Polymetallic mineralisation in the Chillagoe district of north-east Queensland – insights into base metal rich intrusion-related gold systems

Thesis submitted by
Berit Lehrmann (Dipl. Min.)
May 2012

for the degree of Doctor of Philosophy
in the School of Earth & Environmental Sciences
James Cook University

STATEMENT OF ACCESS

I, the undersigned, author of this work, understand that James Cook University will make this thesis available for use within the University Library and, via the Australian Digital Theses network, for us elsewhere.

I understand that, as an unpublished work, a thesis has significant protection under the Copyright Act and, I wish this work to be embargoed until May 31st, 2013.

After which date I do not wish to place any further restriction on access to this work.

All users consulting this thesis will have to sign the following statement "In consulting this thesis I agree not to closely paraphrase it in whole or in part without the written consent of the author; and make proper public written acknowledgement for any assistance that I have obtained from it."

23/05/2012

STATEMENT OF SOURCES
DECLARATION

I declare that this thesis is my own work and has not been submitted in any form for another degree or diploma at any university or other institution of tertiary education. Information derived from the published or unpublished work of others has been acknowledged in the text and a list of references is given.

23/05/2012

ELECTRONIC COPY

I declare that the electronic copy of this thesis provided to the James Cook University Library is an accurate copy of the print thesis submitted, within the limits of the technology available.

23/05/2012

STATEMENT OF CONTRIBUTIONS

Financial contributions included:

- Living stipend and research scholarship from Kagara Ltd & Mungana Goldmines Ltd
- James Cook University Graduate Research School Grant 2009
- James Cook University School of Earth and Environmental Sciences grant 2010

General contributions of others included:

- Prof. T.G. Blenkinsop: supervision throughout the second half of the PhD project and revision of all chapters
- Dr. A.I.S. Kemp: supervision throughout the second half of the project including help in redesigning the project, LA-ICP-MS analysis and revision of some chapter drafts
- Prof. N.H.S. Oliver: supervision throughout the first half of the project, help in designing the project and assistance in the field
- Dr. M.J. Rubenach: supervision throughout the first half of the project and assistance in the field
- Dr. K.L. Blake, Dr. J. Whan, Dr. S. Askew: technical assistance during EMP & CL analysis (chapters 3, 4, 5 and 6) at the Advanced Analytical Centre, James Cook University, Townsville
- Dr. Y. Hu: technical assistance during LA-ICP-MS analysis (chapter 4, 5 and 6) at the Advanced Analytical Centre, James Cook University, Townsville
- Dr. M. Norman: Re-Os isotope analysis (chapter 5) at the Research School of Earth Sciences, Australian National University, Canberra
- Mr Darren Richardson: preparation of all polished thin and thick scetions
- SGS Townsville mineral laboratory assay analysis (chapter 5)

ACKNOWLEDGEMENTS

First I would like to thank Kagara Ltd and Mungana Goldmines Ltd for their financial support, logistic support to and from Chillagoe as well as access to the property, samples and data. I greatly appreciate all the help and support given to me by the geologists, field assistants and other company members from the exploration team, the Townsville office and other persons up in Chillagoe and for sharing their thoughts and knowledge about the deposits and geology. Thanks in particular to Charlie Georgees, Ian Morrison, John Nethery, Robert Henry, Kay Mathews, Rowena Duckworth, and the hard core 'fieldi' crew Kevin, James, Ewen, Macca and Mervin.

I am grateful to Prof. Tom Blenkinsop for redesigning the project and his constructive criticisms, improvements and patience during the revision of all chapter drafts. I also acknowledge Dr. Tony Kemp for redesigning the project, his help during LA-ICP-MS analysis and revision of some chapter drafts. Prof. Nick Oliver and Dr. Mike Rubenach are thanked for their help in getting the project started and providing assistance in the field.

Technical support by Dr. Kevin Blake (EMP, CL), Dr. Yi Hu (LA-ICP-MS), Dr. Jen Whan (EMP, CL), Dr. Shane Askew (EMP, CL) at the AAC-JCU (Townsville) and Re-Os isotope analysis by Dr. Marc Norman (Research School of Earth Sciences, Australian National University, Canberra) is gratefully acknowledged. I also would like to thank Darren Richardson (Ingham Petrographics) for the preparation of thin and thick sections.

Thanks also to everyone else in the SEES & AAC department in particular Glen Connolly, Beth Moore, Judy Botting, Judith Casey for all the help they provided and Clive Grant and Robert Scott for solving numerous computer license and field trip tracker issues.

Finally, I would like to thank the many people far away from home for their constant encouragement, support and patience.

ABSTRACT

The Chillagoe district, located in northeast Queensland, is host to several polymetallic mineral deposits, which comprise three major metallogenic commodities: 1. Cu-Au, 2. Zn-Pb-Cu and 3. Sn-W-Mo. Metals such as W, Mo, Bi, Te, (± As, Sb) vary in concentrations within and between deposits. The deposits occur in a wide range of styles such as porphyries, breccias, skarns, and veins. Previous workers suggested that granites related to four igneous supersuites of the Permo-Carboniferous Kennedy Igneous Province were the source of the diverse metal commodities, whereas the calc-alkaline, metaluminous to weakly peraluminous, I-type, weakly oxidised to reduced, compositionally evolved nature of the oldest supersuite suggests that it alone could be the source for the polymetallic deposits. The mineralisation could be recognised as having affinities to intrusion-related gold deposits (IRG), adding to the increasing number of such systems recognised within the Tasmanides of eastern Australia. Although an IRG system could explain the polymetallic nature of the deposits in general, the economic grade of base metals hosted by deposits of the Chillagoe district is quite unusual for an IRG system.

This thesis investigated three polymetallic deposits (Recap, Mungana and Red Dome) of the Chillagoe district by combining petrographical, electron-microprobe (EMP), laser ablation inductively coupled plasma mass spectrometry (LA-ICP-MS) and radiogenic isotope studies (Re-Os, U-Pb and Lu-Hf) in order to improve the understanding of the metal diversity of IRGs, and provide insights into the processes of magma formation and evolution related to such systems. Petrographical studies showed that skarn formation at all three deposits is very similar and show no differences to the processes in other intrusion-related skarn systems. Mineralisation on the other hand differs regarding their major commodities, with Redcap and Mungana being base metal dominant, but also hosting minor gold mineralisation, whereas Red Dome is dominated by copper mineralisation and also comprises gold mineralisation and a very minor base metal commodity. The difference in the metal commodities and economic grade was caused by the emplacement of two compositionally different magmatic phases. The primary magmatic event (~ 326-320 Ma), characterised by weakly reduced and strongly fractionated rocks, provided the metallogenic diversity typical for an IRG system with some of the metals being incorporated into silicate phases (Sn, Zn) and As-Cu-Sb sulphide minerals (Au). The second magmatic event (more oxidised and less fractionated, ~312-305 Ma) caused remobilisation of metals related to the primary event, as well as adding S and possibly Zn, Cu, Pb to the system at Redcap and Mungana, whereas at Red Dome in addition to the sulphur, Cu and maybe Au was introduced.

Studies of the mineral chemistry showed that composition of garnets and sphalerite have the potential to be used as exploration tool to locate causative intrusions. Due to the complexity of the systems investigated here, the concept should be tested again to establish its use in other multiphase IRG systems.

Trace element concentrations and radiogenic isotope data (Lu-Hf) of zircons on the other hand showed that the diverse metallogeny of the IRG systems can be linked to the most fractionated phase in the magmatic system, with the magma originally being derived from a crustal metasedimentary source (in Chillagoe: ~2.0-2.5 Ga). The great advantage of determining such information from zircons rather than from whole rock data is that the latter can become easily affected by metamorphism, (hydrothermal) alteration and/or weathering, whereas physico-chemically robust zircons preserve their primary information.

TABLE OF CONTENTS

LIST OF TABLES

LIST OF FIGURES

LIST OF PLATES

Chapter 1: Introduction

1.1. General introduction

Granites are related to various metallogenic types (e.g. Cu ± Au, Cu ± Mo, Sn ± W, W ± Mo-Bi & Zn ± Pb-Ag) hosted within a wide range of deposit styles like porphyries, breccias, skarns, stockworks, and veins (Ĉernŷ et al. 2005 and references therein) with granites acting in some cases as metal and fluid source (Blevin & Chappell 1995) and in others as fluid source only, remobilising metals from the wall rocks (Ĉernŷ et al. 2005). Many attempts have been made to establish classification schemes for granite-related mineralisation (Chappell & White 1974; Ishihara 1981; Lehmann 1990; Blevin & Chappell 1992, 1995; Candela 1992; Blevin et al. 1996), but the majority of these schemes are based on whole rock data which can become easily affected by alteration and weathering, so providing misleading results. In addition, all these schemes fail to explain the occurrence of polymetallic mineralisation (Sn-Au-Bi-W-As-Mo-Te-Sb ±Zn, Cu, Pb), which can be found for example in the Tintina Gold Belt of Alaska, Kori Kollo (Bolivia), Jilau (Tajikistan), and eastern Australia (Timbarra and Kidston). This problem is partly addressed by the introduction of a new classification: intrusion-related gold (IRG) deposits (Thompson et al. 1999; Lang et al. 2000; Lang & Baker 2001; Hart 2005, 2007). Although the number of published works on intrusion-related gold deposits increases each year, there is still a lack of detailed deposit descriptions that will help to understand the diversity of polymetallic mineralisation styles. In addition, information about the magma sources is very rare and magmatic evolution processes are not well understood although they are essential to understand the partitioning behaviour of different metals (Lehmann 1990; Candela 1992; Blevin and Chappell 1992; Ĉernŷ et al. 2005).

In this study three polymetallic deposits of the Chillagoe district located in north eastern Queensland were investigated by combining petrographical, mineral chemical, geochronological and radiogenic isotope information with the aim of addressing key questions related to the diversity, formation and discovery of intrusion-related gold systems. In the next sections a review of the major existing classification schemes of granite-related mineralisation styles is provided, the characteristics of IRG systems are outlined and the Chillagoe district is introduced. In addition, the aims of the thesis are presented as well as the methodology to address them is briefly described. The chapter finishes with an outline of the thesis.

1.2. Classification schemes of granite-related metal commodities

Three major classification schemes of granite-related metal commodities exist. They are based on the source (I- and S-type model of Chappell & White 1974), the occurrence of magnetite (magnetite-ilmenite series of Ishihara (1977), redox state (Ishihara 1981; Lehmann 1990; Blevin & Chappell 1992; Candela 1992) or a combination of oxidation state and magma evolution (Blevin & Chappell 1995; Blevin et al. 1996).

In 1974, Chappell & White proposed that granites were either derived from an igneous source (I-type) or from metasedimentary material (S-type), with the I-type being later divided into Andean/Cordilleran and Caledonian subgroups by Pitcher (1982), and two other classes, the M-type (mantle-derived , Whalen et al.1987) and A-type (anorogenic, Loiselle & Wonnes 1979) were introduced. Cordilleran I-types are linked to Cu-Mo ± Au mineralisation, M-types to Cu-Au and S-types to Sn-W ± Mo, and A-type granites are either associated with Be and F or are barren systems like the Caledonian I-types (Fig.1.2.A). One problem with the source classification scheme is that based on compositional and isotopic parameters some granites cannot be clearly classified as S- or I-types (Chappell & White 1992; Ĉernŷ et al. 2005) and that the definition of some A- and I-types overlap, resulting in misclassifications of granites and therefore assigning specific metal suites to the wrong source. Blevin & Chappell (1995) showed that Sn and W mineralisation can be related to S- and I-type granites.

Ishihara (1977) classified granites based on petrographic observation into magnetite bearing (magnetite–series) and magnetite free (ilmenite-series), suggesting that Au, Cu, Pb-Zn and Mo mineralisation are associated with granites of the magnetite series whereas as Sn and W are commonly associated with rocks of the ilmenite-series (Fig. 1.2.B). The dominance of either magnetite or ilmenite is an indicator of the relative oxidation state of the magma, which is supposed to be inherited from the source material and in some places assimilated from the wall rocks (Carmichael 1991; Ĉernŷ et al. 2005) and expressed as the ratio of whole rock Fe_2O_3 versus FeO. The relative oxidation state is a very important control on the partitioning behaviour of metals between melt(s), mineral(s) and fluid(s) (Lehmann 1990; Candela 1992; Blevin and Chappell 1992; Ĉernŷ et al. 2005). While granites of the ilmenite series are reduced and sulphur poor (Burnham & Ohmoto 1980) therefore yielding early sulphur saturation resulting in early magmatic precipitation of sulphides (Ĉernŷ et al. 2005), granites of the magnetite-series retain sulphur in the melt allowing enrichment of metals in the melt which are then available for late exsolution by aqueous fluids (Candela 1992) forming sulphide rich metal deposits.

A)

	Subgroup	Mineralisation
I-type	Cordilleran	Cu-Mo ± Au
	Caledonian	barren
S-type		Sn-W ± Mo
M-type		Cu-Au
A-type		Be,F/barren

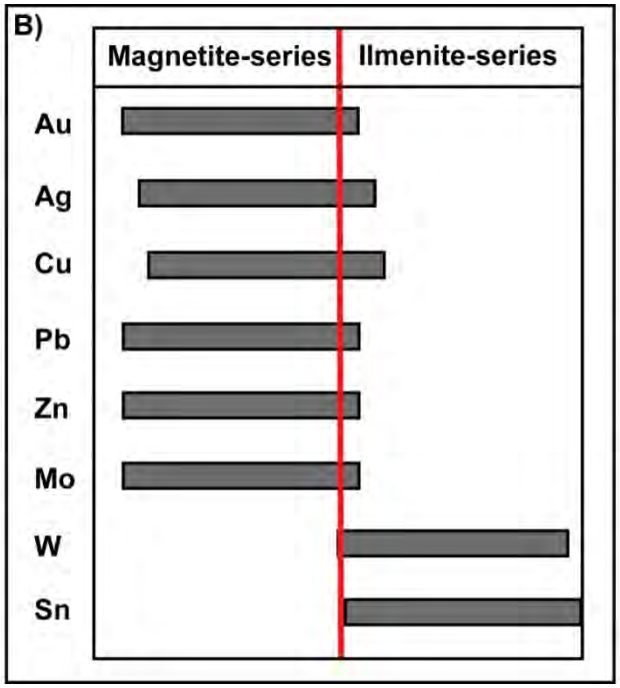

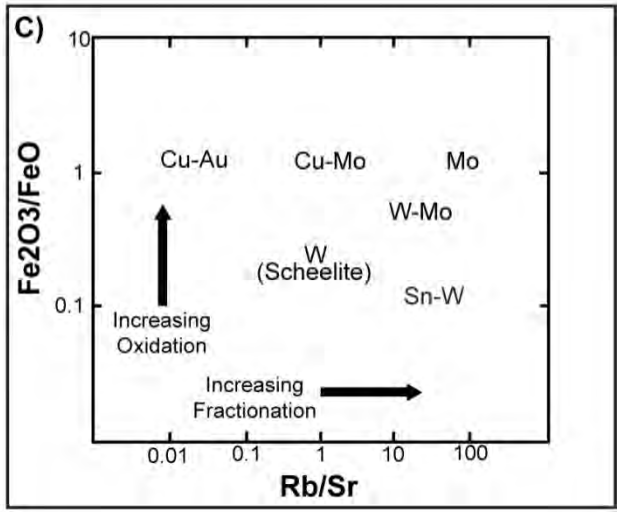

Figure 1.2. Three models for granite-related metal association based on: **A)** their source (Ĉerný et al. 2005), **B)** occurrence of magnetite or ilmenite (modified from Ishihara 1981) and **C)** redox state versus degree of fractional crystallisation (modified from Blevin et al. 1996).

Although the classification scheme of Ishihara is quite good in comparison to the source classification scheme as it includes the relative oxidation state, petrographic and whole rock data can be affected by alteration and weathering providing misleading results. Blevin & Chappell (1992, 1995) emphasised the significance of the oxidation state for metal behaviour, and improved the existing model of Ishihara (1981) by using the degree of fractional crystallisation as a second discrimination parameter resulting in a new classification scheme for the metal potential of granites. The model by Blevin et al. (1996, Fig. 1.2.C) confirmed the link between Cu-Au mineralisation and oxidised, unevolved granites which had been proposed previously by other authors like Burnham & Ohmoto (1980), Ishihara (1981), Candela (1992) and Seedorff et al. (2005). Blevin et al.'s model also confirmed the relationship between Sn-W and reduced, fractionated granites, as suggested by e.g. Lehmann (1990) and Blevin & Chappell (1992). In addition to the established links between Cu-Au and Sn-W mineralisation and specific granite type, Blevin et al. (1996) also made the associations between specific granite types and W-Mo, W and Mo mineralisation, for example with W-Mo mineralisation being related to relative oxidised and fractionated rocks compared to Cu-Au mineralisation. The model of Blevin et al. (1996) helped to improve the understanding of metallogenic relationships and granites. It especially highlighted that the magma source alone is not responsible for the diverse metal styles associated with granites but that other factors like the magmatic composition and evolution play an important role. One problem with the model is that whole rock data were used for discrimination of different granites and their metals, which can provide erroneous results due to alteration. Another issue is that this model, as well as the other two models of Champion & Chappell (1992) and Ishihara (1981), fail to provide an explanation of how polymetallic mineralisation with the contradictory metal association of Sn and Cu-Au mineralisation can be linked to one granitic intrusion as can be observed in Alaska and parts of the Tasmanides of eastern Australia (Fig. 1.3.).

1.3. Polymetallic mineralisation explained by an intrusion-related gold deposit model?

The occurrence of polymetallic mineral deposits with a diverse metallogeny of Au-Bi-W-As-Mo-Te-Sb associated with Sn (W) provinces and wide-ranging grades of base metals has first been described in the Tintina Gold Belt of Alaska by Sillitoe (1991), Newberry et al. (1995), Lang et al. (1997), and McCoy et al. (1997). While existing classification schemes could not explain the diversity of mineral commodities (see previous section), a new deposit style model (intrusion-related gold (IRG) deposit) was introduced which summarises the typical characteristics for these polymetallic deposits (Blevin et al. 1996; Thompson et al. 1999; Lang & Baker 2001; Mustard 2001; Blevin 2004; Bierlein & McKnight 2005; Champion 2005; Hart

2005, 2007). IRGs are also characterised by showing vertical and/or lateral metal zoning within a single deposit (Thompson et al. 1999; Lang & Baker 2001; Blevin 2004; Hart 2005) with some of the mineralisation being located more than 3 km away from the causative intrusion. In addition the mineralisation is hosted in a variety of deposit styles ranging from veins, breccias, skarn and dissemination within intrusive body and country rocks.

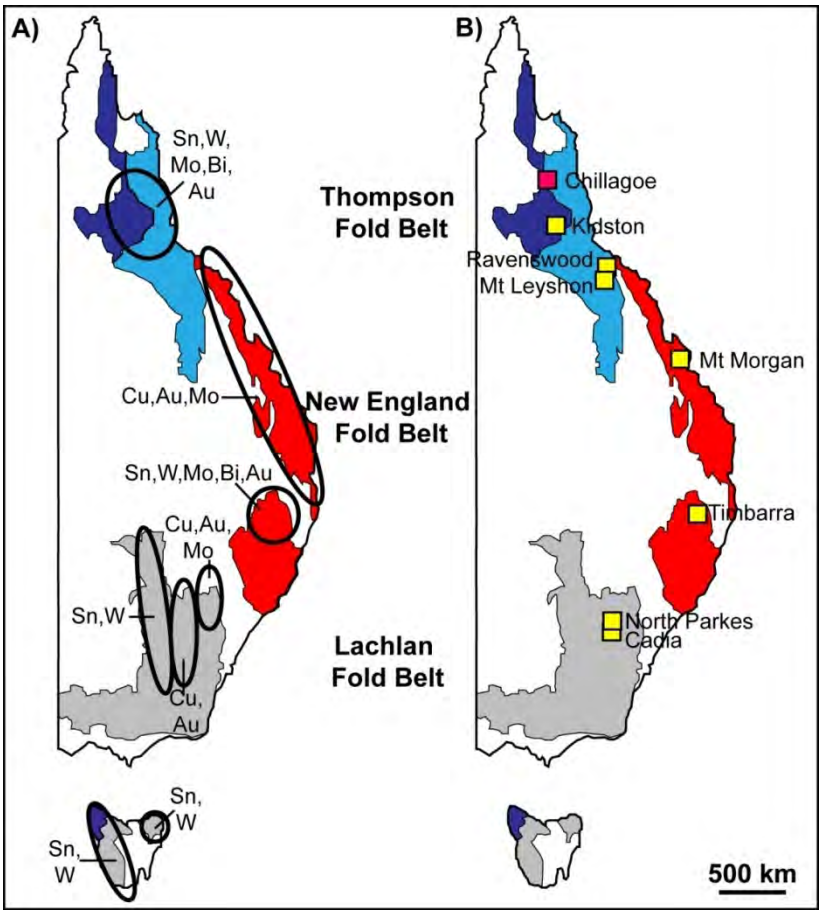

Figure 1.3. Distribution of granite-related Au, Cu, Sn, Mo and W deposits within the Thomson, New England and Lachlan Fold Belt of the Tasmanides of Eastern Australia (**A**) and occurrence of porphyry Cu-Au, Cu-Mo and possible intrusion-related gold deposits within the Tasmanides (**B**); modified from Blevin (2004) and Champion & Blevin (2005).

In general IRGs are related to calc-alkaline, metaluminous to weakly peraluminous, I-types, weakly oxidised to reduced, compositionally evolved granites which show a wide range in composition with SiO_2 ranging from ~ 60 to 75 wt.-% for example (Thompson et al. 1999; Lang & Baker 2001; Blevin 2004; Baker et al. 2005 & Champion 2005). Other characteristics known for IRGs are multiphase igneous complexes (Coulson et al. 2001), in some places associated coeval volcanics (Lang & Baker 2001), and an almost synchronous timing of magmatic and hydrothermal activity (Baker et al. 2005), with very limited isotope data (εND) indicating that the magma was derived from continental crust (Lang et al. 2000), although the influence of a juvenile magma source, as for Kori Kollo, can not be excluded (Lang & Baker 2001). In

addition, calciferous, graphitic or basaltic country rocks as well as structures seem to be an important component of IRGs (Lang & Baker 2001; Champion 2005).

The increasing number of studies in the last years has helped to improve the definition of IRGs. However, due to nomenclature uncertainties and definition overlap with other magmatic-hydrothermal systems like Au-rich copper porphyries, orogenic gold deposits and Au-skarns, exploration strategies are ineffective (Hart 2005). Many aspects of IRGs are still not well understood, such as the diversity of polymetallic mineralisation styles, information about the magma sources and evolution processes including the timing of granite emplacement, metal formation and alteration events. In addition there is a need to identify pathfinder elements which can be used to locate a specific type of mineralisation or the causative intrusion, which is especially important in terrains where granites are buried and deposits are of superimposed nature.

1.4. Polymetallic deposits of the Chillagoe district

To address the above problems this thesis investigates three polymetallic deposits (Recap, Mungana and Red Dome) occurring in the Chillagoe district of north east Queensland (Fig.1.3.B) which show many characteristics typical for IRGs. Amongst them are for example their association with four granitic supersuites of the Permo-Carboniferous Kennedy Igneous Province which are discriminated, based on whole rock data into calk-alkaline, metaluminous to peraluminous types (Fig. 1.4.A), moderate reduced to oxidised (Fig. 1.4.B.), strongly evolved (Fig. 1.4.C) and highly to moderately fractionated (Fig. 1.4.D) rocks. The source of these igneous rocks is either 2.0 to 2.5 Ga metasedimentary crust (whole rock εNd data, Black & McCulloch 1990), a mixture of a felsic and basaltic magma (whole rock Rb-Sr data, Black & Richards 1972a) or parts of old crust assimilated by a juvenile magma as proposed by Champion & Chappell (whole rock εNd data, 1992).Other factors which suggest an IRG origin are the occurrence of many structures with up to 7 deformation events being recognised in the area (e.g. Bell 1980; Vos et al. 2006a) and the abundance of calciferous and basaltic rocks of the Siluro-Devonian Chillagoe Formation (e.g. De Keyser & Wolff 1964; Vos et al. 2006b).

The mineral deposits are all of polymetallic nature with three types being the major commodities: 1. Cu-Au, 2. Zn-Pb-Cu and 3. Sn-W-Mo (e.g. Gregory et al. 1980, Morrison & Beams 1995) with W, Mo, Bi, Te, (± As, Sb) concentrations varying within and between deposits. The majority of metals are related to the oldest granitic supersuite (Tab. 1.4.) as proposed by De Keyser & Wolff (1964); Branch (1966); Sheraton & Labonne (1978) and Georgees & Nethery (1999).

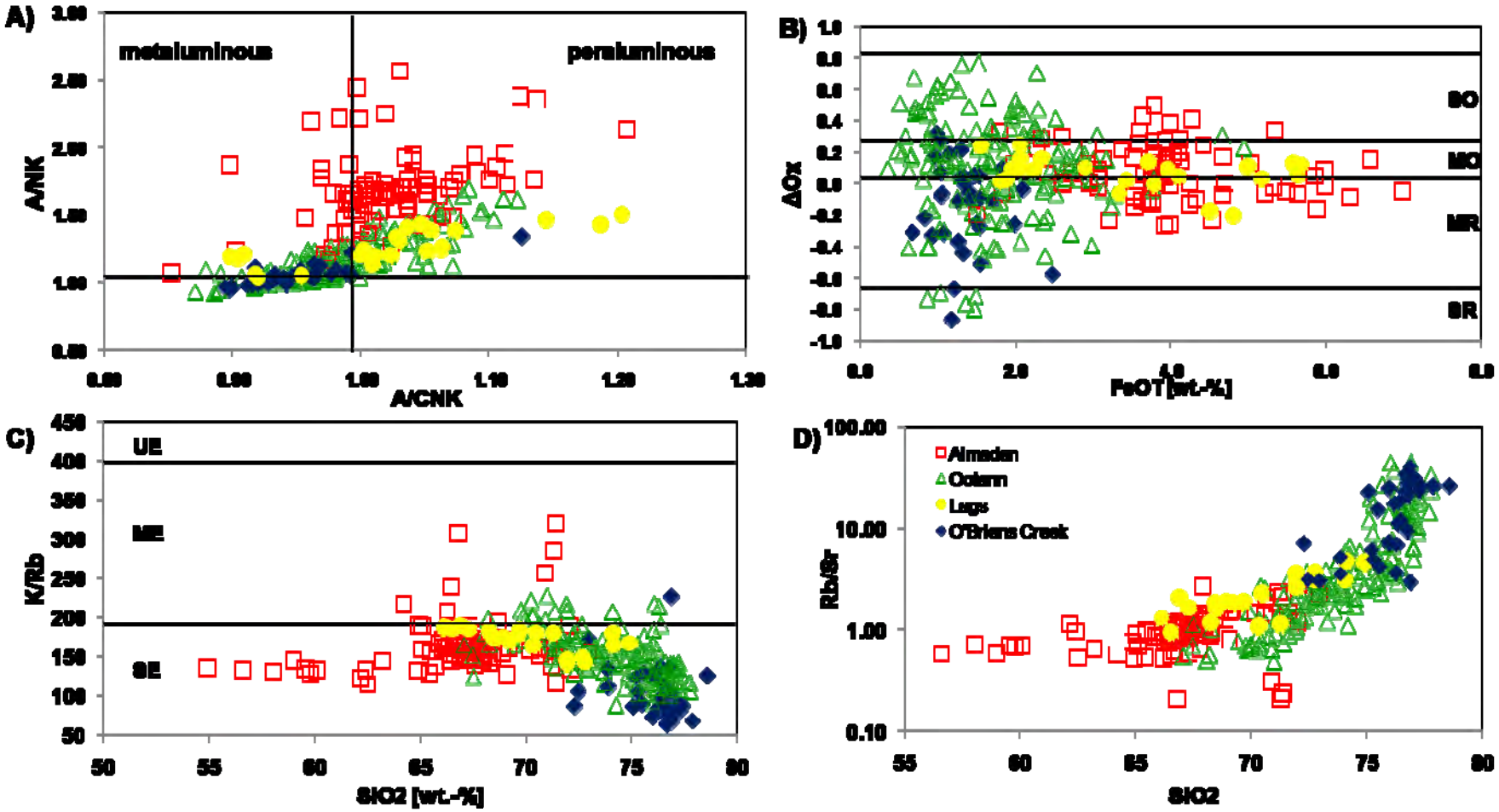

Figure 1.4. Geochemical characteristics of four Permo-Carboniferous Supersuites of the Kennedy Igneous Province; **A**) discrimination diagram of Shand (1943); **B**) relative oxidation state after Blevin (2004) with FeOT being total iron, $\Delta Ox = \log(Fe_2O_3/FeO) + 0.3 + 0.03 \times FeOT$, and SR: strongly reduced, MR: moderate reduced, MO: moderate oxidised, SO: strongly oxidised; **C**) degree of evolvement after Blevin (2004) with SE: strongly evolved, ME: moderate evolved and UE: unevolved; **D**) degree of fractionation expressed as Rb/Sr ratio; whole rock data were taken from OZCHEM (2008).

The deposit styles are also diverse and may encompass porphyry related skarn, breccia or stockwork for Cu-Au mineralisation (Torrey et al. 1986; Ewers et al. 1990; Morrison & Beams 1995; Nethery & Barr 1998; Creighton 2005; Georgees 2007a; Hodkinson et al. 2009), Besshi type VMS and porphyry related skarn for base metal mineralisation (Woodbury 1994; Morrison & Beams 1995; Nethery & Barr 1998) and sediment or granite-hosted Sn-W-Mo mineralisation (Morrison & Beams 1995 and references therein).

Table 1.4. Summary of metal potential of single supersuites for the Chillagoe district

Supersuite	**Geochemical characteristics**				**Mean age**	**associated mineralisation ***
O'Brien's Creek	I-type	felsic	reduced	fractionated	315 Ma	Sn,W,Mo,F,Cu,Au,Ag,Pb, Zn,Bi,Sb
Almaden	I-type	± felsic	oxidised	unfractionated	300 Ma	Cu,Pb,Zn,Ag
Ootann	I-type	felsic	reduced	fractionated	300 Ma	W,Mo,Bi
Lags	A-type	felsic	reduced-oxidised	unfractionated	280 Ma	U,F,Au

* compiled from De Keyser & Wolff (1964); Branch (1966); Sheraton & Labonne (1978), Georgees & Nethery (1999)

The reasons for studying the Redcap, Mungana and Red Dome deposits of the Chillagoe district are that they show different mineral commodities and vary regarding grade although they are located within ~3 km of each other. Investigations will help to better understand the diversity of metal styles and zonation patterns in the district as well as for IRGs in general. In addition, at all deposits more than one igneous body was emplaced resulting in several cycles of overprinting and remobilisation (Georgees 2007a), obliterating the link between granite type and mineralisation, and heavy alteration (Garrad & Bultitude 1999). The use of whole rock geochemistry and isotope studies is thus nearly impossible and other discrimination tools are needed, which are not based on whole rock data and are more resistant to alteration and weathering. Additionally, the majority of igneous bodies are buried (Mungana & Red Dome) or not discovered yet (Redcap) making it hard to locate the causative igneous body and target a specific mineral commodity, creating the need to identify pathfinder elements or minerals which can be used as exploration tools.

1.5. Aims and methodology

The thesis aims are to:

- provide detailed descriptions of polymetallic mineralisation styles occurring in the Chillagoe district which will help to improve the understanding of the metal diversity of

IRGs;

- identify chemically differences of sulphide and silicate phases which can be used as exploration tools to either locate mineralisation or causative intrusions of IRGs;

- determine the absolute timing of mineralisation and emplacement of igneous suites which will help to better understand whether IRG systems are short or long lived magmatic and hydrothermal systems;

- gain information about the magmatic evolution and magma sources which are responsible for the diverse metallogenic potential of IRGs

The results are not only useful for exploration in the Chillagoe district, but also provide valuable information for IRG systems elsewhere.

To achieve these aims a combination of petrographical, electron-microprobe (EMP), laser ablation inductively coupled plasma mass spectrometry (LA-ICP-MS) and radiogenic isotope studies (Re-Os, U-Pb and Lu-Hf) were used to develop a paragenetic sequence for each mineral deposit, determine the mineral chemistry of possible pathfinder minerals (garnet, sphalerite and gold), reveal the timing of igneous emplacements (U-Pb of zircon) and mineral formation (Re-Os of molybdenite) and resolve magma composition, formation processes and source material (trace elements & Lu-Hf of zircon).

Using mineral chemistry as an exploration tool is a relatively old method and commonly applied to garnets in skarn systems (Atkinson & Einaudi 1978; Meinert 1987 & 1992; Jamtveit et al. 1993; Nicolescu et al. 1998; Gaspar et al. 2008), but no studies have been conducted on garnets in IRGs to test whether proposed theories can be applied here as well. Microanalytical investigations of sphalerite by LA-ICP-MS on the other hand are rare with only the work of Cook et al. (2009) providing some information about trace element behaviour of sphalerites in different deposit styles, but, as for the silicate phases, no data for IRGs exist.

The second ore phase investigated in this study was gold, but due to the small nature of the grains the analyses were conducted by EMP. In the past the gold fineness was commonly used as a discrimination tool (Morrison et al. 1991), but recent studies have shown that Ag can become easily depleted (e.g. Hough et al. 2007) as it is more soluble and volatile than gold (Hough et al. 2009). Therefore a different approach was taken, using the Cu content of gold to

characterise the gold of IRG deposits and identify whether different gold compositions can represent different ore grades and if so whether they are related to specific elements like Bi, Te, or Sb which then can be used as pathfinders to locate the gold mineralisation.

To understand the magmatic evolution processes necessary for the formation of IRGs and gain information about the source, trace elements and radiogenic isotope data were collected by LA-ICP-MS and LA-MC-ICP-MS. on zircons. This approach is not known to have been conducted on IRG systems before. While whole rock data can easily become affected by alteration and weathering providing misleading results, zircon has a very high physico-chemical robustness, with work of Murgulov et al. (2008) and Fu et al. (2009) establishing that it can even survive hydrothermal alteration retaining its isotopic compositions at the time of crystallisation. Therefore information on the magmatic differentiation processes expressed as Zr/Hf, Hf/Y and Th/U ratios (e.g. Heaman et al. 1990; Linnen & Keppler 2002; Hoskin & Schaltegger 2003; Claiborne et al. 2006; Bolhar et al. 2008) and degree of oxidation state presented by the Eu and Ce anomalies (Hoskin & Schaltegger 2003) are preserved. The ratio of Ce^{4+}/Ce^{3+} may be useful as exploration tool helping to discriminate between barren and Cu-mineralised porphyry bodies as proposed by Ballard et al. (2002). Whether this can be used in IRG systems will be investigated in this study.

Lu-Hf-isotope studies are useful to track crustal and mantle evolution processes as well as to identify the source from which the zircon originated (Patchett et al. 1981; Vervoort et al. 1996; Blichert-Toft & Albarède 1997; Amelin et al. 1999; Kinny & Maas 2003; Hawkesworth & Kemp 2006; Kemp et al. 2007; Scherer et al. 2007). Especially the nature of the magmatic source will help to give a better understanding whether the diverse metal styles of IRGs originated from old crustal material with the metals being concentrated due to magmatic evolvement as proposed for IRGs of the Tintina Gold Belt, or whether at least some metal commodities were added by the input of juvenile magma as suggested for Kori Kollo (Lang & Baker 2001).

1.6. Thesis outline

The thesis consists of 7 chapters with the outline of the thesis and the content of each chapter presented below.

Chapter 1: Introduction

This chapter provides a general introduction to the mineral deposit styles occurring in the Chillagoe district and puts their occurrence in a broader context. The aims of this thesis are presented and the structure of thesis is outlined.

Chapter 2: Regional and local geology of the Chillagoe district

Chapter 2 describes the regional geology of the Chillagoe district and provides a summary of previous work conducted in the district. The Redcap, Mungana and Red Dome deposits are introduced.

Chapter 3: Petrography and paragenesis of the Redcap, Mungana and Red Dome deposits

In this chapter the petrography of igneous rocks, skarns and mineralisation types of the Redcap, Mungana and Red Dome deposit are presented and a paragenetic sequence chart for each deposit is provided and discussed.

Chapter 4: Mineral chemistry of garnets, clinopyroxenes, sphalerite and gold from Redcap, Mungana and Red Dome

This chapter provides information regarding the potential of silicate phases as an exploration tool, and investigates compositions of zinc and gold phases to identify deposit style and timing.

Chapter 5: Geochronology of igneous rocks and mineralisation from Redcap, Mungana and Red Dome

Chapter 5 presents U-Pb isotope studies of zircons and Re-Os isotopes studies of molybdenite to identify the timing of igneous rock emplacement, skarn formation and timing of the mineralisation. In addition Re-Os concentrations of molybdenite are used to discriminate between different deposit styles.

Chapter 6: Trace element chemistry, Ti-in-zircon thermometry and Hf isotope studies of zircons from the Redcap, Mungana and Red Dome deposits

In this chapter trace element and Hf isotope data of zircons are presented and the source of the igneous rocks, possible link to mineralisation and possible genetic relationships between the different igneous suits are established.

Chapter 7: Summary and discussion

This chapter summarises and discusses the major findings of the study and outlines possible future work.

Chapter 2: Regional and local geology of the Chillagoe district

2.1. Introduction

The Chillagoe district, located 210 km west of Cairns, is situated within the Middle Palaeozoic Hodgkinson Province which is the northernmost part of the Tasmanides in eastern Australia. While first descriptions of the area in general focused on single prospects or groups (Jack 1891; Skertchly 1897, 1899; Jensen 1923, 1940, 1941; Broadhurst 1952, 1953) mapping projects in the 1950's and 1960's conducted by the Bureau of Mineral Resources (BMR) and the Geological Survey of Queensland (GSQ) concentrated more on the regional geological framework of the area (e.g. Best 1962; De Keyser & Wolff 1964; De Keyser & Lucas 1968).

Since then, more studies were carried out in the district with different aims. The GSQ and BMR kept the focus on the regional geology, especially revision of existing stratigraphic units, as well as the occurrence of mineral deposits (Day et al. 1983; Ishaq et al. 1987; Bultitude et al. 1993a & b; Donschak & Bultitude 1994; Bultitude et al. 1997; Garrad & Bultitude 1999) and other authors focused on more specific topics like single stratigraphic units or rocks within these groups and their origin (Arnold & Fawckner 1980; Fawckner 1981; Green et al. 1988; Webb et al. 1989; Bernecker & Webb 1990; Fordham 1990; Green 1990; Vos et al. 2006b), the structural history of the area (De Keyser 1963; Bell 1980; Shaw et al. 1987; Vos et al. 2006a, 2007) or igneous units including their timing and possible link to mineralisation (Branch 1961, 1966; Richards et al. 1966; Black 1968; Black & Richards 1972 a & b; Sheraton & Black 1973; Bailey 1977; Sheraton & Labonne 1978; Richards 1980; Mackenzie 1987, 1988; Champion 1991; Champion & Chappell 1992; Mackenzie & Champion 1994; Perkins & Kennedy 1998; Georgees & Nethery 1999; Champion 2005).

Only a limited amount of research has been carried out on single deposits in the Chillagoe district e.g. Red Dome (Smith 1985; Torrey 1986; Torrey et al. 1986; Ewers & Sun 1988a & b; Ewers et al. 1990; Woodbury 1994; Holland 1994; Nethery & Barr 1998; Creighton 2005), Mungana (Halfpenny 1991; Woodbury 1994; Nethery & Barr 1996; Barr 1998; Georgees 2007a & b; Hodkinson et al. 2009; Rubenach 2010) and Redcap (Paverd 1971, 1981; Musumeci 1974; Rubenach & Cuff 1985; Rubenach & Cartwright 1994).

In this chapter three lithological and structurally distinct provinces in the Chillagoe district will be introduced. These are the Georgetown Province, Hodgkinson Province and Kennedy Igneous Province (Fig. 2.1.). Furthermore a brief outline of the geological evolution as well as the

exploration history of the district will be provided and finally the Redcap, Red Dome and Mungana prospects will be introduced.

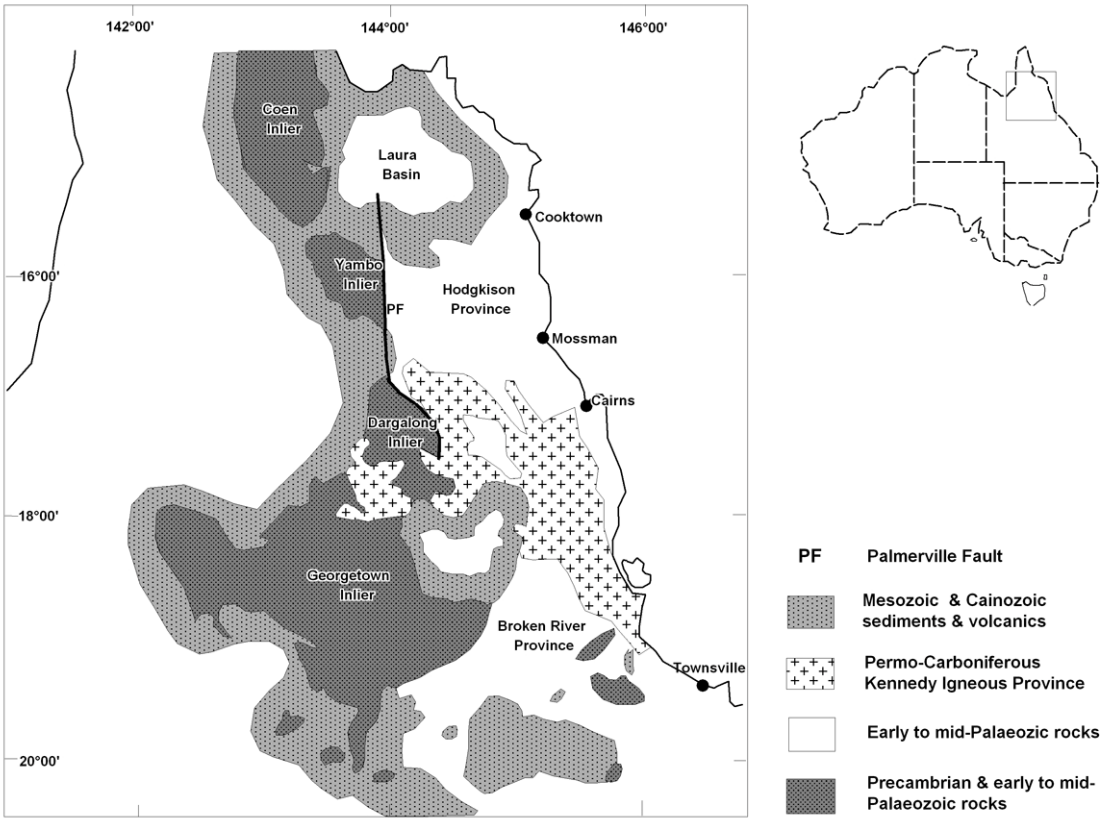

Figure 2.1. Major stratigraphical units in north-east Queensland (modified from Shaw et al. 1987).

2.2. Georgetown Province

The Georgetown Province is separated to the east by the Palmerville Fault from the Hodgkinson Province and is part of the Precambrian basement. The Precambrian rocks are gneisses, schists, amphiboles, quartzite and minor migmatites, and crop out in several inliers, with the one in the Chillagoe district being the Dargalong Inlier. Although very little is known of the depositional environments of the former sediments, it is assumed that the deposition of those sediments took place between 1640Ma and 1580 Ma (Withnall et al. 1997b). At around 1580 Ma emplacement of granites of S-type composition occurred and at around 1575 Ma the whole area was affected by regional metamorphism to up to granulite facies.

Locally the Dargalong Metamorphics are intruded by Silurian Nundah Granodiorite which is part of the Blackman Gap Supersuite. The unfractionated, oxidised, I-type granodiorite was dated by the GSQ and yielded an SHRIMP age of 434 +/- 10 Ma (Donchak & Bultitude 1994).

2.3. Hodgkinson Province

2.3.1. Introduction

The Hodgkinson Province is separated in the west from the Proterozoic Georgetown Province by the Palmerville Fault and in the south from the coeval Broken River Province by the Carboniferous-Permian Kennedy Igneous Province (Fig. 2.1.). To the north the province is overlain by Mesozoic sediments of the Laura Basin and its eastern boundary remains unknown. In the Chillagoe area the Hodgkinson Province is represented by siliciclastic, volcanic and calciferous rocks of four formations which are from west to east: Quadroy Conglomerate, Mulgrave Formation, Chillagoe Formation and Hodgkinson Formation (Fig. 2.3.1.). Although the rocks of the four stratigraphic units were affected by regional metamorphism to lower greenshist facies (Fordham 1990; Vos et al. 2006b), the pre-fix 'meta' is omitted for briefness in this chapter as well as in the remaining part of this thesis.

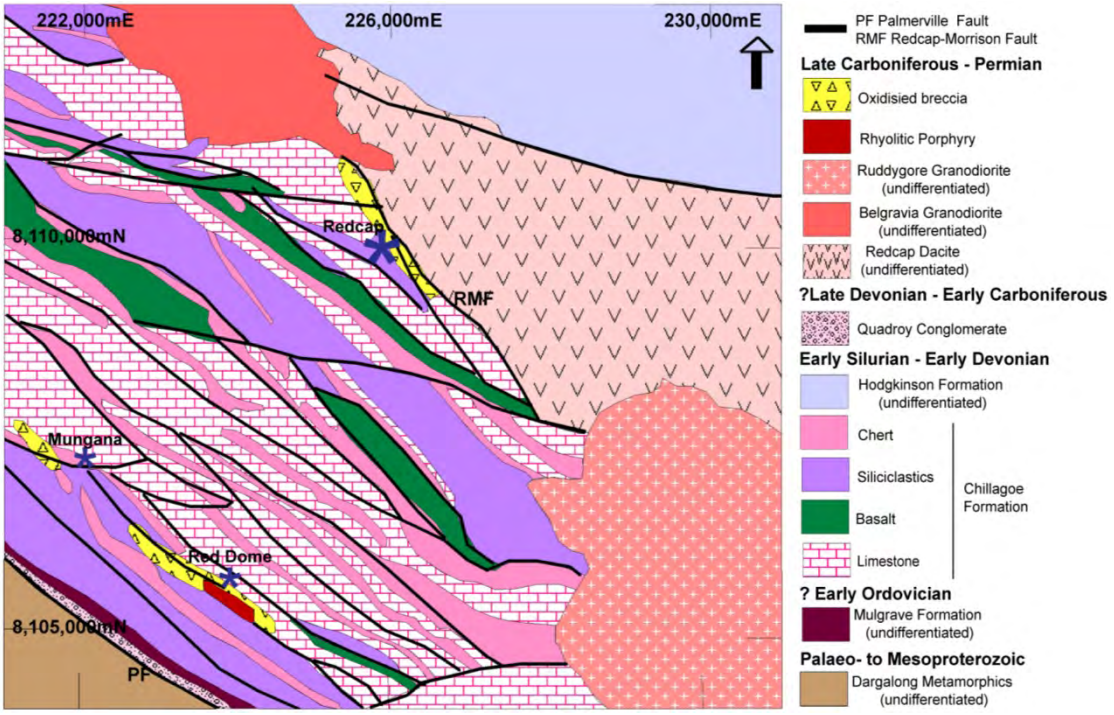

Figure 2.3.1. Map extract of the Chillagoe district showing the different stratigraphic units of the area; modified from Department of Natural Resources and Mines, Queensland, 2003.

The Hodgkinson Province has been intensively studied, but still much information like thickness and boundaries of individual units, depositional environment as well as the exact timing of the sedimentation remain uncertain. Intensive folding and faulting have disrupted single stratigraphic units internally or caused repetition of sequences, while other units only occur in fault-lenses lacking undisturbed contacts to other units. Additionally, many rocks (e.g. siliciclastics of Mulgrave Formation, Hodgkinson Formation and Quadroy Conglomerate) do

not contain any micro- and macrofauna which could be used for biostratigraphy. Therefore it is difficult to get reliable age control of the different units. Only for rocks of the Chillagoe Formation, which is the major host of mineral deposits in the district, has biostratigraphy been applied successfully (Fordham 1990).

2.3.2. Mulgrave Formation

The Mulgrave Formation was first identified by Fawckner (1981) and is bounded to the west by the Palmerville Fault or is unconformably overlain by the Quadroy Conglomerate (Fig. 2.3.1.). Further north (outside the Chillagoe district) Mountain Creek Conglomerate and Van Dyke Litharenite are faulted against or unconformably overlay the Mulgrave Formation. The Mulgrave Formation comprises of quartz-arenite with minor interbedded basalt, chert, siltstone, (haematitic) mudstone and jasper.

Originally Fawckner (1981) claimed that the Mulgrave Formation is younger than the Chillagoe Formation, but this has been revised by Bultitude et al. (1993b) who propose that it is of Ordovician age, because the Ordovician Mountain Creek Conglomerate (age confirmed by conodont fauna and SHRIMP U-Pb age of zircons from clasts) contains clasts which have been derived from the Mulgrave Formation. Additionally, the Mulgrave Formation correlates lithologically well with the Ordovician Judea Formation of the Broken River Province (Withnall et al. 1997a).

2.3.3. Chillagoe Formation

This unit has been first described by Jack and Etheridge (1892) and in more detail by De Keyser & Wolff (1964) and De Keyser & Lucas (1968). It consist of limestone, chert, basalt and various siliciclastic rocks like mudstone, siltstone, greywacke, sandstone and conglomerate with each rock type showing locally strong variations in its abundance (Garrad & Bultitude 1999). Based on biostratigraphic observation by Fordham (1990) the Chillagoe Formation can be divided into a lower, middle and upper part (Fig. 2.3.3.).

The lower part consists of fine grained limestone which is intercalated with thin chert beds. Dominant fossils are brachiopods, bryozoans, ostracods and conodonts in the limestone while in the chert radiolarians occur (Fordham 1990). The upper part of the lower Chillagoe Formation consists of basalts, which partly show pillow textures (De Keyser & Wolff 1964). The basalts were investigated in detail by Holland (1994) and Vos et al. (2006b) with the latter claiming that the basalts of the Chillagoe Formation were derived from an evolved magmatic arc while basalts of the younger Hodgkinson Formation developed from a depleted mantle source.

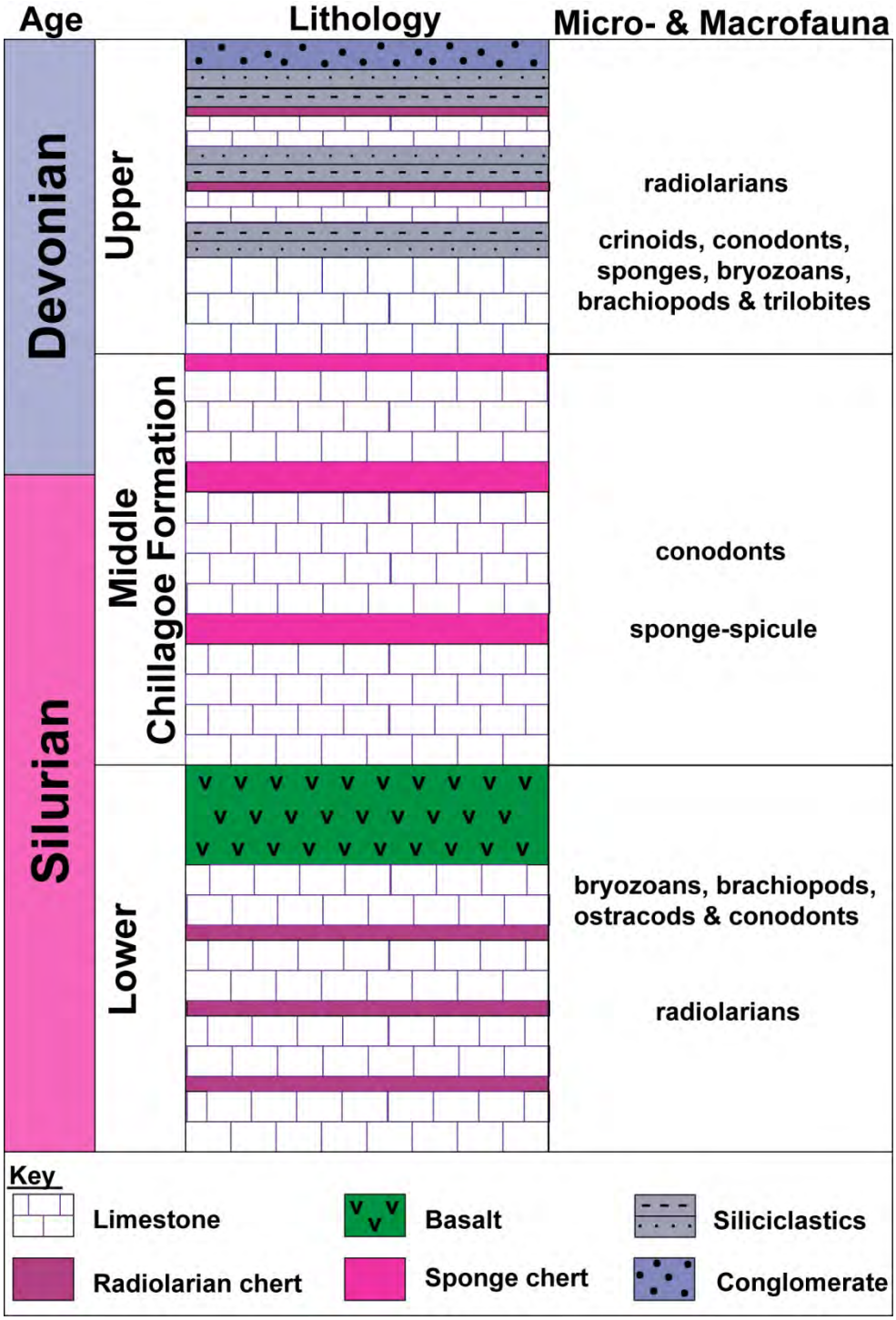

Figure 2.3.3. Stratigraphic profile of the Chillagoe Formation created from data of Fordham (1990).

The middle part of the Chillagoe Formation is dominated by massive limestone (mud- and wackestone) and layers of chert. Comparing to the chert from the lower Chillagoe Formation the chert of the middle part contains sponge spicules and is finely laminated (Fordham 1990). This agrees well with observations made by Broadhurst (1952), who also identified two different

chert types in the formation. In general the middle part is poorer in fossil abundance as well as variety than the lower and upper part of the Chillagoe Formation, with conodonts being the main microfauna (Fordham 1990).

The upper Chillagoe Formation consists of crinoidal dominated packstone and thin layers of radiolarian rich chert, which decrease in abundance towards the top of the unit and give way to greywacke, sandstone and conglomerate with boulder sized clasts. The disappearance of the limestone and the occurrence of the conglomerate are the characteristic features to identify the contact to the overlaying Devonian Hodgkinson Formation. Micro- and macrofauna like conodonts, sponges, bryozoans and trilobites can be found within the limestone beds (Fordham 1990). While all rocks of the Chillagoe Formation were deposited in the marine environment, carbonates and chert were deposited in shallower water levels than the siliciclastic rocks (Garrad & Bultitude 1999), but the geological formation history has been subject to intensive discussions.

Early workers believed that the different lithologies were deposited on a shallow shelf in a marine environment (e.g. De Keyser & Wolff 1964; De Keyser & Lucas 1968), while others postulated that the limestone units are allochthonous blocks, which had broken off shallow water shelves and were deposited into deeper water (e.g. Green et al. 1988, Green 1990). This hypothesis was denied by e.g. Webb et al. (1989) and Bultitude et al. (1993b) who claimed that the limestones were deposited in-situ because of the mud dominated limestones and fossil fauna, both indicating a slow deposition and stable environment. Based on this, it is assumed that the lower and middle parts of the Chillagoe Formation were deposited on isolated mounts and ramps on the margin of a volcanic platform, while the siliciclastics of the upper Chillagoe Formation are flysch which have been deposited in turbiditic currents (Garrad & Bultitude 1999).

2.3.4. Hodgkinson Formation

The Hodgkinson Province conformably overlies the Chillagoe Formation and in earlier works it was called Mount Garnet Formation (De Keyser & Wolff 1964), but later the name was revised and nowadays the Hodgkinson Formation is subdivided into Kitoba Member, OK Member, Larramore Metabasalt and undifferentiated Hodgkinson Formation, with only the Kitoba Member occurring in the Chillagoe district. The Kitoba Member consists of various siliciclastic rocks with sandstone and greywacke being the dominant rock type, with only minor basalt and very rare limestone. Except the basalts, which have evolved from a depleted mantle source (Vos et al. 2006b) during rifting, the siliciclastics represent deposits of turbidity currents like the sedimentary rocks from the older Chillagoe Formation (Garrad & Bultitude 1999). Although the

rocks of the Kitoba Member are poor in fossils, very rarely conodont fauna indicate an early Devonian age for the subunit. In the Chillagoe district no mineralisation is hosted in rocks of the Hodgkinson Formation, but further east (Herberton district, Fig. 2.6), Sn-W-Mo mineralisation occurs within this stratigraphic unit (Garrad & Bultitude 1999).

2.3.5. Quadroy Conglomerate

This unit builds discontinuous lenses adjacent to the Palmerville Fault and was first identified by Fawckner (1981). It consists of siliciclastic rock (mainly conglomerate) which are immature, do not show any sedimentary structures (Garrad & Bultitude 1999) and with the majority of material being derived from rocks of the Dargalong Inlier, although some boulders were originated from Devonian limestone. Therefore it is assumed that the Quadroy Conglomerate is of late Devonian to early Carboniferous age, and, based on its immature composition, may have been deposited in a non-marine fan environment (Garrad & Bultitude 1999).

2.4. Kennedy Igneous Province

2.4.1. Introduction

The third major unit in the Chillagoe district is the Kennedy Igneous Province, which was first introduced by Bultitude et al. (1997) and replaces earlier terms used for Permo-Carboniferous plutonic and volcanic rocks like Coastal Range Igneous Province (Stephenson & Griffin 1976) or the North Queensland Volcanic and Plutonic Province (Day et al. 1983). Single granitic intrusions are nowadays divided into five supersuites (Fig. 2.4.1.) based on geochemical composition with four of them (O'Brien's Creek S., Almaden S., Ootann S., Claret Creek S.) introduced by Champion (1991) and Champion & Chappell (1992) and the fifth one (Lags S.) introduced by Mackenzie et al. (1992). The volcanic rocks are not divided into groups.

In this section old granite classifications from authors prior to the study of Champion (1991) and Mackenzie et al. (1992) will be outlined as well as the new plutonic supersuite classification, as only together can they provide an overview of the mineralisation model of the greater Chillagoe district. Volcanic rocks will not be described in this section, but where relevant briefly outlined in the descriptions of single deposits (e.g. Redcap Dacite at the Redcap deposit, see section 2.7.2.).

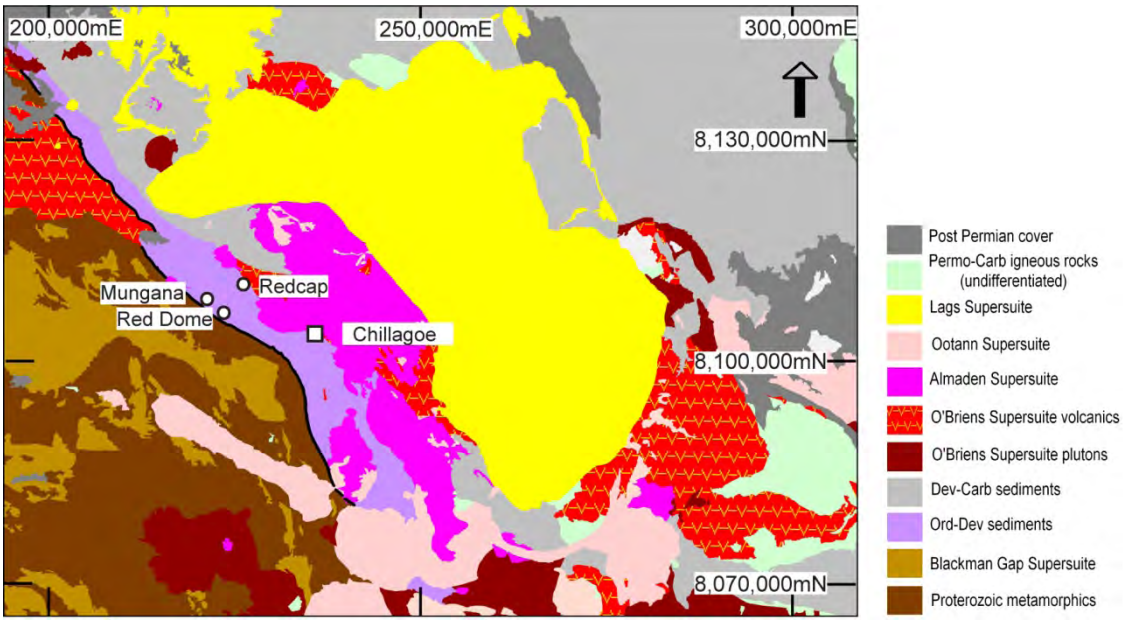

Figure 2.4.1. Plutonic and volcanic rocks of the Kennedy Igneous Province and the distribution of single plutonic supersuites in the greater Chillagoe district; modified from Department of Mines and Energy, Queensland, 1997.

2.4.2. Old granite classification

Within the old granite classification by Branch (1961) and Best (1962) the granites of the greater Chillagoe area were summarised into two geochemically and geochronologically distinctive groups: 1. Elisabeth Creek Granite and 2. Herberton River Granite, while De Keyser & Wolff (1964) divided the occurring granites into 6 units and Black into 10. Based on the controversial grouping, there has been even a greater debate on the origin and associated mineralisation of the granites.

Branch (1961) believed that the biotite leucogranites from the Elisabeth Creek Group and the hornblende-biotite quartzmonzonite and granodiorites of the Herberton River Group were co-magmatic but of different origin, assuming a lower crust or upper mantle source for granites of the Elisabeth Creek Group and an anatectic magma source for the other group (Branch 1966), while De Keyser & Wolff (1964) suggested that all granitic groups were derived from a single batholith. Additionally, Branch (1966) suggested the granites of the Almaden Group, which is a sub-group of the Herberton River Group were formed through assimilation of carbonates of the Chillagoe Formation and igneous rocks of the Herberton River Group, but this theory was rejected by De Keyser & Wolff (1964) and revised by Branch who then suggested that plutonic rocks of the Almaden Group had developed through magma mixing of basaltic magma and the source material of the Herberton River Group.

De Keyser & Wolff (1964) associated base metal and precious metal ore with granites, which belong to the Herberton River Group based on the classification of Branch (tab. 2.4.2). Branch (1966) and Sheraton & Labonne (1978) also linked base metal mineralisation to igneous rocks of the Herberton River Group.

Table 2.4.2. Old granite classification and associated mineralisation

Group	Rock type	Mineralisation		
		De Keyser & Wolff (1964)	Branch (1966)	Sheraton & Labonne (1978)
Elisabeth Creek Group	biotite leucogranite	Sn, W, Mo, F	Sn	Sn, W, Mo, F, Cu, Pb, Ag, Au, Bi, Sb
Herberton River Group	hornblende -biotite monzonite to granodiorite	Cu, Pb, Ag, Au	Cu, Pb	
Almaden Group	hornblende granodiorite			Cu, Pb, Ag, Zn, Bi

All workers also postulated a relationship of tin mineralisation to granites of the Elisabeth Creek Group, but while Branch (1966) associated only tin, De Keyser & Wolff (1964) additionally suggested tungsten, molybdenite and fluorine to be related to granites of the Elisabeth Creek Group and Sheraton & Labonne (1978) also included base metals, gold and antimony. All these correlations have to be seen with caution as mineralisation was linked to the nearest outcropping intrusion, but more recent work has shown that causative intrusions do not crop out at the surface e.g. Red Dome and Mungana.

Richards et al. (1966) were the first to conduct isotopic studies using K-Ar on biotite and hornblende to obtain the age of the granites, yielding an average age of 285 ± 27 Ma. Based on their results they suggested the igneous rock formed during the Permo-Carboniferous, but as they did not distinguished between the two major granite groups, Black & Richards (1972a) conducted further isotopic studies (Rb-Sr on whole rock) to investigate the Branch theory of two distinguishable granite groups regarding their timing and source. For granites of the Elisabeth Creek Group they obtained an age of 327 ± 5 Ma and for igneous rocks of the Herberton River Group they got 320 ± 53 Ma. As the initial Sr isotope ratios between the two groups were indistinguishable, Black & Richards (1972a) postulated that both granitic groups were derived from the same source, which agrees with the theory of De Keyser & Wolff (1964) who also had suggested that all granites were derived from one single source.

The only problem with the Rb-Sr isotopic results of Black & Richards (1972a) is that the standard deviation of age for the Herberton River Group was relatively high and therefore Black & Richards redated this Group and treated the igneous rocks of the Almaden Subgroup as an independent group. The second dating yielded an average age of 318 ± 56 Ma for igneous rocks

of the Herberton River Group and 470 ± 50 Ma for granites of the Almaden Subgroup. As the Almaden Subgroup is always intruding the Elisabeth Creek Group and therefore younger, Black & Richards (1972a) concluded, that those granites of the Almaden Subgroup had two magma sources with distinguishable isotopic signatures, and were formed through mixing as suggested by De Keyser & Wolff (1964) and Branch (1966).

2.4.3. New granite classification

The investigation of the igneous rocks in the greater Chillagoe district continued, and as a result a new granite classification was introduced by Champion (1991) and Champion & Chappell (1992). Based on geochemical and isotopic characteristics they divided the plutonic rocks into four supersuites: O'Brien's Creek, Almaden, Ootann and Claret Creek (Tab. 2.4.3.). Mackenzie et al. (1992) added a fifth group, which is called Lags Supersuite. While the O'Brien's Creek supersuite replaces the Elisabeth Creek Group, Almaden and Ootann Supersuites replace the former Herberton River Group.

Plutonic rocks of the O'Brien's Creek Supersuite belong to the I-type family, are felsic, highly fractionated, mainly reduced biotite (leuco) granites (Garrad & Bultitude 1999). Comparing to the other three supersuites they have very high contents of Nb, Th, U, Y, Zr, Ta, Hf, Cs and F and Sn, Mo, W, F mineralisation is commonly associated with granites of this supersuite (Garrad & Bultitude 1999), although Georgees & Nethery (1999) also link Cu, Au, Ag, Pb, Zn, Bi, Sb mineralisation to the O'Brien's Creek Supersuite, which agrees well with the observations made by Sheraton & Labonne (1978). From the geochronological perspective not much work was conducted recently, and many of the existing ages are related to earlier Rb-Sr isotopic studies of Black & Richards (1972a) yielding 326 to 303 Ma years for granites of the former Elisabeth Creek Group (Fig. 2.4.3.). Only two U-Pb (zircon) isotope ages are available for rhyolitic porphyry intrusions at Red Dome (322 ± 3 Ma, Perkins & Kennedy 1998 and Mungana 317 ± 2 Ma, Georgees 2007a).

The second supersuite in the Chillagoe area is the Almaden Supersuite, which comprises biotite-hornblende granodiorite, biotite granite and (monzo) diorite (Garrad & Bultitude 1999). Rocks of this group are also felsic and of I-type affinity, but compared to members of the O'Brien's Creek Supersuite they are oxidised and unfractionated (Tab. 2.4.3.) with relatively high K_2O, CaO and Sc content and compared to the other supersuites, they are relatively low Ba and Sr content (Champion & Chappell 1992; Garrad & Bultitude 1999).

Table 2.4.3. New granite classification and associated mineralisation

Supersuite	Rock type	Geochemical characteristics				Mean age	associated mineralisation
O'Brien's Creek	biotite (leuco)granite	I-type	felsic	reduced	fractionated	315 Ma	Sn,W,Mo,F,Cu,Au, Ag,Pb,Zn,Bi,Sb
Almaden	biotite-hornblende granodiorite, biotite granite and (monzo) diorite	I-type	± felsic	oxidised	unfractionated	300 Ma	Cu,Pb,Zn,Ag
Ootann	biotite leucogranites to hornblende-biotite granodiorite	I-type	felsic	reduced	fractionated	300 Ma	W,Mo,Bi
Claret Creek	biotite/hornblende granodiorite, tonalite	I-type	felsic	oxidised	unfractionated	290 Ma	-------
Lags	hornblende-biotite microdiorite to biotite microgranite	A-type	felsic	reduced-oxidised	unfractionated	280 Ma	U,F,Au

Typical mineralisation associated with plutonic rocks of this group is Cu, Pb, Zn and Ag (Georgees & Nethery 1999), which agrees with observation made by De Keyser & Wolff (1964), Branch (1966) and Sheraton & Labonne (1978). Isotopic age data (Rb-Sr from Black & Richards 1972a) yielded 303 to 292 Ma years.

The third supersuite is the Ootann Supersuite, which comprises biotite leucogranites to hornblende-biotite granodiorite and is of similar age (306-299 Ma) as the Almaden Supersuite, but it is considered to be younger than the Almaden Supersuite as igneous rocks of the Ootann Supersuite always cross-cut the Almaden Supersuite when they are in direct contact. Geochemically, rocks of the Ootann Supersuite are also felsic and of I-type affinity, but more reduced and fractionated than rocks of the Almaden Supersuite. High Rb and low Sr content are the general characteristics, but in comparison with the also reduced and fractionated O'Brien's Creek Supersuite igneous rocks of the Ootann Supersuite have lower concentrations of HREE and F.

The Claret Creek Supersuite occurs south of the Chillagoe district and builds a ring complex. It consists of biotite- or hornblende-bearing granodiorite and tonalite as well as co-magmatic volcanic rocks. It was first described in detail by Bailey (1977) and is characterised by high Al_2O_3 and Na_2O values and very low K_2O, Rb, Th, Y and U content (Garrad & Bultitude 1999). The emplacement of rocks of the Claret Creek Supersuites took place in Carboniferous time at around 300 Ma and no mineralisation is associated with this Supersuite.

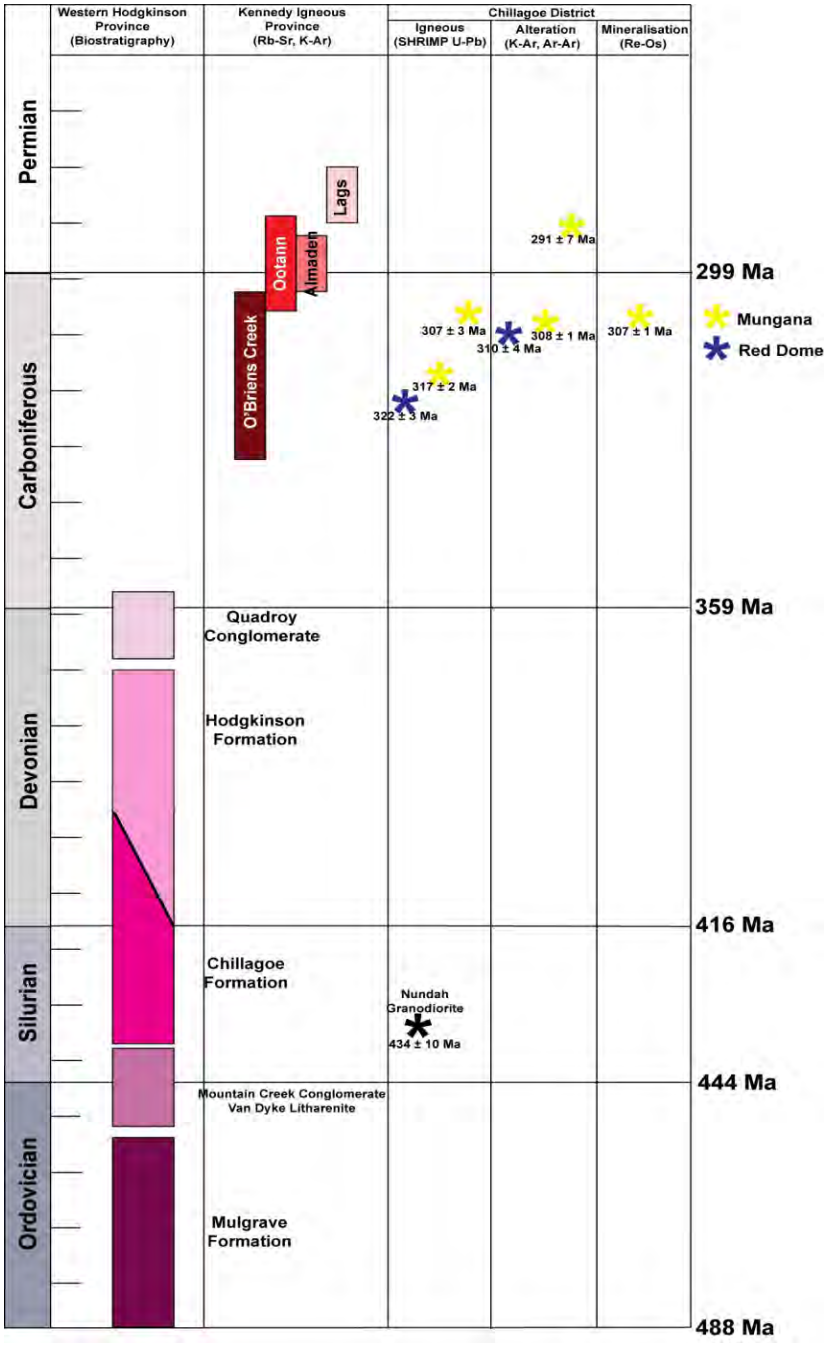

Figure 2.4.3. Geochronological summary of stratigraphic units of the Hodgkinson and Kennedy Igneous Province including isotopic age data of igneous supersuites and single deposits; created from data of Black & Richards (1972a), Fordham (1990), Donchak & Bultitude (1994), Woodbury (1994), Perkins & Kennedy (1998) and Georgees (2007a).

A fifth supersuite in the greater Chillagoe district is called Lags and was first introduced by Mackenzie et al. (1992). The Lags Supersuite consists of hornblende-biotite microdiorite to biotite microgranite, is of A-type affinity and shows distinctive high concentrations of Ba and Zr comparing to the other four supersuites. Isotopic age data indicate a Permian age of 290-280 Ma (Black & Richards 1972a) and minor U, F and Au are associated with this supersuite.

Isotopic characteristics like $^{87}Sr/^{86}Sr$ ratios and ε_{Nd} values have been interpreted to suggest that all igneous rocks of the five supersuites were derived from a long lived crustal source of dacitic to andesitic composition by different degrees of partial melting, fractionation and assimilation of Proterozoic to Devonian country rocks (Champion & Chappell 1992).

2.5. Geological evolution of the Chillagoe district

The geological evolution of the Chillagoe district is still controversial as there is no agreement regarding the timing and number of deformation events, nor does a correlation of events throughout the entire Hodgkinson Province seem to be possible. The only point where all workers agree is that sediments were deposited in the vicinity of an active continental margin, but whether the regime was extensional or compressive or where the exact position of the subduction zone has been remains subject to much debate (Garrad & Bultitude 1999).

The first event in the area was the deposition of deep-water turbidity-current sediments of the Hodgkinson Formation, Mountain Creek Conglomerate and Van Dyke Litharenite with minor eruption of basalts, derived from an evolved magmatic arc (Vos et al. 2006b) during Ordovician time (Fig. 2.5.A). During the Silurian a basin formed, which was caused by movement of the Palmerville Fault, a steeply eastward dipping thrust fault, which may represent a reactivated Precambrian structure (Vos et al. 2006a). Deep-water turbidity-current sediments (Chillagoe Formation) as well as fossiliferous limestones were deposited and basalts erupted on the sea-floor, which were derived from the same source as basalts of Ordovician age (Vos et al. 2006b). Additionally, the Nundah Granodiorite was emplaced during Silurian time (Fig. 2.5.B).

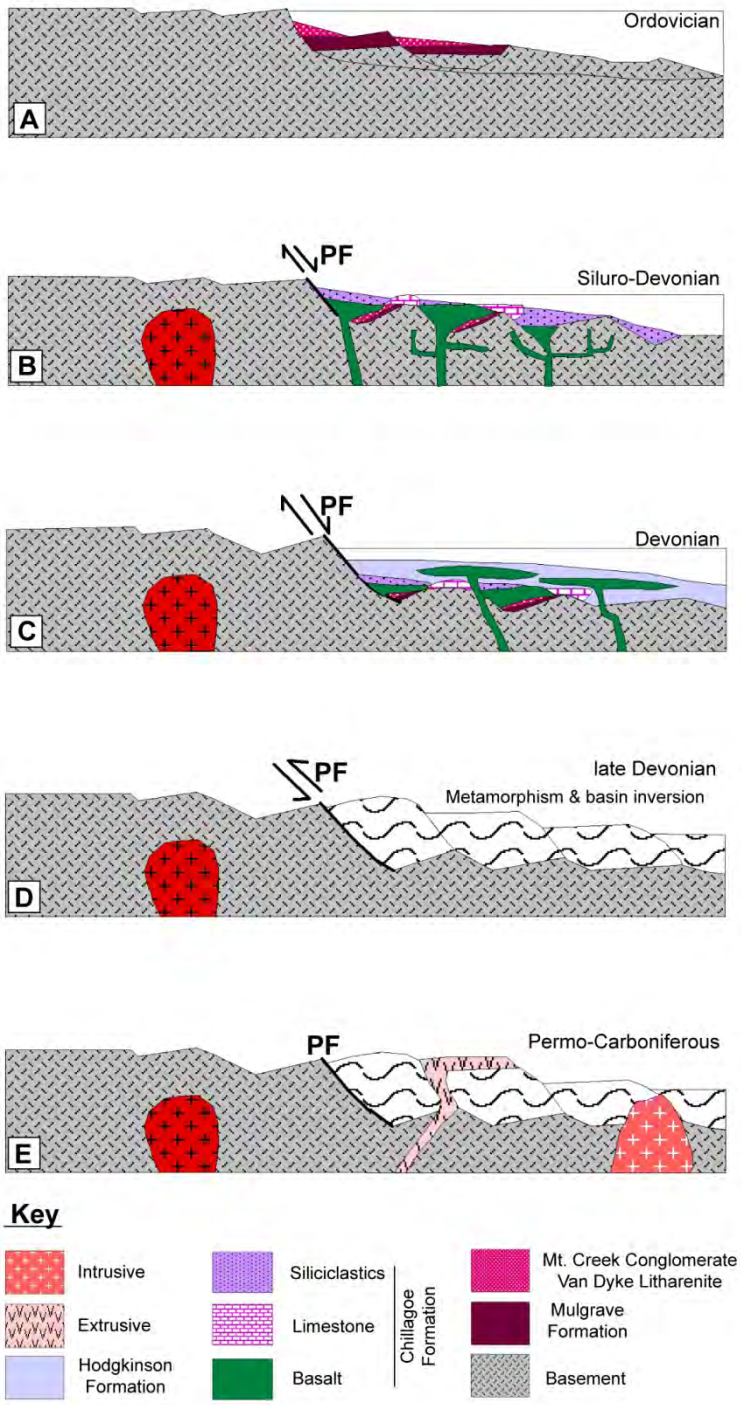

Figure 2.5. Geological evolution of the Chillagoe district; **A**: deposition of sedimentary rocks of the Mulgrave Formation, Mountain Creek Conglomerate and Van Dyke Litharenite (Ordovician); **B**: deposition of sedimentary rocks of the Chillagoe Formation, eruption of basalts and emplacement of the Nundah Granodiorite (Siluro-Devonian); **C**: deposition of sedimentary rocks of the Hodgkinson Formation (Devonian), **D**: deformation (including basin inversion) and metamorphism to lower greenshist facies (late Devonian); **E**: emplacement and eruption of co-magmatic plutonic and volcanic rocks including development of mineral deposits (Permo-Carboniferous); compiled form De Keyser & Wolff (1964) and Vos et al. (2006b).

The sedimentation of the Chillagoe Formation continued into the Devonian, and the formation was conformably overlain by sediments of the Hodgkinson Formation (Fig. 2.5.C). These sediments also consist of flysch and include minor basalt, which, in comparison to older basalts, was derived from a depleted mantle source (Vos et al. 2006b). Another tectonic event, represented by the movement of the Palmerville Fault and regional metamorphism in late Devonian time, resulted in folding, thrusting and inversion of Ordovician to Devonian sedimentary rocks (Fig. 2.5.D). In Permo-Carboniferous time plutonic rocks of the five supersuites and co-magmatic volcanic rocks were emplaced/erupted (Fig. 2.5.E), in some places along fault contacts (e.g. Red Dome, Nethery & Barr 1998). Associated with the plutonic rocks are different styles of mineralisation (Tab. 2.4.3.) like Sn, W, Au, base metals with the O'Brien's Creek Supersuite, base metals with the Almaden Supersuite, W, Mo, Bi with the Ootann Supersuite and minor U, Au and F with the Lags Supersuite. After Permo-Carboniferous time no further movement of the Palmerville Fault occurred as the igneous suites are not displaced (Shaw et al. 1987; Bultitude et al. 1997).

2.6. Exploration and mining history

First examined for gold due to its proximity to the Palmer goldfield (Fig 2.6.), the Chillagoe mining district was primarily exploited for base-metals (Cu, Pb, Ag) from oxidised horizons of the deposits. Zinc, one of the dominant ore phases and in general associated with the lead, was extracted, but it could not been treated due to a lack of suitable ore processing methods during that time.

All together more than 100 prospects, shafts and mines, grouped into seven principal mining centres (Mungana, Redcap, Zillmanton, Chillagoe, Calcifer, Fluorspar, and Dargalong, Fig 2.6.) were exploited in three stages of mining activity between 1888 and 1927 (Broadhurst 1953). In the first mining era (1894-1897) 7,814 tonnes of ore containing 962 tonnes of copper, 250 tonnes of lead, and 32,000 ounces of silver were mined (Broadhurst 1953) and processed in local smelters (e.g. Calcifer, Mungana and Redcap). With the development of central smelters in Chillagoe in 1901, the second era, which was the most successful one, started. In this era (1901-1914) 436,470 tonnes of ore were exploited yielding 14,607 tonnes of copper, 24,643 tonnes of lead and 3,258,600 ounces of silver (Broadhurst 1953). In the last mining period only 99,572 tonnes of ore were mined and 1,327 tonnes of copper, 11,967 tonnes of lead and 876,400 ounces of silver were extracted (Broadhurst 1953).

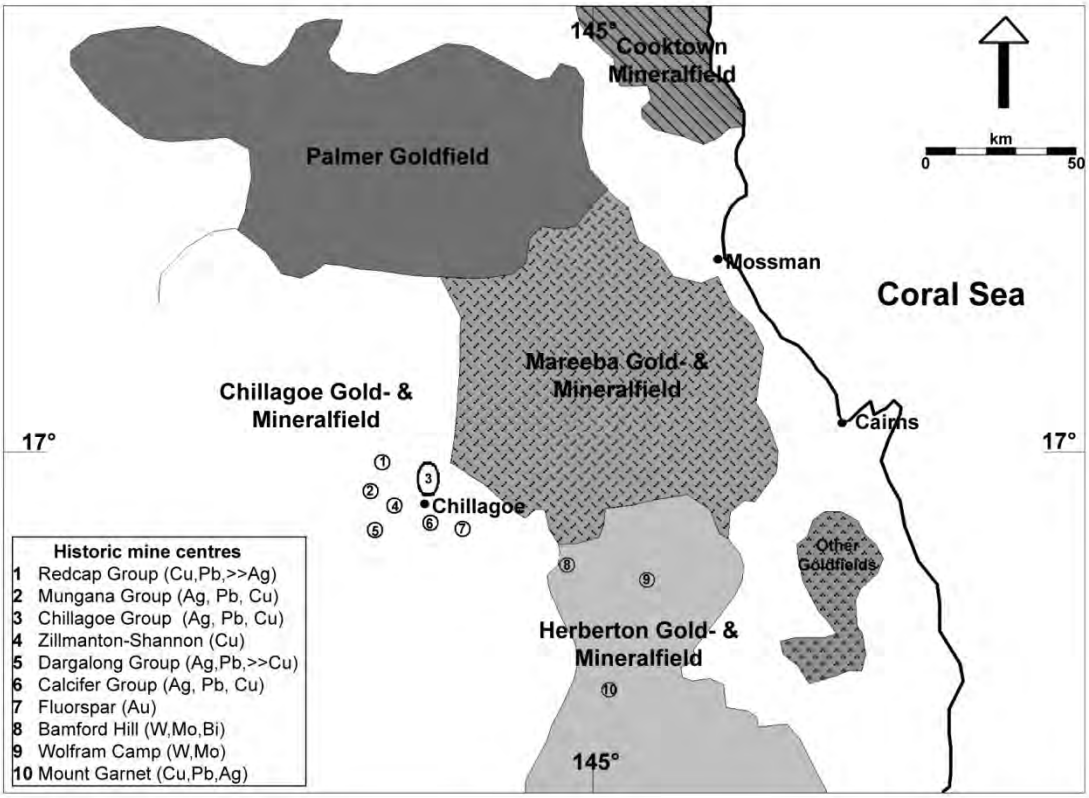

Figure 2.6. Historic mineral fields and mining centres during early mining activity from 1888 to 1964; modified from De Keyser & Lucas (1968).

Although Jack (1891) and Skertchly (1897) had predicted a great potential for the Chillagoe district, the historical production 543,856 tons of ore, which is the equivalent of one year production from Mount Isa in the 1960's (De Keyser and Wolff 1964), stayed well behind their forecast. This had many reason with the majority of the difficulties being not of geological nature, but also technical, economic as well as political problems were responsible. Two of the geological problems were, that due to the complex structural history ore bodies were disrupted internally, and not all ore occurred close to the surface. With the exhaustion of ore close to the surface, mining often stopped as due to technical limitations, as deeper levels (mostly beyond the oxidised zone) could not be accessed. Ore processing methods were also limited and many of the metals remained untreated (e.g. the zinc). Other problems were flooding, fires, low metal prices, mismanagement, transport issues, industrial unrest and a lack of workers during WWI (De Keyser & Lucas 1968).

From the 1930's on a new era started in the Chillagoe district, which was dominated by exploration. Around 20 exploration companies and geological surveys (De Keyser & Wolff 1964; Torrey 1986; Nethery & Barr 1996) investigated the area using various geophysical (e.g. airborne magnetics & radiometric), geological (mapping), geochemical (country rock & soil) and drilling (RC percussion & diamond) methods to reveal the locations of new deposits as well

as to identify source of the mineralisation. This extensive exploration led to a new mining period from 1986 to 1996 with Red Dome being exploited as an open-pit for gold, producing a total of 12.8 Mt ore with 2 g/t Au and 0.5 % Cu grade. Another deposit, Mungana, had also been discovered during that time, but it took another ten years until Kagara Zinc Limited (now Kagara Ltd), started the development of an underground mine at Mungana. Kagara continued exploring the area, focussing on base metal and gold, but since 2010 only focuses on the base metal mineralisation, whereas a spin-off company of Kagara (Mungana Goldmines) took over the exploration for gold.

2.7. Local geology of Redcap, Mungana and Red Dome

2.7.1. Introduction

The Redcap, Mungana and Red Dome deposit are located 18 km, 15 km and 12 km north-west of Chillagoe, respectively (Fig. 2.6.) and are hosted within the Siluro-Devonian Chillagoe Formation. All deposits are of polymetallic nature with Zn-Cu-Pb (Redcap, Mungana) and Cu-Au (Redcap, Red Dome) being the main mineralisation type although other types like Au-As-Bi (Mungana) also exist. The different mineralisation types show characteristics of different deposits styles, these being porphyry (Red Dome, Mungana), skarn (Redcap, Mungana and Red Dome) and hydrothermal breccia (Mungana and Red Dome) environment. In this section the three deposits will be introduced regarding their geological setting and history and a summary of previous work conducted at the deposits will be provided.

2.7.2. Redcap

The Redcap deposit is located about 18 km north-west of Chillagoe and is hosted within the steeply-dipping Chillagoe Formation. In the north-east of the Redcap deposit, the Chillagoe Formation is thrust over Permo-Carboniferous Redcap Dacite along a south-west dipping fault, the Redcap-Morrison Thrust. The Redcap Dacite as well as the Redcap-Morrison Thrust is truncated by the unmineralised Belgravia Granodiorite in the north-west (Bultitude et al. 1993a; Fig. 2.3.1).

The Redcap deposit consists of three main NW-trending mineralisation zones, here called lines, which formed at lithological contacts over a distance of 2.5 kilometres. The mineralisation lines are named after the main historic base metal workings (1888-1927), and are from south-west to north-east the Penzance, Victoria and Redcap-Morrison lines (Fig. 2.7.2.).

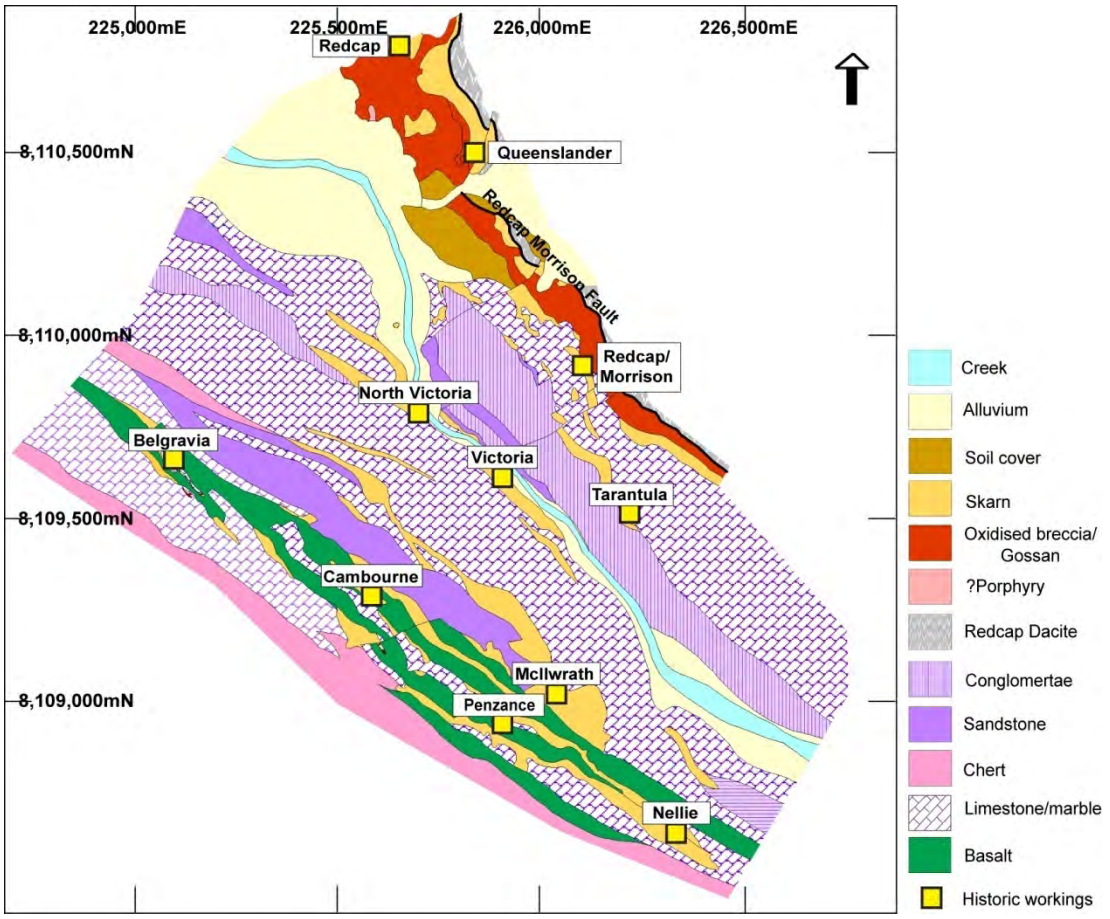

Figure 2.7.2. Geological map of the Redcap deposit including the location of historic workings; modified from Patterson (1996).

An estimated 31 pits and shafts (Ishaq et al. 1987) were worked for copper, silver and lead (no gold reported) mainly from the oxidised zones of the old workings with a general change of mineralisation trend from lead-dominated in the north-west to copper dominated in the south-east (De Keyser & Wolff 1964). Zinc was also extracted, but could not be treated during that time. The mineralisation was hosted in various types of gossanous ferruginous and/or siliceous breccias and gossanous garnet magnetite skarns. Although the workings of the Redcap Group formed historically the largest deposit in the Chillagoe district, only 13,000 tons of ore were extracted yielding 300 tons of copper, 525 tons of lead and 731 kg of silver (Ishaq et al. 1987), while the Mungana Group produced 2/3 of the total production of the Chillagoe district (see section 2.6.).

Since the mining stopped at Redcap in 1927, the area has been the subject of moderate to intensive exploration. Eight companies investigated the area with various geophysical, geochemical and drilling programs, with all of them focusing around the historical workings, but Kagara Ltd was the only company that succeeded by identifying a zinc-dominated base metal lode at the Victoria line in 2005 and 2008 (Coffey 2010).

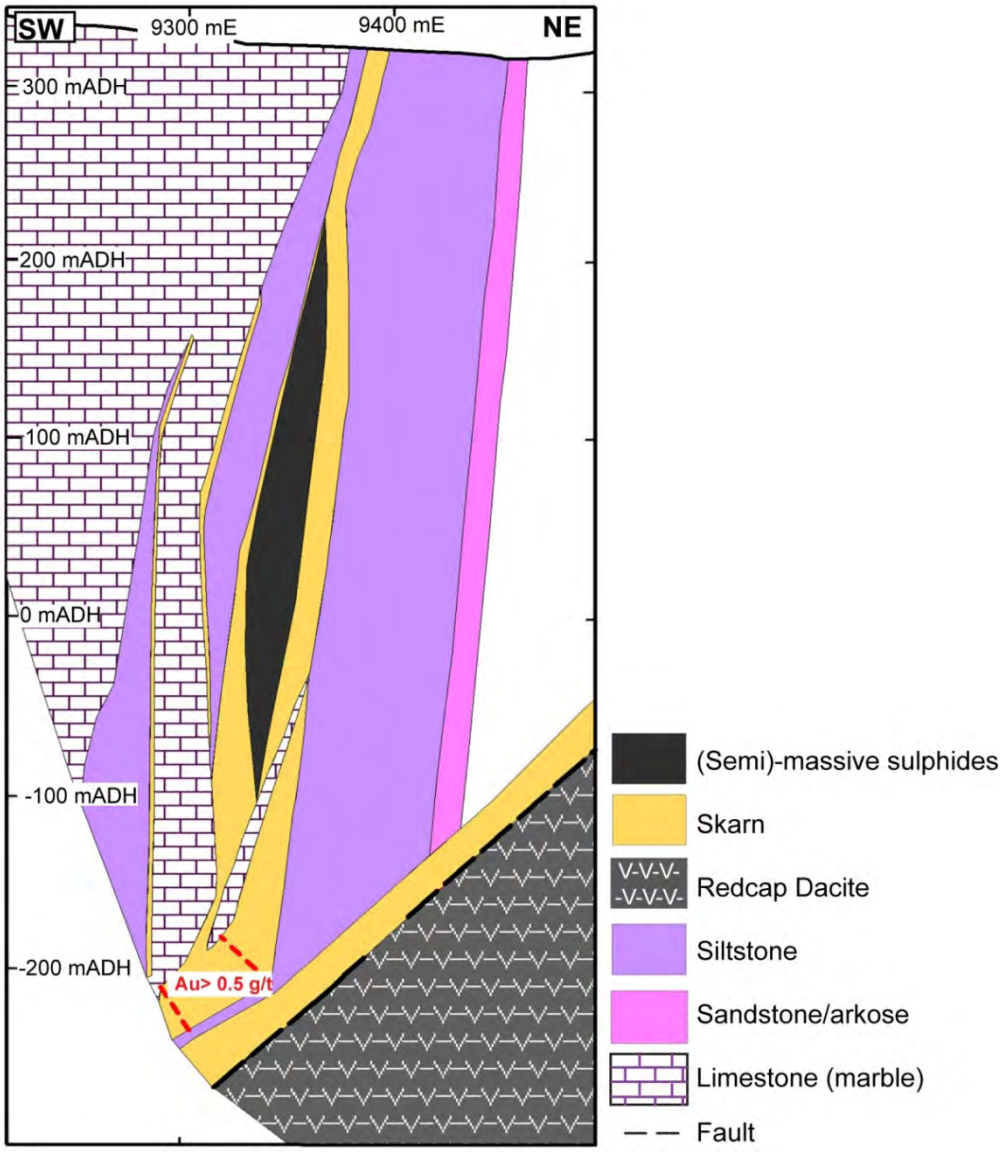

Figure 2.7.2.1. Schematic cross section (5600 E) of Redcap-Victoria showing the different lithologies of the Chillagoe Formation, and the occurrence of skarn lenses, base metal and gold mineralisation; modified from Kagara Ltd (2008).

The Victoria deposit comprises two sulphide-bearing skarn lenses with one, being parallel to the nearly vertical dipping lithological contacts of the country rock, while the second skarn lens is parallel to the Redcap-Morrison Thrust (Fig. 2.7.2.1.). While the first skarn lens, which consists mainly of garnet, wollastonite and vesuvianite (see chapter 3) is dominated by Zn-Cu-Pb mineralisation, the second skarn lens at depth (~ 500 m) comprises pyroxene skarn with minor k-feldspar and garnet and hosts Cu-Au mineralisation. As of June 2008 the resource, which remains open at depth, is estimated to be 3.44 Mt of ore at 5.08 % Zn, 1 % Cu, 22 g/t Ag and 0.14 g/t Au grade (Coffey 2010) with more drilling being underway to define the edges of the ore body and to improve and increase the resource values.

Previous research work of the Redcap deposit is limited to Paverd (1971, 1981), Musumeci (1974), Rubenach & Cuff (1985) and Rubenach & Cartwright (1994). Paverd (1971, 1981) investigated garnets from the Redcap deposit (Redcap and West Victoria prospect) and Zillmanton-Shannon area (ca. 5 km NW of Chillagoe, see Fig. 2.6.) regarding their potential as exploration tool for base metal mineralisation. He observed that skarns containing garnets with less then 55 % andradite component are barren, while nearly pure andradite garnets ($And_{>85}$) are dominated by magnetite and pyrrhotite and only carry less than 5 % sulphides. The best economic mineralisation is hosted by skarn containing garnets with 60 to 85 andradite component.

Musumeci (1974) conducted mapping around Mount Redcap and investigated the breccia, to identify its origin and potential for mineralisation and style, but did not come to any conclusion.

Rubenach & Cuff (1985) and Rubenach & Cartwright (1994) investigated the skarn at Redcap Creek, which formed along marble contacts and is linked to the emplacement of diorite and gabbro dykes cutting the Belgravia Granodiorite, while no skarn or hornfels developed in contact with the Chillagoe Formation (Bultitude et al. 1993a). Rubenach et al.'s (1985 & 1994) field observations and stable isotope studies suggest that the marble was first impermeable, but that a reaction skarn provided permeability resulting in additional skarn formation by fluid flow parallel to the contacts, rather than fluid flow perpendicular to the lithological contacts towards the marble as the general infiltration model suggests (e.g. Meinert et al. 2005). Not only the fluid pathway of skarn formation is unusual, but also the skarn itself. Stage 1 skarn consists of very coarse grained tilleyite which is associated melilite and wollastonite. Originally Rubenach & Cuff (1985) suggested a formation temperature for stage 1 skarn of 800 °C with temperature estimates being obtained by calculating phase-relationships using THERMOCALC. Nearly a decade later Rubenach & Cartwright (1994) revised the formation temperature with their calculations in THERMOCALC indicating only 700 °C.

2.7.3. Mungana

The Mungana deposit is located about 18 km west-north-west of Chillagoe and together with Red Dome it is part of a NW-trending deformed belt ('mine corridor') of internally disrupted, steeply-dipping Chillagoe Formation (Fig. 2.7.3). The Chillagoe Formation comprises limestone, siliciclastic rocks, chert and basalt. Additionally, pipe-like oxidised breccias crop out at the surface. Two intrusive bodies are identified at Mungana, a rhyolitic porphyry and a granite, but their genetic relationship remains unknown (Hodkinson et al. 2009).

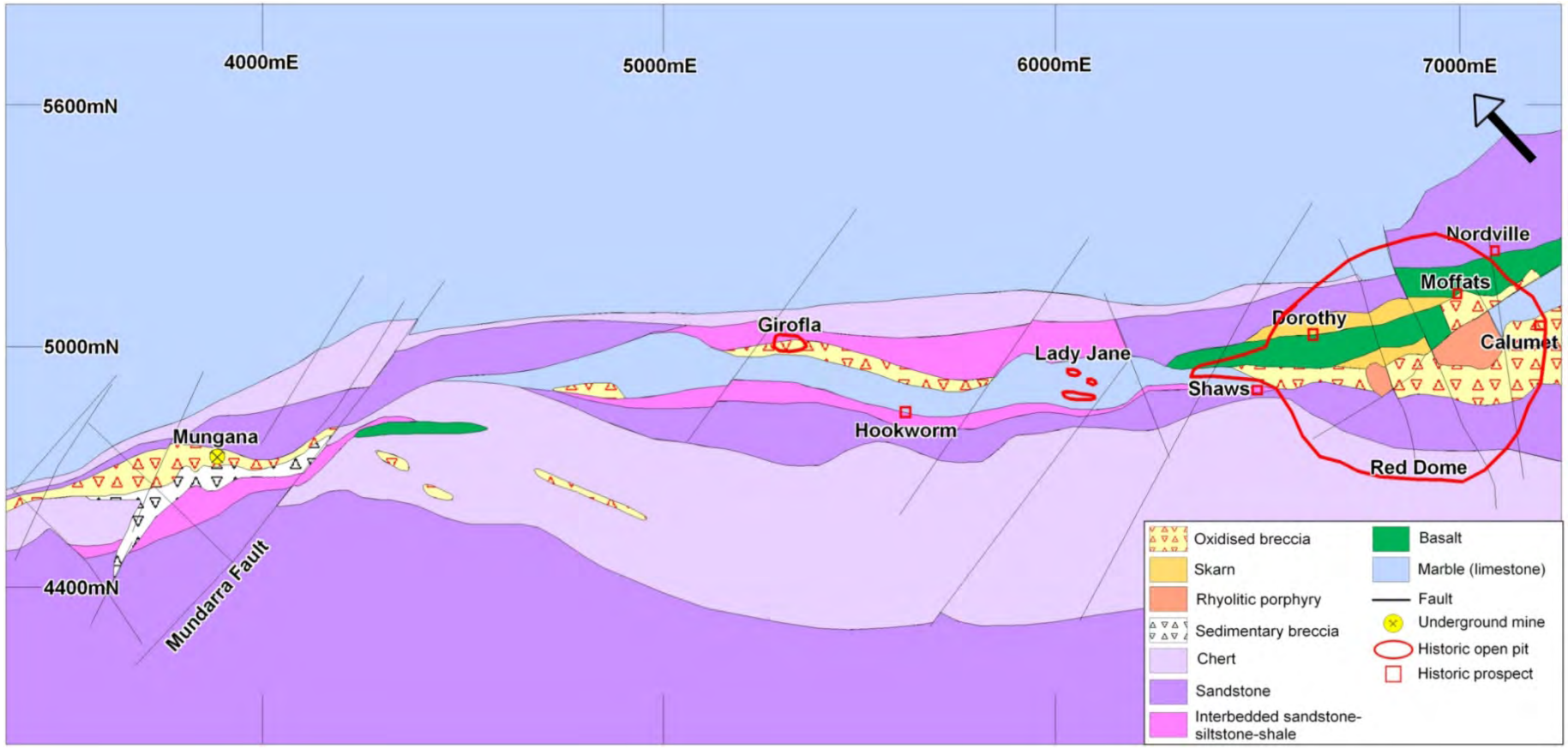

Figure 2.7.3. Geological map of the 'mine corridor', showing the location of historic workings and recent mines; modified from Barr (1998).

Mungana, like Redcap, is a polymetallic mineralised system with base-metal mineralisation (Cu-Zn-Pb) occurring in lenses associated with skarn adjacent to faulted lithological contacts (Fig. 2.7.3.1). A second type of mineralisation is Au-As-Bi which occurs in quartz veins cutting the porphyry and country rocks, mainly sandstone. In the upper part of the deposit a breccia occurs, which originated from a phreatic explosion event first identified by Nethery et al. (1994). Because of the brecciation and additional supergene processes and deep weathering (down to 260 m, Hodkinson et al. 2009), the system is complex and the timing of single events is obscured as earlier processes were overprinted by later events.

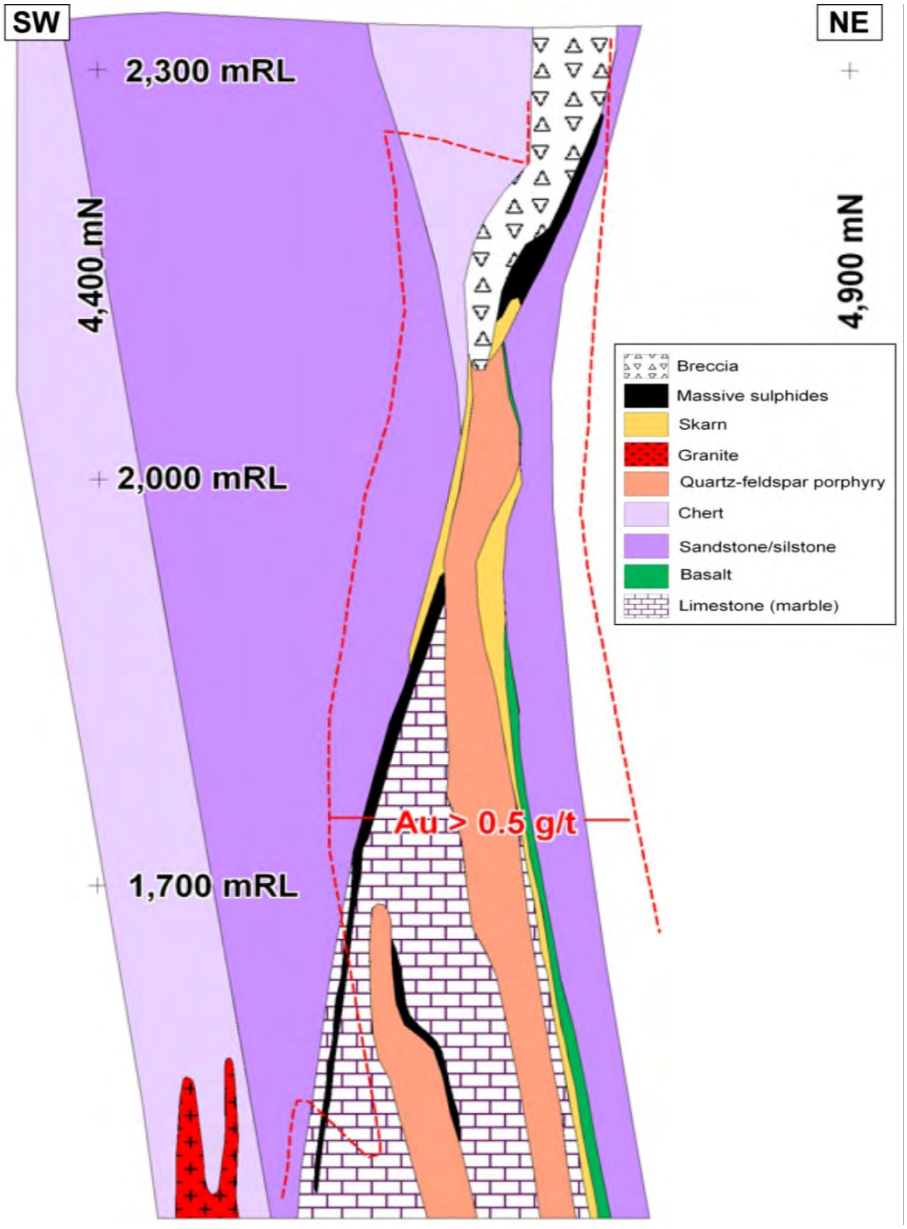

Figure 2.7.3.1. Schematic cross section (3850 E) of the Mungana deposit showing country rocks, intrusions as well as skarn occurrence and distribution of base metal and gold mineralisation; modified from Georgees (2007b).

During the first mining era (1888-1927) a total of 21 prospects were mined (Ishaq et al. 1987) for their copper, lead and silver mineralisation, mainly from the oxidised zone, with Girofla and Lady Jane being the most important producers (2/3 of the total ore production in the Chillagoe district). Other mines included in the Mungana Group were Dorothy, Moffats, Red Dome, Magazine, Nordville, Calumet and Griffith Hill (Fig. 2.7.3.), which would be assigned to the Red Dome deposit today and therefore will be described in the next section.

At the Girofla mine, mineralisation occurred in three vertical siliceous and ferruginous chert breccia pipes. Primarily mineralisation was copper, but production numbers indicate that 6 times more tons of lead was extracted than copper (6000 t; Broadhurst 1953). Secondary copper minerals were especially enriched at around 125 m depth (Broadhurst 1953) and at depth (~ 155 m) copper gave way to lead mineralisation. The Lady Jane mine, located ~ 800 m south east of Girofla, consisted of four shafts which reached down to ~ 125 m (De Keyser & Wolff 1964) and is also referred to as a copper mine, although lead production exceeded the copper extraction. Comparing to Girofla, the Lady Jane deposit occurred in limestone with De Keyser & Lucas (1968) describing the Lady Jane deposit as a contact-metasomatic deposit which grades into hypothermal vein deposits: in today's terminology this would be described as a skarn deposit with intrusion-related quartz stockwork.

After the mining stopped in 1927, only minor exploration was conducted around Mungana until mining at Red Dome commenced in 1986. From then on, four companies started to investigate the area in more detail, drilling more than 90,000 m (Coffey 2010). Mining commenced in 2008 with current resource being an estimate of 32.2 Mt ore at 0.7 % Zn, 0.3 % Pb, 0.2 % Cu, 12 g/t Ag and 0.81 g/t Au grade.

Previous research on the Mungana deposit is limited to Halfpenny (1991), Woodbury (1994), Nethery & Barr (1996), Barr (1998), Georgees (2007a), Hodkinson et al. (2009) and Rubenach (2010). The first study conducted at Mungana was from Halfpenny (1991), who described the prospect geology, developed a paragenetic sequence based on hand specimens and drill core, and investigated the formation and origin of the breccia with the overall aim to compare the Red Dome and Mungana deposit.

Halfpenny suggested that the gold mineralisation occurs together with molybdenite in laminar quartz veins. These quartz veins form a stockwork which cuts porphyry intrusion as well as sandstone, and based on Halfpenny, the gold mineralising event occurs very early, in the contact metamorphic event, although primary fluid inclusions of the quartz yielded temperatures of 250-309 °C (Allen 1989), which are too low for contact metamorphic origin of the quartz. On the

other hand Halfpenny assigned the base-metal mineralisation to a retrograde event as he observed that it occurred together with retrograde altered skarn. Investigations of the oxidised breccia suggested that the breccia had formed after the retrograde mineralisation event, and because of a lack of any exotic clasts and matrix, as well as nearly no abrasion of clasts and no matrix infill, Halfpenny postulated that the breccia had formed through a combined tectonic and karst collapse event. Only a couple of years later, milled and exotic clasts, sulphide matrix infill as well as evidence of fluidisation were discovered, and the origin of the breccia was revised. Early tectonic breccias occur along major shear structures, the second brecciation event was caused by phreatic explosion (Nethery et al. 1994) and a third event is represented by karst collapse (Hodkinson et al. 2009).

Woodbury (1994) also developed a paragenetic sequence for the Mungana deposit. His paragenesis is very similar to the one from Halfpenny (1991) with the only new aspect that after Woodbury the gold-molybdenite-carrying laminar quartz veins are additionally associated with bismuth, tellurium and silver. In addition to the paragenetic sequence Woodbury did some whole rock analysis of porphyry samples from Red Dome and Mungana, conducted studies of fluid inclusions from the gold-bearing laminar quartz veins, determined the sulphur isotopes of bulk sulphide samples and undertook K-Ar isotope studies on sericite from one porphyry sample. He postulates that whole rock data indicate that the porphyry from Mungana shows signs of A-type affinity and that the porphyry bodies from Red Dome and Mungana are unrelated to each other. K-Ar dating of sericite yielded 291 ± 7 Ma, suggesting a Lags Supersuite event at Mungana. His age also disagrees with an Ar-Ar isotopic age of sericite from Perkins & Kennedy (1998) who obtained and age of 308 ± 1 Ma for the alteration at Mungana. Their age on the other hand can possibly show an alteration event caused by the emplacement of the granitic intrusion at 307 ± 3 Ma (SHRIMP U-Pb isotope analysis, Georgees 2007a).

Woodbury's fluid inclusion homogenisation temperatures (277-339 °C) are similar to the ones obtained by Allen (1989), but again the temperature range does not support a very early paragenetic timing of the gold-mineralising event. Finally, his sulphur stable isotope analysis of bulk sulphide samples from the base-metal lode indicate that the sulphides originated from a magmatic fluid, with no influence of meteoric water, and only one sulphur source seems to exist.

In 1996 Nethery & Barr updated the evolution history of Mungana and postulated that the base-metal mineralisation is early in the paragenetic sequence and is hosted by a skarn adjacent to a shear zone. During this time other workers reported the occurrence of Besshi style VMS deposits in the Hodgkinson Province (e.g. Ok mine, ~ 74 km NW of Chillagoe; Mt Molly and

Dianne, ~ 54 and 96 km NW of Cairns, Morrison & Beans 1995), which are characterised by stratabound accumulation of sulphide mineralisation that originated from mafic volcanism at or near the seafloor (Franklin et al. 2005).Based on the occurrence of these deposit style in the region, Nethery and Barr (1996) proposed that the base-metal mineralisation at Mungana originated from a Besshi style VMS event and was later replaced and introduced into the Mungana deposit along shear zones. Georgees (2007a) on the other hand, suggested that the base-metal mineralisation is related to a retrograde skarn, which pre-dates the porphyry, but no information regarding the formation of that skarns exist. Hodkinson et al. (2009) support the hypothesis of Georgees (2007a) as underground exposure show that the sulphides were introduced into the skarn, although the emplacement mechanisms are still not understood.

Barr (1998) conducted a review of the Mungana deposit and especially focused on the different brecciation events as well as different mineralisation and alteration styles. He confirmed the occurrence of the two major mineralisation styles, previously identified by Halfpenny (1991) and Woodbury (1994), but postulated that the Cu-Zn-Pb-Ag mineralisation is associated with a retrograde skarn which pre-dates the emplacement of the porphyry. Additionally, the gold-mineralising event occurred later (post porphyry), and the gold is not associated with molybdenite and/or bismuth and tellurium. Barr suggested a link to arsenic. His major finding was that a late high sulphidation event had occurred after the phreatic explosion and a remobilisation of Cu-Pb-Zn-As-Ag had taken place resulting in clasts embedded into a sulphide matrix which is dominated by sphalerite, colloform galena, as well as tennantite, chalcocite and covellite.

The most recent research of the Mungana deposit was conducted by Rubenach in 2010. He investigated the genesis and timing of gold mineralisation on the basis of quartz generations, which are distinguishable regarding their internal CL structure and trace element geochemistry. Additionally, he tried fluid inclusion studies, but microthermometry failed because of the small inclusion size (Rubenach 2010).

In total Rubenach identified four quartz types: 1. brain rock quartz (Q1), 2. stockwork quartz (Q2), 3. Very fine grained gold-carrying quartz (Q3) and 4. unmineralised quartz cutting earlier quartz veins in porphyry, sandstone and base metal lode (Q4a-c). The Ti concentration determined by LA-ICP-MS used in the titanium-in-quartz-geothermometer by Wark & Watson (2006) yielded temperatures of 650-390 °C for Q1 and Q2 quartz, 400-220 °C for Q3 quartz and 350-220 °C for Q4a-c quartz, with aluminium versus titanium concentration plots indicating that Q1 to Q3 quartz are related to the porphyry while Q4 quartz are likely to be of epithermal origin.

Rubenach postulates that two gold mineralising events exist, with the primary one being related to Q3 quartz and gold occurring as inclusions in arsenopyrite and chalcopyrite as well as being associated with electrum, tennantite and minor bismuth-tellurides. The second gold event classified by Rubenach occurs in form of gold inclusions in loellingite or gold being associated with silver and lead tellurides and all of them being hosted in quartz-carbonate veins.

2.7.4. Red Dome

The Red Dome deposit is located about 15 km west-north-west of Chillagoe and like Mungana it occurs within the 'mine corridor', which comprises internally disrupted, steeply-dipping Chillagoe Formation (Fig. 2.7.3). Two intrusive bodies were described in the past, which are characterised by geochemical and textural features (Torrey 1986).

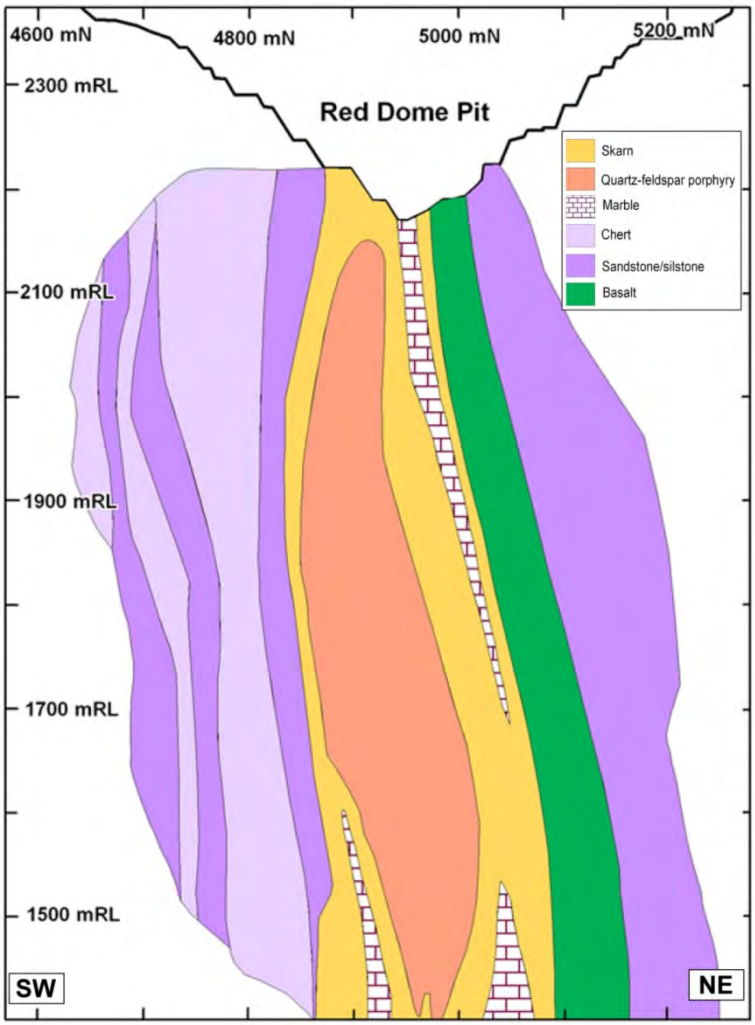

Figure 2.7.4. Schematic cross section (6700 E) of Red Dome showing steeply-dipping lithologies of the Chillagoe Formation and skarn development around the emplaced porphyry; modified from Coffey 2010.

These are the Nested Rhyolite Porphyry identified by micrographic intergrowth of feldspar and quartz as well as crenulate layered quartz, and later Crowded Porphyry Dykes, which consist of coarser grained porphyry with abundant phenocrysts and are richer in potassium than the earlier Nested Porphyry (Ewers & Sun 1988a). More recent drilling has shown that the different porphyries build one porphyry mass at depth (Coffey 2010). Around the porphyry garnet and wollastonite skarn have formed (Fig. 2.7.4.) which host different styles of mineralisation: Cu, Cu-Au-Ag and Cu-Zn-Pb-Ag. The upper part of the Red Dome deposit consists of a polymict karst collapse breccia which was mined for gold-copper and silver.

The Red Dome deposit has experienced two mining periods, one from 1888-1927 and a second one from 1986-1996. During the first mining period small workings like Dorothy, Calumet, Malachite, Nordville, Griffith and Red Dome (Fig. 2.7.3.) were mined down to a depth of maximum 70 m for cupriferous iron flux, malachite, cuprite and azurite nodules which occurred in siliceous ferruginous or jasperised breccias, gossan or skarn (Jensen 1940; De Keyser & Wolff 1964). In total the amount of extracted ore was low (De Keyser & Wolff 1964) and no production data are being reported for single deposits, but it is mentioned that at Red Dome gold occurred (7 dwt per ton, De Keyser & Wolff 1964). In the 1970's a new resource was discovered at Red Dome and extensively explored until mining commenced in 1986. During the second mining period, which lasted until 1996, Cu-Au ore from the oxidised breccia was extracted from open pit yielding a total of 12.8 Mt ore at 0.5 % Cu and 2 g/t Au grade. Kagara purchased the lease in 2003 and conducted further exploration of the Red Dome deposit, especially deep drilling beneath the old pit which resulted in a new estimated resource of 40.1 Mt ore at 0.8 g/t Au and 0.3 % Cu grade.

Previous research work of the Red Dome deposit is limited to Smith 1985, Torrey 1986, Ewers & Sun 1988a & b, Ewers et al. 1990, Woodbury 1994, Nethery & Barr 1998 and Creighton 2005. Smith (1985) focussed on the mineralised breccia in the upper part of the deposit and suggested that it is of karst collapse origin and is the major host of native gold, which originated from tellurides which were hosted in the deeper skarn.

Torrey (1986) investigated the Red Dome deposit in greater detail, developing a paragenetic sequence and conducting fluid inclusion studies of quartz. His paragenetic sequence is divided into four stages: 1. early metasomatic, 2. late metasomatic, 3. early retrograde and 4. late retrograde. Stage 1 is represented by hedenbergite endoskarn and brown andradite exoskarn with minor diopside, magnetite and vesuvianite, while skarn of the second stage is dominated by wollastonite with minor amounts of andradite and diopside. Both stages are linked to the intrusion of the Nested Porphyry, while the stages 3 and 4 are associated with the later Crowded

Porphyry. Stage 3 and 4 are represented by retrograde alteration, which consists of calcite, chlorite, epidote, sericite and quartz and a very late green garnet skarn. Based on Torrey (1986) base-metal mineralisation is associated to the retrograde alteration of stage 3, while gold mineralisation occurs in the form of Au-Ag-tellurides (e.g. sylvanite and petzite) within the wollastonite skarn and copper mineralisation in the garnet-magnetite skarn of stage 2.

Fluid inclusion data for early paragenetic quartz from crenulate layers, microgranitic cavities and quartz stockwork yielded temperatures of 500 to 600 °C with salinity values of 35-65 wt% equivalent NaCl, while a second generation of fluid inclusions from the quartz stockwork generated temperatures of 200 to 375 °C with salinity values of 2-22 wt% equivalent NaCl which were also found in fluorite and quartz of the retrograde base-metal bearing sericite-carbonate-quartz alteration.

Ewers & Sun (1988a) also conducted fluid inclusion studies, but unlike Torrey, they did not experience any problems with the freezing of the inclusions. They also found two types of fluid inclusion which were distinguished by their salinity, but are identical to the ones identified by Torrey. One group (inclusions in fluorite from the rhyolite) yielded salinity values of 30-50 wt% equivalents NaCl, while the second group (garnets from skarn) produced values of 2-24 wt% equivalents NaCl. Ewers & Sun also conducted whole rock analysis of country rocks, skarn and intrusion, and, based on their mass balance calculations, they suggested that Fe, Cu, Mo, Sn, Zn, As, W, S, Pb, Ag and Bi were added to the system and not provided by the country rocks. They also conducted stable isotopes studies and postulated that sulphur isotopes indicate a mixing of two sulphur sources with one originating from the porphyry and the second one from the country rocks, while oxygen isotopes showed that no meteoric water was involved in the ore formation.

The last aspect of Ewers & Sun's work (1988b) was the investigation of the gold occurrence. They observed gold in the form of inclusions hosted in copper minerals and arsenopyrite, associated with bismuth-tellurides and in the form of electrum, but they did not find any gold-silver-tellurides, in contrast to Torrey (1986). Ewers & Sun suggested that the gold is not early and occurs only in wollastonite skarn or retrograde veins, with some of the gold (mainly electrum) being reworked, while Nethery & Barr (1998) assigned the gold-bearing arsenopyrite, which occurs together with molybdenite and quartz in stockwork, to a mesothermal event. Creighton (2005) suggested another theory for the timing of gold. She postulated that the gold is hosted together with silver, bismuth und tellurium in very small-scale carbonate veins, which cut through earlier skarn. In this case the observation by Torrey (1986) and Ewers & Sun

(1988b) would be correct regarding the general gold occurrence (skarn), but it would also show that both of them have missed the very small scaled carbonate veins.

Woodbury (1994) investigated the geochemical composition of the porphyries from Red Dome, but he could not show that the Nested and Crowded Porphyry are distinct geochemically, which could be because all of his samples were heavily altered. However, he postulated that the geochemistry of the porphyries show a A-type affinity and suggested that the porphyries from Red Dome are linked to the Lags Supersuite, although Bultitude et al. (1993b) had shown that the highly fractionated, partly reduced porphyry from Red Dome (it is not known whether they investigated Nested and Crowded Porphyry or only one) is of I-type affinity and also shows other characteristics typical of the O'Brien's Creek Supersuite. As this granitic supersuite is only present further south to the Chillagoe district and is very similar to the Ootann Supersuite, which is quite abundant in the district, Bultitude et al. assigned the Red Dome porphyry to the Ootann Supersuite. Woodbury (1994) additionally conducted K-Ar isotope studies of sericite yielding 310 ± 4 Ma and 304 ± 2 Ma. Perkins & Kennedy (1998) also conducted isotopic dating, but they used the U-Pb isotopic system to determine the age of the Crowded Porphyry. They obtained an age of 322 ± 3 Ma, which is typical for plutonic rocks of the O'Brien's Creek Supersuite, but too old for granites of the Ootann Supersuite and therefore the porphyry at Red Dome can be assigned to the O'Brien's Creek Supersuite.

Chapter 3: Petrography and paragenesis of the Redcap, Mungana and Red Dome deposits

3.1. Introduction

The previous chapter introduced the Red Dome, Mungana and Redcap deposits and summarised the previous work conducted at each. While prior studies have focussed on Red Dome (Smith 1985; Torrey 1986; Torrey et al. 1986; Ewers & Sun 1988a & b; Ewers et al. 1990; Woodbury 1994; Holland 1994; Nethery & Barr 1998) resulting in a detailed paragenetic sequence for the skarn and mineralisation types, only a limited amount of research has been carried out at Mungana (Halfpenny 1991; Woodbury 1994; Nethery & Barr 1996; Barr 1998; Rubenach 2010) and Redcap (Paverd 1971; Musumeci 1974; Rubenach & Cuff 1985) focussing mainly on the surface geology, oxidation zone and breccia environment. So far the geological evolution of the subsurface, unoxidised environment has only been explained partly for the Mungana deposit and not for Redcap at all. With new drill core available at all three deposits, this chapter aims to develop a geological history based on detailed paragenetic sequences of the Mungana and Redcap deposits, as well as to review and update the existing paragenesis for the base and precious metal mineralisation of Red Dome (created by Torrey in 1986).

To achieve this, parts of 36 drill holes (~2,000 m) were re-logged and a suite of about 250 samples from surface outcrops and drill core representing the main lithological units, major skarn types, their alteration and associated mineralisation was collected (listed in appendix 1). From these samples about 150 polished thin and thick sections were made and investigated by transmitted and reflected light microscopy. However, some minerals could not be identified by microscope and in this case they were analysed by electron microprobe using a JEOL JXA 8200 with the analyses being listed in appendix 2. Overall, on the basis of the observations a paragenetic sequence of skarn and ore formation was established and the spatial distribution and mineralogical composition were identified. Special emphasis had been on the gold and base metal occurrences. The chapter concludes with a comparison of all three deposits, highlighting their similarities and major differences.

3.2. Redcap deposit

3.2.1. Field relationships

Mapping was conducted on a 1:1000 scale at Redcap (Fig. 3.2.1), covering the three mineralisation zones (here called lines, see chapter 2), from southwest to northeast: Penzance, Victoria and Redcap-Morrison lines (Plate 3.2.1.A).

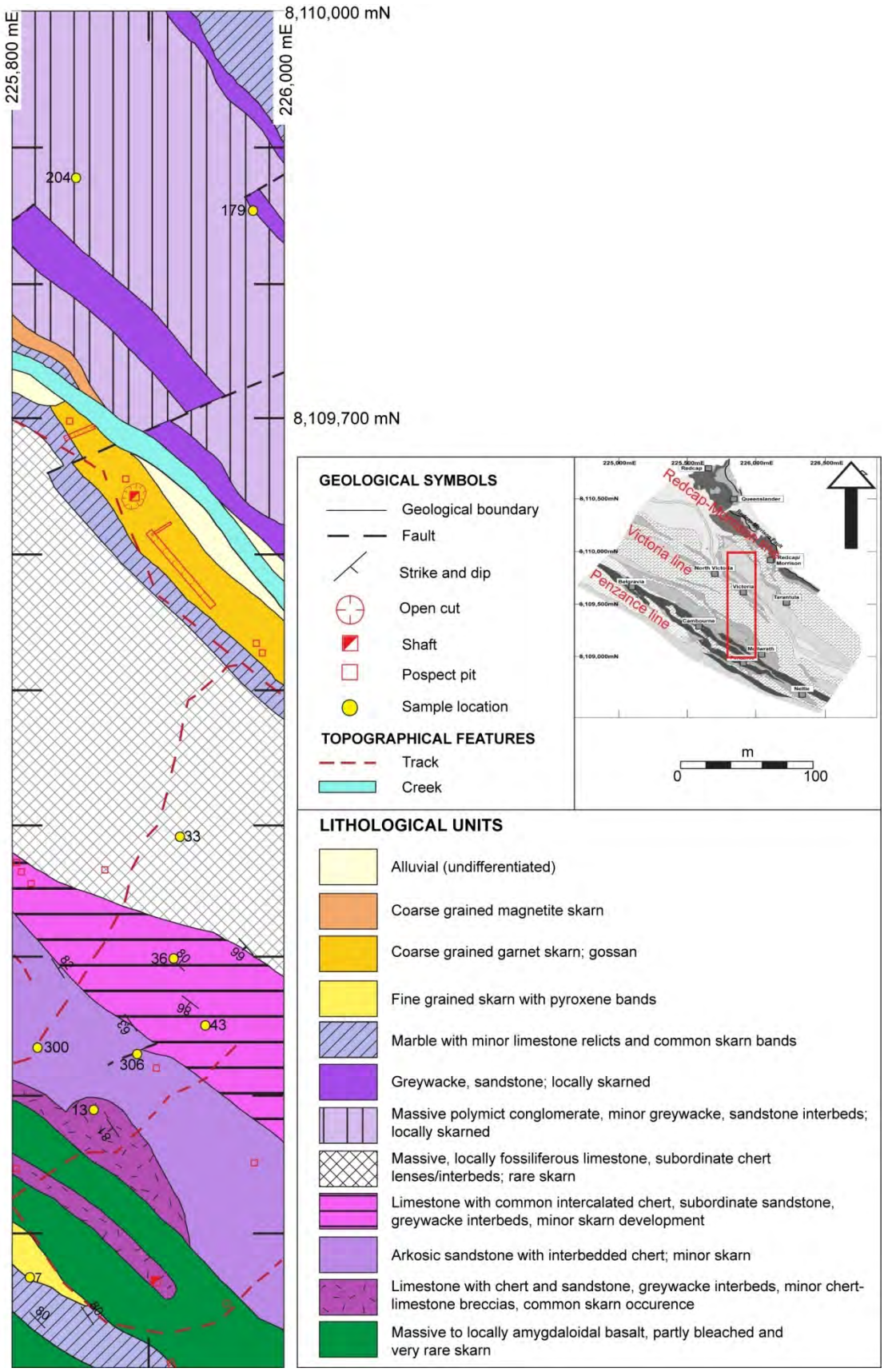

Figure 3.2.1. Map of the Redcap area showing the distribution of lithologies of the Chillagoe Formation and the occurrence of skarns; key sample localities, mentioned in the text, are indicated by circles, except sample BL67, 111 and 254 which are outside of the map area; a full list of sample localities is shown in appendix 1.

The aims of this exercise were to a) get a better understanding of the skarn and ore hosting lithologies (Chillagoe Formation), b) improve an existing map, compiled by Patterson in 1996, regarding the occurrence and classification of skarns and c) check whether any mineralisation occurs at the surface. The Siluro-Devonian Chillagoe Formation consists of NW-trending, in general steeply-dipping (≥80 °) limestone, basalt, and different siliciclastic rocks (Plate 3.2.1.B), with abundance varying within the three mineralisation lines (Fig. 3.2.1.). During late Devonian to middle Carboniferous these rocks experienced regional metamorphism of up to lower greenshist facies (Vos et al. 2006b), but because of briefness the pre-fix ‘meta’ is omitted in the descriptions.

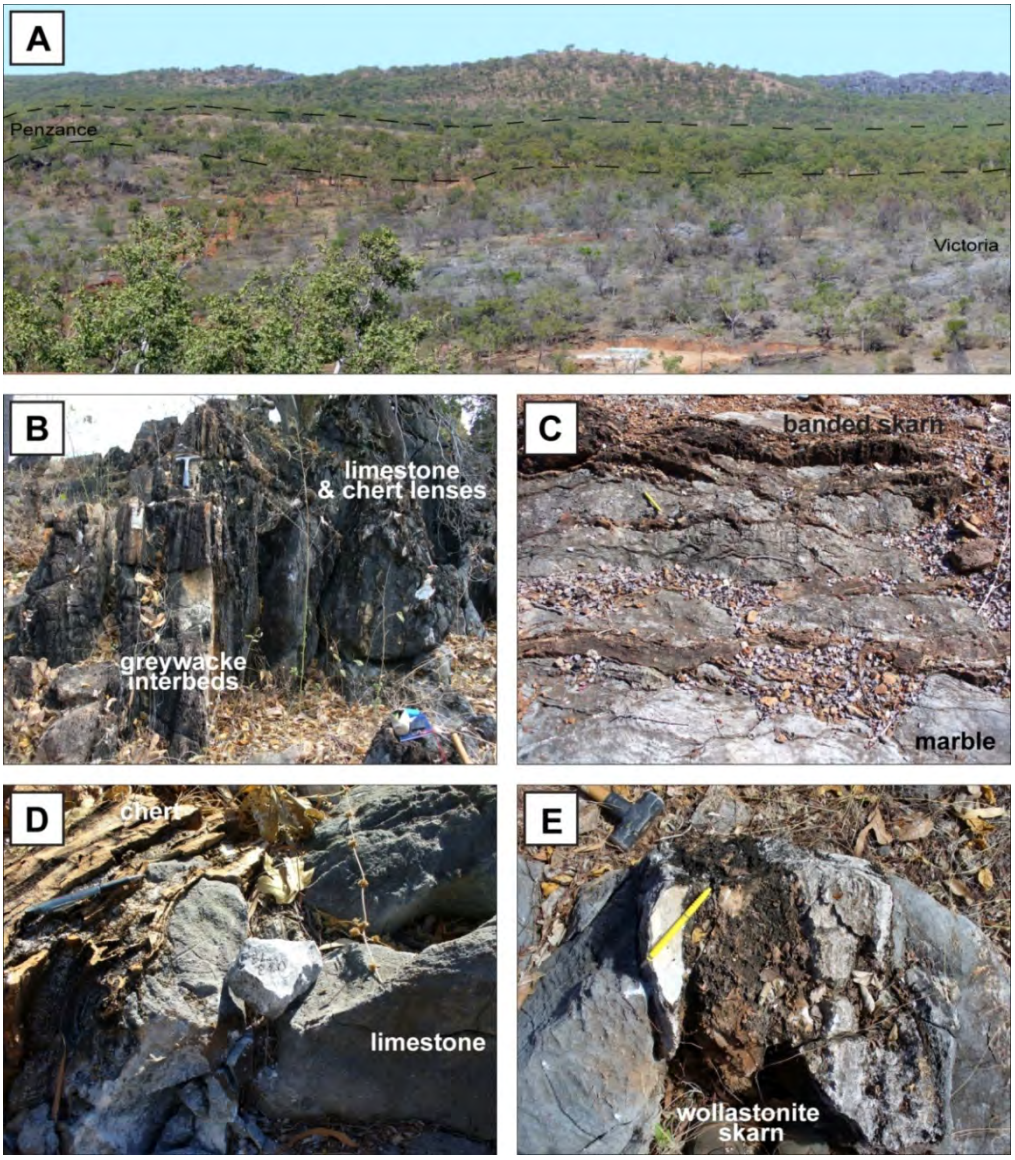

Plate 3.2.1. Photographs of representative outcrops from Redcap; **A**: NW-SE view of the field area showing the Victoria and Penzance lines; **B**: interbeds of steep dipping greywacke and limestone with minor chert lenses and partly skarned contacts; **C**: banded skarn layers in marble at Penzance; **D**: limestone with intercalated chert; **E**: limestone with sharp contacts to marble and skarn.

The Penzance line is dominated by basalt and minor limestone with interbeds of chert, sandstone and greywacke (Plate 3.2.1.C), while the Victoria line is comprised of arkose, limestone units with minor chert and greywacke interbeds and nearly pure, massive limestone units (Plate 3.2.1.B, D, E). The Redcap-Morrison line in the north-eastern part of the Redcap area consists of massive conglomerate with minor interbeds of greywacke. Only a small amount of limestone crops out in this mineralisation line.

The degree of skarn occurrence varies within the area. Massive skarn bodies (maximum 35 metres thickness) are rare and can only be found at the Penzance line and the most north-eastern part of the Victoria line at the banks of the Redcap Creek, while bleaching of siliciclastic units and recrystallisation of limestone to marble are common features throughout the region. In the following part major lithological units of the Chillagoe Formation and their related skarn types will be described

3.2.1.1. Limestone with chert lenses and layers and associated skarn types

This unit typically occurs within the Victoria line and only to a small amount within the Penzance line. The limestone is blue grey in colour, partly contains abundant fossils or their fragments (corals, crinoids and brachiopods) and shows karren eroded bluffs (Plate 3.2.1.1.A & B). In some places the limestone is intercalated with light grey, usually <10 cm thick, chert layers and lenses (Plate 3.2.1.D, Plate 3.2.1.1.C), or occur at interbeds within siliciclastic (mainly greywacke, siltstone and minor sandstone) units (Plate 3.2.1.B). Where karst formation took place the chert-limestone assemblage occurs as breccias with chert comprising angular clasts in a limestone matrix, which is replaced by wollastonite during metasomatism (Plate 3.2.1.1.D).

Due to contact metamorphism the limestone is locally recrystallised to white coarse grained marble, while the chert was affected by bleaching (Plate 3.2.1.1.E), and during later metasomatism wollastonite skarn formed at the contact between the two rock units. The bleached zones are very fine grained, which makes it impossible to determine their mineralogical composition, but based on their hardness it is assumed that those rocks are enriched in silica. Within the bleached rocks rare elliptical or circular zones occur which are usually 1 cm diameter (up to 1.5 cm) and consist from rim to core of <1 mm-sized fibrous vesuvianite, ~1 mm-sized euhedral garnet and on average 0.25 mm-sized anhedral diopside (Plate 3.2.1.1.F). Locally, small amounts of 50 µm to 0.1 mm-sized anhedral grains of chalcopyrite, pyrite and pyrrhotite occur in the wollastonite skarn and vesuvianite-garnet-diopside zones, but they never make up more than 0.5 % of the rocks. Neither rocks are usually

affected by retrograde alteration, but an up to 5 cm thick, porous, brown weathering crust, has developed on the surface.

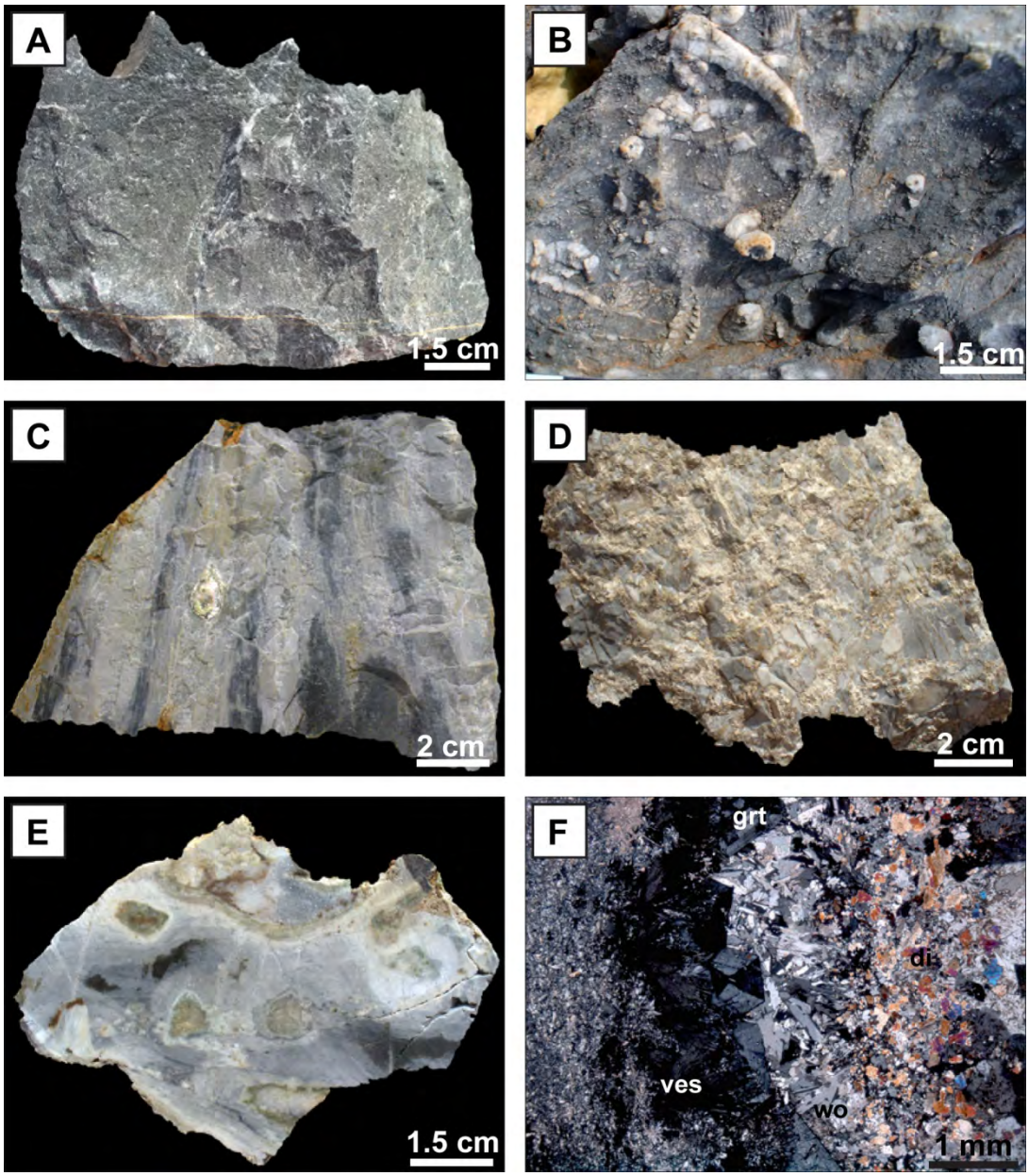

Plate 3.2.1.1. Photographs and transmitted light photomicrographs (XPL: crossed polars) of representative limestone, chert and associated skarns from Redcap; **A**: blue-grey limestone with "mini-karren" eroded surface (BL 33); **B**: fossil bearing limestone partly recrystallised to marble (BL 33); **C**: chert with a 2 cm skarn lenses consisting of vesuvianite, garnet and diopside (BL 43); **D**: former chert-limestone breccia with the limestone component being replaced by wollastonite during metasomatism (BL 13); **E**: bleached skarn with elliptical zones of vesuvianite-garnet-diopside (BL 36b); **F**: close up of elliptical zone with vesuvianite (ves), garnet (grt), wollastonite (wo), diopside (di) from core to rim (XPL, BL 36b).

3.2.1.2. Basalts and associated skarn types and mineralisation

Basalts only crop out along the Penzance line. Where least affected by metamorphism and metasomatism, they are dark green in colour and very fine grained (Plate 3.2.1.2.A), although some amygdaloidal varieties also occur. The basalts consist of 0.2 mm-sized subhedral clinopyroxene and subhedral lath shaped feldspar of the same size with minor 50 µm-sized orange-brown titanium-rich phases, which have been titanomagnetite before contact metamorphism occurred (Holland 1994). The pyroxene and feldspar are almost always affected by alteration resulting in the pyroxenes being replaced by actinolite and feldspar altered to epidote.

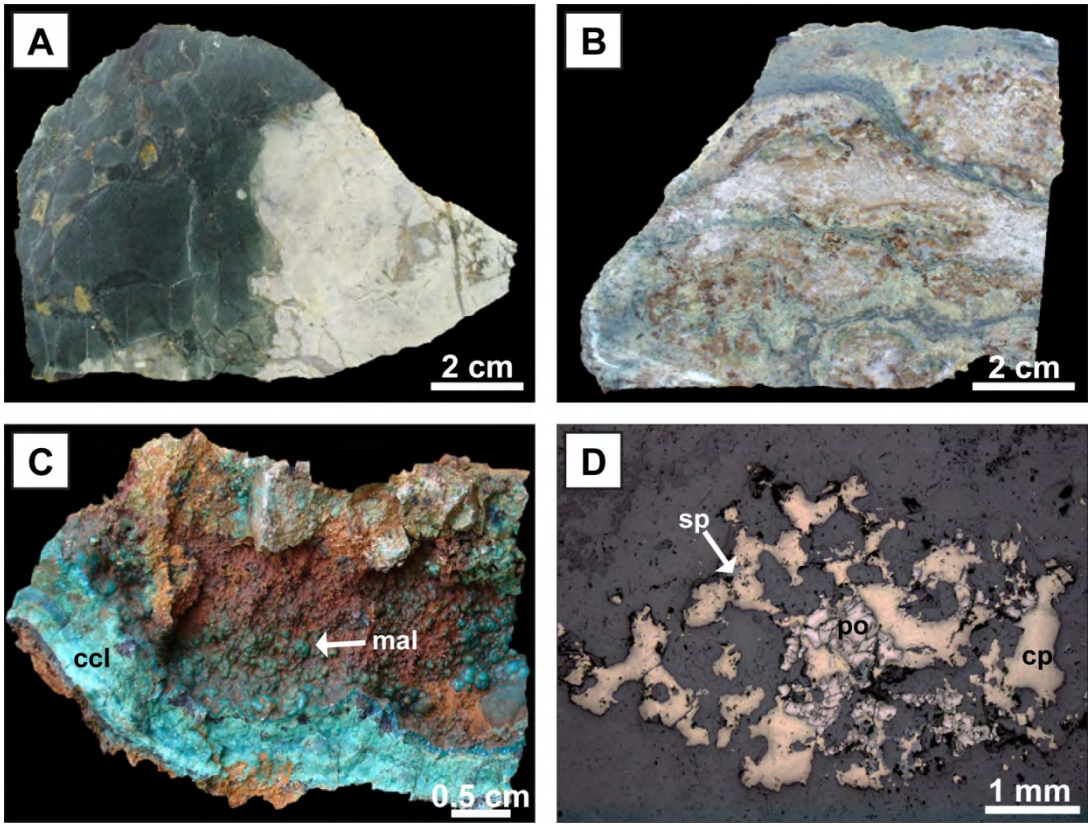

Plate 3.2.1.2. Photographs and reflected light photomicrographs (RL) of representative basalt, associated skarn types and mineralisation from Redcap; **A**: unbleached and bleached basalt (BL 111b); **B**: banded garnet-vesuvianite-wollastonite-clinopyroxene skarn (BL 7); **C**: botryoidal malachite (mal) and chrysocolla (ccl) (BL 67c); **D**: pyrrhotite (po), chalcopyrite (cp) and sphalerite (sp) in skarn vein (RL, BL 111b).

The basalts are usually bleached and cut by skarn veins (Plate 3.2.1.2.A). These veins consist of clinopyroxene and K-feldspar in the outer zone of the vein while the centre of the vein consists mainly of carbonate and quartz hosting some epidote rimmed sulphides. Chalcopyrite is the most abundant ore phase and can make up to 1 % of the skarn zones in the basalt. It is associated with pyrrhotite and very rarely red-brown sphalerite (Plate 3.2.1.2.D). Minor malachite, partly with botryoidal habitus, but also other secondary copper phases like

chrysocolla ($(Cu,Al)_2H_2Si_2O_5(OH)_4$ x nH_2O; Plate 3.2.1.2.C) and azurite on the surface indicate the occurrence of copper mineralisation at depth.

At recrystallised limestone-basalt boundaries typically banded skarn occurs. It consists of a varying amount of 1 mm-sized (up to 5 mm) subhedral to euhedral green garnet and vesuvianite, 0.35 mm, fibrous, white wollastonite and 0.5 mm thick, dark green bands of 0.2 mm-sized anhedral to roughly prismatic clinopyroxene. The rock is commonly affected by retrograde alteration. Wollastonite and vesuvianite have partially broken down to quartz and calcite, and clinopyroxene is retrogressed to actinolite or a chlorite-clay mixture where the process is advanced. Minor mineralisation in form of 0.24 mm-sized anhedral, honey coloured sphalerite, 80 µm-sized chalcopyrite as well as <20 µm grains of pyrite and pyrrhotite also occur in the skarn, but the total abundance of sulphides within this skarn type is less than 1 %.

3.2.1.3. Siliciclastic units and associated skarn types

Siliciclastic rocks occur throughout the Redcap area, but their thickness, abundance and type varies between the three lines. At the Penzance line mainly greywacke and siltstone crop out in form of centimetre to maximum one metre thick beds intercalated within limestone units, while along the Victoria line a massive arkosic unit (up to 100 m thick) is the dominant siliciclastic rock type although a minor amount greywacke, chert and basalt-breccias occur. The Redcap-Morrison line hosts the major amount of siliciclastics, which consist of a massive conglomerate with minor interbeds of greywacke. Together they reach a thickness of nearly 250 m.

Except the arkose and breccias the mineral mode for the siliciclastics is similar and therefore their description is summarised. In general, the siliciclastic rocks are medium to coarse grained and poorly to moderately sorted. The colour ranges from dark grey to greenish-yellow. Major components are quartz, feldspar and fragments of chert, quartzite and other rocks of mainly metamorphic origin. The quartz grains range from 75 µm to 5 mm in size and are angular to subround. Feldspar grains are of 1-2 mm size, angular to subangular and strongly altered to clay. Where relicts are preserved the feldspar can be identified as microcline. The rock fragments consist of chert and quartzite (Plate 3.2.1.3.C & D). The size of the clasts is generally between 0.5 and 5 mm, but within the conglomerate they can be up to 50 cm. Minor mineral phases in the siliciclastics are 40 µm to 1mm lath shaped orange-brown biotite (maximum 3 % of the rock), ~25 µm-sized anhedral rutile as well as up to 60 µm-sized zircons and 20-50 µm-sized (very rarely up to 0.3 mm) anhedral pyrite, pyrrhotite and chalcopyrite, with the sulphides contributing maximum 1 % to the overall rock composition. Only in one sample (BL 179b) 0.12 mm flaky molybdenite, which forms a 1 cm band, occurs (Plate 3.2.1.3.A & C).

The breccias consists of either chert or basalt clasts in a siliceous matrix and crop out in beds of less than 3 m thickness. The clast size ranges from 0.3 to 1 mm with more angular clasts occurring in the chert breccias while the clasts of the basalt breccia show a minor degree of rounding (Plate 3.2.1.3.B). Other mineral phases than clasts and silicified matrix were not observed in the breccias.

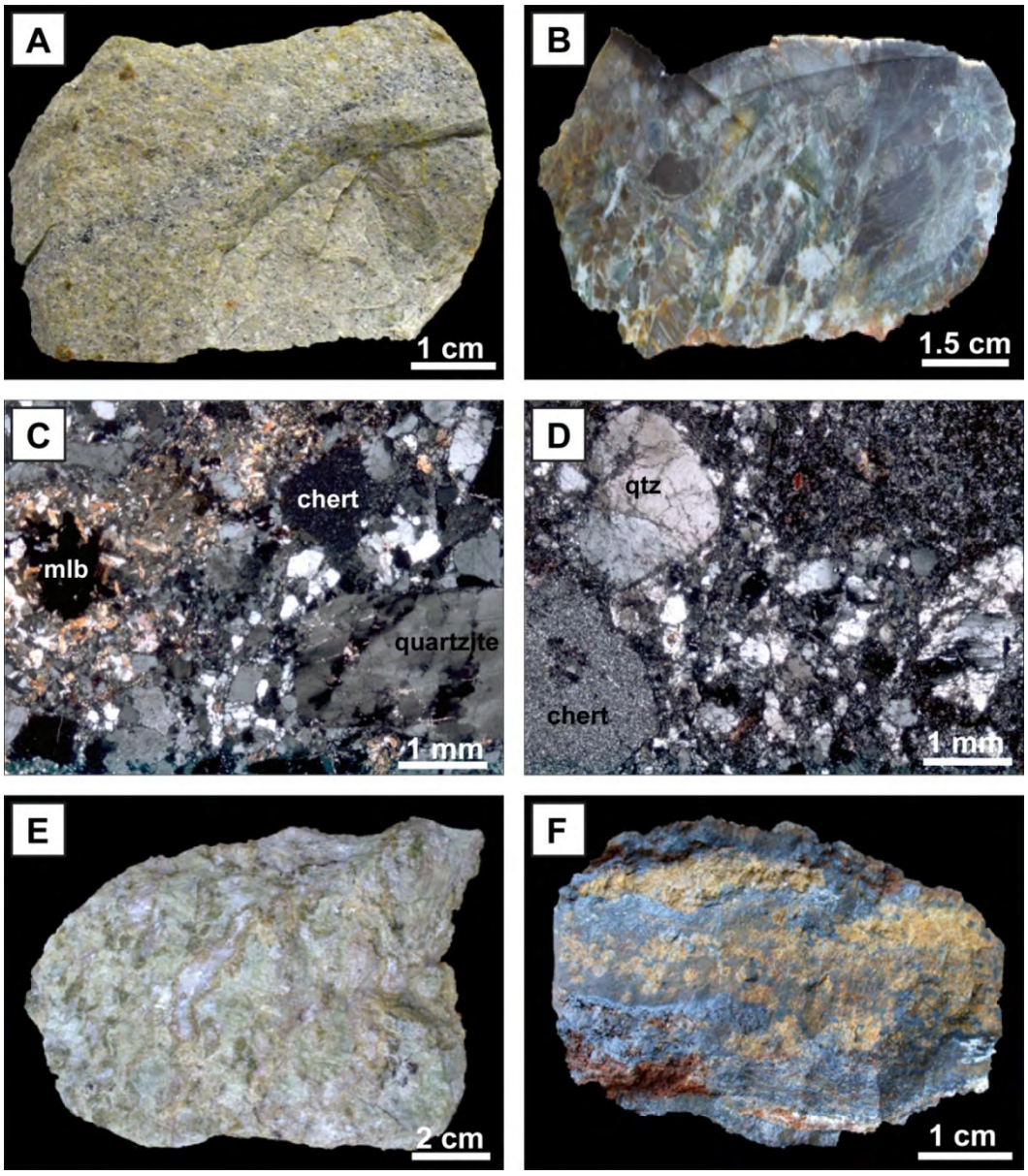

Plate 3.2.1.3. Photographs and transmitted light photomicrographs (XPL: crossed polars) of representative siliciclastics and associated skarn types from Redcap; **A**: epidote altered greywacke with a 1 cm thick band enriched in molybdenite (BL 179b); **B**: breccia consisting of basalt clasts in silicified matrix (BL 306); **C**: greywacke with traces of molybdenite (mlb), (XPL, BL 179b); **D**: fine grained conglomerate with chert and quartz as clasts within a quartz-rich matrix, (XPL, BL 204); **E**: green garnet-wollastonite skarn with relicts of calcite (white), (BL 300); **F**: banded magnetite garnet skarn, with the garnets partly retrogressed to an iron-rich carbonate, (BL 254).

The arkose consists of up to 25 %, on average 0.5 mm-sized angular to subangular feldspar clasts. Its original composition could not be determined, due to advanced alteration. Angular to subrounded quartz of 0.15 to 0.5 mm size, as well as rock fragments of up to 2.5 mm size and 0.15 to 1 mm-sized subhedral, lath shaped, orange brown biotite and 0.25 to 0.7 mm-sized flaky colourless muscovite occur in the rock. The micas can make up to 5 % of the rock.

All siliciclastic rocks, except the breccias, have been affected by alteration with the feldspar component being retrogressed to sericite or epidote and the biotite to chlorite, or, if the process is advanced, to clay minerals. Parts of the siliciclastic sequence have been affected by metasomatism. While some rocks only show bleaching, in general the greywacke, chert-breccias and arkosic unit, other rocks exhibit skarn formation to a varying degree. If the rock has only undergone minor metasomatism, calc-silicate minerals like brown garnet and vesuvianite, green clinopyroxene and white wollastonite occur in elliptical to round zones of maximum 1 cm size (Plate 3.2.1.1.E) with locally traces of up to 0.32 mm-sized anhedral chalcopyrite in the centre of those zones. Where the siliciclastic units are interlayered with limestone units, more skarn has developed along the contact replacing the limestone and building up to 1 m thick beds. This skarn, which can only be found in the SE part of the Victoria line, consists of 0.5 to 3mm-sized subhedral to euhedral green garnet, partly retrogressed to diopside along fractures and on average 0.5 mm-sized fibrous, orange-brown wollastonite rimming calcite (Plate 3.2.1.3.E). No sulphide minerals can be observed.

Another green garnet skarn is associated with magnetite and only crops out at the south eastern banks of Redcap Creek. Its composition varies from pure garnet skarn to garnet magnetite skarn. The green garnet skarn reaches a thickness of up to 35 m, while the garnet magnetite skarn is only 12 m thick. The magnetite is partly altered to hematite or, where advanced, to goethite. Both skarns have been mined in the 1890's for copper, zinc and lead (De Keyser & Wolff 1964).

3.2.2. Redcap Dacite and Belgravia Granodiorite

Two igneous rock units crop out in the north western of the Redcap area. These are the Belgravia Granodiorite, which has intruded into the Chillagoe Formation and Redcap Dacite (Bultitude et al. 1993a), which are bound to the south east by the Redcap-Morrison-Fault. Only the Redcap Dacite is intersected in drill holes (Fig. 3.2.4.) and the fault is represented by a 0.7-3.9 m brecciated zone within the volcanics.

3.2.2.1. Redcap Dacite

The dacite is medium to coarse grained and of light grey to dark brown colour (Plate 3.2.2.1.A). The rock consists of ~25-30 % phenocrysts in an aphanitic groundmass. The phenocrysts are

0.15 to 5 mm-sized angular to subrounded quartz, on average 1.5 mm-sized subhedral to euhedral lath shaped plagioclase and 0.5 to 4 mm-sized subhedral, generally simple twinned, K-feldspar. Up to 5% of the rock consists of orange-brown platy biotite. Associated with biotite are 40 µm to 0.12 mm-sized euhedral zircon, on average 60 µm-sized euhedral apatite, and 40-60 µm-sized cubes of pyrite. Throughout the rock fine disseminated 40 µm to 0.12 mm-sized anhedral pyrrhotite, chalcopyrite and pyrite can occur, but their abundance varies from less than one percent to up to 4 %. The feldspars exhibit partly retrograde alteration to sericite, which gives them a cloudy appearance in thin section. Biotite is partly retrogressed to chlorite. The quartz-molybdenite veins are cut by up to 0.2 mm thick veins consisting of clear quartz and on average 75 µm-sized, anhedral, arsenopyrite (Plate 3.2.2.1.B).

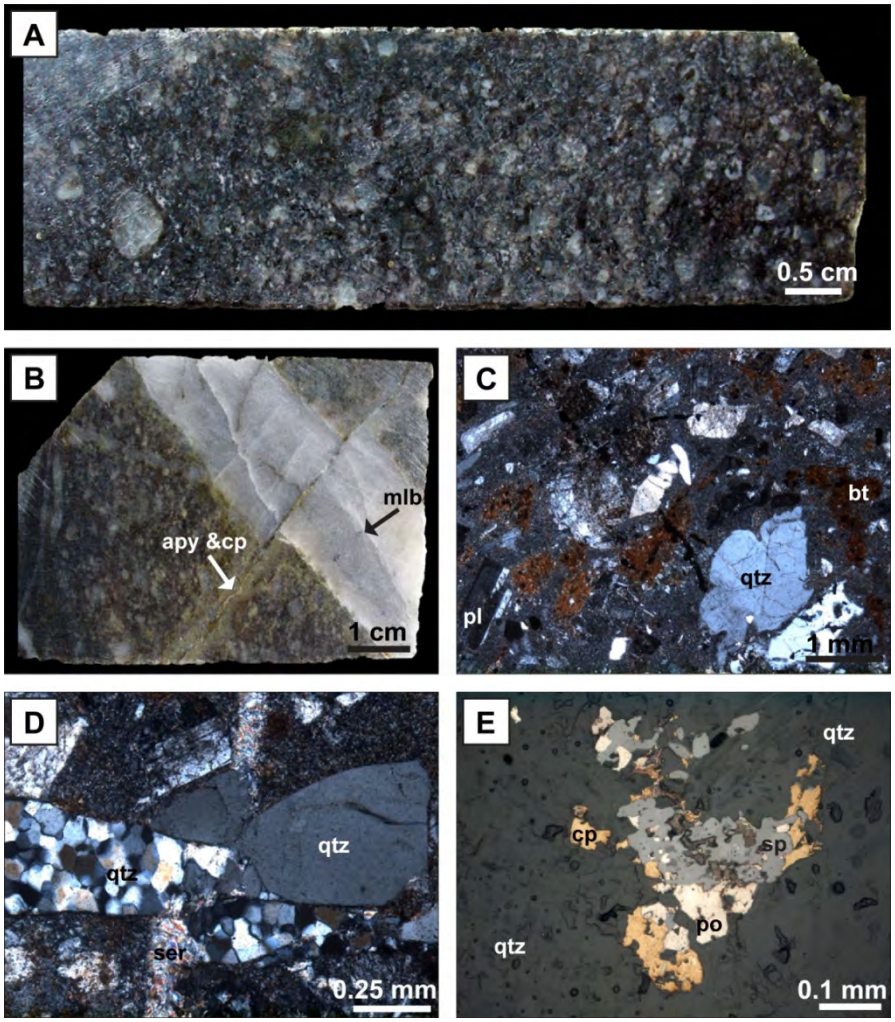

Plate 3.2.2.1. Photographs, transmitted (XPL: crossed polars) and reflected light (RL) photomicrographs of the Redcap Dacite; **A**: dacite with coarse grained phenocrysts (949-525.29); **B**: dacite cut by white quartz-molybdenite vein which is then cut by a clear quartz-arsenopyrite vein (951-601.80); **C**: dacite showing quartz (qtz), plagioclase (pl) and biotite (bt) phenocrysts in an aphanitic groundmass (XPL, 949-525.29); **D**: sugary quartz (qtz) vein cut by a sericite (ser) vein (XPL, 949-525.29); **E**: pyrrhotite (po), chalcopyrite (cp) and sphalerite (sp) in a quartz (qtz) vein (RL, 951-597.90).

Locally the dacite is cut by milky white quartz veins of 2 mm to 15 cm thickness. In the centre of the veins 0.1 mm-sized, flaky molybdenite occurs, while the quartz grains are of 0.5 mm size. Another type of mineralised quartz veins consist of up to 0.5 mm-sized sugary, fluid inclusion rich (~5-10 µm, 30 % vapour phase and pyrite, halite or chalcopyrite daughter crystals) quartz and pyrrhotite, sphalerite and chalcopyrite (3.2.2.1.D & E). The 15 µm to 0.4 mm-sized anhedral pyrrhotite and 40 µm to 0.25 mm-sized chalcopyrite are commonly intergrown. Sphalerite, ranging in size from 0.12 to 0.3 mm, is less abundant than the other two ore phases. While a relationship between the quartz-molybdenite and quartz-arsenopyrite can be observed, the timing of the pyrrhotite-chalcopyrite-sphalerite veins remains unknown.

3.2.2.2. Belgravia Granodiorite

The granodiorite consists of 1-3 mm quartz, on average 1.5 mm lath shaped plagioclase, 1mm simple twinned K-feldspar and 0.75 mm tabular brown biotite and 1.5 mm roughly prismatic brown hornblende (Plate 3.2.2.2.A). Minor phases are 50 µm to 0.15 mm titanomagnetite with rare ilmenite exsolution lamellae (Plate 3.2.2.2.D), on average 75 µm-sized euhedral apatite and <0.12 mm-sized euhedral zircons.

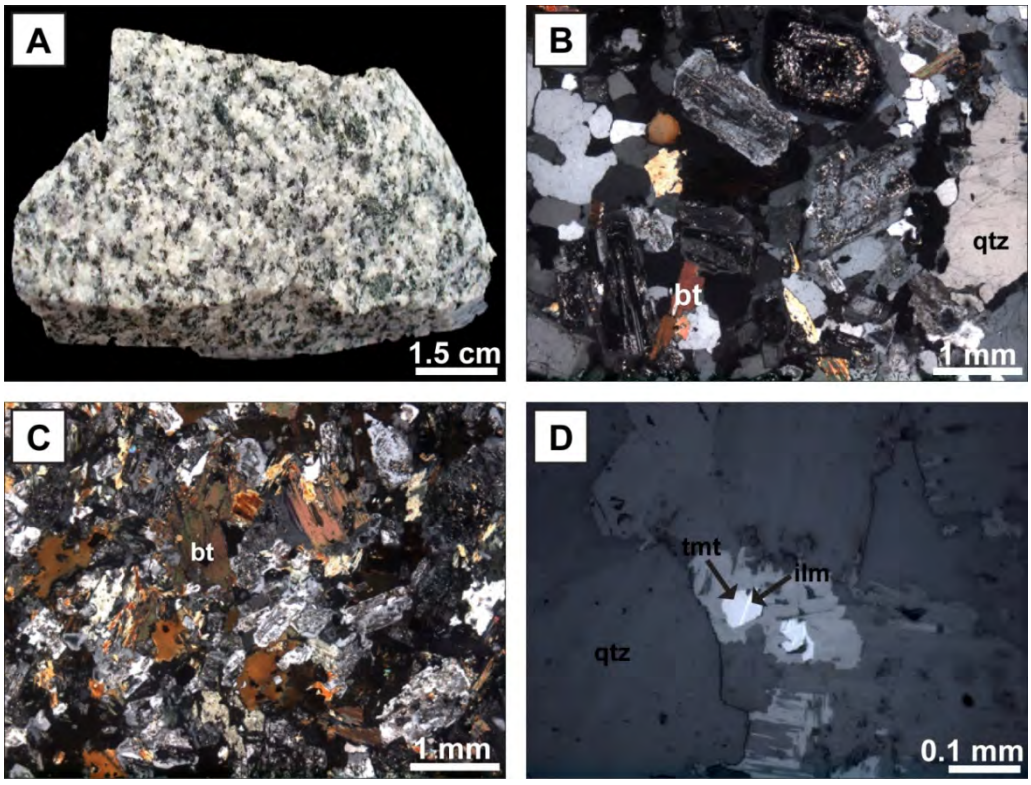

Plate 3.2.2.2. Photographs, transmitted (XPL: crossed polars) and reflected light (RL) photomicrographs of the Belgravia Granodiorite; **A**: granodiorite (BE-1); **B**: typical mineralogy of the granodiorite consisting of quartz (qtz), plagioclase (pl) and biotite (bt) (XPL, BE-1); **C**: microgranular enclave consisting of the same mineralogy as the granodiorite, only with more abundant mafic phases (XPL, BE-1); **D**: titanomagnetite (tmt) with ilmenite (ilm) exsolution lamellae in biotite (medium grey) (RL, BE-1).

In places up to 1.5 cm elliptical enclaves occur in the granodiorite that are enriched in the mafic minerals (Plate 3.2.2.2.C), but quartz and feldspar also occur. Except the enrichment of mafic phases the only other difference between the elliptical zones and the remaining rock is the smaller grain size, which for all minerals is up to 0.75 mm. Only one grain of 75 µm-sized anhedral chalcopyrite was observed. In general the granodiorite seems to be barren (Bultitude et al. 1993a).

3.2.3. Skarn types, alteration and associated mineralisation

Three major skarn types can be distinguished in the subsurface environment along the Victoria line based on their spatial occurrence and mineralogy. These are: 1. garnet skarn, 2. wollastonite skarn and 3. clinopyroxene skarn. The garnet skarn is the most abundant skarn type. Clinopyroxene skarn normally can be found at depth, proximal to the Redcap Dacite, while wollastonite skarn seems to occur only in the south eastern part of the Victoria line. Based on their abundance and mineralogical composition, some skarn types are described below in greater detail than other ones.

3.2.3.1. Garnet skarn

This skarn type consists of either green or brown 1-5 mm subhedral to euhedral garnets. While the green type can be commonly found associated with magnetite or sulphides adjacent to marble contacts (Plate 3.2.3.1.A, B & C), red-brown varieties are more likely to be associated with hedenbergite, and pale brown to buff coloured ones only occur in retrograde altered siltstones. In general the garnets are of 1-5 mm size, subhedral to euhedral, usually show oscillatory growth zones and are optically isotropic in thin section. Only the buff coloured garnets are anisotropic. Mineral chemistry revealed that with exception of the buff coloured garnets, which are grossular, all other garnets are 95-100 % andradite (see chapter 4).

Minor wollastonite and apophyllite ($(K,Na)Ca_4Si_8O_{20}(F,OH) \times 8H_2O$), at skarn-marble contacts only), or on average 1mm prismatic dark green hedenbergite or 0.5 mm anhedral quartz and calcite occur interstitial to the garnets, although the last assemblage is assumed to be of retrograde origin, because the quartz and calcite can also be frequently found as fracture fills within the garnet crystals. The garnets are partly replaced by on average 75 µm-sized anhedral, pale green diopside, which occurs either within or surrounding the garnets (Plate 3.2.3.1.D).

In places the green garnet is intergrown with magnetite, which occurs in several centimetre thick patches or stringers. Both minerals are cut by up to 1 cm thick veins of pyrrhotite which is intimately associated with chalcopyrite. Red-brown sphalerite occurs interstitial to the garnets. The sphalerite grains are up to 1.5 mm in size, but on average 0.5 mm, can show minor

exsolution of <20 µm-sized chalcopyrite or are rimmed by anhedral chalcopyrite. Galena with on average 5 µm-sized native bismuth inclusions also seems to be later than the sphalerite (Plate 3.2.3.1.E). All sulphides are partly rimmed by on average 0.4 mm-sized anhedral, marcasite, which itself is partly retrogressed to goethite. Very rarely, the andradite skarn hosts gold mineralisation, which occurs in the form of electrum and is associated with native bismuth and pilsenite (Bi_4Te_3) in calcite filled fractures.

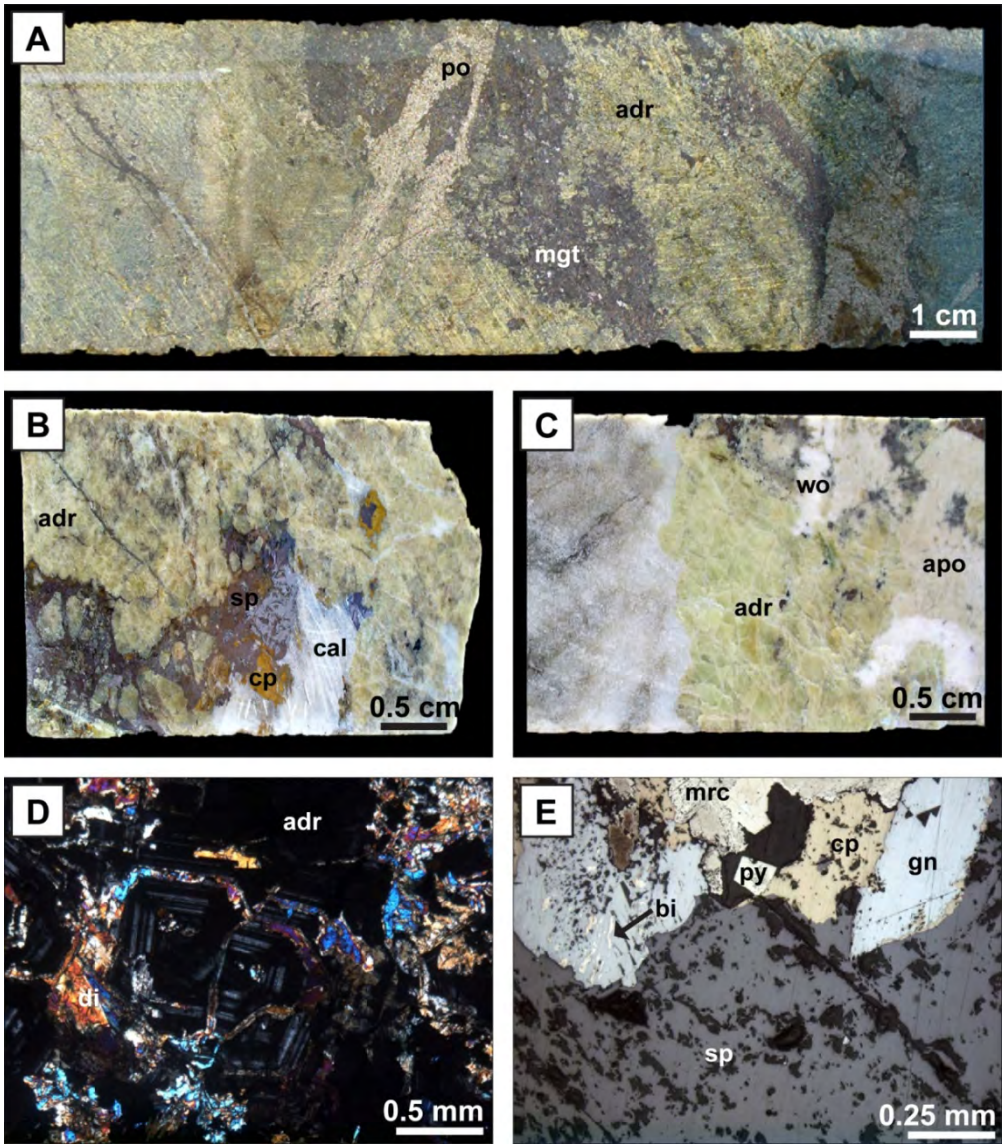

Plate 3.2.3.1. Photographs, transmitted (XPL: crossed polars) and reflected light (RL) photomicrographs of garnet skarn and associated mineralisation; **A**: Green andradite (adr) magnetite (mgt) skarn cut by pyrrhotite (po), (949-220.55); **B**: green andradite (adr) skarn with partly interstitial sphalerite (sp), chalcopyrite (cp) mineralisation and calcite (cal), (949-165.80); **C**: green andradite (adr) skarn at marble contact associated with wollastonite (wo) and apophyllite (apo), (949-172.24); **D**: euhedral andradite (adr) with oscillatory growth zones partly retrogressed to diopside (di), (XPL, 952-575.2 I); **E**: base metal assemblage consisting of sphalerite (sp), later chalcopyrite (cp), galena (gn), native bismuth (bi), pyrite (py) and very late, partly retrogressed marcasite (mrc), (RL, 949-165.80).

3.2.3.2. Wollastonite skarn

Wollastonite skarn is the dominant skarn type in the south eastern part of the Victoria line. It consists of 0.12 to 2 mm-sized fibrous wollastonite, which is intergrown with 0.5 to 5 mm-sized brown garnet (Plate 3.2.3.2.A & B) or up to 1.5 mm-sized radiating rosettes of brown vesuvianite (Plate 3.2.3.2.C & D). Very small grains (1-50 µm) of huttonite ($ThSiO_4$) are disseminated through the rock and were identified by EDS.

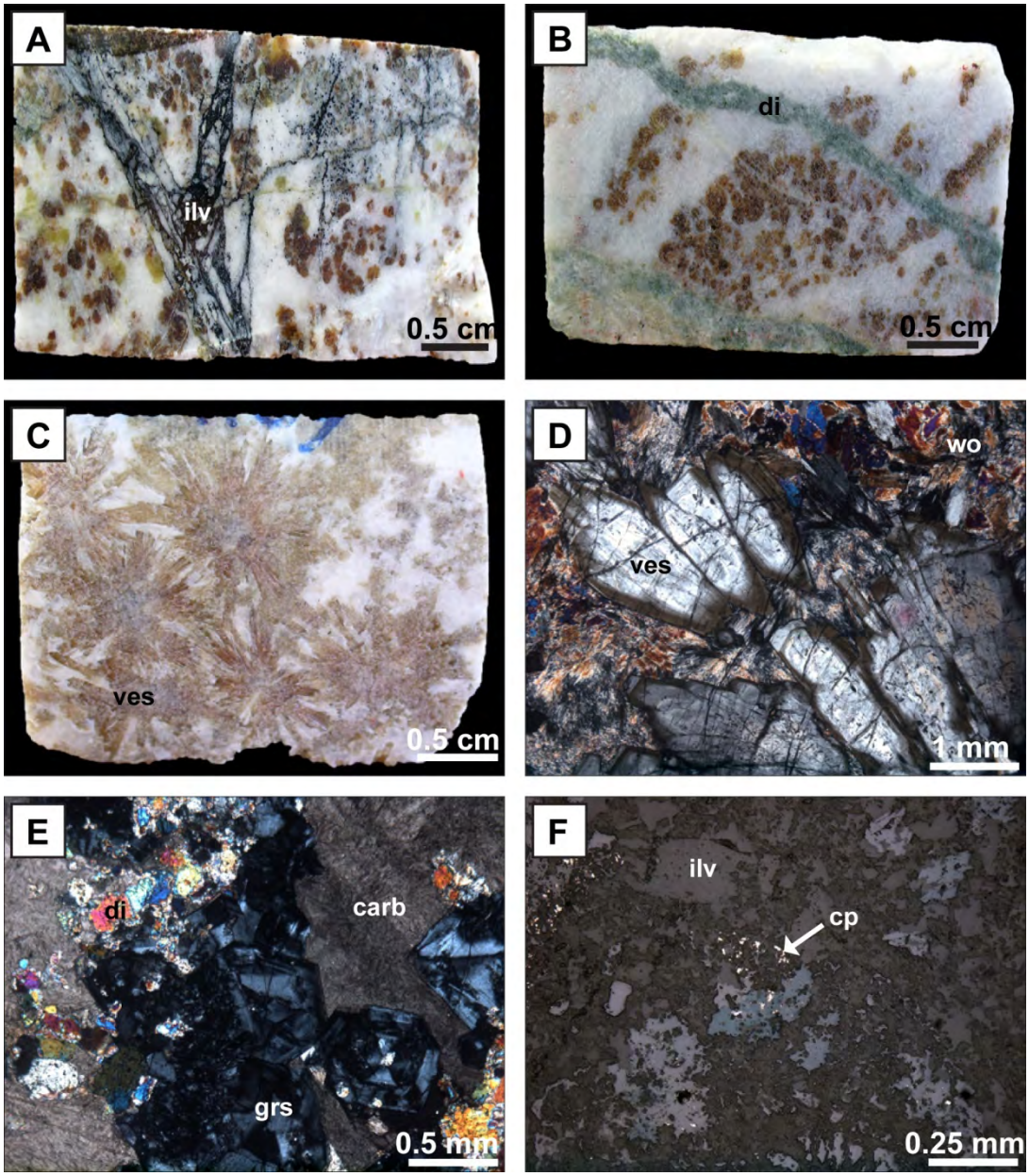

Plate 3.2.3.2. Photographs, transmitted (XPL: crossed polars) and reflected light (RL) photomicrographs of wollastonite skarn and associated mineralisation; **A**: Euhedral, brown and green andradite in wollastonite cut by later ilvaite (ilv), (974-363.14); **B**: brown andradite in wollastonite cut by later diopside (di), (974-351-27); **C**: radiating rosettes of brown vesuvianite (ves) in wollastonite, (974-291.01); **D**: vesuvianite (ves) in wollastonite (wo), (XPL, 974-291.01); **E**: euhedral grossular (grs) associated with diopside (di) and carbonate (carb), (XPL, 974-291.01); **F**: ilvaite with partly associated chalcopyrite, (RL, 974-351.27).

In places the wollastonite skarn is cut by either 0.25 mm-sized green diopside veins or by black 0.25 mm-sized ilvaite ($CaFe^{2+}{}_2Fe^{3+}(Si_2O_7)O(OH)$) veins. The ilvaite sometimes occurs in form of radiating grains and can be very weakly magnetic. Minor anhedral 5-40 µm-sized chalcopyrite (less than 0.5 % of the rock) is associated with the ilvaite (Plate 3.2.3.2.F). Other sulphides were not observed.

The wollastonite skarn shows minor retrograde alteration. The wollastonite broke down to a brownish stained carbonate-quartz mixture preserving the fibrous texture of the original mineral while the brown garnet (original of andraditic composition) retrogressed to grossular and diopside. The grossular garnets are on average of 0.5 mm size, euhedral and yellowish-green in colour, while the diopside with an average size of 0.2 mm is anhedral and pale green (Plate 3.2.3.2. E).

3.2.3.3. Clinopyroxene skarn

Clinopyroxene skarn occurs mainly adjacent to the Redcap-Morrison fault at levels deeper than 400 m beneath surface, and only occurs in a smaller amount in shallower levels (between 100-200 m below surface) rimming semi-massive to massive sulphides zones (see chapter 3.2.4.2.).
The skarn consists of 0.15 to 4 mm-sized anhedral to stubby prismatic, dark green hedenbergite. In places it is associated with up to 1 cm-sized anhedral pink K-feldspar (Plate 3.2.3.3.A), on average 0.25 mm-sized anhedral to subhedral, red-brown andradite (Plate 3.2.3.3.B) or up to several centimetre thick patches or stringers of magnetite (Plate 3.2.3.3.E).

The hedenbergite skarn may be cut by either 2 cm thick veins consisting of 0.25 to 1.5 mm-sized anhedral, pale green diopside or milky white veins consisting of on average 0.3 mm-sized, sugary quartz which hosts 75 µm to 0.45 mm-sized, flaky molybdenite and 50 µm to 0.12 mm-sized, anhedral scheelite. Around these veins there is an alteration halo of on average 0.3 mm-sized blue-green coloured amphibole, which is partly retrogressed to chlorite or where advanced to nontronite ($Na_{0.3}Fe_2((Si,Al)_4O_{10})(OH)_2$ x nH_2O). Electron microprobe analysis of this amphibole did not reveal its composition. Although looking “fresh” the mineral was pervasively altered on the scale of a few microns, such that the analysis reflects a mixture of the original mineral phase and secondary material.

Minor on average 75 µm-sized anhedral, pyrrhotite and chalcopyrite occur in the clinopyroxene skarn. Both are later than magnetite (Plate 3.2.3.3.E) and chalcopyrite also rims earlier molybdenite (Plate 3.2.3.3.F).

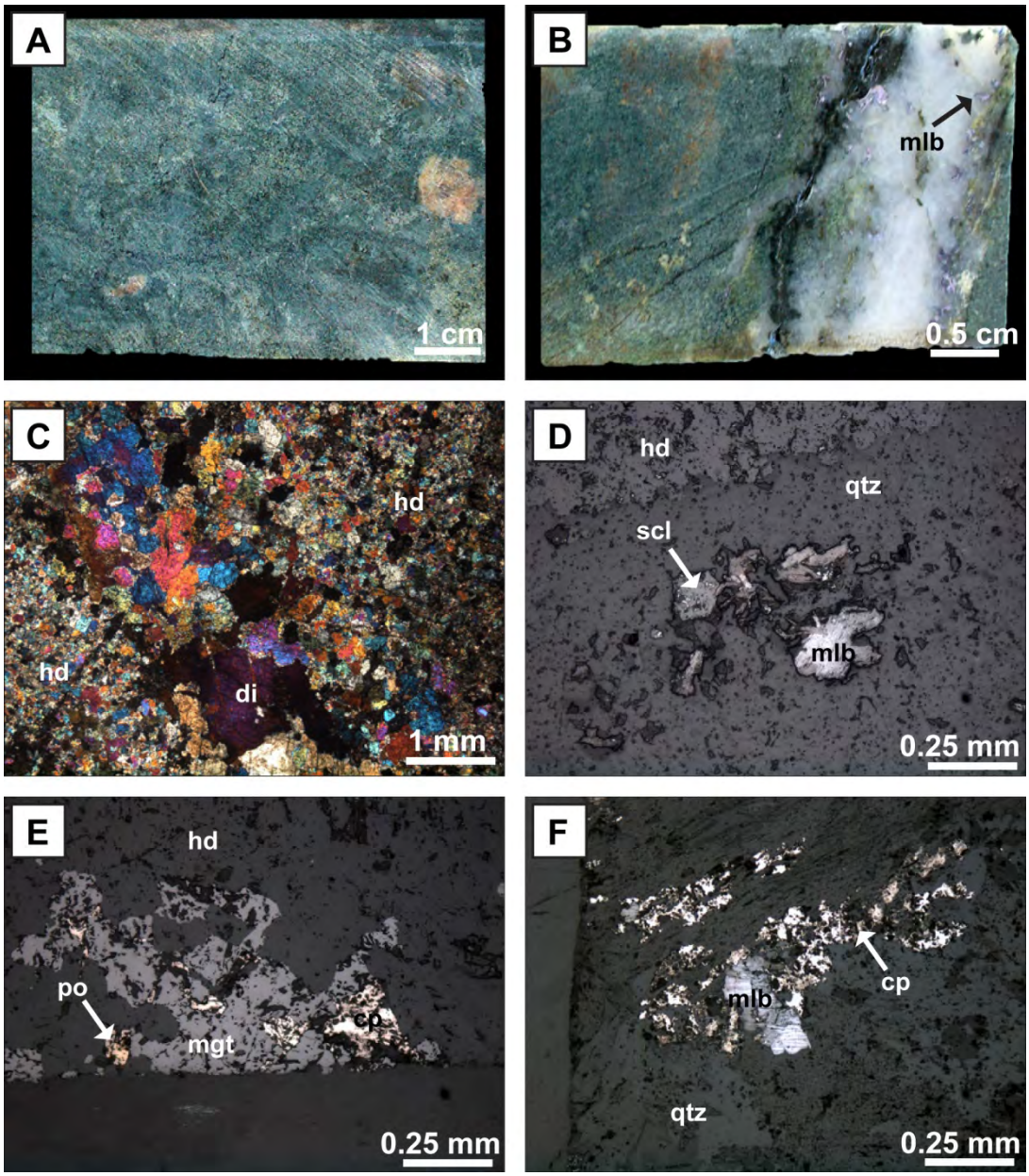

Plate 3.2.3.3. Photographs, transmitted (XPL: crossed polars) and reflected light (RL) photomicrographs of clinopyroxene skarn and associated mineralisation; **A**: Green hedenbergite skarn with K-feldspar, (952-600.14); **B**: green hedenbergite skarn with red-brown andradite cut by a white quartz-molybdenite (mlb)vein, (952-588.14); **C**: hedenbergite (hd) cut by later diopside (di), (XPL, 952-588.14); **D**: scheelite (scl) and molybdenite (mlb) hosted in a quartz (qtz) vein, cutting hedenbergite skarn, (RL, 949-443.68); **E**: magnetite (mgt) in hedenbergite (hd) skarn with later pyrrhotite (po) and chalcopyrite (cp) (RL, 949-443.68); **F**: quartz (qtz) vein hosting molybdenite (mlb) and later chalcopyrite (cp), (RL, 952-590.2).

3.2.4. Mineralisation

Three major types of mineralisation occur along the Victoria line. These are 1. zinc-copper-lead, 2. semi massive to massive iron-copper and 3. gold-bismuth-tellurium, which occur at different levels within the deposit (Fig. 3.2.4).

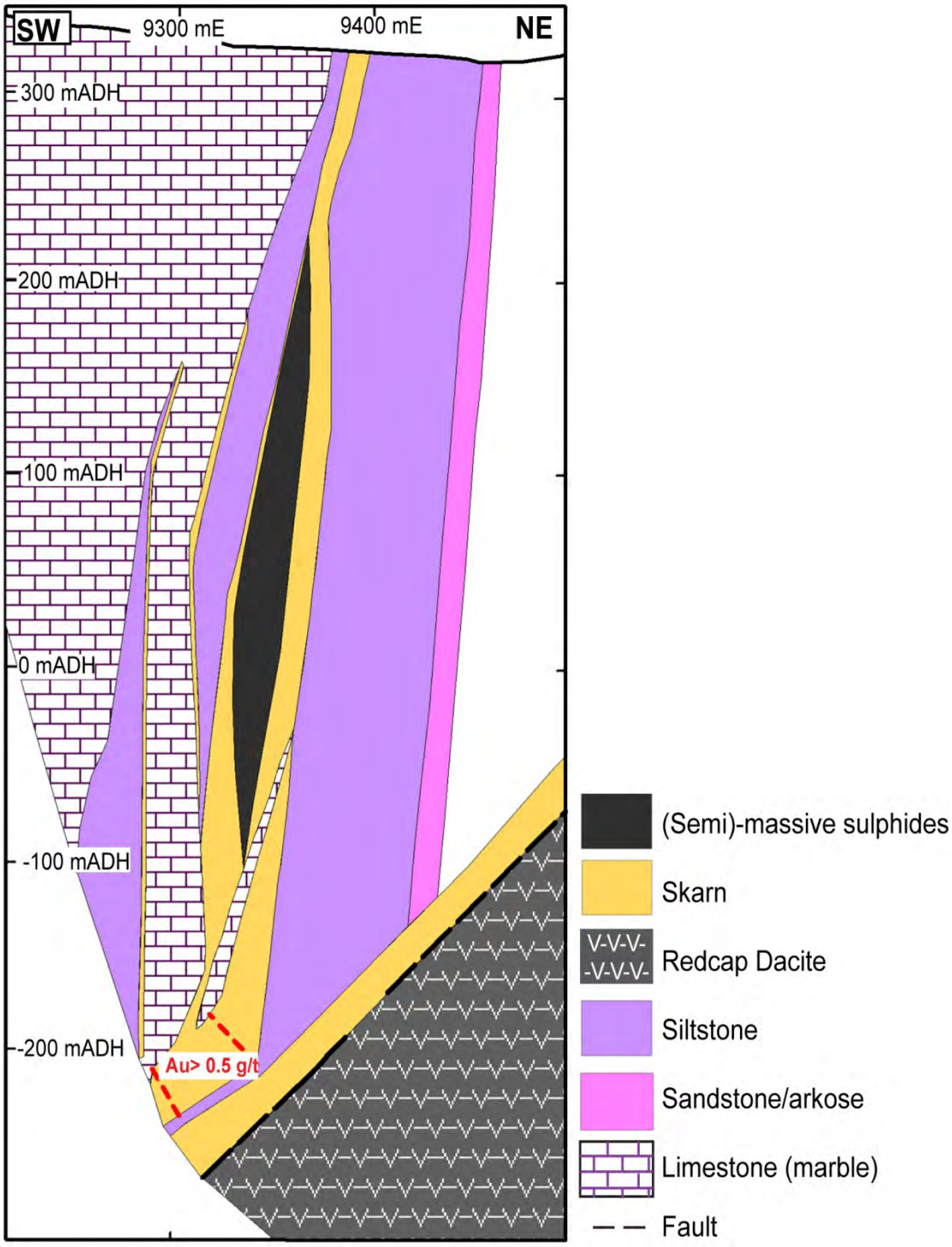

Figure 3.2.4. Schematic cross sections (5600 E) of Redcap-Victoria showing the different lithologies of the Chillagoe Formation, and the occurrence of skarn lenses, base metal and gold mineralisation; modified from Kagara Ltd (2008).

3.2.4.1. Zinc-copper-lead

The zinc-copper-lead mineralisation occurs in the upper part of the deposit and is associated with garnet skarn bodies where it is either interstitial to the calc-silicate minerals or occurs as massive zones (up to 1 metre thick). It is dominated by red-brown anhedral sphalerite, with grain size varying from 0.15 to 5 mm.

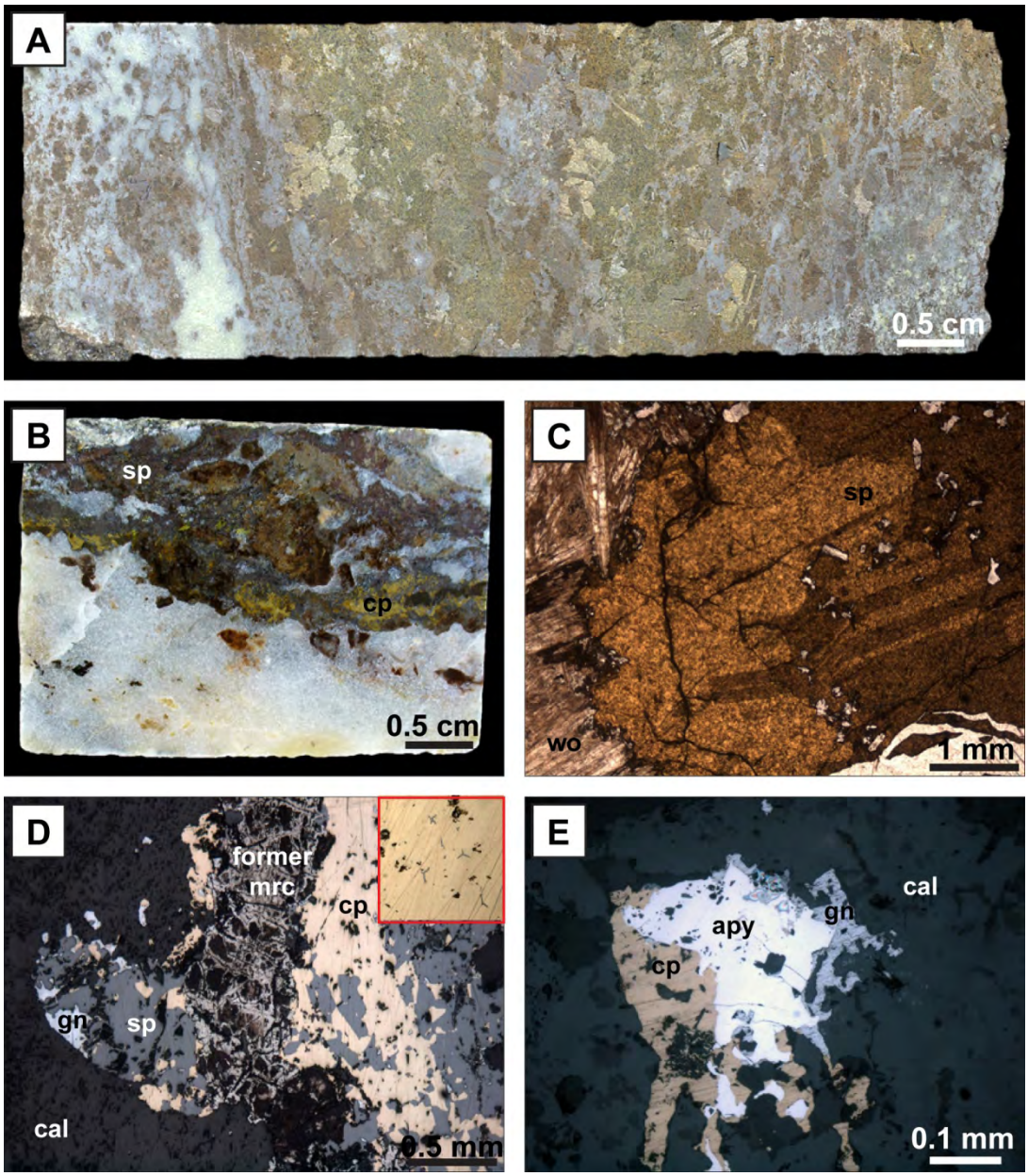

Plate 3.2.4.1. Photographs, transmitted (PPL: plane-polarised) and reflected light (RL) photomicrographs of zinc-copper-lead mineralisation; **A**: Massive honey coloured sphalerite with minor red-brown sphalerite, (949-179.15); **B**: base metal (sphalerite-sp and chalcopyrite-cp) occurrence at marble contact overprinting calc-silicate minerals (not visible in image), (949-161.50); **C**: honey coloured, lamellar sphalerite (sp) with fibrous wollastonite (wo), (PPL, 949-197.53); **D**: sphalerite (sp) with later chalcopyrite(cp), locally showing star shaped exsolution of sphalerite (inset picture) and galena (gn) and heavily altered marcasite (mrc) (RL, 949-159.86A); **E**: arsenopyrite (apy) with later chalcopyrite (cp) and galena (gn), (RL, 949-161.50).

A honey coloured variety of sphalerite can occur, but it is rare (~5 % of total sphalerite occurrence). This iron-poorer type sometimes shows growth lamellae (Plate 3.2.4.1.A & C). In places the sphalerite shows on average 50 µm-sized chalcopyrite exsolution and is commonly rimmed by chalcopyrite, but vice versa chalcopyrite shows in some places star shaped exsolution of sphalerite indicating a high temperature origin (Ramdohr 1980). Lead mineralisation occurs in the form of galena, which seems to be later than sphalerite, but slightly earlier in timing than chalcopyrite (Plate 3.2.3.1.E). Minor on average 5 µm-sized native bismuth inclusions occur within the galena. The sphalerite is cut in places by carbonate veins. One of these veins carries gold-bismuth-telluride minerals (see chapter 3.2.4.3).

3.2.4.2. Semi massive to massive iron-copper mineralisation

This mineralisation type occurs in the upper part of the deposit. It is almost always associated with clinopyroxene and can reach up to three metres in thickness. The dominant mineral phase is pyrrhotite, which occurs in massive zones or less common patches or veins (Plate 3.2.4.2.A). Minor chalcopyrite, which also appears in an anhedral massive form, is intimately intergrown with pyrrhotite. Very rare anhedral red brown sphalerite and roughly cubic pyrite can occur within this mineralisation type. Assay data indicate the presence of arsenic, but no arsenopyrite or other arsenic rich mineral phases were observed.

In places the pyrrhotite is affected by retrograde alteration and is coated with a “dirty” brown layer, which is assumed to have been marcasite which then altered to goethite (Plate 3.2.4.1.D). Chalcopyrite seems to have been less affected by retrograde alteration. Only in one sample the mineral is rimmed by a bluish-white copper-sulphide (soft and black in hand specimen), which could be digenite (Plate 3.2.4.2.D) but due to pervasively alteration of the mineral on the scale of a few microns, electron microprobe analysis did not help to reveal its composition.

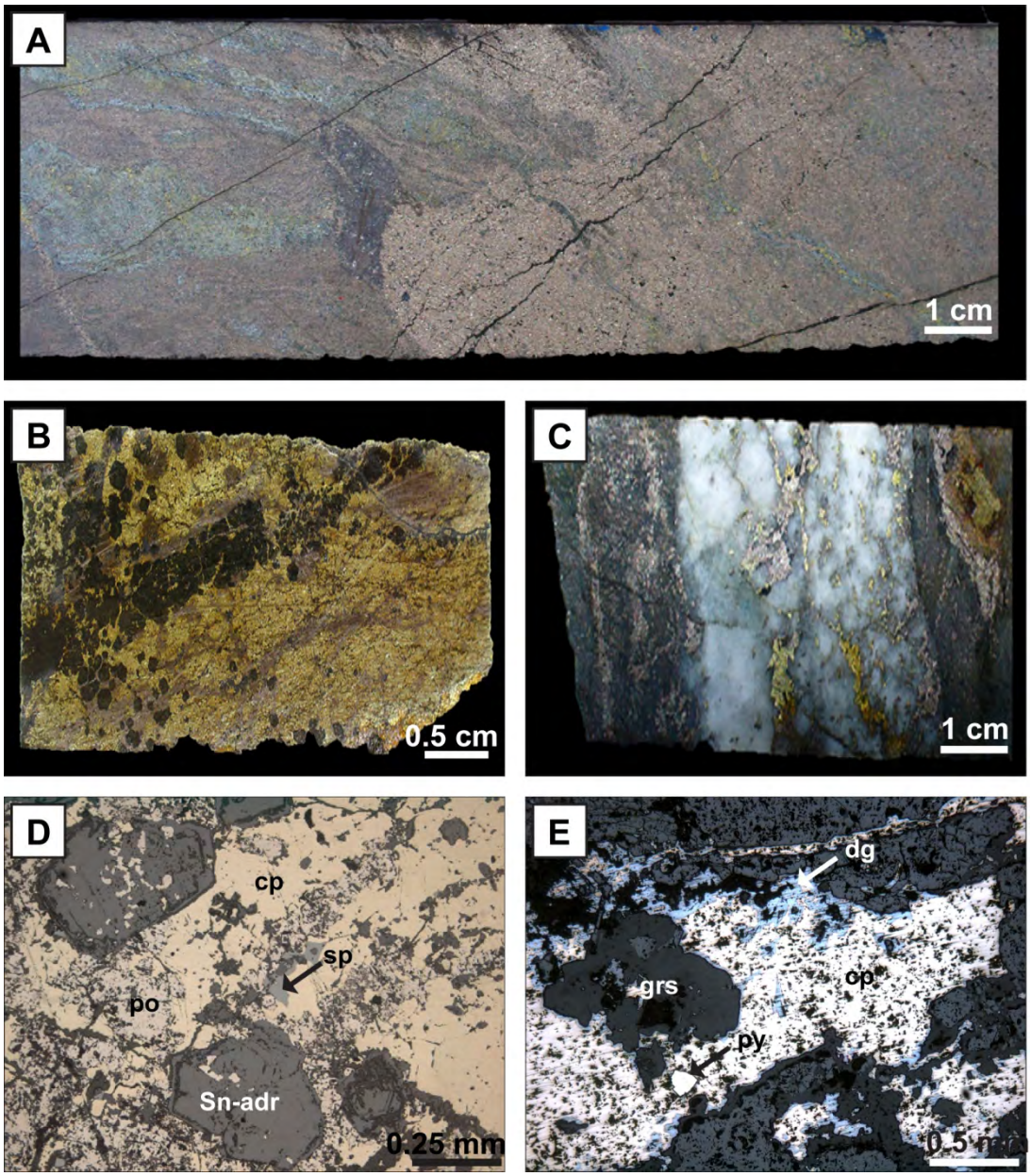

Plate 3.2.4.2. Photographs and reflected light (RL) photomicrographs of semi-massive to massive iron-copper mineralisation; **A**: Massive pyrrhotite with traces of chalcopyrite, (969-132.40); **B**: massive chalcopyrite associated with pyrrhotite later than andradite skarn, (952-574.52); **C**: white quartz vein with pyrrhotite and chalcopyrite in its centre and pyrrhotite distributed within host rock, (949-224.30); **D**: chalcopyrite (cp) associated with pyrrhotite (po) and very rare sphalerite (sp) overprinting earlier tin-rich andradite skarn (Sn-adr), (RL, 952-574.52); **E**: chalcopyrite (cp) rimmed by digenite (dg) overprinting earlier grossular (grs) skarn, (RL, 963-99.20).

3.2.4.3. Gold-bismuth-tellurium mineralisation

This mineralisation type has only been observed in five samples from three different settings. 1. electrum grains are associated with up to 0.15 mm-sized native bismuth, on average 10 µm-sized hedleyite (B_7Te_3) and occur together with chlorite and carbonate in a 0.5 mm thick quartz vein which cuts an earlier quartz vein hosting pyrrhotite and chalcopyrite (Plate 3.2.4.3.A & B);

2. electrum associated with native bismuth, hedleyite, bismuthinite (Bi_2S_3) in a carbonate filled fracture in sphalerite (Plate 3.2.4.3.C);

3. electrum associated with native bismuth and pilsenite in carbonate filled fractures in andradite garnet (Plate 3.2.4.3.D).

In all cases the electrum grains are 1-10 µm in size.

Based on these observations the gold occurs very late in the paragenesis and is part of a retrograde carbonate event.

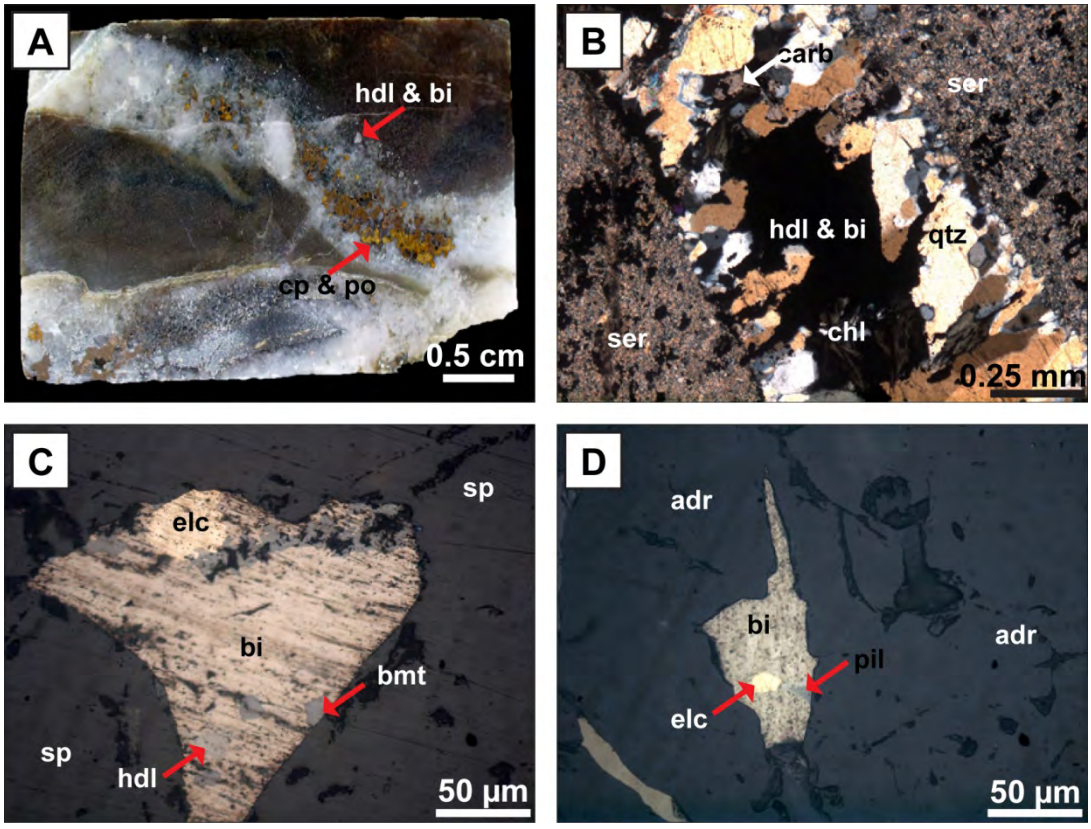

Plate 3.2.4.3. Photographs, transmitted (XPL: crossed polars) and reflected light (RL) photomicrographs of gold-bismuth-tellurium mineralisation; **A**: siltstone cut by a quartz vein carrying chalcopyrite (cp) and pyrrhotite (po) which is cut by a second quartz vein hosting gold-bismuth-tellurium minerals, (949-247.37); **B**: sericite (ser) altered siltstone cut by quartz (qtz) vein hosting gold-bismuth-tellurium mineralisation which is associated with carbonate (carb) and chlorite (chl), (XPL, 949-247.37); **C**: sphalerite hosting electrum (elc), native bismuth (bi), hedleyite (hdl) and bismuthinite (bmt), (RL, 949-197.53), **D**: electrum (elc) associated with native bismuth (bi) and pilsenite (pil) in carbonate filled fractures in andradite (adr) garnet (RL, 952-575.2 III).

3.2.5. Paragenetic sequence

This section summarises the paragenetic sequence for the skarn minerals and mineralisation for the Redcap deposit (Fig. 3.2.5.) based on descriptions outlined in the previous sections.

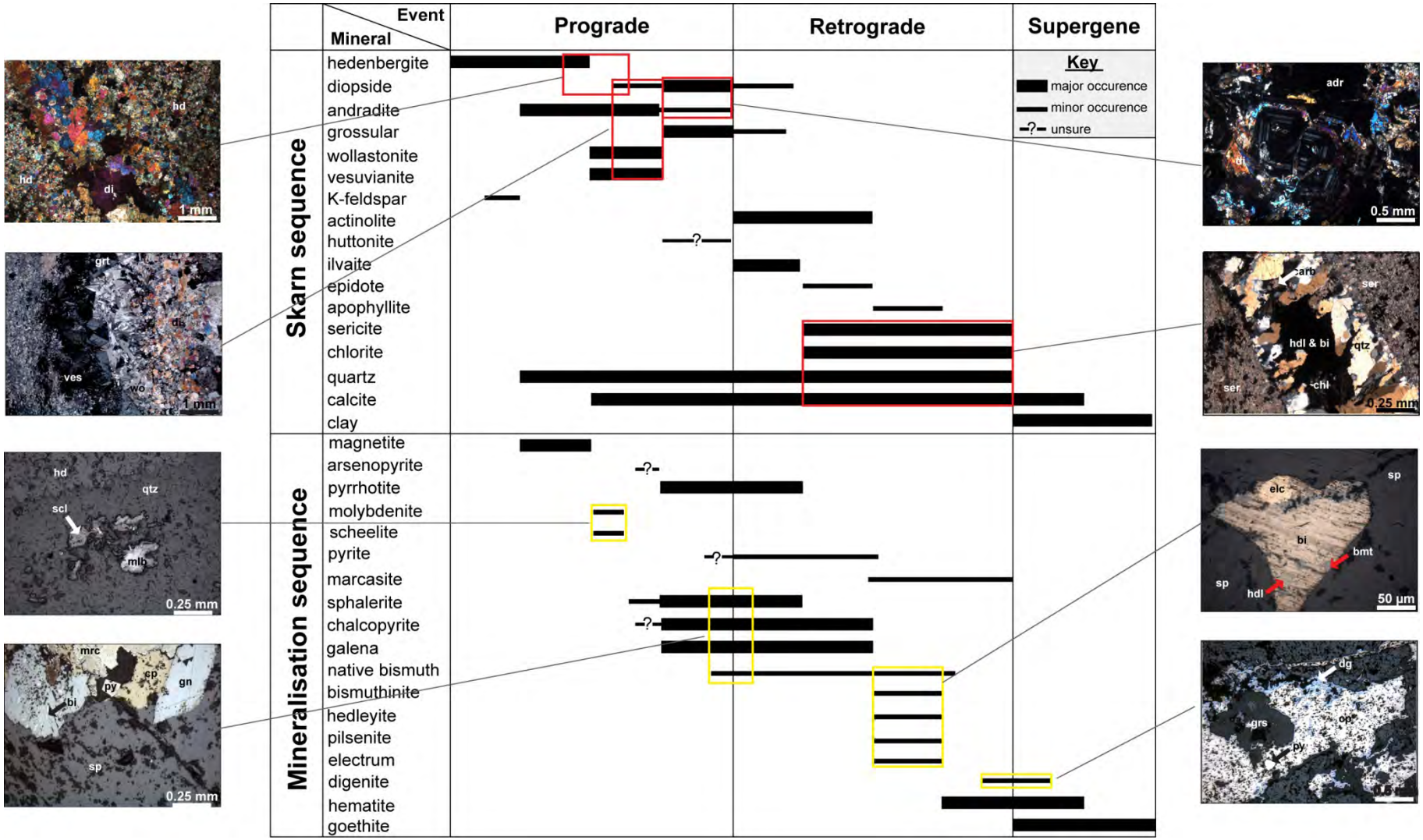

Figure 3.2.5. Paragenetic sequence of skarn minerals and mineralisation at Redcap.

The first stage (not shown in Fig. 3.2.5.) is contact metamorphism, best observed in the field, resulting in the recrystallisation of limestone to marble, bleaching of the siliciclastic units and basalts as well as in the formation of banded skarn. The second event is prograde metasomatism. During this stage hedenbergite-K-feldspar skarns (Plate 3.2.3.3.A) develop mainly adjacent to the Redcap-Morrison Thrust and to a minor amount within veins cutting bleached basalt. During ongoing metasomatism the first skarn assemblage was overprinted by andraditic garnet which is commonly associated with magnetite (Plate 3.2.3.1.A). This replacement follows the reaction suggested by Gustafson (1974):

9 hedenbergite + 2 O_2 ↔ 3 andradite + 9 quartz + magnetite

and occurs at temperature somewhere between 650-550°C (only estimates can be made as necessarily factors to narrow the temperature field like P, P_{fluid}, $X(CO_2)$, $f(O_2)$, $f(S_2)$ and pH are not known).

Possibly through introduction of more calcium into the system, magnetite and quartz react with calcium to form new andradite (Taylor & Liou 1978) while other quartz reacts with the calcium to form wollastonite (Harker & Tuttle 1956). Additionally, vesuvianite occurs with the wollastonite-andradite skarn (Plate 3.2.3.2.A & C). During ongoing metasomatism the vesuvianite-wollastonite assemblage then decomposes after the reaction of Valley et al. (1985) into grossular-diopside-calcite (Plate 3.2.3.2.E). Assumed temperature for this event is less than 450 °C, as vesuvianite is not stable below this temperature (Ito & Arem 1970). This is supported by the occurrence of ilvaite, crosscutting the former assemblage (Plate 3.2.3.2.A) as ilvaite is not stable at temperatures above 440°C (Martin & Gil 2010). With the occurrence of ilvaite the retrograde alteration has started and anhydrous minerals of the prograde cycle get replaced by hydrous minerals, such as epidote, actinolite and chlorite, which get decomposed to calcite, quartz and clay.

The first mineralising event occurs during the prograde stage with the development of magnetite at quite high temperature of ~560 °C (Barton & Skinner 1979). It is followed by the occurrence of molybdenite-scheelite mineralisation in sugary quartz veins (Plate 3.2.3.3.D) and later by arsenopyrite (Plate 3.2.2.1.B) and pyrrhotite-chalcopyrite introduction (Plate 3.2.3.3.E). Still in the prograde phase sphalerite and chalcopyrite with galena develop, mainly at marble contacts (Plate 3.2.4.1.B & D). The temperature for this event ranges between 400-450 °C (Howd & Barnes 1975) and is also confirmed by the star-shaped sphalerite exsolution in chalcopyrite (Ramdohr 1980). The deposition of the sulphides along the marble contact can be explained by neutralisation of the acidic hydrothermal fluid by marble.

During ongoing retrograde alteration pyrrhotite retrogresses to pyrite and then to marcasite, while in rare cases chalcopyrite retrogresses at the rim to digenite (Plate 3.2.4.2.E). Gold mineralisation also occurs at very low temperature with the native bismuth-hedleyite assemblage indicating temperatures below 266 °C (Barton & Skinner 1979).

3.3. Mungana

The Mungana deposit is hosted in steeply-dipping siliciclastic rocks, consisting of chert, sandstone and minor siltstone. Minor limestone is commonly recrystallised to marble and a small band of basalt occurs in the eastern part of the deposit. The skarn body and massive sulphide lenses occur at the flanks of the porphyry intrusion (Fig. 3.3.1.) and will be described in the following section.

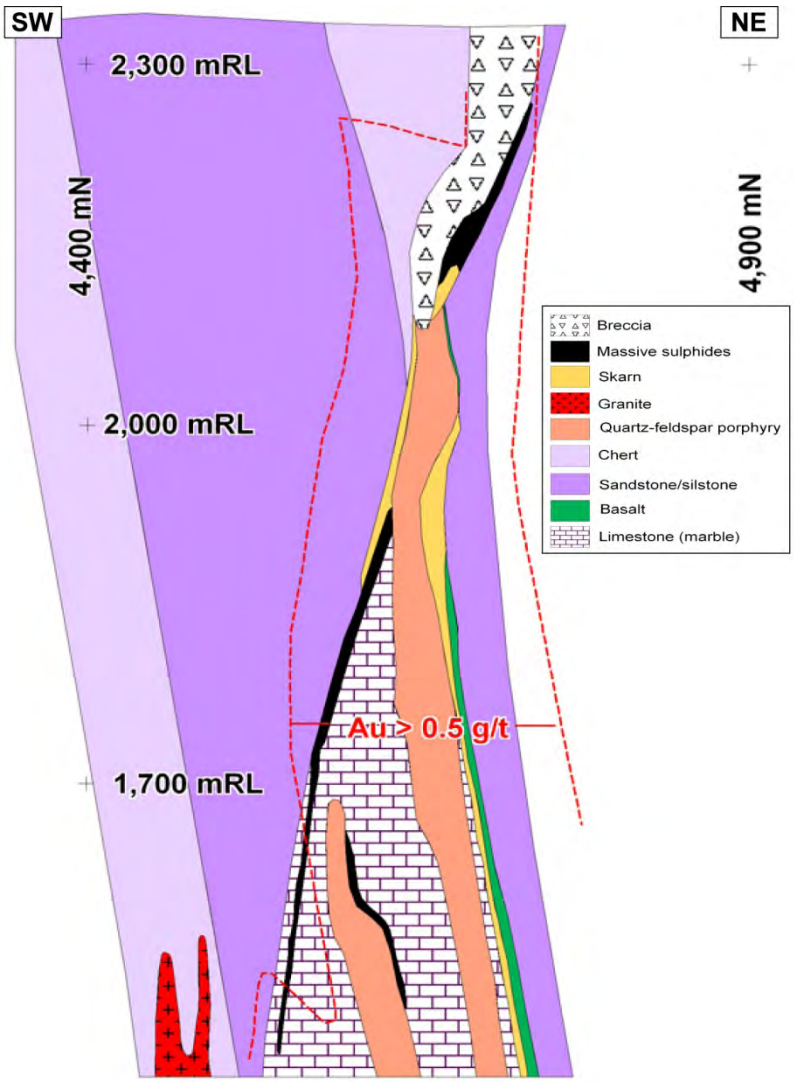

Figure 3.3.1. Schematic cross section (3850 E) of the Mungana deposit showing country rocks, intrusions as well as skarn occurrence and distribution of base metal and gold mineralisation; modified from Georgees (2007b).

3.3.1. Intrusive rocks

Two different intrusive rock types occur at Mungana: a) granite and b) rhyolitic porphyry. The porphyry is relatively abundant but the granite has only been intersected in three drill holes. Intrusive relationships are unknown.

3.3.1.1. Granite

The granite is coarse grained and consists of ~1mm-sized (up to 3 mm) quartz, ~2 mm-sized (up to 5 mm) anhedral to subhedral tabular K-feldspar (pink in hand specimen) with perthite exsolution, ~3mm-sized (up to 5 mm) subhedral lath shaped plagioclase (pale green in hand specimen) and minor ~0.75 mm-sized, platy green brown biotite (Plate 3.3.1.1.A & B). Associated with the biotite are ~0.15 mm-sized euhedral zircons, on average 20 µm-sized opaques (likely to be a titanium phase), and along biotite cleavage, ~0.15 mm-sized elongated subhedral grains of pyrite occur. No other sulphide minerals have been observed. Both feldspars have been subject to alteration resulting in the development of sericite or where the alteration process is advanced to clay (probably kaolinite). The biotite is partly replaced by chlorite.

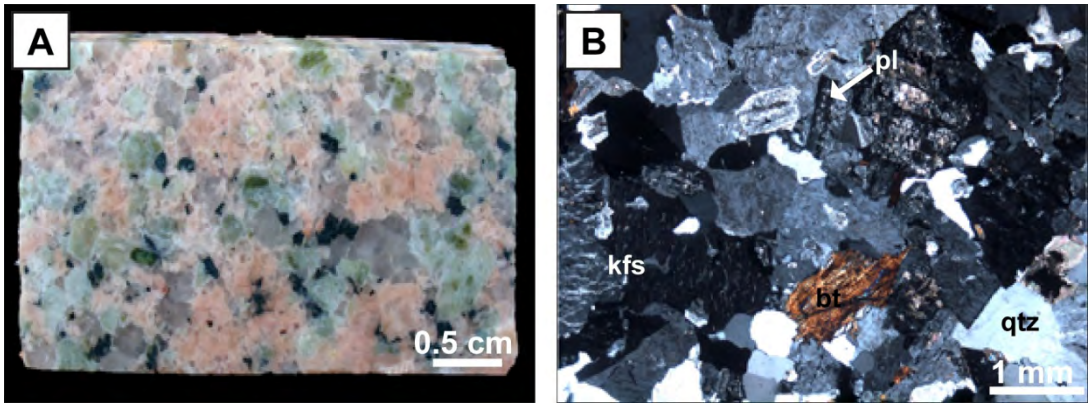

Plate 3.3.1.1. Photograph and transmitted (XPL: crossed polars) light photomicrograph of the Mungana granite; **A**: Mungana granite consisting of quartz (grey), K-feldspar (pink), plagioclase (green) and biotite (black), (883W3-1019.79); **B**: typical micro-scale image of the granite comprising of quartz (qtz), K-feldspar (kfs), plagioclase (pl) and biotite (bt), (XPL, 883W3-1019.79).

3.3.1.2. Rhyolitic porphyry

The porphyry is yellow-green-greyish in hand specimen and has only a small amount of phenocrysts (~5 %). These phenocrysts consist of 1.5-2 mm-sized embayed and partly resorbed quartz, 1.5-2.5 mm-sized lath shaped, simple twinned, cloudy K-feldspar and ~0.5 mm-sized altered biotite (Plate 3.3.1.2.A & B), which is associated with ~60 µm-sized euhedral zircon. The groundmass consists of ~0.15 mm, up to 0.24 mm-sized anhedral quartz and altered feldspar, with some relicts indicating a plagioclase composition.

Up to 2 mm zones (miarolitic cavities) consisting of 0.35-0.5 mm-sized sugary, fluid inclusion rich quartz are associated with ~0.35 mm-sized columnar epidote (pale yellow green in hand specimen) and ~0.25 mm-sized euhedral lozenges or rhomb shaped arsenopyrite (possibly loellingite; Plate 3.3.1.2.C). The epidote also appears in a second mineral assemblage together with ~0.15 mm-sized, anhedral chalcopyrite and Fe-rich sphalerite, which is very rarely rimmed by ~15 µm-sized anhedral galena (Plate 3.3.1.2.D).

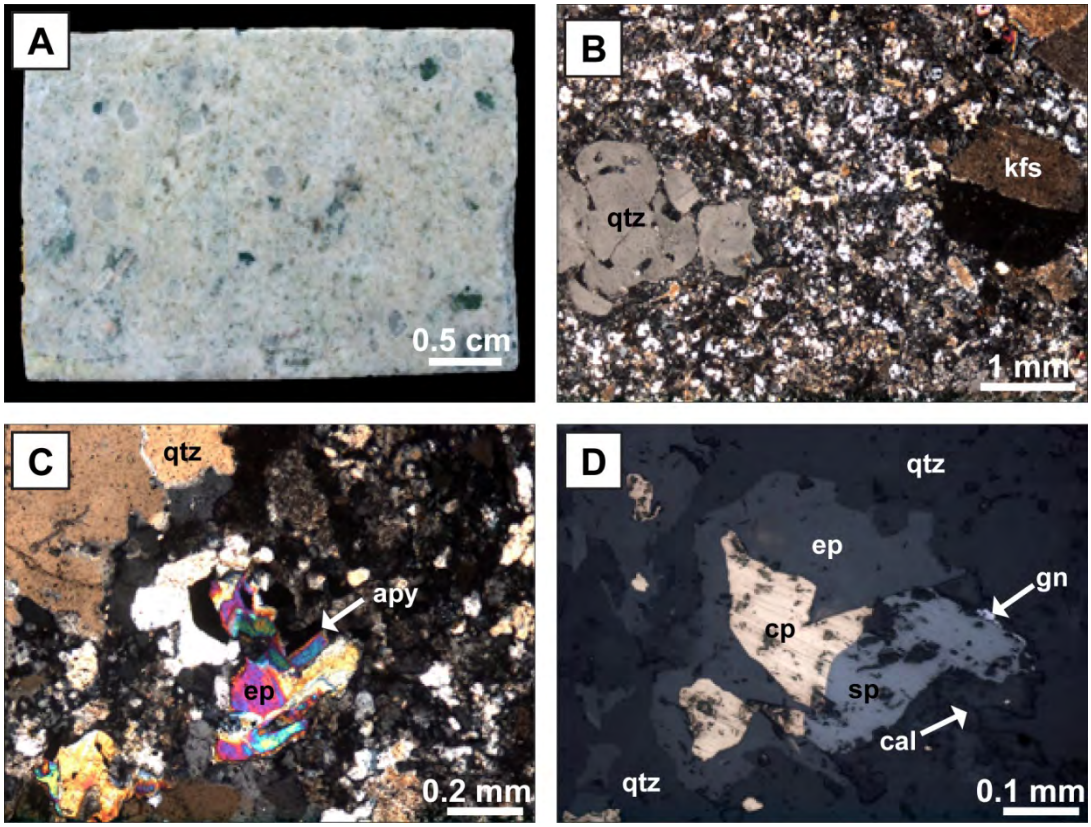

Plate 3.3.1.2. Photographs, transmitted (XPL: crossed polars) and reflected light (RL) photomicrographs of rhyolitic porphyry from Mungana; **A**: yellow green coloured rhyolitic porphyry (883-857.68); **B**: rhyolitic porphyry with quartz (qtz) and K-feldspar (kfs) phenocrysts in a quartz-rich groundmass, (XPL, 883-857.68); **C**: miarolitic cavity filled with quartz (qtz), arsenopyrite (apy) and epidote (ep), (XPL, 883-857.68); **D**: chalcopyrite(cp), sphalerite (sp) and later galena (gn) rimmed by epidote (ep), calcite (cal) in quartz (qtz), (RL, 883-857.68).

3.3.2. Skarn types, alteration and associated mineralisation

Four main skarn types can be distinguished at Mungana based on their spatial occurrence, mineralogical composition and timing. These are: 1. Banded skarn, 2. garnet skarn, 3. wollastonite skarn and 4. clinopyroxene skarn, and are described in the next sections.

3.3.2.1. Banded skarn

This skarn is represented by a variety of types and can be found at marble contacts or where two or more different lithological units are interlayered. This rock type is usually very fine grained,

but some coarser grained types occur as well. The colour of the banded skarn varies based on its mineralogical composition with cream, green, grey and brown being the main types. The abundance of different mineral phases strongly varies within the rock type ranging from 0 % to up to 50 % for the major minerals and 0-25 % for the minor ones.

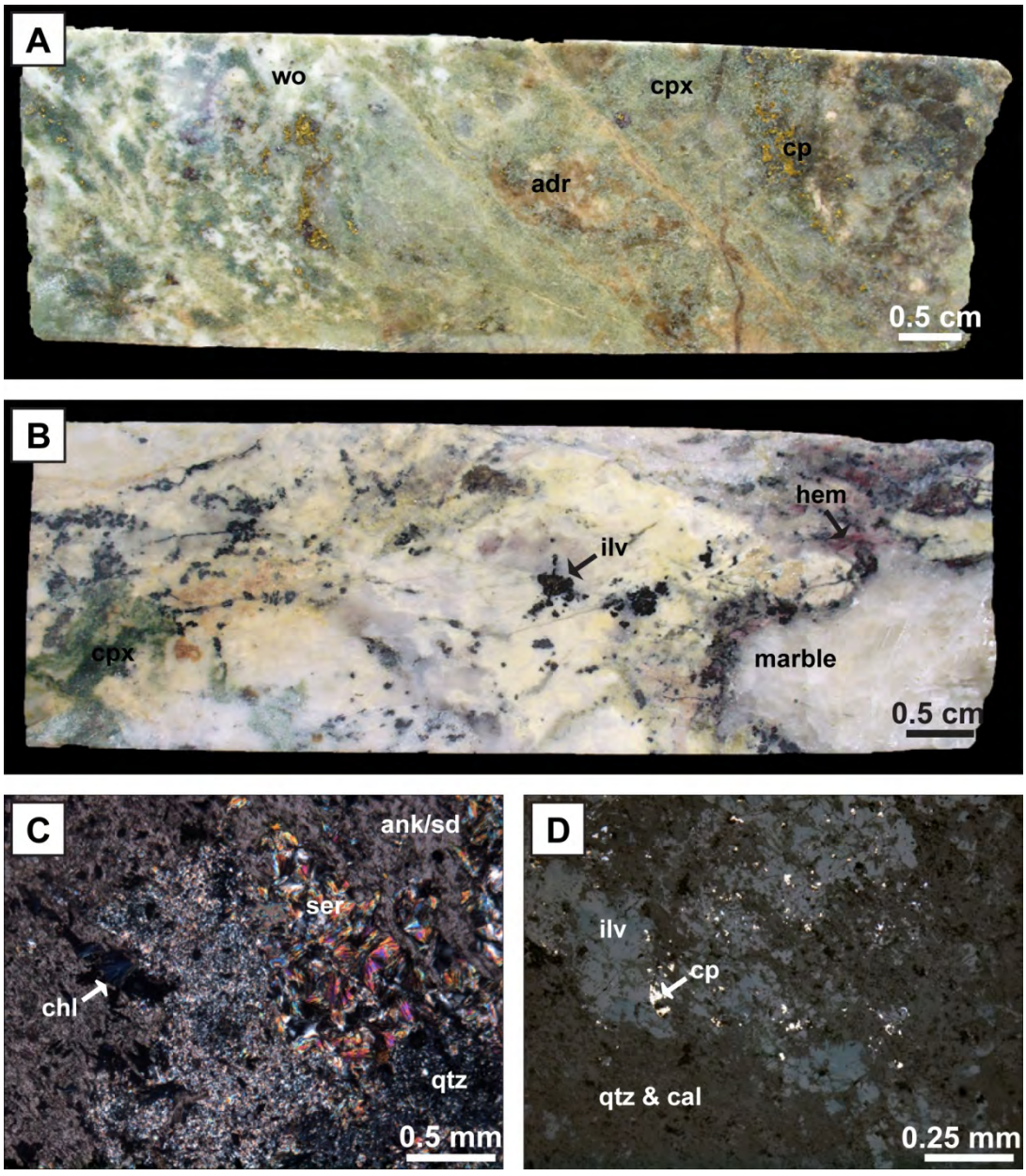

Plate 3.3.2.1. Photographs, transmitted (XPL: crossed polars) and reflected light (RL) photomicrographs of banded skarn from Mungana; **A**: banded skarn consisting of brown andradite (adr), green clinopyroxene (cpx) and minor wollastonite (wo) and traces of chalcopyrite (cp), (742-473.8); **B**: banded skarn consisting of calcite intergrown with garnet (creamy-yellow), green clinopyroxene (cpx), black ilvaite (ilv), later hematite (hem) at marble contact (859-783.5); **C**: retrograde mineral assemblage consisting of sericite (ser), chlorite (chl) and iron-rich carbonate (ank/sid), (XPL, 546-128.3); **D**: ilvaite (ilv) associated with chalcopyrite (cp), quartz (qtz) and calcite (cal), (RL, 859-783.5).

Major mineralogical components are 0.2 mm to 3 mm-sized, euhedral, brown garnet, ~0.2 mm, up to 1 mm-sized, anhedral to stubby prismatic green clinopyroxene, ~1 mm-sized partly radiating prismatic, brown vesuvianite and ~0.6 mm-sized, partly radiating, elongated white wollastonite (Plate 3.3.2.1.A). Rhombohedral K-feldspar and ~0.5 mm-sized (up to 3 mm) anhedral colourless fluorite are associated with the main components, especially with clinopyroxene. Occurring interstitial to or as alteration products of the major minerals are black massive ilvaite (Plate 3.3.2.1.B), a second generation of fine grained clinopyroxene, ~0.25 mm-sized subhedral to prismatic actinolite, flaky sericite, 20 µm to 0.3 mm-sized anhedral to roughly tabular chlorite, 50 µm to 3 mm-sized anhedral quartz and calcite as well as clay (possible kaolinite and nontronite) and hematite.

While the fine grained clinopyroxene is an alteration product of the garnet, the original clinopyroxene is retrogressed to actinolite and an iron carbonate (assumed to be ankerite or siderite), and, where the alteration process is advanced, has broken down to chlorite and clay (Plate 3.3.2.1.C). Quartz and calcite represent the retrograde alteration of wollastonite as well as of vesuvianite. Ilvaite is also a retrograde mineral phase and is always associated with calcite and quartz.

Several sulphides (up to 1.5 % of the skarn) are also present in this skarn type, either as fine disseminations or patches and are commonly, but not always associated with the retrograde mineral assemblages. The most abundant phases are 0.2-0.5 mm-sized anhedral chalcopyrite and 0.2-0.5 mm-sized anhedral to stubby prismatic arsenopyrite while ~0.15mm, up to 0.5 mm-sized flaky molybdenite, anhedral dark coloured sphalerite (Fe-rich), anhedral galena, anhedral tetrahedrite/tennantite and bornite are rare.

The paragenetic position of arsenopyrite as well as of molybdenite can only be inferred as both minerals rarely occur together with the other sulphides. In general arsenopyrite can be found within or interstitial to clinopyroxene and is therefore assumed to be part of the prograde mineral assemblage or if retrograde occurs in a very early stage (Plate 3.3.2.4.C & D). Molybdenite also seems to occur early in the paragenesis, but in one instance it rims arsenopyrite and thus may partly postdate growth of this mineral (Plate 3.3.2.4.E).

Chalcopyrite and sphalerite with inclusions of galena overlap in timing, while tennantite is later than the zinc-copper assemblage as it can be commonly found rimming this mineral association (Plate 3.3.3.1.C). The paragenetic stage of bornite, which occurs as exsolution or retrograde alteration of chalcopyrite remains uncertain. It is definitely later than the sphalerite-chalcopyrite

but lacks a direct occurrence with tennantite/tetrahedrite. Hematite is very late in the paragenesis and occurs as a very thin weathering crust of Fe-rich sphalerite.

3.3.2.2. Garnet skarn

This skarn is the most abundant one at Mungana (~80 %) consists of 0.3-10 mm-sized euhedral, partly fractured garnet with interstitial 0.1-8 mm-sized anhedral quartz and calcite (Plate 3.3.2.2.A.), magnetite or massive anhedral chalcopyrite (Plate 3.3.2.2.B).

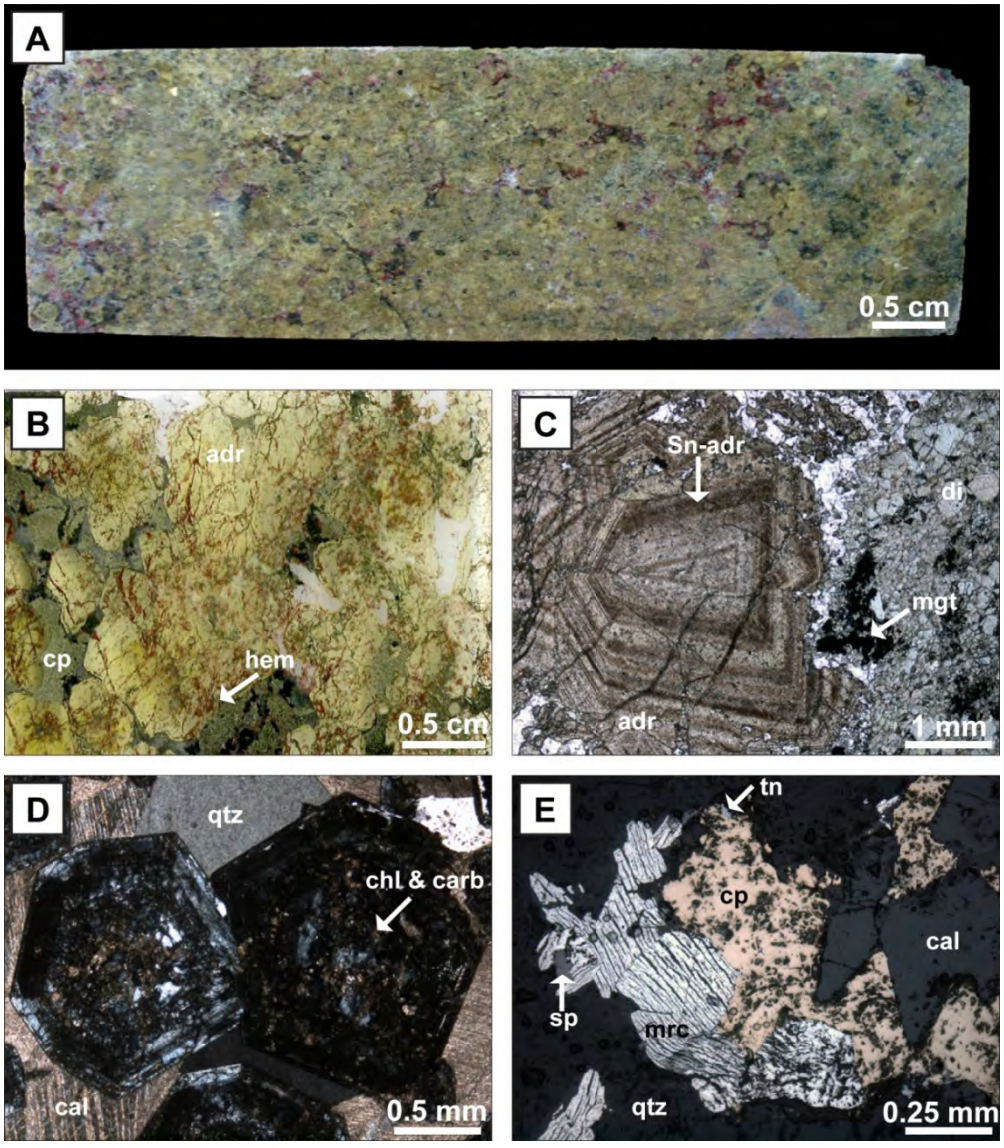

Plate 3.3.2.2. Photographs, transmitted (PPL: plane-polarised, XPL: crossed polars) and reflected light (RL) photomicrographs of garnet skarn from Mungana; **A**: green andradite skarn with interstitial quartz and calcite as well as diopside (green) and hematite (red), (849W1-566.43); **B**: green andradite skarn with interstitial chalcopyrite (cp) and hematite (hem), (859-612.15); **C**: brown andradite with partly tin-rich growth zones (Sn-adr), magnetite (mgt) and diopside (di), (PPL, 859-765.8); **D**: partly chlorite (chl) and carbonate (carb) retrogressed andradite skarn with interstitial calcite (cal) and quartz (qtz), (XPL, 849W1-564.73); **E**: chalcopyrite (cp) with lamellar marcasite (mrc) and rare sphalerite (sp) and tennantite (tn) in interstitial to andradite occurring calcite (cal) and quartz (qtz), (RL, MuD183-158.7).

The andraditic garnet varies in colour from light brown to dark green, is in general slightly anisotropic and commonly shows oscillatory growth zones with some of these zones being enriched in tin (Plate 3.3.2.2.C, see chapter 4). It is partly retrogressed to 20 µm to 0.2 mm-sized anhedral-subhedral diopside or where alteration is advanced to a mixture of Fe-rich chlorite and calcite (Plate 3.3.2.2.C & D). The interstitial quartz-calcite assemblage is also assumed to be of retrograde origin and could have been originally wollastonite based on observations in the other skarn types, although no relicts of the mineral can be found. However, this assemblage is in some places overprinted by chalcopyrite (up to 15 % of the skarn).

The chalcopyrite occurs together with ~0.1 mm, up to 0.5 mm-sized, red brown Fe-rich sphalerite and subhedral pyrite of the same size. These minerals are commonly rimmed by ~0.5 mm, up to 2mm-sized lamellar marcasite (Plate 3.3.2.2.E). Very rare ~50 µm-sized anhedral tennantite encrusts the chalcopyrite and sphalerite, but no relationships to marcasite can be observed. Minor hematite makes up 5 % of the skarn. In some places it occurs on the rims of chalcopyrite and both of the iron sulphides, but a relationship to tennantite is not observed.

3.3.2.3. Wollastonite skarn

This skarn type only makes up ~9 % of the overall skarn occurrence at Mungana and can be found primarily at chert-limestone contacts, but also occurs as a secondary skarn type overprinting garnet and clinopyroxene skarn, where the latter skarn type forms relicts within the wollastonite (Plate 3.3.2.3.A). In general the wollastonite occurs in 0.6-1.5 mm-sized elongated needles, but sometimes radiating rosettes can be found. It is very commonly associated with ~3 mm-sized euhedral red brown andradite which can have up to 0.25 wt-% tin in its structure. Diopside occurs either interstitial to the garnet or replaces it along its growth zones and is 0.25 to 1 mm in size.

Only a minor amount of sulphides (maximum 0.5 %) occur in this skarn type. The dominant phase is up to 1mm, flaky molybdenite which occurs either within the andradite or interstitial to garnets in wollastonite. Other sulphides are 70 µm to 0.25 mm-sized anhedral chalcopyrite and anhedral to stubby prismatic arsenopyrite. Very rarely up to 10 µm-sized native bismuth, bismuthinite and pilsenite occur along fractures in the garnet, but no gold mineralisation has been observed although assays of this rock indicate a gold grade of 2.6 g/t (see appendix 3).

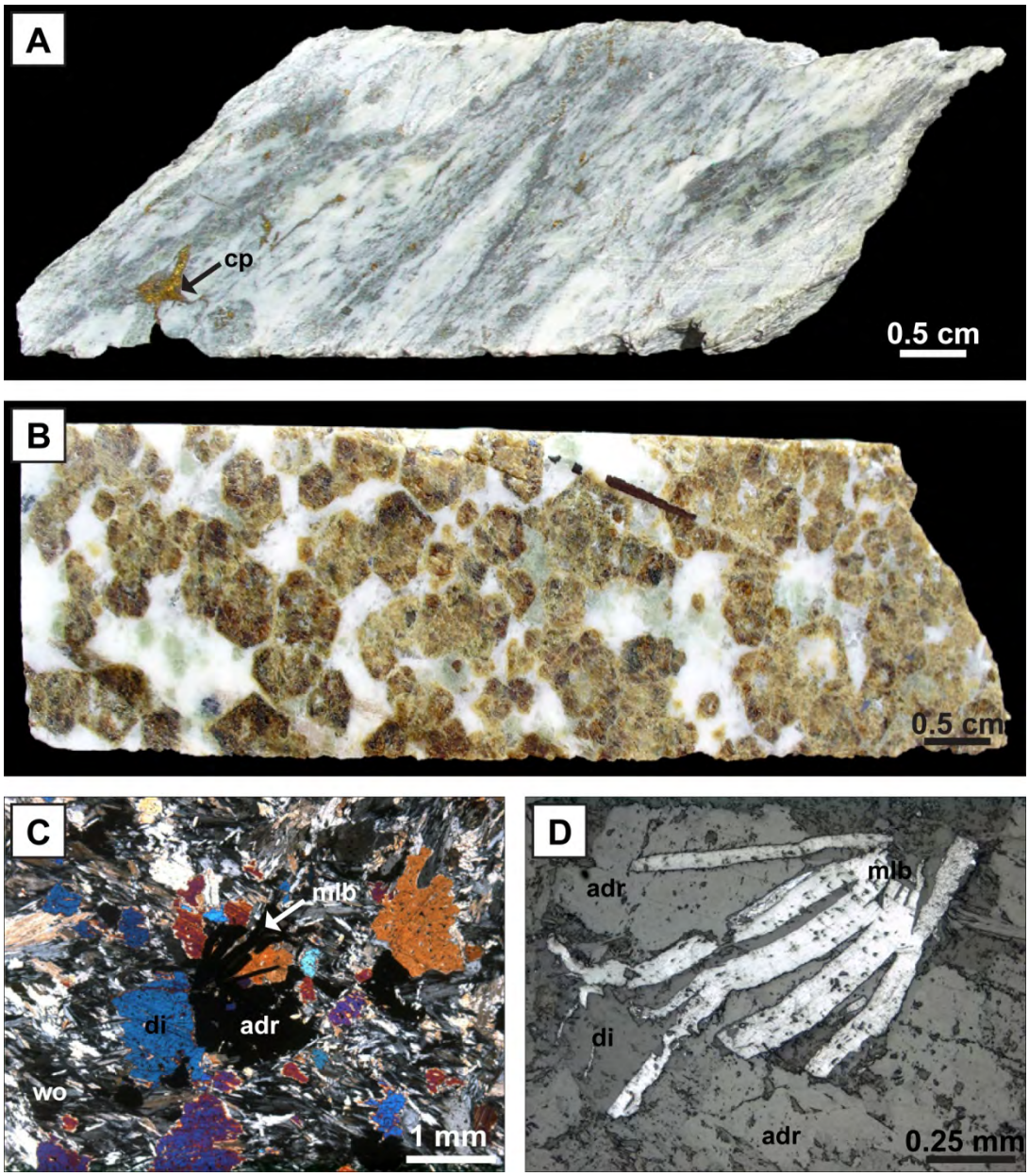

Plate 3.3.2.3. Photographs, transmitted (XPL: crossed polars) and reflected light (RL) photomicrographs of wollastonite skarn from Mungana; **A**: wollastonite skarn with clinopyroxene bands and rare chalcopyrite (cp) (853-536.1); **B**: wollastonite-andradite skarn with minor clinopyroxene (green) and molybdenite (grey) (890W6-787.56); **C**: wollastonite (wo) with diopside (di), andradite (adr) and molybdenite (mlb), (XPL, 890W6-787.56); **D**: flaky molybdenite (mlb) within andradite (adr) and minor diopside (di), (RL, 890W6-787.56).

3.3.2.4. Clinopyroxene skarn

The clinopyroxene skarn is only poorly developed like the wollastonite skarn with a maximum abundance of 11 % of the overall skarn occurrence. It occurs as endoskarn overprinting the porphyry or as exoskarn overprinting sandstone. Both types are green and mostly massive. The endo-clinopyroxene skarn consists of on average 0.3 mm-sized (up to 2 mm) anhedral to subhedral hedenbergite and ~0.5 mm-sized anhedral pink K-feldspar (Plate 3.3.2.4.A). No sulphides can be observed with this skarn type.

The exoskarn variety of the clinopyroxene skarn also consists of ~0.5 mm, up to 2 mm-sized anhedral to stubby prismatic hedenbergite, but is associated with 0.2 mm-sized (up to 6 mm) anhedral brown garnet and ~0.25 mm-sized anhedral brown vesuvianite (Plate 3.3.2.4.B). In some places the clinopyroxene skarn gets cut by up to 2.5 mm thick wollastonite veins (Plate 3.3.2.4.D), clinopyroxene-K-feldspar-arsenopyrite veins (Plate 3.3.2.4.C) or by calcite-quartz-ilvaite veins. Around these veins and as a general alteration type the clinopyroxene is retrogressed to a blue-green pleochroic amphibole, which decomposes during further alteration processes into a mix of chlorite, carbonate and clay (possibly nontronite).

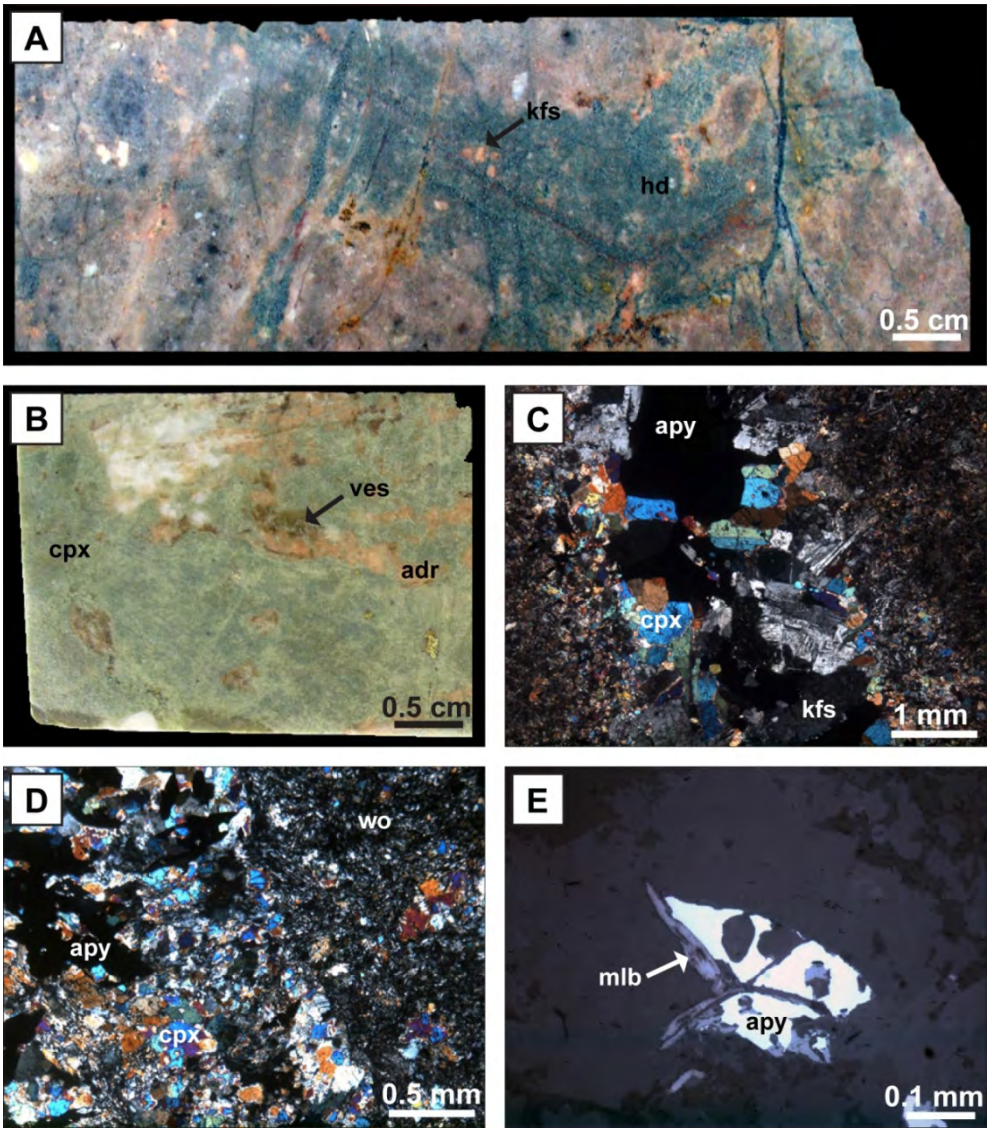

Plate 3.3.2.4. Photographs, transmitted (XPL: crossed polars) and reflected light (RL) photomicrographs of clinopyroxene skarn from Mungana; **A**: hedenbergite (hd) skarn with K-feldspar (kfs) overprinting porphyry, (883W2-871.5); **B**: clinopyroxene skarn with associated brown andradite (adr) and vesuvianite (ves), (742-479.7); **C**: clinopyroxene (cpx), K-feldspar (kfs) and arsenopyrite (apy) vein cutting earlier clinopyroxene skarn (XPL, 883-701.54); **D**: clinopyroxene skarn with arsenopyrite (apy) and a later wollastonite (wo) vein (XPL, 883-701.54); **E**: skeletal arsenopyrite (apy) rimmed molybdenite (mlb), (RL, 883-701.54).

Common mineralisation associated with this skarn type, which can be up to 2 % of the whole skarn, are ~0.5 mm, up to 1.5 mm-sized subhedral-euhedral, partly skeletal lozenges of arsenopyrite, coarse grained blocks of flaky molybdenite, or ~0.15 mm-sized anhedral chalcopyrite. No relationships between chalcopyrite and the other two sulphide phases have been observed, but the molybdenite postdates the arsenopyrite (Plate 3.3.2.4.E).

3.3.3. Mineralisation

Although some of the mineralisation has been already described above, three major mineralisation types will be individually outlined in this section. These are: 1. zinc-copper-lead, 2. copper-arsenic-antimony and 3. gold mineralisation.

3.3.3.1. Zinc-copper-lead

This mineralisation type is the most abundant one within the Mungana deposit. It mainly occurs in (semi) massive lenses which can be found in the upper level within the breccia zone or in lower level associated with skarns (Fig. 3.2.4.).

Dark red brown, 0.2-4 mm-sized anhedral sphalerite is the dominant mineral in this assemblage. It either is associated with chalcopyrite, which forms stringers and patches, and on average 0.5 cm calcite (Plate 3.3.3.1.A) or it is intergrown with euhedral up to 2 cm, native antimony (Plate 3.3.3.1.B) overprinting green garnet skarn. Native antimony is proposed to form either in the hypogene or supergene environment with its formation being related to a decrease in temperature, f_{O2} or f_{S2} (Ramdohr 1980; Williams-Jones & Normad 1997). At Mungana the native antimony is likely to be a supergene product originating from either stibnite or gudmundite.

On average 0.2 mm-sized anhedral chalcopyrite rims the sphalerite or occurs as ~50 µm-sized blebs within the sphalerite, which is assumed to be of exsolution origin. Lead occurs as either ~50 µm-sized altaite (PbTe) or ~0.25 mm-sized galena inclusions within the sphalerite (Plate 3.3.3.1.C & D). Galena commonly has inclusions of 1-5 µm-sized native bismuth or silver tellurides such as hessite (Ag_2Te). Later 50 µm to 0.3 mm-sized tennantite, partly separated by a 5 µm-sized rim of chalcopyrite, rims the sphalerite (Plate 3.3.3.1.C).

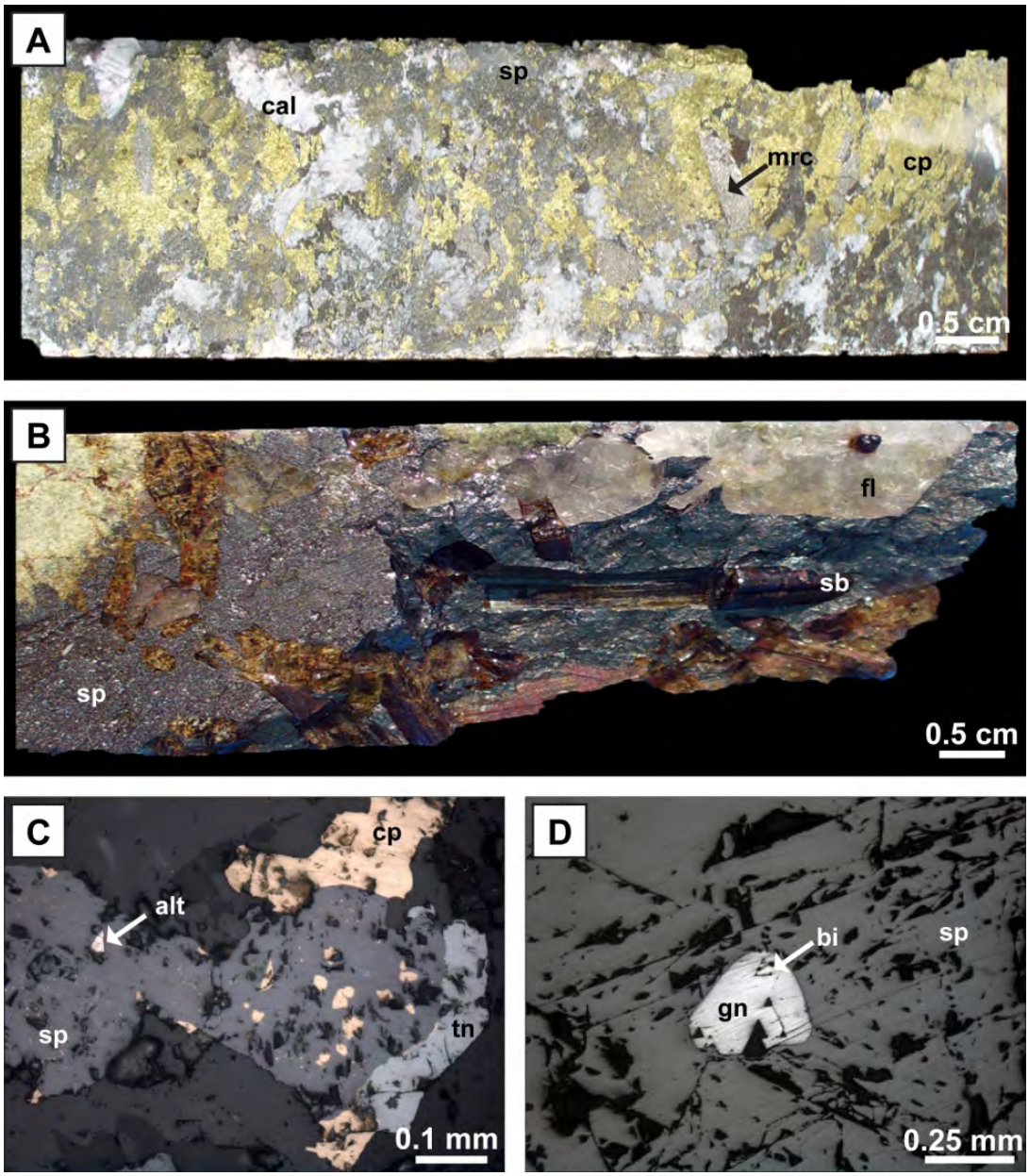

Plate 3.3.3.1. Photographs and reflected light (RL) photomicrographs of zinc-copper-lead mineralisation of the Mungana deposit; **A**: massive sphalerite (sp) with chalcopyrite (cp) later marcasite (mrc) in calcite (cal), (MuD190-139.35); **B**: massive sphalerite (sp) with native antimony (sb), and fluorite (fl) overprinting green garnet skarn (849-746.90); **C**: sphalerite (sp) with chalcopyrite (cp) exsolution and rim, as well as altaite (alt) and later tennantite (tn), (RL, MuD054-74.4); **D**: sphalerite (sp) with galena (gn) and native bismuth (bi) inclusions within the galena (RL, MuD224-88.4).

3.3.3.2. Copper-arsenic-antimony

This mineralisation type can be found within marble (Plate 3.3.3.2.A), in retrograde skarn (Plate 3.3.3.2. B), or in quartz veins cutting porphyry. Copper is mainly present in form of 50 µm to 1 cm-sized chalcopyrite and to a minor amount in 50 µm to 0.25 mm-sized anhedral tetrahedrite, as well as retrograde bornite and covellite. Antimony occurs in the form of tetrahedrite or 50 µm

to 0.15 mm-sized anhedral to roughly euhedral lozenges of gudmundite (FeSbS) while arsenic is only present in the form of arsenopyrite.

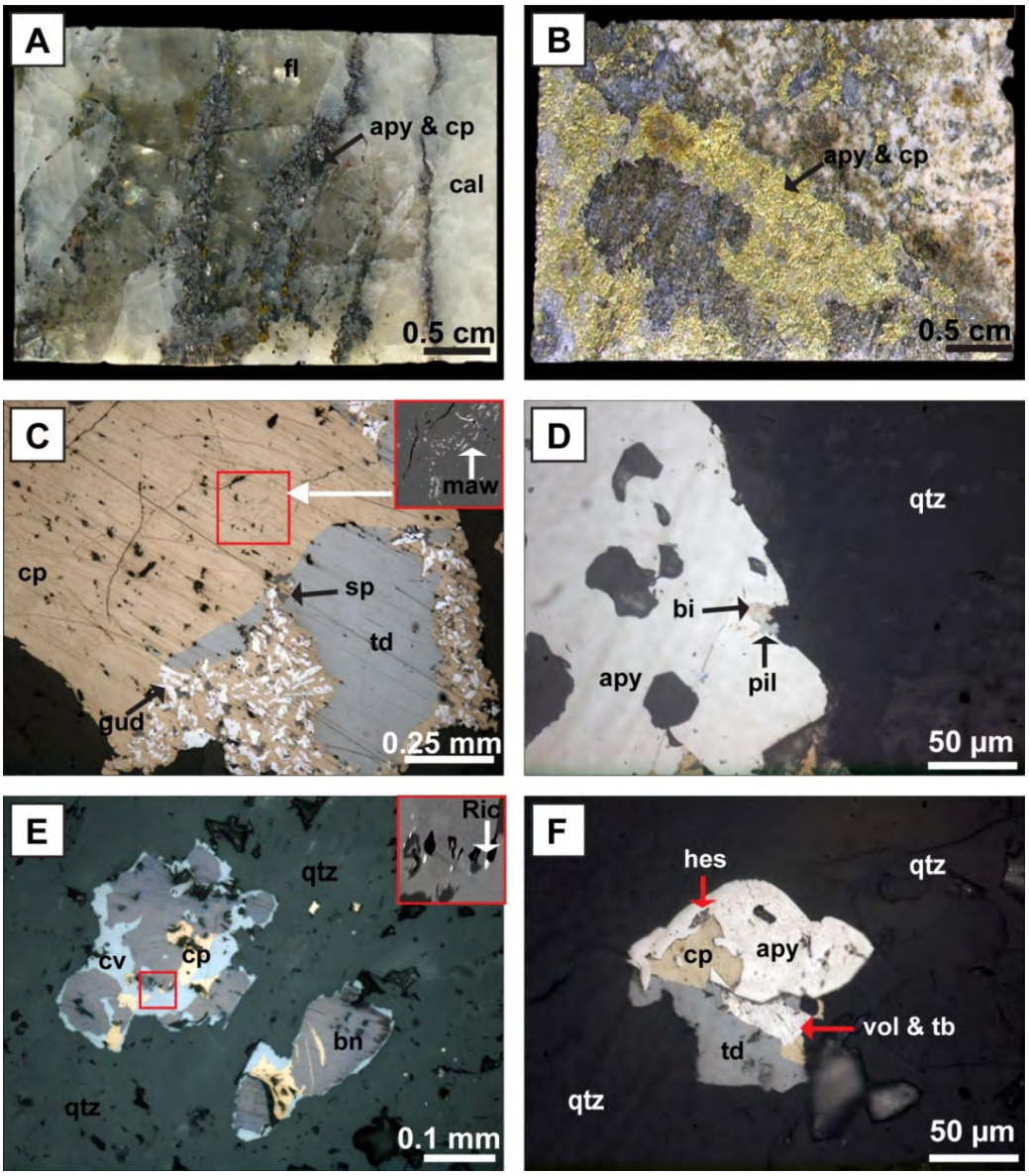

Plate 3.3.3.2. Photographs and reflected light (RL) photomicrographs of copper-arsenic-antimony mineralisation of the Mungana deposit; **A**: arsenopyrite (apy) associated with chalcopyrite (cp) and fluorite (fl) in marble (859-787.4); **B**: arsenopyrite (apy) associated with chalcopyrite (cp) in retrograde skarn (MuD183-102.3); **C**: chalcopyrite (cp) with inclusions of mawsonite (maw) associated with tetrahedrite (td), rare sphalerite (sp) and a retrograde gudmundite (gud), (RL, 859-787.40); **D**: skeletal arsenopyrite (apy) with native bismuth (bi) and pilsenite (pil) in quartz (qtz), (RL, 859-765.8); **E**: chalcopyrite (cp), later bornite (bn), trace of rickardite (ric) and supergene covellite (cv) in quartz (qtz), (RL, MuD054-74.4); **F**: arsenopyrite (apy), chalcopyrite (cp), tetrahedrite (td) and likely exsolved hessite (hes), volynskite (vol) and tellurobismuthite (tb) in quartz (qtz), (RL, MuD054-74.4).

Minor mineral phases in the mineralisation type are 5-15 µm-sized inclusions of mawsonite ($Cu_6Fe_2SnS_8$) in chalcopyrite (Plate 3.3.3.2.C), up to 10 µm-sized native bismuth with

associated pilsenite at the rim of slightly skeletal arsenopyrite (Plate 3.3.3.2.D), <5 µm-sized rickardite (Cu_7Te_5) which occurs at the boundary of chalcopyrite and bornite (Plate 3.3.3.2.E), <10 µm-sized hessite at the rim of chalcopyrite-arsenopyrite border as well as intimately intergrown <50 µm-sized volynskite ($AgBiTe_2$) and tellurobismuthite (Bi_2Te_3) along the borders of chalcopyrite, arsenopyrite and tetrahedrite (Plate 3.3.3.2.F). Chalcopyrite and arsenopyrite are of primary origin, while gudmundite (decay of tetrahedrite next to sphalerite and chalcopyrite), bornite and then covellite (retrograde alteration of chalcopyrite), and rickardite (supergene developed, Ramdohr 1980) are alteration products. Volynskite, tellurobismuthite and hessite were exsolved from tetrahedrite or arsenopyrite during cooling.

3.3.3.3. Gold mineralisation

Gold can be found in four different mineral associations within the Mungana deposit. In the first type it occurs along the grain boundary of tennantite and chalcopyrite together with tellurobismuthite and arsenopyrite in quartz veins cutting skarn and porphyry (Plate 3.3.3.3.A).

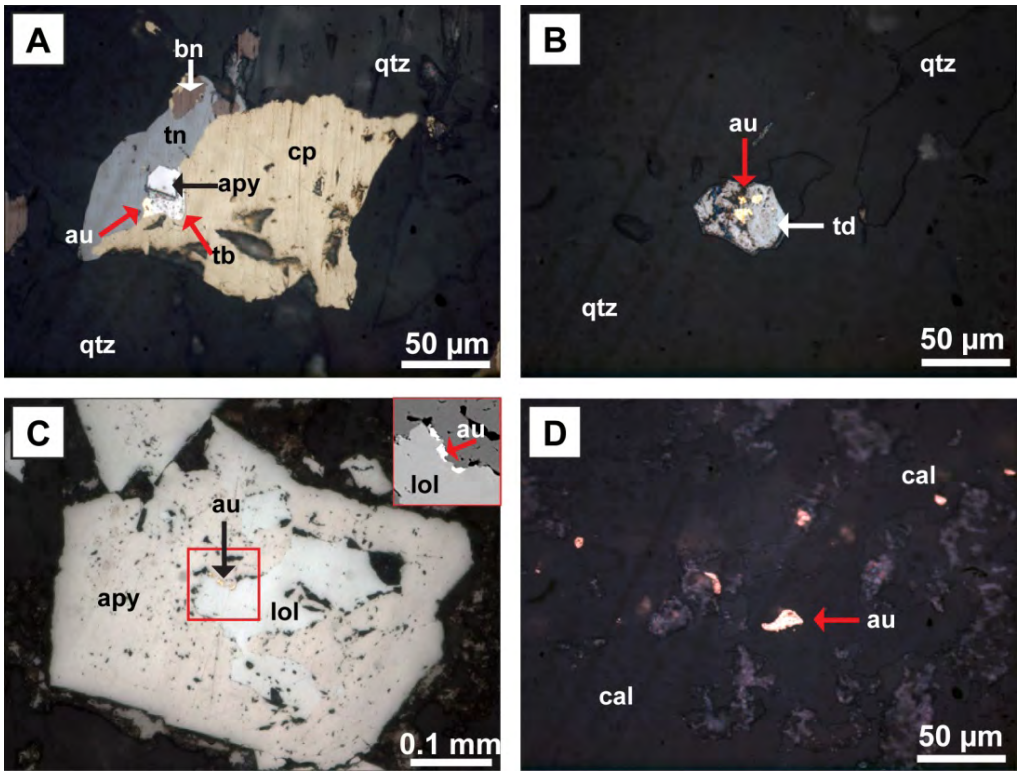

Plate 3.3.3.3. Reflected light (RL) photomicrographs of gold mineralisation of the Mungana deposit; **A**: chalcopyrite (cp), tennantite (tn), later bornite (bn) with the occurrence of arsenopyrite (apy), gold (au) and tellurobismuthite (tb) along the grain boundary of chalcopyrite and tennantite, (RL, MuD054-74.4); **B**: gold (au) within tetrahedrite (td) in a quartz (qtz) vein, (RL, MuD183-117.1); **C**: gold occurring at the boundary of loellingite (lol) and arsenopyrite (apy), (RL, MuD183-117.1); **D**: free gold grains within calcite clasts, (RL, 849W1-581.44).

Type two to three also occur in quartz veins. The gold in these types occurs either within tetrahedrite (Plate 3.3.3.3.B), or along the grain boundary of loellingite and arsenopyrite (Plate 3.3.3.3.C). Type four occurs in form of 5-25 µm-sized free gold grains hosted in calcite clasts within a breccia (Plate 3.3.3.3.D). It is possible that the gold originally was incorporated into the lattice of tetrahedrite, loellingite and chalcopyrite and was exsolved during a decrease in the temperature.

3.3.4. Paragenetic sequence

This section summarises the paragenetic sequence for the skarn minerals and mineralisation for the Mungana deposit (Fig. 3.3.4.) based on descriptions outlined in the previous sections. The skarn formation at Mungana is similar to the one already described for the Redcap deposit with the differences being that banded skarn and fluorite are more abundant at Mungana. Banded skarn commonly develops adjacent to basalt of the Chillagoe Formation, but drill holes from Redcap-Victoria do not intersect basalt and therefore no banded skarn is observed, although at Redcap-Penzance this skarn type is quite common. Fluorite is a common mineral at Mungana and Red Dome and associated with copper-arsenic or copper mineralisation, but so far only the zinc-bearing Victoria line of Redcap has been investigated in detail, while the other two mineralisation lines, Penzance and Redcap-Morrison, were not explored during the course of the study, but due to the paragenetic similarities between Redcap and the other deposits, it is likely that fluorite will occur in one of the other mineralisation lines.

Mineralisation at Mungana is more diverse than at Redcap. Magnetite is again the earliest phase with loellingite, arsenopyrite, molybdenite, sphalerite, galena and chalcopyrite being developed in the prograde phase based on their association with prograde skarn minerals, but later than magnetite. Loellingite/arsenopyrite seems to be the earliest as it is associated with clinopyroxene (Plate 3.3.2.4.C), which is earlier than the wollastonite skarn with associated chalcopyrite and molybdenite (Plate 3.3.2.3.A & B). Additionally the loellingite/arsenopyrite is rimmed by molybdenite (Plate 3.3.2.4.E).

Sphalerite and chalcopyrite are late prograde to retrograde, with the prograde occurrence mainly adjacent to marble contacts, having develop at around 400 to 450 °C (Howd & Barnes 1975). Galena with native bismuth inclusions or altaite is associated with the sphalerite although some of the galena also postdates the sphalerite (Plate 3.3.1.2.D). Tennantite and tetrahedrite postdate chalcopyrite as well as sphalerite, as they can be found rimming the copper and zinc minerals. The edges of chalcopyrite were partly retrogressed to bornite and rickardite (Plate 3.3.3.2.E), with rickardite being considered a secondary mineral based on Ramdohr (1980).

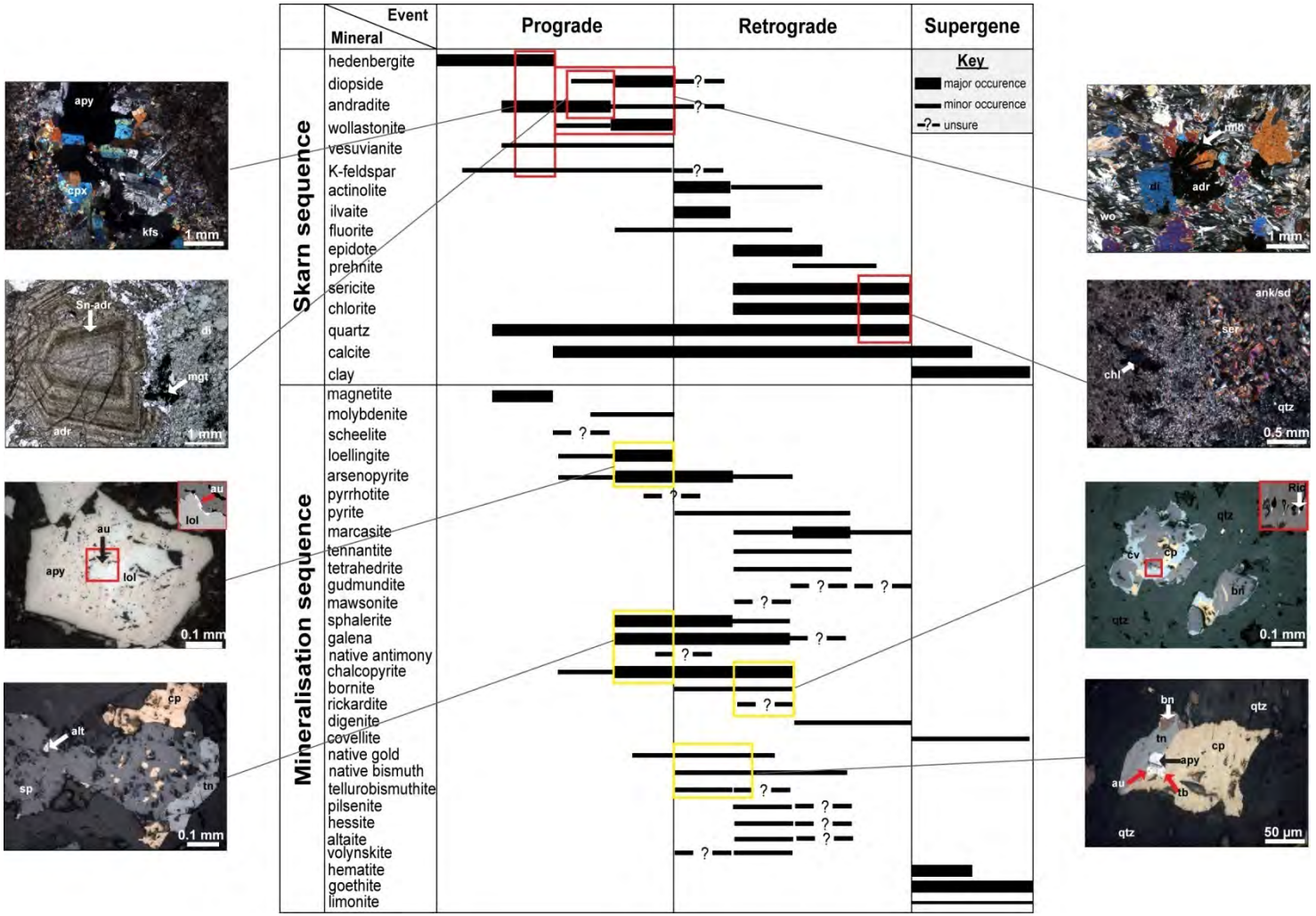

Figure 3.3.4. Paragenetic sequence of skarn minerals and mineralisation from the Mungana deposit.

Bornite has further decomposed to digenite and covellite. All these processes occur at temperatures below 300 °C, but no more precise information could be found in the literature. The decay of the fahlores associated with chalcopyrite and sphalerite to gudmundite (Plate 3.3.3.2.C) on the other hand can be narrowed down to a temperature of less than 290 °C, as gudmundite is not stable above this temperature (Barton & Skinner 1979).

The gold mineralisation at Mungana is different to that observed at Redcap, and occurred at higher temperatures. Originally gold occurred as an invisible component in loellingite and chalcopyrite, as described by Neumayer et al. (1993) and Simon et al (2000). In the case of invisible gold in loellingite the gold was exsolved either during progressive sulphidation at around 500 to 600 °C (Knaak et al. 1995) or during a retrograde event (i.e. temperature decrease) as suggested by Tomkins & Mavrogenes (2001), resulting in the formation of arsenopyrite through reaction of loellingite and pyrrhotite. As gold cannot be incorporated into the structure of arsenopyrite (Neumeyer et al. 1993; Tomkins & Mavrogenes 2001), gold was precipitated at the grain boundary of the two arsenic phases (Plate 3.3.3.3.C; Möller & Kersten 1994). Invisible gold from the chalcopyrite was exsolved from the mineral at temperatures of around 400 °C, indicated by the presence of tellurobismuthite.

3.4. Red Dome

The Red Dome deposit is hosted within the steeply-dipping siliciclastics and basalt of the Siluro-Devonian Chillagoe Formation which is dominated in the western part of Red Dome by chert and sandstone, while in the eastern part of the deposit by sandstone and basalt (Fig. 3.4.). During the emplacement of the porphyry body limestone recrystallised to marble and was later converted to skarn during metasomatism. Skarn types at Red Dome are minor clinopyroxene (~21 %) and wollastonite skarn (~5 %) and the most abundant type is garnet-magnetite skarn, which can be subdivided into brown garnet skarn, brown green garnet skarn and magnetite-garnet skarn. They were all described in detail in previous work by Torrey (1986), and, as they are very similar to the skarns already described at Mungana and Redcap, they will not be outlined again.

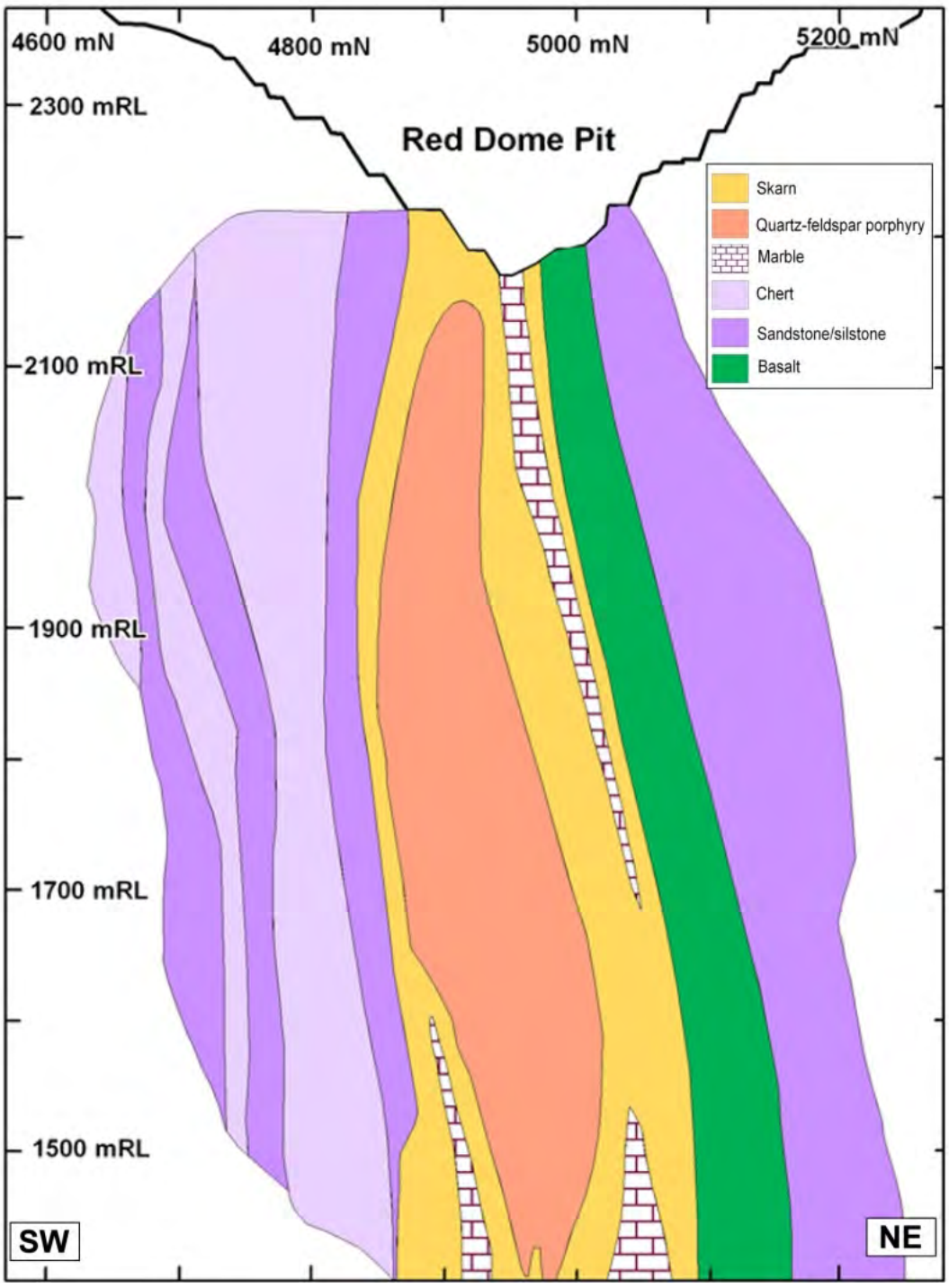

Figure 3.4. Schematic cross section (6700 E) of Red Dome showing steeply-dipping lithologies of the Chillagoe Formation and skarn development around the emplaced porphyry; modified from Coffey 2010.

3.4.1. Intrusive rocks

Only one major intrusive rock type occurs at Red Dome. This porphyry can be divided based on its appearance as well as special distribution into two subunits. Porphyry A shows relatively abundant quartz-feldspar phenocrysts and occurs in the western part of the Red Dome deposit,

while porphyry B is a very fine grained dacitic porphyry and occurs in the eastern part of the deposit. No cross cutting relationships between the porphyry types have been observed.

3.4.1.1. Quartz-feldspar porphyry (type A)

This porphyry appears greenish grey in hand specimen and consists of ~12 % phenocrysts in a very fine grained groundmass (Plate 3.4.1.1.A & B). The phenocrysts are on average 2 mm (up to 3 mm) subangular to rounded and commonly embayed (Plate 3.4.1.1.C), partly showing undulatory extinction and rarely being surrounded by a 0.25 mm inner corona of granophyric quartz-feldspar intergrowth and 0.25 mm outer corona of quartz, and on average 1.5, up to 2.5 mm-sized rounded to subhedral lath shaped, mainly simple twinned K-feldspar, which can be partly retrogressed to 0.5 mm-sized anhedral epidote, flaky sericite (Plate 3.4.1.1.F), but in general is heavily altered to a sericite-clay mixture. Minor on average 0.7 mm-sized heavily altered relicts of biotite occur in the groundmass and are associated with 55 µm-sized euhedral zircons, ~0.17 mm, up to 0.24 mm-sized marcasite and ~20 µm-sized anhedral chalcopyrite.

The groundmass consists of on average 0.25 mm-sized (up to 0.7 mm) heavily altered subhedral lath shaped feldspar with some relicts indicating a K-feldspar composition. Rare ~80 µm, up to 0.12 mm-sized cubic pyrite, and/or smaller 40 µm-sized subhedral arsenopyrite are disseminated within the groundmass. The porphyry is cut by on average 0.25 mm thick veins consisting of ~75 µm-sized sugary textured quartz, ~75 µm thick wollastonite veins or smaller than 0.1 mm-sized carbonate veins, and in places an alteration halo consisting of epidote has developed around the veins (Plate 3.4.1.1.E). No cross cutting relationship of the different veins can be observed.

In general both of the feldspars are affected by retrograde alteration resulting in epidote or sericite and, where the progress is advanced, very fine grained clay (likely kaolinite) occurs. Biotite is also heavily altered to a mixture of chlorite and clay. In a very rare case some of the phenocrysts are replaced by purple fluorite and ~1mm, up to 3 mm-sized anhedral red-brown Fe-rich sphalerite (Plate 3.4.1.2.A & B), which shows ~15 µm-sized chalcopyrite exsolution. Furthermore the sphalerite is associated with 50 µm to 0.15 mm-sized anhedral chalcopyrite and both minerals are rimmed by up to 100 µm-sized, partly lamellar marcasite. Besides the arsenopyrite and pyrite, whose paragenetic timing remains uncertain, the sphalerite, chalcopyrite and marcasite are associated with retrograde alteration.

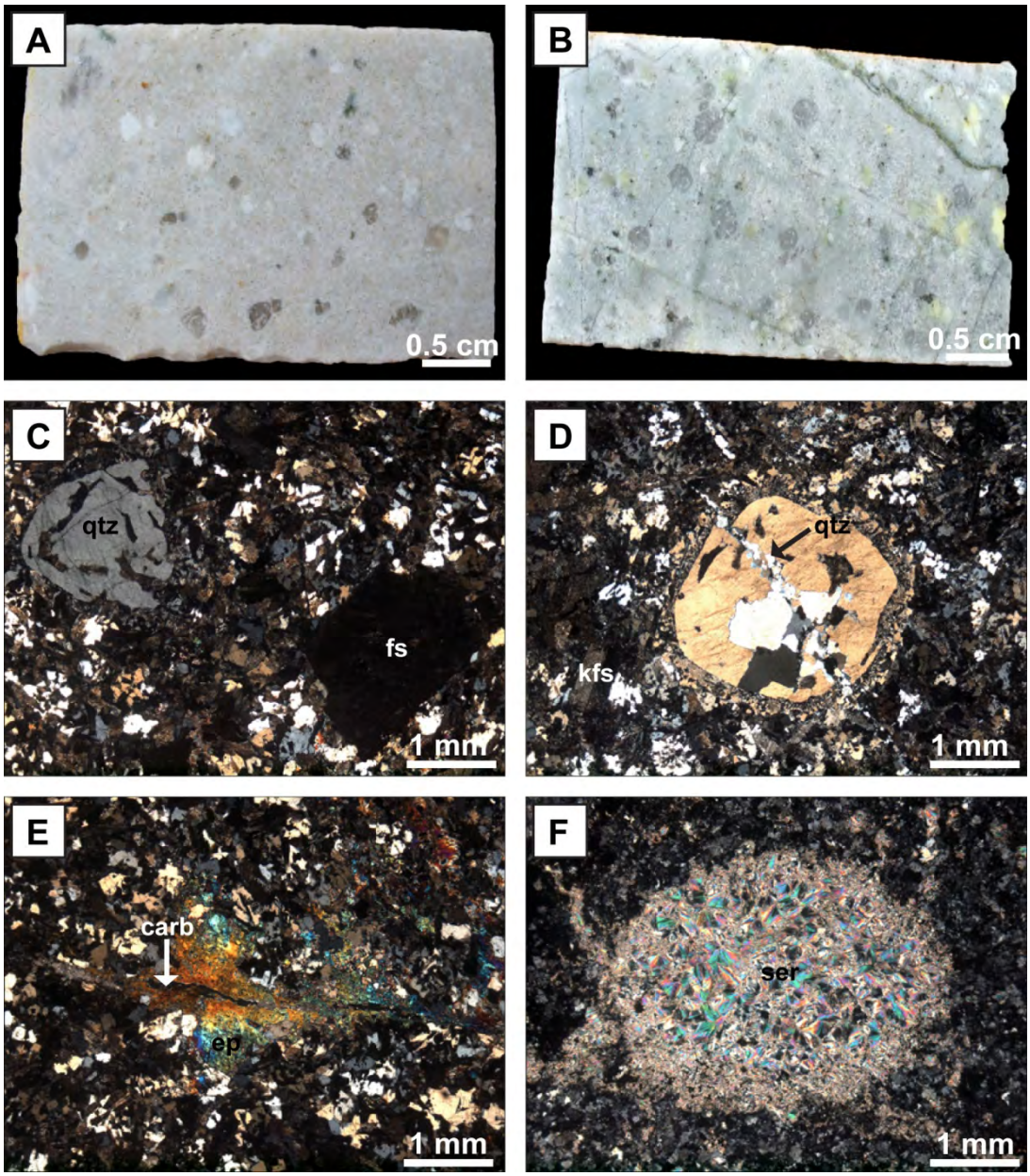

Plate 3.4.1.1 Photographs and transmitted (XPL: crossed polars) photomicrographs of quartz-feldspar porphyries from the Red Dome deposit; **A**: grey quartz-feldspar porphyry (936-635.22); **B**: greenish-grey quartz feldspar porphyry (984-525.26); **C**: quartz-feldspar porphyry with quartz (qtz) and feldspar (fs) as phenocrysts in a fine grained groundmass consisting of the same minerals (XPL, 936-635.22); **D**: quartz (qtz) phenocrysts surrounded by a 0.23 mm inner rim of granophyric quartz-feldspar intergrowth and an outer rim of the same size consisting of quartz (XPL, 984-525.26); **E**: carbonate vein with epidote alteration halo cutting the ground mass (XPL, 936-635.22); **F**: phenocryst completely replaced by sericite (XPL, 983-885.98).

3.4.1.2. Dacitic porphyry (type B)

This porphyry also appears greenish grey in hand specimen, but in comparison to porphyry A it contains sparse, small phenocrysts (Plate 3.4.1.2.C). Very rare ~0.75 mm, up to 1mm-sized, rounded to subhedral lath shaped plagioclase as well as rounded, simple twinned K-feldspar of similar size occur in a fine grained groundmass consisting of ~0.25 mm-sized quartz and

subhedral plagioclase and K-feldspar (Plate 3.4.1.2.D). Both feldspars have been subject to retrograde alteration resulting in sericite or where advanced into clay and leaving the feldspars looking cloudy. Relicts of greenish brown biotite occur in the groundmass and are associated with an orange brown titanium phase (probably rutile) and ~50 µm-sized euhedral zircons. Very rare ~40 µm-sized anhedral chalcopyrite and sphalerite are disseminated throughout the groundmass.

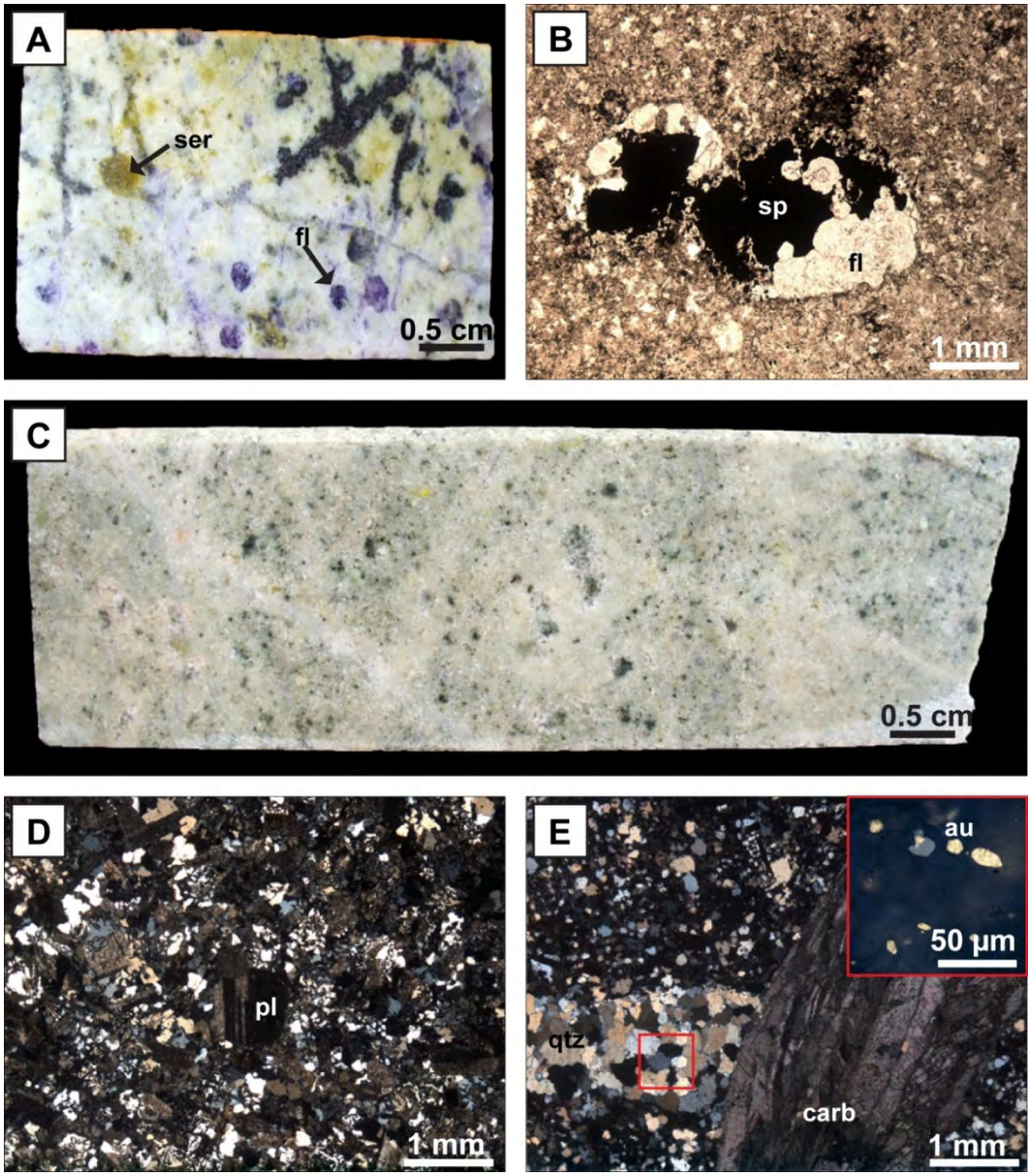

Plate 3.4.1.2. Photographs, transmitted (PPL: plane-polarised, XPL: crossed polars) and reflected light (RL) photomicrographs of a fluorite bearing quartz-feldspar porphyry and dacitic porphyry from the Red Dome deposit; **A**: quartz-feldspar porphyry with some the phenocrysts replaced by sericite (ser) or fluorite (fl), (983-885.98); **B**: phenocrysts replaced by fluorite (fl) and sphalerite (sp), (PPL, 983-885.98); **C**: dacitic porphyry (995-614.15); **D**: dacitic porphyry with plagioclase (pl) building rare phenocrysts (XPL, 995-614.15); **E**: dacitic porphyry cut by gold carrying (RL, small inset) quartz (qtz) vein which then is cut by a later carbonate (carb) vein (XPL, 995-478.59).

The porphyry is cut by a network of up to 2mm wide veins consisting of ~0.25 mm-sized sugary quartz grains, which are rich in <15 µm-sized fluid inclusions (~25 % vapour phase with occasional halite daughter crystals). These quartz stockwork veins can host ~50 µm, up to 0.1 mm-sized chalcopyrite, <15 µm-sized tetrahedrite, <15 µm-sized gold (partly associated with tetrahedrite) and <15 µm-sized hedleyite. Except for the gold-tetrahedrite association no direct relationships between the other ore phases can be observed, so it is assumed that all are part of the same paragenetic sequence. The quartz stockwork is cut by ~2.5 mm laminated carbonate veins, which therefore postdate the gold-copper event (Plate 3.4.1.2.E).

3.4.2. Mineralisation

Three main types of mineralisation occur at Red Dome: 1. zinc-copper-lead, 2. copper-(antimony) and 3. gold. These are described in the next sections.

3.4.2.1. Zinc-copper-lead

This mineralisation type commonly occurs in veins, cavity or fracture fills ranging in size between 1 cm and up to 1 m cutting either hedenbergite or green garnet-magnetite skarn or marble, but these veins also extended into the siliciclastic host lithologies of the Chillagoe Formation.

Dark red-brown, Fe-rich, and rare honey coloured sphalerite are the dominant mineral phases. The sphalerite can be found associated with calcite, quartz and fluorite in veins rimmed by molybdenite (Plate 3.4.2.1.A) or is overprinted by ~0.5 cm, up to 1.5 cm-sized lamellar marcasite (Plate 3.4.2.1.B). Commonly the sphalerite is associated with anhedral chalcopyrite (Plate 3.4.2.1.C & D), which can also be found as micrometre thick exsolution within the sphalerite. Another mineral in this mineralisation type is on average 100 µm, up to 0.25 mm-sized tennantite, overprinting the earlier chalcopyrite and sphalerite. In some localities the Fe-rich sphalerite has a thin weathering crust of hematite (Plate 3.4.2.1.E).

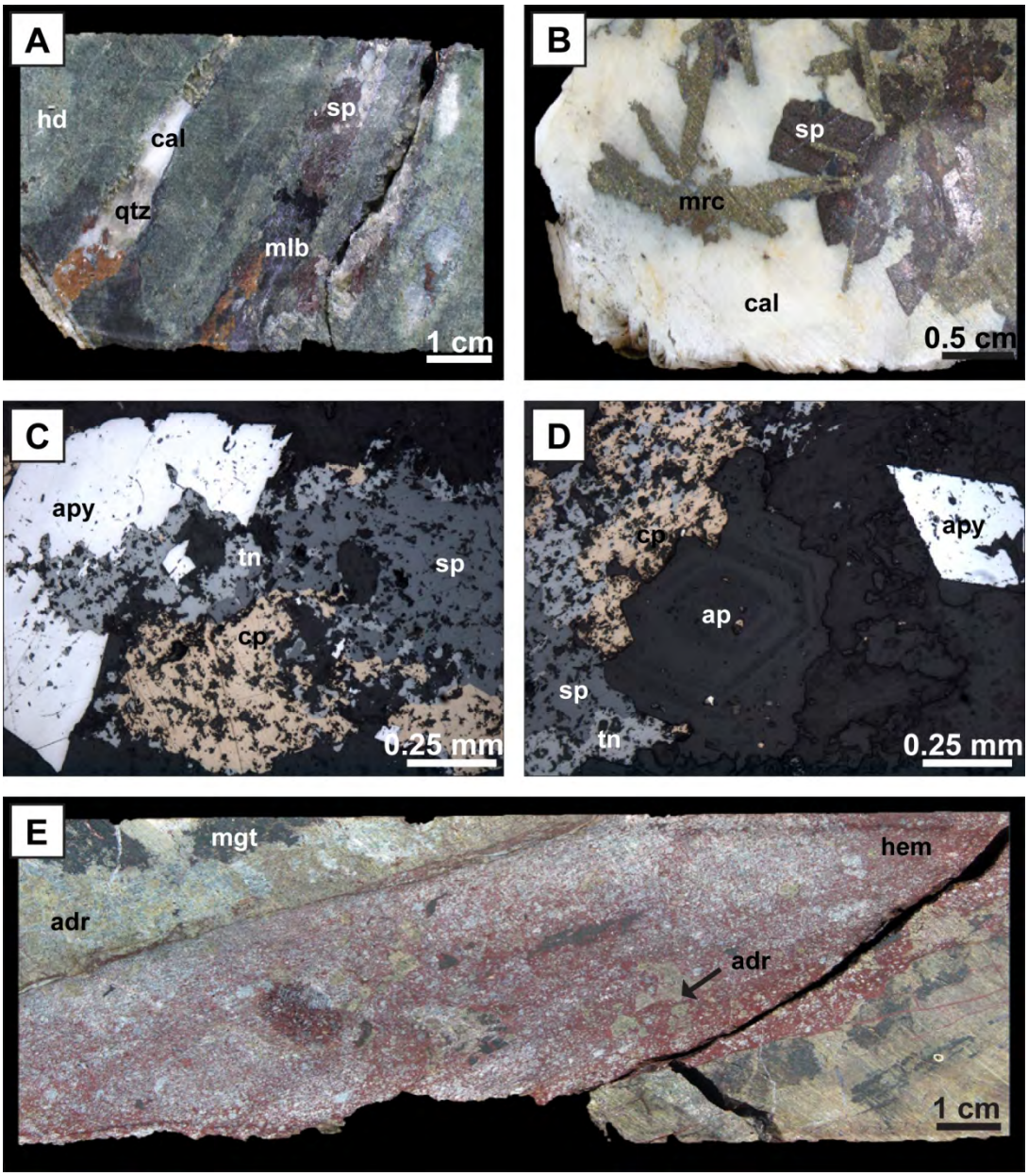

Plate 3.4.2.1. Photographs and reflected light (RL) photomicrographs of zinc-copper-lead mineralisation from the Red Dome deposit; **A**: sphalerite (sp) associated with calcite (cal), quartz (qtz) and molybdenite cutting hedenbergite (hd) skarn (937W4-1133.19); **B**: sphalerite (sp) with slightly later lamellar marcasite (mrc) in calcite (cal), (937W4-999.50); **C**: sphalerite (sp) with chalcopyrite (cp) and later tennantite (tn) and earlier arsenopyrite (apy), (RL, 983-885.71); **D**: sphalerite (sp) associated with chalcopyrite (cp) and later tennantite (tn) overprinting apatite (ap), (RL, 983-885.71); **E**: green andradite (adr) skarn with associated magnetite (mgt) cut by brecciated fault zone of angular andradite clasts in former sphalerite matrix, which is now hematite (hem), (937-1129).

3.4.2.2. Copper-(antimony)

This is the most abundant mineralisation type at Red Dome and can be commonly found associated with green magnetite skarn or marble (Plate 3.4.2.2.A & B). Most abundant copper minerals are 0.25 mm to 1.5 mm anhedral bornite and ~0.25 mm, up to 0.5 mm-sized anhedral chalcopyrite. Both copper minerals commonly show myrmekitic intergrowth or exsolution

lamella of one copper phase in the other and are partly retrogressed to covellite. Other minerals associated with the copper minerals are colourless fluorite, stibnite or chalcostibite ($CuSbS_2$) occurring in form of up to 1 cm veins or in ~0.5 mm-sized anhedral grains as well as 1-10 µm-sized native bismuth, 30 µm to 0.1 mm-sized hessite and ~15 µm-sized altaite and volynskite, with the silver-lead and tellurium phases assumed to have been exsolved from their host mineral during retrograde alteration. Torrey (1986) also observed petzite and sylvanite in this mineralisation type, but no gold-silver-tellurides were observed in this study.

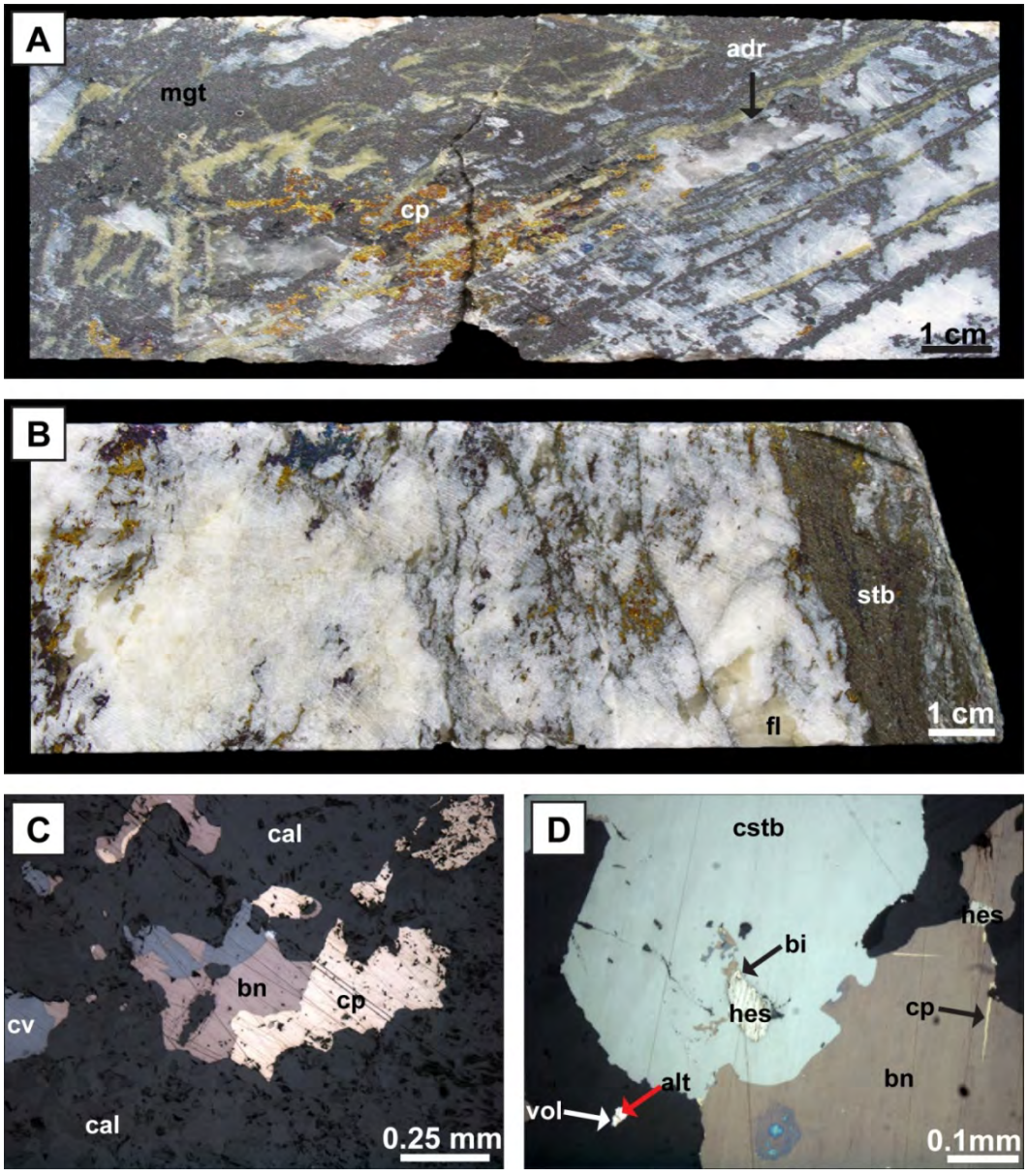

Plate 3.4.2.2. Photographs and reflected light (RL) photomicrographs of copper-(antimony) mineralisation from the Red Dome deposit; **A**: massive magnetite (mgt) associated with green andradite (adr) and minor chalcopyrite (cp) in marble (937W3-999.30); **B**: chalcopyrite, bornite and fluorite (fl) in marble, cut by a stibnite vein (937W5-983); **C**: chalcopyrite (cp) with later bornite (bn) and later covellite (cv) in marble (RL, 937W5-983); **D**: bornite (bn) with rare chalcopyrite (cp) exsolution lamellae and associated chalcostibite (cstb) and minor hessite (hes), volynskite (vol), altaite (alt) and native bismuth (bi), (RL, 937W5-983).

3.4.2.3. Gold

Gold mineralisation occurs in several settings. Free gold grains can be observed in calcite veins cutting green-garnet magnetite skarn (Plate 3.4.2.3.A) or within retrograde altered mineralised fractures cutting porphyry (Plate.3.4.2.3.B).

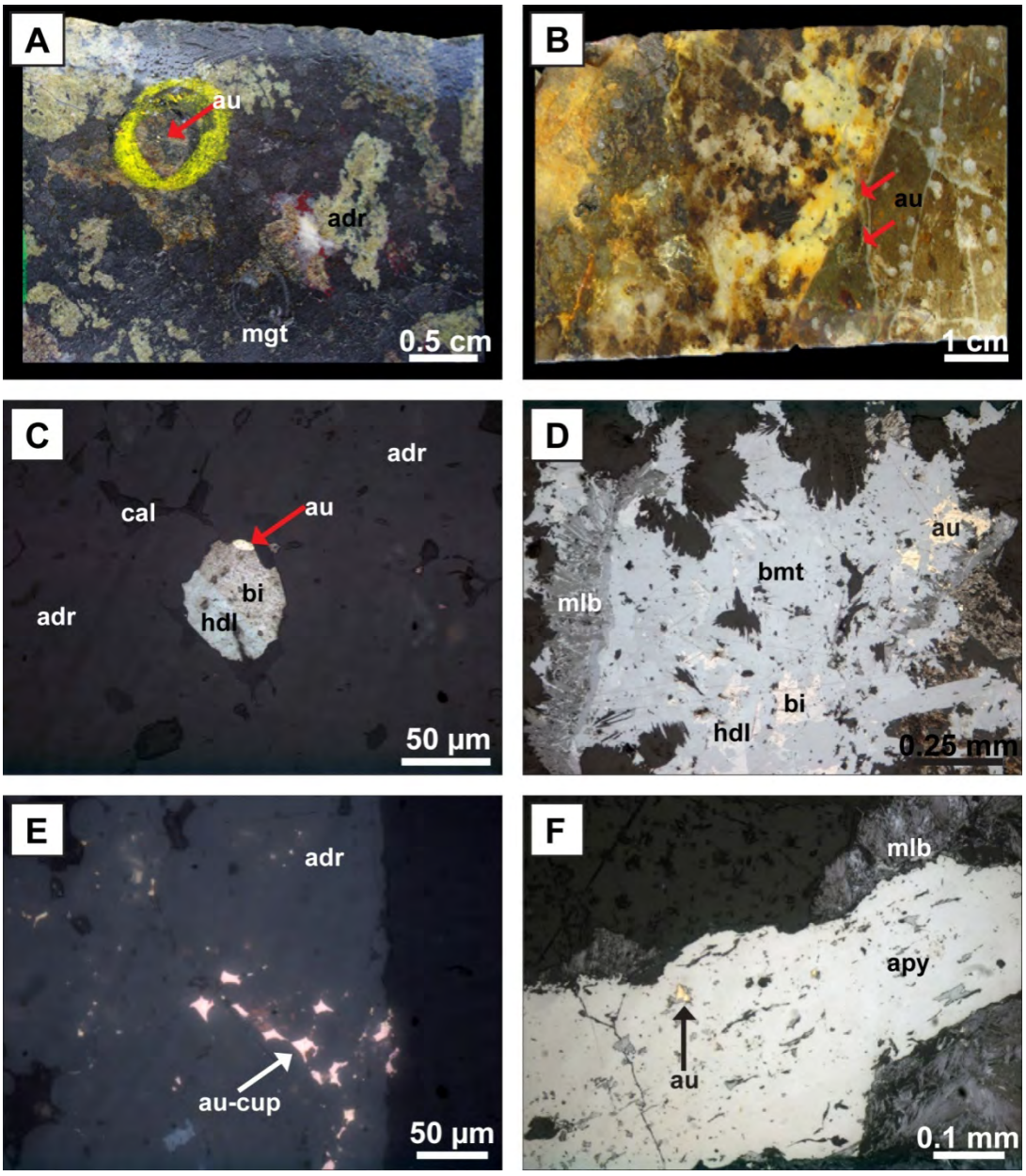

Plate 3.4.2.3. Photographs and reflected light (RL) photomicrographs of gold mineralisation from the Red Dome deposit; **A**: magnetite (mgt) green andradite (adr) skarn cut by very small calcite vein hosting visible gold (au), (937-1153); **B**: retrograde altered mineralised quartz fracture with visible gold (au), (983-879.90); **C**: native gold (au) associated with hedleyite (hdl) native bismuth (bi) and calcite (cal) in andradite (adr) skarn (RL, 937W5-1044A); **D**: native gold (au) associated with native bismuth (bi), hedleyite (hdl) and bismuthtinite (bmt), overprinted by later molybdenite (mlb) in sericite altered porphyry (RL, 983-880.28); **E**: tetra-auricupride (au-cup) along tiny fracture in andradite (adr) skarn (RL, 937W4-1039); **F**: native gold in arsenopyrite rimmed by later molybdenite (mlb) in quartz (RL, 983-880.28).

At a micro scale, 1-10 µm-sized gold grains are intimately associated with ~50 µm-sized native bismuth and hedleyite (Plate 3.4.2.3.C) in late calcite filled fractures cutting through earlier brown garnet skarn. Within the mineralised fracture environment gold is either associated together with native bismuth, hedleyite and bismuthinite, with molybdenite appearing to be younger than the gold-bismuth-tellurium-sulphur assemblage (Plate 3.4.2.3.D) or occurs as inclusions within arsenopyrite, which is rimmed by flaky molybdenite (Plate 3.4.2.3.F). Alternatively tetra-auricupride (AuCu) can be found adjacent to mini fractures in the same skarn (Plate 3.4.2.3.E). A direct relationship between tetra-auricupride and the gold-bismuth-tellurium assemblage could not be observed, although both occur within the sample.

3.4.3. Paragenetic sequence

This section summarises the paragenetic sequence for the mineralisation for the Red Dome deposit (Fig. 3.4.3.) based on descriptions outlined in the previous sections.

Magnetite is, as for Mungana and Redcap, the earliest phase at Red Dome, but while at the other two deposits it is only associated with silicate phases, it occurs at Red Dome additionally together with chalcopyrite and bornite (Plate 3.4.2.2.A) with Simon et al. (2000) suggesting that this Cu-Fe-S assemblage is typical for high temperature porphyry copper-gold deposits. Arsenopyrite, possibly molybdenite as well as stibnite and chalcostibite also occur during the prograde phase, with the latter not being observed by Torrey (1986).

Sphalerite occurs from the late prograde to intermediate retrograde stage, although its main occurrence is the retrograde stage. It is associated with molybdenite (Plate 3.4.2.1.A), chalcopyrite, and earlier arsenopyrite, and it is overprinted by marcasite and tennantite (Plate 3.4.2.1.B & C), with the latter mineral assemblage being also common at Mungana.

Gold mineralisation at Red Dome is retrograde and like at Redcap associated with several Bi-S-Te phases suggesting formation temperatures below 266 °C (Barton & Skinner 1979) with the bismuth-tellurides and sulfosalts assemblage commonly observed in sulfide-poor-Au-systems (Ciobanu et al. 2009) like IRGs of Tintina (Alaska) and Timbarra (Australia) (Baker et al. 2005). In addition to the Au-Bi-Te-S association, gold also occurs in the form of tetra-auricupride (Plate 3.4.3.2.E) at even lower temperatures of 75 and 150 °C (Tomkins & Pinnel 1976), with this mineral likely being a secondary mineral phase developed through gold being substituted by copper as postulated by Knipe and Fleet (1997).

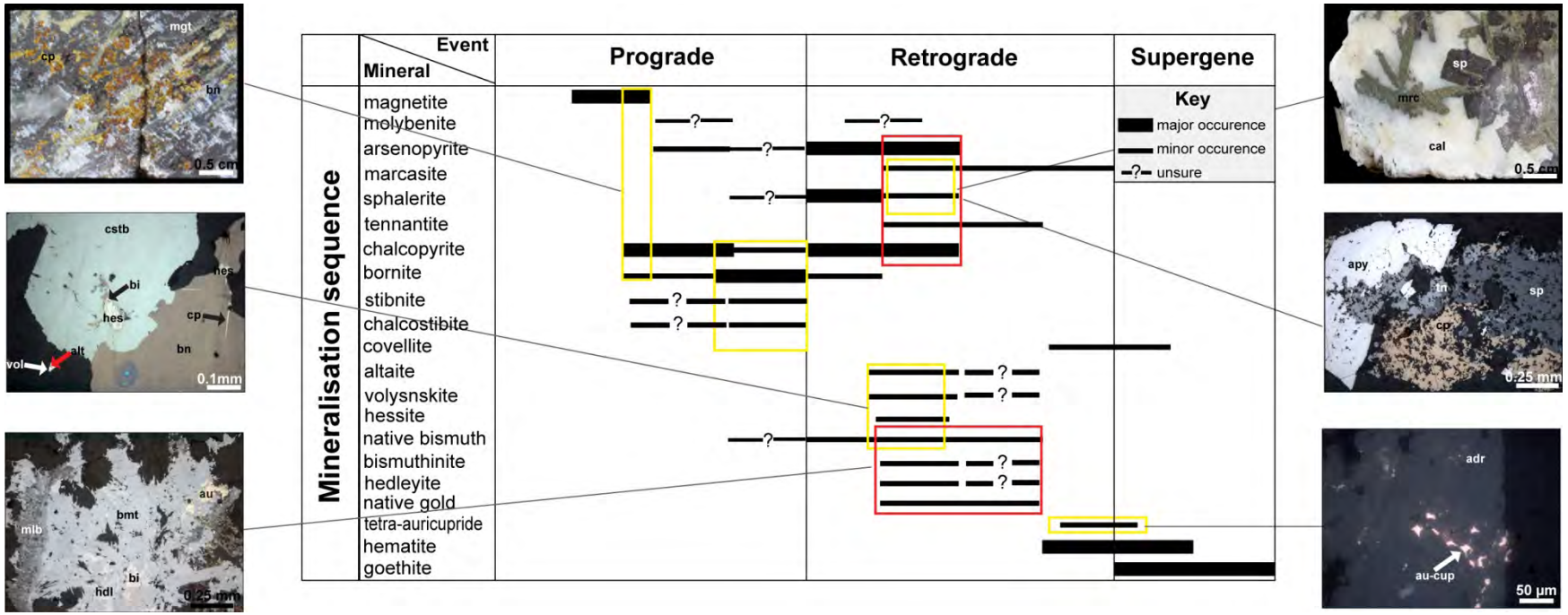

Figure 3.4.3. Paragenetic sequence of the mineralisation from the Red Dome deposit.

3.5. Summary

Four main paragenetic stages of skarn and mineralisation formation occur at Redcap, Red Dome and Mungana. The first stage is represented by contact metamorphism caused by the emplacement of igneous bodies resulting in recrystallisation of limestone to marble, bleaching of the siliciclastic units and basalts as well as in the formation of banded skarn and the development of quartz stockwork. The second stage is characterised by prograde metasomatism resulting in nearly identical skarn sequences at all three deposits (Fig. 3.5.), although the abundance of single skarn types varies at Redcap, Red Dome and Mungana which could be due to different abundance of country rocks as well as composition of the igneous rocks.

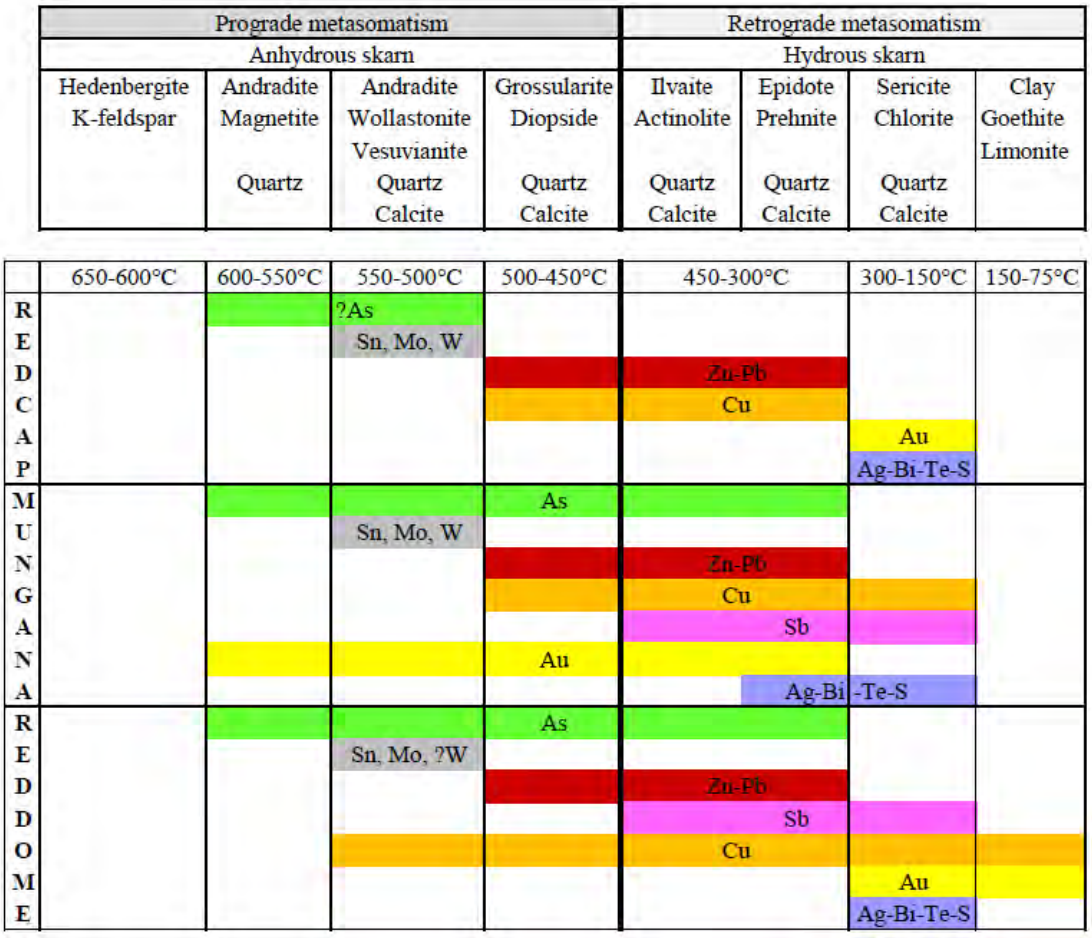

Figure 3.5. Summary of skarn mineral assemblages, formation temperatures and comparison of associated mineralisation types occuring Redcap, Mungana and Red Dome.

While skarn sequences of the three deposits are very similar the mineralisation associated with the second stages differs. At Red Dome, copper is the dominant mineralisation type; at Redcap zinc-copper-lead and iron mineralisation dominates, while at Mungana arsenic-iron-zinc-copper-lead mineralisation is the most abundant mineralisation style. In the third stage of retrograde alteration with again no major difference in the skarn sequence, the mineralisation of

the three deposits is also distinct in some aspects (Fig. 3.5.). At Red Dome zinc mineralisation is rare and associated with arsenic and copper phases, although zinc has also been reported do be incorporated into chlorite (Rule & Radke 1988), but at Redcap and Mungana zinc is associated with copper-lead and to a minor degree iron phases in the form of marcasite.

Gold mineralisation on the other hand is associated with Bi-Te-S minerals at Redcap and Red Dome and developed at very low temperatures (<266 °C) in a possible sulphide-poor environment (Ciobanu et al. 2009), whereas gold at Mungana is associated with arsenic, copper and antimony minerals and formed at higher temperatures of ≥ 400 °C., with the occurrence of gold along grain boundaries suggesting that the gold was originally incorporated into one mineral phase such as loellingite and possibly chalcopyrite. Although this higher temperature event was not observed at Redcap and Red Dome in this study, observations of Ewers & Sun (1988b) indicate that at Red Dome some of the gold may have been originally incorporated into arsenic-copper minerals and therefore suggest that the gold associated with Bi-Te-S phase might be part of a remobilising event.

In summary, the paragenetic sequences of the Redcap, Red Dome and Mungana are very similar regarding the silicate phases, whereas more differences occur in the sulphide mineralisation, with the Redcap deposit lacking arsenic and antimony minerals and also not showing a variety in copper minerals, chalcopyrite being the only economic phase. Whether these differences are related to different igneous sources, (no porphyry body has so far being identified at Redcap), or just indicate that the Redcap deposit is not as intensively explored as the other two deposits and therefore lacks the variety of sulphide minerals can not be inferred from the observations presented in this chapter. Studies of trace elements and radiogenic isotopes of different silicate and sulphide phases presented in the next chapters will address this problem.

Chapter 4: Mineral chemistry of garnets, clinopyroxenes, sphalerite and gold from Redcap, Mungana and Red Dome

4.1. Introduction

In the previous chapter the paragenetic sequences for silicate and sulphide minerals from the Redcap, Mungana and Red Dome deposits were established. While garnets and clinopyroxenes from all three deposits are associated with identical calc-silicate mineral assemblages which have the same timing (early to late prograde) differences in mineral assemblages and timing of the base metal and gold mineralising events occur between Recap, Mungana and Red Dome. Base metal mineralisation at Redcap and Mungana occurs in the late prograde to medium retrograde stage with sphalerite, chalcopyrite and galena being the dominant ore phases, while at Red Dome base metal mineralisation can only be found in the retrograde stage and sphalerite is often associated with marcasite and rare chalcopyrite. Gold mineralisation is similar at Redcap and Red Dome with gold linked to bismuth and telluride mineral phases and occurring very late in the retrograde stage. At Mungana on the other hand, gold is associated with copper, arsenic and antimony and occurs earlier than at the other two deposits in the retrograde stage.

In this chapter garnet, clinopyroxene, sphalerite and gold grains were further investigated by electron microprobe (EMP) and laser ablation inductively coupled plasma mass spectrometry (LA-ICP-MS) for their major and trace elements to check whether the identified petrographic similarities and differences are also reflected in the mineral chemistry. The question of whether garnet compositions can be used as exploration tool, as suggested by Paverd (1981), is addressed. Additionally, trace element data from sphalerite will be used to identify the deposit style, as at Mungana two hypothesis for the origin of the base metal mineralisation exist, with Georgees (2007a) suggesting the base metal mineralisation was associated with an early skarn while Nethery & Barr (1996) suggesting a VMS deposit style. Furthermore the copper content of gold will be used to examine the number of gold events occurring in the Red Dome, Mungana and Redcap area, as well as to identify the deposit style. The results are presented in the following sections and the EMP and LA-ICP-MS data are provided in appendices 4-7 and 9-11.

4.2. Major and trace elements in garnets and clinopyroxenes

Skarn deposits are classified based on their main ore commodities into seven types: Cu, Fe, Mo, Sn, W, Zn (Einaudi et al. 1981) and Au (Meinert 1989). Meinert (1992) showed that some of the

skarn types are represented by specific calc-silicate mineral compositions (in this case garnets and clinopyroxenes), while others show a wide range of compositional variety, but even those skarn systems do show general zonation patterns representing fluid pathways and evolution as well as changes in temperature, with a combination of them being used as exploration tool (Meinert 1987). These zonation patterns can either be a change in the overall mineral occurrence with garnets occurring proximal to the magmatic source, pyroxenes distal, and wollastonite-vesuvianite assemblages at the skarn-marble contact (Meinert et al. 2005) or it can be a change of colour within a single mineral group as observed by Atkinson & Einaudi (1978) for garnets. They observed that garnets proximal to the intrusion are dark red-brown, become lighter brown distal to the intrusion and have pale yellow-green colours adjacent to the marble front although there is still discussion about whether different garnet colours are controlled by major elements only (Deer et al. 1992) or a combination of major and trace elements (Meinert et al. 2005).

The overall problem with the kind of “regional” zonation is that some skarn deposits are not explored to the edge and therefore some patterns can not be observed and may misdirect exploration. Based on this problem other authors took a different approach and investigated compositional variations within single garnet grains regarding their major and trace element composition (Jamtveit 1991; Yardley et al. 1991; Jamtveit et al. 1993; Jamtveit & Hervig 1994), stable isotopes (Bowman 1998; Crowe et al. 2001) or REE (Nicolescu et al. 1998; Whitney & Olmsted 1998; Smith et al. 2004; Gaspar et al. 2008) to reveal the evolution of skarn systems. Jamtveit et al. (1993) observed that cores representing the composition of the intrusion are in general more grossular rich, while rims, which reflect a reaction with infiltrating fluids, are of more andraditic composition. Such core-rim variations were also observed by Nicolescu et al. (1998) who also detected that the Fe-richer cores are LREE-poorer while the Fe-richer rims are enriched in LREE. Since systems are complex in the Chillagoe district due to single events being obliterated by multiple events of reactivation and remobilisation (Nethery & Barr 1998; Georgess & Nethery 1999; Georgees 2007a, Hodkinson et al. 2009), it was decided to use intra-grain scale analyses to reveal the history of the skarn and mineralisation formation.

4.2.1. Methodology

After a detailed petrographic study of garnets and clinopyroxenes, fourteen samples representing different optical and textural features (Tab. 4.2.1.) were selected for major and trace element analyses.

Table 4.2.1. Sample location and description of garnets and clinopyroxenes

			GARNET			CLINOPYROXENE		
Deposit	**DH-interval**	**Colour**	**Optical property**	**Texture**	**Comp.**	**Colour**	**Comp.**	**Mineralisation**
Redcap	949-165.80	brown	anisotropic	growth zoning	Adr_{100-75}	----	----	sp-gn-cp
Redcap	949-179.15	brown	anisotropic	growth zoning	Adr_{95-66}	----	----	later sp
Redcap	949-443.68	----	----	----	----	dark green	Hd_{94-91}	mgt
Redcap	952-574.42	yellow-green	isotropic	none	Adr_{100-67}	----	----	later cp-po
Redcap	952-575.2III	red-brown	anisotropic	growth zoning	Adr_{100-84}	----	----	mgt-po; late Au-Bi
Redcap	974-291.01	brown	weakly anisotropic	sector twinning	Grs_{88-92}	pale green	Di_{94-78}	-----
Redcap	974-349.86	orange-brown	isotropic	none	Adr_{100-98}	----	----	-----
Mungana	859-612.5	yellow-green	isotropic	weak zoning	Adr_{100-96}	----	----	later cp
Mungana	859-765.8	brown	anisotropic	growth zoning	Adr_{100-99}	----	----	-----
Mungana	890W6-787.56	orange brown	isotropic	patchy	Adr_{97-87}	pale green	Di_{72-63}	mlb
Red Dome	841-530.1	yellow-brown	isotropic	none	Adr_{100}	----	----	-----
Red Dome	939-731.9	yellow green	isotropic	none	Adr_{100-14}	----	----	mlb
Red Dome	939-772.2	brown	anisotropic	growth zoning	Adr_{83-72}	----	----	-----
Red Dome	939-1103.02	red-brown	anisotropic	growth zoning	Adr_{100-83}	dark green	Hd_{98}	mgt

Major elements were determined in situ in polished thick sections (thickness 70 µm-100 µm) using a JEOL JXA 8200 electron microprobe with five wavelength dispersive spectrometers at the AAC-JCU (Townsville) with the following standards being used for calibration: almandine (Si, Fe), spessartine (Mn, Al), olivine (Mg), wollastonite (Ca), TiO_2 (Ti), albite (Na) and orthoclase (K). Operating conditions were 20 nA beam current, 15 kV accelerating voltage and 10 µm beam diameter with 20 seconds counting time on the Kα peak and 10 seconds on the background. Trace element data were obtained with a GeoLas 193 nm ArF laser coupled to a Varian 820 quadrupole ICP-MS unit. The laser was operated a 10 HZ pulse rate and the laser energy was 6 J/cm^2. Spots without visible inclusions and alteration, as well as without any cracks were selected and on average 5-10 spot analyses (depending on the size of the garnet/clinopyroxene) from core to rim were conducted with the spot size ranging from 24 to 44 µm. Calibration was performed using NIST 610 as a primary standard and NIST 612 as a secondary one to check for reproducibility and accuracy. Data were processed using Ca as internal standard (previously determined EMP values) and the data reduction software GLITTER 4.4.2. (Van Achterbergh et al. 2001).

Element maps of garnets were quantified by electron microprobe spot analyses using a JEOL JXA 8200. First of all the area, which should be mapped, was selected (in this case a whole garnet grain) and the map size defined (best resolution, i.e. in general 500 x 500 pixel, except of one map 500 x 350 pixel). Depending of the grain and map size the number of required spot analyses was calculated with spot analyses being conducted every 2, 5 or 8 µm. Elements analysed include Al, Fe, Mn and Sn with the following standards being used for calibration: almandine (Fe), spessartine (Mn, Al) and cassiterite (Sn). Operating conditions were 20 nA beam current, 15 kV accelerating voltage and 2 to 6 µm beam diameter.

4.2.2. Garnet and clinopyroxene petrography

Garnets at Redcap, Red Dome and Mungana occur in barren and mineralised skarns with base metals (dominated by chalcopyrite and sphalerite) or magnetite being the most common mineralisation types. Garnets show a variety of colours, textural features and compositions (Tab. 4.2.1). Different shades of brown are the dominant colour (Plate 4.2.2.A & C), while pale yellow to green garnets (Plate 4.2.2.E, G & I) are less common. In transmitted light some garnets are completely isotropic, but in back-scatter some of them show internal textures like patchy zoning (Plate 4.2.2.B) and very weak growth zoning (Plate 4.2.2.F) while others remain featureless (Plate 4.2.2.J).

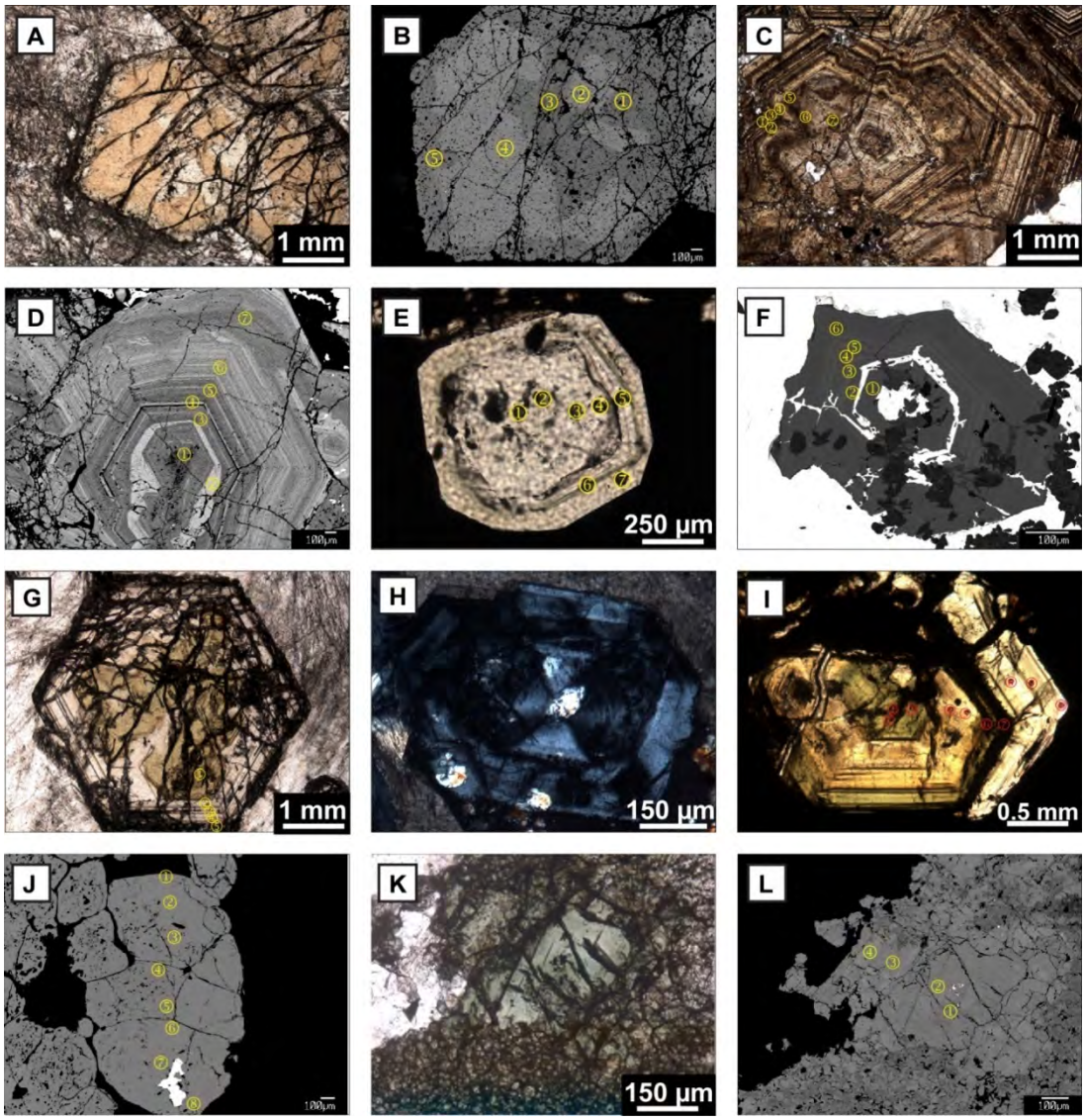

Plate 4.2.2. Transmitted light photomicrographs (PPL: plane-polarised light & XPL: crossed polars) and back-scattered electron images (BSE) of representative garnet and clinopyroxene grains form Redcap, Mungana and Red Dome; **A**: orange brown andradite garnet in wollastonite skarn (PPL, 890W6-787.56); **B**: previous garnet showing patchy zoning (BSE); **C**: brown, anisotropic andradite with growth zoning (PPL, 859-765.8); **D**: anisotropic andradite with growth zoning (BSE, 949-165.80); **E**: very pale yellow andradite with visible growth zones towards the rim (PPL, 859-612.15); **F**: andradite surrounded by massive sphalerite (white), (BSE, 949-179.15); **G**: yellow-green andradite core with a nearly colourless rim (PPL, 939-731.9); **H**: grossular with sector twinning (XPL, 974-291.01); **I**: green-yellow andradite with broad growth zones in chalcopyrite (black), (PPL, 952-574.42); **J**: featureless andradite with arsenopyrite inclusion (white), (BSE, 841-530.10); **K**: massive hedenbergite skarn (PPL, 949-443.68); **L**: previous clinopyroxene showing dark and light patches (BSE, 949-443.68).

Anisotropic garnets on the other hand show growth zoning ranging from very fine scaled to broad bands (Plate 4.2.2.C, D, G & I). One garnet shows sector twinning (Plate 4.2.2.H). Almost all garnets are fractured with some of the fractures being filled with either quartz or calcite, which can be associated with ore minerals like arsenopyrite, scheelite, molybdenite, chalcopyrite or native bismuth and bismuth-tellurides.

Only a few grains of clinopyroxene were analysed in this study. Most of them are part of a barren skarn with only a few being associated with magnetite or pyrrhotite. Compared to the garnets they do not show many variations in colour or internal texture. In general the clinopyroxenes are pale to dark green (Plate 4.2.2.K) and in back-scatter they show patches of darker and lighter zones.

4.2.3. Garnet and clinopyroxene composition

All garnets from the Redcap, Red Dome and Mungana deposit are part of the calcic grandite family ranging in composition from end-member andradite to 92% grossular (Fig. 4.2.3.1.). While some garnets are homogenous in their composition (e.g. 841-530.1, 859-612.15, 859-765.80, 952-574.42), others show a huge compositional variety from core to rim from pure andradite in the core over nearly end-member grossular in the middle grain part back to andradite with 60-70% andradite component (e.g. 939-731.9, 949-165.80, 949-179.15). This change can neither be observed in the colour pattern nor is it reflected within the internal texture. The only correlation which seems to exists is that darker colours in the back-scattered electron images represent Fe-poorer zones than lighter colours, but the difference in the iron content can be as little as 0.02 wt.-%.

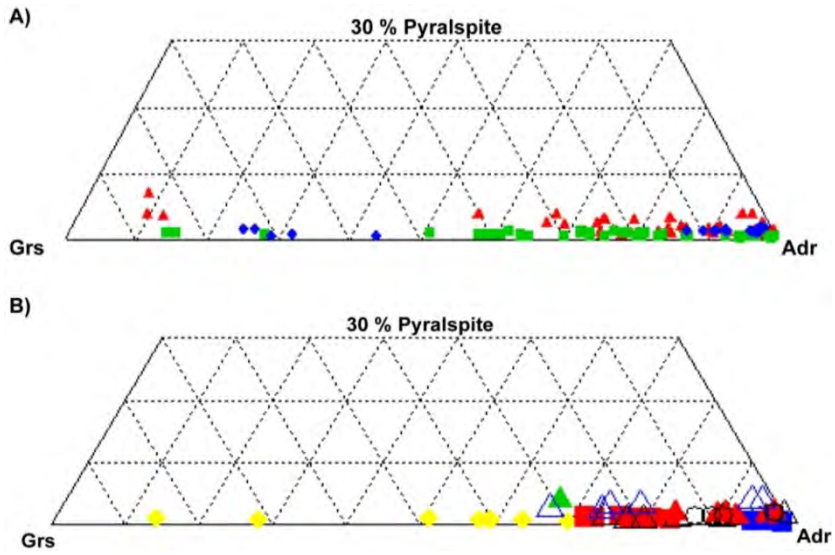

Figure 4.2.3.1. Ternary diagram of garnet compositions within the Redcap (▲,Δ, Δ, ▲), Red Dome (■, ♦, ■) and Mungana (●, ○) deposits (**A**) and within single grains (**B**); grs: grossular, adr: andradite, pyralspite: pyrobe + almandine + spessartine.

Garnets at Redcap, Red Dome and Mungana occur either in a barren skarn or are associated with three different types of mineralisation: a) magnetite, b) tin and c) sulphides (mainly base metals). The composition from garnets associated with barren skarns ranges from 0-60 wt.-% andraditic component (n=17), while magnetite dominated skarns consist of 85-100 wt.-%

andradite (n=33) (Fig. 4.2.3.2.). Garnets from sulphide rich skarns show an andraditic composition of 60-95 wt.-% (n=43), but in general the composition just reaches 85 wt.-% andradite. The last of the four garnets types investigated is tin bearing garnet, which has not been previously identified in the Chillagoe area and will be described later in this section. Garnets associated with tin mineralisation are almost always of pure andraditic composition (n = 44). Based on these observation there seems to be a link between the garnet composition and the occurrence and type of mineralisation as suggested by Paverd (1981), which could be used as exploration tool.

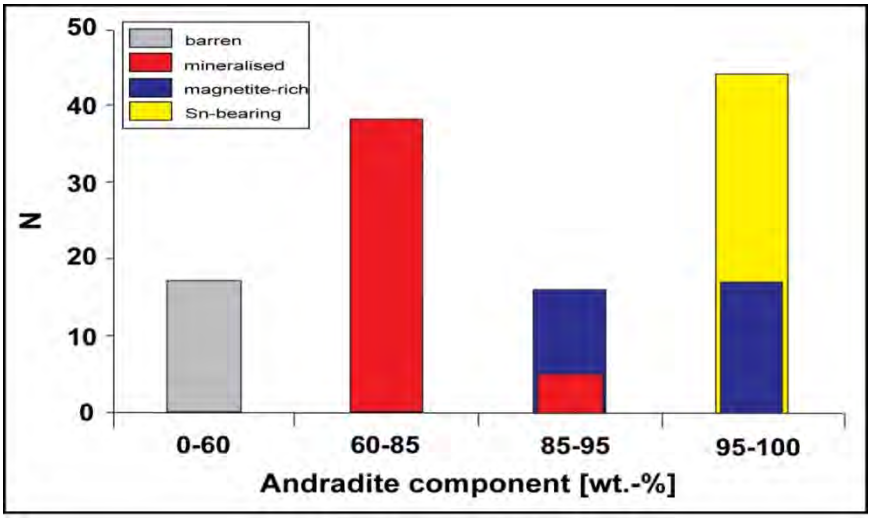

Figure 4.2.3.2. Garnet composition reflecting different skarn types ranging from barren skarns to sulphide rich skarns.

Clinopyroxenes from the three deposits are part of the calcic diopside-hedenbergite series and range in composition from nearly pure diopside to end-member hedenbergite (Fig. 4.2.3.3.) with dark green clinopyroxenes being more iron-rich while pale green ones more magnesium-rich.

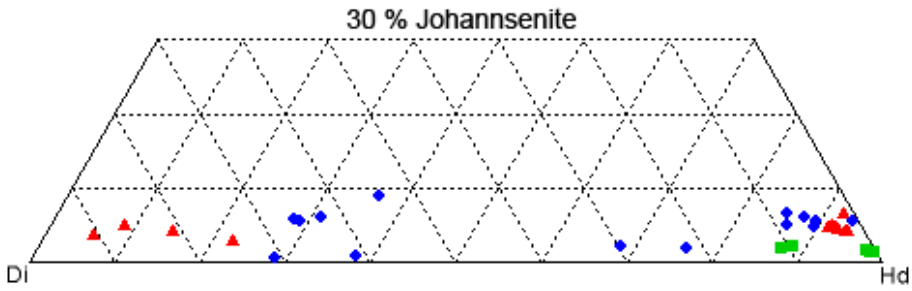

Figure 4.2.3.3. Ternary diagram of clinopyroxene compositions within the Redcap (▲), Red Dome (■) and Mungana (●) deposits and individual clinopyroxene grains; di: diopside, hd: hedenbergite.

Manganese is incorporated in all clinopyroxenes but while at Redcap and Mungana concentrations can reach up to 3 wt.-% which is a typical feature of Zn skarn systems (Meinert

et al. 2005), Mn values at Red Dome do not exceed 0.5 wt.-%. The darker and lighter patchy zones observed in back-scattered electron images again reflect the iron content with dark zones being iron-poor and lighter zones being iron-rich with a difference being as low as for the garnets.

4.2.4. Trace elements of garnets and clinopyroxenes

Trace element concentration in garnet are low for the majority of analysed elements and range between 1 to 80 ppm, such as B (7-21), Nb (1-32), Sc (1-17), Sr (1-26), V (1-81), Y (1-81), Zn (2-50) and Zr (1-78), with values above 80 ppm (4 outliners within V, Y, Zn, Zr) being linked to accidentally analysed subsurface inclusions. Elements exceeding concentrations of 80 ppm in garnets are As (109-1528), Ga (106-999), Ge (85-576), In (160-763) and Sn (84-29105). The high arsenic values occur only in two samples (859-612.15 & 952-574.42) with massive chalcopyrite, and can be linked to the chalcopyrite. Ga, Ge, In and Sn seem to be incorporated in the garnet structure. Gallium, germanium and indium concentrations are high in the yellow-green garnet skarn (100-1000 ppm), while in brown or red-brown garnets the concentrations of these elements rarely exceed values of 50 ppm. Within this element group, concentrations of Ga seem to control the colour with green garnets having values of 106-122 ppm, the yellow coloured part of the garnet showing concentrations of 220-222 ppm, brownish yellow garnets have 420-430 ppm and colourless parts reaching values of 780-1000 ppm. In this case it looks as though colour variations are not only controlled by iron and manganese as suggested by Deer et al. (1992) with the green-yellow-colourless garnet of this study being end-member andradite, but that trace element chemistry does play a role in the garnet colour, but more work is needed to confirm this.

Table 4.2.4.1. Summary of the occurrence and composition of Sn-bearing garnets

Locality	Country	SnO_2 [wt.-%]	Composition	Other Sn phases	References
Pitkäranta	Russia	0.32-1.44	Adr_{63}	n.a.	Saksela 1951, Hellwege 1956
Plavno	Czech Republic	1.07-1.36	Adr_{90}	stannite, cassiterite	Dadak & Novak 1965
El Hamman	Morocco	~ 3.5	Adr	malayaite	Sonnett 1981
Davib Ost	Namibia	0.4-5.82	Adr_{95-99}	n.a.	McIver & Mihalik 1975
Tsumo	Japan	0.76	Adr	malayaite, cassiterite	Amthauer et al. 1979
Cassiar district	Canada	0.9	Adr_{100}	n.a.	Mulligan & Jambor 1968
Gumble	Australia	2.87	Adr_{59-79}	malayaite, cassiterite	Mulholland 1984
Doradilla	Australia	0.47-3.07	Adr_{69-86}	malayaite, cassiterite	Plimer 1984

n.a.: not available, Adr: andradite

Natural tin-bearing garnets are relatively rare with occurrences being reported from Australia, Canada, Czech Republic, Japan, Morocco, Namibia and Russia (Tab. 4.2.4.1.). Garnets containing more than 0.01 % SnO_2 are considered as tin-bearing garnets (Dadák & Novák 1965), whereas toturite, a tin-garnet, shows average values of 32.6 % SnO_2 (Galuskina et al. 2010). Tin-bearing garnets generally form early in the contact metamorphic or metasomatic stage with some skarns not containing any other Sn-bearing phases, whereas other skarns show late stage developed other Sn-bearing phases, with the Sn of these minerals originating from the tin-bearing garnets.

In the Chillagoe district they can be observed at all three deposits (Fig. 4.2.4.1), but while some garnets show a nearly homogenous distribution of tin from core to rim (e.g. 890W6: 2143-2799 ppm) other garnets show concentration varying by several orders of magnitude (e.g. 939-731.9: 24-5207 ppm).

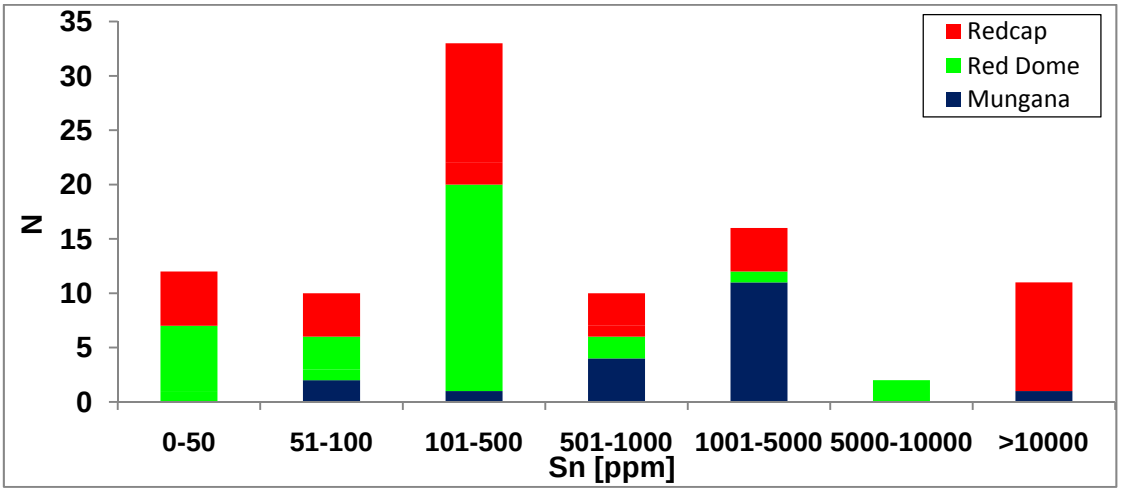

Figure 4.2.4.1. Tin concentration in garnets from the Redcap, Red Dome and Mungana deposits

Comparing the compositions of homogenous and very heterogenous tin-bearing garnets it appears that there is a link between the general garnet composition and the occurrence of tin. Tin only occurs in early paragenetic andraditic garnets with the highest concentrations being found in nearly end-member andradite garnet. Other tin minerals are only reported from the Mungana deposit occurring in the massive sulphide lenses (Hodkinson et al. 2009), whereas at Red Dome only one occurrence of cassiterite is known from a heavily altered sample and at Redcap so far no other Sn-phase have been identified.

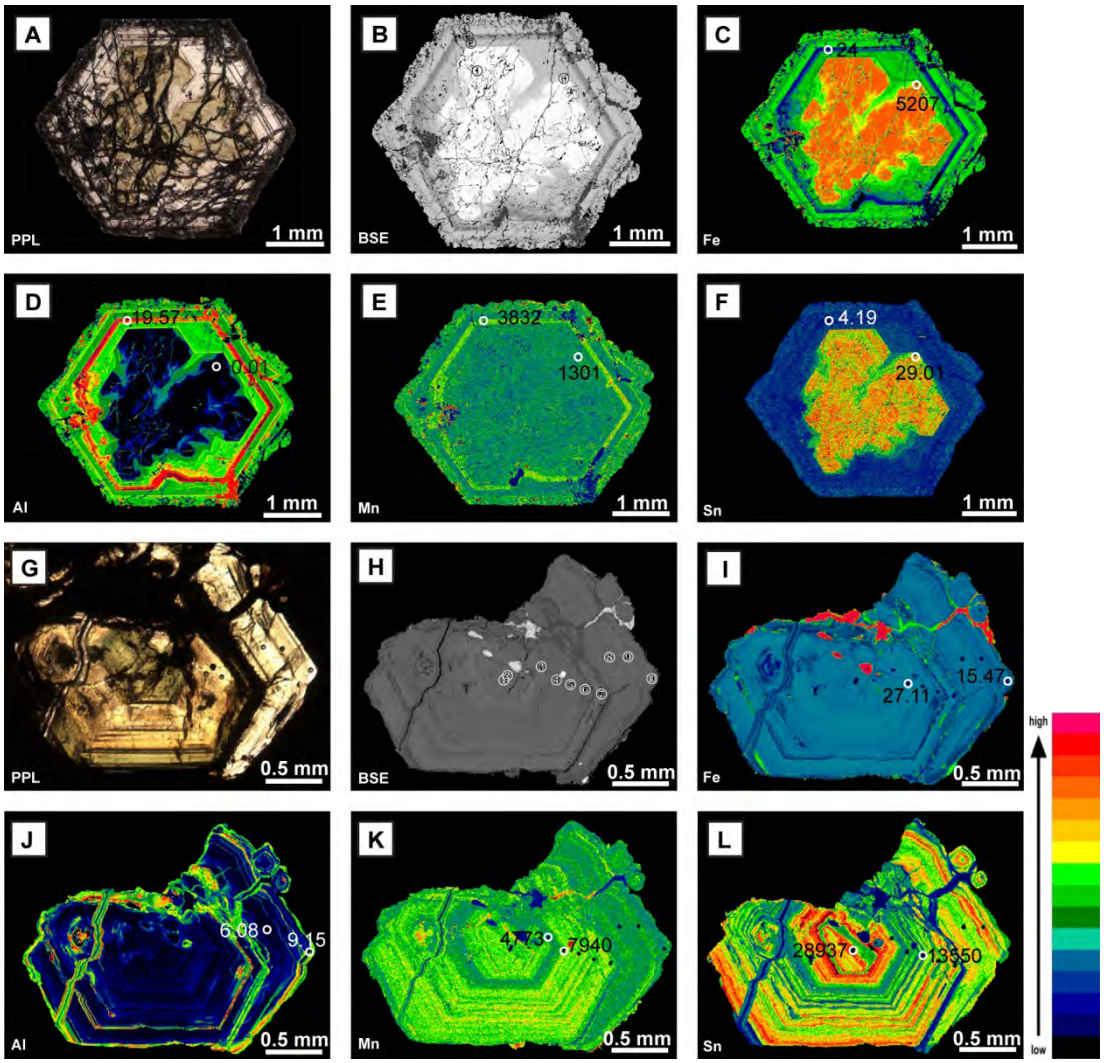

Plate 4.2.4. Transmitted light (PPL), back scattered electron images (BSE) and element maps of two garnet grains from Red Dome (A-F: 939-731.9) and Redcap (G-L: 952-574.42) with highest and lowest concentration of each element shown in wt.-% (FeO, Al_2O_3) and ppm (Mn, Sn); **A**: yellow green core surrounded by colourless rim (PPL); **B**: bright centre with medium grey rim (BSE); **C**: Fe-element map with warm colours indicating high element concentration and cold colours low concentration; **D**: element map showing the distribution of Al; **E**: element map of Mn occurrence; **F**: element map of Sn distribution; **G**: yellow green core surrounded by colourless rim (PPL); **H**: back-scattered electron image of the same grain; **I**: element map of Fe; **J**: element map of Al; **K**: element map of Mn; **L**: element map showing the distribution of Sn.

Samples which are homogenous in their composition like 890W6 also show nearly homogenous tin concentrations, while other samples which are heterogenous in their overall composition (e.g. 939-731.9: 100% andradite to 85 % grossular) show also a very heterogenous tin concentrations. This observation can be confirmed in element maps of garnets using different colours to express the concentration of a specific element (Plate 4.2.4).

Based on these maps it becomes clear that Sn only occurs in area of high iron and low aluminium concentrations (Plate 4.2.4. C, D, F, I, J, L). This link has already been identified by

Amthauer et al. (1970) who suggest that in tin-bearing garnets Fe gets substituted by Sn which they express in the following equation: 2 $Fe^{3+} \leftrightarrow Sn^{4+} + Fe^{2+}$. However element maps from another garnet grain also show that manganese together with iron might play a role, suggesting a coupled substitution which could be expressed as the following: 8 $Fe^{3+} \leftrightarrow 3\ Sn^{4+} + 3\ Fe^{2+} + 3\ Mn^{2+}$.

The majority of trace elements analysed in clinopyroxene do not exceed concentrations of 20 ppm with zinc being the only exception. The occurrence of natural zinc-bearing clinopyroxene is also quite rare with zincian clinopyroxenes being reported from Japan, USA, Italy and Czech Republic (Tab. 4.2.4.2.).

Table 4.2.4.2. Summary of the occurrence and composition of zincian clinopyroxenes

Locality	Country	ZnO [wt.-%]	composition	References
Příbram	Czech Republic	1.23-3.12	hed_{77-96}	Ettler et al. 2001
46 deposits	Japan	0.01-0.31	hed_{11-95}	Nakano et al. 1994, Burton et al. 1982
New Jersey	USA	3.27-10.15	joh_{52}	Fondel & Ito 1966
New Mexico	USA	0.06-0.18	hed_{39-78}	Burton et al. 1982
Idaho	USA	0.05-0.07	hed_{81}	Burton et al. 1982
California	USA	0.11-0.15	hed_{77-88}	Burton et al. 1982
Temperino	Italy	0.09-0.13	hed_{87}	Burton et al. 1982

Clinopyroxenes containing more than 100 ppm Zn are considered Zn-bearing (Nakano 1998), whereas petedunnite, a Zn-pyroxene, shows values of up to 12. 5 % ZnO (Essene & Peacor 1987). Nakano (1998) observed that clinopyroxenes are only enriched in Zn along contacts to sphalerite with the enriched zones being as thin as 100 microns, but the clinopyroxene composition on the other hand is not relevant. Based on its similar ionic radius, Zn substitutes in diopsidic clinopyroxene for Mg, while in hedenbergitic rich clinopyroxenes it exchanges with Fe (Shannon & Prewitt 1969). More interesting is that Nakano (1998) has used the Zn concentration in clinopyroxenes to determine whether the system is a Cu-Fe skarn (< 200 ppm) or a Pb-Zn skarn (> 200 ppm).

Zinc concentration ranges from clinopyroxenes of the Redcap, Mungana and Red Dome deposits range from 335 to 1072 ppm (Fig. 4.2.4.2) and do not depend on whether the clinopyroxene is of hedenbergitic or diopsidic composition. With all Zn concentrations being higher than 200 ppm Zn the Redcap, Mungana and Red Dome deposits should be zinc-skarns after the theory of Nakano (1998).

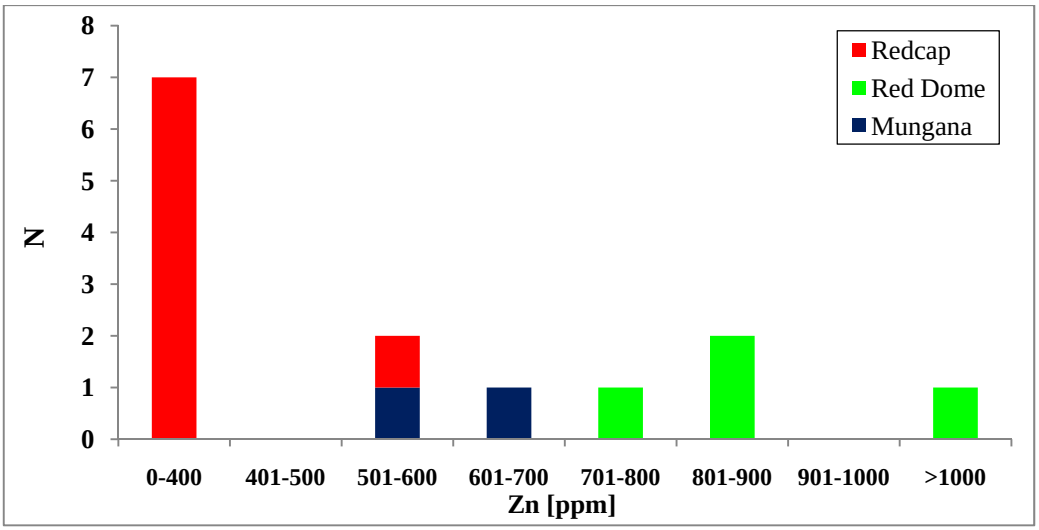

Figure 4.2.4.2. Zinc concentration in clinopyroxenes from the Redcap, Red Dome and Mungana deposits

This is indeed true for the Redcap and Mungana deposits, but it cannot be applied to the Red Dome deposit, where copper is the dominant mineralisation type. In this case it might show that the source of the mineralisation had a polymetallic budget, but due to a lack of sulphur Zn was incorporated into clinopyroxene and possible vesuvianite (in which it can occupy up to 3 wt.-% in its structure, Fitzgerald et al. 1986). The Zn may have been liberated during break down of the mineral and formed sphalerite with a later introduced sulphur source. This hypothesis can also be possible for the Mungana and Redcap deposits, with the only difference being that the sulphur carrying fluid also contained Zn.

4.2.5. REE chemistry of garnets and clinopyroxenes

Fe-rich garnets from the Redcap, Red Dome and Mungana deposits are in general enriched in the LREE elements and depleted in HREE (Fig. 4.2.5.a-f), which is very common in this type of garnets (Gaspar et al. 2008), while Al-rich garnets show the opposite behaviour in REE elements (Fig. 4.2.5.f Grs_{85}). The major difference in the garnets from the three deposits occurs in form of different Eu-anomalies. The most common Eu-anomaly is strong positive with Eu/Eu* values from >2 to up to 59 (Fig. 4.2.5.a, b). While some grains are very homogenous from core to rim with identical REE patterns (Fig. 4.2.5.a), others show a change in REE concentrations, although they have an identical REE pattern (Fig. 4.2.5.b). The change of magnitude in the REE pattern may represent heterogeneity of the fluid as suggested by Gaspar et al. (2008). A second type of REE pattern shows a strong negative Eu-anomaly with Eu/Eu* ratios between 0.1 and 0.3 (Fig. 4.2.5.c). Gaspar et al. (2008) suggest that this type of pattern is related to a more granditic garnet composition, but as the garnet here ranges from 95 to 100 wt.-% andradite this seems not to be the case.

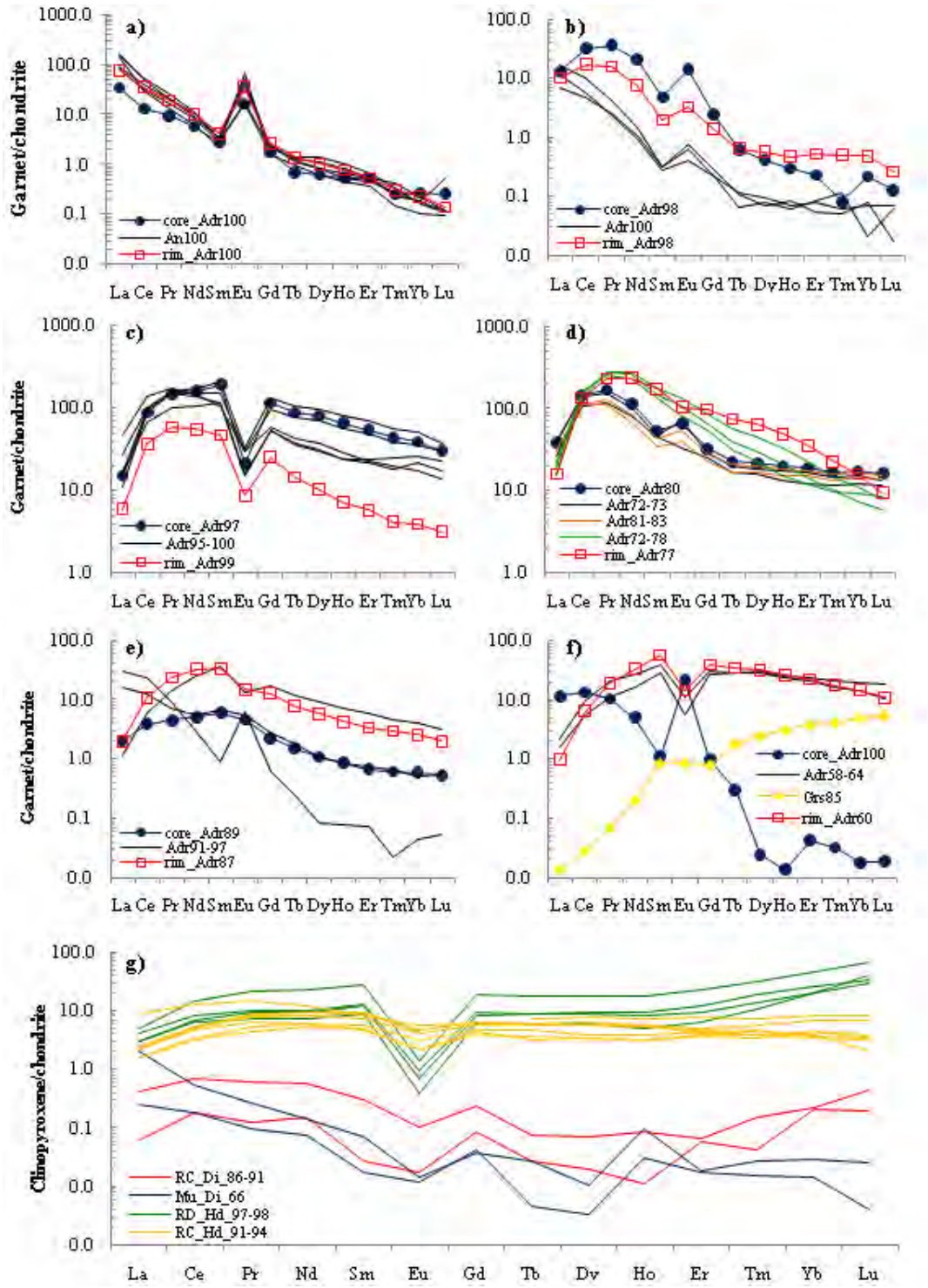

Figure 4.2.5. Chondrite-normalised REE patterns of garnets and clinopyroxenes from the Redcap, Red Dome and Mungana deposits with samples being normalised to chondrite values from Anders and Grevesse (1989); **a**: pure andradite garnet with strong positive Eu-anomaly (859-765.80); **b**: andraditic garnet with core rim variations in the overall REE concentrations and strong positive Eu-anomaly (974-349.86); **c**: core rim profile of andraditic garnet showing a strong negative Eu-anomaly (939-1103.2); **d**: 72-83 wt.-% andraditic garnet with two different REE patterns (939-772.2); **e**: 87-97 wt.-% andraditic rich garnet showing different REE patterns with a weak to non Eu-anomaly and a strong positive one (890W6); **f**: grossular to pure andraditic garnet with three different REE patterns ranging from one with strong negative Eu-anomaly over non visible anomaly to a strong positive Eu-anomaly (939-731.9); **g**: REE pattern of clinopyroxene from all three deposits (890W6, 939-1103.2, 974-291.01, 949-443.68).

Nicolescu et al. (1998) on the other hand propose that this kind of REE patterns with strong negative Eu-anomalies indicate that the causative intrusion acted as a heat source only and that the material in the skarn has been derived from limestone. Additionally to the two described patterns with obvious Eu-anomalies, some garnets show a third type of REE pattern, which do not show any form of anomaly , but follow the overall trend of LREE-enriched and HREE-depleted pattern (Fig. 4.2.5.d & e). Again a major compositional change in the garnet grain does not exist.

One explanation for the difference of the third REE pattern in comparison to the other two patterns already described could be that the “smooth” pattern is related to mixed analyses, i.e. that because of very small scaled growth zoning, garnet zones of different composition were analysed. A second explanation is that they are of geological nature and the distinguishable patterns do reflect different fluids. A change of REE pattern due to different garnet composition as suggested by Gaspar et al. (2008) can be seen in figure 4.2.5.f. The grossular-rich garnet shows the typical pattern for Al-rich garnets with depletion of the LREE and enrichment of the HREE. The pure andraditic garnet shows a strong positive Eu-anomaly while zones of the garnets with intermediate composition show negative Eu-anomalies.

Clinopyroxenes show different patterns. Hedenbergite-rich clinopyroxenes show either strong negative Eu-anomalies or “smooth” patterns with a very weak to non observable Eu-anomaly. Interestingly the clinopyroxene REE pattern from Red Dome (939-1103.2) shows the identical form regarding the Eu-anomaly as the one from a garnet of the same sample. Therefore it can be assumed that both calc-silicate phases are co-genetic and derived from the same fluid. The “smooth” pattern can again be of analytical nature representing mixed analyses, but can also reflect a different fluid. Diopsidic clinopyroxenes are very poor in REE with concentrations rarely exceeding the detection limit. Based on this it seems that they cannot incorporate the REE into their structure.

4.3. Major and trace elements in sphalerite

Major and trace element compositions of sphalerite have been used in a wide range of topics. Early work mainly focused on using the Fe-concentration of sphalerite as geobarometer and –thermometer (Scott & Barnes 1971; Hutchinson & Scott 1981). However, as the sensitivity of required conditions and their uncertainties are still controversial (Martín & Gil 2005) and most of the time not met, the use of the geobarometer is nowadays limited. Other authors used the sphalerite chemistry to reveal the nature of different colours, formation temperatures (Oftedahl 1940), deposit styles (Qian 1987; Cook et al. 2009; Ye et al. 2011), and for ore processing

duties (Boulton et al. 2005) or environmental hazard studies (Kossof et al. 2008) with the major milestone being the application of LA-ICP-MS analyses to determine the trace element composition of sphalerite, which proved to be an accurate and efficient method (Watling et al. 1995; Axelsson & Rodushkin 2001). In this study trace element concentrations of sphalerite were determined to identify the geochemical differences between sphalerite of different paragenetic stages within a single deposit, but also on a more regional scale to get information regarding their formation temperature and deposit style.

4.3.1. Methodology

Based on petrographic studies of sphalerite, six samples representing two major sphalerite types from each deposit were selected for major and trace element analyses (Tab. 4.3.1).

Table 4.3.1. Sample locality and description of analysed sphalerite

Deposit	DH_interval	Occurrence	Colour	Texture	Paragenesis
Redcap	949-165.80	garnet skarn	dark red-brown	featureless	cp-gn
Redcap	949-179.15	semi massive sulphide lenses	yellow-orange	lamellae	Au-Bi
Mungana	849W1-579.72	semi massive sulphide lenses	dark red-brown	featureless	cp-gn
Mungana	888-710.7	quartz gangue	orange	featureless	cp-apy
Red Dome	937W4-1133.19	quartz vein in cpx skarn	dark red-brown	featureless	cp-mlb
Red Dome	983-885.71	quartz vein in porphyry	green-brown	featureless	cp-tn-apy

Major elements were determined in situ in polished thick sections (thickness 70 µm-100 µm) using a JEOL JXA 8200 electron microprobe with the following standards used for calibration: sphalerite (Zn), pentlandite (Fe), sphalerite (S). Operating conditions were 20 nA beam current, 20 kV accelerating voltage and 10 µm beam diameter with 20 seconds counting time on the Kα peak and 10 seconds on the background. Trace element data were obtained with a GeoLas 193 nm ArF laser coupled to a Varian 820 quadrupole ICP-MS unit. The laser was operated a 10 HZ pulse rate and the laser energy was 6 J/cm^2. Spots without visible inclusions and alteration, as well as without any cracks were selected and on average 6-10 spot analyses (depending on the size of the sphalerite) from core to rim were conducted with the spot size being 32 µm. Calibration was performed using NIST 610 as a primary standard and NIST 612 as a secondary one to check for reproducibility and accuracy. Data were processed using Fe as internal standard (previously determined EMP values) and the data reduction software GLITTER 4.4.2. (Van Achterbergh et al. 2001).

4.3.2. Sphalerite Petrography

Two different sphalerite types were identified at the Redcap, Red Dome and Mungana deposits (Tab.4.3.1.): a red-brown sphalerite (Plate 4.3.2.A, C, E) and a honey coloured type (Plate 4.3.2.G, I, K), with the latter occurring later in the paragenetic sequence than the former.

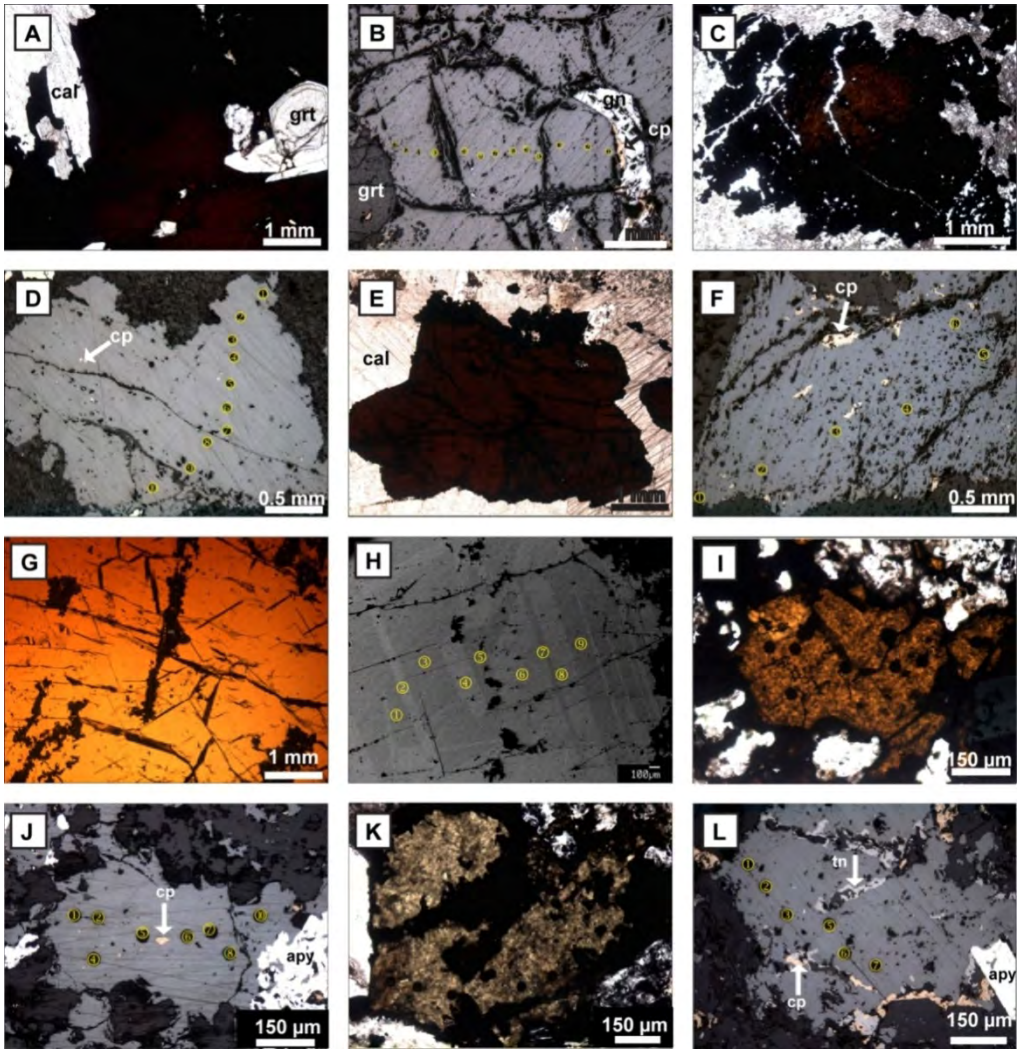

Plate 4.3.2. Photomicrographs of representative sphalerite grains from Redcap, Red Dome and Mungana; PPL: plane-polarised light, RL: reflected light, BSE: back-scattered electron image; **A**: red-brown sphalerite in andradite skarn (grt) adjacent to marble contact (cal) from Redcap, (PPL, 949-165.80); **B**: sphalerite with garnet (grt), chalcopyrite (cp) and galena (gn), (RL, 949-165.80); **C**: red-brown sphalerite in skarn at Mungana (PPL, 849W1-579.72); **D**: sphalerite from Mungana with rare "chalcopyrite disease" (RL, 849W1-579.72); **E**: red-brown sphalerite in calcite vein at Red Dome (PPL, 937W4-1133.19); **F**: sphalerite from Red Dome with "chalcopyrite disease" (RL, 937W4-1133.19); **G**: yellow-orange coloured sphalerite from Redcap (PPL, 949-179.15); **H**: same sphalerite grain as in previous image showing lamellae (BSE, 949-179.15); **I**: yellow-brown coloured sphalerite from Mungana (PPL, 888-710.7); **J**: same sphalerite grain as in previous image with rare "chalcopyrite disease" and arsenopyrite (apy) at grain boundaries (RL, 888-710.7); **K**: pale yellow brown sphalerite from Red Dome (PPL, 983-885.71); **L**: same sphalerite grain as in previous image with minor "chalcopyrite disease" and tennantite (tn) inclusions (RL, 983-885.71).

Red-brown sphalerite occurs within skarn or massive sulphides bodies at the Redcap and Mungana deposits, while at Red Dome it can be found in veins. Honey coloured sphalerite occurs in veins (Red Dome and Mungana) but can also be part of semi massive to massive sulphide lenses (Redcap). The sphalerite is often associated with galena, arsenopyrite or tennantite (Plate 4.3.2.B, J, K) and in many cases it shows signs of "chalcopyrite disease" (Plate 4.3.2. D, F, J). The majority of sphalerite grains are featureless regarding their internal textures except one grain which shows lamellae in transmitted light and back scattered electron imagery (Plate 4.3.2.H).

4.3.3. Mineral chemistry of sphalerite

Iron is present in all samples with two major populations of concentrations. Dark red-brown sphalerite shows iron values of 7.24 to 12.59 wt.-%, while the iron content of honey coloured sphalerite samples varies between 0.74 to 4.57 wt.-% (Fig. 4.3.3.1.a). Iron-poorer zones are again represented by darker back-scattered electron images, which can be observed in the sample with lamellae. In this study the iron content of sphalerite samples has not been used in the geobarometer by Scott & Barnes (1971), as the required co-existing mineral assemblages (pyrite and/or pyrrhotite) were not observed.

Typical trace elements occurring in sphalerite from Redcap, Red Dome and Mungana are Mn (112-8283 ppm), Cd (1702-5213 ppm), Co (0.2-276) ppm, In (8-154 ppm) and Se (1-59 ppm), all showing a smooth ablation pattern and therefore suggesting that these elements occur in solid solution. Trace element data from sphalerite samples from other skarn deposits as well as from other deposit types are listed in table 4.3.3. for comparison. Other elements like Ag, Bi, Cu, Pb and Sb show very noisy patterns or peaks and represent inclusions of galena, chalcopyrite, silver-bismuth minerals and tetrahedrite.

Table. 4.3.3. Summary of element concentrations in sphalerite from different deposit types

Deposit type	Mn [ppm]	Cd [ppm]	Co [ppm]	In [ppm]	Se [ppm]	Reference
Skarn	601-36136	1688-7999	2.4-2828	0.01-98.9	1.1-81.5	Cook et al. 2009, Ye et al. 2011
Epithermal	711-18451	1015-11044	0.02-7.82	0.05-281	1.5-56.8	Cook et al. 2009
SEDEX	675-6537	4659-8564	0.01-7.5	3.5-415	0-13.9	Ye et al. 2011
VMS	165-4744	2720-5088	0.02-0.17	0.04-13.7	0.82-4.1	Cook et al. 2009
Sediment-hosted	1.1-1937	187-68552	0.73-25.6	0-1.4	0-3.7	Ye et al. 2011

Manganese concentrations in the red brown sphalerite are in general one order of magnitude higher (2734-8283 ppm) than in the honey coloured ones (112-892 ppm), with the only exceptions being honey coloured sphalerite from Redcap with concentrations between 3588 and

5993 ppm (Fig. 4.3.3.1.b). The red-brown sphalerite from Mungana seems to have some zoning which is reflected in the change of Mn concentration, but this could not be observed in thin sections.

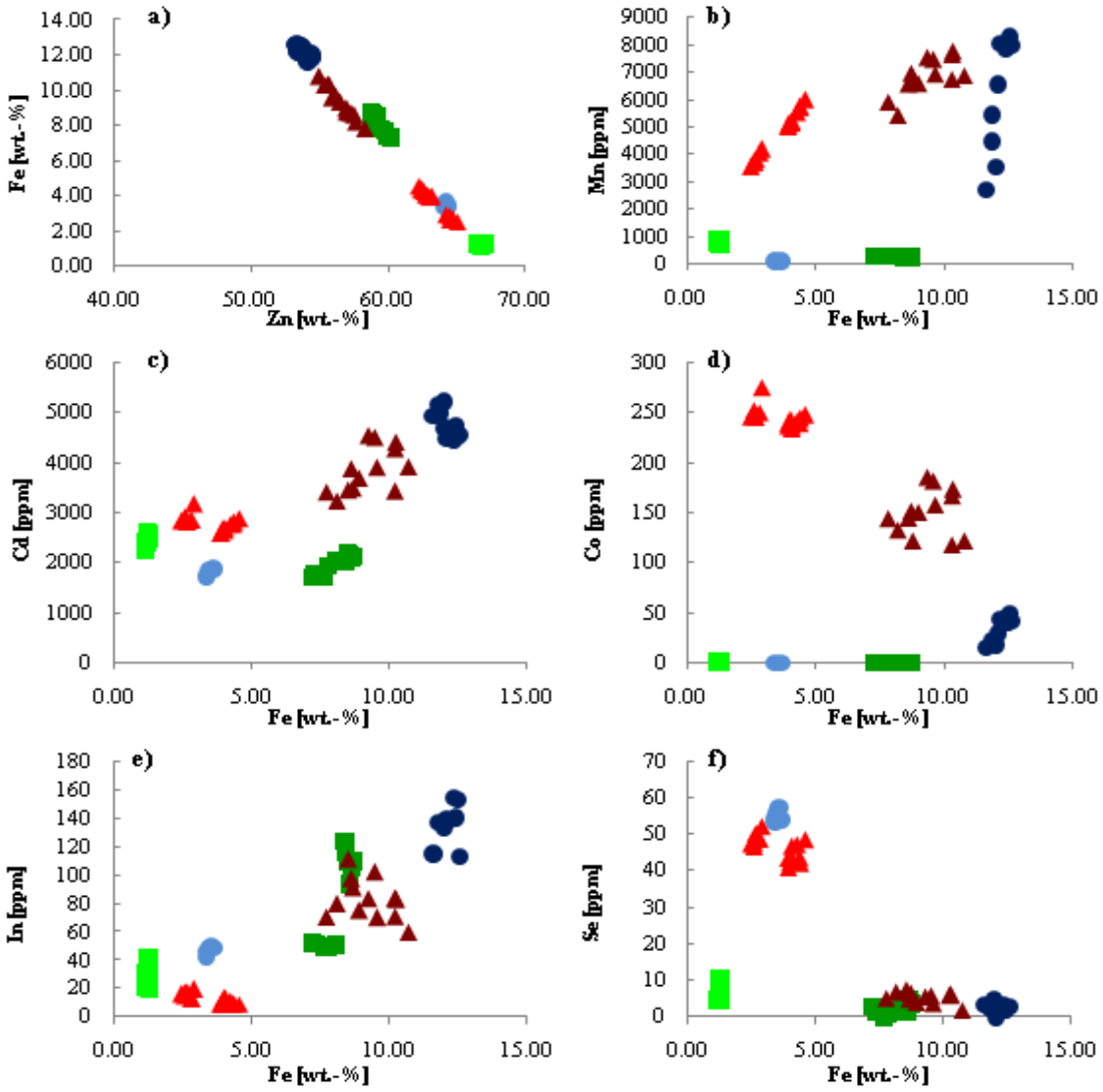

Figure 4.3.3.1. Trace element distributions in different sphalerite samples from Redcap, Red Dome and Mungana; binary plot of Fe vs. Zn (**a**), Mn vs. Fe (**b**), Cd vs. Fe (**c**), Co vs. Fe (**d**), In vs. Fe (**e**) and Se vs. Fe (**f**); ▲: dark red-brown sphalerite (Redcap), ▲: honey coloured sphalerite (Redcap), ●: dark red-brown sphalerite (Mungana), ●: honey coloured sphalerite (Mungana), ■: dark red-brown sphalerite (Red Dome), ■: honey coloured sphalerite (Red Dome).

Cadmium is present in all samples analysed (Fig. 4.3.3.1.c). Honey coloured sphalerite has again lower concentrations values as the dark sphalerite, with the sample from Red Dome being an exception. Both sphalerite samples have similar concentration values. The highest cobalt values occur in the honey coloured sample from Redcap with concentrations of 237-276 ppm. Red-brown sphalerite from Redcap and Mungana is also enriched in Co, with values between

16-186 ppm, while concentrations in the other samples rarely exceed the detection limit (Fig.4.3.3.1.d). Based on the hypothesis postulated by Oftedahl (1940) that trace element concentrations in sphalerite sample can provide information regarding the minerals formation temperature, in this case that ores of hypothermal to mesothermal origin have high concentrations of Co and In, sphalerite from the Redcap deposits as well the red-brown sphalerite from Mungana were formed at higher temperatures than the honey coloured sphalerite from Red Dome and Mungana together with the red-brown sphalerite from Red Dome. This confirms the observations made in the paragenesis.

Cook et al. (2009) suggested that In concentrations could represent the distance to the magmatic source with high values indicating proximity to the intrusive body, while low values mean that the sphalerite occurs distal to the magmatic source. All red-brown sphalerite grains have higher In values (60-154 ppm, Fig. 4.3.3.1.e) than the honey coloured sphalerite samples (8-49 ppm), suggesting that the iron-richer sphalerite are closer to the magmatic source. Selenium concentrations of the different sphalerite samples confirm this observation. Honey coloured sphalerite yielded higher Se values (exception Red Dome), suggesting formed distal to the distal to the igneous body whereas the darker sphalerite have low Se values (Fig. 4.3.3.1.f), indicating that they formed more proximal to the intrusion.

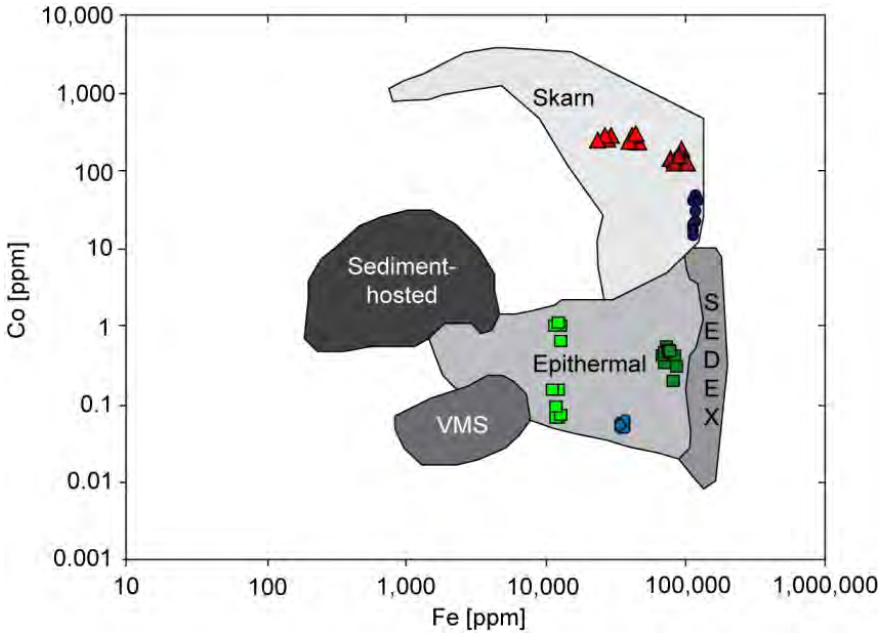

Figure 4.3.3.2. Binary plot of Co vs. Fe of sphalerite samples occurring in different deposit styles (field constructed from data by Cook et al. 2009; Ye et al. 2011) and the occurrence of samples from the Redcap, Red Dome and Mungana deposits; ▲: dark red-brown sphalerite (Redcap), ▲: honey coloured sphalerite (Redcap), ●: dark red-brown sphalerite (Mungana), ●: honey coloured sphalerite (Mungana), ■: dark red-brown sphalerite (Red Dome), ■: honey coloured sphalerite (Red Dome).

To check for the different deposit styles, Co-Fe values of sphalerite samples from the Redcap, Red Dome and Mungana deposits were plotted against each other and compared to typical sphalerite compositions from skarn, epithermal, sediment-hosted, SEDEX and VMS deposits (Tab. 4.3.3.; Fig. 4.3.3.2.) with fields constructed from data by Cook et al. (2009) and Ye et al. (2011). Based on this comparison it becomes obvious that none of the sphalerite samples analysed in this study is related to a VMS deposit style as suggested by Nethery & Barr (1996) for the Mungana deposit. The red-brown sphalerite samples from Redcap and Mungana, as well as the honey coloured sample from Redcap plot in the skarn field, while the other honey coloured samples from Red Dome and Mungana and the red-brown sphalerite from Red Dome lie in the field of epithermal deposit style. However, classification of deposit types based on a distinct chemical signature of sphalerite is still in its initial stage, as the metal portioning behaviour between sphalerite and coexisting phases during and post crystallisation is not well constrained yet (Cook et al. 2009).

4.4. Gold

Gold mineralisation occurs within many different deposit styles, e.g. orogenic, slate belts, volcanic massive sulphide, skarn, porphyry, plutonic and epithermal deposits (Morrison et al. 1991), but it can also occur in placer deposits where the source of the gold often remains uncertain or unknown. To reveal the source of the gold occurring placer deposits, many workers have applied micro analyses to determine the chemistry of gold grains (e.g. Stumpfl & Clark 1965; Saager 1969; Desborough 1970; Desborough et al. 1970; Leake et al. 1998; Outridge et al. 1998; Chapman et al. 2000; Townley et al. 2003) with work from Morrison et al. (1991) indicating that gold grains of different deposit styles show characteristic chemical signatures.
In the majority of cases silver concentrations has been used, which is the most common alloy in gold grains (Boyle 1979). Other trace elements can include Bi, Cu, Hg, Pd (Boyle 1979), but only Cu was analysed in this study.

Recent studies have shown that Ag can become easily depleted (Groen et al. 1990), based on being more soluble and volatile than gold (Hough et al. 2009) and therefore a source model only for the gold fineness might be erroneous. Townley et al. (2003) included copper concentrations of gold grains to identify the source of alluvial gold grains in porphyry environments in Chile and found that Cu concentrations of more than 0.75 wt.-% are typical for Au-rich copper deposits while gold grains from Au-porphyries and epithermal deposits have Cu values of less than 0.1 wt.-%.

Although attempts were made to employ LA-ICP-MS for determining trace elements in gold grains, electron microprobe analyses are still considered to provide more reliable results. One reason is that calibration based only on external standards provides wrong results (McCandless et al. 1997) and that through a lack of Au and Ag having minor isotopes no internal standards can be used for calibration. Furthermore the laser set up plays an important role (Outridge et al. 1998), and the grains analysed should be coarse grained (Townley et al. 2003).

As for the Chillagoe area gold mineralisation is assumed to be porphyry related (Nethery & Barr 1998; Georgees & Nethery 1999; Georgees 2007a; Hodkinson et al. 2009) the approach of Townley et al. 2003 was used in this study and based on the small size of the analysed gold grains (in general less than 15 µm) the electron microprobe was used.

4.4.1. Methodology

Nine samples representing different gold occurrences were selected for electron microprobe analyses (Tab. 4.4.1.). Again a JEOL JXA 8200 electron microprobe was used with the following operating conditions: 20 kV accelerating voltage, 20 nA beam current and 1 µm beam diameter. Calibration was performed using chalcopyrite (Cu), pure Au (Au) and pure Ag (Ag) as standards. The counting time was 40 seconds on the Kα/Lα peak and 20 seconds on the background.

Correlation matrixes for Redcap, Mungana and Red Dome were calculated in Discover using the assay data (all elements in ppm) from an unpublished data base of Kagara Ltd. (2008).

Table 4.4.1. Sample location and description of analysed gold

Deposit	DH_interval	Occurrence	Paragenesis	Au [wt.-%]	Ag [wt.-%]	Cu [wt.-%]	Fineness*
Recap	949_197.53	calcite vein in massive sulphides	Bi-Te-S	62	38	-----	621
Recap	949_247.38	calcite-chlorite- quartz vein in siltstone	Bi-Te	76-78	22-24	-----	756-779
Recap	952_575.2III	calcite fracture fill in andradite skarn	Bi-Te	58-63	37-42	-----	581-633
Mungana	MuD54_74.4	quartz vein in skarn	cp-apy-tn	81-85	13-15	1.8-4.3	848-867
Mungana	1960	quartz vein in porphyry	cp-td, apy-lol	96-97	2-4	0.4-1.2	964-979
Mungana	849W1_581.44	calcite clasts in breccia	-----	82-90	9-16	0.5-2.0	839-909
Griffiths Hill	995_478.59	quartz vein in porphyry	-----	87-92	8-13	-----	869-921
Red Dome	983_880.28	quartz vein in porphyry	Bi-Te-S	81-91	9-19	-----	808-911
Red Dome	937W4_1039	calcite fracture fill in andradite skarn	Bi	86	14	-----	855
			-----	74-76	-----	24-26	n/a

$* \frac{(1000 \text{ x } \mathrm{Au[wt.-\%]})}{(\mathrm{Au[wt.-\%]+Ag\ [wt.-\%]})}$

4.4.2. Gold petrography

As previously described in chapter 3, gold can be found either associated with Bi-Te minerals (Redcap and Red Dome) or occurs together with copper-arsenic-antimony minerals (Mungana).

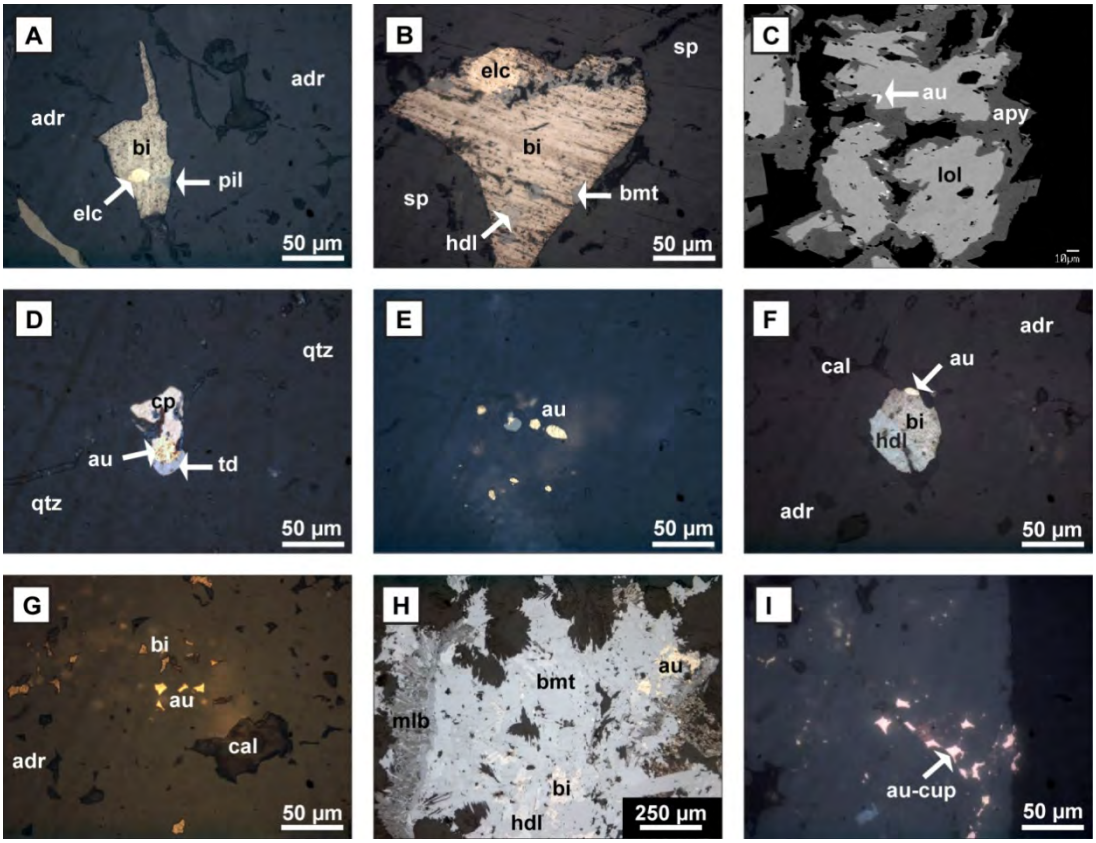

Plate 4.4.2. Photomicrographs (RL: reflected light) and back-scattered electron image (BSE) of representative gold grains from Redcap, Red Dome and Mungana; **A**: electrum (elc) associated with native bismuth (bi) and pilsenite (pil) in carbonate filled fractures in andradite (adr) skarn (RL, 952-575.2 III); **B**: electrum (elc), native bismuth (bi), hedleyite (hdl) and bismuthinite (bmt) hosted in sphalerite (RL, 949-197.53); **C**: gold occurring at the boundary of loellingite (lol) and arsenopyrite (apy), (BSE, MuD183-117.1); **D**: gold (au) within tetrahedrite (td) and chalcopyrite (cp) in a quartz (qtz) vein, (RL, 1960); **E**: gold (au) carrying quartz (qtz) vein in dacitic porphyry (RL, 995-478.59); **F**: native gold (au) associated with hedleyite (hdl), native bismuth (bi) and calcite (cal) in andradite (adr) skarn (RL, 937W5-1044A); **G**: native gold (au), adjacent to native bismuth (bi) in andradite (adr) skarn (RL, 937W4-1039); **H**: native gold (au) associated with native bismuth (bi), hedleyite (hdl) and bismuthinite (bmt), overprinted by later molybdenite (mlb) in sericite altered porphyry (RL, 983-880.28); **I**: tetra-auricupride (au-cup) along tiny fracture in andradite (adr) skarn (RL, 937W4-1039).

At Redcap gold in form of electrum is always associated with native bismuth and bismuth-telluride (pilsenite or hedleyite) replacing calcite filled fractures in andradite skarn or massive sphalerite (Plate.4.4.2.A, B) or it occurs together with chlorite and calcite in comb-quartz veins.

At Mungana gold can be found at the border of arsenopyrite and loellingite (Plate 4.4.2.C) or chalcopyrite and tetrahedrite (Plate 4.4.2.D), which indicates that originally the gold was

included in one or the other mineral and was exsolved during temperature change. Gold grains from Griffiths Hill occur as free grains within quartz veins cutting dacitic porphyry (Plate 4.4.2.E), while at Red Dome gold can be found associated with bismuth and telluride phases (Plate 4.4.2.F, H), as free gold grains in the vicinity of native bismuth (Plate 4.4.2.G) or in form of tetra-auricupride replacing calcite in andradite skarn (Plate 4.4.2.I).

4.4.3. Gold chemistry

The petrographically observed association of gold with either Bi-Te or Cu-As-Sb mineral phases in the Redcap, Red Dome and Mungana deposit is well reflected in the assay data. Correlation matrixes for the Redcap and Red Dome show that a strong positive correlation between Au-Bi-Te exists with correlation coefficient being between 0.6 and 1.0 (Fig. 4.4.3.1.a, b) with Au-Bi correlation coefficient of > 0.6 being typical for IRGs (Baker et al. 2005). At Mungana the correlation between Au and Bi is low (Fig. 4.4.3.1.c) and no statement can be made regarding possible correlation with tellurium, as this element has not been determined.

a)	Au	Cu	Sb	As	Bi	Te
Au		0.4	0.0	0.1	0.6	1.0
Cu			0.2	0.3	0.6	0.6
Sb				0.5	0.3	0.0
As					0.3	-0.1
Bi						1.0
Te						

b)	Au	Cu	Sb	As	Bi	Te
Au		0.1	0.1	0.3	0.6	0.9
Cu			0.5	0.3	0.2	0.4
Sb				0.5	0.0	0.3
As					0.4	0.4
Bi						1.0
Te						

c)	Au	Cu	Sb	As	Bi	Te
Au		0.6	0.6	0.5	0.4	----
Cu			0.9	0.6	0.7	----
Sb				0.7	0.8	----
As					0.4	----
Bi						----
Te						

Figure 4.4.3.1. Correlation matrix for the Redcap (**a**), Red Dome (**b**) and Mungana (**c**) deposits compiled from assay data (unpublished data base from Kagara Ltd 2008) with correlations relevant for this section being highlighted in yellow.

Arsenic, copper and antimony correlate very well with values ranging between 0.6 and 0.9, but they also show a correlation with gold as observed in thin sections. Assay data can help to point out which elements gold is associated with and this might help to identify its occurrence in drill core.

Silver concentrations in gold grains vary between the deposits with 2-16 wt.-% at Mungana, 8-19 wt.-% at Red Dome and 22-44 wt.-% at Redcap. Calculations of the fineness expressed by the formula [1000 x Au/(Au+Ag)] yield values ranging between 581-779 for gold grains from the Redcap deposit, 809-921 for Griffiths Hill and Red Dome and 839-979 for Mungana. Based on work from Morrison et al. (1991) who used the fineness to identify different styles of gold-mineralising environments, the values from deposits of the Chillagoe area could represent anything from plutonic (825), porphyritic (700-1000), volcanogenic (650-850) to epithermal (440-1000) deposit styles. Considering that recent studies have shown that Ag concentration can

vary within an otherwise homogenous grain (Hough et al. 2007) and that silver is more soluble and volatile (Hough et al. 2009) than gold in gold-silver alloys and therefore can easily become depleted (Groen et al. 1990), using the fineness of gold grains to identify the gold-mineralising environment is kind of useless.

To reduce the effect of possible Ag depletion Townley et al. (2003) determined Cu in addition to the Au and Ag concentrations in gold grains and found that gold grains from Au-rich copper porphyries have Cu values higher than 0.75 wt.-% with varying amounts of silver, while gold grains from gold-rich porphyries and epithermal deposits have Cu concentrations of less than 0.1 wt.-%. Gold grain analyses from the Mungana, Redcap and Red Dome plus Griffiths Hill deposits show different concentrations in Cu (Fig. 4.4.3.2), with grains from Mungana showing values between 0.4 to 4.3. wt.-%, while grains from the other deposits show no sign of copper.

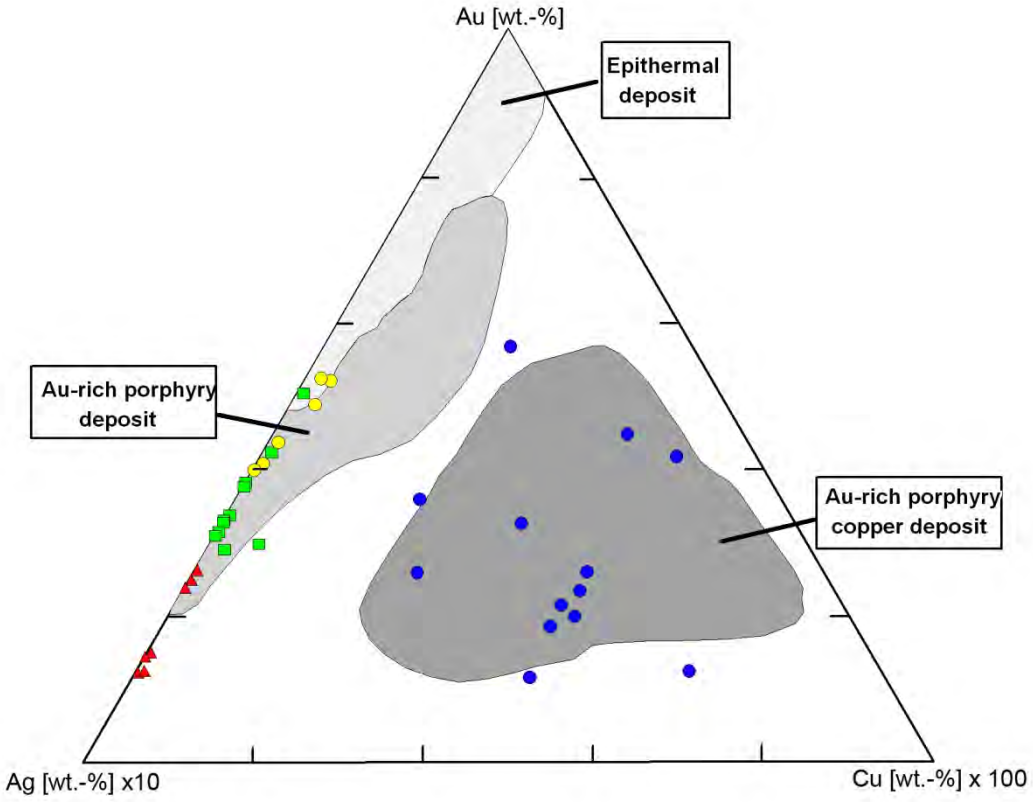

Figure 4.4.3.2. Triangular plot showing the compositional differences of gold grains from different deposit styles (fields from Townley et al. 2003) and gold grains from the Redcap (▲), Red Dome (■), Griffiths Hill (●) and Mungana (●) deposits.

In comparison with the data from Townley et al. (2003), gold from the Redcap, Red Dome and Griffiths Hill deposits plot in the field of Au-rich porphyries while gold grains from Mungana can be assigned to Au-bearing Cu-porphyries, but as geochemical data of porphyry samples from the Red Dome and Mungana deposit do not show a difference between the two porphyries

and U-Pb isotopes studies yield nearly identical ages for both porphyry bodies (see chapter 5) it is unlikely that two different commodity hosting porphyry systems exists. Thus another explanation for the different gold grain compositions is required. The most obvious one is that the distinctive compositions do not represent a different deposit style, but that they represent two different mineralising events with the copper-rich gold representing the primary event (indicated by lower grade) and the copper-poor gold, which is almost always associated with bismuth-telluride assemblages, representing the second event (indicated by high grade). Evidence for this hypothesis would be that sphalerite hosted electrum (Redcap: 949_179.15) is an indicator for remobilisation (Hurley & Crocket 1985), and that a Bi-Te-S melts are able to extract gold from pre-existing arsenopyrite (Oberthür & Weiser 2008).

A remaining problem is the occurrence of tetra-auricupride (AuCu) at the Red Dome deposit. Not much is known about this mineral which has been described by Ramdohr (1980) as “red gold” and became accepted as a new mineral based on work by Chen et al. (1983). Its natural occurrence is rare with observations of tetra-auricupride only being reported from Borneo (Stumpfl & Clark 1965), Canada (Knipe & Fleet 1997), China (Chen et al. 1983), Greenland (Bird et al. 1991), Morocco (Oen & Kieft 1974), Russia (Shcheka et al. 2004) and South Africa (Verryn et al. 1991). All of these deposits have in common that they are either layered mafic intrusions or altered ultramafic rocks with associated placer deposits which almost always host PGM (Knight & Leitch 2001) with Pt and Pd partly being incorporated in the structure of tetra-auricupride with values ranging between 0.78-3.86 wt.-% Pd and 1.87-13.91 wt.-% Pt (Shcheka et al. 2004). The only known mafic rocks occurring in the Chillagoe area are Silurian-Devonian basalts of the Chillagoe Formation, which are assumed to have nothing to do with the mineralisation in the area. Based on the theory that the described gold-mineralisation at Red Dome represents a second event with grade enrichment through remobilisation, in this case it is more likely that the observed Au-Cu alloy is not a primary mineral, but rather a replacement product where copper substitutes for gold. Knipe & Fleet (1997) observed this in tetra-auricupride samples from Ontario, where the gold was replaced by copper in a very late stage event at low temperatures which are assumed to be between 75 and 150 °C (Tomkins & Pinnel 1976).

4.5. Summary

For deposits from Redcap, Red Dome and Mungana it seems that the overall garnet composition does reflect a specific type of mineralisation as suggested by Paverd (1981) and therefore indicating that a specific garnet composition can be used as exploration tool to identify a specific type of mineralisation. Colour variations of garnet on the other hand are considered not

suitable as still more work needs to be done to get a better understanding of which elements are responsible for a specific colour type and whether the occurrence of those elements is temperature independent or not.

The occurrence of tin in garnets from all three deposits can have two meanings: 1. All deposits have an O'Briens Creek supersuite event involved within their development history as this is the only one known to be associated with Sn mineralisation (Georgees & Nethery 1999) or 2. The source of the tin is in rocks of the Chillagoe Formation, where all the deposits occur. Since in the Mount Garnet area, further east to the Chillagoe district, tin originally also occurred within calc-silicate phases and deposits there are clearly linked to O'Briens Creek intrusions and are hosted by the Hodgkinson Formation, the first hypothesis of the origin of tin mineralisation seems to be more likely, as sandstone, greywacke and basalt do not show elevated tin concentrations with the majority of samples yielding values below the detection limit (OZCHEM 2008). However, the discovery that metals become structurally bound in the lattice of silicate phases of IRG systems indicates that the metal diversity of IRG system has been underestimated.

Mn-concentrations of clinopyroxenes and in occupied Zn indicate that the Redcap and Mungana deposit are Zn-skarns, while Red Dome based on its low Mn-values is not linked to this deposit style, with sphalerite being only a very minor sulphide phase at Red Dome. Alternatively the occurrence of Zn in clinopyroxene could mean that through a lack of sulphur in the system Zn was incorporated into the calc-silicate minerals, but while at Redcap and Mungana a later source introduced sulphur and possibly more zinc, at Red Dome either the later event did not occur or was a sulphur-poor system, resulting in the majority of Zn remaining in the clinopyroxene and chlorite as reported by Rule & Radke (1988).

The major difference between the two sphalerite types is their concentration in Fe and Mn, with the darker red-brown one having up to 3-10 times more Fe and one magnitude higher Mn concentrations. Other trace elements like cobalt, indium and selenium indicate that the dark red-brown sphalerite samples are of higher temperature origin (except Red Dome) and more proximal to the intrusion, while the honey coloured sphalerite samples (except Redcap) experienced lower formation temperatures and are located more distal to the intrusion. By comparison with data from Cook et al. (2009) sphalerite samples from Redcap, Red Dome and Mungana plot in the epithermal and skarn field, but not in the VMS field. Therefore a VMS deposit styles as suggested by Nethery & Barr (1996) is unlikely.

The existing correlation between gold and Bi-(Te) in the assay data, which can also be confirmed by petrographical observations, is the most useful tool to locate gold mineralisation. Silver concentrations of gold grains from Redcap, Red Dome and Mungana do not help to distinguish between different styles. Copper concentrations suggest that gold from Redcap, Red Dome (including Griffiths Hill) can be associated with Au-rich porphyries while gold from Mungana can be related to Au-rich copper porphyries, but as porphyry bodies from Red Dome and Mungana are of nearly identical chemical composition and age, this approach also did not help to identify the nature of the gold mineralisation, suggesting that copper concentrations in gold can not be used as discrimination tool between different ore deposits within polymetallic systems. However, the different Cu concentrations show that the analysed gold grains represent two events, with the one from Mungana being assumed to be the primary one with gold exsolved from arsenic, copper and antimony-rich mineral phases which has also been reported to occur at Red Dome (Ewers & Sun 1988b) while gold at Redcap and Red Dome represents the second event, with gold being remobilised and enriched with bismuth acting as an scavenger.

Chapter 5: Geochronology of igneous rocks from Redcap, Mungana and Red Dome

5.1. Introduction

Previous geochronological work in the greater Chillagoe area (including the Herberton district) is mainly restricted to K-Ar and Rb-Sr ages collected in the 1960's to 1990's (Richards et al. 1966; Black & Richards 1972a & b, Black 1978, 1980; Woodbury 1994). Only a few SHRIMP U-Pb zircon (3) and Re-Os molybdenite ages (2) exist and these are summarised in table 5.1.

Table 5.1. Summary of U-Pb and Re-Os isotope age data in the greater Chillagoe district

Locality	Rock type	Age [Ma]	Methodology	Mineral	Reference
Red Dome	"crowded" porphyry	322.4 ± 2.8*	SHRIMP U-Pb	zircon	Perkins & Kennedy 1998
Mungana	porphyry	317.3 ± 2.3*	SHRIMP U-Pb	zircon	Georgees 2007a
Mungana	granite	307.1 ± 2.5*	SHRIMP U-Pb	zircon	Georgees 2007a
Mungana	-------	307.1 ± 1.3*	Re-Os	molybdenite	Georgees 2007a
Bamford	-------	303 ± 2*	Re-Os	molybdenite	Norman et al. 2004

* Uncertainties of quoted age errors are 1 σ for data from Perkins & Kennedy but are not mentioned for the ages from other authors

Unfortunately, for the majority of existing data listed in table 5.1., additional information like sample locality (for the Red Dome porphyry), isotope concentrations (all samples) and used methodology (Re-Os molybdenite age from Mungana) could not be traced. The low number of available age data and the many uncertainties within the data set are insufficient to fully document the geological history of the Red Dome and Mungana deposit, especially the timing of skarn formation and mineralising event. Additionally, the Redcap deposit has not been investigated geochronologically so far. This chapter therefore aims to constrain the timing of emplacement of the igneous rocks, the skarn formation and the mineralisation for all three deposits.

A total of 14 samples (Tab. 5.1.1.) were selected for LA-ICP-MS U-Pb dating of zircon at the AAC-JCU (Townsville) and Re-Os dating of molybdenite at the RSES-ANU (Canberra). The results are presented in the following sections, the sample localities are shown in appendix 1, and the data can be found in appendices 13 and 14.

Table 5.1.1. Summary of samples analysed for isotope geochronology

Deposit	Sample ID	Rock type	Method	Mineral analysed
Redcap	949	Dacite	U-Pb	Zircon
Redcap	950	Clinopyroxene skarn	Re-Os	Molybdenite
Redcap	952W1	Dacite	U-Pb	Zircon
Redcap	955	Molybdenite -quartz vein	Re-Os	Molybdenite
Redcap	BE-1	Granodiorite	U-Pb	Zircon
Mungana	883W2	Rhyolitic porphyry	U-Pb	Zircon
Mungana	883W3	Granite	U-Pb	Zircon
Mungana	890W6	Andradite-wollastonite skarn	Re-Os	Molybdenite
Red Dome	936	Quartz-feldspar porphyry	U-Pb	Zircon
Red Dome	982	Clinopyroxene skarn	Re-Os	Molybdenite
Red Dome	983	Gold-molybdenite- quartz vein	U-Pb	Zircon
Red Dome	983	Gold-molybdenite- quartz vein	Re-Os	Molybdenite
Red Dome	984	Quartz-feldspar porphyry	U-Pb	Zircon
Red Dome	995	Dacitic porphyry	U-Pb	Zircon

5.2. U-Pb isotope geochronology of zircons

In comparison with other isotopic decay systems the U-Pb isotope decay system of zircon is a very powerful tool to reveal the geological history of complex systems with multiple overprinting events as assumed for the Chillagoe district (Nethery & Barr 1996; Georgees & Nethery 1999; Hodkinson et al. 2009) due to the mineral's robust nature and high closure temperature (Finch & Hanchar 2003). Zircon can survive magmatic, metamorphic and sedimentary processes and does not only preserve its original age, but can also record further formation periods in the form of new growth zones (Hoskin & Schaltegger 2003; Corfu et al. 2003). In combination with trace element studies (see chapter 6) it can even be possible to identify the source from which the zircons crystallised (Kinny & Maas 2003). For further details on the U-Pb decay system, LA-ICP-MS technique and other aspects regarding zircons the reader is referred to work from Hanchar and Hoskins (2003) and references therein.

5.2.1. Methodology

Nine samples (Tab. 5.1.1.) were crushed to a grain size smaller than 0.5 mm and zircons were separated by conventional magnetic separation and heavy liquid techniques. On average 50 grains were picked from the samples with special attention paid to cover a variety of morphologies and grain sizes. The grains were then mounted in an epoxy resign and polished to

reveal their interior. In addition to the epoxy grain mount, zircons from the mineralised quartz vein (983) were also analysed in situ in two polished thin sections.

Cathodoluminescence (CL) images were made to reveal the internal structure of the zircons by using a JEOL JSM 5410LV Scanning Electron Microscope in monochromatic greyscale mode and ~20kV accelerating voltage. Based on the shape and internal structure of individual zircon grains 20 to 25 grains were selected for analysis. Due to the relatively small nature of zircons as well as to avoid cracks and inclusions, that may provide erroneous results, only 1 spot within a single grain was analysed for the majority of samples. The material was ablated by a GeoLas 193 nm ArF laser and transported by a mixed argon-helium gas into a Varian 820 quadrupole ICP-MS. Background data were obtained for 35 seconds and followed by 40 seconds of ablation with the laser fluence kept at 6 J/cm^2 and a repetition rate of 10 Hz. Where possible the spot diameter was kept at 24 μm, but for zircon within the polished thin section it was reduced to 16 μm as these zircons were very rich in inclusions. In total eight isotopes were measured, which were assigned different dwell times: ^{29}Si (10ms), ^{204}Pb, ^{206}Pb, ^{208}Pb, ^{232}Th, ^{238}U (20ms), ^{235}U (30ms) and ^{207}Pb (40ms).

The reference zircon Plešovice (^{206}Pb/^{238}U age 337.8 ± 1.9 Ma, Sláma et al. 2008) was used as primary zircon standard and GJ-1 (^{206}Pb/^{238}U age 599.8 ± 2.4 Ma, Jackson et al. 2004) was used as a secondary one, except for the zircon analysis in the polished sections where GJ-1 was used as a primary standard. Standards were run every 10-12 analyses to check for reproducibility and accuracy. The reproducibility in ^{206}Pb/^{238}U age (1 RSD) for Plešovice was 1 % for the first session (n= 13 with 338.2 ± 3.4 Ma), and 0.7 % for the second session (n=18 with 338.2 ± 2.4), while for GJ-1 it was 0.95 % in session one (n=24, 595.4 ± 5.7), 0.89 % (n=9 with 597 ± 5) in session two and 0.59 % (n=6, 600.9 ± 3.6 Ma) in the third session (in situ analyses of zircons in polished thin sections).

Age data were processed using data reduction software GLITTER 4.4.2 (Van Achterbergh et al. 2001) filtering each signal for outliers as required. Data were assessed, calculated and plotted with ISOPLOT/EX 3.70 (Ludwig 2008). U-Pb isotope data (uncorrected for common Pb) are presented as Tera-Wasserburg diagrams to better illustrate the scatter of the error ellipses (Ludwig 2008). The apparent ages quoted for each sample are reported as weighted mean ^{206}Pb/^{238}U ages corrected for common lead based on the 207Pb method (e.g. Williams 1998) using the present day terrestrial lead value of Stacey & Kramers (1975). ^{206}Pb/^{238}U ages are the most robust ones for rocks of Permo-Carboniferous age.

5.2.2. Morphology and internal structures of zircons from the Recap deposit

Three igneous samples from the Redcap deposit were investigated regarding their morphology and internal structures. Two of the samples are from the Redcap dacite (949 & 952W1) and one sample from the Belgravia granodiorite (BE-1). Representative zircons grains of each sample are shown in plate 5.2.2.1 to 5.2.2.3.

5.2.2.1. Redcap dacite

Zircons from one of the dacite samples (949) are euhedral prismatic (Plate 5.2.2.1.a) or needle-shaped (Plate 5.2.2.1.c) ranging in size from 230 to 110 µm and an average length-width ratio of 3:1, which is typical for zircons of magmatic origin (Corfu et al. 2003).

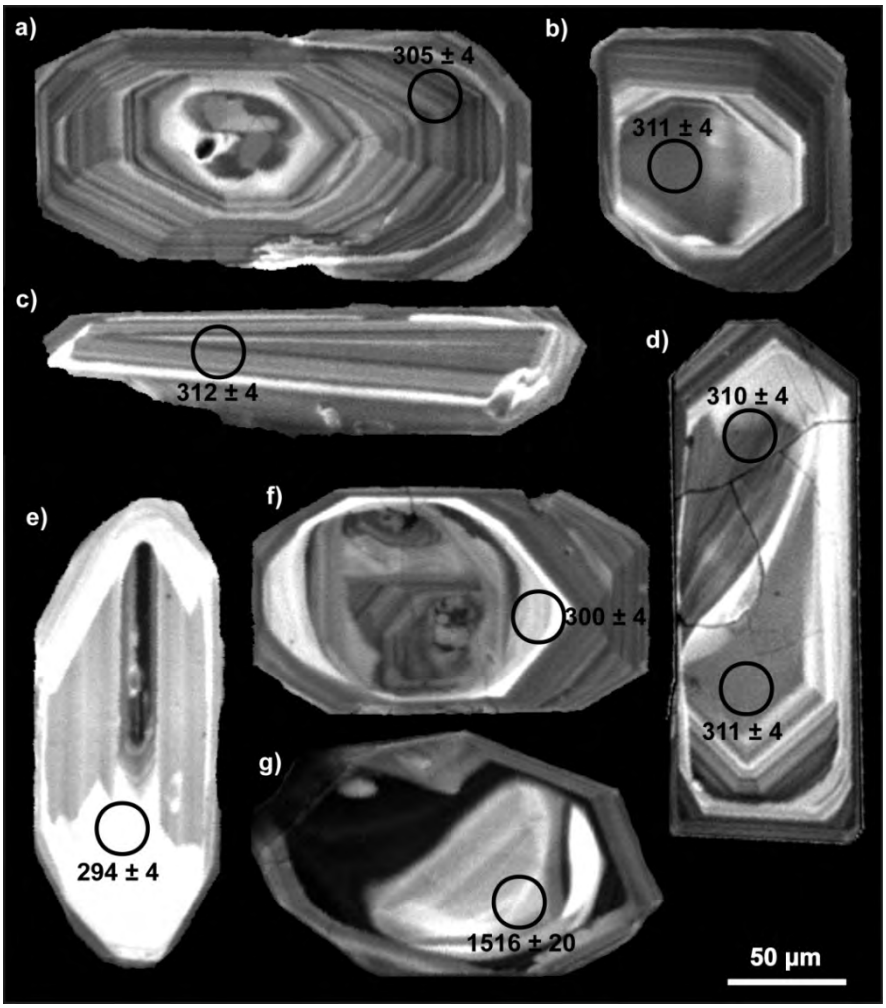

Plate 5.2.2.1. Cathodoluminescence images of representative zircon grains from a Redcap dacite (949) with the circle (not scaled) showing the locality of the analysis and related $^{206}Pb/^{238}U$ age in Ma; **a**) inherited core overgrown by oscillatory growth zones; **b**) featureless core overgrown by oscillatory growth zones; **c**) needle-shaped zircon with possibly growth bands; **d**) featureless, locally recrystallised core overprinted by a thin oscillatory growth zoned rim; **e**) bright CL rim overgrowing weakly growth zoning; **f**) convolute zoned core separated by bright CL zone from oscillatory growth zoned rim; **g**) inherited core surrounded by a zone of very dark CL and overgrown by weakly oscillatory zones towards rim.

Fine scale oscillatory growth zoning is a common feature of zircons from this rock type. In some places it is overgrowing embayed, possible inherited cores (Plate 5.2.2.1.a) or featureless cores (Plate 5.2.2.1.b), both being mantled by bright CL-zones. Other structures are growth bands parallel to the elongated shape of the zircon (Plate 5.2.2.1.c), featureless cores locally recrystallised and then overgrown by fine scaled oscillatory growth zoning (Plate 5.2.2.1.d) with the latter partly being very bright in CL (Plate 5.2.2.1.e). Convolute zoned or inherited cores can also be observed (Plate 5.2.2.1.f & g), but are rare.

Zircons from a second dacite sample from Redcap (952) also show blocky prismatic shapes ranging in size from 245 to 136 µm with typical length-width ratios of 2:1.

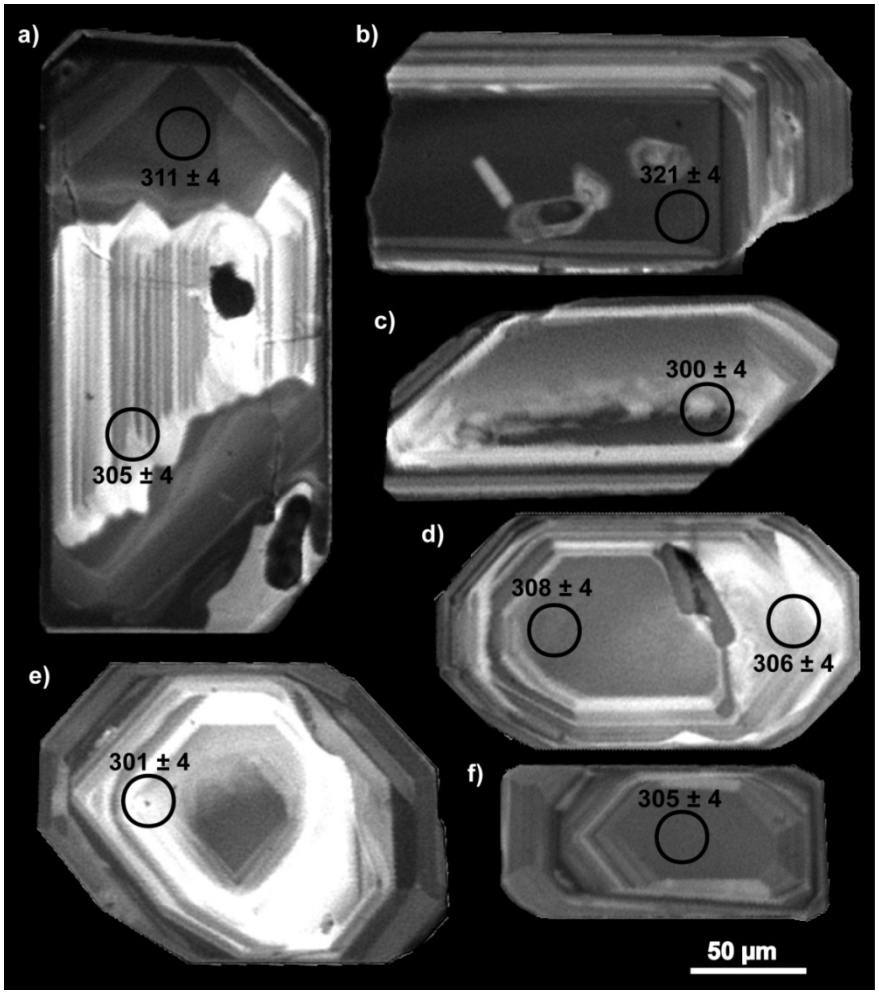

Plate 5.2.2.2. Cathodoluminescence images of representative zircon grains from a Redcap dacite (952W1) with the circle (not scaled) showing the locality of the analysis and related $^{206}Pb/^{238}U$ age in Ma; **a**) core with bright CL and oscillatory growth zones overgrown by dark, weakly growth zones towards the rim; **b**) featureless, dark core overgrown by fine scaled oscillatory growth zones; **c**) patchy core with weak growth zoned rim wards; **d**) featureless core with oscillatory zoning in rims; **e**) featureless core surrounded by a very bright CL zones and medium scaled growth bands towards the rim; **f**) featureless core with oscillatory growth zones rim wards.

Oscillatory growth zones are not as abundant as in sample 949, but occur either in the form of very bright zones in the core (Plate 5.2.2.2.a) or towards the rim (Plate 5.2.2.2.b, c & f). Featureless cores are relatively common (Plate5.2.2.2.b, d & f) and have medium to dark CL colour, indicating U-rich zones while bright CL zones on the other hand are normally U-low (Rubatto & Gebauer 2001).

5.2.2.2. Belgravia granodiorite

Zircons from the Belgravia granodiorite (BE-1) are often euhedral to subhedral, blocky prismatic (Plate 5.2.2.3.a, c-i), although some needle-shaped grains occur (Plate 5.2.2.3.b & j). The size ranges from 404 to 132 µm and is on average 200 µm.

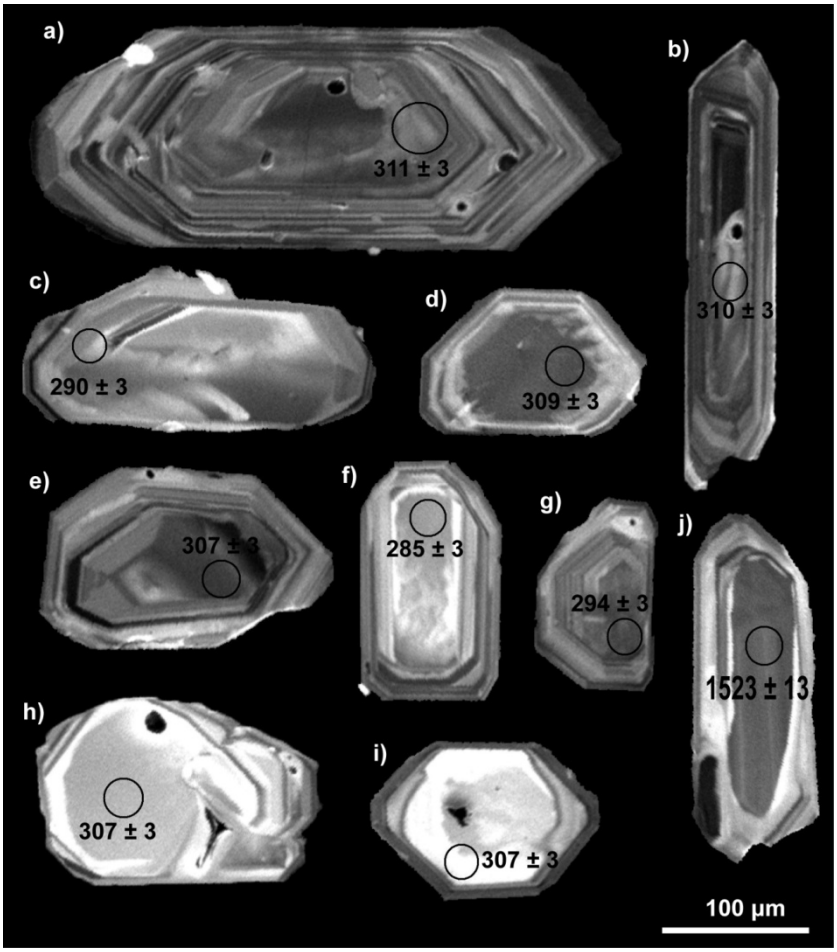

Plate 5.2.2.3. Cathodoluminescence images of zircons from the Belgravia granodiorite at Redcap (BE-1) with the circle (not scaled) showing the locality of the analysis and related $^{206}Pb/^{238}U$ age in Ma; **a**) zircon with oscillatory growth zoning; **b**) dark CL core locally recrystallised and overgrown by oscillatory zoning; **c**) featureless core overgrown by very weak growth zones; **d**) dark core rimmed with bright CL "flame-like" structure; **e**) featureless core with oscillatory growth zoning towards the rim; **f**) flame-like bright CL overprinting a featureless core (very weak form of convolute zoning), and rimmed by oscillatory growth zones; **g**) oscillatory growth zoned zircon; **h & i**) patchy bright CL core with darker faded oscillatory growth zoned rim; **j**) dark CL, inherited core with brighter growth zones towards the rim.

Length-width ratios vary from 2:1 to 5:1 with the ratio of 2:1 being most common. Internal CL structures show oscillatory growth zoning (Plate 5.2.2.3.a, e & g) which almost always occurs towards the rims (Plate5.2.2.3.b). Featureless, dark cores locally show signs of recrystallisation represented by irregular or convolute zoning (Plate 5.2.2.3.b). Some grains are completely featureless (Plate 5.2.2.3.c) or show bright "flame-like" structures rimming or intruding featureless dark core representing a weak form of convolute zoning (Plate 5.2.2.3.d & f). Other grains show patchy CL images of light grey to very bright areas and are often rimmed by a slightly darker zone (Plate 5.2.2.3.h & i). One inherited core was observed in this rock and is characterised by a subrounded, elongated, featureless, dark core overgrown by relatively bright growth bands (Plate 5.2.2.3.j).

5.2.3. U-Pb isotope data of Redcap

Twenty-five spot analyses were conducted on zircon grains from two samples of the Redcap dacite (949 & 952W1) and one sample of the Belgravia granodiorite (BE-1) to cover the majority of different CL structures. Data are plotted on Tera-Wasserburg diagrams (Fig. 5.2.3.1 and 5.2.3.2) and the results reported as ^{207}Pb corrected weighted mean ^{206}Pb/^{238}U age.

5.2.3.1. Redcap dacite

Twenty five spots have been analysed on sample 949 (Plate 5.2.3.1.A). Zircons with featureless, dark CL structures as well as dark zones with oscillatory growth zoning and weak convolute zoning yielded similar ages of around 310 Ma. Three zircon grains with very bright CL on the other hand are on average 15 Ma younger. These analyses were rejected (red ellipses on Tera-Wasserburg diagrams) for age calculation as they may have been subject to Pb loss, although high CL intensity suggest low U concentrations (Rubatto & Gebauer 2001) and therefore being less sensitive to Pb loss or these grains represent a younger zircon population (294 ± 2 Ma, n=3, 2STD). Additionally one inherited core with a Mesoproterozoic ^{206}Pb/^{238}U age of 1516 ± 20 Ma was not considered for the age calculations. The remaining 21 analyses yielded a ^{207}Pb corrected weighted mean ^{206}Pb/^{238}U age of 310 ± 2 Ma (2σ, MSWD 1.5).

For age calculation of the second dacite sample from Redcap (952W1) 20 analyses were used. Three analyses which are on average 321 Ma old were rejected as they may be inherited cores (featureless, dark CL) representing a slightly older group of Redcap dacite and two other zircon grains of ~ 296 Ma years, which have very bright CL were discarded for the same reason (Pb loss) as zircon grains from sample 949 with similar CL. The remaining zircon grains yielded a ^{207}Pb corrected weighted mean ^{206}Pb/^{238}U age of 306 ± 2 Ma (2σ, MSWD 1.5).

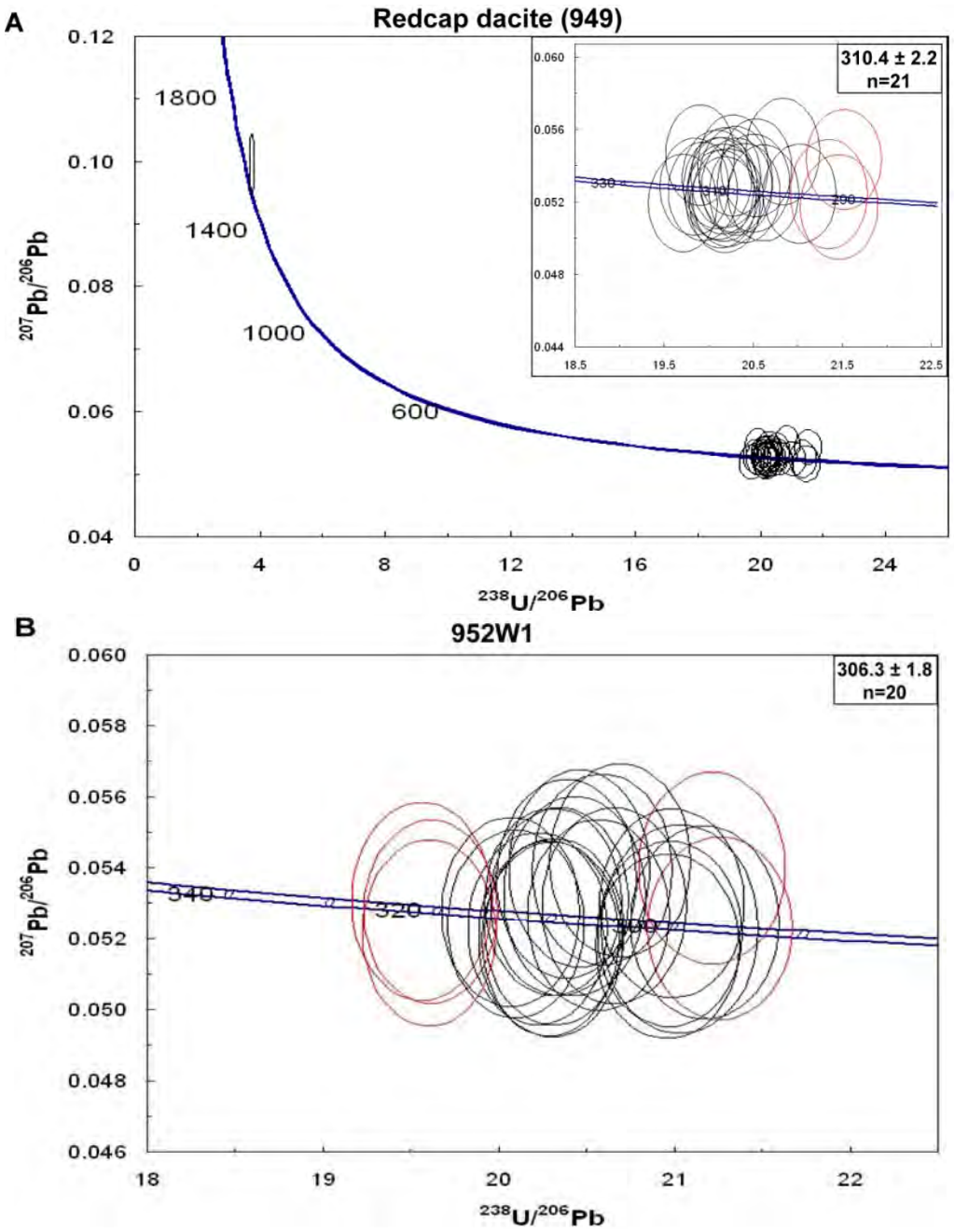

Figure 5.2.3.1. Tera-Wasserburg plots of zircons from two Redcap dacite samples; **A**) sample 949: main diagram showing all 25 analyses and the inset shows those analyses used to calculate the weighted mean $^{206}Pb/^{238}U$ age for the samples as well as the rejected analyses (in red); **B**) U-Pb isotope data for sample 952W1 with discarded analyses in red.

5.2.3.2. Belgravia Granodiorite

Twenty-five spots have been analysed from sample BE-1 (Plate 5.2.3.2.A & B). One inherited core of Mesoproterozoic age (1523 ± 13 Ma) was identified. The remaining 24 analyses represent two age populations, which can be distinguished based on their internal structure. The older population has dark, featureless or oscillatory zoned internal structure (Plate 5.2.2.3.a, d & e). Thirteen zircon grains are assigned to this group (Fig. 5.2.3.2.A), which yielded a ^{207}Pb corrected weighted mean $^{206}Pb/^{238}U$ age of 309 ± 2 Ma (2σ, MSWD 1.6).

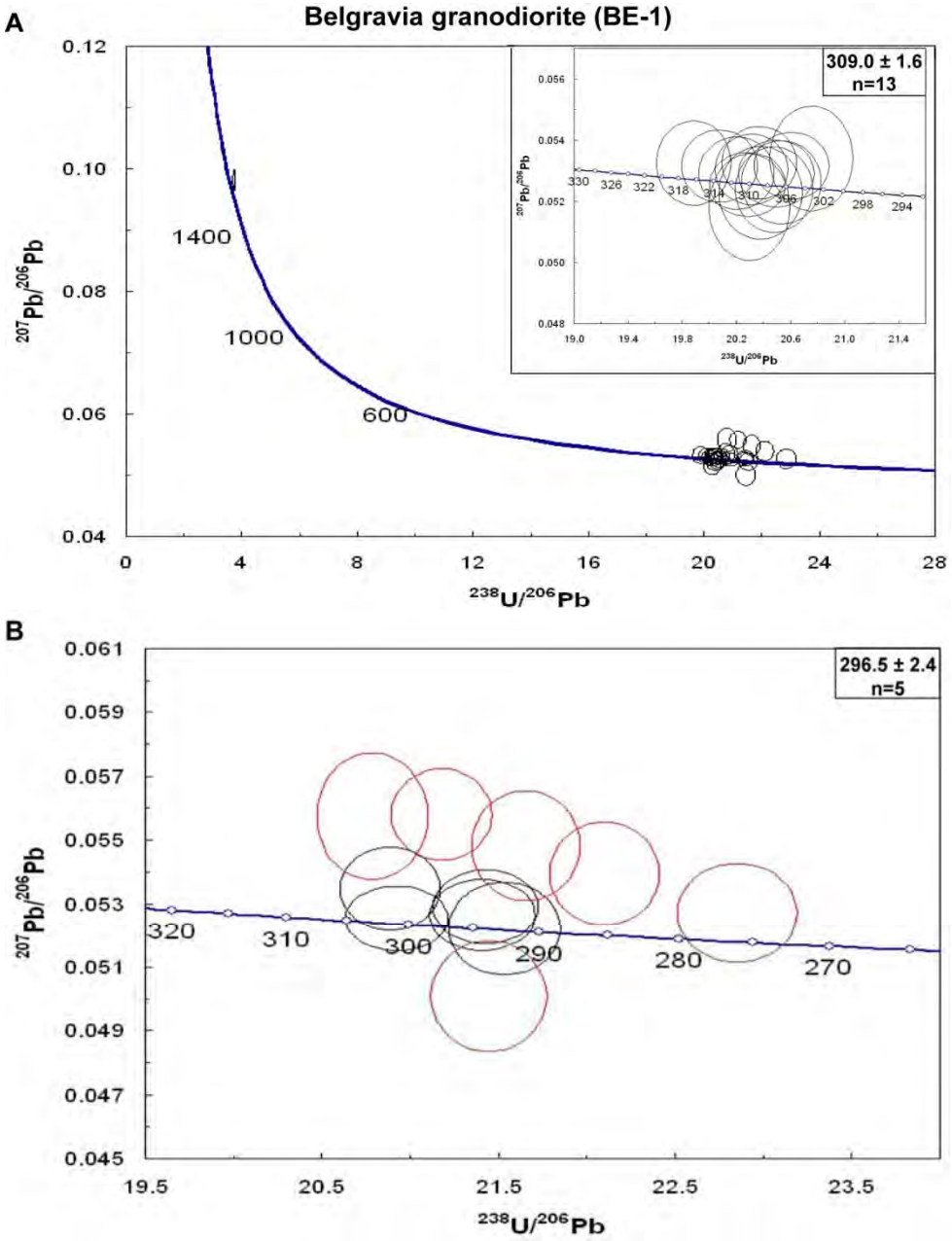

Figure 5.2.3.2. Tera-Wasserburg plots of zircons from the Belgravia granodiorite (BE-1); **A**) main diagram showing all 25 analyses and the inset shows the older age population; **B**) analyses used to calculate the weighted mean $^{206}Pb/^{238}U$ age of the younger age group and the ones discarded (red ellipses).

One grain is this population is slightly older than the others (316 Ma), has a medium grey CL and may represent a slightly older population within the Belgravia granodiorite. The younger population is represented by zircon grains which have bright CL and show weak to moderate convolute zoning (e.g. Plate 5.2.2.3f). Eleven grains can be assigned to this group (Fig. 5.2.3.2.B), but only 5 analyses were used for age calculation as the majority of the grains are discordant, probably due to a combination of common lead and radiogenic lead loss. The ^{207}Pb corrected weighted mean $^{206}Pb/^{238}U$ age for this group is 297 ± 2 (2σ, MSWD 2.4).

5.2.4. Morphology and internal structures of zircons from igneous rocks of the Mungana deposit

Two igneous samples from the Mungana deposit were investigated regarding their morphology and internal structures. These samples are a rhyolitic porphyry (883W2) and a granite (883W3), with representative zircons grains of each sample being shown in plate 5.2.4.1 and 5.2.4.2.

5.2.4.1. Rhyolitic porphyry

Zircons from the rhyolitic porphyry (883W2) are roughly blocky prismatic, range in size from 291 to 111 µm and have length-width ratios of 2:1. CL imaging reveals homogenous, featureless cores (Plate 5.2.4.1.a, b & c).

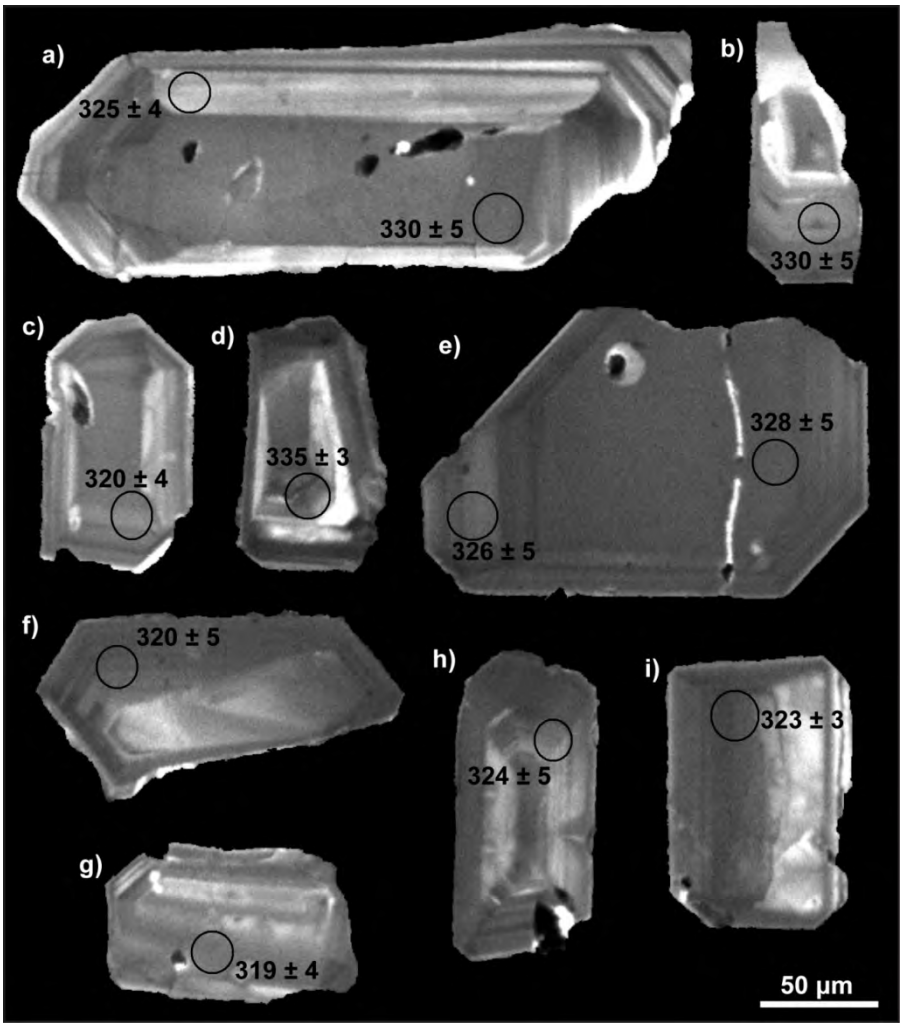

Plate 5.2.4.1. Cathodoluminescence images of representative zircon grain from the Mungana porphyry (883W2) with the circle (not scaled) showing the locality of the analysis and its related $^{206}Pb/^{238}U$ age in Ma; **a, c, e, f**) homogenous, featureless core with weak oscillatory zoned overgrowth; **b & d**) weak growth bands, mantled by a zone of very bright CL; **g & i**) patchy zoning; **h**) sector zoning.

Towards the rim weak oscillatory growth zoning can occur which sometimes has brighter CL than the core (Plate 5.2.3.1.a) or the same CL intensity as the core (Plate 5.2.4.1.e). Other grains have a dark featureless core which is mantled by a band of bright CL between core and rim (Plate 5.2.4.1.b & d) or show patchy zoning (Plate 5.2.4.1.g & i). One grain shows weak sector zoning (Plate 5.2.4.1.h). No convolute zoning, signs of local recrystallisation or inherited cores were observed.

5.2.4.2. Granite

Zircons from the Mungana granite (883W3) are euhedral prismatic (Plate 5.2.4.2.a) or needle-shaped (Plate 5.2.4.2.c). The size ranges from 225 to 79 µm and the length-width ratios are 5:1 to 1:1.

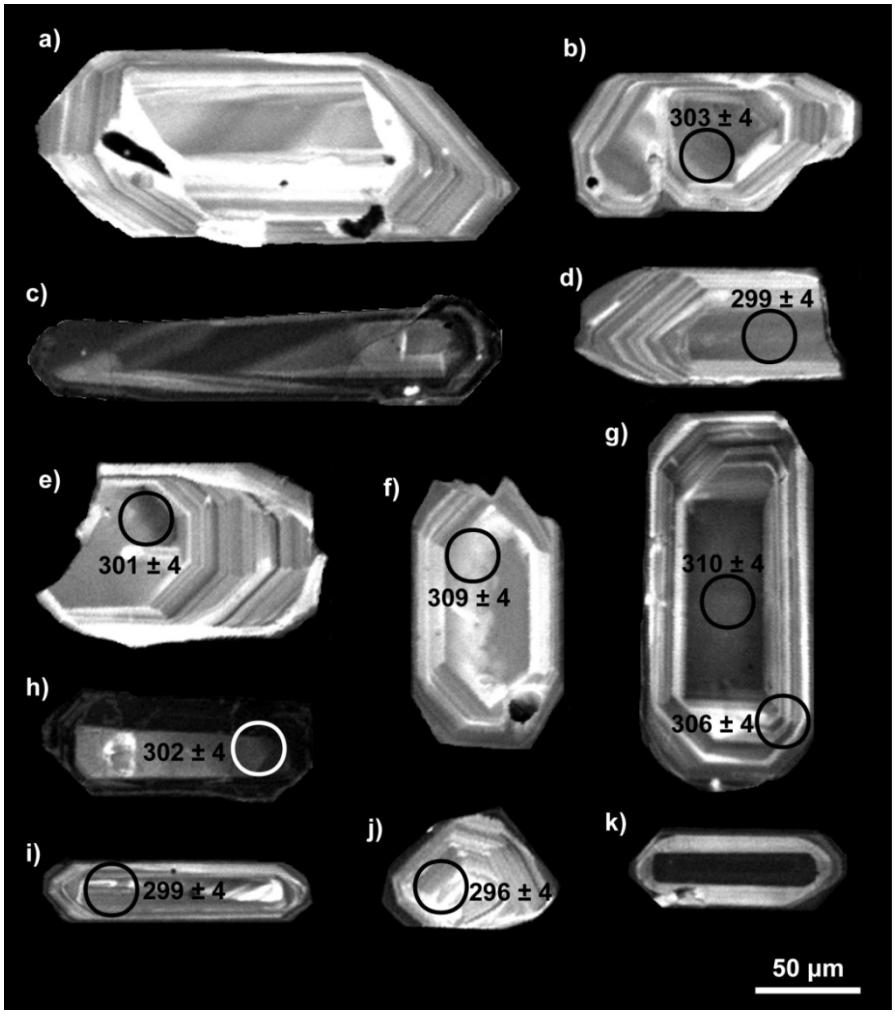

Plate 5.2.4.2. Cathodoluminescence images of representative zircon grains from the Mungana granite (883W3) with the circle (not scaled) showing the locality of the analysis and its related $^{206}Pb/^{238}U$ age in Ma; **a, f, i & j**) bright CL core with in some places very weak convolute zoning overgrown by oscillatory zoning towards the rim; **b**) patchy zoning in the core with oscillatory growth zoning towards the rim; **d, e, g & k**) homogenous, featureless core oscillatory growth zoned rim; **c & h**) nearly featureless grains with very low CL intensity.

CL images show patches or growth bands in the core (Plate 5.2.3.2.a, i & j) overgrown by oscillatory zoning towards rim (Plate 5.2.4.2.a & j) with other grains showing the same structure, but having relatively dark CL cores (Plate 5.2.4.2.d & e). Some grains are CL dark with featureless cores (Plate 5.2.4.2.c & h) or have a dark featureless core overgrown by a brighter oscillatory zoned rim (Plate 5.2.4.2.g & k) while other grains have a patchy core which is again overgrown by oscillatory zoning towards rim (Plate 5.2.4.2.b & f).

5.2.5. U-Pb isotope data of Mungana

Twenty spot analyses were conducted on zircon grains from two igneous samples of the Mungana deposit. These samples are a rhyolitic porphyry (883W2) and a granite (883W3). Data are plotted on Tera-Wasserburg diagrams (Fig. 5.2.5.1 and 5.2.5.2) and the results reported as ^{207}Pb corrected weighted mean ^{206}Pb/^{238}U age.

5.2.5.1. Rhyolitic porphyry

Twenty spots have been analysed from the porphyry sample (883W2). Nineteen out of twenty grains yielded a ^{207}Pb corrected weighted mean ^{206}Pb/^{238}U age of 324 ± 2 Ma (2σ, MSWD 1.1). The single discarded analysis, which yielded a ^{206}Pb/^{238}U age of 338 Ma, was rejected as during the analysis relatively high counts on mass 204 suggest the presence of significant common lead.

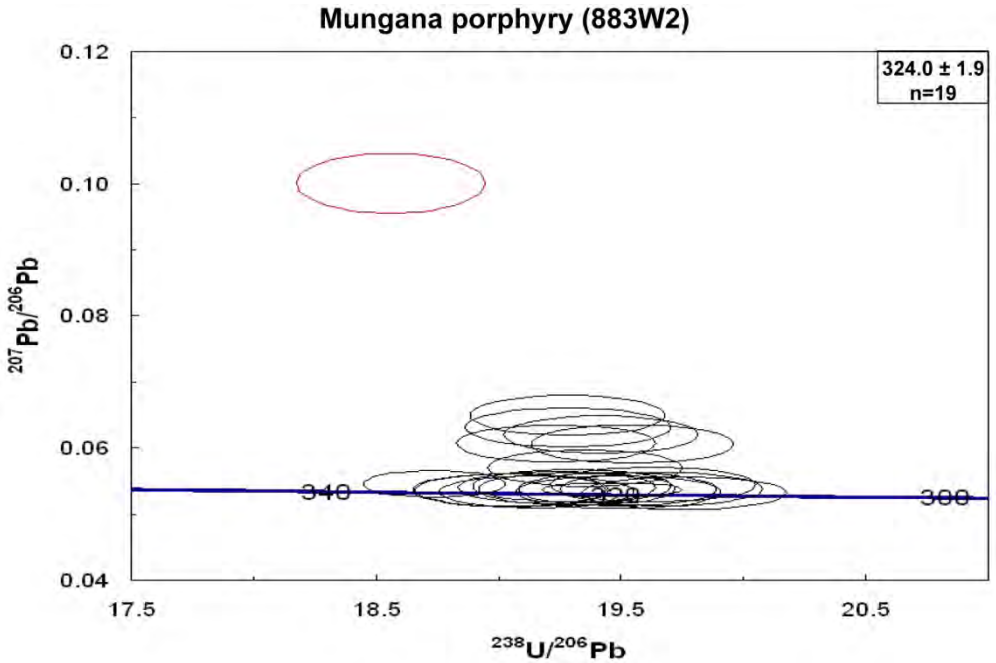

Figure 5.2.5.1. Tera-Wasserburg plot of zircon analyses from a porphyry from Mungana (883W2) showing the analyses used to calculate the ^{207}Pb corrected weighted mean ^{206}Pb/^{238}U age and one rejected analysis (red ellipse).

5.2.5.2. Granite

Twenty zircons from the Mungana granite were analysed, yielding a ^{207}Pb corrected weighted mean $^{206}Pb/^{238}U$ age of 305 ± 2 (2σ, MSWD 0.95) (Fig. 5.2.5.2).

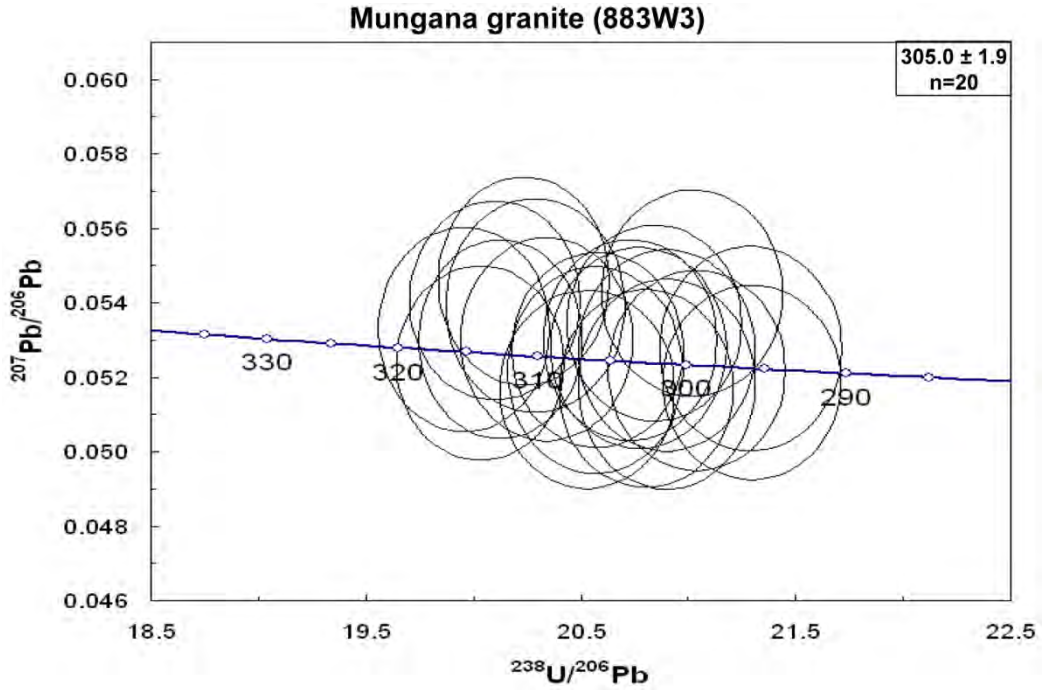

Figure 5.2.5.2. Tera-Wasserburg plots of zircon analyses from a granite sample from Mungana (883W3) showing the analyses used to calculate the ^{207}Pb corrected weighted mean $^{206}Pb/^{238}U$ age.

5.2.6. Morphology and internal structures of zircons from igneous rocks and mineralised quartz vein from the Red Dome deposit

Three igneous samples from the Red Dome deposit and one zircon bearing mineralised quartz vein (983) were investigated regarding their morphology and internal structures. Two of the samples are quartz-feldspar porphyries (936 & 984) and one sample is a dacitic porphyry (995), Representative zircons grains of each sample are shown in plate 5.2.6.1.A & B, 5.2.6.2 and 5.2.6.3.

5.2.6.1. Quartz-feldspar porphyry

Zircons from one quartz-feldspar porphyry (936) are euhedral, blocky prismatic in shape and range in size from 185 to 81 µm. Their length-width ratio is 2:1. CL imaging reveals broad oscillatory growth zoning (Plate 5.2.6.1.A_a) with partly very bright CL zones. Some grains are very dark in CL and are almost featureless (Plate 5.2.6.1.A_b) while others have patchy zoning in the centre, which is overgrown by very broad bands (Plate 5.2.6.1.A_c & j). Zircons with dark cores (Plate 5.2.6.1.A_d, h &i) which may have been resorbed (Plate 5.2.6.1.A_e) and

possibly inherited cores (Plate 5.2.6.1.A_g) are mantled by a bright CL zone, which becomes darker again towards the rim. One grain shows sector zoning (Plate 5.2.6.1.A_f).

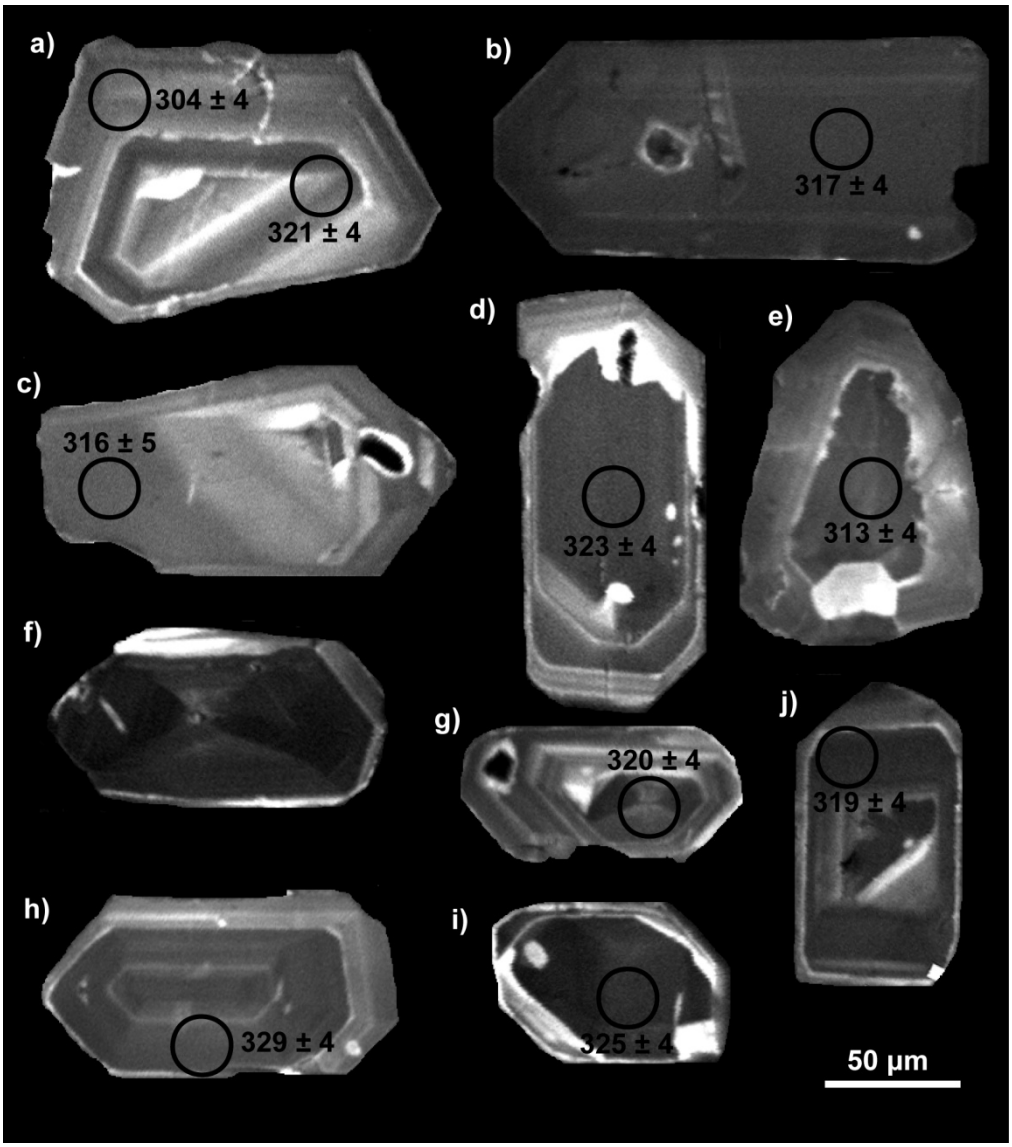

Plate 5.2.6.1.A Cathodoluminescence images of representative zircon grains from quartz-feldspar porphyry(936) at Red Dome with the circle (not scaled) showing the locality of the analysis and related $^{206}Pb/^{238}U$ age in Ma; **a**) broad oscillatory growth zoning; **b**) homogenous, featureless zircon; **c & j**) patchy core with broadly zoned overgrowths; **d-e, h-i**) inherited, partly resorbed, very dark core, overgrown by weak, broad oscillatory zones; **f**) sector zoning.

Zircons from a second quartz-feldspar porphyry sample from Red Dome (984) show a roughly prismatic shape, but some elongated, partly needle-shaped ones also occur. The size ranges from 222 to 94 µm and length width ratio is on average of 2:1 (maximum 5:1). Compared to sample 936, the internal structures are relatively simple. Some grains are featureless or only show weak growth bands (Plate 5.2.6.1.B_a, c, f, h, I & j). Other grains have dark cores and a

brighter rim with partly visible oscillatory growth zoning (Plate 5.2.6.1.B_e & f) and only a few zircons show oscillatory growth zoning within the entire grain (Plate 5.2.6.1.B_d).

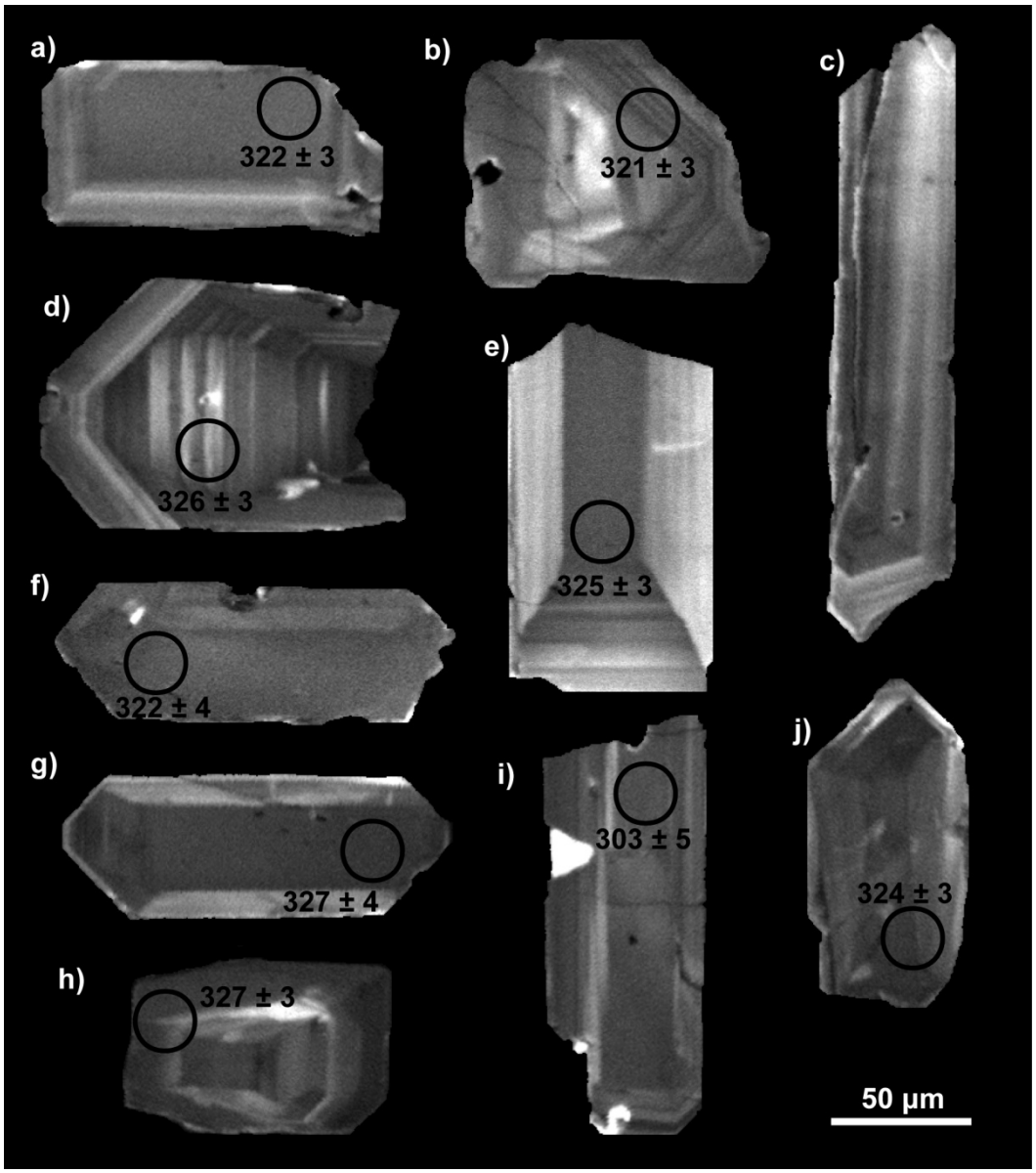

Plate 5.2.6.1.B Cathodoluminescence images of representative zircons from a second quartz-feldspar porphyry (984) from Red Dome with the circle (not scaled) showing the locality of the analysis and related $^{206}Pb/^{238}U$ age in Ma; **a, c, f, i & j**) nearly featureless structure; **b & g**) patchy core and broad growth zones or oscillatory growth zones towards the rim; **d**) zircon grain with oscillatory growth zoning; **e & g**) homogenous dark core with bright band at rim.

5.2.6.2. Dacitic porphyry

Zircons from the dacitic porphyry (995) from Red Dome are needle-shaped or prismatic with either bi-pyramidal or flat edges. They range in size from 250 to 138 µm and have a length-width ratio of 2:1 (maximum 4:1). Internal structures show oscillatory growth zones or bands and are weak (Plate 5.2.6.2.a, b, c, g & f). Some of the growth zones occur only towards the rim

with grains having a homogenous, featureless core while others show the zoning through the entire grain. Some are more or less featureless (Plate 5.2.6.2.d) and rarely grains with a dark inherited core occur (Plate 5.2.6.2.e).

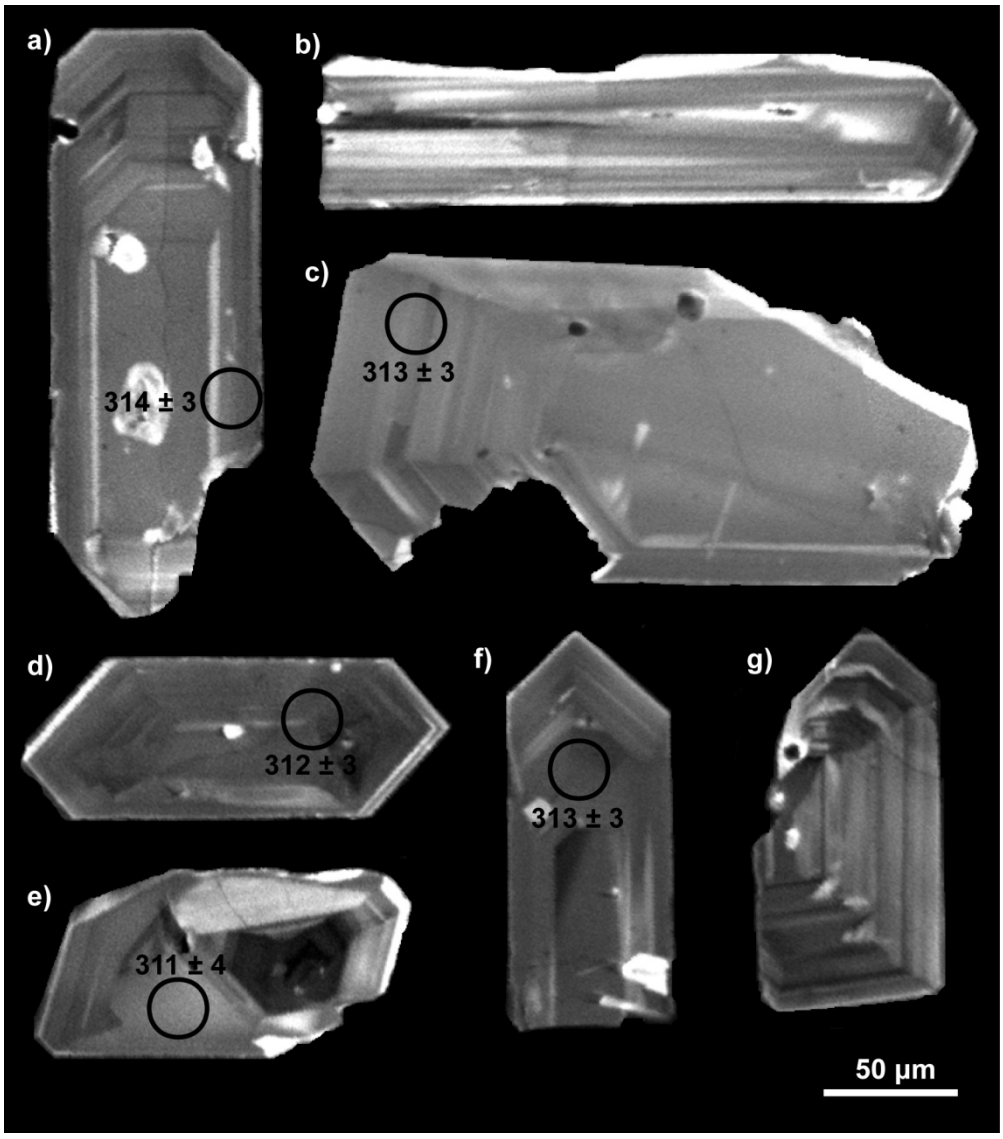

Plate 5.2.6.2. Cathodoluminescence images of representative zircons from a dacitic porphyry (995) from Red Dome with the circle (not scaled) showing the locality of the analysis and related $^{206}Pb/^{238}U$ age in Ma; **a, c & f**) featureless core overgrown by oscillatory growth zoning towards the rim; **b & g**) oscillatory growth zoning throughout the entire grain; **d**) nearly featureless zircon; **e**) dark, inherited core overgrown by brighter zones with no obvious feature.

5.2.6.3. Mineralised quartz vein in fluorite bearing quartz-feldspar porphyry

Zircons from the mineralised quartz vein were investigated within two polished thin sections (983-880.28 & 983-885.71) and within an epoxy grain mount (983). Only zircons from the grain mount were imaged by CL.

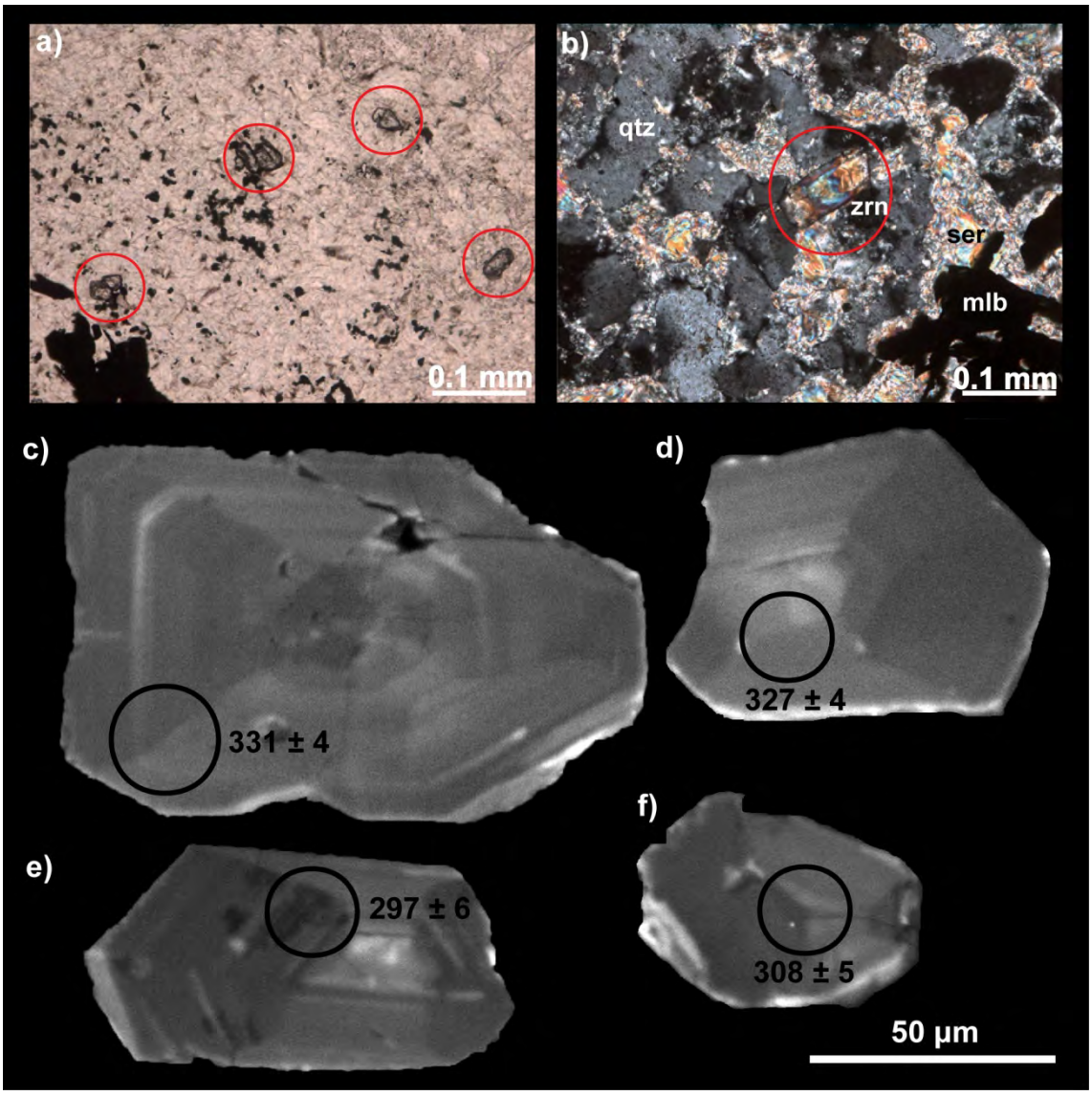

Plate 5.2.6.3. Photomicrographs (PPL: plane-polarised, XPL: crossed polars) and cathodoluminescence images of representative zircon grains from a mineralised quartz vein in a fluorite bearing quartz-feldspar-porphyry (983) from Red Dome with the circle (not scaled) showing the locality of the analysis and related $^{206}Pb/^{238}U$ age in Ma; **a**) trail of single zircons and pairs (red circles) within the quartz vein(PPL, 983-885.71); **b**) euhedral prismatic zircon (zrn) in sericite (ser) altered, molybdenite (mlb) mineralised quartz (qtz) vein (XPL, 983-885.71); **c, d & f**) weak to very sector zoning; **e**) coarse oscillatory growth zoning.

Polished thin section investigation show that zircons from the mineralised quartz vein occur commonly in pairs along a trail (Plate 5.2.6.3.a) within the quartz vein. While some zircon grains are subrounded (Plate 5.2.6.3.a & f) others are of subhedral to roughly prismatic shape (Plate 5.2.6.3.b, c, d & e). Compared to zircons from the other porphyry samples of Red Dome, zircons from this sample are small with a size ranging from 118 to 50 µm. Length-width ratios are 2:1 to 1:1. Only very poor internal structures are developed. Weak to very weak sector zoning (Plate 5.2.6.3.c, d & f) can be observed in some grains, while others show weak oscillatory growth zoning (Plate 5.2.6.3.e).

5.2.7. U-Pb isotope data of the Red Dome deposit

Twenty spot analyses have been conducted on zircon grains from two samples of a quartz-feldspar porphyry (936 & 984) and a dacitic porphyry (995) from the Red Dome deposit. Additionally five spots of zircons from a mineralised quartz vein (epoxy grain mount: 983) as well as 13 spots in situ in two polished thin sections (983-880.29 & -885.71) were analysed. Data are plotted on Tera-Wasserburg diagrams (Fig. 5.2.7.1.A & B, 5.2.7.2. and 5.2.7.3.) and the results reported as ^{207}Pb corrected weighted mean ^{206}Pb/^{238}U age.

5.2.7.1. Quartz-feldspar porphyry

Twenty grains of both the quartz-feldspar porphyries (936 & 984) were analysed and their results plotted on Tera-Wasserburg diagrams (Fig. 5.2.7.1.A & B). Sixteen out of twenty grains from sample 936 yielded ^{207}Pb corrected weighted mean ^{206}Pb/^{238}U age of 322 ± 2 Ma (2σ, MSWD 1.09).

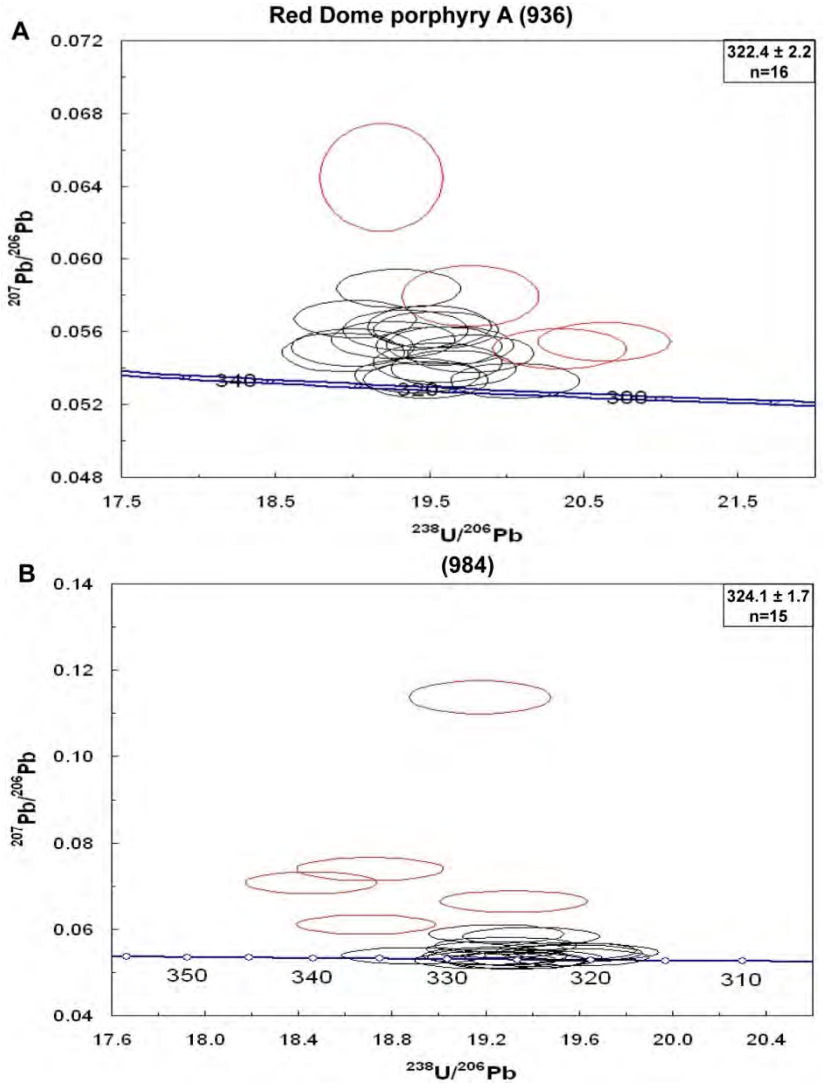

Figure 5.2.7.1. Tera-Wasserburg plots of zircon analyses from two quartz-feldspar porphyry samples (936: **A** & 984: **B**) from the Red Dome deposit showing the analyses used to calculate the ^{207}Pb corrected weighted mean ^{206}Pb/^{238}U age and the rejected analyses in red ellipses.

The two youngest analyses were rejected because their ablation profiles are complex being possibly caused by zoning and the two most discordant analyses were discarded as during analysis high levels of ^{204}Pb were detected. Fifteen zircons from the second quartz-feldspar porphyry sample (984) yielded a ^{207}Pb corrected weighted mean ^{206}Pb/^{238}U age of 324 ± 2 Ma (2σ, MSWD 0.93). Five analyses were discarded as during analysis high levels of ^{204}Pb were detected.

5.2.7.2. Dacitic porphyry

Twenty grains of the dacitic porphyry (995) from the Red Dome deposit were analysed and their results plotted on a Tera-Wasserburg diagram (Fig. 5.2.7.2). Fifteen grains yielded a ^{207}Pb corrected weighted mean ^{206}Pb/^{238}U age of 311 ± 2 Ma (2σ, MSWD 1.3). The two youngest as well as the oldest analysis and the two most discordant analyses were discarded because of high ^{204}Pb concentrations during analysis and down-hole complexity in ratios probably caused by analysing non homogenous zones.

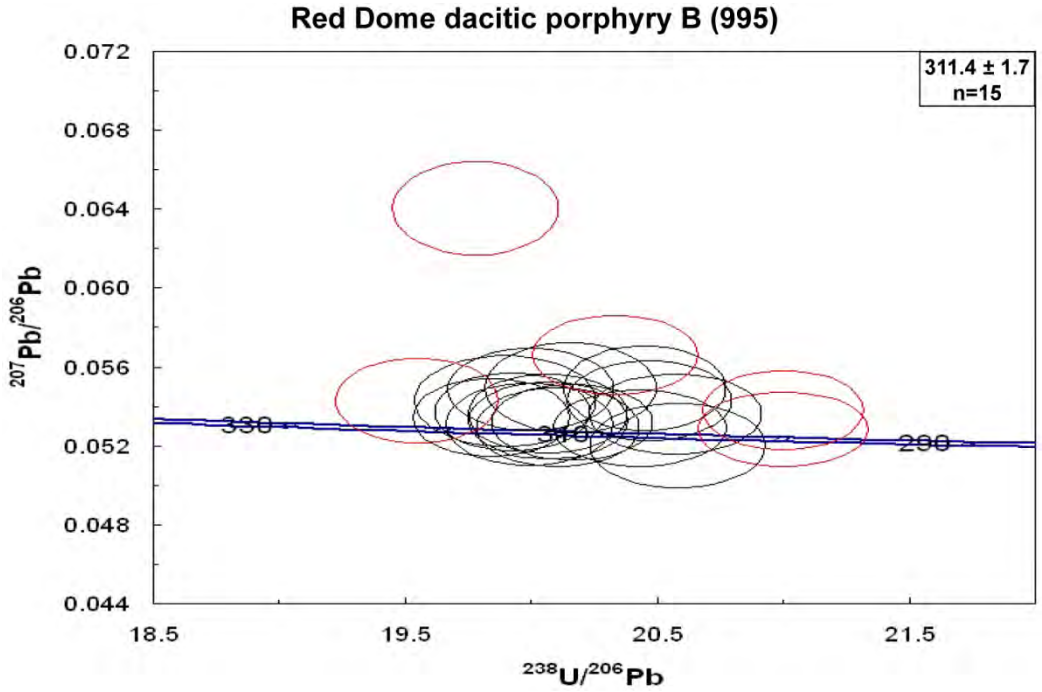

Figure 5.2.7.2. Tera-Wasserburg plots of zircon analyses from a dacitic porphyry sample (995) from the Red Dome deposit showing the analyses used to calculate the ^{207}Pb corrected weighted mean ^{206}Pb/^{238}U age and the rejected analyses in red ellipses.

5.2.7.3. Mineralised quartz vein in fluorite bearing quartz-feldspar porphyry

Eighteen zircon grains of this sample (983) were analysed with 13 of them in situ in polished thin sections (983-880.29 & -885.71) and five grains in the epoxy grain mount. Unlike all other zircons analysed in this study, zircons from the mineralised quartz vein were standardised to the reference zircon GJ-1 (see section 5.2.1.). The scatter of the U-Pb data of zircons from sample

983 is large (Fig. 5.2.7.3.A). With the seven most discordant, youngest and oldest analyses removed a ^{207}Pb corrected weighted mean ^{206}Pb/^{238}U age of 322 ± 2 Ma (2σ, MSWD 1.6) is obtained.

This sample also contained molybdenite and the results of the Re-Os dating will be presented and discussed in the next section.

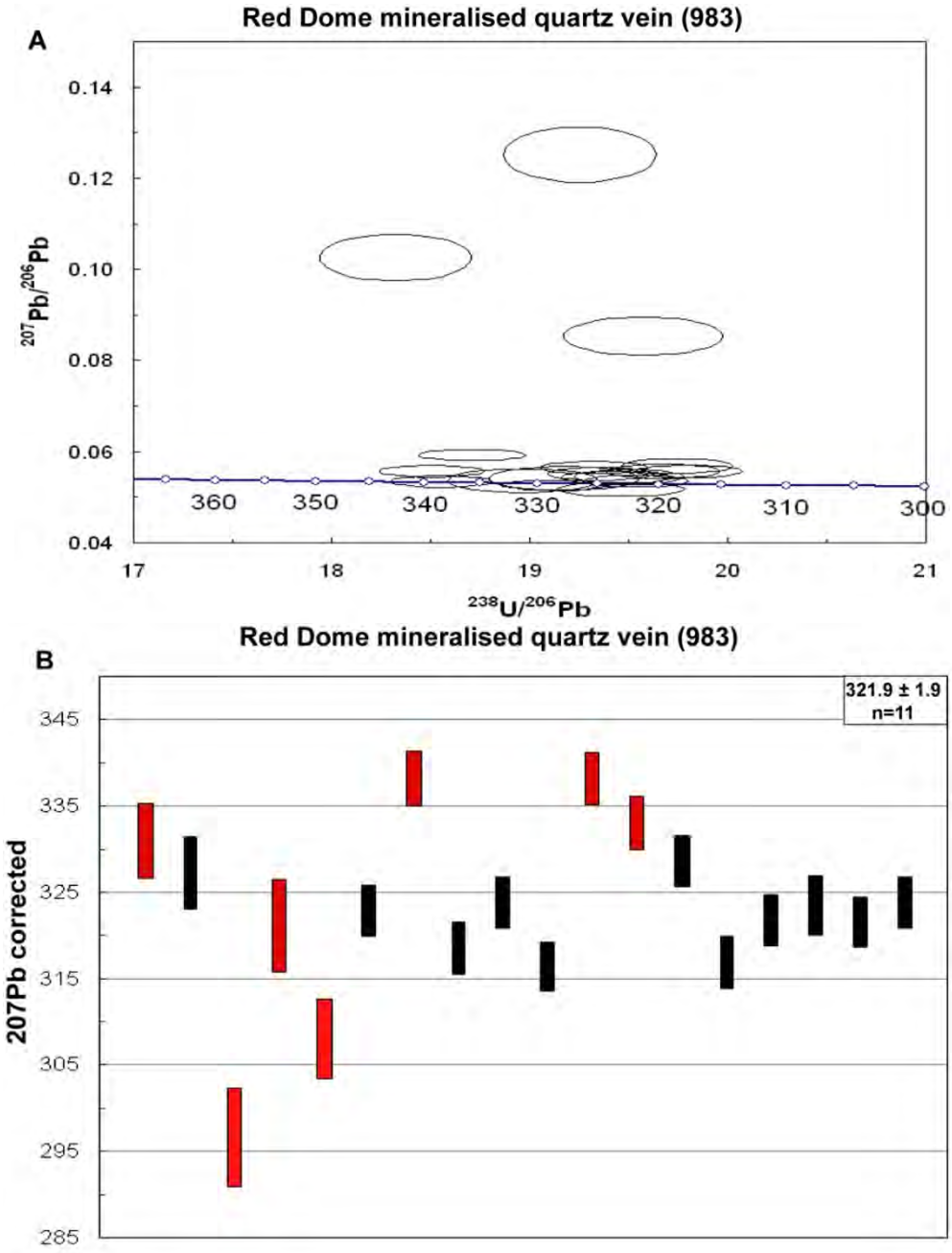

Figure 5.2.7.3. A. Tera-Wasserburg plots of zircon analyses from a mineralised quartz vein (983) from the Red Dome deposit **B.** diagram showing the ^{207}Pb corrected ^{206}Pb/^{238}U ages used to calculate the ^{207}Pb corrected weighted mean ^{206}Pb/^{238}U age and the rejected analyses in red.

5.3. Re-Os molybdenite

Rhenium-osmium dating of molybdenite is considered as an important tool for revealing ore-formation as the mineralisation is dated directly (Selby & Creaser 2001; Stein et al. 2001; Norman et al. 2004). Although it is an accepted dating tool there is still discussion about the robustness of the geochronometer. The major problem is that rhenium and osmium isotopes can become decoupled (Stein et al. 2001 and references therein; Stein et al. 2003; Selby & Creaser 2004), with ^{187}Os being the mobile phase (Stein et al. 2003). However, due to a lack of other minerals incorporating Os and the unusual structure of molybdenite (Stein et al. 2003) ^{187}Os stays within the molybdenite crystal and therefore the isotopic systems remains closed. McCandless et al. (1993) postulated that this may only be true for one of the two natural occurring molybdenite polytypes (2-H and 3-R), but while the 3-R polytype seems to be sensitive for ^{187}Os loss, the more common 2-H polytype (≥99 %) is not.

Furthermore, Xiong & Wood (1999) and Suzuki et al. (2001) showed in independent studies that low temperature hydrothermal alteration causes a loss of Re in molybdenite, but Stein et al. (2001) as well as Selby & Creaser (2001) claimed the opposite. Based on all these studies it is assumed that the Re-Os systems is suitable as a geochronometer, however some problems still exist. Selby & Creaser (2004) showed that with increasing grain size and age the decoupling of parent-daughter isotopes increases and they as well as Stein et al. (2001, 2003) emphasis how important the right sample size and homogeneity are to obtain accurate and reproducible ages. One last problem with the Re-Os isotope system of molybdenite is that all previous authors assumed that single molybdenite grains are of homogenous geochronological and chemical compositions, but Aleinikoff et al. (2012) showed that one single molybdenite crystal can show differences regarding its age and composition from core to rim being caused by multiple growth periods.

5.3.1. Methodology

Five samples of molybdenite were selected for this study (Tab. 5.3.1.; Plate 5.3.1.). Two of the samples have molybdenite mineralisation associated with pyroxene skarn (Redcap 950 & Red Dome 982; Plate 5.3.1.A & D) and should provide an indirect age for skarn formation. Another two samples (Redcap 955 and Red Dome 983; Plate 5.3.1.B & E) represent molybdenite-gold mineralisation in quartz veins (gold in these samples was confirmed by assay analysis and petrography, chapter 3). The fifth sample was taken from Mungana (890W6, Plate 5.3.1.C) to check the reliability of the existing Re-Os age. This molybdenite is relatively coarse grained (0.3 mm) and occurs in wollastonite-andradite skarn. Gold in this sample has also been confirmed by assay analysis, but only Bi-Te mineral phases were observed in thin sections.

Table 5.3.1. Overview of molybdenite samples analysed in this study

Deposit	DH	Interval [m]	Rock type	Au-grade
Redcap	950	472.05-472.16	Clinopyroxene skarn	n/a*
Redcap	955	405.21-405.32	Molybdenite -quartz vein	2.58 g/t
Mungana	890W6	787.56-787.8	Andradite-wollastonite skarn	2.72 g/t
Red Dome	982	1013.72-1013.81	Clinopyroxene skarn	n/a*
Red Dome	983	880.20-880.43	Gold-molybdenite- quartz vein	92.8 g/t

* not analysed

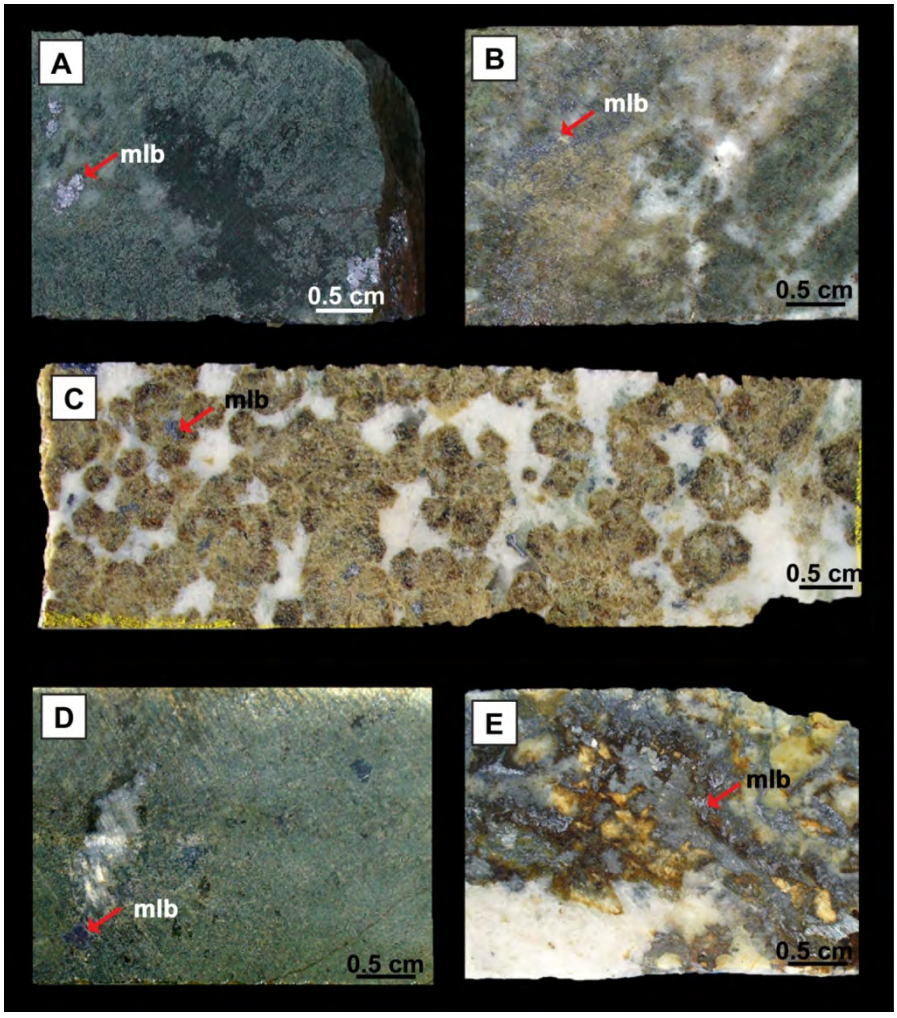

Plate 5.3.1. Photographs of molybdenite (mlb) bearing samples analysed in this study; **A**: clinopyroxene skarn from Redcap (950); **B**: molybdenite carrying quartz vein in clinopyroxene skarn from Redcap (955); **C**: andradite-wollastonite skarn from Mungana (890W6); **D**: clinopyroxene skarn from Red Dome (982); **E**: mineralised quartz vein in sericite altered quartz-feldspar porphyry from Red Dome (983).

The Re-Os analysis were carried out at the RSES, ANU (Canberra) by Marc Norman and only a brief summary of the methodology used is outlined here, while details for this study can be found in Norman et al. (2004) or in a more general way in Reisberg & Meisel (2002).

The molybdenite samples were crushed and processed by conventional heavy liquid techniques and hand picked to high purity (~ 98 %). The samples were then spiked with ^{185}Re and normal Os isotopic solutions and dissolved in reverse aqua regia, sealed in a carius tube and heated for 12 hours at ~240 °C. After cooling the oxidised volatile Os was purged directly into a Finnigan Neptune MC-ICP-MS while the rhenium (remains in the residual solution) was separated by anion exchange chromatography and was analysed by ICP-MS. Data were corrected for mass fractionation. With each sample batch standards (HLP5: Huanglongpu-a carbonatite hosted Mo-Pb deposit) were analysed as well to check for complete sample digestion and spike equilibration. They yield an age of 221.1 ± 0.8 Ma for the first run (samples 950 & 982) and 220.9 ± 1.1 Ma for the second batch (955, 983, 890W6 and 950-rerun) which lies within error of the accepted age of 221.5 ± 0.3 Ma for HLP-5 with (Stein et al. 1997).

Furthermore molybdenite samples from all three deposits were selected to investigate the timing of the mineralisation as well as to obtain an indirect age of the skarns, which are partly associated with molybdenite.

5.3.2. Results

The molybdenite samples of the skarn samples 950 and 982 yielded an age of 315.1 ± 13.1 Ma and 314.9 ± 1.0 Ma, respectively. While the result from 982 gave an acceptable error, the first run of sample 950 was considered unreliable due to possible incomplete spike sample equilibration (per. comm. M. Norman) and it was decided to repeat the analysis with the second batch of samples, where the sample yielded similar Re and Os concentrations (see table 5.3.2) as in the previous run, but the error within the concentrations was reduced.

Table 5.3.2. Re-Os isotope data for molybdenite from the Redcap, Mungana and Red Dome deposit

Sample	Description	sample mass [mg]	Re [ppm]	^{187}Os [ppb]	Age ± 1 σ [Ma]
Redcap					
950_1*	cpx-skarn	254.7	9.26 ± 0.03	30.64 ± 117.99	315.1 ± 13.1
950-2	cpx-skarn	99.8	10.00 ± 0.23	30.92 ± 0.33	294.5 ± 1.0
955	qtz-vein	51.2	53.12 ± 1.35	166.47 ± 0.65	298 ± 1.0
Mungana					
890W6	grt-wo-skarn	194.1	0.39 ± 0.004	1.35 ± 0.07	335.6 ± 1.2
Red Dome					
982	cpx-skarn	150.1	1.72 ± 0.01	5.69 ± 0.15	314.9 ± 1.0
983	qtz-vein	202.5	0.76 ± 0.08	2.61 ± 0.23	327.2 ± 1.6

* considered as unreliable due to possible incomplete spike sample equilibration (per. comm. M. Norman)

In the second run sample 950 yielded nearly the same Re and but this time the error of the analysis was only 1 Ma. The other samples yielded an age of 298 ± 1.0 Ma for the gold hosting quartz vein at Redcap (sample 955), 327.2 ± 1.6 Ma for the gold hosting quartz vein from Red Dome (983) and 335.6 ± 1.2 Ma for the gold bearing skarn sample from Mungana.

In addition to ages, the Re and Os concentrations determined in this study were plotted against each other (Fig. 5.3.2.) and compared to Re and Os values of a porphyry Cu-Au deposit of the Ertsberg district of Indonesia (Mathur et al. 2005), a porphyry Cu deposit of the Cananea district, Mexico (Valencia et al. 2006), a porphyry Mo deposit of Endako, Canada (Selby & Creaser 2001), a porphyry Cu-Mo deposit of the Collahuasi district, Chile (Masterman et al. 2004) and two IRG deposits of the Tintina Gold Belt, Alaska (Selby et al. 2002).

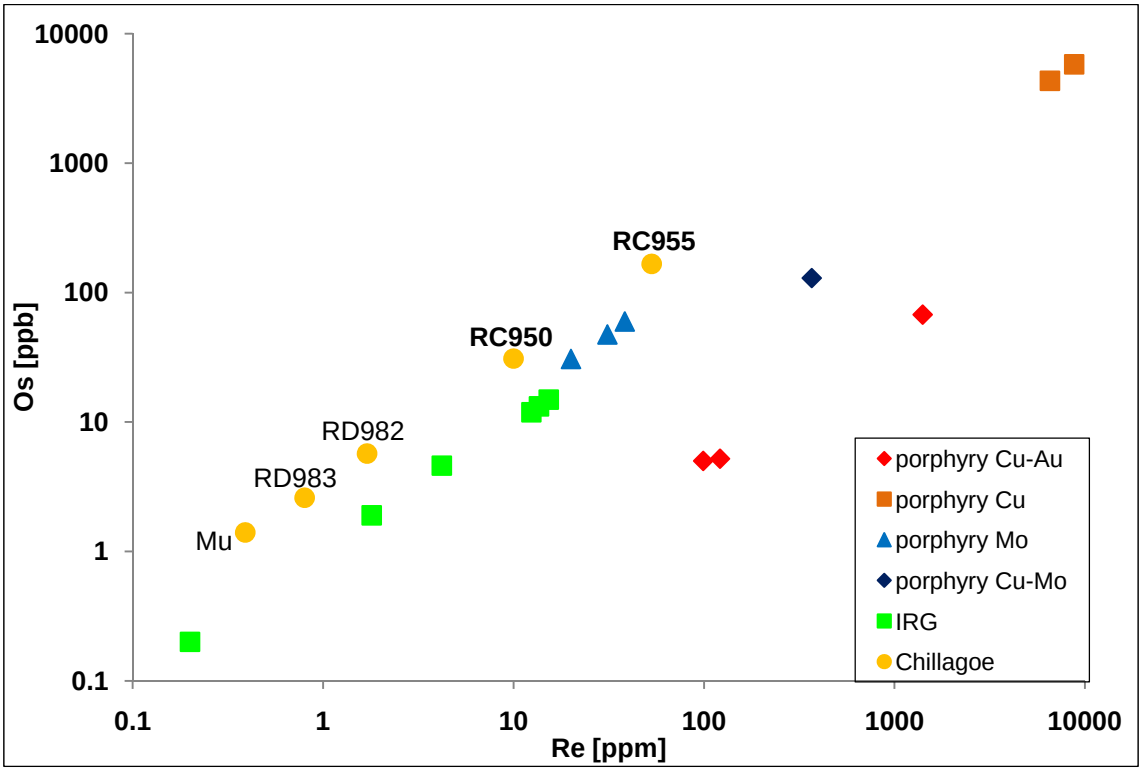

Figure 5.3.2. Log-plot of Re versus Os concentrations of molybdenite from different porphyry deposit styles and intrusion-related gold deposits (IRG) and samples from Redcap, Red Dome and Mungana; other data taken from Mathur et al. 2005 (porphyry Cu-Au), Valencia et al. 2006 (porphyry Cu), Selby & Creaser 2001 (porphyry Mo), Masterman et al. 2004 (Porphyry Cu-Mo) and from Selby et al. 2002 (IRG).

Molybdenite samples from Red Dome (982 & 983) and Mungana (890W6) plot adjacent to molybdenite samples from intrusion-related gold deposits, although the Os concentrations of the Chillagoe samples are always higher than the values determined by Selby et al. (2002) which could indicate that these Chillagoe samples have experienced minor Re loss as suggested earlier in this section. One molybdenite from Redcap (950) plots at the border of IRG and porphyry Mo

while the second molybdenite sample from Redcap (955) shows Re and Os concentrations well above the values of the porphyry Mo deposit of Selby & Creaser (2001). The difference between the Re and Os concentrations of the molybdenite samples from the Redcap deposit to the ones determined for the Red Dome and Mungana deposit could be related to a disturbance of the isotope system resulting in loss of either Re or Os or could indicate that the metals at Redcap were derived from a different magmatic source than at the other two deposits with the latter one being investigated through Hf isotope studies of zircons in the next chapter.

5.4. Summary

Zircons from the two Redcap dacites (949 & 952W1) and the Belgravia granodiorite (BE-1) have very similar shapes, sizes and CL structures. Featureless, dark cores are widespread and rarely represent inherited cores of Mesoproterozoic age (twice identified). Another common feature is oscillatory zoning mainly occurring at the rim. Intensive convolute zoning is rare, but a weak form as bright CL “flame structure” occurs in some places. These weak convolute zones as well as zones with very bright CL are almost always younger (~290-300 Ma) than featureless cores or oscillatory zoned areas with darker CL (>300-315 Ma).

Based on the ages of the Belgravia granodiorite and the two Redcap dacite samples it is possible that these two igneous units are approximately coeval (Fig. 5.4), at least within the uncertainty limits of the techniques employed here, which is common within the Chillagoe district (Garrad & Bultitude 1999). Bultitude et al. (1993a) suggested, however, that the Redcap dacite must be older than the Belgravia granodiorite as the latter truncates the Redcap dacite and Redcap Fault. One way to explain both observations is that parts of the Redcap dacite, which is divided into four subunits (Department of Natural Resource and Mines-Queensland 2003) are older than the Belgravia granodiorite (also divided into two subunits, Department of Natural Resource and Mines-Queensland 2003), while other parts, investigated in this study are coeval. A supporting argument for the hypothesis from Bultitude et al. (1993a) can be found within the zircon population from sample 952W1 where a small group of older grains (321 Ma) was identified. Regarding the possible coeval nature of the two igneous unit, as suggested in general for the Chillagoe district by Garrad & Bultitude (1999) further investigations are necessary and were conducted through trace element studies of zircons from these rocks (see chapter 6).

The Re-Os isotope data from two molybdenite samples from the Redcap yielded some potentially controversial results (Tab. 5.4., Fig. 5.4.). While the sample from the gold-bearing quartz vein yielded 299 Ma, which lies within the error of the younger zircon population identified within the Belgravia granodiorite, the other sample from molybdenite bearing

clinopyroxene skarn (955) yielded 315 Ma in the first dating round and 295 Ma in the second dating round. The younger result for this sample would well agree with the other molybdenite sample, but as sample 955 is nearly identical to sample 982 from Red Dome and from the same paragenetic sequence, the older age seems to be more realistic.

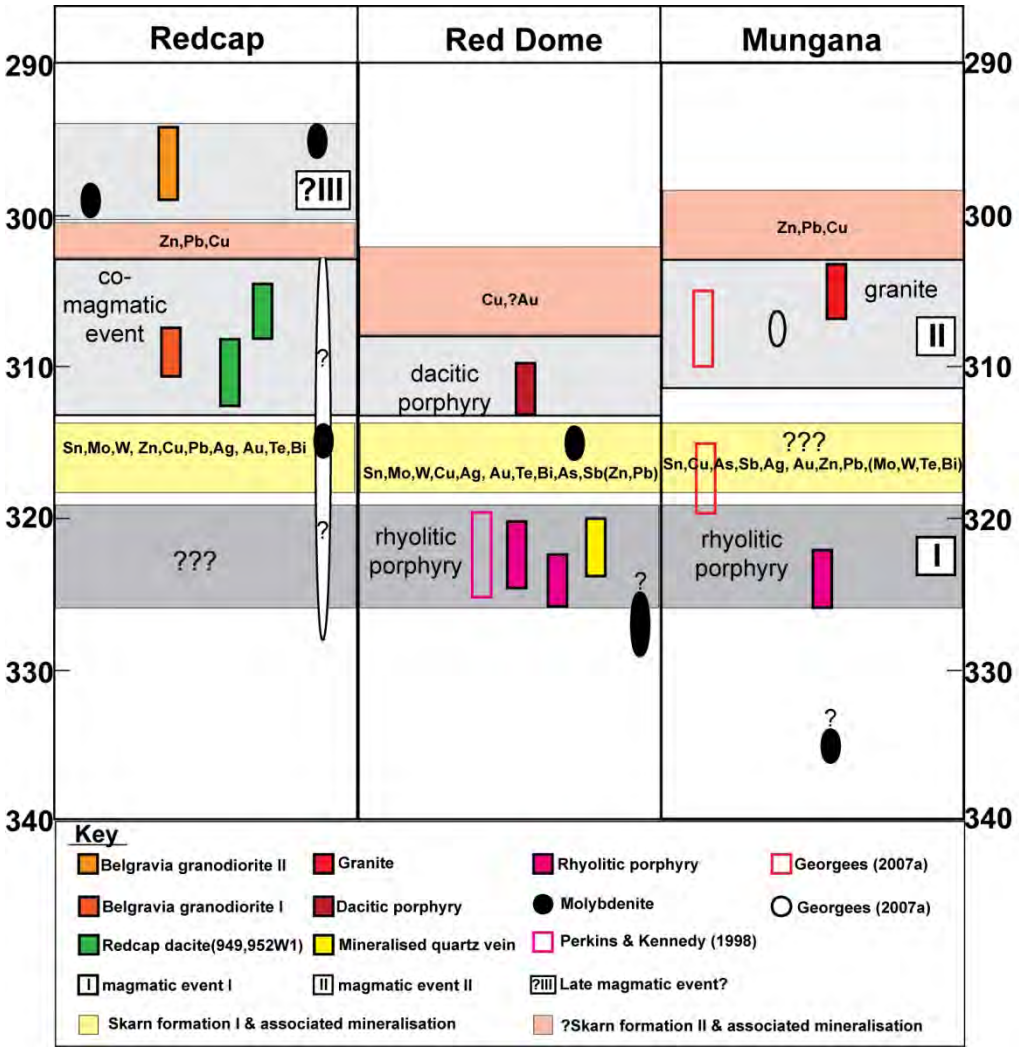

Figure 5.4. Geochronological overview of single magmatic and mineralising events for the Redcap, Red Dome and Mungana deposits and their possible correlation.

One reason for the age difference of 20 Ma could be an unidentified analytical problem. Another possible explanation is that the Re-Os isotope system was disturbed through a hydrothermal fluid resulting in Re-loss of the molybdenite and causing an age that is too young. Stein et al. (2001) deny that hydrothermal alteration can affect the Re-Os isotope system, but studies from Suzuki et al. (2001) and Zhang et al. (2012) have shown that a halogen-rich aqueous fluid can influence the Re-Os decay system. An argument for the presence of such a fluid can be found within the younger zircon population of the Belgravia granodiorite.

Table 5.4. Summary of geochronological data from Redcap, Mungana and Red Dome

Sample ID	Deposit	Rock type	Method	Age range [Ma]	Weighted Mean [Ma]	Inherited core [Ma]
949	Redcap	Dacite	U-Pb	292-319	310 ± 2* (n= 21/25)	1 grain: 1516 ± 20
950	Redcap	Clinopyroxene skarn	Re-Os	-----	a) 315 ± 13* b) 295 ± 1*	-----
952W1	Redcap	Dacite	U-Pb	296-321	306 ± 2* (n=20/25)	-----
955	Redcap	Molybdenite -quartz vein	Re-Os	-----	299 ± 1*	-----
BE-1	Redcap	Granodiorite	U-Pb	276-316	a) 309 ± 2* (n=13/25) b) 297 ± 2* (n=5/25)	1 grain: 1523 ± 13
883W2	Mungana	Rhyolitic porphyry	U-Pb	318-335	324 ± 2* (n=19/20)	-----
883W3	Mungana	Granite	U-Pb	296-315	305 ± 2* (n=20/20)	-----
890W6	Mungana	Andradite-wollastonite skarn	Re-Os	-----	335 ± 1*	-----
936	Red Dome	Quartz-feldspar porphyry	U-Pb	304-331	322 ± 2* (n=16/20)	-----
982	Red Dome	Clinopyroxene skarn	Re-Os	-----	315 ±1*	-----
983	Red Dome	Gold-molybdenite- quartz vein	U-Pb	297-338	322 ± 2* (n=11/18)	-----
983	Red Dome	Gold-molybdenite- quartz vein	Re-Os	-----	327 ± 2*	-----
984	Red Dome	Quartz-feldspar porphyry	U-Pb	303-333	324 ± 2* (n=15/20)	-----
995	Red Dome	Dacitic porphyry	U-Pb	299-321	311 ± 2* (n=15/20)	-----

*Uncertainties for U-Pb isotope ages 2σ and for Re-Os isotope ages 1 σ

Although zircons are considered to be very robust (Finch & Hanchar 2003), a fluorine rich aqueous fluid is able to alter zircon (Valero et al. 1998; Rasmussen 2005). Zircons from the younger Belgravia granodiorite sample all have bright CL and patchy, “flame-like” structures, which, after Geisler et al. (2007) indicate an alteration of the zircons. These features were also present within the zircon population from Redcap dacite. One way to overcome the problems with the controversial molybdenite ages is to investigate more samples to get a better overview about Re-Os concentrations and distributions within a sample and conduct geochemical investigations like trace element or sulphur isotope studies prior to age dating. This will help to check for heterogeneity within a single sample, as observed by Barkov et al. (2000) and Voundouris et al. (2009), but also to confirm that based on macroscopic features distinguishable samples really represent different generations of molybdenite.

Zircons of two igneous rocks from the Mungana deposit are smaller than zircons from the Redcap deposit with averages of 110 and 150 µm for the porphyry sample (883W2) and granite (883W3). Subhedral to euhedral prismatic shapes are dominant with only zircons from the granite rarely having a needle shape. CL structures of the porphyry sample are in general dark and very weak developed. Featureless cores overgrown by weak oscillatory zones are the most common structures. Very weak convolute zoning, represented by “flame-like” textures were only observed in two cases. Zircons from the granite on the other hand have well developed internal structures, which are similar to the ones observed in zircons from the Redcap deposit. Dark, featureless cores are commonly overgrown by oscillatory zoning, in the granite, and bright CL zones and weak convolute zoning (flame-like texture) also occur.

A previously dated porphyry sample from the Mungana deposits yielded a SHRIMP U-Pb (zircon) age of 317.3 ± 2.3 Ma (Georgees 2007a). This SHRIMP result is 2.1% younger than the age of 324.0 ± 1.9 Ma determined by LA-ICP-MS in this study (Fig. 5.4.). As the porphyry sample investigated in this study was not only taken from the same drill hole as the one analysed by Georgees (2007a), but also adjacent to the sample of Georgees, the relative age difference of the porphyry is unlikely to be related to the sample, and it is more probable that the age difference is caused by the two analytical techniques, as also observed by other authors (e.g. Ballard et al. 2001), but could also be related to the use of different standards or calculating methods, with such information not being available for the age data of Georgees (2007a).

Re-Os isotope dating of molybdenite from Mungana provided controversial results. A previous investigated sample of molybdenite hosted in a clinopyroxene bearing andradite-wollastonite skarn yielded an age of 307.1 ± 1.3 Ma (Georgees 2007a), identical to the age of the Mungana granite (307.1 ± 2.5 Ma), but the granite appears to be unrelated to any mineralisation (Georgees

2007a). A second molybdenite sample from a nearly identical rock type (andradite-wollastonite skarn with traces of clinopyroxene) from a different drill hole was dated in this study and yielded an age of 335.6 ± 1.2 Ma (Fig. 5.4.). As no event of such age is known in the Chillagoe district (pers. com. C. Georgees) the old age as well as the age difference of nearly 29 Ma between the two dated molybdenite samples is interesting. The Mungana deposit experienced supergene enrichment and it is possible that a fluid, likely of halogen-rich aqueous composition, may have influenced the Re-Os concentration of the molybdenite. Based on work from McCandless et al. (1993) erroneous ages can be caused by the loss of some rhenium from the system after it has decayed to ^{187}Os, while the osmium in the system remains stable. An indicator that the molybdenite sample dated in this study has experienced such a Re-loss is the very low Re concentration of 0.39 ppm, which is one to two magnitudes lower than the Re concentration measured in samples from the Redcap deposit. Like the Redcap deposit, further studies of molybdenite are required to resolve the existing problem with the two controversial Re-Os ages at Mungana.

Zircons from two quartz-feldspar porphyry samples (936 & 984) from Red Dome are of similar size, shape and CL structures and nearly identical to the ones observed for the rhyolitic porphyry of Mungana. The two samples yielded ages of 322 ± 2 Ma and 324 ± 2, respectively (Fig. 5.4.). Both ages agree well with the existing SHRIMP U-Pb zircon age of 322.4 ± 2.8 Ma reported by Perkins & Kennedy (1998).

Zircon grains from the dacitic porphyry (995) are on average 50 µm larger than zircons from the two quartz-feldspar porphyries, but exhibit almost identical CL structures with featureless, homogenous cores being the most common ones. Although no intrusive relationship is evident in drill core, the U-Pb age of 311 ± 2 Ma indicates that the dacitic porphyry post-dates the quartz-feldspar porphyry and therefore supports the argument of previous workers like Torrey (1986), Ewers & Sun (1988a) and Nethery & Barr (1998), who all suggested that a second, younger porphyry body exists at Red Dome. Whether a genetic relationship to the older porphyry exists will be investigated in this study and the outcome of this topic can be found in chapter 6.

In addition to the two porphyry types, zircons from a mineralised quartz vein, which is hosted in a fluorite bearing, sericite altered, quartz-feldspar porphyry were investigated. Zircons from this sample are 25 to 50 % smaller than zircons from other samples investigated at Red Dome and are on average 75 µm in size. Two major shapes occur; these being roughly prismatic and subrounded. All grains show weak to very weak internal structures with sector zoning being the most common one. The rounded shape of some zircons, as well their occurrence in trails within

the mineralised quartz vein may indicate a hydrothermal origin for some of the zircons, but neither their occurrence nor their morphology alone can be used to determine their origin (Hoskin & Schaltegger 2003). Analyses from an epoxy grain mount as well as two polished thin section yielded an age of 322 ± 2 Ma. This age lies within the uncertainty of the other ages yielded for the quartz-feldspar porphyry (Fig. 5.4.), but the presence of fluorite in the sample could indicate that a least some of zircons of the mineralised quartz vein may be of hydrothermal origin, as a fluorine-rich fluid has the ability to mobilise zirconium (Valero et al. 1998; Rasmussen 2005), while other zircons could have been incorporated from the host rock (quartz-feldspar porphyry) retaining their original U-Pb signature. Distinguishing whether zircons of this sample are magmatic or hydrothermal can be done with trace element studies, as presented in the next chapter.

Two molybdenite samples (982 & 983) from the Red Dome deposit were investigated. While sample 982 is hosted in clinopyroxene skarn, sample 983 is from the mineralised quartz-vein. Sample 982 yielded a Re-Os age of 315 ± 1 Ma, suggesting that skarn formation and molybdenite mineralisation are related to the quartz-feldspar porphyry. The other molybdenite sample from Red Dome yielded an age of 327 ± 2 Ma. This age is slightly older than the quartz-feldspar porphyry as well as the age determined from zircons of the same sample (Fig. 5.4.). One explanation for the age difference can be explained by Re-loss after it has decayed from ^{187}Os through an aqueous, likely halogen rich fluid. An evidence for the presence of such a fluid can be found in the abundance of fluorite within the vein and quartz-feldspar porphyry. A second argument can be the low Re concentration (0.76 ppm) of the sample which is one order of magnitude lower than the Re-concentrations from the other investigated sample (982).

Comparisons of Re-Os concentration from molybdenite samples from the Chillagoe district with Re-Os concentration of other molybdenite bearing porphyry and IRG deposits around the world indicate that molybdenite from the Chillagoe district correlates well with molybdenite from an IRG system. Low Re-Os concentrations are typical for this style and also indicate that the molybdenite originated from an evolved, crustal source (Stein et al. 2001) which is common for IRGs (Thompson et al. 1999; Lang & Baker 2001; Baker et al. 2005). However, the major problem with using Re and Os concentration to distinguish the deposit style in which the molybdenite formed remains that the amount of either Re or Os loss cannot be estimated, and therefore making it unsuitable as a stand alone discrimination tool.

From a regional perspective, two major igneous events were identified (I & II, Fig. 5.4) in the Chillagoe district with each of the events being followed by skarn formation, although based on petrographical studies it is not possible to assign a certain skarn type to a specific magmatic

event. An older event (I) is represented in form of rhyolitic porphyry which can be geochemically (e.g. Ewers & Sun 1988a) and geochronologically assigned to the O'Briens Creek supersuite. At the Redcap deposit such a porphyry body has yet to be discovered, but the similarity between the paragenetic sequences (chapter 3) from all deposits as well as very similar geochemical composition of Sn-bearing garnets and sphalerite at Redcap and Mungana (chapter 4) suggest that an O'Briens Creek supersuite event must have occurred there.

The second magmatic event is represented at all three deposits and occurred between 312 and 305 Ma. While at Redcap the Redcap dacite and Belgravia granodiorite can be assigned to the Almaden supersuite based on their geochemical characteristics, at Mungana a granite was emplaced (geochemistry indicates either the Ootann or Almaden supersuite) and at Red Dome a second porphyry, which can be assigned to either the O'Briens Creek or Ootann supersuite, although far more geochemistry is need to make the assignment to a specific supersuite. Not only the different igneous rock types, but also the relationship to different supersuites may be responsible for the differences between the deposits. At Mungana no mineralisation was introduced within the second event, although a remobilisation may have occurred, but only of the base metals and not of the gold (no secondary gold mineralisation was identified, chapter 4). At Red Dome the dacitic porphyry could have remobilised gold, which was originally deposited within the first igneous event. At Redcap the second event probably also did not introduce any new mineralisation, but caused a remobilisation and enrichment of the base metals. The late event at around 295 Ma, if it really occurred may have been responsible for remobilisation of the gold, but whether this late event represents a low temperature part of the second igneous event or is related to another yet undiscovered intrusion remains unknown.

Chapter 6: Trace element chemistry, Ti-in-zircon thermometry and Hf isotope studies of zircons from igneous rocks of the Redcap, Mungana and Red Dome deposits

6.1. Introduction

Zircon is a widespread accessory mineral in many felsic to ultramafic igneous rocks (e.g. Heaman et al. 1990; Belousova et al. 2002; Hoskin & Schaltegger 2003). The mineral also occurs in metamorphic and sedimentary rocks (e.g. Finch & Hanchar 2003; Hoskin & Schaltegger 2003) and additionally zircon has been reported to be of hydrothermal origin (e.g. Hoskin & Schaltegger 2003; Hoskin 2005; Schaltegger 2007).

Due to the mineral's physico-chemical robustness and high closure temperature for Pb (Lee et al. 2001) zircon is able to preserve its isotopic and chemical information (Finch & Hanchar 2003). Because of these properties the mineral is commonly used for U-Pb geochronological studies (Hoskin & Schaltegger 2003), but in the last decades there has been an increasing number of studies in which the trace element and isotope composition of zircon were used for a different purpose: identification of crystallisation environment, magmatic evolution and source rocks (e.g. Heaman et al. 1990; Hoskin & Ireland 2000; Belousova et al. 2002; Hoskin & Schaltegger 2003; Kinny & Maas 2003).

Zircon has the ability to incorporate a significant number of trace elements (20-25) by simple or coupled substitution in its structure (Hoskin & Schaltegger 2003). The majority of trace elements only reach concentrations of ppm-level (Kinny & Maas 2003), while concentrations of Hf can be up to percent level (typically 0.5-2.0 wt.-% HfO_2, Hoskin & Schaltegger 2003). To reveal the conditions under which the zircon and its host rock have formed, different trace elements, their ratios or isotopes are combined. For example, thorium-uranium ratios can be used to distinguish between magmatic and metamorphic zircons (Hoskin & Schaltegger 2003) and additionally the ratio can be used together with Zr/Hf ratios to identify a compositional change of the crystallisation environment (e.g. fractionation) (Linnen & Keppler 2002; Hoskin & Schaltegger 2003; Claiborne et al. 2006; Bolhar et al. 2008). Additionally, chondrite-normalised REE patterns are useful to distinguish mantle derived zircons from zircons formed in a crustal environment (Heaman et al. 1990, Hoskin & Ireland 2000; Hoskin & Schaltegger 2003), while the values of the Ce and Eu anomalies (expressed as Ce/Ce* and Eu/Eu*) provide information of the oxygen fugacity of the magma (Ballard et al. 2002; Hoskin & Schaltegger 2003). In addition, Ti concentrations in zircon are used to estimate the crystallisation

temperature (Watson et al. 2006; Ferry & Watson 2007; Fu et al. 2008) whereas Hf-isotope studies are useful to determine the crustal evolution and source (Vervoort et al. 1996; Griffin et al. 2002; Kinny & Maas 2003 and many more).

In this study trace elements (Th-U, Zr-Hf, Y, Ti & REE) and Hf isotope studies of zircons from the Redcap, Red Dome and Mungana deposit were combined to reveal the magmatic history and nature of source rocks of the igneous rocks of the Chillagoe district. The results are presented in the following sections and the data are listed in appendices 12-13 and 15.

6.2. U and Th concentrations

Uranium and thorium get incorporated into the zircon lattice by simple substitution of Zr^{4+} (Ahrens 1965; Ahrens et al. 1967), because both elements have ionic radii (U: 1.0 Å & Th: 1.05 Å) that are similar to zirconium (0.84 Å), although U is four times more compatible than Th (Mahood & Hildreth 1983; Hoskin & Schaltegger 2003). The element concentrations as well as their ratios can be used for two different purposes: a) to observe changes in magmatic composition (Ahrens et al. 1967; Heaman et al. 1990; Belousova et al. 2002; Hoskin & Schaltegger 2003; Bolhar et al. 2008) and b) to distinguish between magmatic and metamorphic zircons (Ahrens et al. 1967; Heaman et al. 1990; Hoskin & Schaltegger 2003; Bolhar et al. 2008). Ahrens et al. (1967) investigated zircons from kimberlite and granite samples and observed that the U and Th concentrations of the zircons are different. Zircons from kimberlites had incorporated very low amounts of Th and U (2-7 & 7-28 ppm), while zircons from granitic samples showed high concentrations (~40-4700 ppm). They postulated that zircons with low Th and U concentrations were derived from a primitive source, while zircons with high U and Th abundance originated from a more evolved source. The hypothesis of Ahrens et al. (1967) was confirmed several times by later workers. Heaman et al. (1990) and Belousova et al. (2002) also observed that mantle-derived zircons have low Th and U concentrations, while zircons formed in a highly fractionated crystal environment have Th and U concentrations which are several orders of magnitude higher than those of kimberlitic zircons. Additionally, Bolhar et al. (2008) observed that with increasing differentiation the Th/U ratio decreases as well as that the ratio can correlate with the crystallisation temperature.

The second use of thorium and uranium is in form of their ratio to distinguish between magmatic and metamorphic zircons. The typical values for the Th/U ratio for zircon in the majority of igneous rocks is between 0.1 and 1 (Belousova et al. 2002) with general values of ≥ 0.5 (Hoskin & Scherer 2003), while metamorphic zircons can have very low ratios (Ahrens et

al. 1967; Heaman et al. 1990), which are on average 0.01 or even lower (Hoskin & Schaltegger 2003).

Zircons from igneous rocks of the Redcap, Red Dome and Mungana deposits are all supposed to be of magmatic origin as suggested by CL microstructures and therefore the U and Th concentrations as well as the Th/U ratio will be used in this study to examine whether any changes in crystallisation environment of the zircons can be observed. Thorium and uranium were determined during the U-Pb isotope studies (see chapter 5.2.1.) and the concentration calculated relative to the NIST 610 standard glass, assuming a stoichiometric SiO_2 concentration in zircon of 33 wt.-%. A summary of the Th and U concentrations and Th/U ratio for zircons from igneous rocks of the Redcap, Red Dome and Mungana is provided in table 6.2., while the whole data set is listed in appendix 13.

Table 6.2. Th and U concentrations of zircons from different igneous rocks of the Redcap, Red Dome and Mungana deposits

Deposit	Sample ID	Rock type	Age ± 2σ [Ma]	Th [ppm]	U [ppm]	Th/U
Redcap	949	Dacite	310 ± 2	41-294	91-468	0.2-0.6
Redcap	952W1	Dacite	306 ± 2	46-245	133-581	0.3-0.6
Redcap	BE-1	Granodiorite	309 ± 2 297 ± 2	42-357 67-222	69-549 90-521	0.5-0.9 0.4-0.9
Redcap	----	Inherited grains (n=2)	Ø1520 ± 17	53-117	176-326	0.3-0.4
Mungana	883W2	Rhyolitic porphyry	324.0 ± 1.9	287-1060	357-1163	0.8-1.4
Mungana	883W3	Granite	305.0 ± 1.8	68-381	111-720	0.3-0.9
Red Dome	936	Quartz-feldspar porphyry	322.4 ± 2.2	383-1202	497-1358	0.7-1.3
Red Dome	984	Quartz-feldspar porphyry	324.1 ± 1.7	229-1130	303-804	0.8-1.7
Red Dome	983	Mineralised quartz vein	321.9 ± 1.9	902-3661	985-2755	0.9-1.4
Red Dome	995	Dacitic porphyry	311.4 ± 1.7	201-1476	302-778	0.8-1.9

6.2.1. Redcap

The two Redcap dacite samples (949 & 952W1) have very similar Th and U concentrations as well as Th/U ratios and are therefore described together (Tab. 6.2.; Fig. 6.2.1.). Their Th concentrations range between 41 to 294 ppm Th and their U concentrations between 91 to 581 ppm yielding Th/U ratios of 0.2 to 0.6, respectively. Neither the small zircon population of 321 Ma from 952W1 nor the zircon population <301 Ma from 949 do distinguish based on their concentration or ratio from the other zircon grains from the two Redcap dacites.

Zircon grains from the Belgravia granodiorite were divided based on CL microstructures and age in an older (P-I) and younger population (P-II) (see chapter 5). Group P-I has Th and U concentrations of 42 to 357 ppm and 69 to 549 ppm which are within the range of the concentrations determined for the Redcap dacite samples, although the Th/U ratios with values between 0.5 and 0.9 are almost always higher than the ratios determined for the Redcap dacite samples (Fig. 6.2.1.). The second zircon population of the Belgravia granodiorite (P-II) yielded also very similar Th and U concentrations as other zircon grains from the Redcap deposit, but their Th/U ratios are with values of 0.4 to 0.9 very similar to the ratios of the other Belgravia granodiorite zircon group.

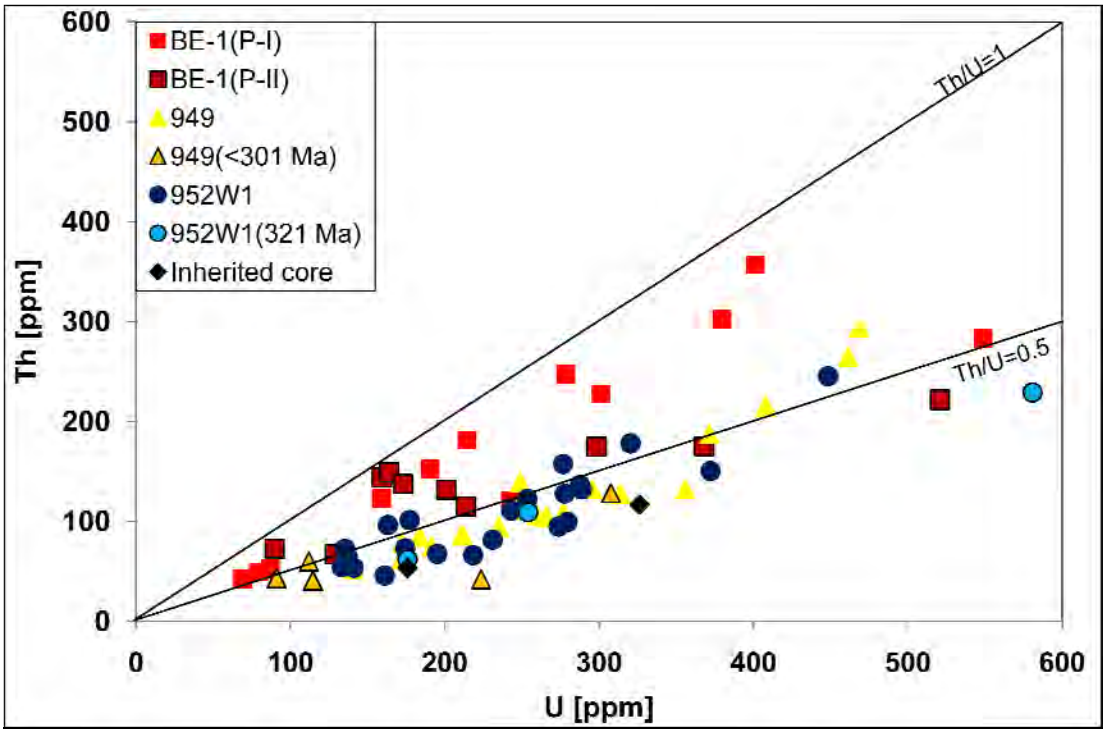

Figure 6.2.1. Plot of Th against U concentrations of zircons from igneous rocks of the Redcap deposit; 949 & 952W1: Redcap dacite, BE-1(P-1): old zircon group of the Belgravia granodiorite, BE-1(P-II): younger zircon group of the Belgravia granodiorite, 2 inherited cores.

Two Mesoproterozoic cores were identified in a zircon grain from the Belgravia granodiorite (BE-1) and in a zircon grain from one Redcap dacite (949). Their Th and U concentrations fall within the range of concentrations determined for the Redcap dacite samples and are 53-117 ppm Th and 176-326 ppm U, respectively yielding Th/U ratios of 0.3 to 0.4.

6.2.2. Mungana

Zircons from the porphyry sample (883W2) from Mungana have Th concentrations which range between 287 to 1060 ppm, while U concentrations are between 357 to 1163 ppm (Fig. 6.2.2.)

yielding Th/U ratios of 0.8 to 1.4 indicating that these zircons crystallised in an environment where other Th and U bearing phases like e.g. monazite or allanite were absent.

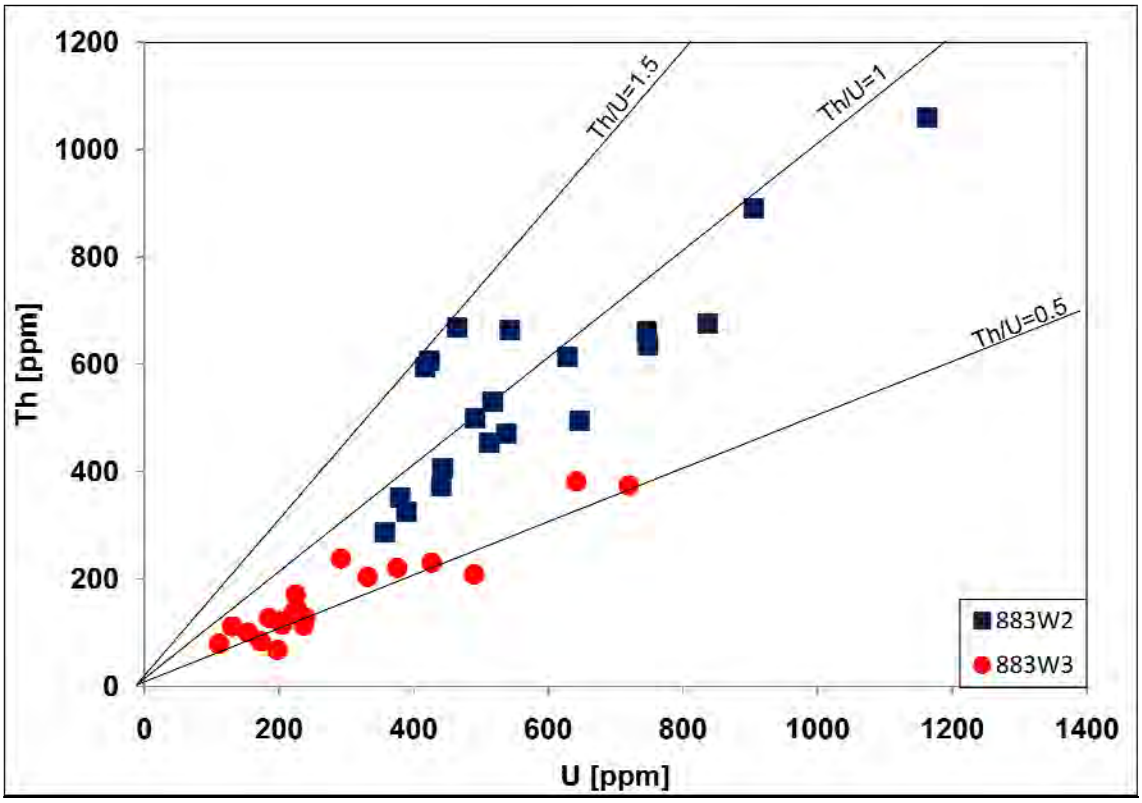

Figure 6.2.2. Plot of Th against U concentrations of zircons from igneous rocks of the Mungana deposit; 883W2: porphyry, 883W3: granite.

Thorium and U concentrations of the granite sample (883W3) range from 68 to 381 ppm and from 111 to 720 ppm, respectively, being lower than the concentrations obtained for the porphyry sample, but within the rang of the ones already described for the Belgravia granodiorite. The Th/U ratios, which range from 0.3 to 0.9, are also lower than the ratios determined for the porphyry, but again very similar to the ones obtained for the Belgravia granodiorite zircon groups. Considering that the Th and U concentrations can be used to identify a compositional change of the crystallisation environment (Ahrens et al. 1967; Heaman et al. 1990; Belousova et al. 2002), it seems that the Mungana porphyry could have been derived from a more evolved source than the Mungana granite.

6.2.3. Red Dome

Zircon grains from one of the quartz-feldspar porphyries (936) from Red Dome yielded Th concentrations of 383 to 1202 ppm and similar concentrations of U ranging from 497 to 1358 ppm yielding Th/U ratios of 0.7 to 1.3 (Fig. 6.2.3.). The second quartz-feldspar porphyry sample of Red Dome (984) shows on average lower concentrations of Th and U (~200 ppm) than

sample 936, but very similar Th and U content to the Mungana porphyry with concentrations of sample 984 ranging between 229 to 1130 ppm Th and 303 to 804 ppm U, respectively (Fig. 6.2.3.). Their Th/U ratios range from 0.8 to 1.7 with three grains exceeding a ratio of 1.5.

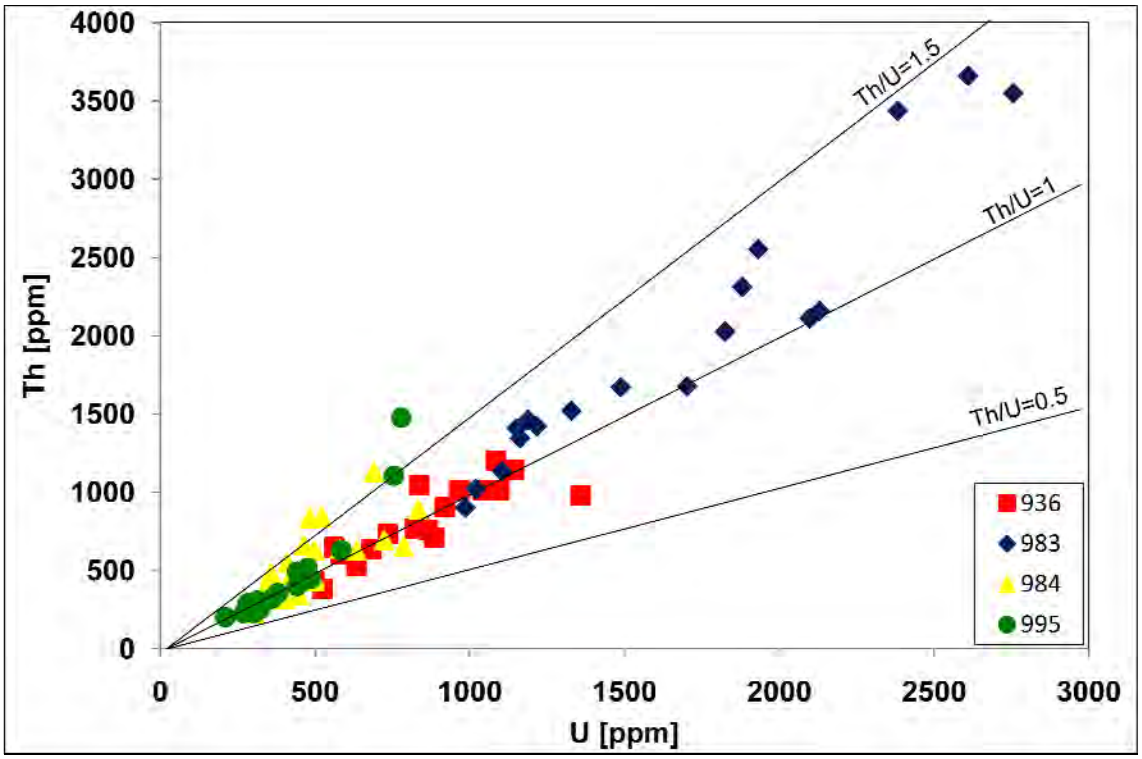

Figure 6.2.3. Plot of Th against U concentrations of zircons from igneous rocks of the Red Dome deposit; 936 & 984: quartz-feldspar porphyries, 995: dacitic porphyry, 983: mineralised quartz vein.

Zircons from the dacitic porphyry (995) show lower Th and U contents than the previously described quartz-feldspar porphyry (984) ranging from 201 to 1476 ppm and 302 to 778 ppm respectively, but their ratios being similar to the ones obtained for the other porphyry samples, ranging form 0.8 to 1.9, with only two values exceeding a ratio of 1.5. The last sample investigated from the Red Dome deposit is a mineralised quartz vein (983). Zircons from this sample have the highest Th and U concentrations of all zircons analysed in this study. Thorium content ranges between 902 to 3661 ppm and U values are between 985 to 2755 ppm, while the Th/U ratios are with values of 0.9 to 1.4 similar to ratios obtained for the other samples of the Red Dome deposit.

In general a trend of decreasing Th and U concentrations from sample 983 via 936 and 984 to 995 can be observed, although minor overlapping of individual samples occur, suggesting a decrease of the fractionation degree from 936 via 984 to 995, with the less evolved sample (995) also being the youngest.

6.3. Zr, Hf and Y concentrations

Hafnium and yttrium are some of the only trace elements in zircon which can have concentrations of percent-level. Typical HfO_2 concentrations in zircons range from 0.5 to 2.0 wt.-% (Hoskin & Schaltegger 2003), while Y commonly occurs with concentration between 0.1 to 1 wt.-% (Hoskin & Schaltegger 2003), although much higher values are reported for both elements in hydrothermal zircons with concentrations of 3 to 8 wt.-% HfO_2 and 1.3 to 2.1 wt.-% Y_2O_3, respectively (Hoskin 2005). Like thorium and uranium, Hf and Y concentrations and ratios can be used to monitor changes in the crystallisation environment (Belousova et al. 2002; Linnen & Keppler 2002; Claiborne et al. 2006; Bolhar et al. 2008). Ahrens et al. (1967) observed that mantle derived zircons had in general one order of magnitude lower Y concentrations than zircons which originated from a more evolved magma, while the Hf/Y ratio of kimberlitic and granitic zircons behave the opposite, i.e. that the ratio decreases from mantle derived zircons to zircons that form in the crustal environment (Belousova et al. 2002). The same trend can be observed for Hf concentrations and Zr/Hf ratios. Increasing magmatic fractionation raises the Hf concentrations lowers the Zr/Hf ratios (Linnen & Keppler 2002; Hoskin & Schaltegger 2003; Claiborne et al. 2006), while mantle derived zircons show low Hf concentrations and high Zr/Hf ratios (Heaman et al. 1990). Like the Th/U ratio, the Zr/Hf ratio can correlate with the crystallisation temperature (Bolhar et al. 2008).

6.3.1. Methodology

Trace element data of zircons were obtained from the same samples already investigated by U-Pb isotope studies (see chapter 5) and where possible spots were analysed from the same zone that the U-Pb age analyses were made, although small grain size, cracks and inclusions sometimes did not allow such an approach. Major elements of zircon (Si, Zr, Hf) were determined using a JEOL JXA 8200 electron microprobe with five wavelength dispersive spectrometers at the AAC-JCU (Townsville). Calibration was made using natural 91500 zircon (Si, Zr) and synthetic HfO_2 (Hf) standard. Operating conditions were 50 nA beam current, 15 kV accelerating voltage and 10 µm beam diameter with 20 seconds counting time on the Kα and Lα peak of Si and Zr and 60 seconds counting time on Lα peak of Hf while the background counting was 10 and 30 seconds. The reference zircon 91500 (ZrO_2 = 66.17 ± 54, SiO_2= 32.69 ± 30, Wiedenbeck et al. 2004) was analysed as unknown every 20-25 analyses yielding a reproducibility rate (1RSD) of 1.4 % for ZrO_2 (67.09 ± 0.21, n=15) and 0.1 % for SiO_2 (32.67 ±0.1, n=15).

The same spot analysed by EMP was then ablated by a GeoLas 193 nm ArF laser and the material transported by a mixed argon-helium gas through sample cell and mixing bulb into a

Varian 820 quadrupole ICP-MS. Background data were obtained for 35 seconds followed by 40 seconds of ablation with the following elements being analysed with dwell times ranging between 10 to 40 ms: ^{29}Si, ^{31}P, ^{44}Ca, ^{49}Ti, ^{88}Sr, ^{89}Y, ^{93}Nb, ^{139}La, ^{140}Ce, ^{141}Pr, ^{143}Nd, ^{147}Sm, ^{151}Eu, ^{160}Gd, ^{159}Tb, ^{163}Dy, ^{165}Ho, ^{167}Er, ^{169}Tm, ^{171}Yb, ^{175}Lu, ^{179}Hf, ^{232}Th and ^{238}U. The laser energy output was kept at 6J/cm^2 and a repetition rate of 10 Hz. Where possible the spot diameter was kept at 24 μm, but for some inclusion rich zircons it was reduced to 16 μm.

Calibration was carried out using NIST 610, while NIST 612 and zircon standard 91500 were analysed as unknowns every 10-15 analyses to check for data quality with the reference zircon 91500 (Y = 140 ± 13, Lu= 13.1 ± 1, Wiedenbeck et al. 2004) yielding a reproducibility rate (1RSD) of 2% for Y (143 ± 5, n=16) and 3% for Lu (13.5 ± 1, n=16).Data were processed using Hf as internal standard (previously determined EMP values) and the data reduction software GLITTER 4.4.2. (Van Achterbergh et al. 2001). The signals were filtered for outliers and some analyses or parts of their signal were excluded because high P, Ca and LREE peak indicated that subsurface inclusions (apatite) were ablated by accident.

A summary of concentration ranges of ZrO_2, HfO_2 and Y for each zircon population from the igneous rocks of the Redcap, Red Dome and Mungana deposit are listed in table 6.3.1, whereas the whole data set can be found in appendices 8 and 12.

Table 6.3.1. Zr, Hf and Y concentrations of zircons from igneous rocks of the Redcap, Red Dome and Mungana deposits

Deposit	Sample ID	Rock type	ZrO_2 [wt.-%]	HfO_2 [wt.-%]	Y [ppm]	Zr/Hf
Redcap	949	Dacite	64.83-66.93	1.06-1.65	601-3144	34-58
Redcap	952W1	Dacite	64.56-66.65	1.10-1.67	702-2695	34-52
Redcap	BE 1	Granodiorite	65.22-66.56	1.16-1.52	555-2086	39-50
Redcap	----	Inherited grains (n=2)	65.53-66.28	1.51-1.52	438-742	38
Mungana	883W2	Rhyolitic porphyry	64.47-66.40	1.20-1.48	1329-4771	38-48
Mungana	883W3	Granite	63.76-67.07	1.02-1.36	949-2674	42-57
Red Dome	936	Quartz-feldspar porphyry	64.26-66.08	1.38-1.56	2008-5311	36-40
Red Dome	984	Quartz-feldspar porphyry	64.68-66.44	1.27-1.49	1720-5232	38-46
Red Dome	983	Mineralised quartz vein	64.12-64.70	1.47-1.60	3606-9614	35-38
Red Dome	995	Dacitic porphyry	64.50-66.47	1.09-1.34	1397-4156	43-48

ZrO_2 and HfO_2: EMP, Y: LA-ICP-MS

6.3.2. Redcap

The two samples of the Redcap dacite (949 & 952W1) have very similar concentrations of HfO_2, ZrO_2 and Y ranging from 1.06 to 1.67 wt.-% HfO_2 and 601 to 3144 ppm Y (Tab. 6.3.1. and Fig. 6.3.2.A & B). Their Zr/Hf ratios rang from 34 to 58 whereas their Hf/Y ranges from 3 to 17. Neither the old zircon grain population of sample 952W1 nor the young zircon group of sample 949 do differ regarding their Zr, Hf and Y concentration from the other zircons.

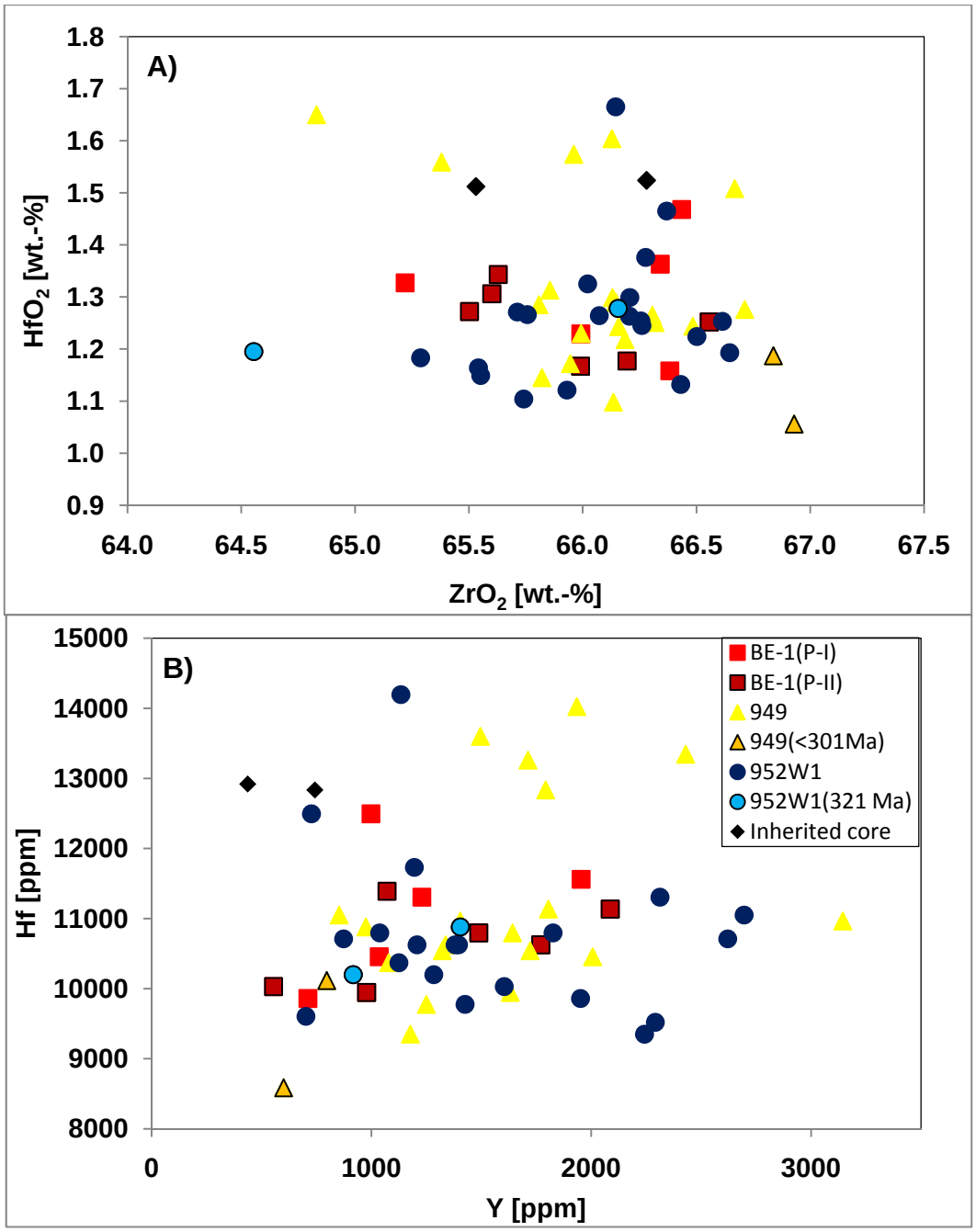

Figure 6.3.2. Plot of zirconium, hafnium and yttrium concentrations of zircons from igneous rocks of the Redcap deposit; **A**) HfO_2 against ZrO_2 (both in wt.-%) and **B**) Hf against Y (both in ppm); 949 & 952W1: Redcap dacite, BE-1(PI) and (PII) older and younger zircon group of the Belgravia granodiorite and 2 inherited grains.

Zircons from the Belgravia granodiorite (BE-1) yielded nearly identical concentrations of HfO_2, ZrO_2 and Y to the samples of the Redcap dacites (Tab. 6.3.1. and Fig. 6.3.2.). Their HfO_2 contents are between 1.16 to 1.47 wt.-%, while Y values range between 555 to 2086 ppm yielding Zr/Hf ratios of 39 to 50 and Hf/Y ratios of 5 to 18, respectively with no difference between the old and younger zircon population observable. Based on the similar Zr, Hf and Y concentration it appears that the Redcap dacite as well as both population of the Belgravia granodiorite were derived from the same source, supporting the assumption that are coeval.

The two inherited cores from 949 and BE-1 have HfO_2 concentrations of 1.3 wt.-% and a Zr/Hf ratio of 38. Yttrium values of one grain are within the range of the concentration from zircon grains from the other three samples (742 ppm), while the second grain yielded a quite low value of 438 ppm. Because of the different Y concentrations, their Hf/Y ratios are also distinct. One grain yielded a ratio of 17, within the range of the other zircons from Redcap, while the other one has a ratio of 30 suggesting a different source for this zircon grain, which will be tested by Hf isotope studies (see chapter 6.6).

6.3.3. Mungana

Zircons from the rhyolitic porphyry (883W2) have HfO_2 concentrations of 1.20 to 1.48 wt.-% and Zr/Hf ratios of 38 to 48 (Tab. 6.3.1. and Fig. 6.3.3.). A comparison between the grains indicate that the Hf content increases from core towards rim, but whether this is also true within a single grain could not be determined, as the zircons from the porphyry were too small to conduct more than one analysis on them. Yttrium contents of zircons from 883W2 range from 1329 to 4771 ppm, yielding Hf/Y ratios of 2 to 8.

The granite from Mungana (883W3) has slightly lower HfO_2 values than the porphyry, ranging from 1.02 to 1.36 wt.-% (Tab. 6.3.1. and Fig. 6.3.3.), but higher Zr/Hf ratios which are similar to the ones observed in zircons from Redcap. The Zr/Hf ratios yielded values of 42 to 57. Values of the Hf/Y ratios are between 4 and 11 with the average ratio being higher than in zircon grains from the porphyry, but within range of the ratios determined for zircon grains from the Redcap deposit. While lower ratios occur in the core, higher Hf/Y ratios are observed at rims. However, due to the small nature of the grains no intra grain observation could be made, as the size only allowed one analysis per grain. In general, Hf and Y concentrations as well as the ratios indicate that the granite was derived from a slightly less fractionated source than the porphyry.

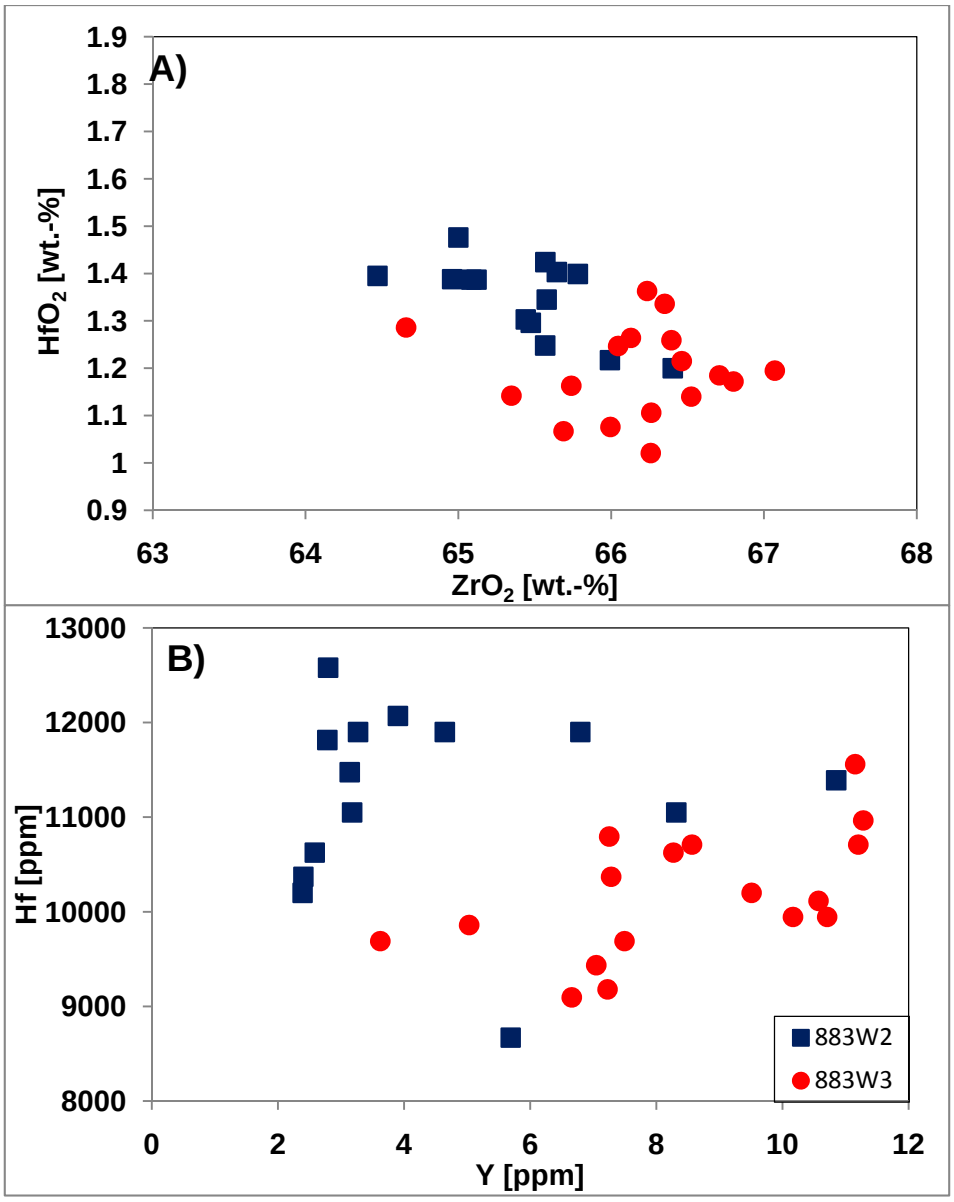

Figure 6.3.3. Plot of zirconium, hafnium and yttrium concentrations against each other of zircons from igneous rocks of the Mungana deposit; **A**) HfO_2 against ZrO_2 (both in wt.-%) and **B**) Hf against Y (both in ppm); 883W2: porphyry, 883W3: granite.

6.3.4. Red Dome

Yttrium and HfO_2 content of zircons from one of the quartz-feldspar porphyries (936) are slightly higher than the concentrations determined from the rhyolitic porphyry from Mungana. They yielded values of 1.38 to 1.56 wt.-% HfO_2 and yttrium concentrations of 2008 to 5311 ppm (Tab. 6.3.1. and Fig. 6.3.4.). The Zr/Hf and Hf/Y ratios yielded values of 36 to 40 and 2 to 6, respectively. Zircons from the second quartz-feldspar porphyry sample (984) have similar HfO_2 and Y content sample 936 yielding values of 1.27 to 1.49 wt.-% HfO_2 and yttrium concentrations of 1720 to 5232 ppm (Tab. 6.3.1. and Fig. 6.3.4.) and also yielding similar Zr/Hf and Hf/Y ratios as sample 936 with values ranging from 38 to 46 for the Zr/Hf ratio and values between 2 to 7 for the Hf/Y ratio. It appears that the Hf content increases from core to rim, but

this observation is based on inter grain examinations only, as again the grains from all porphyry samples of Red Dome were only big enough to conduct one analysis.

The dacitic porphyry is distinct from the two quartz-feldspar porphyries in HfO_2 and Y content, but also in its Zr/Hf and Hf/Y ratios. The HfO_2 concentrations are lower, with values between 1.09 and 1.34 wt.-% and the Y content ranging from 1397 to 4156 ppm. The Zr/Hf ratios range from 43 to 48 and the values of the Hf/Y ratio are between 3 and 8.

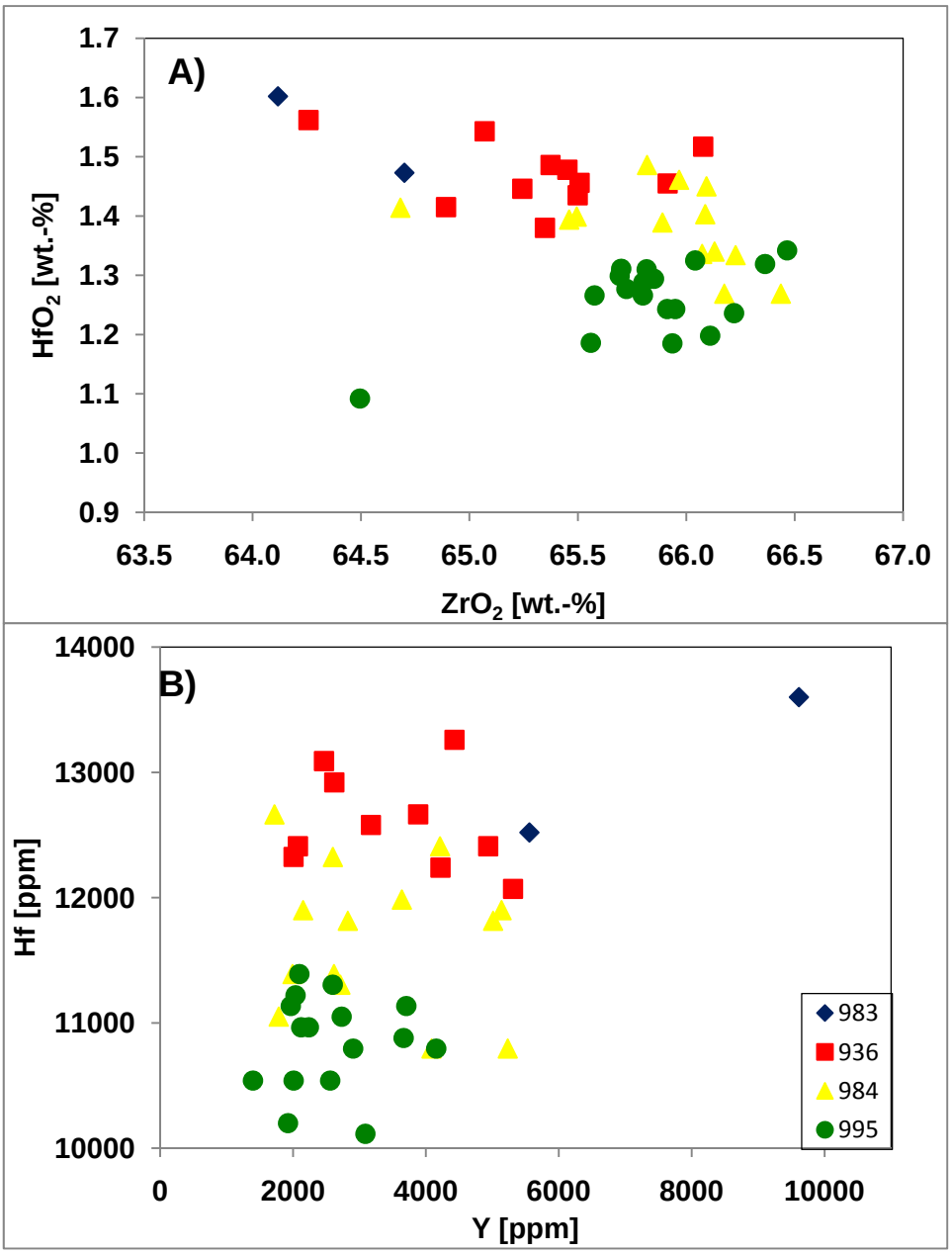

Figure 6.3.4. Plot of zirconium, hafnium and yttrium concentrations against each other of zircons igneous rocks of the Red Dome deposit; **A**) HfO_2 against ZrO_2 (both in wt.-%) and **B**) Hf against Y (both in ppm); 936 & 984: quartz-feldspar porphyries, 995: dacitic porphyry and 983: mineralised quartz vein.

Only three zircon grains from the mineralised quartz vein (983) were analysed, as due to their small nature and enrichment in inclusions and cracks, there was rarely a clear spot after the geochronological studies were done. The HfO_2 content ranges between 1.47 to 1.60 wt.-% (Tab. 6.3.1. and Fig. 6.3.4.) and is the highest observed within the Red Dome deposit as well as in comparison to zircons from the other deposits. The yttrium concentrations are also very high, yielding values of 3606 to 9614 ppm. The Zr/Hf ratio lies between 35 and 38, while the Hf/Y ratio is between 1 and 2, but based on the low number of analyses the data have to been treated with caution.

In general a decreasing trend of Zr/Hf and Hf/Y ratios from 936 via 984 to 995 occurs, suggesting that a change of crystallisation environment occurs from more fractionated for the quartz-feldspar porphyries to less fractionated for the younger dacitic porphyry.

6.4. Ti in zircon thermometry

Titanium concentration in zircon can be used as geothermometer that was developed by Watson & Harrison (2005), who observed that the incorporation of Ti into zircon is temperature dependent, although the Ti concentration in terrestrial zircon rarely exceed values of 20 ppm (Fu et al. 2008). Watson et al. (2006) postulated that changes in pressure would nearly not affect the thermometer and assumed that any diffusive re-equilibration of zircon rarely occurred, as studies of the behaviour of tetravalent cation by Cherniak et al. (1997a & b) showed that diffusion only takes place at a level that can hardly be measured. They calibrated the thermometer to rutile saturated conditions; other titaniferous phases like titanite, ilmenite, titanomagnetite or even titanium in quartz would fulfil the required TiO_2 saturated conditions needed for the thermometer. Watson et al. (2006) also postulated that even under continuing fractionation the saturated rutile condition would remain stable. Ferry and Watson (2007) presented a revised Ti-in-zircon thermometer, which considered the activity of TiO_2 and SiO_2 for temperatures estimates as Watson & Harrison (2005) had already shown that the , but also to the TiO_2 and SiO_2 activity. Although the revision of the geothermometer by Ferry and Watson (2007) increased the possibilities of usage, they could not explain why crystallisation temperatures of zircon were lower than other temperature estimates, for example zircon saturation temperatures (Fu et al. 2008). Fu et al. (2008) assumed that the incorporation of Ti into zircon is not only influenced by the temperature and TiO_2 and SiO_2 activity, but a combination of other factors like calibration inaccuracies of the thermometer, resetting of the Ti amount through alteration or diffusion, disequilibrium conditions and/or non-Henry's Law substitution, which may influence the Ti uptake into zircon.

In this study zircon crystallisation temperatures were estimated using the Ti concentration determined by LA-ICP-MS (see section 6.3.1. for methodology) and equation 7 of Watson et al. (2006): $T\ (°C) = \frac{5080 \pm 30}{(6.01 \pm 0.03) - \log(Ti)} - 273$. The activities of TiO_2 and SiO_2 were assumed to saturated (=1) and additionally no pressure corrections were made. A summary of Ti concentrations and temperatures for zircons from igneous rocks of the Redcap, Mungana and Red Dome deposit are provided in table 6.4, while the whole data set is listed in appendix 12.

Table 6.4. Summary of Ti concentrations and temperature estimates for zircons from igneous rocks of the Redcap, Mungana and Red Dome deposits

Deposit	Sample ID	Rock type	Ti [ppm]	T [°C]
Redcap	949	Dacite	2-19	611-800
Redcap	952W1	Dacite	2-16	628-785
Redcap	BE 1	Granodiorite	7-15	712-779
Redcap	----	Inherited grains (n=2)	13,15	762,780
Mungana	883W2	Rhyolitic porphyry	2-5	603-684
Mungana	883W3	Granite	2-13	612-766
Red Dome	936	Quartz-feldspar porphyry	3-7	638-711
Red Dome	984	Quartz-feldspar porphyry	2-5	611-685
Red Dome	983	Mineralised quartz vein	4	666
Red Dome	995	Dacitic porphyry	2-6	628-692

6.4.1. Redcap

Zircons of the two age groups of the Belgravia granodiorite (BE-1) have Ti concentrations of 7 to 15 (Tab. 6.4.) and yielded crystallisation temperatures of 712 to 779 °C (Fig. 6.4.1.). While zircon cores of both populations have crystallisation temperatures of on average 770 °C, rims yielded on average temperatures which are 30 °C lower than the average of 740 °C. No correlation between the temperatures with the Th/U and Zr/Hf ratios exist.

The two Redcap dacite samples (949 & 952W1) are again summarised, due to their similarity. The Ti content of zircons of these samples range from 2 to 19 ppm (Tab. 6.4.). Titanium values equal or above the average of 10 are observed in the core and yielded an average crystallisation temperature of 764 °C ± 16 (n=22, 2STD), very similar to the temperature calculated for zircons of the Belgravia granodiorite. Twenty-one rim analyses yielded an average temperature of 712 °C ± 35 (n=21, 2 STD). Neither the older zircon group of 952W1 nor the younger zircon populations of sample 949 are distinct from the other zircon grains. Again no correlation between the Th/U and Zr/Hf ratios and temperatures can be observed.

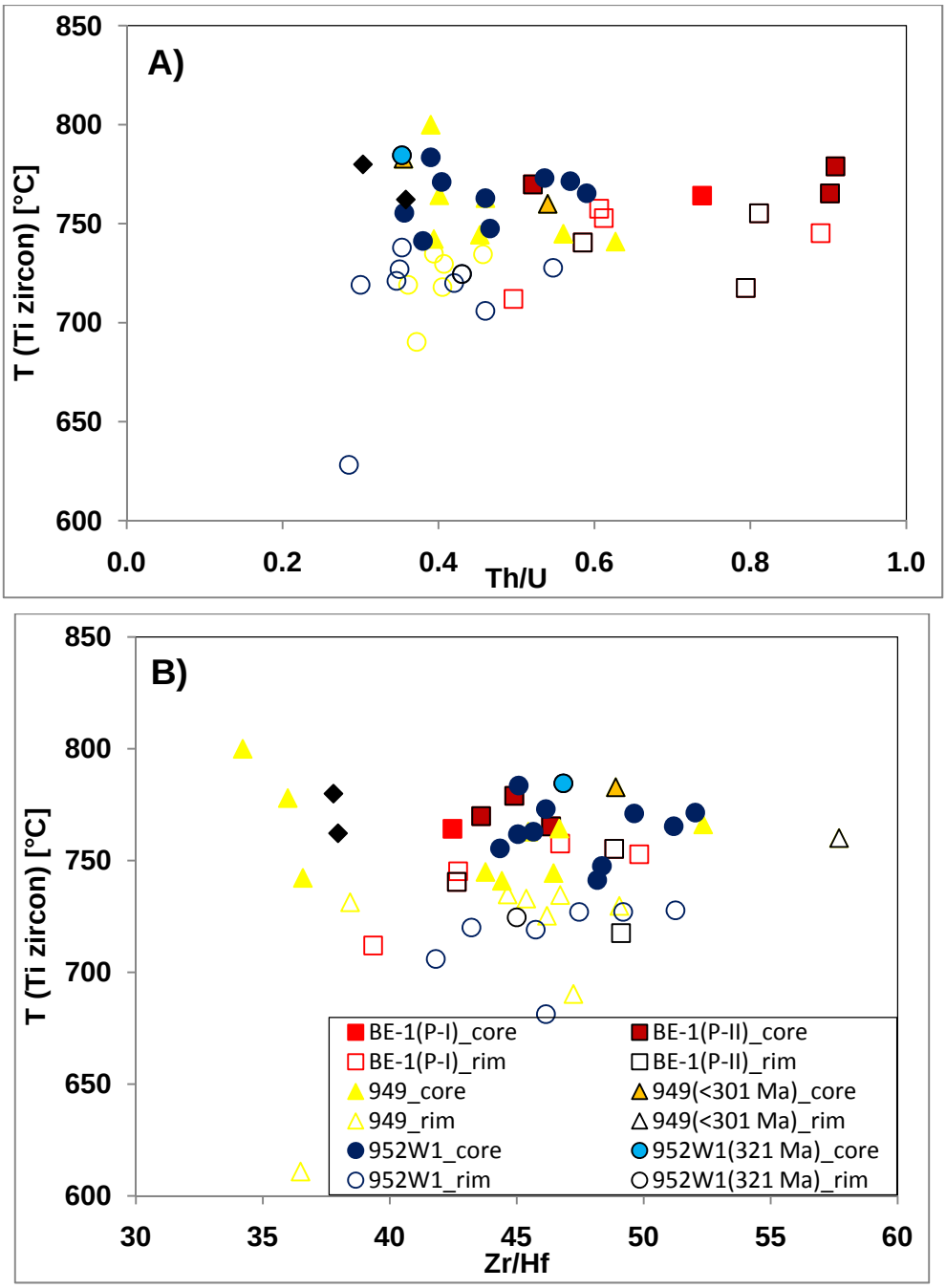

Figure 6.4.1 Plot of Ti-in zircon temperatures against Th/U ratios (**A**) and Zr/Hf ratios (**B**) from igneous rocks of the Redcap deposit; 949 & 952W1: Redcap dacite, BE-1(PI) and (PII) older and younger zircon group of the Belgravia granodiorite and 2 inherited grains.

The two inherited, Mesoproterozoic cores have similar titanium concentration than zircons from the other three samples ranging between 13 to 15 ppm and also yielding similar crystallisation temperatures of 762 and 780 °C, respectively. Due to similarity of all samples it is likely that all rocks at Redcap were derived from the same source as Th, U, Zr, Hf and Y concentration already suggested.

6.4.2. Mungana

Zircon grains from the rhyolitic porphyry (883W2) of Mungana only show a limited variation in their Ti content, ranging from 2 and 5 ppm (Tab. 6.4). Nine out of 13 analyses of rims yielded an average crystallisation temperature of 625 °C ± 15 (2 STD), while the average core temperature is 44 °C higher (669 °C ± 15, 2 STD). In this case a correlation between Th/U (Fig. 6.4.2.A) and Zr/Hf (Fig. 6.4.2.B) can be observed.

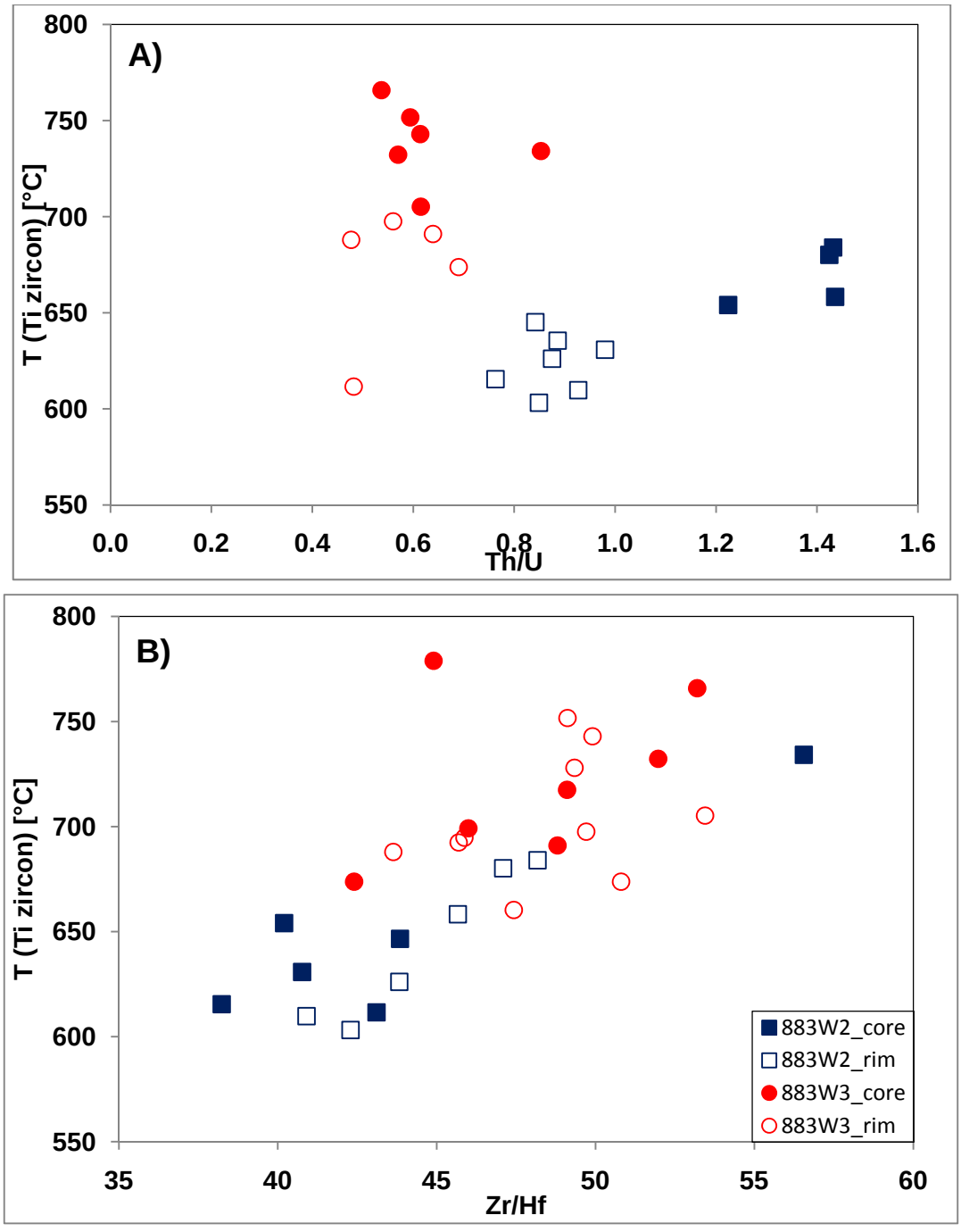

Figure 6.4.2. Plot of Ti-in zircon temperatures against Th/U (**A**) and Zr/Hf ratios (**B**) from igneous rocks of the Mungana deposit; 883W2: porphyry, 883W3: granite.

Zircon cores with higher crystallisation temperatures also have higher Th/U ratios (≥ 1.0) and additionally show slightly higher Zr/Hf ratios than zircons from the rim, suggesting that during crystallisation of the zircons a very weak change of the crystallisation environment occurred and that cores were derived from a less fractionated source than the rims.

The granite sample has higher and broader Ti concentrations than the porphyry, ranging from 2 to 13 ppm. Titanium concentrations above the average occur in the core, yielding an average temperature of 737 °C ± 19 (2 STD), whereas zircon rims (n=10) are on average 59 °C cooler (Ø 678 °C ± 27, 2 STD). No correlation between Th/U ratio and temperature exists (Fig. 6.4.2.A), but the Zr/Hf ratio is almost always higher for zircon cores than for zircon rims, except three grains which overlap regarding their ratio (Fig. 6.4.2.B).This indicates that the cores of the zircons were derived from a more fractionated source whereas the rims crystallised in a slightly as less evolved environment.

6.4.3. Red Dome

One of the quartz-feldspar porphyry samples (936) has titanium concentrations between 3 to 7 ppm, with four out of 10 analyses being below the detection limit. Three out of the remaining 6 zircon grains yielded a core temperature of 692 °C ± 20 (2 STD), whereas rims have an average temperature of 647 °C ± 15 (2STD). The second quartz-feldspar porphyry (984) yielded Ti concentrations identical to the ones detected for the Mungana porphyry sample and almost identical to the values of sample 936 (Tab. 6.4.). Difference of temperatures between core and rim are only 26 °C with cores yielding an average temperature of 668 °C ± 11 (2STD) and rims of 642 °C ± 14 (2STD), with the core temperature being identical to the one calculated for zircon cores from the Mungana porphyry.

Titanium concentrations of the dacitic porphyry also do not vary much and range from 2 to 6 ppm (Tab. 6.4.) with only one analysis being below the detection limit. Eight cores out of 15 analyses yielded an average crystallisation temperature of 676 °C ± 12 (2STD), whereas rims are 30 °C cooler with an average temperature of 646 °C ± 9 (2STD). Only three analyses were conducted on zircons from the mineralised quartz vein (983), with two out of three having Ti concentrations below the detection limit. The remaining analysis yielded a temperature of 666 °C ± 6, which falls within the range of temperatures calculated for the other porphyries of Red Dome and the Mungana porphyry and at least for this zircon a magmatic origin can be assumed because the temperature is too high for a hydrothermal event.

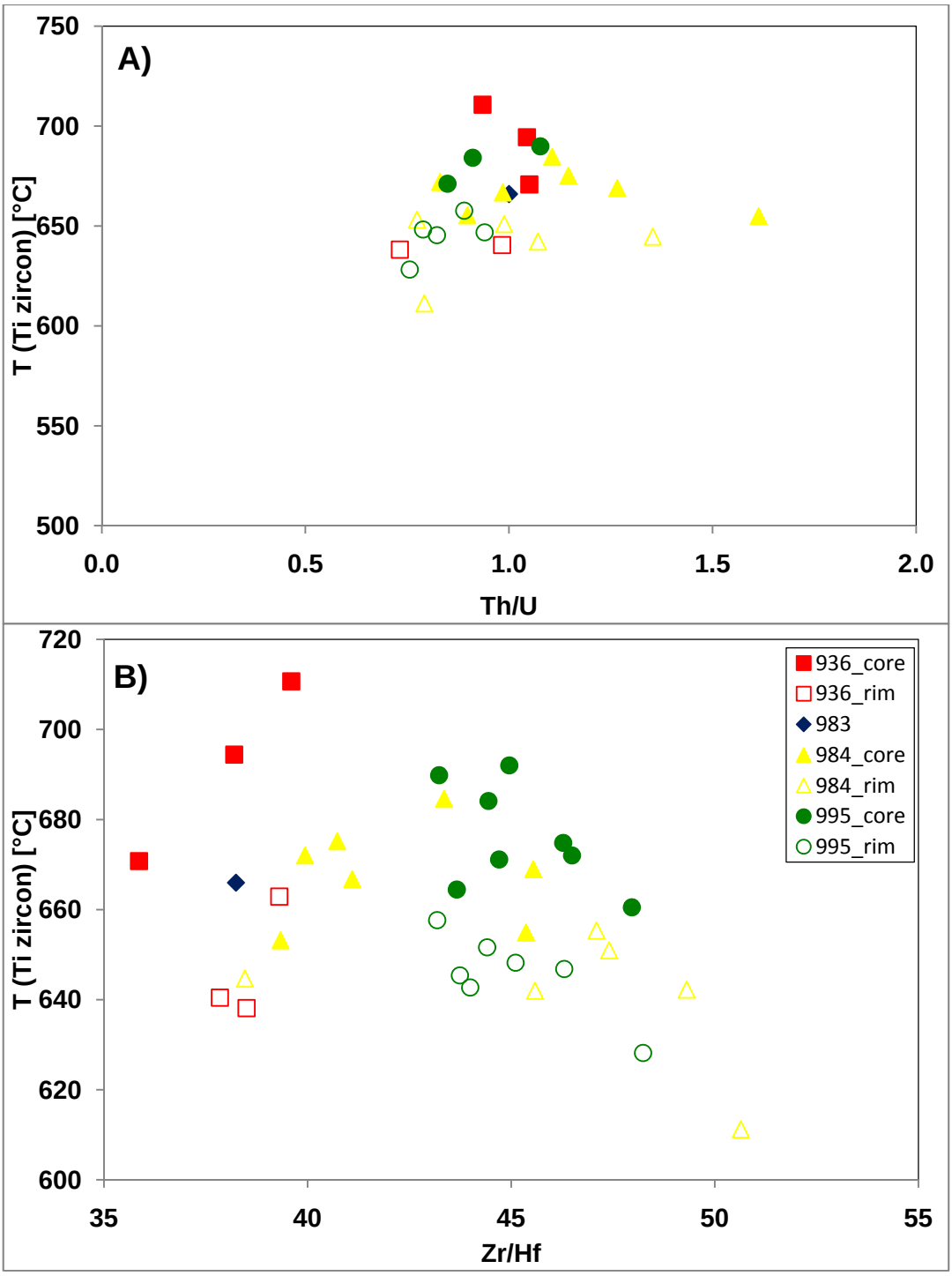

Figure 6.4.3. Plot of Ti-in zircon temperatures against Th/U (**A**) and Zr/Hf ratios (**B**) from igneous rocks of the Red Dome deposit; 936 & 984: quartz-feldspar porphyries, 995: dacitic porphyry and 983: mineralised quartz vein.

A comparison of the zircon crystallisation temperatures of the single samples with their Th/U and Zr/Hf ratios (Fig. 6.4.3.A & B) shows that no correlation between the Th/U ratio and crystallisation temperatures exists. On the other hand a clear trend can be observed for the Zr/Hf ratios. The Zr/Hf ratios increase from 936 (~35-40) via 984 (~38-46) to sample 995 (~43-48)

with only a small overlap existing between sample 984 and 995. This trend can be observed not only within zircon cores, but also within zircon rims, suggesting a change of the source where the zircons from the older quartz-feldspar porphyries were derived from a more fractionated (936) source than zircons from the younger dacitic porphyry (995).

6.5. REE abundance

The group of rare earth elements (REE) comprises 14 elements which can be divided into three subgroups these being the light REE (La-Eu), medium REE (Gd-Ho) and heavy REE (Er-Lu) with the latter being more compatible into the zircon lattice based on their smaller ionic radii. The total abundance of REE in zircons from different igneous rocks can vary by several orders of magnitude (Heaman et al. 1990; Hoskin & Ireland 2000; Belousova et al. 2002; Hoskin & Schaltegger 2003), but this difference cannot be used for the majority of rocks as discrimination tool with one exception. Zircons that originated from a mantle source are characterised by very low REE concentrations with values being less than 50 ppm (Hoskin & Ireland 2000; Belousova et al. 2002), whereas zircons derived from a crustal source show a broad range of total REE content typically ranging from 250 ppm to 0.5 wt.-% (Hoskin & Schaltegger 2003).

The chondrite normalised REE pattern may also be distinctive for mantle derived zircons (Hoskin & Schaltegger 2003), but does not help to discriminate zircons from rocks which originated from a crustal source. In general the normalised REE pattern of zircon show a steep rise from LREE to HREE with LREE commonly exhibiting values of less than 10 times chondrite, whereas values of MREE range from 1 to 100 and HREE show values of 1000 to 10000's (Hoskin & Schaltegger 2003). The steepness of the slopes for the LREE and HREE can be calculated by dividing chondrite normalised values of Sm and La for LREE and Lu and Gd for HREE with the former one being used in combination with the Ce anomaly as a discrimination tool to distinguish between hydrothermal and magmatic zircons (Hoskin 2005), whereas the value of $(Lu/Gd)_N$ can be used to differentiate between crustal and mantle derived zircons with the latter typically yielding low $(Lu/Gd)_N$ values of 1 to 10 (Hoskin & Schaltegger 2003).

Two anomalies occur within the chondrite normalised REE pattern: a positive Ce anomaly (Ce/Ce*) with values of ≥ 1 and a usually negative Eu anomaly (Eu/Eu*) which ranges from 0 to 1 (Hoskin & Schaltegger 2003). The magnitude of the anomalies is calculated by using the following equations: $\mathrm{Ce/Ce} * = \frac{\mathrm{CeN}}{\sqrt{(\mathrm{LaN\ x\ PrN})}}$ & $\mathrm{Eu/Eu} * = \frac{\mathrm{EuN}}{\sqrt{(\mathrm{SmN\ x\ GdN})}}$.While zircons that originate from a crustal source show varieties within their degree of anomaly, mantle derived zircons are generally characterised by insignificant to no Ce- and Eu anomalies (Hoskin &

Schaltegger 2003). In addition to the usage of Ce/Ce* and Eu/Eu* magnitudes to distinguish between mantle and crustal zircons, the anomalies also give information on the oxygen fugacity of the environment in which the zircons formed (Ballard et al. 2002; Hoskin & Schaltegger 2003; Bolhar et al. 2008) or in some circumstances help to discriminate between barren and Cu-mineralised systems with Ce/Ce* values >70 and Eu/Eu* > 0.4 being required for the latter (Ballard et al. 2002).

Cerium and europium are the only elements within the group of lanthanides which occur in a trivalent oxidation state like the other 12 elements but also have a second oxidation state in the form of Ce^{4+} and Eu^{2+} with both elements thus being redox sensitive (Bolhar et al. 2008). Hinton & Upton (1991) showed that tetravalent cerium is more compatible in the zircon lattice than Ce^{3+} under oxidised conditions and gets enriched relative to La and Pr, which causes the large anomaly whereas under reduced conditions no Ce anomaly is exhibited (Hoskin & Schaltegger 2003).

Table 6.5. Summary of total REE abundance, magnitude of anomalies and steepness of patterns of zircon grains from igneous rocks of the Redcap, Mungana and Red Dome deposit

Sample ID	Rock type	Age ± 2σ [Ma]	∑REE [ppm]	Lu/Gd_N	Eu/Eu*	Ce/Ce*
949	Dacite	310 ± 2	420-2280	17-37	0.03-0.12	9-98
952W1	Dacite	306 ± 2	478-1945	18-52	0.04-0.12	8-103
BE-1 (P-I)	Granodiorite	309 ± 2	483-1335	20-49	0.17-0.20	80-243
BE-1 (P-II)	Granodiorite	297 ± 2	383-1413	19-36	0.18-0.21	60-282
----	Inherited grains	Ø1520	200; 505	1; 29	0.01;0.35	23; 90
883W2	Rhyolitic porphyry	324 ± 2	903-3343	12-30	0.16-0.20	22-130
883W3	Granite	305 ± 2	683-1995	15-31	0.15-0.32	22-248
936	Quartz-feldspar porphyry	322 ± 2	1322-3375	19-31	0.11-0.17	6-29
984	Quartz-feldspar porphyry	324 ± 2	1177-3804	13-29	0.17-0.20	20-172
983	Mineralised quartz vein	322 ± 2	2310-5243	17-28	0.10-0.24	6-207
995	Dacitic porphyry	311 ± 2	953-2856	15-26	0.17-0.29	7-209

The europium anomaly indicates a depletion of Eu relative to Sm and Gd. Although under oxidised conditions theoretically no Eu-anomaly should develop, it is commonly exhibit with Drake (1975) and Hoskin et al. (2000) proposing that plagioclase fractionation before or during zircon crystallisation can produce magmas depleted in Eu resulting in negative Eu anomalies under oxidised conditions.

In this section zircons from Redcap, Red Dome and Mungana were investigated regarding their REE concentrations and normalised patterns, as well as magnitudes of the Eu/Eu* and Ce/Ce* anomalies and steepness of the patterns are described with a summary of the data being provided in table 6.5 whereas additional data are listed in appendix 11.

6.5.1. Redcap

Zircons from Redcap dacite sample 949 have total REE concentrations of 420 to 2280 ppm (Tab. 6.5). Four core-rim analyses indicate that the REE concentrations in the core are on average 275 ppm higher than in the rims. Zircons from the second Redcap dacite sample (952W1) have nearly identical total REE concentrations with values ranging from 478 to 1945 ppm (Tab. 6.5). Two zircons grains with 321 Ma ages and possibly part of an older population (see chapter 5), cannot be distinguished based on their total REE concentrations from the others. Five core-rim analyses show that a decrease of total REE abundance of on average 460 ppm from core to rim occurs.

Chondrite-normalised REE patterns of the two Redcap dacite sample are, like their total REE abundance, very similar (Fig. 6.5.1.1.) and will be described together. Both samples show uniform patterns with steep LREE and HREE pattern, positive Ce-anomaly and negative Eu-anomaly. In general a decrease of REE concentrations from core to rim occurs, with one exception in sample 949. Neither the group of younger than 301 Ma from sample 949 nor the 321 Ma group of sample 952W1 can be distinguished based on their REE-pattern from the other zircons grains.

Zircons from the Belgravia granodiorite (BE-1) sample were divided into two populations based on their age (see chapter 5).

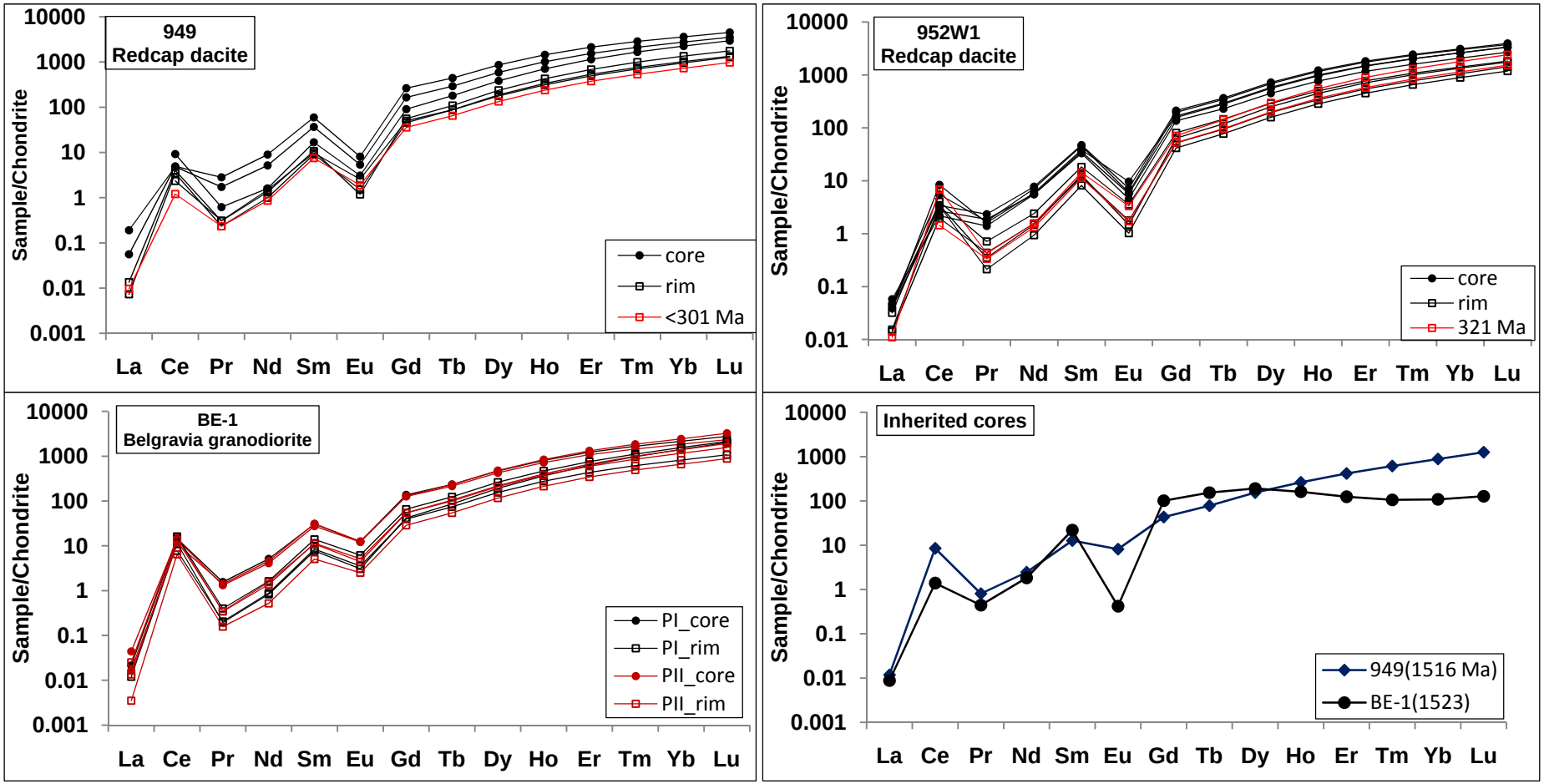

Figure 6.5.1.1. Chondrite normalised REE patterns of zircons from the Redcap dacites (949 & 952W1), two zircon populations of the Belgravia granodiorite (P-I: 309 ± 2 Ma and P-II: 297 ± 2 Ma) and two inherited cores; all data are normalised to chondrite values of Anders & Grevesse (1989).

The older population (P-I) has average total REE concentrations of 829 ± 318 ppm (n= 5), whereas the total REE abundance of the younger population (P-II) shows average values of 908 ± 369 ppm (n=6). Rare earth concentrations of core and rim analyses of P-I are on average 100 ppm higher than in the younger group P-II, but both populations show a concentration variation of around 600 ppm between core and rim. This is also reflected in the chondrite-normalised REE patterns (Fig. 6.5.1.1.). In general the REE pattern is similar to the ones already described for the Redcap dacite samples, with steep rise of LREE and HREE, positive Ce- and negative Eu-anomalies, although the Ce-anomaly is an order of magnitude stronger and the Eu-anomaly weaker than in samples 949 & 952W1 (Tab. 6.5., Fig. 6.5.1.2.).

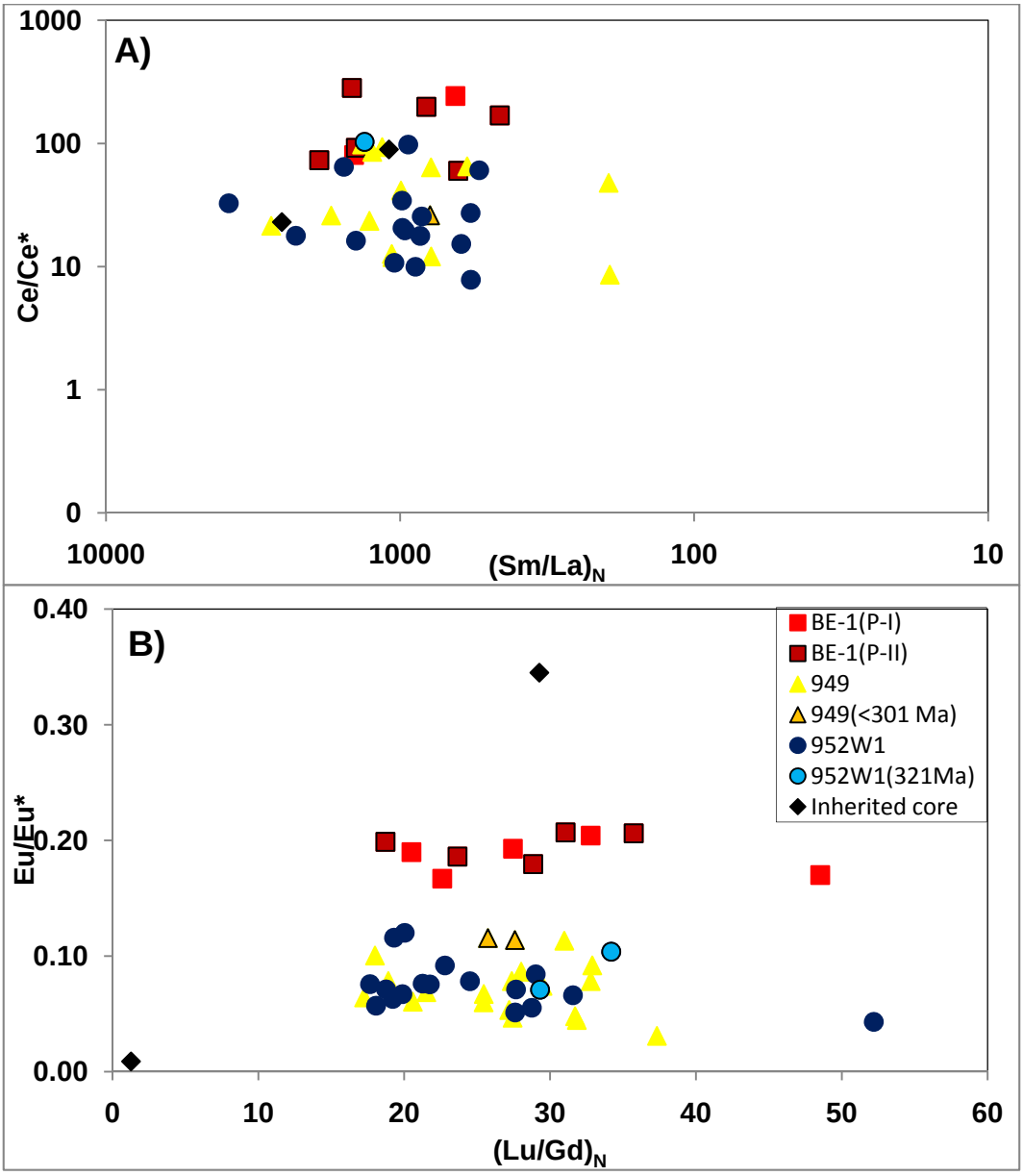

Figure 6.5.1.2. Plot of Ce/Ce* versus $(Sm/La)_N$ (**A**) and Eu/Eu* versus $(Lu/Gd)_N$ (**B**) of zircons from the Redcap dacites (949 & 952W1), two zircon populations of the Belgravia granodiorite (P-I: 309 ± 2 Ma and P-II: 297 ± 2 Ma) and two inherited cores.

The two inherited cores of Mesoproterozoic age are very different. While the zircon from sample BE-1 has total REE concentrations of 200 ppm (Tab. 6.5.) the zircon grain from 949 has a REE concentration of 505 ppm (Tab. 6.5.) which is within the range of the Permo-Carboniferous zircon populations. The chondrite-normalised patterns also vary between the two different grains. The zircon grain from 949 exhibits a steep rise for LREE and HREE with a positive Ce-anomaly and a moderate negative Eu-anomaly (Fig. 6.5.1.1.), whereas the inherited core from sample BE-1 shows an order of magnitude lower rise within the LREE pattern and a very flat HREE pattern, but a steep negative Eu-anomaly, suggesting that although both grains are of similar age, they were derived from a different source or alternatively that one grain (BE-1) was affected by metamorphism with such an event occurred at around 1550 Ma in the area (Black et. al. 1998).

As the degree of steepness of the HREE pattern, expressed as $(Lu/Gd)_N$, and the level of the Ce- and Eu-anomaly can help to discriminate between mantle and crustal derived zircons they will be described separately. Forty-three zircon grains from two Redcap dacite samples (949 & 952W1) show Ce-anomalies which range from 8 to 103 with an average of 38 ± 30 (Tab. 6.5., Fig. 6.5.1.2.A). The Ce-anomalies of the two Belgravia granodiorite populations are on average higher, yielding values of 162 ± 115 for the older and 146 ± 87 for the younger group although both populations do overlap (Tab. 6.5. and Fig. 6.5.1.2.A.), but in comparison to the Redcap dacite zircons both zircons groups of the Belgravia granodiorite crystallised from a more oxidised magma than the Redcap dacites. The two inherited cores plot within the range of the dacite and granodiorite (Fig. 6.5.1.2.A).

The negative Eu-anomaly of zircons from the Redcap dacites is quite steep, yielding values of 0.03 to 0.11 with an average of 0.1 ± 0.05 (n=39, 2 STD). The 321 Ma old grains of sample 952W1 as well as the very young grains (<301 Ma) of sample 949 cannot be distinguished from the remaining grains which is also true for the HREE, which yield an average of 26 ± 7 (2 STD) suggesting a crustal source. Both zircon groups of the Belgravia granodiorite show similar $(Lu/Gd)_N$ values of 30 ± 11 (2 STD) for the older group and 28 ± 7 (2 STD) for the younger group suggesting also a crustal origin, but the Eu-anomaly is slightly less negative then the ones from the Redcap dacites (Fig. 6.5.1.2.B), with average values of 0.18 ± 0.02 and 0.20 ± 0.01 for the older and younger populations. The two inherited cores are very different in comparison to the zircon grains from the other samples and to each other (Fig. 6.5.1.2.B). One grain has a $(Lu/Gd)_N$ value of 1 and a strong negative Eu-anomaly suggesting formation in either a reduced environment or in an oxidised environment in the presence of plagioclase. The other grain yielded a $(Lu/Gd)_N$ value of 29 which falls within the range of the Redcap dacite and Belgravia granodiorite samples (Tab. 6.5.), but with an Eu/Eu* value of 0.35 it has a weaker Eu-anomaly

then all the other samples from Redcap suggesting that it was derived from a more oxidised source or crystallised in an environment which lacks plagioclase.

6.5.2. Mungana

Zircons from the Mungana porphyry (883W2) have total REE concentrations of 903 to 3343 ppm (Tab. 6.5.) with an average of 2341 ± 737 ppm (n=17). Two out of 17 grains yielded values well above 3000 ppm and are relatively enriched in LREE which could indicate accidental analyses of LREE-rich apatite inclusions. The chondrite-normalised REE patterns are uniform with a steep slope for LREE and HREE and positive Ce and negative Eu-anomalies (Fig. 6.5.2.1.). Although no core-rim analyses were conducted, the general trend shows that cores exhibit higher REE concentrations than rims. The steepness of the Ce-anomaly with values of 22 to 130 and an average of 49 ± 31 (2 STD) (Tab. 6.5., Fig. 6.5.2.2.A) is typical for a fractionated, oxidised crustal source. The HREE ratio of $(Lu/Gd)_N$ also suggests a crustal origin of the porphyry with values ranging between 12 and 30 (Tab. 6.5., Fig. 6.5.2.2.B).

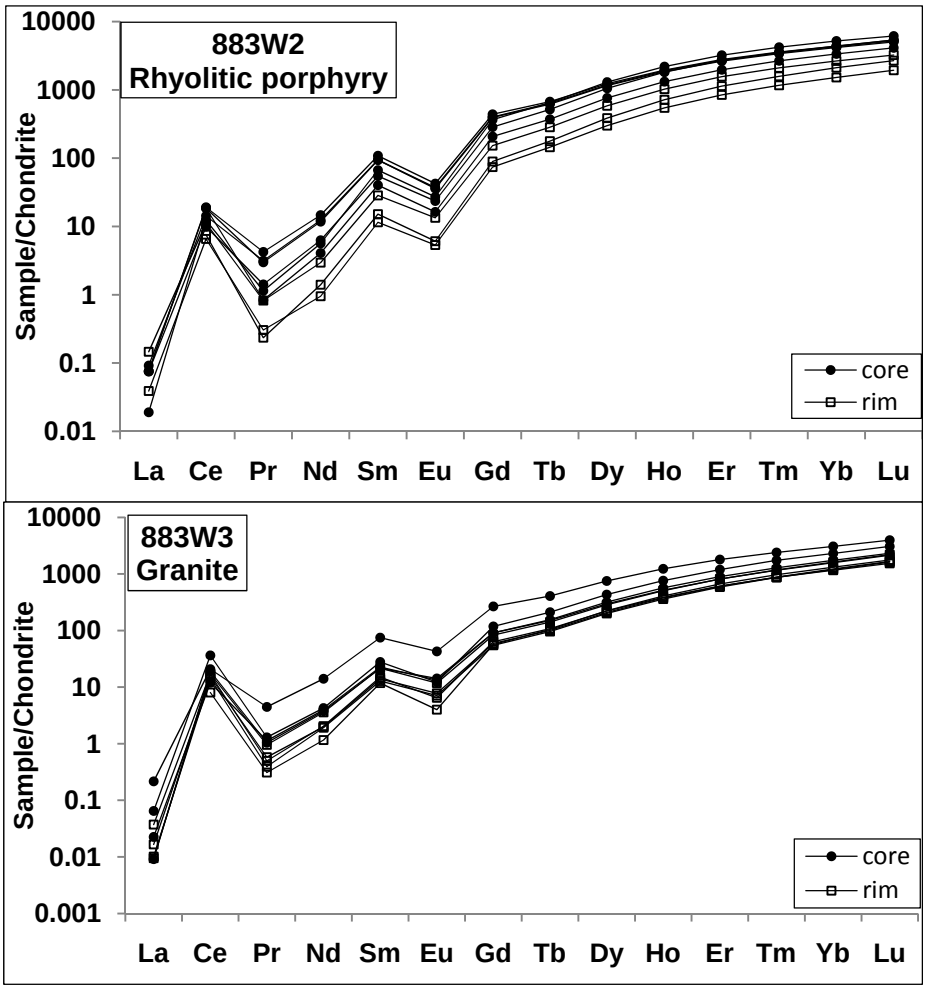

Figure 6.5.2.1. Chondrite normalised REE patterns of zircons from the Mungana porphyry (883W2) and granite (883W3); all data are normalised to chondrite values of Anders & Grevesse (1989).

The degree of the Eu-anomaly yielded an average value of 0.18 ± 0.01 (n=14, 2 STD), which is identical to the one obtained for the Belgravia granodiorite sample from Redcap.

Zircons from the Mungana granite (883W3) have lower total REE concentrations than the porphyry yielding an average value of 953 ± 321 ppm (n=17), but falling within the range of total REE abundance of the dacite and granodiorite samples from the Redcap deposit. Their chondrite-normalised REE pattern is similar to the one observed within the porphyry (Fig. 6.5.2.1.), but the Ce-anomaly is more positive with average values of 126 ± 74 and weaker negative Eu-anomalies with an average of 0.26 ± 0.05 (Fig. 6.5.2.2.A & B), suggesting that the granite formed from a more oxidised and evolved source than the porphyry. The HREE ratio of $(Lu/Gd)_N$ which ranges from 15 to 31 (Tab. 6.5.) supports the assumption of a crustal source for the granite.

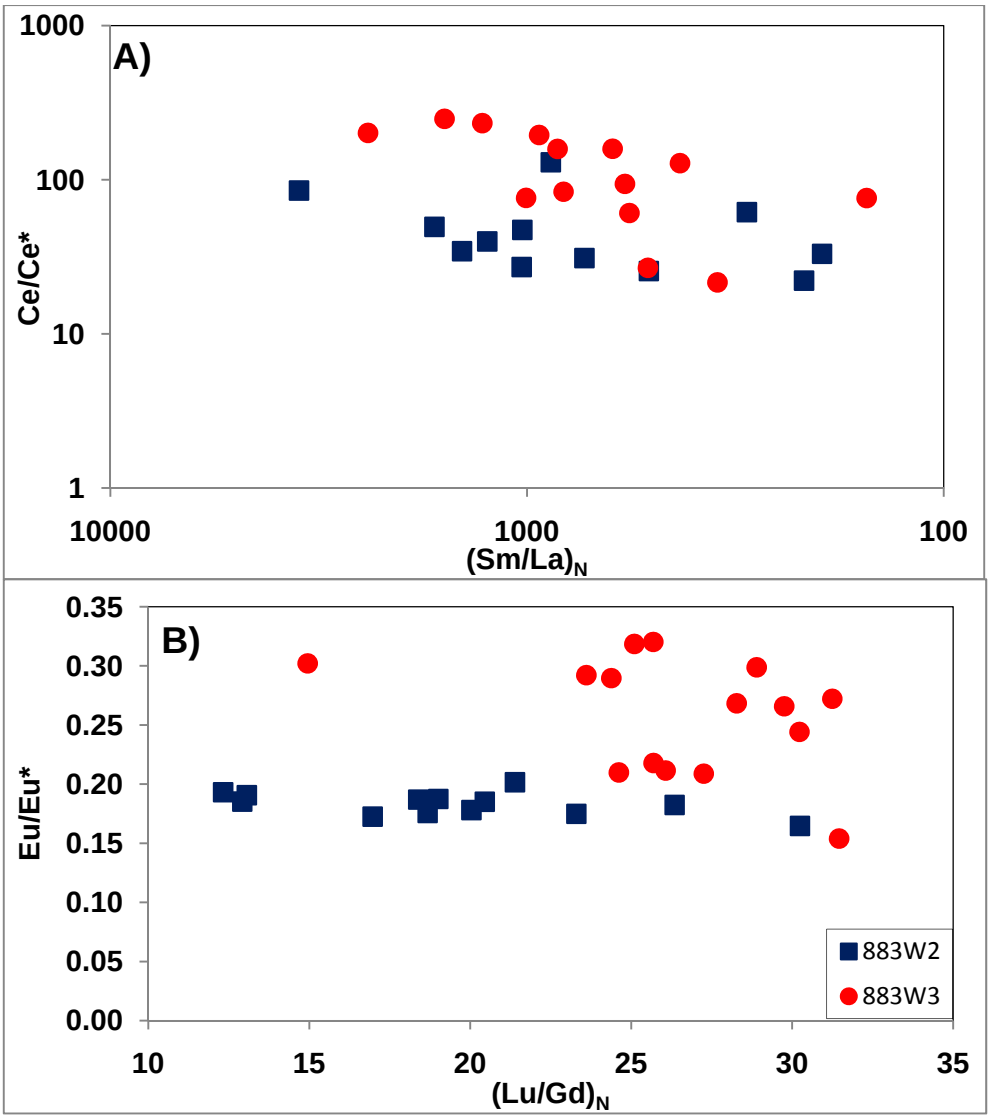

Figure 6.5.2.2. Plot of Ce/Ce* versus $(Sm/La)_N$ (**A**) and Eu/Eu* versus $(Lu/Gd)_N$ (**B**) of zircons from the Mungana porphyry (883W2) and granite (883W3).

6.5.3. Red Dome

Zircon grains from one of the quartz-feldspar porphyries (936) from Red Dome yielded total REE concentrations between 1322 and 3375 ppm (Tab. 6.5.) with an average of 2344 ± 807 ppm (n=10), which is similar to the concentrations observed in the Mungana porphyry. Chondrite-normalised REE patterns are uniform with positive Ce- and negative Eu-anomaly and show that cores have higher REE concentrations than rims. The second quartz-feldspar porphyry sample (984) has total REE concentrations of 1177 to 3804 ppm (Tab. 6.5.) with an average of 2263 ± 897 ppm (n=14) falling within the range of sample 936 and the 883W2 from Mungana. The Chondrite-normalised patterns are similar ones to the ones from 936, but the LREE are more enriched in 984 than in 936 (Fig. 6.5.3.1.) and the Ce-anomaly is also stronger than in sample 936. No core-rim pair could be analysed due to the small nature of the zircon grains, but inter-grain analyses suggest that cores in general have higher REE concentrations than rims.

The dacitic porphyry (995) yielded total REE concentrations of 953 to 2856 ppm with an average of 1778 ± 498 ppm (n=16). In comparison with the other porphyry samples from Red Dome and Mungana the total REE average value of 995 is around 550 ppm lower, but around 800 ppm higher than all samples from Redcap and the Mungana granite. The chondrite-normalised patterns are slightly heterogeneous (Fig. 6.5.3.1.), with the majority of zircon grains showing patterns similar to the ones observed in sample 984, whereas four zircon grains show patterns similar to the ones from sample 936 with weaker LREE and Ce-anomalies.

Zircons from the mineralised quartz-vein yielded very high total REE concentrations ranging from 2310 to 5243 ppm, but due their richness in inclusions and small size subsurface inclusions could not been avoided. This is confirmed by high P and Ca values as well as enrichment in LREE. Two out of three analysed zircon grains show uniform chondrite-normalised REE patterns with positive Ce- and negative Eu-anomalies (Fig. 6.5.3.1.), similar to the patterns observed in samples 936 and 984. The pattern from the third grain of 983 shows a very week positive Ce-anomaly with a value of 6 (Tab. 6.5.), but the HREE show similar patterns to the other porphyry samples. As the chondrite-normalised REE patterns are all similar and indicate a crustal source, the degree of the Ce- and Eu-anomalies as well as the steepness of HREE will be described in more detail.

Zircons from sample 936 have Ce-anomaly values of 6 to 29 with an average of 15 ± 9 (n=9, 2 STD), which suggest a crustal source, but the values of the Ce-anomaly are to low for the porphyry do be linked to Cu mineralisation as suggested by Ballard et al. (2002).

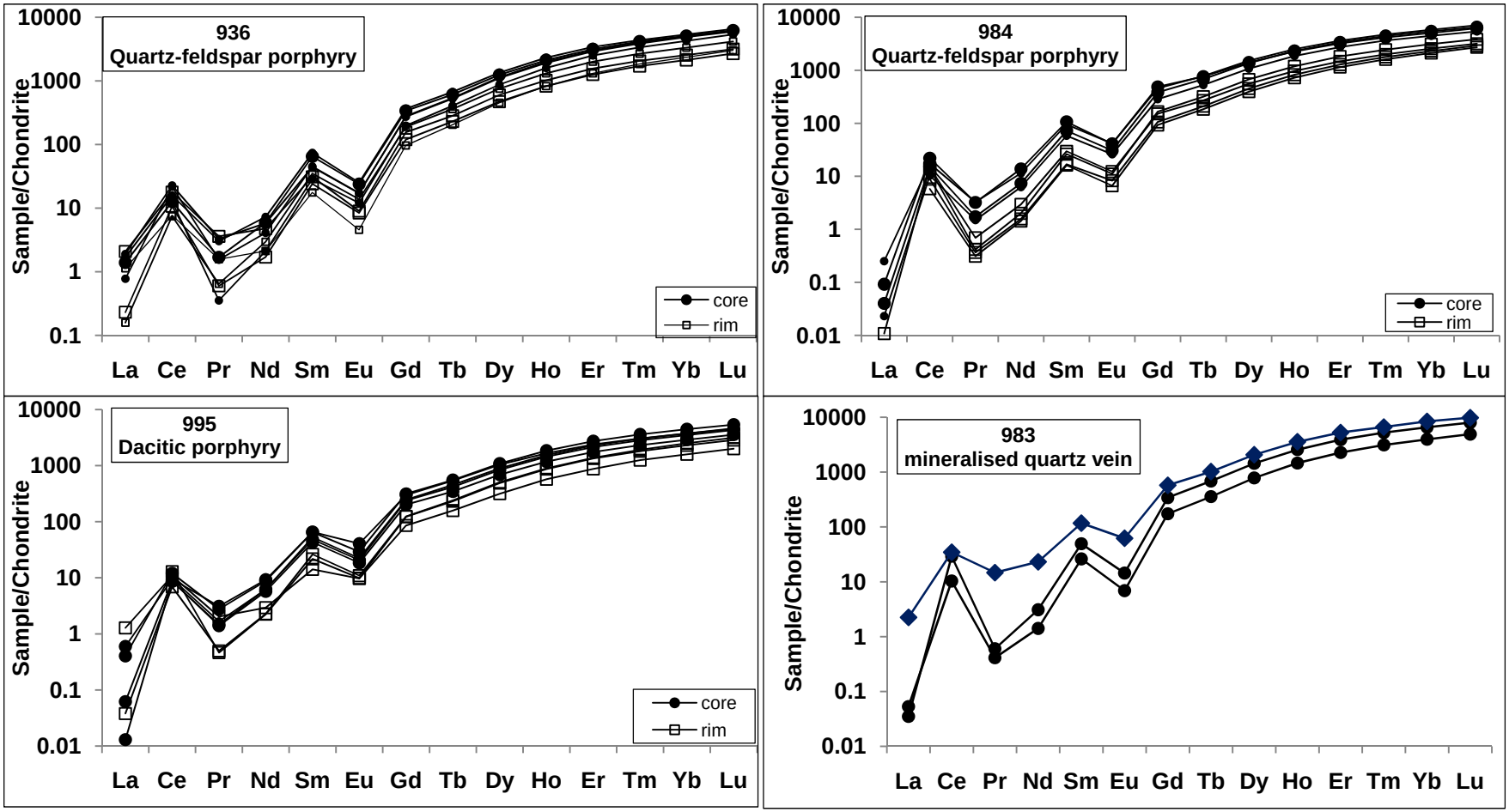

Figure 6.5.3.1. Chondrite normalised REE patterns of zircons from two quartz-feldspar porphyries (936 & 984), one dacitic porphyry (995) and one mineralised quartz vein from the Red Dome deposit; all data are normalised to chondrite values of Anders & Grevesse (1989).

The steepness of HREE expressed as $(Lu/Gd)_N$ ranges from 19 to 34, with an average of 24 ± 4 (2 STD) which is typical for crustal derived zircons (Fig. 6.5.3.2.B). Sample 984 shows stronger Ce-anomalies with values 20 to 172 (Tab. 6.5.) and an average of 69 ± 44 (n=14, 2 STD), suggesting that this porphyry was derived from a slightly more evolved source than sample 936, but the values are too low to be the source for copper mineralisation. The HREE in the form of $(Lu/Gd)_N$ fall within the range of sample 936 (Fig. 6.5.3.2.B: values of 13 to 29), but the Eu-anomaly of sample 984 is slightly less negative with an average value of 0.19 ± 0.01 (n=14, 2 STD) than sample 936.

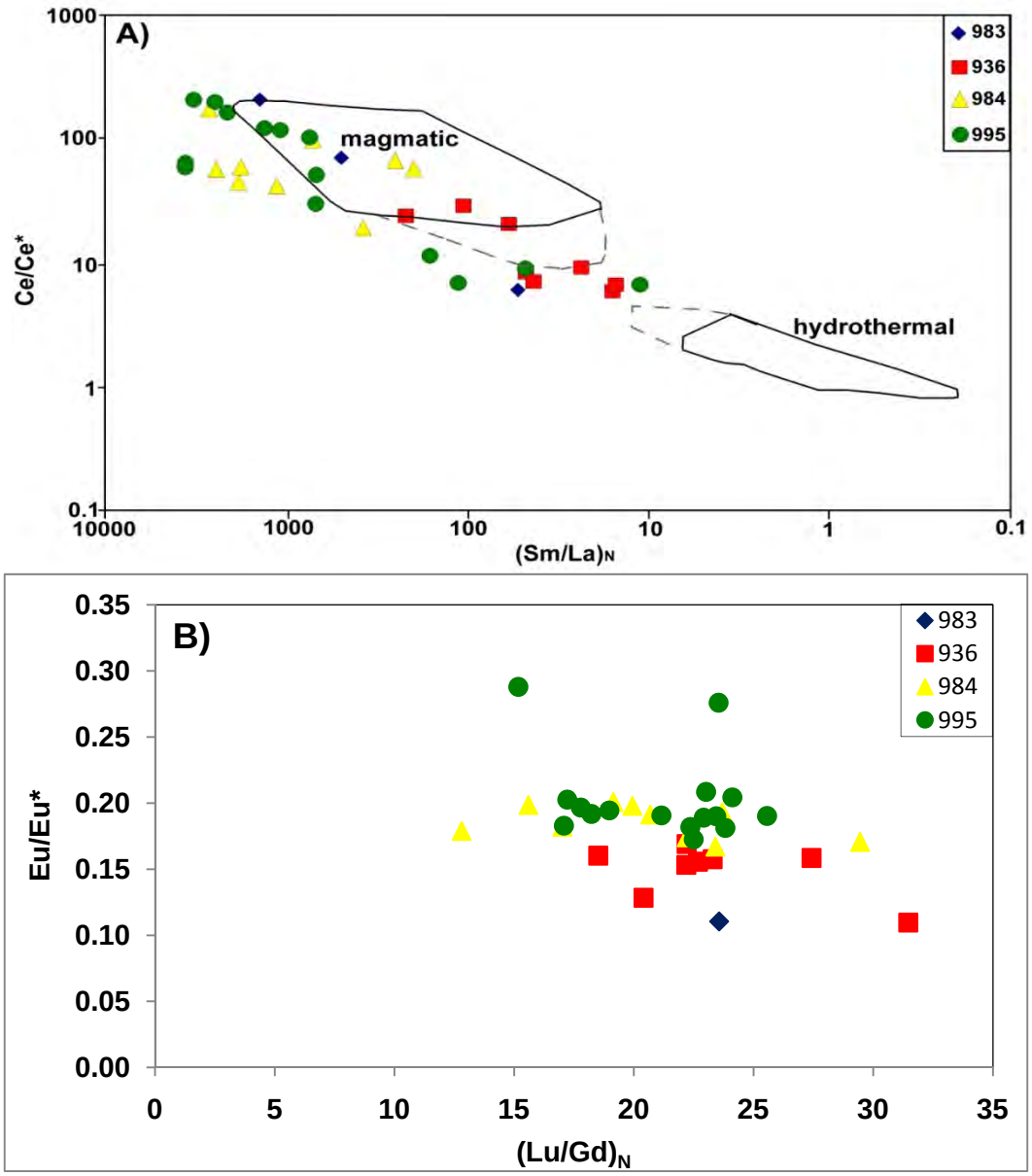

Figure 6.5.3.2. Plot of Ce/Ce* versus $(Sm/La)_N$ (**A**) and Eu/Eu* versus $(Lu/Gd)_N$ (**B**) of zircons from two quartz-feldspar porphyries (936 & 984), one dacitic porphyry (995) and one mineralised quartz vein from the Red Dome deposit with magmatic and hydrothermal field taken from Hoskin (2005).

The majority of zircon grains from the dacitic porphyry (995) show again stronger positive Ce-anomalies than the two quartz-feldspar porphyries 936 and 984 with an average of 82 ± 71 (2 STD). Four out of 14 analyses yielded very low Ce/Ce* values, but as La concentrations of these analyses are one order of magnitude higher than for the remaining grains, it is possible that LREE subsurface inclusions were accidentally hit. The Eu-anomaly of sample 995 reached similar values to sample 984 (Fig. 6.5.3.2.B), ranging from 0.17 to 0.29 (Tab. 6.5), whereas $(Lu/Gd)_N$ yielded an average of 21 ± 3 (n=16), suggesting a crustal source.

Only three analyses of zircons from the mineralised quartz vein (983) were obtained, yielding a variety of results for the Ce-anomaly and only one result for Eu/Eu* and $(Lu/Gd)_N$ (Tab. 6.5.), but the values for the Ce-anomaly plotted against the steepness of the LREE (expressed as Sm/La_N, Fig. 6.5.3.2.A) suggests that these zircons are of magmatic origin and not hydrothermal.

6.6. Hf isotopes

The Lu-Hf isotope system of zircon can be used to track crustal and mantle evolution processes as well as to identify the source from which the zircon originated (Patchett et al. 1981; Patchett, 1983; Vervoort et al. 1996; Blichert-Toft & Albarède 1997; Amelin et al. 1999; Kinny & Maas 2003; Hawkesworth & Kemp 2006; Kemp et al. 2007; Scherer et al. 2007). While Hf concentrations in zircon can range from 0.5 to 2 wt.-% (Hoskin & Schaltegger 2003; Wu et al. 2006), lutetium content of zircon is relatively low resulting in very low Lu/Hf ratios of typically 0.002 or much less (Kinny & Maas 2003). During magma development the mantle gets depleted in Hf as it is more compatible than Lu in the melt than in the residual mantle, resulting in Lu/Hf ratios higher than chondrite values in the depleted mantle and Lu/Hf ratios lower than chondrite values in the crust (Kinny & Maas 2003; Scherer et al. 2007). Due to β-decay of ^{176}Lu to ^{176}Hf the $^{176}Hf/^{177}Hf$ ratio of the mantle will therefore become more radiogenic over time whereas the $^{176}Hf/^{177}Hf$ ratio of the crust becomes relatively unradiogenic. Due to low Lu/Hf ratios, zircon will retain a near-initial $^{176}Hf/^{177}Hf$ ratio and therefore preserve its information of the source at the time of its formation (Kinny & Mass 2003). The difference between the $^{176}Hf/^{177}Hf$ ratio of a sample and the $^{176}Hf/^{177}Hf$ ratio of chondrites in parts per ten thousand is expressed as epsilon units.

While the bulk silicate earth is conventionally assumed to have ε_{Hf} values of zero, zircons derived from depleted mantle exhibit positive ε_{Hf} values whereas zircons which originated from existing crustal material may have negative ε_{Hf} values (Fig. 6.6.).

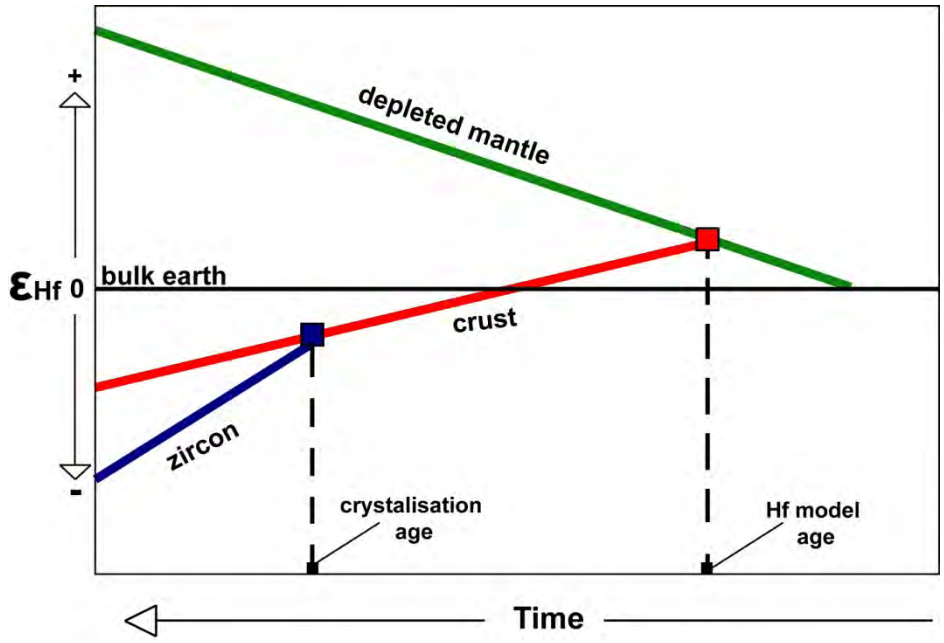

Figure 6.6. Schematic evolution of ε_{Hf} versus time; modified from (Scherer et al. 2007).

In addition to the initial $^{176}Hf/^{177}Hf$ ratio and ε_{Hf} value at the time of magma crystallisation, it is also possible to estimate the time at which the crustal source material was extracted from the depleted mantle. This age is called the Hf model age.

6.6.1. Methodology

Hafnium isotopes were determined using a GeoLas 193 nm ArF laser coupled to a Thermo-Scientific Neptune multi-collector ICP-MS at the AAC-JCU (Townsville). The ablated material was transported by a gas mixture of argon, helium and nitrogen into the MC-ICP-MS unit with the nitrogen reducing possible oxide formation and enhancing the sensitivity (Iizuka & Hirata 2005). Data were collected for 60 seconds with the laser fluence kept at 6 J/cm^2 and a repetition rate of 4 Hz. Where possible the spot size was kept at 60 µm, but in some places it had to be reduced to 44 µm to make sure that no mixing of different growth zones, especially inherited cores, occurred. In total eight isotopes were measured these being ^{171}Yb (L4), ^{173}Yb (L3), ^{175}Lu (L2), ^{176}Hf, ^{176}Lu, ^{176}Yb (L1), ^{177}Hf (C), ^{178}Hf (H1), ^{179}(H2) and ^{180}Hf (H3), with the Faraday cup configuration for each isotope being mentioned in brackets.

The reference zircon Mud Tank ($^{176}Hf/^{177}Hf$ 0.282507 ± 6, Woodhead & Hergt 2005) was used for external calibration, whereas reference zircons FC1 ($^{176}Hf/^{177}Hf$ 0.282184 ± 16, Woodhead & Hergt 2005) and GJ-1 ($^{176}Hf/^{177}Hf$ 0.282000 ± 5, Morel et al. 2008) were used as secondary standards as monitors of data quality. The raw isotope data were corrected for the isobaric interference of ^{176}Lu and ^{176}Yb on ^{176}Hf following the method of Kemp et al. (2009) and using

the $^{176}Yb/^{171}Yb$ value of Segal et al. (2003) and $^{176}Lu/^{175}Lu$ value of Vervoort et al. (2004). Initial $^{176}Hf/^{177}Hf$ ratios and $\varepsilon_{Hf(t)}$ units were then calculated using the measured $^{176}Lu/^{177}Hf$ and $^{176}Hf/^{177}Hf$, the $^{176}Lu/^{177}Hf_{CHUR}$ and $^{176}Hf/^{177}Hf_{CHUR}$ parameters of Bouvier et al. (2008) and the ^{176}Lu decay constant of Söderlund et al. (2004), whereas Hf depleted mantle model ages (T_{DM}) were calculated using $^{176}Lu/^{177}Hf_{DM}$ and $^{176}Hf/^{177}Hf_{DM}$ parameters of Griffin et al. (2002). In general the ^{207}Pb corrected weighted mean $^{206}Pb/^{238}U$ ages were used as crystallisation age (see chapter 5), except for the inherited cores where the individual measured ages were used.

In this section Hf isotopes of zircons from Redcap, Red Dome and Mungana are presented with a summary of the data being provided in table 6.6 whereas additional data are listed in appendix 15.

Table 6.6.1. Summary of initial $^{176}Hf/^{177}Hf$ and $\varepsilon Hf_{(t)}$ values for zircons from igneous rocks of Redcap, Red Dome and Mungana

Sample ID	Rock type	Age ± 2σ [Ma]	Initial $^{176}Hf/^{177}Hf$	$\varepsilon_{Hf(t)}$
949	Dacite	310 ± 2	0.282242-0.282413	(-12.3)-(-6.3)
952W1	Dacite	306 ± 2	0.282258-0.282383	(-11.8)-(-7.4)
BE-1 (P-I)	Granodiorite	309 ± 2	0.282414-0.282453	(-6.3)-(-4.9)
BE-1 (P-II)	Granodiorite	297 ± 2	0.282320-0.282407	(-9.8)-(-6.8)
----	Inherited grains	1516 ± 20 1523 ± 13	0.281694-0.282349	(-4.4)-(-4.0)
883W2	Rhyolitic porphyry	324 ± 2	0.282328-0.282368	(-8.9)-(-7.5)
883W3	Granite	305 ± 2	0.282250-0.282330	(-12.2)-(-9.3)
936	Quartz-feldspar porphyry	322 ± 2	0.282285-0.282358	(-10.5)-(-7.9)
984	Quartz-feldspar porphyry	324 ± 2	0.282321-0.282366	(-9.2)-(-7.6)
983	Mineralised quartz vein	322 ± 2	0.282294-0.282325	(-10.2)-(-9.1)
995	Dacitic porphyry	311 ± 2	0.282350-0.282387	(-8.5)-(-7.2)

6.6.2. Redcap

Zircon grains from the Redcap dacite sample 949 have very similar initial $^{176}Hf/^{177}Hf$ ratios ranging from 0.282242 to 0.282413 (Tab. 6.6.1., Fig. 6.6.2.1.A) with an average of 0.282355 ± 34 (n=21, 2STD). The ε_{Hf} values at time of crystallisation (310 Ma) range from -12.3 to -6.3 with an average of -8.3 ± 1.2 (Fig. 6.6.2.1.B). Only one out of the 21 grains yielded a value well below the average, with an ε_{Hf} of -12.3. This and the difference of 6 ε units between the single zircon grains could indicate that either the source was contaminated by assimilation of country rocks as suggested by Champion and Chappell (1992) or that the source material was heterogeneous. In general, however, the Hf isotope compositions indicate that the host magma from which the zircons crystallised was derived from old crustal material. The depleted mantle model age of the zircons yielded an average of 1260 ± 51 Ma (n=21, 2STD).

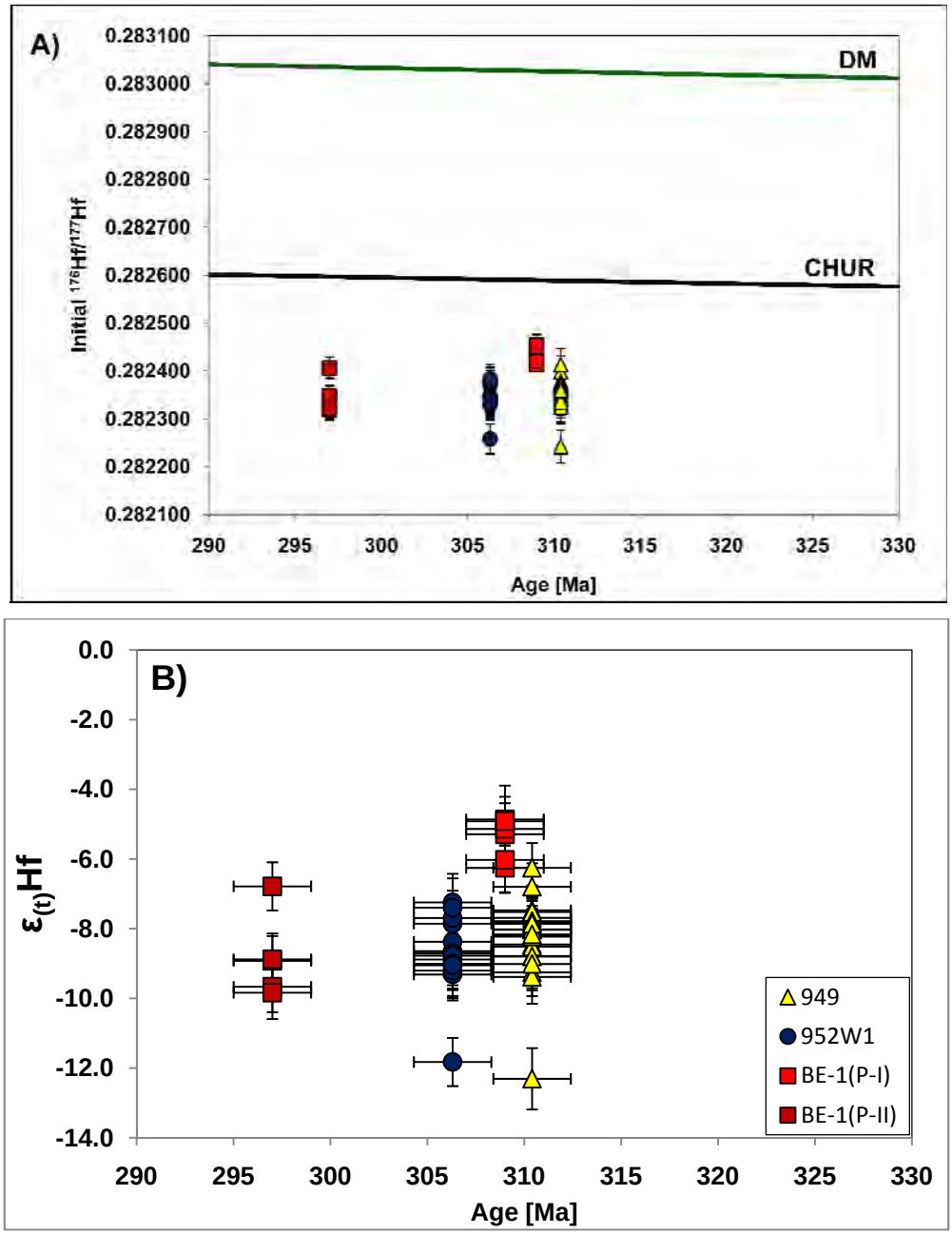

Figure 6.6.2.1. Plot of initial $^{176}Hf/^{177}Hf$ concentrations (**A**) and εHf(t) values (**B**) versus crystallisation age of zircons from two Redcap dacites (949 & 952W1) and two zircon populations of the Belgravia granodiorite; the black line in A, and in all subsequent 176Hf/177Hf versus time plots, is the chondritic uniform reservoir (CHUR) evolution curve calculated using the values of Bouvier et al (2008) and the green line being the depleted mantle (DM) evolution curve calculated using the values of Griffin et al. (2002).

The second Redcap dacite sample (952W1) yielded nearly identical initial Hf isotope compositions with an average of 0.282345 ± 31 (2 STD) and an average ε_{Hf} value (t=306 Ma) of -8.7 ± 1.1 (n=14). The model ages (T_{DM}) are also similar to the ones observed in sample 949 ranging from 1223 to 1392 with an average of 1276 ± 43. As for sample 949, the difference in ε_{Hf} value is relatively high at 4.4 units. One out of 14 grains has lower than average initial $^{176}Hf/^{177}Hf$ with 0.282258 ± 17 (Fig.6.6.2.1.A) and shows also the lowest ε_{Hf} value (-11.8, Fig.

6.6.2.1.B) and depleted mantle model age (1392 Ma). As the CL microstructure of this grain shows fine oscillatory zoning, the Hf ratio is likely caused by sampling material with different isotope signatures, suggesting again a mixed source or assimilation of the country rocks.

The two zircon populations of the Belgravia granodiorite identified from age and CL characteristics (BE-1) are distinguished regarding their initial Hf isotope composition and epsilon values. While the older zircon group (P-I: 309 Ma) has $^{176}Hf/^{177}Hf$ ratios of on average 0.282438 ± 48 (n=6), ε_{Hf} values of -5.4 ± 0.6 (Fig.6.6.2.1.A & B) and T_{DM} age of 1150 ± 24, suggesting a more juvenile source, the younger zircon population (P-II: 297 Ma) yielded Hf isotope concentrations of on average 0.282348 ± 22 and ε_{Hf} values of on average -8.8 ± 1.2 (n=5), which are within the error of the ones observed in sample 949 and 952W1.

Four analyses of Mesoproterozoic cores have nearly identical initial $^{176}Hf/^{177}Hf$ and ε_{Hf} values of 0.281700 ± 5 (n=4, 2 STD) and -4.2 ± 0.2, respectively (Fig. 6.6.2.2.A & B). Hafnium model ages of the depleted mantle yielded an average of 2126 Ma ± 6.

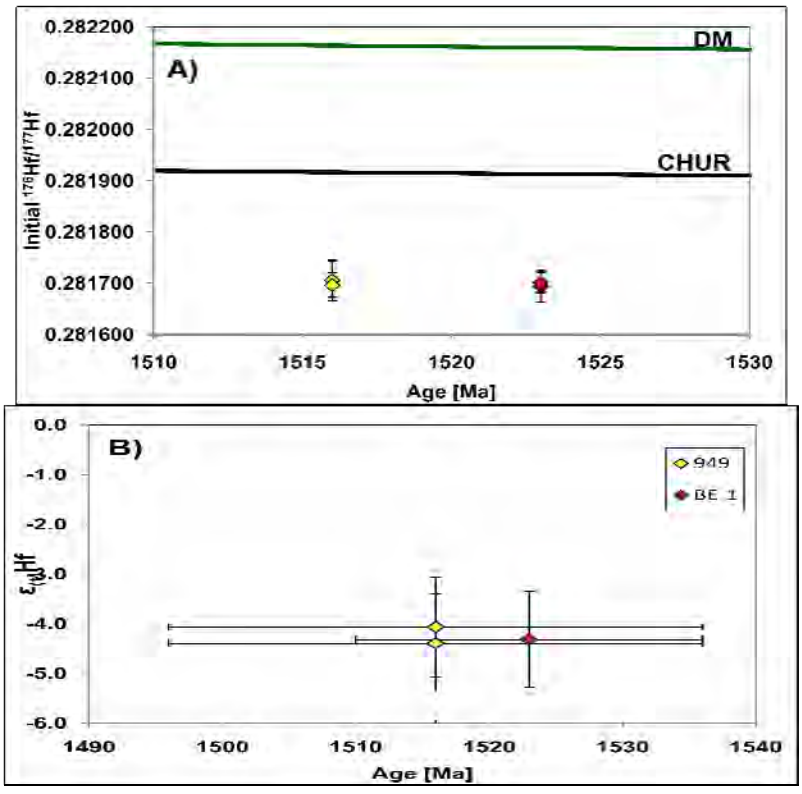

Figure 6.6.2.2. Plot of initial $^{176}Hf/^{177}Hf$ concentrations (**A**) and $\varepsilon_{(t)}Hf$ values (**B**) versus crystallisation age of zircons from the inherited cores of Redcap.

6.6.3. Mungana

Zircons from the rhyolitic porphyry (883W2) of Mungana yielded very similar initial $^{176}Hf/^{177}Hf$ concentrations of 0.282328 to 0.282368 with an average of 0.282344 ± 20 (Tab.6.6.1, Fig. 6.6.3.A.). The ε_{Hf} values are also similar ranging from -8.9 to -7.5 (Tab.6.6.1, Fig. 6.6.3.B.) with an average of -8.4 ± 0.4 (t= 324 Ma, n= 14), suggesting an old crust as source. The Hf isotope compositions of the porphyry are within error of the values determined for the two Redcap dacites (949 & 952 W1) and the younger zircon population from the Belgravia granodiorite, but are more homogenous and have a slightly older Hf model age of 1307 Ma ± 20, although the model ages overlap.

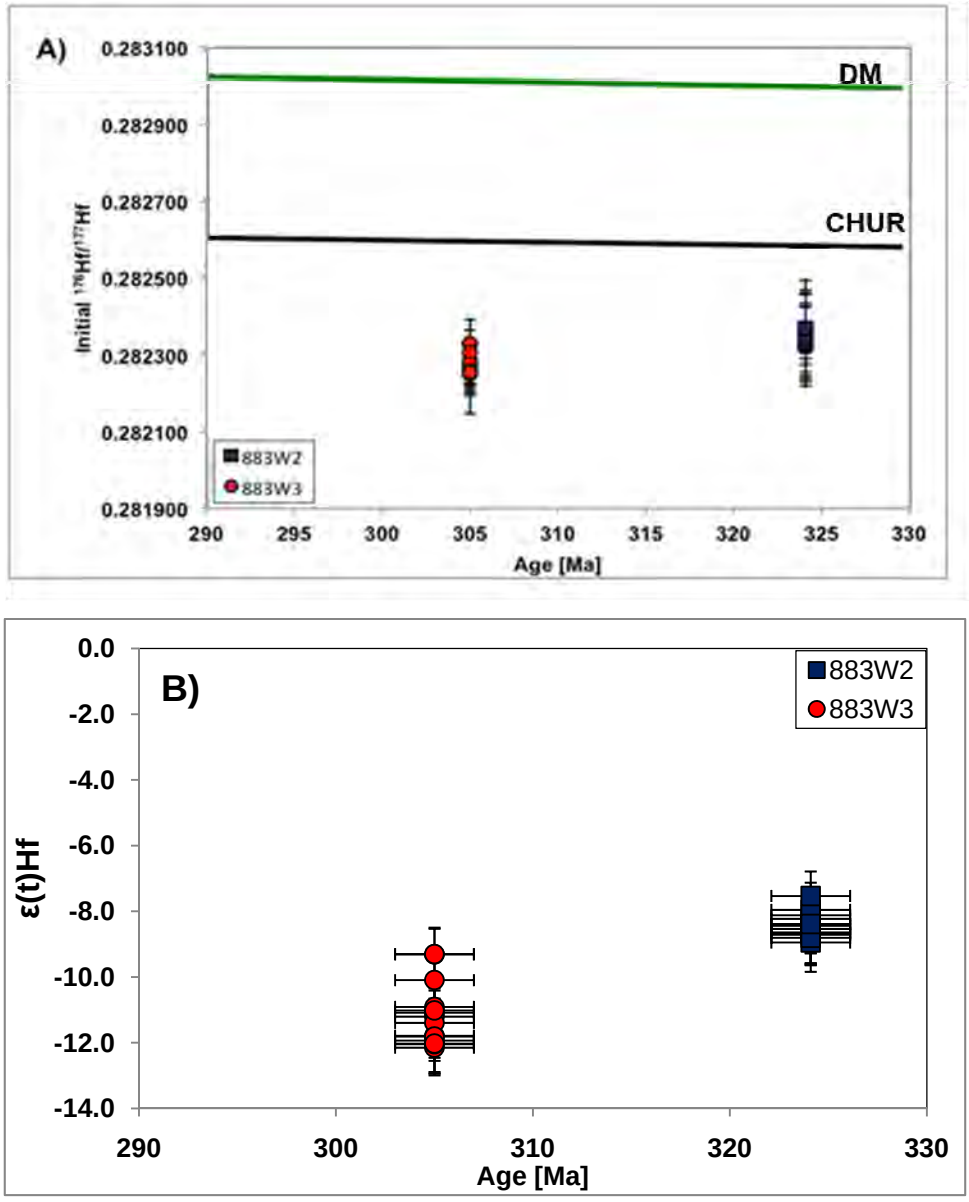

Figure 6.6.3. Plot of initial $^{176}Hf/^{177}Hf$ concentrations (**A**) and $\varepsilon_{(t)}Hf$ values (**B**) versus crystallisation age of zircons from a porphyry (883W2) and granite (883W3) of Mungana.

The Mungana granite (883W3) has different $^{176}Hf/^{177}Hf$ ratios from the porphyry ranging from 0.282250 to 0.282330 with an average of 0.282277 ± 27 (n= 15, 2 STD) and ε_{Hf} values of on average -11.2 ± 0.9 (Fig. 6.6.3.B), suggesting that the granite was derived from a crustal source which is less radiogenic, and thus possibly older, than the ones for the other igneous rocks investigated in this study. The depleted mantle model age (average 1377 Ma ± 31, n=15) is slightly older than the one calculated for the Mungana porphyry.

6.6.4. Red Dome

Zircon grains from one of the two quartz-feldspar porphyries (936) of Red Dome yielded very similar average initial $^{176}Hf/^{177}Hf$ concentrations of on 0.282325 ± 24 (n = 11, 2 STD) and average ε_{Hf} values of -9.1 ± 0.9 (Fig. 6.6.4.A & B), all indicating that zircons were derived from an old crustal source. Three out of 11 analyses with ε_{Hf} values of -10.2 to -10.5 form a separate group with these lower than average values perhaps caused by assimilation of country rock material. Depleted mantle model ages yielded on average 1377 Ma ± 31, which falls within the error of the model age calculated for the Mungana porphyry (883W2). The second quartz-feldspar porphyry sample (984) yielded very similar ε_{Hf} values and Hf model ages to sample 936.

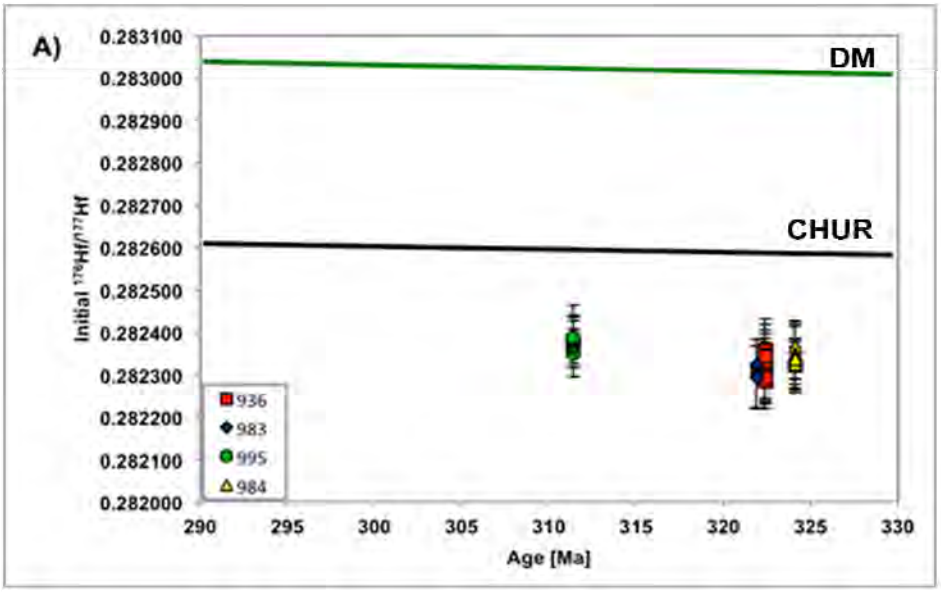

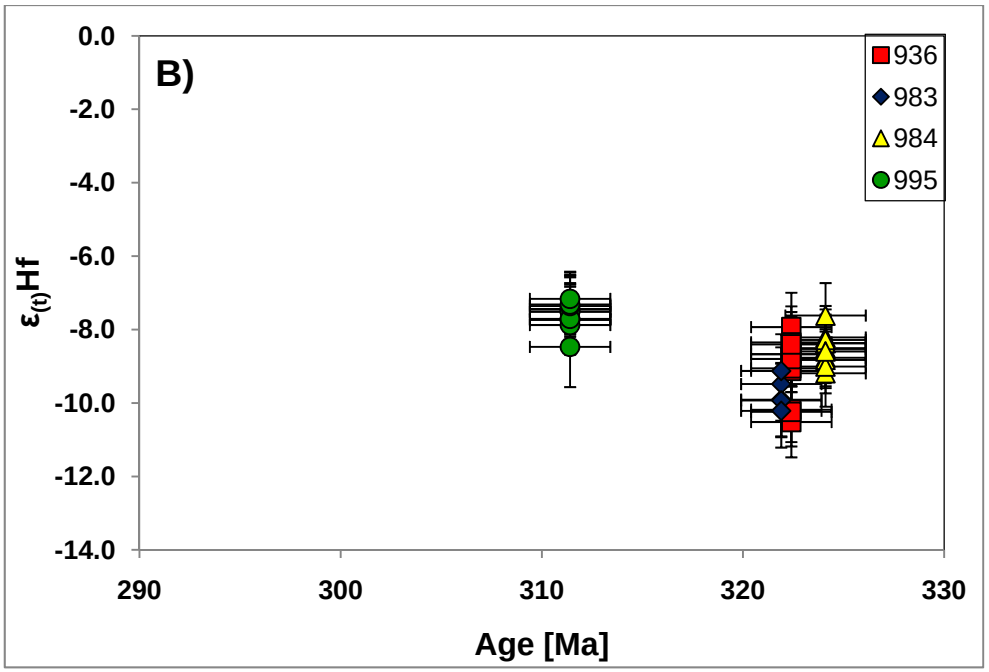

Figure 6.6.4. Plot of initial $^{176}Hf/^{177}Hf$ concentrations (**A**) and $\varepsilon_{(t)}Hf$ values (**B**) versus crystallisation age of zircons from two quartz-feldspar porphyries (936 & 984), one dacitic porphyry (995) and one mineralised quartz vein (983) from the Red Dome deposit.

The initial $^{176}Hf/^{177}Hf$ ratios range from 0.282321 to 0.282366 with an average of 0.282340 ± 12 (n = 12, 2 STD), ε_{Hf} values of -9.2 to -7.6 with an average of -8.5 ± 0.4 (Fig. 6.6.4.A & B) and average depleted mantle model ages of 1312 Ma ± 12. Only five analyses of the mineralised quartz-vein (983) were obtained yielding average $^{176}Hf/^{177}Hf$ of 0.282307 ± 12, average ε_{Hf} values of -9.7 ± 0.4 and average Hf model ages of 1396 ± 14 Ma with all values being similar to the ones obtained for samples 936 and 984.

Zircon grains from the dacitic porphyry (995) have very similar $^{176}Hf/^{177}Hf$ ratios with an average of 0.282374 ± 20 (n =15, 2 STD), similar to the values of the other three porphyry samples (Fig. 6.6.4.A & B). The ε_{Hf} values range from -8.5 to -7.2 with an average of -7.6 ± 0.4 and Hf model ages yielded on average 1258 ± 30 Ma, which is similar to those calculated for 949, 952W1 and the younger zircon group of the Belgravia granodiorite.

6.7. Summary

Zircon grains from the two Redcap dacite samples have nearly identical Th, U, Zr, Hf and Y concentrations, very similar crystallisation temperatures, Ce- and Eu-anomalies and initial $^{176}Hf/^{177}Hf$ and depleted mantle model ages. Neither the younger than 301 Ma zircon population of 949 nor the 321 Ma zircon group of sample 952W1 can be distinguished from the majority of other zircons based on trace elements and Hf isotopes. Based on nearly identical trace element

chemistry and Hf isotope concentrations it can be concluded that both dacites are derived from the same source, with no juvenile material input (Fig. 6.7.1).

The two zircon populations of the Belgravia granodiorite are chemically very similar to each other and the Redcap dacites, except that the Eu-anomalies of the Belgravia granodiorite zircons are slightly smaller than in the dacite and that Ce-anomalies indicate a little more oxidised environment (Fig. 6.7.2.). The only differences between the two age populations of the Belgravia granodiorite are their ε_{Hf} values (Fig. 6.7.1.). While the younger zircon group shows very similar values to the Redcap dacites, the older zircon group has more radiogenic values, indicating that a more juvenile component was involved, which suggests that two sources with distinguishable isotope signatures were mixed. These sources may have been a basaltic and felsic magma as proposed by De Keyser & Wolff (1964), Branch (1966) and Black & Richards (1972a), or an assimilation of country rock material by a mantle derived magma as assumed by Black & McCulloch (1990) and Champion & Chappell (1992), which would shift the isotope ratios towards radiogenic values. The latter theory was also suggested in the Lachlan Fold Belt by Kemp et al. (2007).

The two Mesoproterozoic zircon grains cannot be distinguished from the other igneous rocks of the Redcap deposits based on their Th, U, Zr, Hf and Y concentrations and crystallisation temperatures, but can be differentiated based on their REE pattern, Eu-anomalies and initial Hf isotope ratios. One grain (BE-1) has low total REE and HREE concentrations, suggesting that the zircon experienced metamorphism. The other zircon grain (949) does not differ from the Redcap dacite and Belgravia granodiorite. Hf isotope ratios of both grains yielded identical εHf values (Fig. 6.7.1.) suggesting that they were derived from the same source with depleted model ages of 2126 Ma confirming this assumption. Therefore the different trace element behaviour cannot be related to two different sources, but could be due to a metamorphic event. At around 1550 Ma granulite facies metamorphism occurred in the area (Black et al. 1998), which caused the recrystallisation and resetting of zircons, indicated by convolute zoned CL structures of grain 949. While the Lu and Hf isotope concentrations were not affected by the metamorphism due to their very low diffusion rate (Cherniak et al. 1997a), trace elements, especially LREE, become expelled from the zircon lattice, resulting in flatter LREE patterns and very weak to undeveloped Ce-anomalies as observed on zircons from the Georgetown Region by Hoskin & Black (2000).

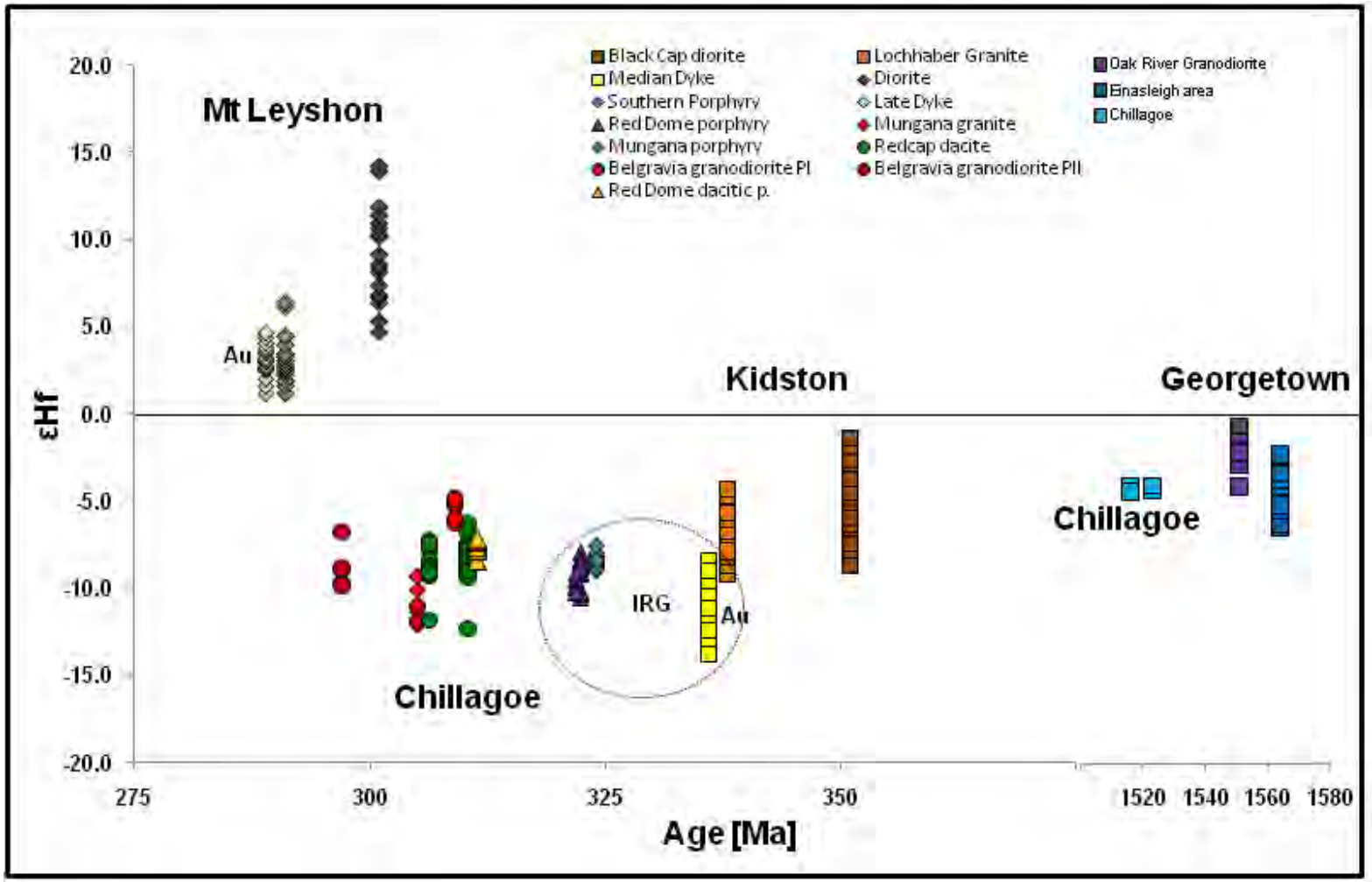

Figure 6.7.1. Summary of εHf values of igneous rocks of the Chillagoe district, and selected εHf values of igneous rocks of the Mt Leyshon and Kidston deposits and the Georgetown inlier with εHf values other than Chillagoe taken from Murgulov et al. (2007, 2008, 2009) and Au indicating the gold-bearing intrusions at Mt Leyshon and Kidston. The circle indicates a link between intrusions and IRG mineralisation.

The general similarity of the inherited zircon grains and the ones from the Redcap dacite and Belgravia granodiorite and the model age of 2126 Ma, supports the theory of Black & McCulloch (1990) that 2.0 to 2.5 Ga metasedimentary crust has been remelted in three stages at around 1550 Ma (the inherited grain), at ~420 Ma (not observed) and ~300Ma (igneous rocks of Redcap) resulting in an increasing degree of fractionation of the rocks with the inherited grains being less fractionated than the Belgravia granodiorite (Fig. 6.7.2.)

Zircon grains from the Mungana porphyry have higher Th, Hf, Y total REE and HREE concentrations than the Mungana granite, but lower Zr concentrations, crystallisation temperatures and Ce- and Eu-anomalies. The higher crystallisation temperatures of the granite as well as higher Zr/Hf and Hf/Y ratios suggest that the granite was derived from a less chemically evolved, but more oxidised system than the porphyry (Fig. 6.7.2.). Due to chemical and isotopic similarities of the Mungana granite to the Redcap dacites and Belgravia granodiorite it is possible that it was derived from the same source (Fig. 6.7.1.), but like for the Redcap samples it remains uncertain whether any country rock material was assimilated or metasedimentary crust was remelted by juvenile magma. One way to check whether sedimentary material was assimilated by mantle derived magma would be oxygen isotope studies of the zircon grains, as these isotopes can help to distinguish between igneous and sedimentary reworked zircons (e.g. Hawkesworth & Kemp 2006). This would also be important to get a better understanding of the origin of the mineralisation, as either metal input by juvenile basaltic magma like at Mt Leyshon (Murgulov et al. 2008) took place, or multi stage remelting of old crustal material resulted in metal enrichment in the most fractionated phase as proposed by Lang & Baker (2001) and proposed by Murgulov et al. (2009) within the Kidston deposit.

Zircon grains from the mineralised quartz-vein (983), the two quartz-feldspar porphyries (936 & 984) and the dacitic porphyry (995) of the Red Dome deposit show a trend regarding their trace element chemistry from 983 via 936 and 984 to 995. While Th, U, Hf, Y and REE concentrations decrease from 983 to 995 with minor overlapping of samples 936 and 984, Zr/Hf &Hf/Y ratios, Ce- and Eu anomalies increase from 983 to 995, whereas the crystallisation temperatures of all samples exhibit very similar values. This trend suggests that zircons from the mineralised quartz vein and the quartz-feldspar porphyries were derived from a more fractionated and less oxidised source than the dacitic porphyry (Fig. 6.7.2.). In addition zircons from the mineralized quartz vein do not show any evidence for a juvenile input linked to mineralisation, as suggested by Murgulov et al. (2008) for the Mt. Leyshon deposit, with their Hf isotope concentrations being similar to samples 936 and 984, suggesting that they originated from the same source.

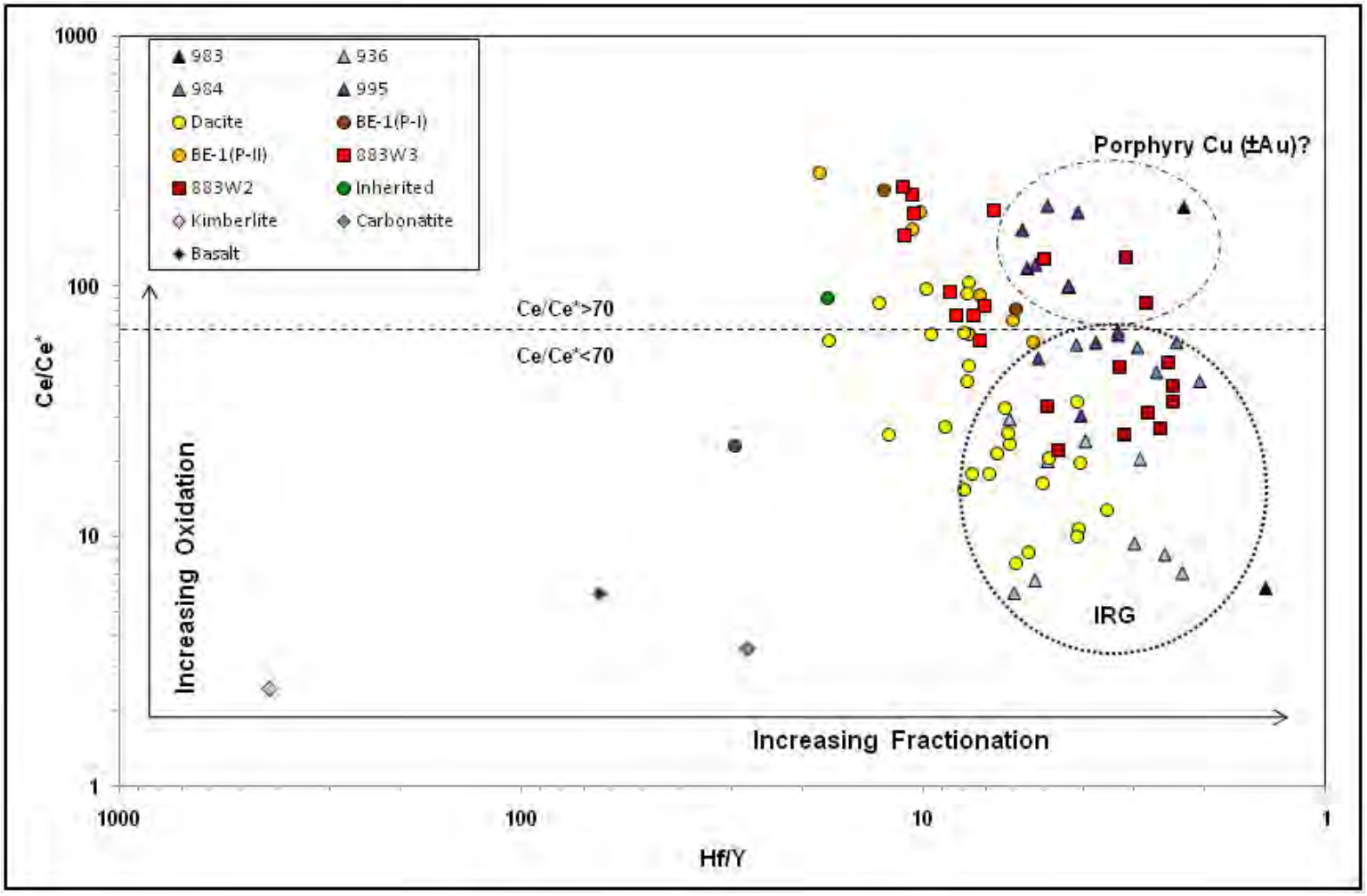

Figure 6.7.2. Plot of oxidation state versus degree of fractionation for igneous rocks of the Redcap, Mungana and Red Dome deposit with oxidation state being expressed as Ce/Ce* and degree of fractionation as Hf/Y ratio; kimberlite, carbonatite and basalt values taken from Belousova et al. 2002, Ce/Ce* </>70 (dashed line) from Ballard et al. 2002 and dotted and dashed circles showing possible discrimination fields for IRG and porphyry Cu deposits.

Trace element and Hf isotopes of zircons from 936 and 984 are very similar to the ones obtained for the porphyry of Mungana (883W2), suggesting that they were derived from a similar source (Fig. 6.7.1.). The Ce-anomalies of samples 936, 984 and 883W2 (15 ± 9, 61 ± 19 and 40 ± 18, respectively, 2STD) are well below the minium of 70 suggested by Ballard et al. (2002) for Cu porphyry systems, whereas Ce-anomalies of 995 indicate that the porphyry was oxidised enough to be the source for Cu mineralisation (Fig. 6.7.2.), which would also explain why copper is one of the dominant ore phases at Red Dome, but not at Mungana. Hf isotope concentrations and Hf model ages of 936, 983, 984 and 883W2, on the other hand are within the error of Hf isotope signatures of the gold-bearing porphyry of the Kidston deposit (Murgulov et al. 2009), suggesting that these porphyries might have been the source of the gold mineralisation at the Red Dome and Mungana deposit under the assumption that gold was enriched in the most fractionated phase due to multi stage reworking of older crustal material which is suggested for IRG systems (Lang & Baker 2001).

Chapter 7: Summary and discussion

7.1. Introduction

This chapter summarises and discusses the results of petrographical, mineral chemical, geochronological and isotopic studies of the Redcap, Mungana and Red Dome deposits in the context of previous work and the general aims of this thesis. In the next sections the genesis of the Redcap, Mungana and Red Dome deposit is presented, the use of mineral chemistry and isotope concentrations of silicate and sulphide phases as exploration tools is outlined, and information about the evolution of the magmatic system including its source environment and relative duration are provided.

7.2. Genesis of the polymetallic Redcap, Mungana and Red Dome deposits

The polymetallic Redcap, Mungana and Red Dome deposits are multiphase systems comprising four stages of host rock formation and alteration (chapter 3), as well as two major cycles of mineralising events related to the occurrence of two magmatic events (chapter 5 & 6, Fig. 7.2). Both events are present at the Mungana and Red Dome deposits whereas the occurrence of the first intrusive phase is only assumed for Redcap based on the similarities of the three deposits to each other. The initial phase (~326-320 Ma) was the emplacement of rhyolitic porphyries (~750-650°C) causing contact metamorphism and resulting in recrystallisation of limestone to marble, bleaching of the siliciclastic units and basalts as well as in the formation of banded skarn (chapter 3: plate 3.2.1.1.E, plate 3.2.1.2.A & B) and the development of quartz stockwork with these characteristics agreeing well with the descriptions made by Rose & Burt (1979) and Einaudi et al. (1981) for general evolution of skarn deposits. The second stage is prograde metasomatism (~650-440°C), which can be subdivided into early hedenbergite-K-feldspar skarn (chapter 3: plate 3.3.2.4.), andradite-garnet skarn with associated magnetite (chapter 3: plate 3.2.3.1.), andradite-wollastonite-vesuvianite skarn (chapter 3: plate 3.3.2.3.) and late grossular-diopside-calcite skarn (chapter 3: plate 3.2.3.2.). The abundance of single types varies at the three deposits, which could be due to different proportions of various country rocks. With the exception of the wollastonite-garnet-(± vesuvianite) skarn the formation of the other three skarn types again agrees well with the descriptions of Rose & Burt (1979) and Einaudi et al. (1981). While Torrey (1986) proposed that the wollastonite-garnet skarn at Red Dome is related to the second magmatic event, Sn-bearing garnets in the wollastonite skarn (observed in all three deposits, chapter 4: section 4.2.4.) and a Re-Os age (335 Ma) of molybdenite intergrown with wollastonite from Mungana (chapter 5: plate 5.3.1.) suggest that the wollastonite skarn can be related to the first magmatic event and formed by continuing metasomatism and decomposition

after the equations 1 to 3 with the skarn front moving towards the marble contact as proposed by Meinert et al. (2005).

1.) 9 hedenbergite + 2 O_2 ↔ 3 andradite + 9 quartz + magnetite (Gustafson 1974)

2.) 18 quartz + 18 calcite + 4 magnetite + O_2 ↔ 6 andradite + 18 CO_2 (Taylor & Liou 1978)

3.) quartz + calcite ↔ wollastonite + CO_2 (Harker & Tuttle 1956)

4.) 2 vesuvianite + 5 wollastonite + 6 CO_2 ↔ 11 grossular + 4 diopside + 6 calcite + 9 H_2O (Valley et al. 1985)

5.) 3 grossular + 5 CO_2 + H_2O ↔ 2 epidote + 5 calcite + 3 quartz (Valley et al. 1985)

6.) diopside + calcite ↔ actinolite + CO_2 (Valley et al. 1985)

The wollastonite skarn then retrogresses to grossular-diopside-calcite skarn following equation 4 with minerals from this skarn type getting replaced by hydrous minerals (equation 5 & 6), such as epidote, actinolite, sericite and chlorite (chapter 3: plate 3.3.2.1.C, plate 3.4.1.1.E & F), which are typical minerals of stage three (retrograde metasomatism: <400 °C), again agreeing with the skarn evolution described by Rose & Burt (1969) and Einaudi et al. (1981). The last stage is represented by weathering, resulting in the formation of clay minerals (e.g. kaolinite, nontronite and many more) as well as iron-hydroxides such as goethite and limonite.

Rose & Burt (1979) and Einaudi et al. (1981) suggested that the skarn formation can be accompanied by mineralising events ranging from the prograde high T metasomatic stage (~500 °C) to the retrograde low T stage (~200 °C). Their theory is valid for the Redcap, Mungana and Red Dome deposits in general, although mineral deposition started at higher temperatures (≤ ~600 °C), and continued to even lower temperatures than 200 °C.

Overall the skarn formation related to an intrusion-related gold (IRG) system is similar to the processes in other intrusion-related skarn systems as described in detail by Rose & Burt (1979), Einaudi et al. (1981) and Meinert et al. (2005). The mineralisation hosted in the skarns on the other hand is more diverse at the Redcap, Mungana and Red Dome deposit of the Chillagoe district than in classic Cu Fe, Mo, Sn, W, Zn and Au skarns as described by Einaudi et al. (1981) and Meinert (1989). The three deposits show some similarities regarding the mineral assemblages related to the primary magmatic event, but differ regarding commodity type and abundance linked to the second magmatic event (Fig. 7.2.). Mineralisation related to the first magmatic event comprises Sn (incorporated in garnets), Zn (incorporated into hedenbergite and diopside; chapter 4), as well as molybdenite and scheelite either intergrown with calc-silicate phases or associated with quartz crosscutting either igneous rocks or skarn (chapter 3: plate 3.2.3.3.).

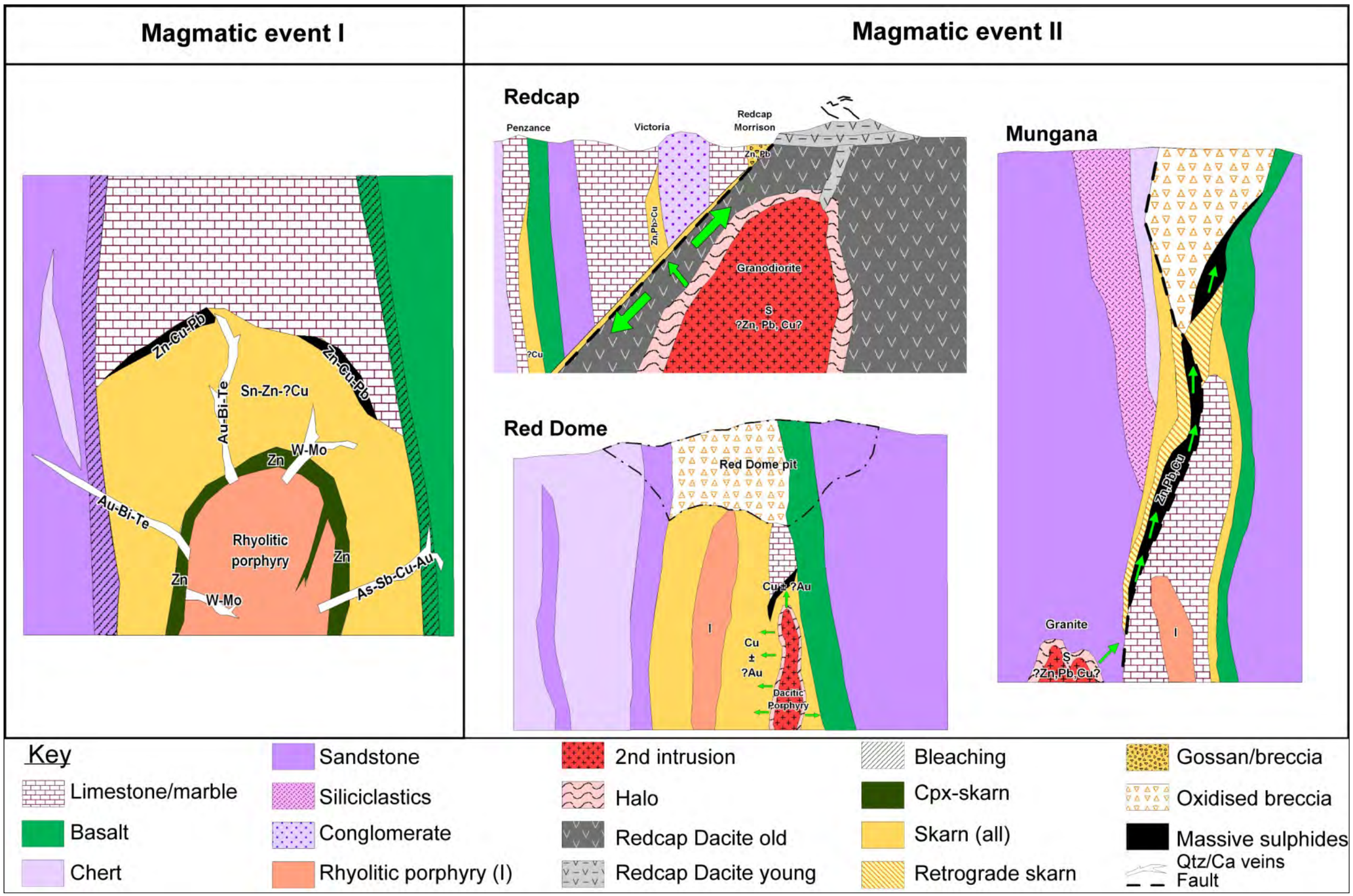

Figure 7.2. First and second magmatic event and their related metal commodities.

In addition arsenic bearing phases (loellingite and arsenopyrite; chapter 3: plate 3.3.3.2.) are also present although this commodity is not as abundant at Redcap as at Red Dome and Mungana, which could be because only the zinc-bearing Victoria line was investigated in detail in this study. Other metals like Au, Ag, Bi, Cu, Te, Pb and Sb can also be linked to the primary magmatic event (chapter 3: plate 3.3.3.2., plate 3.3.3.3., plate 3.4.2.3.), but their occurrence and abundance varies between the three deposits as outlined later in this section.

Especially interesting is the discovery that Sn and Zn were incorporated into the lattice of silicate phases (chapter 4: section 4.2.4.), as this indicates that the primary intrusion must have been reduced (confirmed by trace element chemistry of zircons, chapter 6), diverse regarding its metal potential, and sulphur poor allowing no major sulphide precipitation, which is typical for IRG systems (Lang & Baker 2001). Overall it remains unknown whether metal incorporation into silicate phases is a common feature for IRG systems as there are no data for comparison, but if it is common this would explain why some IRG systems lack obvious base metal mineralisation.

From the economic perspective the Recap, Mungana and Red Dome deposits differ regarding their major commodities (chapter 2: section 2.7.2. to 2.7.4. resource estimates). Redcap and Mungana are base metal dominant, which is unusual in comparison to other IRG deposits (Thompson et al. 1999), but they are also host to gold mineralisation, although the gold is associated with different metal assemblages. Red Dome, on the other hand, is dominated by copper mineralisation, with its abundance being unusually high for an IRG system (Thompson et al. 1999), and also contains gold mineralisation and a very minor base metal commodity.

The base metal mineralisation, which comprises sphalerite, chalcopyrite and galena as dominant ore phases (chapter 3: plate 3.2.4.1., plate 3.3.3.1.), is related to both magmatic events, with the second one being responsible for the untypical high grade of base metals for IRG systems (Fig. 7.2.). During the primary magmatic event Zn was first incorporated into the clinopyroxene, but due to ongoing metasomatism and decomposition of the pyroxenes, Zn became expelled from the lattice and available to a sulphide bearing fluid, with the change of loellingite to arsenopyrite indicating that at Mungana progressive sulphidation occurred. This is the reason that base metals can be found at Mungana intimately intergrown with skarn minerals of the prograde stage (Georgees 2007b), and the process also explains why previous workers assigned the base metal event to a “retrograde” looking early skarn (Halfpenny 1991; Nethery & Barr 1996; Barr 1998; Georgees 2007a and Hodkinson et al. 2009). At Red Dome the Zn either remained in the clinopyroxene, with clinopyroxenes having higher Zn concentration than those

from Redcap and Mungana (chapter 4: Fig. 4.2.4.2.), or the Zn was incorporated into chlorite, with values of up to 30 wt.-% being detected by Rule and Radke (1988).

The emplacement of the second magmatic phase (~313-303 Ma) caused the difference in the base metal grades at the three deposits. While at Red Dome only a very small amounts of sphalerite formed (chapter 3: plate 3.4.2.1.), with trace element chemistry of zircons from the dacitic porphyry indicating a Cu porphyry system (chapter 6: Fig. 6.7.2.), at Redcap and Mungana the oxidised and less fractionated granodiorite and granite, which show an affinity to igneous rocks of the Almaden supersuite, not only introduced more Cu, Zn, Pb (±Ag) and S, but also remobilised existing mineralisation as shown by colloform galena as well as base metal rich matrix in the breccia in the upper part of the Mungana deposit (Barr 1998).

Gold mineralisation at Mungana is hosted in quartz veins and associated with arsenic, copper and antimony minerals (chapter 3: plate 3.3.3.3 & chapter 4: plate 4.4.2.), with correlation matrixes of assay data (chapter 4: Fig. 4.4.3.1.) confirming this link. Originally the gold was incorporated in the lattice of loellingite, chalcopyrite, tennantite and/or tetrahedrite, as suggested by Rubenach (2010) for Mungana and for Red Dome by Ewers & Sun (1988b), and in general by Neumayer et al. (1993) and Simon et al. (2000). During a progressive sulphidation event as in the case of loellingite being changed to arsenopyrite at temperatures between 600 and 500 °C (Knaak et al. 1995, chapter 3: plate 3.3.3.3.C) or decomposition of chalcopyrite to bornite at temperatures of >400 °C, indicated by the simultaneous precipitation of tellurobismuthite (Barton & Skinner 1979), ,gold exsolved and precipitated along the grain boundaries of the primary host mineral and the secondary developed phase (chapter 4: plate 4.4.2.C & D). The temperatures at which the gold precipitated, inferred from the observed sulphide assemblages in this study, do not agree with temperatures determined by fluid inclusion studies of gold-bearing quartz veins from Allen (1989), Woodbury (1994) and Rubenach (2010) with their temperatures of 400-220 °C being to low. The reason for the temperature differences could be that previous workers sampled late stage quartz which is known to contain the best preserved and largest fluid inclusions (Nash 1976), but on the other hand does not represent the important stage of the mineralising event. Alternatively, the fluid inclusions may have changed their original composition due to leaking or imploding as suggested by Passchier & Trouw (2005).

Another supporting argument for the gold exsolution from copper minerals might be that gold at Mungana exhibits Cu concentrations of 0.5 to 4.3 wt.-% (chapter 4: Tab. 4.4.1., Fig. 4.4.3.2.) suggesting that some Cu from the original mineral was incorporated into the gold.

An association of gold with As, Sb, and Cu is not uncommon for IRG systems (Lang & Baker 2001), although association with Bi-Te mineral phases is more general (Thompson et al. 1999; Lang & Baker 2001), as observed at the Redcap and Red Dome deposits investigated in this study. Gold mineralisation at Redcap and Red Dome correlates well with Bi and Te as shown by the correlation coefficients of 0.6 for Bi, which is a typical value for an IRG system (Baker et al. 2005) and 0.9-1.0 for Te. Gold forms at temperatures below 266 °C (Baton & Skinner 1979) with the bismuth-telluride and sulfosalt assemblage being commonly observed in sulphide poor Au systems like IRGs (Ciobanu et al. 2009). The gold occurrence in tiny carbonate veins cutting earlier skarn as observed in this study and proposed by Creighton (2005) indicates that the gold is not only late in the paragenetic sequence but may have been remobilised with gold originally being hosted in As-Sb-Cu minerals as observed at Mungana, and suggested by Ewers & Sun (1988b) for Red Dome. Evidence for this hypothesis is that at Redcap electrum is hosted by sphalerite with this assemblage indicating remobilisation (Hurley & Crocket 1985).

It is proposed that two gold mineralising events occurred with gold of the primary event being incorporated into As-Sb-Cu, although for the Redcap deposit this still needs to be confirmed. The second gold event is linked to Bi-Te minerals. Bi-Te melts are able to extract gold from pre-existing arsenic minerals (Oberthür & Weiser 2008) with bismuth acting as a scavenger (Ciobanu et al. 2005, 2010; Tooth et al. 2011). At the Red Dome deposit it is also possible that more gold was introduced during the second Cu-bearing magmatic event, with the dacitic porphyry (995) being cut by gold and chalcopyrite bearing quartz veins (see chapter 3, Plate 3.4.1.2.E).

7.3. Mineral chemistry and isotope concentrations of silicate and sulphide phases as exploration tool

Clinopyroxene, garnet, sphalerite, gold and molybdenite were investigated for their potential as exploration tools. While clinopyroxene did not provide any results, the percentage of the andradite component of garnets might be useful, suggesting that garnets ranging from 0 to 60 wt.-% andradite are barren systems whereas garnets with 60 to 85 wt.-% andradite component can be linked to mineralisation as suggested by Paverd (1981). A potential problem is that in this study two magmatic events occurred. Petrographic studies did not allow a distinction between skarn related to the first emplacement phase and the second igneous event. Therefore it is possible that the different garnet compositions do not provide evidence for mineralised or barren systems but only discriminate between garnet formation related to the primary and secondary event. In this case both magmatic events are associated with mineralisation and therefore suggest the use of garnet composition as exploration tool, but to establish its use in

other multiphase IRG systems, and in a single magmatic IRG system for comparison, this theory should be tested again.

Oftendahl (1940) and Cook et al. (2009) suggested that Co and In concentrations in sphalerite can be used to estimate the formation temperature which correlates with the distance to the intrusive body. In general, early paragenetic sphalerite grains exhibit higher Co and In as well as Se concentrations, but, as with garnets, multiphase systems may be more complex. To establish whether different trace element concentrations of sphalerite can be used in Chillagoe as pathfinder to locate the intrusion or whether they only reflect sphalerites which formed in different magmatic events, the distribution of Co and In concentrations of sphalerite concentration should be shown in a deposit model.

The use of copper concentrations in gold as discrimination tool seems to differ between Au-bearing Cu porphyries and Au porphyries (Townley et al. 2003), but its use in polymetallic systems is considered to be unreliable. In this study copper concentrations in gold help to identify the primary gold event in which gold was exsolved from As-Sb-Cu minerals and incorporated some Cu in its lattice, but the occurrence of tetra-auricupride at Red Dome (see chapter 3, Plate 3.4.2.3.) has also shown that Cu can substitute for gold at temperatures of 75 to 150 °C (Tomkins & Pinnel 1976). On the other hand correlation matrixes calculated from assay data agree well with petrographical observation, therefore making this a useful tool, especially when the distribution of gold-correlating elements is shown in deposit models: such elements can be used as pathfinders to locate mineralisation.

Re-Os concentrations of molybdenite were tested for their ability to discriminate between IRG systems and different porphyry styles. A comparison of samples from Redcap, Mungana and Red Dome deposit with Re and Os concentrations of molybdenite from an IRG system investigated by Selby et al. (2002) showed that all samples yielded very low concentrations, with such low values being typical for an evolved, crustal derived system (Stein et al. 2001) which is common for IRGs (Thompson et al. 1999; Lang & Baker 2001; Baker et al. 2005). On the other hand the controversial molybdenite ages of the Chillagoe samples, which are either too old in comparison to U-Pb zircon ages (Mungana, Red Dome) or too young (Redcap) indicate that the molybdenite might have experienced Re and/or Os loss. Some workers postulates that this is not possible (Selby & Creaser 2001; Stein et al. 2001) whereas other studies confirm the loss of either Re or Os (McCandless et al. 1993; Xiong & Wood 1999; Suzuki et al. 2001). Therefore the use of Re-Os concentrations is not recommended as a stand alone discrimination tool, but where age control through more reliable geochronometers like U-Pb on zircons is

provided, the reliability of the determined Re-Os concentrations can be estimated, and then, in combination with other data, they may deliver some useful information.

7.4. Timing, magmatic evolution and source environment implications

Trace element chemistry and radiogenic isotope studies of zircons from igneous rocks of the Redcap deposit showed that the Belgravia granodiorite and Redcap dacite are coeval (chapter 5: Fig. 5.4., chapter 6: Fig. 6.2.1., Fig. 6.3.2.). A small population of 321 Ma aged zircons indicates the presence of the primary magmatic event at Redcap with an intrusive body that has not been discovered yet. For the Mungana and Red Dome deposits the occurrence of two magmatic events was confirmed, but the issues with the Re-Os molybdenite ages (chapter 5: section 5.3.) preclude determination of the exact timing of the skarn formation and the mineralising event, and therefore do not provide new information about whether magmatic and hydrothermal activity in IRG systems are almost synchronous as proposed by Baker et al. (2005).

The degree of the Ce anomaly as well as the Hf/Y ratio of zircons proved to be useful tools to identify the magmatic evolution of igneous rocks (chapter 6: Fig. 6.7.2.), with data of this study showing that the igneous rocks of the primary magmatic event are more reduced and fractionated than the igneous rocks related to the second magmatic event. These observations also helped to understand the metal potential of the different magmatic events, with gold being related to the most fractionated phase, as proposed by Lang & Baker (2001) for an IRG system and confirmed by Murgulov et al. (2009) for the Kidston deposit. This study also confirmed that the critical value of $Ce/Ce^* > 70$ for Cu porphyry of Ballard et al. (2001) is correct, with the second intrusion at Red Dome being a Cu porphyry, which explains why Red Dome has higher economic grades of Cu than the other two deposits (chapter 2: section 2.7.2 to 2.7.4.). A trace element concentration plot of Ce/Ce^* versus Hf/Y ratio seems to be a useful alternative to the Blevin et al. (1996) classification scheme where whole rock data cannot be used due to intensive alteration. Alternatively the Zr/Hf ratio can also be used to determine the degree of fractionation.

Negative εHf of all igneous rocks suggests that they were derived from a crustal source as typical for IRG systems (Lang & Baker 2001; chapter 6: Fig. 6.7.1.). The decrease of the εHf from the inherited zircons to more negative values suggests that the rocks formed through multistage remelting of metasedimentary crust (Black & McCulloch 1990).

Trace element and radiogenic isotope data from zircon demonstrated that useful information about the magmatic system such as magma source and evolution parameters, like degree of oxidation and fractionation, can be determined, with zircons having the great advantage that due to their physico-chemical robustness they are not as easily affected as whole rock data by metamorphism, (hydrothermal) alteration and/or weathering.

7.5. Conclusions

A combination of petrographic, geochemical, geochronological and isotopic data showed that:

- mineralisation at the Redcap, Mungana and Red Dome deposits is linked to two magmatic events with the primary event being assigned to an IRG system, whereas the second magmatic event caused reworking and enrichment of existing metals.

- skarns formed in an IRG system do not differ regarding their mineral assemblage from skarns formed in other intrusion-related systems.

- metal commodities in IRG systems are more diverse than in classic skarn deposits, with the overall metal diversity being underestimated as some metals (in this study: Sn, Zn) are structurally bound in the lattice of silicate phases.

- gold in IRG systems can be structurally bound within As-Cu-Sb minerals, can be associated with Bi-Te-S minerals or can occur free.

- the geochemical composition of garnet, sphalerite and gold may be useful to discriminate between barren and mineralised systems as well as act as pathfinder to locate the causative intrusion or mineralisation.

- Re-Os concentrations of molybdenite and trace element geochemistry of zircons may help to discriminate between IRG systems and other porphyry styles.

- Hf isotopes of zircons provide valuable information regarding the magma source from which IRG systems were derived.

7.6. Future work

Further investigations of silicate phases regarding their potential to incorporate certain metals into their mineral structure are needed to reveal the full metal diversity of IRG systems and gain information on why some deposits lack certain metals, although their magmatic evolution and

source may be very similar to other deposits with different mineral commodities. For the Chillagoe district examination of minerals other than garnet and clinopyroxene would be useful with special emphasis on identifying Cu-bearing silicate minerals to further explain the different Cu grades at Redcap and Mungana.

This study showed that gold in IRG systems can either occur free, associated with Bi-Te phases, or incorporated in As-Cu-Sb minerals. Little attention has been paid to the latter, although a better understanding of the occurrence and mineral assemblages of gold would help to clarify metal precipitation mechanism. This understanding would also provide useful information for mining companies for selection of ore processing methods, and allow modelling of the distribution of gold-associated elements, which can be used as vectors to locate mineralisation.

Trace element compositions of garnets and sphalerite determined in this study indicated that they might be useful exploration tools, but further work by LA-ICP-MS analyses and EMP mapping is needed to identify possible limitations in complex multiphase magmatic systems, and to establish their use in single magmatic systems. In addition coexisting mineral phases need to be investigated to fully understand how the presence of certain minerals may influence the trace element distribution within garnet and sphalerite. Additionally, detailed studies on the intra-grain behaviour of trace elements is required as some elements might become mobile, i.e. being sensitive to enrichment or loss.

Radiogenic studies of molybdenite did not allow determination of the exact timing of the mineralisation, but the use of the concentration to discriminate between IRG and porphyry related molybdenite showed some potential, although further work is needed. This includes a better understanding of mechanisms which can cause loss or gain of Re and/or Os in molybdenite. Trace element and sulphur isotope concentrations of molybdenite from Chillagoe need to be checked to confirm that two molybdenite generations were really present, as inferred from petrographical studies.

Further work on trace element chemistry of zircons is also needed to better characterise the magmatic evolution processes related to IRG systems, especially when these systems are not distinguished regarding their metallogeny commodities. Hf isotope studies in this work have shown that the magma was derived from a crustal source, but to exclude any input of a juvenile source, oxygen isotope data of zircons would be useful.

Bibliography

Ahrens, LH, 1965, 'Some observations on the uranium and thorium distributions in accessory zircon from granitic rocks', *Geochimica et Cosmochimica Acta*, vol. 29, pp. 711-716.

Ahrens, LH, Cherry, RD & Erlank, AJ, 1967, 'Observations on the Th-U relationship in zircons from granitic rocks and from kimberlites', *Geochimica et Cosmochimica Acta*, vol. 31, pp. 2379-2387.

Aleinikoff, JN, Creaser, RA, Lowers, HA, Maggee Jr, CW & Grauch, RI, 2012, 'Multiple age components in individual molybdenite grains', *Chemical Geology*, vol. 300-301, pp. 55-60.

Allen, JM, 1989, *Petrology of fourteen drill hole samples from the northwest Mungana prospect, Queensland*, Chartered mineral services report for Elders Resources.

Amelin, Y, Lee, D-C, Halliday, AN & Pidgeon, RT, 1999, 'Nature of the earth's earliest crust from hafnium isotopes in single detrital zircons', *Nature*, vol. 399, pp. 252-255.

Amthauer, G, McIver, JR & Viljoen, EA, 1979, '^{57}Fe and ^{119}Sn Mössbauer studies of natural tin-bearing garnets', *Physics and Chemistry of Minerals*, vol. 4, pp. 235-244.

Anders, E & Grevesse, N, 1989, 'Abundance of the elements: meteoritic and solar', *Geochimica et Cosmochimica Acta*, vol. 53, pp. 197-214.

Arnold, GO & Fawckner, JF, 1980, 'The Broken River and Hodgkinson Provinces', in RA Henderson & PJ Stephenson (eds.), *The geology and geophysics of northeastern Australia*, Geological Society of Australia, Queensland Division, Brisbane, pp. 175-189.

Atkinson, WW, & Einaudi, MT, 1978, 'Skarn formation and mineralisation in the contact aureole at Carr Fork, Bingham, Utah', *Economic Geology*, vol. 73, pp. 1326-1365.

Axelsson, MD & Rodushkin, I, 2001, 'Determination of major and trace elements in sphalerite using laser ablation double focusing sector field ICP-MS', *Journal of Geochemical Exploration*, vol. 72, pp. 81-89.

Bailey, JC, 1977, 'Petrochemistry of the Claret Creek Ring Complex, northeast Queensland', *Journal of the Geological Society of Australia*, vol. 24, pp. 1-14.

Baker, T, Pollard, PJ, Mustard, R, Mark, G, & Graham, JL, 2005, 'A comparison of granite-related tin, tungsten, and gold-bismuth deposits: implications for exploration', *Society of Economic Geology Newsletter*, vol. 61, pp. 5, 10-17.

Ballard, JR, Palin, JM, Williams, IS & Campbell, IH, 2001, 'Two ages of porphyry intrusion resolved for the super-giant Chuquicamata copper deposit of northern Chile by ELA-ICP-MS and SHRIMP', *Geology*, vol. 29, pp. 383-386.

Ballard, JR, Palin, JM & Campbell, IH, 2002, 'Relative oxidation states of magmas inferred from Ce(IV)/Ce(III) in zircon: application to porphyry copper deposits of northern Chile', *Contributions to Mineralogy and Petrology*, vol. 144, pp. 347-364.

Barkov, AY, Martin, RF & Poirier, G, 2000, 'Zoned tungstenoan molybdenite from a fenitised megaxenolith in the Khibina alkaline complex, Kola Peninsula, Russia', *The Canadian Mineralogist*, vol. 38, pp. 1377-1385.

Barr, MJ, 1998, 'A review of the Mungana Au-Cu- base metal deposit North Queensland, with special reference to late high sulphidation mineralisation', M.Sc. thesis, James Cook University, Townsville.

Barton, PB & Skinner, BJ, 1979, 'Sulfide mineral stabilities', in HL Barnes (ed.), *Geochemistry of hydrothermal ore deposits*, 2nd edn, John Wiley and Sons, New York, pp. 278-403.

Bell, TH, 1980, 'The deformational history of northeastern Queensland – a new framework', in RA Henderson & PJ Stephenson (eds.), *The geology and geophysics of northeastern Australia*, Geological Society of Australia, Queensland Division, Brisbane, pp. 307-313.

Belousova, EA, Griffin, WL, O'Reilly, SY & Fisher, NI, 2002, 'Igneous zircon: trace element composition as an indicator of source rock type', *Contributions to Mineralogy and Petrology*, vol. 143, pp. 602-622.

Bernecker, T & Webb, JA, 1990, 'Limestone microfacies distribution of the Chillagoe Formation (Siluro-Devonian), Mungana area, Hodgkinson basin, north Queensland and its structural implications', *Geological Society of Australia abstracts*, vol. 25, pp. 49.

Best, JG, 1962, Atherton, Queensland, 1:250,000 geological series, Explanatory Notes SE/55-5, Bureau of Mineral Resources, Australia.

Bierlein, FP & McKnight, S, 2005, 'Possible intrusion-related gold systems in the western Lachlan Orogen, southeast Australia', *Economic Geology*, vol. 100, pp. 385-398.

Bird, DK, Brooks, CK, Gannicott, RA & Turner, PA, 1991, 'A gold-bearing horizon in the Skaergaard intrusion, east Greenland', *Economic Geology*, vol. 86, pp. 1083-1092.

Black, LP, 1978, *Isotopic ages of rocks from the Georgetown-Mount Garnet-Herberton area, north Queensland*, report 200, Bureau of Mineral Resources Australia.

Black, LP, 1980, 'Rb-Sr systematics of the Claret Creek Ring Complex and their bearing on the origin of Upper Palaeozoic igneous rocks in northeast Queensland', *Journal of the Geological Society of Australia*, vol. 27, pp.157-166.

Black, LP & Richards, JR, 1972a, 'Rb-Sr study of some igneous rocks near Chillagoe and Herberton, north eastern Queensland', *Journal of the Geological Society of Australia*, vol. 19, pp. 271-279.

Black, LP & Richards, JR, 1972b, 'Rock lead isotopes in north eastern Queensland', *Journal of the Geological Society of Australia*, vol. 19, pp. 321-330.

Black, LP & McCulloch, MT, 1990, 'Isotopic evidence for the dependence of recurrent felsic magmatism on new crust formation; an example from the Georgetown region of north-eastern Australia', *Geochimica et Cosmochimica Acta*, vol. 54, pp. 183-196.

Black, LP, Gregory, P, Withnall, IW & Bain, JHC, 1998, 'U-Pb zircon age for the Etheridge Group, Georgetown region, north Queensland: implications for relationships with the Broken Hill and Mt Isa sequences', *Australian Journal of Earth Sciences*, vol. 45, pp. 925-935.

Blevin, PL, 2004, 'Redox and compositional parameters for interpreting the granitoids metallogeny of eastern Australia: implications for gold-rich ore systems', *Resource Geology*, vol. 54, pp. 241-252.

Blevin, PL & Chappell, BW, 1992, 'The role of magma sources, oxidation states and fractionation in determining the granite metallogeny of eastern Australia', *Transactions of the Royal Society of Edinburgh: Earth Sciences*, vol.83, pp. 305-316.

Blevin, PL & Chappell, BW, 1995, 'Chemistry, origin, and evolution of mineralised granites in the Lachlan Fold Belt, Australia: the metallogeny of I- and S-type granites', *Economic Geology*, vol. 90, pp. 1604-1619.

Blevin, PL, Chappell, BW & Allen, CM, 1996, 'Intrusive metallogenic provinces in eastern Australia based on granite source and composition', *Transactions Royal Society of Edinburgh: Earth Sciences*, vol. 87, pp. 281-290.

Blichert-Toft, J & Albarède, F, 1997, 'The Lu-Hf isotope geochemistry of chondrites and the evolution of the mantle-crust system', *Earth and Planetary Science Letters*, vol. 148, pp. 243-258.

Bolhar, R, Weaver, SD, Palin, JM, Cole, JW & Paterson, LA, 2008, 'Systematics of zircon crystallisation in the Cretaceous Separation Point Suite, New Zealand, using U/Pb isotopes, REE and Ti geothermometry', *Contributions to Mineralogy and Petrology*, vol. 156, pp. 133-160.

Boulton, A, Fornasiero, D & Ralston, J, 2005, 'Effect of iron content in sphalerite on flotation', *Minerals Engineering*, vol. 18, pp. 1120-1122.

Bouvier, A, Vervoort, JD & Patchett, PJ, 2008, 'The Lu-Hf and Sm-Nd isotopic composition of CHUR: Constraints from unequillibrated chondrites and implications for the bulk composition of terrestrial planets', *Earth and Planetary Science Letters*, vol. 273, pp. 48-57.

Bowman, JR, 1998, 'Stable isotope systematics of skarns', in DR Lentz (ed.), *Mineralised intrusion-related skarn systems*, Mineralogical Association of Canada Short Course series, vol. 26, pp. 99-145.

Boyle, RW, 1979, *The geochemistry of gold and its deposits*, Bulletin 280, Geological Survey of Canada.

Branch, CD, 1961, *A new intrusion mechanism for some high-level granites, and the relationship with ignimbrites in north Queensland*, Australian Association of Advanced Science, Brisbane.

Branch, CD, 1966, *Volcanic cauldrons, ring complexes and associated granites of the Georgetown Inlier, Queensland*, bulletin 76, Bureau of Mineral Resources, Geology and Geophysics, Australia.

Broadhurst, E, 1952, *The geology of the Mungana-Redcap area, Chillagoe district*, Proceedings of the Australasian Institute of Mining and Metallurgy, vol. 164-165.

Broadhurst, E, 1953, 'The Chillagoe copper lead field', in AB Edwards (ed.), *Geology of Australian ore deposits*, Australasian Institute of Mining and Metallurgy, Melbourne, pp. 768-782.

Bultitude, RJ, Champion, DC & Mackenzie, DE, 1993 a, *New and revised intrusive units in the Chillagoe region, north Queensland*, Queensland geological record 1993/28, Geological Survey of Queensland.

Bultitude, RJ, Donchak, PJT, Domagala, J & Fordham, BG, 1993b, *The pre-Mesozoic stratigraphy and structure of the western Hodgkinson Province and environs*, Queensland geological Record 1993/29, Geological Survey of Queensland.

Bultitude, RJ, Garrad, PD, Donchak, PJT, Domagala, J, Champion, DC, Rees, ID, Mackenzie, DE, Wellman, P, Knutson, J, Fanning, CM, Fordham, BG, Grimes, KG, Oversby, BS, Rienks, IP, Stephenson, PJ, Chappell, BW, Pain, CF, Wilford, JR, Rigby, JF & Woodbury, MJ, 1997, 'Chapter 7: Cairns region', in JHC Bain & JJ Draper, *North Queensland geology*, Bulletin 240, Australian Geological Survey Organisation/Queensland geology series no. 9, Department of Mines and Energy, Brisbane, pp. 225-325.

Burnham, CW & Ohmoto, H, 1980, 'Late-stage processes of felsic magmatism', *Mining Geology*, vol. 8, pp. 1-11.

Burton, JC, Taylor, LA & Chou, I-M, 1982, 'The f_{O2}-T and f_{S2}-T stability relations of hedenbergite and of hedenbergite-johannsenite solid solutions', *Economic Geology*, vol. 77, pp. 764-783.

Candela, PA, 1992, 'Controls on ore metal ratios in granite-related ore systems, an experimental and computational approach', *Transactions of the Royal Society of Edinburgh: Earth Sciences*, vol. 83, pp. 317-326.

Carmichael, ISE, 1991, 'The redox states of basic and silicic magmas: a reflection of their source regions?', *Contributions to Mineralogy and Petrology*, vol. 106, pp. 129-142.

Ĉernŷ, P, Blevin, PL, Cuney, M & London, D, 2005, 'Granite-related ore deposits', in JW Hedenquist, JFH Thompson, RJ Goldfarb & JP Richards, *Economic geology 100th Anniversary volume*, Society of Economic Geologists, Littleton, pp.337-370.

Champion, DC, 1991, 'Petrogenesis of the felsic granitoids of far north Queensland', PhD thesis, Australian National University, Canberra.

Champion, D, 2005, 'Prospects look good in northern Queensland', *Geoscience Australia news*, issue 79.

Champion, DC & Chappell, BW, 1992, 'Petrogenesis of felsic I-type granites; an example from northern Queensland', *Transactions of the Royal Society of Edinburgh: Earth Sciences*, vol. 83, pp. 115-126.

Champion, DC & Blevin, PL, 2005, 'New insights into intrusion-related gold-copper systems in the Tasmanides', presentation given at Mining 2005, Brisbane, 26th of October, www.ga.gov.au/minerals/research/pubs/presentations/irg_mining2005.jsp.

Chapman, RJ, Leake, RC, Moles, NR, Earls, G, Cooper, C, Harrington, K, & Berzins, R, 2000, 'The application of microchemical analysis of alluvial gold grains to the understanding of complex local and regional gold mineralisation: a case study in the Irish and Scottish Caledonides', *Economic Geology*, vol. 95, pp. 1753-1773.

Chappell, BW & White, AJR, 1974, 'The two contrasting, granite types', *Pacific Geology*, vol. 8. pp. 173-174.

Chappell, BW & White, AJR, 1992, 'I-type and S-type granites in the Lachlan Fold Belt', *Transactions of the Royal Society of Edinburgh: Earth Sciences*, vol. 83, pp. 1-26.

Chen, K, Yu, T, Zhang, Y & Peng, Z, 1983, 'Tetra-auricupride, CuAu, discovered in China', in PJ Dunn, M Fleischer, GY Chao, LJ Cabri & JA Mandarino (eds.) 'New mineral names', *American Mineralogist*, vol. 68, pp. 1248-1252.

Cherniak, DJ, Hanchar, JM & Watson, EB, 1997a, 'Diffusion of tetravalent cations in zircon', *Contributions to Mineralogy and Petrology*, vol. 127, pp. 383-390.

Cherniak, DJ, Hanchar, JM & Watson, EB, 1997b, 'Rare-earth diffusion in zircon', *Chemical Geology*, vol. 134, pp. 289-301.

Ciobanu, CL, Cook, NJ & Pring, A, 2005, 'Bismuth tellurides as gold scavengers', in JW Mao & FP Bierlein (eds.), *Mineral deposit research: meeting the global challenge*, Springer, Berlin, pp. 1383-1386.

Ciobanu, CL, Cook, NJ, Pring, A, Brugger, J, Danyushevsky, LV & Masaaki, S, 2009, 'Invisbile gold in bismuth chalcogenides', *Geochimica et Cosmochimica Acta*, vol 73., pp. 1970-1999.

Ciobanu, CL, Birch, WD, Cook, NJ, Pring, A & Grundler, PV, 2010, 'Petrogenetic significance of Au-Bi-Te-S associations: the example of Maldon, Central Victorian gold province, Australia', *Lithos*, vol. 116, pp. 1-17.

Claiborne, LL, Miller, CF, Walker, BA, Wooden, JL, Mazdab, FK & Bea, F, 2006, 'Tracking magmatic processes through Zr/Hf ratios in rocks and Hf and Ti zoning in zircons: an example from the Spirit Mountain batholith, Nevada', *Mineralogical Magazine*, vol. 70, pp. 517-543.

Coffey Mining Pty Ltd, 2010, *Independent geologists report – Chillagoe gold project*.

Cook, NJ, Ciobanu, CL, Pring, A, Skinner, W, Shimizu, M, Danyushevsky, L, Saini-Eidukat, B & Melcher, F 2009, 'Trace and minor elements in sphalerite: a LA-ICP-MS study, *Geochimica et Cosmochimica Acta*, vol.73, pp. 4761-4791.

Corfu F, Hanchar JM, Hoskin PWO & Kinny PD, 2003, 'Atlas of zircon textures', in JM Hanchar & PWO Hoskins (eds.), *Zircon*, Mineralogical Society of America/Geochemical Society, Reviews in Mineralogy and Geochemistry, vol. 53, pp. 468-500.

Coulson, IM, Dipple, GM & Raudsepp, M, 2001, 'Evolution of HF and HCL activity in magmatic volatiles of the gold-mineralised Emerald Lake pluton, Yukon Territory, Canada', *Mineralium Deposita*, vol. 36, pp. 594-606.

Creighton, K, 2005, Paragenesis of the Red Dome gold skarn, Mungana, North-Queensland, B.Sc. (Hons), University of Newcastle.

Crowe, DE, Riciputi, LR, Bezenek, S & Ignatiev, A, 2001, 'Oxygen isotope and trace element zoning in hydrothermal garnets: windows into large-scale fluid-flow behaviour', *Geology*, vol. 29, pp. 479-782.

Day, RW, Whitaker, WG, Murray, CG, Wilson, IH & Grimes, KG, 1983, *Queensland Geology-a companion volume to the 1:250,000 scale geological map 1975*, Geological Survey of Queensland, publication 383.

Deer, WA, Howie, RA, & Zussman, J, 1992, *An introduction to rock-forming minerals*, 2nd edn, Pearson, Harlow.

De Keyser, F, 1963, 'The Palmerville Fault – a'fundamental' structure in north Queensland', *Journal of the Geological Society of Australia*, vol. 10, pp. 273-278.

De Keyser, F & Wolff, KW, 1964, *The geology and mineral resources of the Chillagoe area, Queensland*, bulletin 84, Bureau of Mineral Resources, Geology and Geophysics, Australia.

De Keyser, F & Lucas, KG, 1968, *Geology of the Hodgkinson and Laura basins, north Queensland*, bulletin 70, Bureau of Mineral Resources, Geology and Geophysics, Australia.

Department of Mines and Energy, Queensland 1997, Hodgkinson Province geology, Australia 1:500,000 geological special, Department of Mines and Energy, Queensland, Brisbane.

Department of Natural Resources and Mines, Queensland 2003, Mungana, Australia 1:100,000 geological series, sheet 7763, Department of Natural Resources and Mines, Queensland, Brisbane.

Desborough, GA, 1970, 'Silver depletion indicated by microanalysis of gold from placer occurrences, western United States', *Economic Geology*, vol. 65, pp. 304-311.

Desborough, GA, Raymond, WH & Iagmin, PJ 1970, 'Distribution of silver and copper in placer gold derived from the northeastern part of the Colorado Mineral Belt', *Economic Geology*, vol. 65, pp. 937-944.

Donchak, PJT & Bultitude, RJ, 1994, *Geology of the Atherton 1:250000 sheet*, Queensland Geological Record, 1994/5, Geological Survey of Queensland.

Drake, MJ, 1975, 'The oxidation state of europium as an indicator of oxygen fugacity', *Geochimica et Cosmochimica Acta*, vol. 39, pp. 55-64.

Einaudi, MT, Meinert, LD & Newberry, RJ, 1981, Skarn deposits, in BJ Skinner (ed.), *Economic Geology 75th Anniversary Volume*, Society of Economic Geologists, Littleton, pp. 317-391.

Essene, EJ & Peacor, DR, 1987, 'Petedunnite ($CaZnSi_2O_6$), a new zinc clinopyroxene from Franklin, New Jersey, and phase equilibria for zincian pyroxenes', *The American Mineralogist*, vol. 72, pp. 157-166.

Ettler, V, Legendre, O, Bodénan, F & Touray, J-C, 2001, 'Primary phases and natural weathering of old lead-zinc pyrometallurgical slag from Příbram, Czech Republic', *The Canadian Mineralogist*, vol. 39, pp. 873-888.

Ewers, GR & Sun, SS, 1988a, The genesis of the Red Dome Au skarn deposit, northeast Queensland, in RR Keays, WRH Ramsay & DI Groves (eds.), *The geology of gold deposits: the perspective in 1988*, Economic geology publishing company, New Haven, Economic Geology monographs, no. 6, pp. 218-232.

Ewers, GR & Sun, SS, 1988b, 'Genesis of the Red Dome deposit, northeast Queensland', *Geological Society of Australia abstracts*, vol. 22, pp. 110-115.

Ewers, GR, Torrey, CE & Erceg, MM, 1990, 'Red Dome gold deposit' in FE Hughes (ed.), *Geology of the mineral deposits of Australia and New Guinea*, The Australasian Institute of Mining and Metallurgy, Melbourne, pp. 1455-1460.

Fawckner, JF, 1981, 'Structural and stratigraphic relations and a tectonic interpretation of the Western Hodgkinson Province, northeastern Australia', PhD thesis, James Cook University, Townsville.

Ferry, JM & Watson, EB, 2007, 'New thermodynamic models and revised calibrations for the Ti-in-zircon and Zr-in-rutile thermometers', *Contributions to Mineralogy and Petrology*, vol. 154, pp. 429-437.

Finch, RJ & Hanchar, JM, 2003, Structure and chemistry of zircon and zircon-group minerals, in JM Hanchar & PWO Hoskins (eds.), *Zircon*, Mineralogical Society of America/Geological Society, Reviews in Mineralogy and Geochemistry, vol. 53, pp. 1-25.

Fitzgerald, S, Rheingold, AL & Leavens, PB, 1986, 'Crystal structure of a Cu-bearing vesuvianite', *American Mineralogist*, vol. 71, pp. 1011-1014.

Fondel, C & Ito, J, 1966, 'Zincian aegirine augite and jeffersonite from franklin, New Jersey', *The American Mineralogist*, vol. 51, pp. 1406-1413.

Fordham, BG, 1990, 'Microfossils and gross structures and stratigraphy of the Silurian-Devonian Chillagoe formation, western Hodgkinson province northeast Australia', *Geological Society of Australia, abstracts*, vol. 25, pp. 48-49.

Franklin, JM, Gibson, HL, Galley, AG, and Jonasson, IR, 2005, 'Volcanogenic Massive Sulfide Deposits', in JW Hedenquist, JFH Thompson, RJ Goldfarb & JP Richards, *Economic geology 100th Anniversary Volume*, Society of Economic Geologists, Littleton, pp. 523-560.

Fu, B, Zeb Page, F, Cavosie, AJ, Fournelle, J, Kita, NT, Lackey, JS, Wilde, SA & Valley, JW, 2008, 'Ti-in-zircon thermometry: applications and limitations', *Contributions to Mineralogy and Petrology*, vol. 156, pp. 197-215.

Fu, B, Mernagh, TP, Kita, NT, Kemp, AIS & Valley, JW, 2009, 'Distinguishing magmatic zircon from hydrothermal zircon: a case study from the Gidginbung high-sulphidation Au-Ag-(Cu) deposit, SE Australia', *Chemical Geology*, vol. 259, pp. 131-142.

Galuskina, IO, Galuskin, EV, Dzierżanowski, P, Gazeev, VM, Prusik, K, Pertsev, NN, Winiarski, A, Zadov, AE & Wrzalik, R, 2010, 'Toturite $Ca_3Sn_2Fe_2SiO_{12}$-a new mineral species of the garnet group', *American Mineralogist*, vol. 95, pp. 1305-1311.

Garrad, PD & Bultitude, GPD, 1999, *Geology, mining history and mineralisation of the Hodgkinson and Kennedy provinces, Cairns region, North Queensland*, Queensland minerals and energy review series, Department of Mines and Energy, Brisbane.

Gaspar, M, Knaak, C, Meinert, LD & Moretti, R, 2008, 'REE in skarn systems: a LA-ICP-MS study of garnets from the Crown Jewel gold deposit', *Geochimica et Cosmochimica Acta*, vol. 72, pp. 185-205.

Geisler, T, Schaltegger, U & Tomaschek, F, 2007, 'Re-equilibration of zircon in aqueous fluids and melts', *Elements*, vol. 3, pp. 43-50.

Georgees, C, 2007a, *The Mungana porphyry-related polymetallic deposit*, Bulletin of the Australasian Institute of Geoscientists, no. 46, pp. 47-48.

Georgees, C, 2007b, The Mungana porphyry-related polymetallic deposit, north Queensland, presentation given at Mines & Wines conference, Sydney, September.

Georgees, C & Nethery, JE, 1999, 'The mid Carboniferous tin gold connection', Far North Queensland Conference, Cairns, Australasian Institute of Mining and Metallurgy, Melbourne

Green, PM, Domagala, J & Bultitude, RJ, 1988, 'Chillagoe Formation – a record of a collapsed Silurian-Devonian carbonate shelf', *Geological Society of Australia, abstracts*, vol. 21, pp. 162-163.

Green, PM, 1990, 'Evidence for allochtonous blocks, Chillagoe Formation, Queensland', *Queensland Government Mining Journal*, vol. 91, pp. 357-366.

Gregory, PW, Taylor, RG & White, AH, 1980, 'Mineralisation in the Broken River and Hodgkinson Province', in RA Henderson & PJ Stephenson (eds.), *The geology and geophysics of northeastern Australia*, Geological Society of Australia, Queensland Division, Brisbane, pp. 191-200.

Griffin, WL, Wang, X, Jackson, SE, Pearson, NJ, O'Reilly, SY, Xu, X & Zhou, X, 2002, 'Zircon chemistry and magma mixing, SE China: in-situ analysis of Hf isotopes, Tonglu and Pingtan igneous complexes', *Lithos*, vol. 61, pp. 237-269.

Groen, JC, Craig, JR & Rimstidt, JD, 1990, 'Gold-rich rim formation on electrum grains in placers', *The Canadian Mineralogist*, vol. 28, pp. 207-228.

Gustafson, WI, 1974, 'The stability of andradite, hedenbergite and related minerals in the system Ca-Fe-Si-O-H', *Journal of Petrology*, vol. 15, pp. 455-496.

Halfpenny, RW, 1991, 'Carbonate hosted zoned porphyry Au-Cu-Pb-Zn style mineralisation, north west Mungana, North Queensland', M.Sc. thesis, James Cook University, Townsville.

Hanchar, JM & Hoskins, PWO, 2003, *Zircon*, Mineralogical Society of America/Geochemical Society, Reviews in mineralogy and geochemistry, vol. 53.

Harker, RI & Tuttle, OF, 1956, 'Experimental data on the P_{co2}-T curve for the reaction: calcite + quartz ↔ wollastonite+ carbon dioxide', *American Journal of Science*, vol. 254, pp. 239-256.

Hart, CJR, 2005, 'Classifying, distinguishing and exploring for intrusion-related gold systems', *The Gangue: Newsletter of the Geological Association of Canada Mineral Deposits Division*, vol. 87, pp. 1, 4-9.

Hart, CJR, 2007, 'Reduced intrusion-related gold systems', in WD Goodfellow (ed.), *Mineral deposits of Canada: a synthesis of major deposit types, district, metallogeny, the evolution of geological provinces, and exploration methods*, Geological Association of Canada, Mineral Division, special publication no. 5, pp. 95-112.

Hawkesworth, CJ & Kemp, AIS, 2006, 'Using hafnium and oxygen isotopes in zircons to unravel the record of crustal evolution', *Chemical Geology*, vol. 226, pp. 144-162.

Heaman, LM, Bowins, R & Crocket, J, 1990, 'The chemical composition of igneous zircon suites: implications for geochemical tracer studies', *Geochimica et Cosmochimica Acta*, vol. 54, pp. 1597-1607.

Hellwege, H, 1956, 'The occurrence of tin as trace element in minerals', in Fr. K. Drescher-Kaden (ed.), *Hamburger Beiträge zur angewandten Mineralogie und Kristallphysik-Festschrift zum 70. Geburtstag Hermann Rose's*, Bornträger, Berlin, pp.73-136.

Hinton, RW & Upton, BGJ, 1991, 'The chemistry of zircon: variations within and between large crystals from syenite and alkali basalt xenoliths', *Geochimica et Cosmochimica Acta*, vol. 55, pp. 3287-3302.

Hodkinson, I, Whitelock, J, McDonnel, M & Hayduk, A, 2009, 'Mungana-a porphyry gold overprint on a replacement Zn-Cu-Pb deposit', *Bulletin of the Australasian Institute of Geoscience*, vol. 49, pp.49-56.

Holland, CL, 1994, 'Physical and chemical processes involved in the bleaching of basalt at the Red Dome gold skarn deposit', B.Sc. (Hons) thesis, James Cook University, Townsville.

Hoskin, PWO, 2005, 'Trace-element composition of hydrothermal zircon and the alteration of Hadean zircon from the Jack Hills, Australia', *Geochimica et Cosmochimica Acta*, vol. 69, pp. 637-648.

Hoskin, PWO & Black, LP, 2000, 'Metamorphic zircon formation by solid-state recrystallisation of protolith igneous zircon', *Journal of Metamorphic Geology*, vol. 18, pp. 423-439.

Hoskin, PWO & Ireland, TR, 2000, 'Rare earth element chemistry of zircon and its use as a provenance indicator', *Geology*, vol. 28, pp. 627-630.

Hoskin, PWO & Schaltegger, U, 2003, The composition of zircon and igneous and metamorphic petrogenesis, in JM Hanchar & PWO Hoskins (eds.), *Zircon*, Mineralogical Society of America/Geochemical Society, Reviews in Mineralogy and Geochemistry, vol. 53, pp. 27-62.

Hoskin, PWO, Kinny, PD, Wyborn, D & Chappell, BW, 2000, 'Identifying accessory mineral saturation during differentiation in granitoids magmas: an integrated approach', *Journal of Petrology*, vol. 41, pp. 1365-1396.

Hough, RM, Butt, CRM, Reddy, SM & Verrall, M, 2007, 'Gold nuggets: supergene or hypogene?', *Australian Journal of Earth Sciences*, vol. 54, pp. 959-964.

Hough, RM, Butt, CRM & Fischer-Bühner, J, 2009, 'The crystallography, metallography and composition of gold', *Elements*, vol. 5, pp. 297-302.

Howd, FH & Barnes, HL, 1975, 'Ore solution chemistry IV. Replacement of marble by sulfides at 450 °C', *Economic Geology*, vol. 70, pp. 968-981.

Hurley, TD & Crocket, JH, 1985, 'A gold-sphalerite association in a volcanogenic base-metal-sulfide deposit near Tilt Cove, Newfoundland', *The Canadian Mineralogist*, vol. 23, pp. 423-430.

Hutchinson, MN & Scott, SD, 1981, 'Sphalerite geobarometry in the Cu-Fe-Zn-S system', *Economic Geology*, vol. 76, pp.143-153.

Iizuka, T & Hirata, T, 2005, 'Improvements of precision and accuracy in situ Hf isotope microanalysis of zircon using the laser ablation MC-ICPMS technique', *Chemical Geology*, vol. 220, pp. 121–137.

Ishaq, S, Dash, PH, Sawers, J, Kay, J, Cooper, W, Krosch, N, Lam, J, Garrad, P & Mitchell, G, 1987, *Mineral occurrence data sheets-Mungana 1:100,000 sheet area, metallogenic studies program*, Queensland geological record 29, Geological Survey of Queensland.

Ishihara, S, 1977, 'The magnetite-series and ilmenite-series granitic rocks', *Mining geology*, vol. 27, pp. 293-305.

Ishihara, S, 1981, the granitoids series and mineralisation, in BJ Skinner (ed.), Economic Geology 75th Anniversary volume, pp. 458-484.

Ito, J & Arem, JE, 1970, 'Indocrase, synthesis, phase relations and crystal chemistry', *American Mineralogists*, vol. 55, pp. 880-912.

Jack, RL, 1891, *Chillagoe and Koorboora district*, Publication of the Geological Survey of Queensland, vol. 69.

Jack, RL & Etheridge, R, 1892, *The geology and palaeontology of Queensland and New Guinea*, Publication of the Geological Survey of Queensland, vol. 92.

Jackson, SE, Pearson, NM, Griffin, WL & Belousova, EA, 2004, 'The application of laser ablation-inductively couples plasma-mass spectrometry to in situ U-Pb zircon geochronology', *Chemical Geology*, vol. 211, pp.47-69.

Jamtveit, B, 1991, 'Oscillatory zonation patterns in hydrothermal grossular-andradite garnets: nonlinear behaviour in regions of immiscibility', *American Mineralogist*, vol. 76, pp. 1319-1327.

Jamtveit, B, Wogelius, RA, Fraser, DG, 1993, 'Zonation patterns of skarn garnets; record of hydrothermal system evolution', *Geology*, vol. 21, pp. 113-116.

Jamtveit, B & Hervig, RL, 1994, 'Constrains on transport and kinetics in hydrothermal systems from zoned garnet', *Science*, vol. 263, pp. 505-508.

Jensen, HI, 1923, *Geology of the Cairns Hinterland and other parts of North Queensland*, Publication of the Geological Survey of Queensland, vol. 274.

Jensen, HI, 1940, *The Palmer River district*, Aerial Geological and Geophysical Survey of north Australia, Queensland, report 40.

Jensen, HI, 1941, *The Chillagoe district*, Aerial Geological and Geophysical Survey of north Australia, Queensland, report 53.

Kagara Ltd, 2008, Schematic cross section of Redcap-Victoria.

Kemp, AIS, Hawkesworth, CJ, Foster, GL, Paterson, BA, Woodhead, JD, Hergt, JM, Gray, CM & Whitehouse, MJ, 2007, 'Magmatic and crustal differentiation history of granitic rocks from Hf-O isotopes in zircon, *Science*, vol. 315, pp. 980-983.

Kemp, AIS, Foster, GL, Scherstén, A, Whitehouse, MJ, Draling, J & Storey, C, 2009, 'Concurrent Pb-Hf isotope analysis of zircon by laser ablation multi-collector ICP-MS, with implications for the crustal evolution of Greenland and the Himalayas', *Chemical Geology*, vol 261, pp. 244-260.

Kinny, PD & Maas, R, 2003, 'Lu-Hf and Sm-Nd isotope systems in zircon' in JM Hanchar & PWO Hoskins (eds.), *Zircon*, Mineralogical Society of America/Geological Society, Reviews in Mineralogy and Geochemistry, vol. 53, pp. 327-341.

Knaak, ML, Dalstra, HJ & Ridley, JR, 1995, 'Sulpharsenide textures in high-temperature gold deposits: examples from the Southern Cross province, western Australia', in J Pašava, B Kříbek & K Žák, (eds.), *Mineral deposits: from their origin to their environmental impacts*, Balkema, Rotterdam, pp. 125-128.

Knight, J & Leitch, CHB, 2001, 'Phase relations in the system Au-Cu-Ag at low temperatures, based on natural assemblages', *The Canadian Mineralogist*, vol. 39, pp. 889-905.

Knipe, SW & Fleet, ME, 1997, 'Gold-copper alloy minerals from the Kerr mine, Ontario', *The Canadian Mineralogist*, vol. 35, pp. 573-586.

Kossoff, D, Hudson-Edwards, KA, Dubbin, WE & Alfredsson, M, 2008, 'Incongruent weathering of Cd and Zn from mine tailings', *Mineralogical Magazine*, vol. 72, pp. 81-84.

Lang, JR & Baker, T, 2001, 'Intrusion-related gold systems: the present level of understanding', *Mineralium Deposita*, vol. 36, pp. 477-489.

Lang, JR, Thompson, JFH, Mortensen, JK & Baker, T, 1997, 'Intrusion-related Au mineralisation associated with lithophile elements: an under-recognised metallogenic association', *Geological Society of America, abstracts with programs*, vol. 29, p. 358.

Lang, JR, Baker, T, Hart, CJR & Mortensen, JK, 2000, 'An exploration model for the intrusion-related gold-systems', *Society of Economic Geology Newsletter*, vol. 40, pp. 1, 6-15.

Leake, RC, Chapman, RJ, Bland, DJ, Stone, P, Cameron, DG & Styles, MT, 1998, 'The origin of alluvial gold in the Leadhills area of Scotland: evidence from internal chemical characteristics', *Journal of Geochemical Exploration*, vol. 63, pp. 7-36.

Lee, JK, Williams, IS & Ellis, DJ, 2001, 'Pb, U and Th diffusion in natural zircon', *Nature*, vol. 390, pp. 159-162.

Lehmann, B, 1990, *Metallogeny of tin*, Berlin, Springer.

Linnen, RL & Keppler, H, 2002, 'Melt composition control of Zr/Hf fractionation in magmatic processes', *Geochimica et Cosmochimica Acta*, vol. 66, pp. 3293-3301.

Loiselle, MC, Wones, DR, 1979, 'Characteristics and origin of anorogenic granites', *Geological Society of America abstracts with programs*, vol. 11, pp.468.

Ludwig, KR, 2008, Isoplot/Ex Version 3.70: a Geochronological Toolkit for Microsoft Excel, Berkeley Geochronology Centre, Berkeley, CA.

Maas, R , Kinny, PD, Williams, IS, Froude, DO & Compston, W, 1992, 'The earth's oldest known crust: a geochronological and geochemical study of 3900-4200 Ma old detrital zircons from Mt Narryer and Jack Hills, Western Australia', *Geochimica et Cosmochimica Acta*, vol. 56, pp. 1281-1300.

Mackenzie, DE 1987, 'Geology, petrology and mineralisation of the Permo-Carboniferous Featherbed Volcanic Complex, Northeastern Queensland', in *Pacific Rim Congress 87: an international congress on the geology, structure, mineralisation and economics of the Pacific Rim*, Australasian Institute of Mining and Metallurgy, Parkville, pp. 297-301.

Mackenzie, DE, 1988, 'Petrological and structural evolution of the Permo-Carboniferous Featherbed Volcanics, Northeastern Queensland, and their relationship to mineralisation', *Geological Society of Australia Abstracts*, vol. 21, pp. 264-265.

Mackenzie, DE, Bultitude, RJ & Rienks, IP, 1992, *Geology of the Featherbed Cauldron Complex, north Queensland*, Australian Geological Survey Organisation, Canberra.

Mackenzie, DE & Champion, DC, 1994, 'Permian-Carboniferous magmatism and metallogeny in north Queensland-a new perspective' in RA Henderson & BK Davis (eds.), *New developments in geology and metallogeny: northern Tasman orogenic zone*, Contribution to the Economic Geology Research Unit, James Cook University, Townsville, vol. 50 pp. 67-68.

Mahood, G & Hildreth, W, 1983, 'Large partition coefficients for trace elements in high-silica rhyolites', *Geochimica et Cosmochimica Acta*, vol. 47, pp. 11-30.

Martín, JD & Gil, ASI, 2005, 'An integrated thermodynamic mixing model for sphalerite geobarometry from 300 to 850 °C and up to 1GPa', *Geochimica et Cosmochimica Acta*, vol.69, pp. 995-1006.

Martín, JD & Gill, AS, 2010, 'Ilvaite stability in skarns from the northern contact of the Maladeta batholith, central Pyrenees (Spain)', *European Journal of Mineralogy*, vol. 22, pp. 363-380.

Masterman, GJ, Crooke, DR, Berry, RF, Clark, AH, Archibald, DA, Mathur, R, Walshe, JL & Duran, M, 2004, '40Ar/39Ar and Re-Os geochronology of porphyry copper-molybdenum deposits and related copper-silver veins in the Collahuasi district, Northern Chile', *Economic Geology*, vol. 99, pp. 673-690.

Mathur, R, Titleya, S, Ruiza, J, Gibbinsa, S & Friehauf, K, 2005, 'A Re–Os isotope study of sedimentary rocks and copper–gold ores from the Ertsberg District, West Papua, Indonesia', *Ore Geology Reviews*, vol. 26, pp. 207–226.

McCandless, TE, Ruis, J & Campbell, AR, 1993, 'Rhenium behaviour in molybdenite in hypogene and near-surface environments: implications for Re-Os geochronometry', *Geochimica et Cosmochimica Acta*, vol. 57, pp. 889-905.

McCandless, TE, Baker, ME & Ruiz, J, 1997, 'Trace element analysis of natural gold by laser ablation ICP-MS: a combined external/internal standardisation approach', *Geostandards Newsletter*, vol. 21, pp. 271-278.

McCoy, D, Newberry, RJ, Layer, P, Dimarchi, JJ, Bakke, A, Masterman, JS & Minehane, DL, 1997, 'Plutonic-related gold deposits of interior Alaska', in RJ Goldfarb & LD Miler (eds.) *Ore Deposits of Alaska*, Economic geology publishing company, New Haven, Economic Geology monographs, no. 9, pp. 191-241.

McIver, JR & Mihálik, P, 1975, 'Stannian andradite from "Davib Ost", South Africa', *The Canadian Mineralogist*, vol. 13, pp. 217-221.

Meinert, LD, 1987, 'Skarn zonation and fluid evolution in the groundhog Mine, central mining district, New Mexico', *Economic Geology*, vol. 82, pp. 523-545.

Meinert, LD, 1989, Gold skarn deposits – geology and exploration criteria, in RR Keays, WRH Ramsay & DI Groves (eds.), *The geology of gold deposits: the perspective in 1988*, Economic geology publishing company, New Haven, Economic Geology monographs, no. 6, pp. 537-552.

Meinert, LD, 1992, Skarns and skarn deposits, *Geoscience Canada*, vol. 19, pp.145–162.

Meinert, LD, Dipple, GM & Nicolescu, S, 2005, 'World skarn deposits', in JW Hedenquist, JFH Thompson, RJ Goldfarb & JP Richards, *Economic geology 100th Anniversary Volume*, Society of Economic Geologists, Littleton, pp.299-336.

Möller, P & Kersten, G, 1994, 'Electrochemical accumulation of visible gold on pyrite and arsenopyrite surfaces', *Mineralium Deposita*, vol. 29, pp. 404-413.

Morel, MLA, Nebel, O, Nebel-Jackson, YJ, Miller, JS & Vroon, PZ, 2008, 'Hafnium isotope characterisation of the GJ-1 zircon reference material by solution and laser-ablation MC-ICPMS', *Chemical Geology*, vol. 255, pp. 231-235.

Morrison, GW & Beams, SD, 1995, 'Geological setting and mineralisation style of ore deposits of northeast Queensland', in SD Beams (ed.), Mineral deposits of northeast Queensland: geology and geochemistry, Contribution to the Economic Geology Research Unit, James Cook University, Townsville, vol. 52, pp. 1-32.

Morrison, GW, Rose, WJ & Jaireth, S, 1991, 'Geological and geochemical controls on the silver content (fineness) of gold in gold-silver deposits', *Ore Geology Reviews*, vol. 6, pp. 333-364.

Mulholland, IR, 1984, 'Malayaite and tin-bearing garnet from a skarn at Gumble, NSW, Australia', *Mineralogical Magazine*, vol. 48, pp. 27-30.

Mulligan, R & Jambor, JL, 1968, 'Tin-bearing silicates from skarn in the Cassiar district, northern British Columbia', *The Canadian Mineralogist*, vol. 9, pp. 358-370.

Murgulov, V, Beyer, E, Griffin, WL, O'Reilly, SY, Walters, SG & Stephens, D, 2007, 'Crustal evolution in the Georgetown Inlier, North Queensland, Australia: a detrital zircon grain study', *Chemical Geology*, vol. 245, pp. 198-218.

Murgulov, V, O'Reilly, SY, Griffin, WL & Blevin PL, 2008, 'Magma sources and gold mineralisation in the Mount Leyshon and Tuckers Igneous Complexes, Queensland, Australia: U-Pb and Hf isotope evidence', *Lithos*, vol. 101, pp. 281-307.

Murgulov, V, Griffin, WL & O'Reilly, SY, 2009, 'Temporal and genetic relationships between the Kidston gold-bearing Breccia Pipe and the Lochaber Ring Dyke Complex, North Queensland, Australia: insights from in situ U-Pb and Hf-isotope analysis of zircon', *Mineralogy and Petrology*, vol. 95, pp. 17-45.

Mustard, R, 2001, 'Granite-hosted gold mineralisation at Timbarra, northern New South Wales, Australia', *Mineralium Deposita*, vol. 36, pp. 542-562.

Musumeci, AJ, 1974, 'A study of the Redcap Area, near Chillagoe, North Queensland - with particular reference to the breccia at Mount Redcap', B.Sc. thesis, James Cook University, Townsville.

Nakano, T, 1998, 'Pyroxene geochemistry as an indicator for skarn metallogenesis in Japan', in DR Lentz (ed.), *Mineralised intrusion-related skarn systems*, Mineralogical Association of Canada, Short Course series, vol. 26, pp. 147-168.

Nakano, T, Yoshino, T, Shimazaki, H & Shimizu, M, 1994, 'Pyroxene composition as an indicator in the classification of skarn deposits', *Economic Geology*, vol. 89, pp. 1567-1580.

Nash, JT, 1976, 'Fluid inclusion petrology – data from porphyry copper deposits and applications to exploration', in *Geological survey professional papers*, vol. 907-D, United States government printing, Washington.

Nethery, JE, Barr, M & Woodbury, M, 1994, 'Chillagoe district gold, silver, base metal deposits – hydrothermal to epithermal overprinting', in RA Henderson & BK Davis (eds.)**, '***New developments in geology and metallogeny: northern Tasman Orogenic Zone'*, Contribution to the Economic Geology Research Unit, James Cook University, Townsville, vol. 50, pp. 71-74.

Nethery, J & Barr, M, 1996, 'Mungana-perennial Wallflower of the Chillagoe district', in *Recent gold discoveries in north Queensland program and abstracts*, Australasian Institute of Mining and Metallurgy, Townsville, pp.10-13.

Nethery, JE & Barr, MJ, 1998, 'Red Dome and Mungana gold-silver-copper-lead-zinc deposits', in DA Berkman & DH Mackenzie (eds.), *Geology of Australian and Papua New Guinean Mineral Deposits*, Australasian Institute of Mining and Metallurgy, Melbourne, pp. 723-728.

Neumayer, P, Cabri, LJ, Groves, DI, Mikucki, EJ & Jackman, LA, 1993, 'The mineralogical distribution of gold and relative timing of gold mineralisation in two Archaean settings of high metamorphic grade in Australia', *The Canadian Mineralogist*, vol. 31, pp. 711-725.

Newberry, RJ, McCoy, DT & Brew, DA, 1995, 'Plutonic-hosted gold ores in Alaska: igneous versus metamorphic origins', *Resource Geology*, vol. 18, pp.57-100.

Nicolescu, S, Cornell, DH, Sondervall, U & Odelius, H, 1998, 'Secondary ion mass spectrometry analysis of rare earth elements in grandite garnet and other skarn related silicates', *European Journal of Mineralogy*, vol. 10, pp. 251-259.

Norman, M, Bennett, V, Blevin, P & McCulloch, M, 2004, 'New Re-Os ages from molybdenite from granite-related deposits of Eastern Australia using an improved multi-collector ICP-MS technique', *Geological Society of Australia abstracts*, vol. 74, pp. 129-132.

Oberthür, T & Weiser, TW, 2008, 'Gold-bismuth-telluride-sulphide assemblages at the Viceroy Mine, Harare-Bindura-Shamva greenstone belt, Zimbabwe', *Mineralogical Magazine*, vol. 72, pp.953-970.

Oen, IS & Kieft, C, 1974, 'Nickeline with pyrrhotite and cubanite exsolution, Ni-Co rich loellingite and an Au-Cu alloy in Cr-Ni ores from Beni Bousera, Morocco', *Neues Jahrbuch der Mineralogie, Monatshefte*, pp. 1-8.

Oftendahl, I 1940, 'Untersuchung über die Nebenbestandteile von Erzmineralien norwegischer zinkblendführender Vorkommen', *Skriften Norske Videnskap-akadami Oslo, Mathematik Naturvidenskapeling*, Klasse 8, pp.1-103.

Outridge, PM, Doherty, W & Gregoire, DC, 1998, 'Determination of trace elemental signatures in placer gold by laser-ablation inductively coupled plasma mass spectrometry as a potential aid for gold exploration', *Journal of Geochemical Exploration*, vol. 60, pp. 229-240.

OZCHEM, 2008, National whole rock geochemistry database, Geoscience Australia.

Passchier, CW & Trouw, RAJ, 2005, *Micro-tectonics*, 2nd edn., Springer, Berlin-New York.

Patchett, JP, 1983, 'The importance of the Lu-Hf isotopic system in studies of planetary chronology and chemical evolution', *Geochimica et Cosmochimica Acta*, vol. 47, pp.81-91.

Patchett, JP, Kouvo, O, Hedge, CE & Tatsumoto, M, 1981, 'Evolution of continental crust and mantle heterogeneity: evidence from Hf isotopes', *Contributions to Mineralogy and Petrology*, vol. 78, pp. 279-297.

Patterson, J, 1996, *Redcap prospect work summary, internal company report*, Niugini Mining Ltd.

Paverd, AL, 1971, 'Contact metamorphism and mineralization at Mt. Redcap, Chillagoe, North Queensland', PhD thesis, James Cook University, Townsville.

Paverd, PL, 1981, 'Skarn mineralogy in relation to Cu-Zn-Pb mineralisation' in DM Hausen (ed.), *Process Mineralogy: extractive metallurgy, mineral exploration, energy resources*, American Institute of Mining and Metallurgy, New York, pp.179-186.

Perkins, C & Kennedy, AK, 1998, 'Permo-Carboniferous gold epoch of northeast Queensland', *Australian Journal of Earth Sciences*, vol. 45, pp. 185-200.

Pitcher, WS, 1982, Granitoid type and tectonic environment, in KJ Hsu (ed.), *Mountain building processes*, Academic Press, London, pp. 19-40.

Plimer, IR 1984, 'Malayaite and tin-bearing silicates from a skarn at Doradilla via Bourke, New South Wales', *Australian Journal of Earth Sciences*, vol. 31, pp. 147-153.

Qian, Z, 1987, 'Trace elements in galena and sphalerite and their geochemical significance in distinguishing the genetic types of Pb-Zn ore deposits', *Chinese Journal of Geochemistry*, vol. 6, pp.177-190.

Ramdohr, P, 1980, *The ore minerals and their intergrowths*, 2nd edn., Pergamon Press, Oxford.

Rasmussen, B, 2005, 'Zircon growth in very low grade metasedimentary rocks: evidence for zirconium mobility at ~250 °C', *Contributions to Mineralogy and Petrology*, vol. 150, pp. 146-155.

Reisberg, L & Meisel, T, 2002, 'The Re-Os isotopic system: a review of analytical techniques' *Geostandards Newsletter*, vol. 26, pp. 249-267.

Richards, JR, White, DA, Webb, AW & Branch, CD, 1966, *Isotopic ages of acid igneous rocks in the Cairns hinterland, north Queensland*, bulletin 88, Bureau of Mineral Resources, Geology and Geophysics, Australia.

Richards, DNG, 1980, 'Palaeozoic granites of north eastern Australia' in RA Henderson & PJ Stephenson (eds.), *The geology and geophysics of northeastern Australia*, Geological Society of Australia, Queensland Division, Brisbane, pp. 229-246.

Rose, AW & Burt, DM, 1979, 'Hydrothermal alteration', in HL Barnes (ed.), *The geochemistry of hydrothermal ore deposits*, 2nd edn, John Wiley and Sons, pp. 173-235.

Rubatto, D & Gebauer, D, 2000, 'Use of Cathodoluminescence for U-Pb zircon dating by ion microprobe; some examples from the western Alps', in M Pagel, V Barbin, P Blanc & D Ohnestetter (eds.), *Cathodoluminescence in geosciences*, Springer, Berlin-Tokyo, pp. 373-400.

Rubenach, MJ & Cuff, C, 1985, 'The occurrence of coarse-grained massive tilleyite in the Redcap Creek magmatic skarn, north Queensland', *Mineralogical Magazine*, vol. 49, pp. 71-75.

Rubenach, MJ & Cartwright, I, 1994, 'Stable isotope fronts in high-temperature skarns at Chillagoe, Queensland', *Geological Society of Australia abstracts*, vol. 37, p. 317.

Rubenach, D, 2010, The petrography, geochemistry and genesis of gold mineralisation at Mungana, Chillagoe, Queensland, B.Sc. (Hons), James Cook University, Townsville.

Rule, AC & Radke, F, 1988, 'Baileychlore, the Zn end member of the trioctahedral chlorite series', *American Mineralogist*, vol. 73, pp. 135-139.

Saager, R, 1969, 'The relationship of the silver and gold in the Basal Reef of the Witwatersrand, South Africa', *Mineralium Deposita*, vol. 3, pp. 93-113.

Saksela, M, 1951, 'Mineralogy and origin of the Pitkäranta orebodies', *Bulletin de la Commison Géologique de Finlande*, vol. 24, pp. 181-231.

Schaltegger, U, 2007, 'Hydrothermal zircon', *Elements*, vol. 3, pp. 78-79.

Scherer, EE, Whitehouse, MJ & Münker, C, 2007, 'Zircon as a monitor of crustal growth', *Elements*, vol. 3, pp. 19-24.

Scott, SD & Barnes, HL, 1971, 'Sphalerite geothermometry and geobarometry', *Economic Geology*, vol. 6, pp. 653-669.

Seedorff, E, Dilles, JH, Proffett, JM, Einaudi, MT, Zurcher, L, Stavast, WJA, Johnson, DA & Barton, MD, 2005, 'Porphyry deposits: characteristics and origin of hypogene features', in JW Hedenquist, JFH Thompson, RJ Goldfarb & JP Richards (eds.), *Economic Geology 100th Anniversary volume*, Society of Economic Geologists, Littleton, pp. 251-298.

Segal, I, Halicz, L & Platzner, IT, 2003, 'Accurate isotope ratio measurements of ytterbium by multiple collection inductively coupled plasma mass spectrometry applying erbium and hafnium in an improved double external normalisation procedure', *Journal of Analytical Atomic Spectrometry*, vol. 18, pp. 1217-1223.

Selby, D & Creaser, RA, 2001, 'Re-Os geochronology and systematics in molybdenite from the Endako porphyry molybdenum deposit, British Columbia, Canada', *Economic Geology*, vol. 96, pp. 197-2004.

Selby, D & Creaser, RA, 2004, 'Macroscale NTIMS and microscale LA-MC-ICP-MS Re-Os isotopic analysis of molybdenite: testing spatial restrictions for reliable Re-Os age determinations, and implications for the decoupling of Re and Os within molybdenite', *Geochimica et Cosmochimica Acta*, vol. 68, pp. 3897-3908.

Selby, D, Creaser RA, Hart, CJR, Rombach, CS, Thomson, JFH, Smith, MT, Bakke, AA & Goldfarb, RJ, 2002, 'Absolute timing of sulphide and gold mineralisation: a comparison of Re-Os molybdenite and Ar-Ar mica methods from the Tintina gold belt, Alaska', *Geology*, vol. 30, pp. 791-794.

Shand, SJ, 1943, *Eruptive rocks, their genesis, composition, classification, and their relation to ore deposits with a chapter on meteorite*, John Wiley & Son, New York.

Shannon, RD & Prewitt, CT, 1969, 'Effective ionic radii in oxides and fluorides', *Acta Crystallographica*, B25, pp. 925-946.

Shaw, Rd, Fawckner, JF & Bultitude, RJ, 1987, 'The Palmerville Fault system: a major imbricate thrust system in the northern Tasmanides, north Queensland', *Australian Journal of Earth Science*, vol. 34, pp.69-93.

Shcheka, G, Lehmann, B, Gerth, E, Gömann, K & Wallianos, A, 2004, 'Macrocrystals of Pt-Fe alloy from the Kondyor PGE placer deposit, Khabarovskiy, Russia: trace-element content, mineral inclusions and reaction assemblages', *The Canadian Mineralogist*, vol. 42, pp. 601-617.

Sheraton, JW & Black, LP, 1973, 'Geochemistry of mineralised granitic rocks of northeast Queensland', *Journal of Geochemical Exploration*, vol 2, pp. 331-348.

Sheraton, JW & Labonne, B, 1978, *Petrology and geochemistry of acid igneous rocks of north eastern Queensland*, bulletin 169, Bureau of Mineral Resources, Australia.

Sillitoe, RH, 1991, Intrusion-related gold deposits, in RP Foster (ed.), *Gold metallogeny and exploration*, Blackie, Glasgow, pp. 165-200.

Simon, G, Kesler, SE & Essene, EJ, 2000, 'Gold in porphyry copper deposits: experimental determination of the distribution of gold in the Cu-Fe-S system at 400° to 700 °C', *Economic Geology*, vol. 95, pp. 259-270.

Skertchly, SDJ, 1897, *Report on the tin mines of Watsonville and on various tin, silver, gold and copper mines at Herberton, Mount Albion, Irvinebank, Muldiva, Calcifer, Chillagoe, California Creek, and Tate River*, publication 119, Geological Survey of Queensland.

Skertchly, SDJ, 1899, ,The geology and mineral deposits of the country around Herberton, Watsonville and Chillagoe, North Queensland, *Proceedings of the Royal Society of Queensland*, vol. 14, pp. 9-27.

Sláma J, Košler J, Condon DJ, Crowley JL, Gerdes A, Hanchar JM, Horstwood MSA, Morris GA, Nasdala L, Norberg N, Schaltegger U, Schoene B, Tubrett MN & Whitehouse MJ, 2008, 'Plešovice zircon — a new natural reference material for U–Pb and Hf isotopic microanalysis', *Chemical Geology*, vol. 249, pp. 1–35.

Smith, JT, 1985, 'A mineralized solution collapse Breccia Red Dome, Mungana, North Queensland', B.Sc. thesis, James Cook University, Townsville.

Smith, MP, Hendersen, P, Jeffries, TER, Long, G & Williams, CT, 2004, 'The rare earth elements and uranium in garnets from the Beinn an Dubhaich aureole, Skye, Scotland, UK: constrains on processes in a dynamic hydrothermal system', *Journal of Petrology*, vol. 45, pp. 457-484.

Söderlund, U Patchett, PJ, Vervoort, JD & Isachsen, CE, 2004, 'The ^{176}Lu decay constant determined by Lu-Hf and U-Pb isotope systematics of Precambrian mafic intrusions', *Earth and Planetary Science Letters*, vol. 219, pp. 311-324.

Sonnet, PM 1981, 'Burite, calcium hexahydroxostannate, a new mineral from El Hamman, Central Morocco', *The Canadian Mineralogists*, vol. 19, pp. 397-401.

Stacey, JS & Kramer, JD, 1975, 'Approximation of terrestrial lead isotope evolution by a two-stage model', *Earth and Planetary Science Letters*, vol. 26, pp. 207-221.

Stein, HJ, Markey, RJ, Morgan, JW, Du, A & Sun, Y, 1997, 'Highly precise and accurate Re-Os ages from molybdenite from the East Quingling molybdenum belt, Shaanxi Province, China', *Economic Geology*, vol. 92, pp. 827-835.

Stein, HJ, Markey, RJ, Morgan, JW, Hannah, JL & Schersten, A, 2001, 'The remarkable Re-Os chronometer in molybdenite: how and why it works', *Terra Nova*, vol. 13, pp. 479-486.

Stein, H, Scherstén, A, Hannah, J & Markey, R, 2003, 'Subgrain-scale decoupling of Re and ^{187}Os and assessment of laser ablation ICP-MS spot dating in molybdenite', *Geochimica et Cosmochimica Acta*, vol. 67, pp. 3673-3686.

Stephenson, PJ & Griffin, TG, 1976, 'Cainozoic volcanicity of north Queensland' in JHC Bain & JJ Draper (eds.), 1997, *North Queensland geology*, Bulletin no. 240, Australian Geological Survey Organisation/Queensland geology series no. 9, Department of Mines and Energy, Brisbane.

Stumpfl, EF & Clarke, AM, 1965, 'Electron-probe micro-analysis of gold-platinoid concentrates from southeast Borneo', *Transactions of the Institution of Mining and Metallurgy*, vol. 74, pp. 933-946.

Suzuki, K, Feely, M & O'Reilly, C, 2001, 'Disturbance of the Re-Os chronometer of molybdenites from the late-Caledonian Galway granite, Ireland, by hydrothermal fluid circulation', *Geochemical Journal*, vol. 35, pp. 29-35.

Taylor, BE & Liou, JG, 1978, 'The low-temperature stability of andradite in C-O-H fluids', *American Mineralogist*, vol. 63, pp. 378-393.

Thompson, JFH, Sillitoe, RH, Baker, T, Lang, JR & Mortensen, JK, 1999, 'Intrusion-related gold deposits associated with tungsten-tin provinces', *Mineralium Deposita*, vol. 34, pp. 323-334.

Tomkins, AG & Mavrogenes, JA, 2001, 'Redistribution of gold within arsenopyrite and löllingite during pro- and retrograde metamorphism: application to timing of mineralisation', *Economic Geology*, vol. 96, pp. 525-534.

Tomkins, HG & Pinnel, MR, 1976, 'Low-temperature diffusion of copper through gold', Journal of Applied Physics, vol. 47, pp. 3804-3812.

Tooth, B, Ciobanu, CL, Green, L, O'Neill, B & Brugger, J, 2011, 'Bi-melt formation and gold scavenging from hydrothermal fluids: an experimental study', *Geochimica et Cosmochimica Acta*, vol. 75, pp. 5423-5443.

Torrey, CE, 1986, 'The geology and genesis of the Red Dome (Mungana) gold skarn deposit, north Queensland', M.Sc. thesis, James Cook University, Townsville.

Torrey, CE, Karjalainen, H, Joyce, PJ, Erceg, M & Stevens, M, 1986, *Geology and mineralisation of the Red Dome (Mungana), gold skarn deposit, north Queensland, Australia*, Contribution to the Economic Geology Research Unit, James Cook University, Townsville, vol. 21.

Townley, BK, Hérail, G, Maksaev, V, Palacios, C, de Parseval, P, Sepulveda, F, Orellana, R, Rivas, P, Ulloa, C, 2003, 'Gold grain morphology and composition as an exploration tool: application to gold exploration in covered areas', *Geochemistry: Exploration, Environment, Analysis*, vol. 3, pp. 29-38.

Valencia, VA, Noguez-Alcantara, B, Barra, F, Ruiz, J, Gehrels, G, Quintanar, F & Valencia-Moreno, M, 2006, 'Re-Os molybdenite and LA-ICP-MS U-Pb zircon geochronology for the Milpillas porphyry copper deposit: insights for the timing of mineralisation in the Cananea district, Sonora, Mexico, *Revista Mexicana de Ciencias Geologicas*, vol. 23, pp. 39-53.

Valero, R, Durand, B, Guth, J-L & Chopin, T, 1998, 'Mechanism of hydrothermal synthesis of zircon in a fluoride medium', *Journal of Sol-Gel Science and Technology*, vol. 13, pp. 119-124.

Valley, JW, Peacor, D, Bowman, JR, Essene, EJ & Allard, MJ, 1985, 'Crystal chemistry of a Mg-vesuvianite and implications of phase equilibria in the system CaO-MgO-Al_2O_3-SiO_2-H_2O-CO_2', *Journal of Metamorphic Geology*, vol. 3, pp. 137-153.

Van Achterbergh, E, Ryan CG, Jackson SE &Griffin WL, 2001, 'Data reduction software for LA-ICP-MS: appendix' in PJ Sylvester (ed.), *Laser Ablation-ICP-Mass Spectrometry in the Erath Sciences; Principles and Applications*, Mineralogical Association of Canada, Short Course Series, vol. 29, pp. 239-243.

Verryn, SMC, Merkle, RKW & von Gruenewaldt, G, 1991, 'Gold and associated ore minerals of the Waaikraal deposit, northwest of Brits, Bushveld Complex', *European Journal of Mineralogy*, vol. 3, pp. 451-466.

Vervoort, JD, Patchett, PJ, Gehrels, GE & Nutman, AP, 1996, 'Constraints on early earth differentiation from hafnium and neodymium isotopes', *Nature*, vol. 379, pp. 624-627.

Vervoort, JD, Patchett, PJ, Söderlund, U & Baker, M, 2004, 'Isotopic composition of Yb and the determination of Lu concentrations and Lu/Hf ratios by isotope dilution using MC-ICPMS', *Geochemistry Geophysics Geosystems*, vol. 5, pp. 1-15.

Vos, IMA, Bierlein FP, Barlow, MA & Betts, PG, 2006a, 'Resolving the nature and geometry of major fault systems from geophysical and structural analysis: the Palmerville Fault in north east Queensland, Australia', *Journal of Structural Geology*, vol. 28, pp. 2097-2108.

Vos, IMA, Bierlein FP & Webb, EJ, 2006b, 'Geochemistry of Early–Middle Palaeozoic basalts in the Hodgkinson Province: a key to tectono-magmatic evolution of the Tasman Fold Belt System in northeastern Queensland, Australia', *International Journal of Earth Science*, vol. 95, pp. 569–585.

Vos, IMA, Bierlein, FP, Barlow, MA & Betts, PG, 2007, 'Resolving the nature and geometry of major fault systems from geophysical and structural analysis: the Palmerville Fault in NE Queensland, Australia', *Journal of Structural Geology*, vol. 28, pp. 2097-2108.

Voundouris, PC, Melfos, V, Spry, PG, Bindi, L, Kartal, T, Arikas, K, Moritz, R & Ortelli, M, 2009, 'Rhenium-rich molybdenite and rhenite in the Pagoni Rachi Mo-Cu-Te-Ag-Au prospect, northern Greece: implications for the Re geochemistry of porphyry-style Cu-Mo and Mo mineralisation', *The Canadian Mineralogist*, vol. 47, pp. 1013-1036.

Wark, DA & Watson, EB, 2006, 'TitaniQ: a titanium-in-quartz geothermometer', *Contributions to Mineralogy and Petrology*, vol. 152, pp. 743-754.

Watling, RJ, Herbert, HK & Abell, ID, 1995, 'The application of laser ablation-inductively coupled plasma-mass spectrometry (LA-ICP-MS) to the analysis of selected sulphide minerals', *Chemical Geology*, vol. 124, pp. 67-81.

Watson, EB & Harrison, TM, 2005, 'Zircon thermometer reveals minimum melting conditions on earliest earth', *Science*, vol. 308, pp. 841-844.

Watson, EB, Wark, DA, & Thomas, JB, 2006, 'Crystallisation thermometers for zircon and rutile', *Contribution to Mineralogy and Petrology*, vol. 151, pp. 413-433.

Webb, JA, Bernecker, T & Fordham, BG, 1989, 'Early Silurian to Early Devonian limestone and cherts of the Chillagoe Formation, northeast Australia', *Geological Society of Australia, abstracts*, vol. 28, pp. 340-341.

Whalen, JB, Currie, KL & Chappell, BW, 1987, 'A-type granites - geochemical characteristics, discrimination and petrogenesis', *Contribution to Mineralogy and Petrology*, vol. 95, pp. 407-419.

Whitney, PR & Olmstedt, JF, 1998, 'Rare earth element metasomatism in hydrothermal systems: the Willsboro-Lewis wollastonite ores, New York, USA', *Geochimica et Cosmochimica Acta*, vol. 62, pp. 2965-2977.

Wiedenbeck, M, Hanchar, JM, Peck, WH, Sylvester, P, Valley, J, Whitehouse, M, Kronz, A, Morishita, Y, Nasdala, L, Fiebig, J, Franchi, I, Girard, J-P, Greenwood, RC, Hinton, R, Kita, N, Mason, PRD, Norman, M, Ogasawara, M, Piccoli, PM, Rhede, D, Satoh, H, Schulz-Dobrick, B, Skår, Ǿ, Spicuzza, MJ, Terada, K, Tindle, A , Togashi, S, Vennemann, T, Xie, Q & Zheng, Y-F, 2004, 'Further characterisation of the 91500 zircon crystal', *Geostandards and Geoanalytical Research*, vol. 28, pp. 9-39.

Williams, IS, 1998, 'U-Th-Pb geochronology by Ion Microprobe', in MA McKibben, WC Shanks & WI Ridley (eds.), *Applications of microanalytical techniques to understanding mineralising processes*, Society of Economic Geology, Reviews in Economic Geology, vol. 7, pp. 1-35.

Williams-Jones, AE & Normad, C, 1997, 'Controls of mineral paragenesis in the system Fe-Sb-S-O', *Economic Geology*, vol. 92, pp.308-324.

Withnall, IW, Lang, SC, Lam, JS, Draper, JJ, Knutson, J, Grimes, KG & Wellman, P, 1997a, 'Chapter 8: Broken River Region', in JHC Bain & JJ Draper, (eds.), *North Queensland Geology*,. Bulletin no. 240, Australian Geological Survey Organisation/Queensland geology series no. 9, Department of Mines and Energy, Brisbane.

Withnall, IW, Mackenzie, DE, Denaro, TJ, Bain, JHC, Oversby, BS, Knutson, J, Donchak, PJT, Champion, DC, Wellman, P, Cruikshank, BI, Sun, S-S & Pain, CF, 1997b, 'Chapter 3: Georgetown Region' in JHC Bain & JJ Draper, (eds.), *North Queensland Geology*,. Bulletin no. 240, Australian Geological Survey Organisation/Queensland geology series no. 9, Department of Mines and Energy, Brisbane.

Woodbury, MJ, 1994, 'Red Dome and Mungana porphyry Cu-Au and base metal skarns of north-east Queensland', B.Sc. (Hons) thesis, Australian National University, Canberra.

Woodhead, JD & Hergt, JM, 2005, 'A preliminary appraisal of seven natural zircon reference materials for in situ Hf isotope determination', *Geostandards and Geoanalytical Research*, vol. 29, pp. 183-195.

Wu, F-Y, Yang, Y-H, Xie, L-W, Yang, J-H & Xu, P, 2006, 'Hf isotopic compositions of the standard zircons and baddeleyites used in U-Pb geochronology', *Chemical Geology*, vol. 234, pp. 105-126.

Xiong, Y & Wood, SA, 1999, Experimental determination of the solubility of ReO_2 and the dominant oxidation state of rhenium in hydrothermal solutions', *Chemical Geology*, vol. 158, pp. 245-256.

Yardley, BWD, Rochelle, CA, Barnicoat, AC & Lloyd, GE, 1991, 'Oscillatory zoning in metamorphic minerals: an indicator of infiltration metasomatism', *Mineralogical Magazine*, vol. 55, pp. 357-365.

Ye, L, Cook, NJ, Ciobanu, CL, Liu, Y, Quian, Z, Tiegeng, L, Wei, G, Yulong, Y & Danyushevskiy, L, 2011, 'Trace and minor elements in sphalerite from base metal deposits in South China: a LA-ICPMS study', *Ore geology reviews*, vol. 39, pp. 188-217.

Zhang, L, Audétat, A & Dolejš, D, 2012, 'Solubility of molybdenite (MoS_2) in aqueous fluids at 600-800 °C, 200 M Pa: a synthetic fluid inclusion study', *Geochimica et Cosmochimica Acta*, vol. 77, pp. 175-185.

Appendices

Appendix 1: List of field and drill core samples and sample location map

Field samples

Sample	Rock type	MGA-94 E	MGA-94 N	PTS
BE-1	Granodiorite	224895	8111470	✔
BE-2	Dacite	225325	8111021	✔
BL 2	Banded skarn	225815	8108990	✔
BL 7	Banded skarn	225812	8109067	✔
BL 13	Wollastonite chert breccia	225859	8109190	✔
BL 19b	Garnet-vesuvianite-wollastonite skarn	226067	8109575	✔
BL 33	Limestone	225922	8109393	---
BL 36a&b	Garnet-vesuvianite-wollastonite skarn	225918	8109303	✔
BL 43	Chert	225942	8109254	---
BL 61a, e	Breccia	225937	8109283	✔
BL 67c	Secondary Cu mineralisation	226001	8108966	---
BL 86	Breccia	225875	8109225	+
BL 111b	Basalt	225747	8108974	✔
BL 126	Banded skarn	225775	8109068	✔
BL 179b	Greywacke	225977	8109854	✔
BL 204	Conglomerate	225848	8109879	✔
BL 205	Conglomerate	225830	8109860	✔
BL 213	Conglomerate	225914	8109701	+
BL 236	Milled Breccia	226133	8110097	+
BL 254	Magnetite-garnet skarn	225791	8109758	---
BL 271	Arkosic sandstone	225820	8109222	✔
BL 300	Garnet-wollastonite skarn	225819	8109237	---
BL 302	Banded skarn	225871	8109298	✔
BL 306	Breccia	225892	8109233	✔

PTS: polished thin section; +: thin section; ---: no section

DH location map

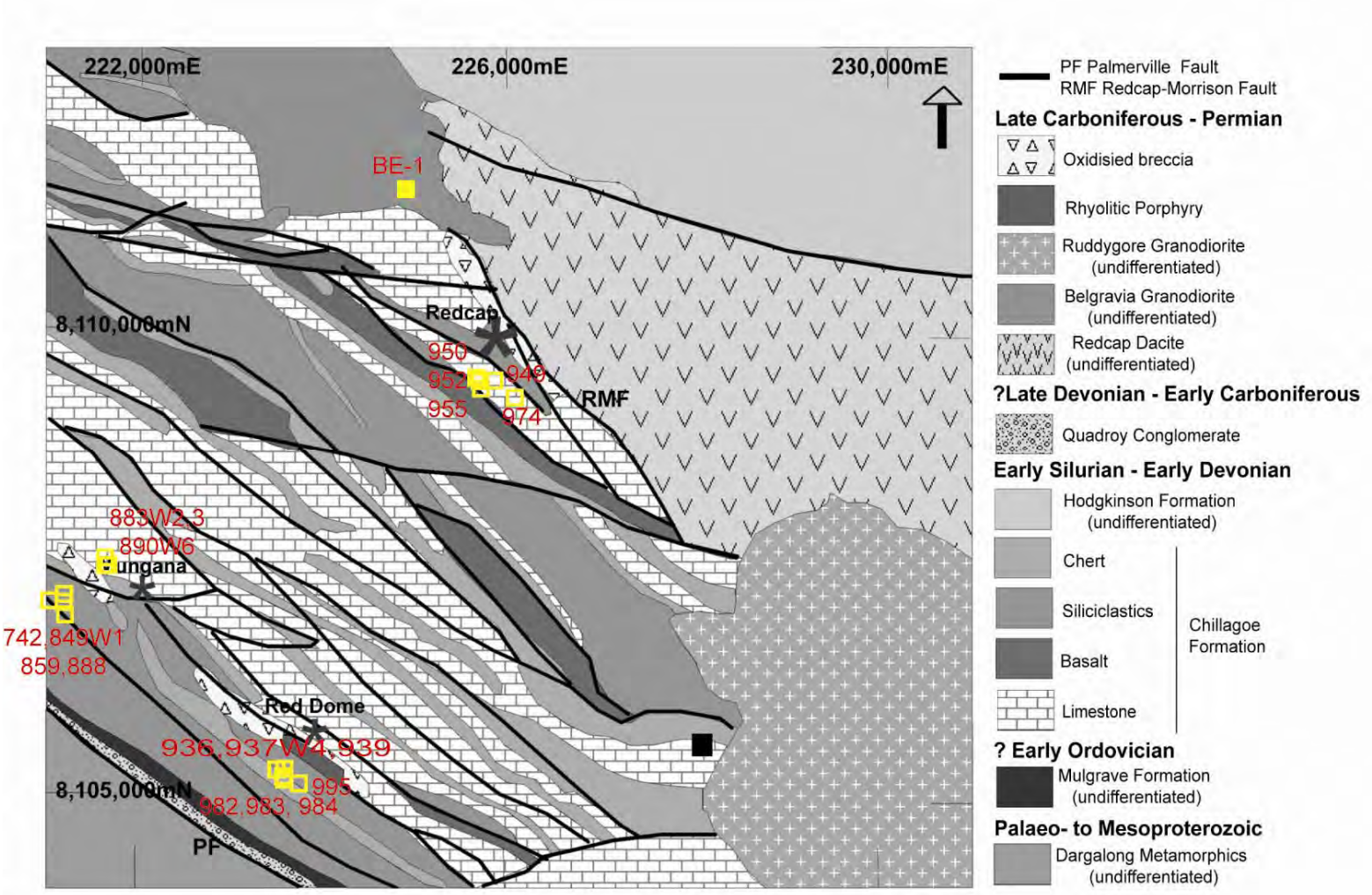

Drill core samples

Sample	Rock type	PTS	EMP						LA-ICP-MS				Geochronology		Lu-Hf
			Grt	Cpx	Sp	Au	MAP	Zrn	Grt	Cpx	Sp	Zrn	U-Pb	Re-Os	
BE-1	Belgravia granodiorite	✔						✔				✔	✔		✔
949-165.80	Brown garnet skarn	✔	✔		✔				✔		✔				
949-179.15	Brown garnet skarn + Zn-Cu-Pb mineralisation	✔	✔		✔				✔		✔				
949-197.53	Semi massive sulphides (Zn-Cu)	✔				✔									
949-247.37	Siltstone with Au-Bi-Te in quartz vein	✔				✔									
949-443.68	Clinopyroxene skarn	✔		✔						✔					
949-525.29-526.91	Redcap dacite	✔						✔				✔	✔		✔
950-472.05-472.16	Clinopyroxene skarn with disseminated Mo	✔												✔	
952-574.42	Massive sulphides (Cu)	✔	✔				✔		✔						
952-575.2III	Brown garnet-magnetite skarn	✔	✔			✔			✔						
952WI-603.53-668.05	Redcap dacite	✔						✔				✔	✔		✔
955-405.21-405.32	Clinopyroxene skarn with quartz-Mo vein	✔												✔	
974-291.01	Brown garnet-wollastonite skarn	✔	✔	✔					✔	✔					
974-349.86	Brown garnet-wollastonite skarn	✔	✔						✔						
742-479.7	Clinopyroxene skarn	✔	✔	✔											
849WI-579.72	Retrograde skarn with semi massive sulphides (Zn)	✔			✔						✔				
849WI-581.44	Carbonate breccia	*				✔									
859-612.15	Green garnet skarn with semi massive sulphides (Cu)	✔	✔				✔		✔						
859-765.8	Brown garnet skarn	✔	✔	✔			✔		✔						
883W2_1019.79-1022.25	Rhyolitic porphyry	✔						✔				✔		✔	✔
883W3_905.37-909.22	Granite	✔						✔				✔		✔	✔
888-710.7	Semi massive sulphides (Zn-Cu)	✔			✔						✔				
890W6-787.56-787.8	Brown garnet-wollastonite skarn	✔	✔	✔					✔	✔				✔	
MuD054-74.4	Basalt with quartz-Cu-As-Sb-Au vein	*				✔									

Sample	Rock type	PTS	EMP						LA-ICP-MS				Geochronology		Lu-Hf
			Grt	Cpx	Sp	Au	MAP	Zrn	Grt	Cpx	Sp	Zrn	U-Pb	Re-Os	
1960	quartz stockwork	*				✔									
841-530.1	Brown garnet skarn	✔	✔						✔						
936-635.22-367.69	Quartz-feldspar porphyry	✔						✔				✔	✔		✔
937W4-1133.19	Clinopyroxene skarn with quartz-Zn vein	✔			✔						✔				
939-731.9	Green garnet skarn	✔	✔				✔		✔						
939-772.2	Brown garnet skarn	✔	✔	✔					✔						
939-1103.02	Brown garnet-magnetite-clinopyroxene skarn	✔	✔	✔					✔	✔					
982-1013.72-1013.81	Clinopyroxene skarn with disseminated Mo	✔												✔	
983-880.28-880.41	Quartz-feldspar porphyry with quartz-Au-Mo-Bi-Te	✔				✔		✔				✔	✔	✔	✔
983-885.71	Quartz-feldspar porphyry with quartz-Au-Mo-Bi-Te	✔			✔			✔			✔		✔		
984-525.26-525.89	Quartz-feldspar porphyry	✔						✔				✔	✔		✔
995-478.59	Dacitic porphyry with quartz-Au vein	✔				✔									
995-614.15-615.8	Dacitic porphyry	✔						✔				✔	✔		✔

*: samples from Kagara Ltd and Rubenach (2010)

Samples highlighted in bold are those used in chapter 5 & 6 where only the drill hole number is provided.

Appendix 2: EMP analyses of rare silicates and sulphides

Mineral	Formula	SiO_2	Al_2O_3	CaO	FeO	Fe_2O_3	Na_2O	K_2O	H_2O	F	ThO_2
Apophyllite	$(K,Na)Ca_4Si_8O_{20}(F,OH) \times 8H_2O$	52.37	0.18	24.96	0.12	-----	-----	3	16.41	2.09	-----
Huttonite	$ThSiO_4$	18.97	-----	-----	-----	-----	-----	-----	-----	-----	80.74
Ilvaite	$CaFe^{2+}{}_2Fe^{3+}(Si_2O_7)O(OH))$	29.17	-----	13.27	-----	51.89	-----	-----	2.01	-----	-----
Nontronite	$Na_{0.3}Fe_2((Si,Al)_4O_{10})(OH)_2 \times nH_2O$	37.29	11.86	-----	-----	31.78	1.53	-----	17.46	-----	-----

Mineral	Formula	Ag	As	Au	Bi	Cu	Fe	Pb	S	Sb	Sn	Te
Altaite	PbTe	-----	-----	-----	-----	-----	-----	52.49	-----	-----	46.65	-----
Bismuthinite	Bi_2S_3	-----	-----	-----	82.19		-----	-----	17.71	-----	-----	-----
Chalcostibite	$CuSbS_2$	-----	-----	-----	-----	25.31	-----	-----	24.57	49.12	-----	-----
Covellite	CuS	-----	-----	-----	-----	65.55	-----	-----	34.45	-----	-----	-----
Digenite	Cu_9S_5	-----	-----	-----	-----	78.04	-----	-----	21.78	-----	-----	-----
Electrum	------	35.6	-----	64.4	-----	-----	-----	-----	-----	-----	-----	-----
Gudmundite	FeSbS	-----	-----	-----	-----	-----	22.64	-----	14.34	59.32	-----	-----
Hedleyite	B_7Te_3	-----	-----	-----	80.03	-----	-----	-----	-----	-----	-----	17.97
Hessite	Ag_2Te	63.7	-----	-----	-----	-----	-----	-----	-----	-----	-----	36.28
Mawsonite	$Cu_6Fe_2SnS_8$	-----	-----	-----	-----	31.29	18.38	-----	31.111	-----	15.37	-----
Pilsenite	Bi_4Te_3	-----	-----	-----	69.71	-----	-----	-----	-----	-----	-----	30.25
Rickardite	Cu_7Te_5	-----	-----	-----	-----	38.85	-----	-----	-----	-----	-----	61.12
Stibnite	Sb_2S_3	-----	-----	-----	-----	-----	-----	-----	29.12	70.57	-----	-----
Tellurobismuthite	Bi_2Te_3	-----	-----	-----	52.57	-----	-----	-----	-----	-----	-----	47.07
Tennantite	$Cu_{12}As_4S_{13}$	-----	20.53	-----	-----	44.09	5.33	-----	30.05	-----	-----	-----
Tetra-auricupride	AuCu	-----	-----	75.43	-----	24.58	-----	-----	-----	-----	-----	-----
Tetrahedrite	$Cu_{12}Sb_4S_{13}$	-----	-----	-----	-----	34.44	10.04	-----	24.55	30.77	-----	-----
Volynskite	$AgBiTe_2$	17.81	-----	-----	38.23	-----	-----	-----	-----	-----	-----	43.85

All values are reported in wt.-%.

Appendix 3: Assay data for selected “molybdenite” samples

SAMPLE	Au [ppm]	Ag [ppm]	As [ppm]	Bi [ppm]	Co [ppm]	Cr [ppm]	Cu [ppm]	Mo [ppm]	Ni [ppm]	Pb [ppm]	Sb [ppm]	Sn [ppm]	Te [ppm]	W [ppm]	Zn [ppm]
detection limit	*0.01*	*0.5*	*3*	*5*	*1*	*10*	*5*	*5*	*5*	*5*	*2*	*2*	*10*	*10*	*5*
955	2.58	2.3	3	320	10	100	1150	8950	6	14	<2	74	50	200	416
983	92.8	510	6730	61500	190	60	1610	20500	406	21200	2890	93	1650	<10	468
890W6	2.72	2.7	43	267	<1	50	15	2310	<5	68	2	1270	20	40	74

A short ¼ NQ2 drill core interval (9-24 cm), i.e. whole rock, was selected for assay analyses. Samples were analysed by SGS Townsville Minerals using the following methods: FAA505 for Au and ICP40Q and ICP43Q for the other elements.

Appendix 4: EMP analyses of garnets

	949.00 165.80	949.00 165.80	949.00 165.80	949.00 165.80	949.00 165.80	949.00 165.80	949.00 165.80	949.00 165.80	949.00 165.80	949.00 165.80	949.00 165.80	949.00 165.80	949.00 165.80	949.00 165.80	949.00 165.80	949.00 165.80	949 179.15	949 179.15
wt.-%	**A_1**	**A_2**	**A_3**	**A_4**	**A_5**	**A_6**	**A_7**	**A_8**	**A_9**	**D_1**	**D_2**	**D_3**	**D_4**	**D_5**	**D_6**	**D_7**	**D_1**	**D_2**
SiO_2	35.16	36.03	35.21	36.04	35.85	35.50	34.74	35.77	35.71	32.52	35.33	35.51	35.47	35.63	35.19	35.97	36.12	35.81
Fe_2O_3 *	30.70	23.81	29.75	23.01	24.94	25.72	29.16	23.64	26.39	24.16	31.37	24.50	27.98	25.31	30.28	23.76	23.13	22.70
MnO	0.10	0.17	0.08	0.32	0.22	0.26	0.42	0.29	0.20	0.17	0.11	0.20	0.09	0.23	0.22	0.30	0.75	0.88
MgO	0.16	0.08	0.14	0.09	0.08	0.12	0.32	0.18	0.11	0.12	0.12	0.06	0.16	0.06	0.23	0.10	0.16	0.23
CaO	33.68	34.23	33.76	34.37	34.42	34.14	33.31	34.57	34.50	34.18	33.47	34.36	33.49	34.68	33.59	34.67	34.13	33.87
Al_2O_3	0.21	5.22	0.99	5.90	4.60	3.81	1.03	5.01	3.39	4.20	0.03	5.01	1.67	4.72	0.53	5.68	5.30	4.64
TiO_2	<mdl	0.22	0.04	0.06	0.07	0.04	<mdl	<mdl	0.02	0.23	0.02	0.15	0.38	<mdl	0.06	<mdl	0.62	1.00
Na_2O	<mdl	<mdl	<mdl	<mdl	<mdl	<mdl	<mdl	<mdl	<mdl	0.13	<mdl	<mdl	<mdl	<mdl	<mdl	<mdl	<mdl	<mdl
K_2O	<mdl	<mdl	<mdl	<mdl	<mdl	<mdl	<mdl	<mdl	<mdl	0.04	<mdl	<mdl	<mdl	0.02	<mdl	<mdl	<mdl	<mdl
TOTAL	**100.01**	**99.76**	**99.97**	**99.79**	**100.18**	**99.60**	**98.99**	**99.47**	**100.34**	**95.74**	**100.48**	**99.79**	**99.25**	**100.65**	**100.11**	**100.48**	**100.21**	**99.15**
Adr [%]	100.00	74.95	96.38	72.44	78.94	82.63	96.60	76.32	84.70	84.44	99.93	77.60	90.66	79.91	98.54	74.63	73.39	74.18
Grs [%]		24.34	2.86	26.47	20.24	16.26	1.10	22.33	14.39	14.69		21.69	8.47	19.34	0.02	24.30	24.27	22.90
Pas [%]		0.71	0.76	1.09	0.82	1.10	2.30	1.35	0.91	0.87	0,07	0.70	0.87	0.75	1.44	1.07	2.34	2.92

Adr: andradite, grs: grossular, pas: pyralspite

*all Fe assumed as Fe^{3+}

	949	949	949	949	949	949	949	949	952	952	952	952	952	952	952	952	952	952
	179.15	179.15	179.15	179.15	179.15	179.15	179.15	179.15	574.42	574.42	574.42	574.42	574.42	574.42	574.42	574.42	574.42	574.42
wt.-%	**D_3**	**D_4**	**D_5**	**D_6**	**C_1**	**C_2**	**C_3**	**C_4**	**A_2**	**A_3**	**A_4**	**A_5**	**A_6**	**A_7**	**A_8**	**A_9**	**C_1**	**C_2**
SiO_2	34.92	35.69	34.82	36.46	35.44	35.86	35.43	36.06	34.77	34.30	34.34	34.03	33.92	34.18	34.25	35.45	34.63	34.13
Fe_2O_3	28.85	24.60	28.26	21.27	22.05	28.54	28.60	21.82	25.04	30.13	30.11	29.07	29.80	29.69	29.74	17.19	29.99	28.98
MnO	1.31	1.02	1.06	0.88	0.64	0.50	0.71	0.84	0.78	1.04	1.25	1.30	1.33	1.24	1.26	1.07	0.88	0.86
MgO	0.17	0.14	0.30	0.12	0.39	0.02	0.04	0.09	0.38	0.37	0.31	0.22	0.25	0.22	0.33	0.34	0.41	0.33
CaO	33.05	33.79	33.04	34.06	34.13	33.67	33.53	34.49	33.56	32.35	32.37	32.52	32.31	32.26	32.60	34.41	32.68	32.59
Al_2O_3	1.50	4.72	1.80	6.90	3.81	2.42	2.22	6.74	3.74	0.14	0.15	0.17	0.13	0.08	0.20	9.15	0.17	0.10
TiO_2	<mdl	0.05	<mdl	0.33	2.51	<mdl	<mdl	0.07	<mdl	0.03	<mdl	<mdl	0.04	<mdl	0.04	0.21	<mdl	0.06
Na_2O	<mdl	<mdl	0.02	<mdl	<mdl	<mdl	<mdl	<mdl	<mdl	<mdl	<mdl	<mdl	<mdl	<mdl	<mdl	<mdl	0.03	<mdl
K_2O	<mdl	<mdl	<mdl	<mdl	<mdl	<mdl	<mdl	<mdl	<mdl	<mdl	<mdl	<mdl	<mdl	<mdl	<mdl	<mdl	<mdl	<mdl
TOTAL	**99.80**	**100.01**	**99.30**	**100.01**	**98.96**	**101.02**	**100.53**	**100.12**	**98.27**	**98.35**	**98.55**	**97.32**	**97.80**	**97.67**	**98.41**	**97.83**	**98.79**	**97.06**
Adr [%]	94.63	78.47	93.12	66.45	74.00	89.48	90.97	68.90	83.29	99.92	99.99	100.00	99.87	100.00	99.88	56.11	100.00	99.79
Grs [%]	1.66	18.65	3.21	31.10	23.04	9.28	7.23	28.86	13.42							40.20		
Pas [%]	3.70	2.88	3.66	2.45	2.95	1.24	1.79	2.24	3.29	0.08	0.01		0.13		0.12	3.70		0.21

	952 574.42	952 574.42	952 574.42	952 574.42	952 574.42	952 574.42	952 574.42	952 574.42	952 574.42	952 574.42	952 574.42	952 574.42	952 574.42	952 575.2III	952 575.2III	952 575.2III	952 575.2III	952 575.2III
wt.-%	**C_3**	**C_4**	**C_5**	**C_6**	**C_7**	**C_8**	**C_9**	**D_1**	**D_2**	**D_3**	**D_4**	**D_5**	**D_6**	**A_1**	**A_2**	**A_3**	**A_4**	**A_5**
SiO_2	33.89	34.59	34.50	34.74	33.94	35.24	34.13	33.62	34.11	33.78	34.81	34.63	33.84	36.15	36.29	35.83	36.14	36.04
Fe_2O_3	28.95	30.22	29.48	29.93	28.75	20.19	29.25	28.98	29.90	29.04	30.05	30.02	29.45	31.08	26.99	29.88	28.56	29.75
MnO	0.97	0.69	0.91	0.99	0.94	1.01	0.95	0.97	0.94	1.12	0.91	0.92	1.04	0.47	0.57	0.45	0.53	0.38
MgO	0.27	0.41	0.25	0.54	0.42	0.39	0.20	0.37	0.48	0.30	0.38	0.32	0.13	0.29	0.07	0.26	0.06	0.11
CaO	32.30	32.74	32.94	32.90	31.87	33.98	32.70	32.57	32.81	33.05	32.86	32.74	32.17	32.85	33.38	33.25	33.40	33.53
Al_2O_3	0.08	0.23	0.15	0.31	0.07	6.78	0.20	0.18	0.25	0.14	0.16	0.03	0.11	0.12	3.15	0.56	2.09	0.72
TiO_2	0.05	0.04	<mdl	0.02	<mdl	0.10	<mdl	0.03	<mdl	<mdl	<mdl	0.02	<mdl	<mdl	0.39	0.06	0.14	<mdl
Na_2O	0.02	<mdl	<mdl	0.02	<mdl	<mdl	<mdl	<mdl	<mdl	<mdl	<mdl	<mdl	<mdl	<mdl	<mdl	<mdl	<mdl	<mdl
K_2O	<mdl	<mdl	<mdl	<mdl	0.02	<mdl	<mdl	<mdl	<mdl	<mdl	<mdl	<mdl	<mdl	<mdl	0.02	<mdl	<mdl	<mdl
TOTAL	**96.54**	**98.92**	**98.23**	**99.45**	**96.02**	**97.70**	**97.44**	**96.72**	**98.50**	**97.45**	**99.18**	**98.69**	**96.74**	**100.97**	**100.85**	**100.30**	**100.92**	**100.55**
Adr [%]	99.82	99.86	100.00	99.91	99.93	66.98	99.97	99.89	100.00	99.96	100.00	99.93	100.00	99.99	83.87	96.95	89.49	96.30
Grs [%]						29.21									14.53	0.94	9.04	2.37
Pas [%]	0.18	0.14		0.09	0.07	3.81	0.03	0.11		0.04		0.07		0.01	1.59	2.11	1.47	1.33

	952 575.2III	952 575.2l.	952 575.2l.	962 575.2l.	952 575.2l.	952 575.2l.	952 575.2l.	952 575.2l	952 575.2.l	952 575.2l.	939 731.9	939 731.9	939 731.9	939 731.9	939 731.9	939 731.9	939 731.9
wt.-%	**A_6**	**A_7**	**A_8**	**A_9**	**C_1**	**C_2**	**C_3**	**C_4**	**C_5**	**C_6**	**B_1**	**B_2**	**B_3**	**B_4**	**B_5**	**B_6**	**A1**
SiO_2	36.09	35.92	36.34	35.79	35.48	35.89	35.73	35.66	35.73	35.25	37.18	35.37	35.95	35.73	37.51	37.34	35.89
Fe_2O_3	29.35	30.93	28.73	30.08	31.11	27.73	27.61	30.42	29.06	30.90	16.71	31.75	31.55	22.24	9.37	19.37	25.22
MnO	0.33	0.51	0.59	0.54	0.41	0.73	0.57	0.46	0.46	0.40	0.32	0.14	0.11	0.20	0.33	0.24	0.16
MgO	0.11	0.06	0.07	0.22	0.19	0.05	0.06	0.11	0.05	0.05	0.10	0.03	<mdl	<mdl	<mdl	0.07	<mdl
CaO	33.43	32.51	33.23	32.83	33.39	33.01	33.26	33.21	33.43	33.15	36.09	33.99	34.36	35.47	37.02	35.79	35.07
Al_2O_3	1.55	0.21	1.80	0.21	0.14	3.19	3.03	0.85	1.81	0.73	10.74	0.04	<mdl	7.00	16.50	8.72	4.21
TiO_2	0.03	0.03	0.15	<mdl	<mdl	0.24	0.21	0.02	0.04	<mdl	0.73	<mdl	<mdl	<mdl	<mdl	0.11	<mdl
Na_2O	<mdl	0.02	<mdl	<mdl	<mdl	<mdl	0.02	<mdl	<mdl	<mdl	<mdl	<mdl	<mdl	<mdl	<mdl	<mdl	<mdl
K_2O	<mdl	<mdl	<mdl	<mdl	<mdl	<mdl	<mdl	<mdl	<mdl	<mdl	<mdl	<mdl	<mdl	<mdl	<mdl	<mdl	<mdl
TOTAL	**100.89**	**100.18**	**100.91**	**99.68**	**100.73**	**100.84**	**100.49**	**100.75**	**100.59**	**100.49**	**101.89**	**101.32**	**101.99**	**100.66**	**100.74**	**101.64**	**100.56**
Adr [%]	92.27	98.87	90.65	98.91	100.00	85.48	86.20	96.43	91.86	98.05	50.59	99.99	99.97	69.92	27.83	59.29	80.83
Grs [%]	6.52		7.69			12.60	12.20	2.03	6.85	0.79	48.32			29.63	71.48	39.91	18.78
Pas [%]	1.20	1.13	1.66	1.09		1.92	1.60	1.54	1.29	1.17	1.09		0.03	0.45	0.69	0.80	0.39

	939	939	939	939	939	939	939	939	939	939	939	939	939	939	939	939	939	939
	731.9	731.9	731.9	731.9	731.9	731.9	731.9	731.9	731.9	731.9	731.9	731.9	731.9	731.9	772.2	772.2	772.2	772.2
wt.-%	**A2**	**A3**	**A4**	**B_1**	**B_2**	**B_3**	**B_4**	**B_5**	**C_1**	**C_2**	**C_3**	**C_4**	**C_5**	**C_6**	**B_1**	**B_2**	**B_3**	**A_1**
SiO_2	36.26	36.32	35.89	35.40	37.15	38.15	37.01	37.06	36.62	35.56	37.48	38.12	37.22	36.87	36.37	35.92	36.52	36.84
Fe_2O_3	23.64	20.77	20.30	32.27	18.77	4.66	20.64	19.50	19.68	31.55	18.77	5.12	19.80	19.79	26.45	28.19	24.41	25.63
MnO	0.17	0.18	0.19	0.14	0.18	0.38	0.17	0.23	0.17	0.16	0.16	0.40	0.16	0.27	0.22	0.18	0.18	0.10
MgO	<mdl	0.02	0.02	<mdl	0.11	0.04	0.11	0.05	0.21	0.03	0.12	0.04	0.11	0.05	<mdl	<mdl	<mdl	0.17
CaO	35.22	35.70	35.48	33.99	35.90	37.46	35.46	35.73	35.66	33.98	35.82	37.19	35.74	36.02	33.95	33.94	34.84	34.58
Al_2O_3	5.98	7.87	8.18	<mdl	9.15	19.57	7.87	9.11	7.45	0.04	8.87	19.24	8.34	8.74	4.52	2.94	5.36	3.88
TiO_2	<mdl	0.03	<mdl	<mdl	0.28	0.07	0.08	0.15	1.63	<mdl	0.22	0.08	0.25	0.16	0.06	0.04	0.07	0.20
Na_2O	<mdl	<mdl	<mdl	0.05	0.06	<mdl	<mdl	<mdl	<mdl	<mdl	0.02	<mdl	<mdl	<mdl	<mdl	<mdl	0.02	<mdl
K_2O	<mdl	<mdl	<mdl	<mdl	<mdl	<mdl	<mdl	<mdl	<mdl	<mdl	<mdl	<mdl	<mdl	<mdl	<mdl	<mdl	<mdl	<mdl
TOTAL	**101.28**	**100.89**	**100.07**	**101.87**	**101.59**	**100.34**	**101.33**	**101.82**	**101.42**	**101.32**	**101.47**	**100.19**	**101.63**	**101.90**	**101.57**	**101.21**	**101.41**	**101.39**
Adr [%]	73.57	64.78	63.75	100.00	57.55	13.70	63.48	59.10	61.70	100.00	57.63	15.05	60.80	60.75	80.14	87.40	75.47	80.33
Grs [%]	26.04	34.73	35.73		41.65	85.33	35.73	40.23	37.12		41.56	83.97	38.41	38.46	19.35	12.18	24.08	18.77
Pas [%]	0.40	0.48	0.52		0.80	0.97	0.79	0.67	1.17		0.80	0.98	0.79	0.79	0.51	0.41	0.45	0.90

	939	939	939	939	939	939	939	939	939	939	939	974	974	974	974	974	974	974
	772.2	772.2	772.2	772.2	772.2	772.2	772.2	772.2	772.2	772.2	772.2	349.86	349.86	349.86	349.86	349.86	349.86	349.86
wt.-%	**A_2**	**A_3**	**A_4**	**A_5**	**A_6**	**A_7**	**A_8**	**A_9**	**C_1**	**C_2**	**C_3**	**B_1**	**B_2**	**B_3**	**C_1**	**C_2**	**C_3**	**C_4**
SiO_2	37.31	37.17	36.75	36.81	37.08	37.10	36.79	37.14	36.31	36.45	36.86	35.45	35.25	35.46	35.67	35.58	35.58	35.80
Fe_2O_3	23.52	23.73	25.52	26.67	23.23	25.75	25.02	24.78	28.29	26.96	25.98	31.28	31.95	32.94	31.23	32.14	32.34	32.48
MnO	0.17	0.15	0.13	0.11	0.16	0.18	0.09	0.14	0.19	0.16	0.11	0.24	0.18	0.25	0.22	0.23	0.22	0.22
MgO	0.23	0.19	0.21	0.15	0.19	0.12	0.17	0.23	<mdl	<mdl	0.16	0.02	0.05	<mdl	<mdl	0.07	<mdl	<mdl
CaO	34.61	34.86	34.54	34.44	34.77	34.30	34.60	34.78	33.18	33.38	34.17	33.21	33.22	32.85	33.86	33.40	33.29	33.59
Al_2O_3	5.92	5.52	3.80	3.31	5.85	4.46	4.43	4.73	2.70	3.51	3.95	0.96	0.30	0.10	0.71	0.07	0.12	0.18
TiO_2	0.05	0.06	0.11	0.12	0.06	0.03	0.09	0.15	0.04	0.02	0.10	0.03	0.03	0.02	0.06	<mdl	<mdl	0.02
Na_2O	<mdl	<mdl	<mdl	<mdl	<mdl	<mdl	<mdl	<mdl	<mdl	0.02	0.03	0.03	0.03	0.02	<mdl	0.03	<mdl	<mdl
K_2O	<mdl	<mdl	<mdl	<mdl	<mdl	<mdl	<mdl	<mdl	<mdl	<mdl	0.01	<mdl	<mdl	<mdl	<mdl	<mdl	<mdl	<mdl
TOTAL	**101.81**	**101.67**	**101.06**	**101.62**	**101.36**	**101.96**	**101.19**	**101.96**	**100.73**	**100.50**	**101.37**	**101.21**	**101.01**	**101.65**	**101.77**	**101.53**	**101.57**	**102.30**
Adr [%]	71.63	73.19	80.81	83.42	71.71	78.59	78.09	76.63	86.89	83.02	80.53	97.31	99.93	99.96	98.11	99.96	99.98	99.93
Grs [%]	27.08	25.74	18.06	15.75	27.15	20.50	21.02	22.16	12.59	16.60	18.58	2.03			1.36			
Pas [%]	1.29	1.07	1.13	0.83	1.14	0.91	0.89	1.21	0.51	0.38	0.89	0.66	0.07	0.04	0.53	0.81	0.02	0.07

	974	859	859	859	859	859	859	859	859	859	859	859	859	859	859	859	859	841
	349.86	612.5	612.5	612.5	612.5	612.5	612.5	612.5	612.5	612.5	612.5	612.5	612.5	612.5	612.5	612.5	612.5	530.1
wt.-%	**C_5**	**A_1**	**A_2**	**A_3**	**A_4**	**A_5**	**A_6**	**A_7**	**C_1**	**C_2**	**C_3**	**C_4**	**C_5**	**D_1**	**D_2**	**D_3**	**D_4**	**B_1**
SiO_2	35.88	35.17	35.55	35.41	35.13	35.14	35.18	35.60	35.38	35.40	35.32	35.34	35.72	35.21	35.33	35.44	35.62	35.28
Fe_2O_3	31.43	30.71	31.46	30.54	30.72	30.82	31.75	29.60	31.24	31.16	30.90	31.27	30.01	30.31	30.94	31.11	29.93	31.53
MnO	0.18	2.04	0.45	1.20	0.23	0.40	0.60	0.31	1.79	1.60	1.48	1.46	0.25	1.24	1.40	1.14	0.31	0.12
MgO	0.03	0.22	0.13	0.11	0.23	<mdl	<mdl	0.12	0.15	0.10	0.06	0.12	0.08	0.09	0.08	0.05	0.12	0.03
CaO	34.06	32.21	33.72	33.30	34.06	33.83	33.51	34.20	32.62	32.88	32.93	32.98	34.37	33.00	32.99	33.26	33.61	34.14
Al_2O_3	0.75	0.13	0.02	<mdl	0.31	0.03	<mdl	1.15	0.14	0.10	0.04	0.10	0.96	0.49	0.17	0.05	0.98	<mdl
TiO_2	0.07	<mdl	<mdl	<mdl	<mdl	<mdl	<mdl	<mdl	0.05	<mdl	<mdl	<mdl	0.05	<mdl	<mdl	0.02	<mdl	<mdl
Na_2O	0.04	<mdl	<mdl	<mdl	0.02	<mdl	0.02	<mdl	<mdl	<mdl	<mdl	<mdl	0.02	<mdl	0.02	<mdl	<mdl	<mdl
K_2O	<mdl	<mdl	<mdl	<mdl	<mdl	<mdl	<mdl	<mdl	<mdl	<mdl	<mdl	<mdl	<mdl	<mdl	<mdl	<mdl	<mdl	<mdl
TOTAL	**102.43**	**100.50**	**101.32**	**100.58**	**100.71**	**100.23**	**101.07**	**100.99**	**101.37**	**101.26**	**100.73**	**101.28**	**101.47**	**100.35**	**100.94**	**101.07**	**100.58**	**101.11**
Adr [%]	98.07	100.00	99.99	99.96	99.99	99.99	100.00	95.62	99.83	99.94	99.98	100.00	96.47	98.79	99.96	99.94	95.87	100.00
Grs [%]	1.37							3.17					2.62				2.90	
Pas [%]	0.56			0.04				1.21	0.17	0.06	0.02		0.91	1.20	0.04	0.06	1.23	

	841 530.1	841 530.1	841 530.1	841 530.1	841 530.1	841 530.1	841 530.1	841 530.1	841 530.1	841 530.1	841 530.1	841 530.1	841 530.1	841 530.1	841 530.1	841 530.1	841 530.1	974 291.01
wt.-%	**B_2**	**B_3**	**A_1**	**A_2**	**A_3**	**A_4**	**A_5**	**A_6**	**A_7**	**A_8**	**C_1**	**C_2**	**C_3**	**D_1**	**D_2**	**D_3**	**D_4**	**A_1**
SiO_2	35.39	35.28	35.66	35.56	35.46	35.31	35.08	34.98	35.63	35.25	35.65	35.55	35.27	35.58	35.62	35.68	35.71	36.32
Fe_2O_3	31.60	31.55	31.53	31.18	31.87	31.54	31.45	31.22	31.72	31.76	31.78	31.30	31.51	31.84	31.95	31.21	31.78	3.12
MnO	0.09	0.08	0.11	0.21	0.26	0.15	0.30	0.20	0.10	0.21	0.07	0.08	0.09	0.12	0.09	0.11	0.14	1.70
MgO	0.03	0.03	0.02	0.02	0.14	0.16	0.16	0.04	0.03	0.04	0.05	0.05	0.03	0.06	<mdl	<mdl	0.03	0.02
CaO	34.13	34.10	34.15	34.06	34.15	34.22	34.02	34.38	34.13	34.21	34.36	34.52	34.51	34.13	34.24	34.09	33.66	37.05
Al_2O_3	<mdl	<mdl	<mdl	<mdl	<mdl	<mdl	<mdl	<mdl	<mdl	<mdl	<mdl	0.02	<mdl	<mdl	<mdl	0.02	<mdl	19.68
TiO_2	0.03	<mdl	<mdl	<mdl	0.04	0.02	<mdl	<mdl	<mdl	0.06	<mdl	0.03	<mdl	<mdl	<mdl	<mdl	<mdl	0.18
Na_2O	<mdl	0.03	<mdl	<mdl	0.02	<mdl	0.02	0.03	<mdl	<mdl	<mdl	0.03	<mdl	<mdl	<mdl	<mdl	<mdl	0.02
K_2O	<mdl	<mdl	<mdl	<mdl	<mdl	<mdl	0.02	<mdl	<mdl	0.02	<mdl	<mdl	<mdl	<mdl	<mdl	<mdl	<mdl	<mdl
TOTAL	**101.28**	**101.09**	**101.51**	**101.04**	**101.95**	**101.40**	**101.05**	**100.85**	**101.62**	**101.57**	**101.94**	**101.57**	**101.43**	**101.75**	**101.92**	**101.11**	**101.32**	**98.10**
Adr [%]	99.90	99.96	99.95	100.00	99.87	99.95	100.00	100.00	99.98	99.83	100.01	99.92	100.00	99.99	99.99	100.01	100.00	9.83
Grs [%]																		86.60
Pas [%]	0.10	0.04	0.05		0.13	0.05			0.02	0.20		0.08						3.57

	974	974	939	939	939	939	939	939	939	939	939	939	939	939	939	939	939	859
	291.01	291.01	1103.2	1103.2	1103.2	1103.2	1103.2	1103.2	1103.2	1103.2	1103.2	1103.2	1103.2	1103.2	1103.2	1103.2	1103.2	765.8
wt.-%	**A_2**	**A_3**	**C_1**	**C_2**	**C_3**	**C_4**	**C_5**	**C_6**	**C_7**	**C_8**	**B_1**	**B_2**	**B_3**	**B_4**	**B_5**	**B_6**	**B_7**	**A_1**
SiO_2	37.51	37.79	35.47	35.67	36.05	35.92	35.80	36.34	35.55	35.78	35.32	35.95	35.73	35.33	35.76	35.97	35.42	35.55
Fe_2O_3	2.70	4.02	30.46	32.50	30.66	32.00	29.31	26.95	31.56	31.61	29.96	30.00	31.45	29.73	32.03	31.82	30.38	31.64
MnO	3.28	1.60	0.13	0.12	0.17	0.14	0.16	0.18	0.17	0.13	0.12	0.16	0.14	0.13	0.17	0.16	0.13	0.29
MgO	<mdl	<mdl	0.02	0.02	0.03	0.06	0.03	0.05	<mdl	<mdl	<mdl	<mdl	0.02	0.03	<mdl	0.03	<mdl	0.03
CaO	35.24	36.65	33.80	33.60	33.88	33.84	33.77	34.19	33.73	34.01	33.16	33.69	33.99	33.98	33.72	33.58	33.52	33.31
Al_2O_3	19.89	19.32	0.96	0.07	1.13	0.09	1.01	3.72	0.77	0.54	1.33	1.80	0.43	1.64	0.07	0.24	1.03	0.14
TiO_2	0.10	<mdl	0.04	<mdl	0.09	<mdl	0.02	0.08	<mdl	0.02	0.03	0.05	<mdl	0.02	0.03	<mdl	0.03	<mdl
Na_2O	<mdl	<mdl	0.03	<mdl	<mdl	<mdl	<mdl	<mdl	<mdl	0.02	0.07	0.03	0.02	0.03	0.03	0.03	<mdl	0.03
K_2O	<mdl	<mdl	<mdl	<mdl	<mdl	<mdl	<mdl	<mdl	<mdl	<mdl	0.04	<mdl	<mdl	0.02	<mdl	<mdl	<mdl	<mdl
TOTAL	**98.73**	**99.40**	**100.93**	**101.98**	**102.00**	**102.06**	**100.11**	**101.52**	**101.79**	**102.11**	**100.05**	**101.67**	**101.79**	**100.91**	**101.81**	**101.83**	**100.55**	**101.01**
Adr [%]	8.27	12.18	96.77	100.00	95.38	99.99	94.81	83.12	98.50	99.05	94.69	92.65	99.30	94.32	99.89	99.43	96.24	99.95
Grs [%]	84.84	84.46	2.84		4.13		4.70	16.27	1.07	0.61	4.96	6.98	0.30	5.26		0.07	3.41	
Pas [%]	6.89	3.36	0.39		0.50	0.57	0.49	0.61	0.43	0.34	0.35	0.37	0.39	0.42	0.11	0.49	0.36	0.05

	859 765.8	859 765.8	859 765.8	859 765.8	859 765.8	859 765.8	859 765.8	859 765.8	859 765.8	859 765.8	859 765.8	859 765.8	859 765.8	859 765.8	859 765.8	859 765.8	890W6 787.56	890W6 787.56
wt.-%	**A_2**	**A_3**	**A_4**	**A_5**	**A_6**	**A_7**	**A_8**	**E_1**	**E_2**	**E_3**	**E_4**	**E_5**	**B_1**	**B_2**	**B_3**	**B_4**	**C_1**	**C_2**
SiO_2	34.86	34.78	35.09	35.21	35.15	34.94	35.25	34.57	35.28	34.56	34.50	35.10	34.65	35.85	35.53	35.53	36.25	35.95
Fe_2O_3	30.70	31.92	30.92	31.21	31.36	32.01	31.14	30.70	30.67	31.24	31.95	31.13	31.83	31.00	31.45	30.84	28.21	30.86
MnO	0.53	0.57	0.43	0.39	0.40	0.44	0.31	0.42	0.33	0.40	0.46	0.42	0.49	0.33	0.74	0.43	0.40	0.55
MgO	0.22	0.21	0.14	0.11	0.23	0.13	0.30	0.15	0.21	0.08	0.10	0.13	0.17	0.23	0.24	0.35	0.09	0.13
CaO	33.16	33.53	33.75	33.80	33.80	33.59	33.67	33.71	34.02	33.49	33.24	33.61	33.24	33.27	32.59	33.35	33.79	32.75
Al_2O_3	0.02	0.05	0.19	0.34	0.11	0.02	0.21	0.65	0.34	0.02	<mdl	0.04	0.03	0.22	0.07	0.03	2.22	0.57
TiO_2	<mdl	0.04	<mdl	<mdl	<mdl	0.02	0.04	<mdl	<mdl	<mdl	<mdl	<mdl	<mdl	<mdl	<mdl	<mdl	<mdl	<mdl
Na_2O	<mdl	0.02	<mdl	<mdl	<mdl	0.03	<mdl	<mdl	<mdl	0.02	<mdl	<mdl	<mdl	<mdl	<mdl	0.02	<mdl	0.02
K_2O	<mdl	<mdl	<mdl	<mdl	<mdl	<mdl	<mdl	<mdl	<mdl	<mdl	<mdl	<mdl	<mdl	<mdl	<mdl	<mdl	0.02	<mdl
TOTAL	**99.51**	**101.11**	**100.51**	**101.07**	**101.06**	**101.18**	**100.92**	**100.21**	**100.85**	**99.82**	**100.28**	**100.44**	**100.43**	**100.89**	**100.63**	**100.56**	**100.98**	**100.83**
Adr [%]	99.96	99.88	100.00	100.00	100.00	99.93	99.86	99.96	99.99	99.96	99.99	100.00	99.99	98.92	99.99	100.00	89.03	97.19
Grs [%]																	9.68	0.97
Pas [%]	0.04	0.12				0.07	0.14	0.04		0.04				1.08			1.30	1.85

	890W6 787.56	890W6 787.56	890W6 787.56	890W6 787.56	890W6 787.56	890W6 787.56	890W6 787.56	890W6 787.56	890W6 787.56	890W6 787.56	890W6 787.56	890W6 787.56	742 479.7	742 479.7	742 479.7	742 479.7
wt.-%	**C_3**	**C_4**	**C_5**	**B_1**	**B_2**	**B_3**	**B_4**	**B_5**	**B_6**	**E_1**	**E_2**	**E_3**	**E_1**	**E_2**	**E_3**	**E_4**
SiO_2	36.02	35.90	36.23	35.92	35.66	35.29	35.89	35.57	35.75	36.05	35.70	35.84	37.85	38.06	38.60	37.83
Fe_2O_3	28.18	30.67	27.65	28.46	29.02	31.45	29.26	30.67	30.40	28.91	30.31	28.83	8.90	14.63	9.82	8.42
MnO	0.37	0.60	0.54	0.47	0.47	0.63	0.51	0.65	0.45	0.39	0.61	0.46	0.69	0.10	0.08	0.68
MgO	0.10	0.10	0.04	0.07	0.09	0.14	0.08	0.09	<mdl	0.09	0.10	0.05	0.02	0.10	0.11	<mdl
CaO	33.49	32.59	33.34	34.14	34.26	33.01	33.98	33.33	34.00	34.01	33.49	34.27	35.21	35.54	35.90	35.47
Al_2O_3	1.88	0.56	2.71	2.08	2.01	0.46	1.99	0.50	0.90	1.64	0.84	1.80	16.28	12.12	15.44	16.86
TiO_2	<mdl	<mdl	0.06	0.02	<mdl	<mdl	0.02	<mdl	0.02	0.02	0.03	0.02	0.70	0.12	0.58	0.62
Na_2O	<mdl	<mdl	<mdl	<mdl	<mdl	<mdl	<mdl	0.03	0.02	<mdl	<mdl	<mdl	0.02	<mdl	0.05	<mdl
K_2O	<mdl	<mdl	<mdl	<mdl	<mdl	<mdl	<mdl	<mdl	<mdl	<mdl	<mdl	<mdl	<mdl	<mdl	<mdl	<mdl
TOTAL	**100.05**	**100.43**	**100.57**	**101.16**	**101.50**	**100.99**	**101.74**	**100.85**	**101.54**	**101.11**	**101.09**	**101.29**	**99.68**	**100.68**	**100.58**	**99.92**
Adr [%]	90.53	97.22	86.54	90.68	92.32	99.67	91.98	98.32	96.80	92.13	96.64	92.26	25.99	43.49	28.62	24.49
Grs [%]	8.22	0.94	12.02	7.98	6.28		6.53		2.11	6.61	1.53	6.46	72.42	55.90	70.77	73.96
Pas [%]	1.25	1.84	1.43	1.34	1.40	0.33	1.48	1.68	1.08	1.26	1.83	1.27	1.59	0.61	0.61	1.54

Appendix 5: EMP analyses of clinopyroxene

Sample	**949**	**949**	**949**	**949**	**949**	**949**	**949**	**974**	**974**	**939**	**939**	**939**	**939**	**890W6**	**890W6**
	443.68	**443.68**	**443.68**	**443.68**	**443.68**	**443.68**	**443.68**	**291.01**	**291.01**	**1103.2**	**1103.2**	**1103.2**	**1103.2**	**787.56**	**787.56**
[wt.-%]	D_1	D_2	D_3	D_4	B_1	B_2	B_3	A_1	A_2	A_2	A_3	B_1	B_2	A_1	A_2
SiO_2	48.05	47.75	48.04	48.30	46.63	48.28	48.11	53.56	54.84	48.08	48.16	49.26	48.27	52.27	52.97
TiO_2	0.02	<mdl	<mdl	<mdl	<mdl	<mdl	<mdl	0.03	0.03	<mdl	0.02	<mdl	0.04	<mdl	<mdl
Al_2O_3	0.23	0.49	0.43	0.13	0.31	0.15	0.19	0.18	0.09	1.06	0.82	0.02	0.60	0.08	0.02
FeO	27.56	28.61	28.73	28.15	26.95	29.04	28.09	2.66	1.81	28.88	28.71	25.52	28.93	9.22	9.03
MnO	1.34	1.17	1.19	1.94	1.41	1.34	1.37	1.41	1.03	0.37	0.42	0.40	0.41	1.71	1.80
MgO	0.69	0.35	0.42	0.20	0.58	0.52	0.52	14.63	15.88	0.05	0.22	1.93	0.10	11.71	11.90
CaO	22.11	22.37	22.01	22.25	22.69	21.87	22.41	26.29	26.06	21.57	22.60	23.61	22.17	24.85	25.08
Na_2O	0.15	0.17	0.28	0.11	0.16	0.14	0.09	0.02	0.05	0.47	0.28	0.08	0.38	<mdl	<mdl
K_2O	<mdl	<mdl	<mdl	0.02	<mdl	<mdl	<mdl	<mdl	<mdl	<mdl	<mdl	<mdl	<mdl	<mdl	0.02
TOTAL	**100.15**	**100.92**	**101.11**	**101.10**	**98.73**	**101.35**	**100.77**	**98.78**	**99.80**	**100.50**	**101.22**	**100.83**	**100.91**	**99.85**	**100.82**
Number of ions calculated on the basis of 6 oxygen and ∑Fe as Fe^{2+}															
Si	1.980	1.963	1.969	1.981	1.958	1.976	1.976	1.997	2.007	1.974	1.966	1.990	1.977	1.986	1.990
Al	0.011	0.024	0.021	0.006	0.015	0.007	0.009	0.008	0.004	0.051	0.040	0.001	0.029	0.003	0.001
Fe	0.950	0.983	0.985	0.966	0.946	0.994	0.965	0.083	0.055	0.991	0.980	0.862	0.991	0.293	0.284
Ca	0.976	0.985	0.967	0.978	1.021	0.959	0.986	1.050	1.022	0.949	0.988	1.022	0.973	1.011	1.010
Ti	0.001	0.000	0.000	0.000	0.000	0.000	0.000	0.001	0.001	0.000	0.000	0.000	0.001	0.000	0.000
Mg	0.042	0.022	0.026	0.012	0.036	0.032	0.032	0.813	0.867	0.003	0.013	0.116	0.006	0.663	0.667
Mn	0.047	0.041	0.041	0.067	0.050	0.046	0.048	0.045	0.032	0.013	0.014	0.014	0.014	0.055	0.057
Na	0.012	0.013	0.022	0.008	0.013	0.011	0.007	0.001	0.003	0.037	0.022	0.006	0.030	0.000	0.000
K	0.000	0.000	0.000	0.001	0.000	0.000	0.000	0.000	0.000	0.000	0.000	0.000	0.000	0.000	0.001
Di [%]	4.08	2.07	2.44	1.16	3.49	2.98	3.03	86.45	90.83	0.32	0.92	0.32	0.62	65.59	66.16
Hd [%]	91.42	94.04	93.63	92.39	91.65	92.69	92.40	8.82	5.81	98.39	97.47	98.39	97.96	28.97	28.16
Jh [%]	4.50	3.89	3.93	6.45	4.86	4.33	4.56	4.73	3.36	1.29	1.61	1.29	1.42	5.44	5.68

Sample	**974**	**974**	**939**	**939**	**939**	**859**	**859**	**742**	**742**	**742**	**742**	**742**	**742**	**742**	**742**	**890W6**	**890W6**
	291.01	**291.01**	**772.2**	**1103.2**	**1103.2**	**765.8**	**765.8**	**479.7**	**479.7**	**479.7**	**479.7**	**479.7**	**479.7**	**479.7**	**479.7**	**787.56**	**787.56**
[wt.-%]	B_1	B_2	A	A_1	B_3	B_1	B_2	C_1	C_2	C_3	A_1	A_2	A_3	A_4	E	A_3	A_4
SiO_2	53.57	53.21	49.46	51.80	48.72	49.44	50.11	47.99	49.26	49.20	52.44	42.89	48.56	49.11	48.69	52.33	51.88
TiO_2	<mdl	<mdl	0.04	<mdl	<mdl	0.02	<mdl	<mdl	<mdl	<mdl	<mdl	0.56	<mdl	0.04	0.06	<mdl	<mdl
Al_2O_3	0.10	0.19	0.14	0.49	0.07	0.18	0.08	0.09	0.33	0.12	0.36	8.17	0.15	0.16	0.61	0.06	0.03
FeO	4.72	6.97	26.33	27.70	26.17	23.29	20.81	24.22	26.18	25.56	9.03	7.03	24.80	25.57	26.32	9.66	11.30
MnO	1.29	0.85	0.59	0.45	0.49	0.54	0.60	1.79	1.60	1.68	0.18	0.13	1.42	1.36	1.53	1.81	2.73
MgO	14.63	13.08	1.54	0.15	1.82	3.78	5.02	1.23	0.81	0.98	12.57	6.38	1.37	0.88	0.07	10.86	9.45
CaO	25.97	25.70	23.22	20.37	22.60	23.56	23.85	23.16	23.12	23.08	25.07	29.87	22.82	22.98	23.02	24.96	24.60
Na_2O	0.09	0.05	0.12	0.33	0.09	0.08	0.10	0.05	0.05	<mdl	0.06	0.14	0.08	0.10	0.07	<mdl	0.07
K_2O	<mdl	<mdl	<mdl	<mdl	0.05	<mdl	<mdl	<mdl	<mdl	<mdl	<mdl	0.10	<mdl	<mdl	<mdl	<mdl	<mdl
TOTAL	**100.37**	**100.05**	**101.44**	**101.30**	**100.01**	**100.88**	**100.58**	**98.55**	**101.36**	**100.62**	**99.72**	**95.27**	**99.22**	**100.21**	**100.36**	**99.70**	**100.06**
Number of ions calculated on the basis of 6 oxygen and ∑Fe as Fe^{2+}																	
Si	1.983	1.991	1.991	2.067	1.990	1.976	1.986	1.991	1.992	2.000	1.980	1.730	1.997	2.003	1.992	1.996	1.994
Al	0.004	0.008	0.007	0.023	0.003	0.008	0.004	0.005	0.016	0.006	0.016	0.388	0.007	0.007	0.029	0.003	0.001
Fe	0.146	0.218	0.886	0.924	0.894	0.778	0.690	0.840	0.885	0.869	0.285	0.237	0.853	0.872	0.900	0.308	0.363
Ca	1.030	1.030	1.002	0.871	0.989	1.009	1.013	1.029	1.002	1.005	1.014	1.291	1.005	1.004	1.009	1.020	1.013
Ti	0.000	0.000	0.001	0.000	0.000	0.001	0.000	0.000	0.000	0.000	0.000	0.017	0.000	0.001	0.002	0.000	0.000
Mg	0.807	0.730	0.092	0.009	0.111	0.225	0.297	0.076	0.049	0.060	0.708	0.384	0.084	0.054	0.004	0.617	0.542
Mn	0.040	0.027	0.020	0.015	0.017	0.018	0.020	0.063	0.055	0.058	0.006	0.004	0.049	0.047	0.053	0.058	0.089
Na	0.006	0.003	0.010	0.026	0.007	0.006	0.008	0.004	0.004	0.000	0.005	0.011	0.007	0.008	0.006	0.001	0.005
K	0.000	0.000	0.000	0.000	0.003	0.000	0.000	0.000	0.000	0.000	0.001	0.005	0.000	0.001	0.000	0.000	0.000
Di [%]	81.23	74.85	9.26	0.92	10.85	22.04	29.47	7.78	4.95	6.04	70.88	61.37	8.54	5.51	0.46	62.75	54.50
Hd [%]	14.70	22.37	88.73	97.47	87.50	76.17	68.53	85.80	89.51	88.09	28.56	37.93	86.45	89.66	94.01	31.31	36.55
Jh [%]	4.07	2.77	2.01	1.61	1.65	1.79	2.00	6.42	5.54	5.86	0.56	0.70	5.01	4.83	5.53	5.94	8.94

Appendix 6: EMP analyses of sphalerite

DH	949	949	949	949	949	949	949	949	949	949	949	949	949	949	949	949	949
m	179_15	179_15	179_15	179_15	179_15	179_15	179_15	179_15	179_15	179_15	179_15	179_15	179_15	179_15	179_15	179_15	179_15
grain	B	B	B	B	B	B	B	B	B	B	B	B	B	B	B	B	B
Fe	2.53	2.53	2.58	2.55	2.47	2.54	2.46	2.49	2.61	2.92	3.00	2.68	2.62	2.83	2.87	2.88	2.92
Zn	64.44	64.85	64.85	64.79	64.96	64.63	64.99	65.06	64.49	64.20	64.57	64.71	64.53	64.50	64.25	63.51	63.96
S	33.91	34.33	34.48	34.19	34.23	34.49	34.20	34.22	34.09	34.15	34.13	34.15	34.24	34.54	34.55	34.17	34.59
TOTAL	**100.87**	**101.71**	**101.92**	**101.54**	**101.69**	**101.66**	**101.69**	**101.77**	**101.21**	**101.26**	**101.71**	**101.54**	**101.39**	**101.87**	**101.67**	**100.56**	**101.48**

DH	949	949	949	949	949	949	949	949	949	949	949	949	949	949	949	949	949
m	179_15	179_15	179_15	179_15	179_15	179_15	179_15	179_15	179_15	165_80	165_80	165_80	165_80	165_80	165_80	165_80	165_80
grain	C	C	C	C	C	C	C	C	C	I	I	I	I	I	I	II	II
Fe	3.92	3.91	4.00	4.05	4.05	4.25	4.38	4.35	4.57	7.59	8.44	9.97	9.70	9.90	10.04	10.26	8.56
Zn	63.00	63.14	63.18	62.87	62.74	62.63	62.45	62.48	62.27	58.67	56.73	55.50	55.50	55.57	55.32	55.36	57.45
S	34.52	34.46	34.24	34.29	34.15	34.59	34.10	33.97	34.31	34.75	34.59	34.75	34.95	34.82	34.91	34.83	34.60
TOTAL	**101.44**	**101.51**	**101.41**	**101.23**	**100.94**	**101.47**	**100.93**	**100.82**	**101.16**	**101.01**	**99.82**	**100.29**	**100.16**	**100.34**	**100.27**	**100.48**	**100.61**

DH	949	949	949	949	949	949	949	949	949	949	949	937W4	937W4	937W4	937W4	937W4	937W4
m	165_80	165_80	165_80	165_80	165_80	165_80	165_80	165_80	165_80	165_80	165_80	1133	1133	1133	1133	1133	1133
grain	II	II	II	II	II	II	II	II	II	II	II	B	B	B	B	B	B
Fe	7.78	8.15	8.95	9.61	10.27	10.30	9.53	9.30	8.67	8.73	10.75	7.24	7.38	7.35	7.68	7.79	8.07
Zn	58.24	57.59	56.91	56.14	55.59	55.64	55.86	56.44	57.21	56.93	54.93	60.18	60.19	59.87	59.79	59.40	59.19
S	34.32	34.34	34.43	34.41	34.77	34.69	34.48	34.62	34.57	34.53	34.97	34.67	34.50	34.39	34.57	34.41	34.47
TOTAL	**100.34**	**100.07**	**100.30**	**100.16**	**100.63**	**100.63**	**99.89**	**100.35**	**100.47**	**100.20**	**100.64**	**102.08**	**102.07**	**101.61**	**102.04**	**101.60**	**101.74**

All values are reported in wt.-%; In general more than one sphalerite grain was analysed within a sample. Therefore different grains are labelled A-D or 1-II.

DH	937W4	937W4	937W4	937W4	937W4	937W4	983	983	983	983	983	983	983	983	983	983	983
m	1133	1133	1133	1133	1133	1133	885	885	885	885	885	885	885	885	885	885	885
grain	A	A	A	A	A	A	A	A	A	A	A	A	A	D	D	D	D
Fe	8.42	8.46	8.72	8.66	8.51	8.61	1.29	1.15	1.22	1.20	1.22	1.25	1.28	1.26	1.19	1.21	1.19
Zn	58.87	58.87	58.79	58.77	59.14	58.82	66.94	66.80	66.73	66.75	66.59	66.72	66.62	66.46	66.54	67.17	66.82
S	34.72	34.35	34.29	34.61	34.62	34.53	34.28	34.29	34.34	34.51	34.47	34.38	34.10	34.18	34.50	34.93	34.80
TOTAL	**102.01**	**101.74**	**101.82**	**102.09**	**102.27**	**101.97**	**102.51**	**102.23**	**102.29**	**102.46**	**102.30**	**102.34**	**102.00**	**101.91**	**102.24**	**103.31**	**102.82**

DH	983	983	983	849W1	849W1	849W1	849W1	849W1	849W1	849W1	849W1	849W1	849W1	849W1	849W1	849W1	849W1
m	885	885	885	579	579	579	579	579	579	579	579	579	579	579	579	579	579
grain	D	D	D	B	B	B	B	B	B	B	B	B	B	A	A	A	B
Fe	1.27	1.31	1.35	11.63	12.00	11.81	11.85	12.05	12.46	12.13	12.51	12.38	12.59	0.74	1.72	12.27	8.12
Zn	67.06	66.83	66.35	54.13	54.34	54.40	54.23	53.94	53.51	53.45	53.60	53.36	53.32	67.02	66.19	53.52	55.42
S	34.69	34.51	34.60	34.43	34.33	34.55	34.59	35.05	34.59	34.46	34.84	34.60	34.78	34.01	34.26	34.43	34.23
TOTAL	**103.02**	**102.64**	**102.30**	**100.19**	**100.68**	**100.77**	**100.72**	**101.04**	**100.56**	**100.04**	**100.94**	**100.34**	**100.69**	**101.78**	**102.16**	**100.23**	**97.76**

DH	849W1	849W1	849W1	849W1	849W1	849W1	849W1	849W1	888	888	888	888	888	888	888	888	888
m	579	579	579	579	579	579	579	579	710	710	710	710	710	710	710	710	710
grain	B	B	B	B	B	B	B	B	D	D	D	D	D	D	D	D	C
Fe	9.07	9.02	9.32	9.51	8.78	8.72	7.48	1.08	3.16	3.17	3.20	3.14	3.21	3.18	3.26	3.07	3.47
Zn	53.06	52.81	52.83	52.72	53.07	53.90	55.66	66.80	64.74	64.52	64.90	64.78	64.71	64.84	64.55	64.53	64.36
S	34.47	34.68	34.70	34.69	34.67	34.09	33.65	34.37	34.57	34.76	34.54	34.10	34.59	34.36	34.82	34.34	34.28
TOTAL	**96.60**	**96.51**	**96.88**	**96.95**	**96.51**	**96.75**	**96.81**	**102.25**	**102.48**	**102.45**	**102.71**	**102.02**	**102.52**	**102.38**	**102.63**	**102.00**	**102.11**

DH	888	888	888	888	888	888	888	888	888
m	710	710	710	710	710	710	710	710	710
grain	C	C	C	C	C	C	C	C	C
Fe	3.61	3.56	3.63	3.47	3.40	3.52	3.28	3.57	3.40
Zn	63.70	64.23	64.24	64.24	64.10	64.05	63.92	63.87	64.37
S	34.46	34.24	34.38	34.54	34.44	34.45	34.56	34.59	34.21
TOTAL	**101.79**	**102.03**	**102.24**	**102.28**	**101.96**	**102.08**	**101.79**	**102.11**	**101.98**

Appendix 7: EMP analyses of gold

Deposit	Sample	Cu [wt.-%]	Ag [wt.-%]	Au [wt.-%]	Fineness
Redcap	949_197_1	<mdl	37.88	62.12	621
Redcap	949_247_1	<mdl	23.34	76.66	767
Redcap	949_247_2	<mdl	24.41	75.59	756
Redcap	949_247_3	<mdl	22.08	77.92	779
Redcap	952_575II_1	<mdl	36.72	63.27	633
Redcap	952_575III_1	<mdl	41.88	58.12	581
Redcap	952_575_III_2	<mdl	41.07	58.91	589
Mungana	MuD54_74_1	4.26	14.56	81.18	848
Mungana	MuD54_74_3_1	1.82	13.06	85.11	867
Mungana	849W1_2	1.60	9.40	89.00	904
Mungana	849W2_1	2.04	13.52	84.44	862
Mungana	849W1_3	0.98	9.00	90.02	909
Mungana	849W1_3_2	0.85	15.45	83.70	844
Mungana	849W1_3_3	0.54	10.46	89.00	895
Mungana	849W1_3_5	1.77	11.16	87.07	886
Mungana	849W1_3_6	2.02	15.74	82.24	839
Mungana	1960_1_1	0.37	3.60	96.04	964
Mungana	1960_2	1.15	2.11	96.74	979
Mungana	1960_4_1	0.90	2.85	96.25	971
Mungana	1960_1_2	0.15	3.13	96.72	100
Mungana	1960_4_2	0.15	2.04	97.82	100
Griffith's Hill	995_478_1	0.03	8.04	91.93	920
Griffith's Hill	995_478_7	<mdl	13.06	86.94	869
Griffith's Hill	995_478_3	0.05	8.97	90.99	910
Griffith's Hill	995_478_5	<mdl	11.19	88.79	888
Griffith's Hill	995_478_6	<mdl	12.51	87.48	875
Griffith's Hill	995_4788	0.05	7.94	92.01	921
Red Dome	983_880_1	<mdl	13.93	86.07	861
Red Dome	983_880_2	<mdl	8.87	91.13	911
Red Dome	983_880_5	<mdl	11.73	88.25	883
Red Dome	983_880_6	<mdl	17.89	82.11	821
Red Dome	983_880_7	<mdl	14.18	85.82	858
Red Dome	983_880_9	0.06	19.22	80.72	808
Red Dome	983_880_8_1	<mdl	16.83	83.17	832
Red Dome	983_880_8_2	<mdl	17.12	82.88	829
Red Dome	983_880_8_3	<mdl	18.23	81.77	818
Red Dome	983_880_8_4	0.16	17.75	82.09	822
Red Dome	983_880_8_5	<mdl	16.34	83.65	837
Red Dome	937W4_1039_3_1	<mdl	14.36	84.56	855
Red Dome	937W4_1039_4_1	23.73	0.06	78.94	-----
Red Dome	937W4_1039_4_2	24.24	<mdl	77.73	-----
Red Dome	937W4_1039_4_4	25.59	<mdl	74.41	-----
Red Dome	937W4_1039_4_5	25.01	<mdl	74.12	-----
Red Dome	937W4_1039_4_6	26.43	<mdl	73.57	-----
Red Dome	937W4_1039_4_7b	24.60	<mdl	75.60	-----

Appendix 8: EMP analyses of zircon

#	SiO_2[wt.-%]	ZrO_2[wt.-%]	HfO_2[wt.-%]	Total
949_1	32.72	66.84	1.19	100.75
949_2	32.40	65.81	1.29	99.49
949_3	32.14	65.38	1.56	99.08
949_4	32.00	65.95	1.17	99.12
949_5_b	32.49	66.67	1.51	100.67
949_5_a	32.46	66.32	1.25	100.03
949_6	32.56	66.19	1.22	99.97
949_7_a	32.49	66.31	1.27	100.06
949_7_b	32.43	66.48	1.24	100.16
949_8_b	32.36	66.15	1.29	99.79
949_8_a	32.62	66.16	1.24	100.02
949_9	32.46	65.96	1.57	100.00
949_10	32.30	64.83	1.65	98.79
949_11	32.67	66.71	1.28	100.66
949_12	32.38	65.99	1.23	99.61
949_14	32.43	65.86	1.31	99.60
949_15	32.62	66.13	1.30	100.05
949_16_a	32.54	66.93	1.06	100.53
949_16_b	32.52	66.14	1.10	99.75
949_17	32.59	65.82	1.15	99.56
949_18	32.54	66.13	1.60	100.27
952W1_1_a	32.52	65.54	1.16	99.22
952W1_1_b	32.59	65.71	1.27	99.58
952W1_2	32.52	66.07	1.26	99.86
952W1_3_a	32.34	66.28	1.38	100.00
952W1_3_b	32.63	66.26	1.25	100.14
952W1_6	32.59	66.43	1.13	100.16
952W1_4	32.51	66.21	1.30	100.01
952W1_5	32.47	65.93	1.12	99.52
952W1_7	32.34	65.74	1.10	99.19
952W1_8	32.42	65.76	1.27	99.44
952W1_9_a	32.52	66.21	1.26	99.99
952W1_9_b	32.60	66.50	1.22	100.33
952W1_10	32.54	66.02	1.33	99.89
952W1_11_a	32.65	65.55	1.15	99.35
952W1_11_b	32.39	66.37	1.47	100.22
952W1_12_a	32.64	65.29	1.18	99.11
952W1_12_b	32.37	66.15	1.67	100.18
952W1_13	32.46	66.26	1.25	99.97
952W1_14	32.44	66.16	1.28	99.88
952W1_15	32.51	64.56	1.20	98.26
952W1_16	32.55	66.65	1.19	100.39
952W1_17	32.71	66.61	1.25	100.58
BE1_2 _PI	32.38	66.34	1.36	100.09
BE1_15_PI	32.35	66.44	1.47	100.26
BE1_17_PI	32.52	65.99	1.23	99.74
BE1_20 _PI	32.36	66.38	1.16	99.90
BE1_22 _PI	32.56	65.22	1.33	99.10
BE1_10 _PI	32.65	65.99	1.17	99.80

#	SiO_2[wt.-%]	ZrO_2[wt.-%]	HfO_2[wt.-%]	Total
BE1_3_PII	32.47	65.63	1.34	99.44
BE1_5_PII	32.41	66.56	1.25	100.21
BE1_19_PII	32.64	65.60	1.31	99.54
BE1_21_PII	32.39	66.20	1.18	99.76
BE1_7_PII	32.61	65.50	1.27	99.39
BE1_8	32.42	66.28	1.52	100.23
949_13	32.48	65.53	1.51	99.53
883W2_11	32.43	65.99	1.22	99.64
883W2_a	32.46	65.47	1.30	99.23
883W2_13	32.56	65.09	1.39	99.04
883W2_1	32.42	65.57	1.42	99.41
883W2_3	32.62	66.40	1.20	100.22
883W2_4	32.38	65.57	1.25	99.19
883W2_14	32.38	65.78	1.40	99.56
883W2_2	32.34	65.44	1.30	99.08
883W2_8	32.30	65.58	1.35	99.22
883W2_19	32.44	65.00	1.48	98.91
883W2_18	32.27	64.47	1.40	98.14
883W2_6	32.54	65.65	1.40	99.59
883W2_c	32.07	65.12	1.39	98.57
883W2_b	32.26	64.96	1.39	98.61
883W3_1	32.54	65.35	1.14	99.03
883W3_2_a	32.68	66.00	1.08	99.75
883W3_2_b	32.60	66.24	1.36	100.20
883W3_3	32.30	63.76	1.80	97.86
883W3_4	32.63	67.07	1.20	100.89
883W3_7_a	32.57	66.26	1.11	99.94
883W3_7_b	32.35	66.13	1.26	99.74
883W3_5	32.53	65.74	1.16	99.43
883W3_6	32.65	66.71	1.19	100.54
883W3_8	32.43	66.46	1.22	100.11
883W3_9	32.55	65.69	1.07	99.31
883W3_10	32.62	66.80	1.17	100.59
883W3_11_a	32.70	66.52	1.14	100.36
883W3_11_b	32.58	66.39	1.26	100.23
883W3_12	32.45	64.66	1.29	98.40
883W3_13	32.58	66.05	1.25	99.87
883W3_14	32.64	66.35	1.34	100.33
883W3_15	32.56	66.26	1.02	99.84
936_18	32.29	65.51	1.46	99.26
936_7	32.38	65.91	1.46	99.75
936_17	32.19	65.24	1.45	98.88
936_15	32.35	64.89	1.42	98.66
936_12	32.35	65.07	1.54	98.97
936_11	32.07	65.35	1.38	98.79
936_10	32.10	65.50	1.44	99.04
936_13	31.82	64.26	1.56	97.64
936_5	32.19	65.45	1.48	99.12
936_4	32.11	65.37	1.49	98.97
936_a	32.16	66.08	1.52	99.75

#	SiO_2[wt.-%]	ZrO_2 [wt.-%]	HfO_2[wt.-%]	Total
983_1	32.10	64.70	1.47	98.27
983_2	32.12	64.12	1.60	97.84
984_2	32.46	65.82	1.49	99.77
984_3	32.37	66.18	1.27	99.82
984_1	32.36	66.09	1.45	99.90
984_a	32.36	66.13	1.34	99.83
984_6	32.40	65.50	1.40	99.29
984_7	32.35	65.89	1.39	99.63
984_9	32.44	66.09	1.40	99.93
984_10	32.30	65.46	1.39	99.15
984_12	32.43	65.97	1.46	99.86
984_13	32.40	64.68	1.41	98.49
984_14	32.48	66.23	1.33	100.04
984_15	32.54	66.07	1.34	99.95
984_16	32.42	66.44	1.27	100.13
984_17	32.21	65.83	1.30	99.34
995_8	32.51	66.47	1.34	100.32
995_1	32.59	65.95	1.24	99.79
995_11	32.66	65.80	1.29	99.75
995_10	32.39	65.85	1.29	99.53
995_h	32.56	65.94	1.19	99.68
995_j	32.41	64.50	1.09	97.99
995_5	32.56	65.69	1.30	99.55
995_g	32.29	66.22	1.24	99.75
995_f	32.56	66.11	1.20	99.87
995_e	32.53	65.80	1.27	99.60
995_d	32.64	65.70	1.31	99.65
995_c	32.59	65.58	1.27	99.44
995_b	32.52	65.91	1.24	99.68
995_15	32.52	65.82	1.31	99.64
995_a	32.48	65.56	1.19	99.23
995_21	32.59	65.72	1.28	99.59
995_16	32.48	66.04	1.33	99.85
995_17	32.42	66.36	1.32	100.10

Appendix 9: LA-ICP-MS analyses of garnet

	939 731_9	939 731_9	939 731_9	939 731_9	939 731_9	939 731_9	939 731_9	939 731_9	939 731_9	939 731_9
[ppm]	A_1	A_2	A_3	A_4	A_5	B_1	B_2	B_3	B_4	B_5
Al27	1383	46912	98177	42739	44931	40647	115	110	45816	89333
Si29	170687	197301	214049	193196	194499	198781	177613	178113	198156	207245
Ca43	242927	256578	267727	253433	255363	257936	242927	245571	253504	264582
Sc45	1.2	5.2	4.0	3.3	2.0	16.7	1.3	1.3	2.0	3.5
Ti49	<0.2	1842.5	757.2	2889.9	1700.5	9658.1	0.5	90.0	1799.0	476.8
V51	<0.02	38.3	57.4	111.4	27.0	148.7	0.0	<0.02	78.9	41.6
Cr53	<1.3	20.6	3.4	6.6	6.9	69.7	1.5	<1.2	4.5	2.5
Mn55	1301	1675	3832	1479	1822	1789	1361	994	1737	3300
Cu65	<0.2	0.3	<0.3	<0.2	<0.2	0.4	<0.2	<0.2	<0.2	0.2
Zn66	24.5	4.4	2.7	3.7	5.8	7.5	24.1	15.1	7.5	2.3
Ga71										
Ge72										
As75										
Sr88	0.1	0.1	0.0	0.1	0.1	0.5	0.1	0.0	0.1	0.0
Y89	0.0	50.4	5.8	46.6	56.0	68.8	0.0	0.1	132.9	4.4
Zr90	0.0	68.5	14.1	70.0	76.6	239.1	<0.01	<0.01	67.9	8.9
Nb93	0.0	6.2	5.2	6.9	2.7	31.6	<0.01	0.0	5.1	4.0
Cd111										
In115										
Sn119	5052.5	315.3	24.4	80.4	580.8	102.2	5507.3	3170.2	470.9	70.3
Sn118	<0.1	355.9	28.9	91.8	656.6	115.6	<0.1	1671.6	532.8	80.3
Ta181										
Th232	0.0	0.1	<0.01	0.3	0.1	0.0	0.0	0.0	0.0	0.0
U238	0.1	0.5	0.0	0.3	0.6	0.4	0.0	0.0	0.7	0.0
Sn115										
La139	2.7	0.5	<0.001	0.4	0.2	0.4	0.9	0.4	0.5	0.0
Ce140	8.1	5.8	0.0	3.3	3.9	2.4	0.7	0.5	7.2	0.0
Pr141	0.9	1.8	0.0	1.0	1.7	0.6	0.0	0.0	2.9	0.0
Nd143	2.3	12.1	0.1	7.4	15.0	4.6	0.0	0.1	27.5	0.1
Sm147	0.2	5.8	0.1	4.2	8.4	2.8	<0.001	0.0	20.4	0.1
Eu151	1.2	0.6	0.0	0.3	0.8	0.4	0.3	0.1	0.8	0.1
Gd157	0.2	6.1	0.2	5.3	7.7	4.2	0.1	0.0	22.7	0.2
Tb159	0.0	1.0	0.1	1.0	1.3	0.9	0.0	0.0	3.8	0.0
Dy163	0.0	6.7	0.6	7.2	7.7	7.8	<0.01	0.0	23.5	0.5
Ho165	0.0	1.3	0.2	1.4	1.4	1.8	<0.01	0.0	4.2	0.1
Er167	<0.01	3.3	0.6	3.9	3.6	5.8	<0.01	<0.01	9.7	0.5
Tm169	<0.001	0.4	0.1	0.5	0.4	0.8	<0.001	<0.001	1.1	0.1
Yb171	<0.003	2.4	0.8	3.3	2.4	5.6	<0.01	<0.01	5.7	0.7
Lu175	<0.001	0.3	0.1	0.4	0.3	0.7	<0.00	0.0	0.5	0.1

blank cells: not analysed, <0.0..: < minimum detection limit

	939 731_9	939 772_2	939 772_2	939 772_2	939 772_2	939 772_2	939 772_2	939 772_2	939 772_2	939 772_2
[ppm]	B_6	A_1	A_2	A_3	A_4	A_5	A_6	A_7	A_8	A_9
B11										
Al27	41459	17118	18083	19149	18659	21118	17083	11746	13305	15839
Si29	192347	185805	188290	193184	191105	191351	194697	188849	215173	192835
Ca43	255791	247144	247358	249145	246858	246143	248502	245142	247287	248573
Sc45	2.0	4.9	4.6	2.6	5.5	3.9	2.7	2.3	1.8	1.6
Ti49	708.0	841.2	473.6	497.9	975.9	834.8	382.9	438.2	355.1	320.5
V51	37.7	14.3	12.8	10.5	16.1	12.7	21.6	21.9	24.3	23.2
Cr53	4.7	20.5	15.7	11.5	30.5	22.4	4.6	5.0	4.1	3.4
Mn55	1507	819	832	1087	888	872	999	967	145	1181
Co59										
Cu65	0.2	0.2	0.1	<0.1	0.2	0.2	1.5	0.2	0.3	<0.1
Zn66	3.5	8.7	8.5	10.3	8.0	8.5	99.9	10.6	237.7	19.0
Ga71										
Ge72										
As75										
Sr88	0.1	0.1	0.1	0.1	0.1	0.2	2.6	0.1	0.9	0.3
Y89	27.6	40.2	34.3	23.1	36.6	28.7	55.8	27.8	36.9	81.1
Zr90	22.2	66.9	65.0	69.5	70.6	56.1	27.8	36.2	16.8	10.6
Nb93	1.2	9.8	9.1	10.4	8.3	8.4	9.1	8.4	7.3	9.0
Cd111										
In115										
Sn119	68.0	294.8	346.4	114.0	286.0	216.2	409.9	373.0	351.0	468.3
Sn118	76.6	334.7	390.2	127.5	323.3	246.3	461.1	418.2	393.4	528.0
Ta181										
Th232	0.1	9.3	9.2	11.8	8.9	10.7	4.9	5.1	4.9	5.1
U238	0.6	3.9	2.9	13.2	3.2	2.5	8.5	6.9	7.6	6.8
Sn115										
Dy160										
La139	0.7	9.0	9.4	6.1	6.9	7.3	3.5	5.2	4.5	3.7
Ce140	5.7	87.8	83.6	64.4	67.7	66.2	81.7	97.1	94.3	81.2
Pr141	1.5	14.9	13.5	10.5	11.3	9.9	24.4	22.0	25.0	20.7
Nd143	10.4	51.7	45.8	37.5	38.5	30.6	122.9	103.6	119.7	106.4
Sm147	5.1	7.9	7.1	6.7	6.2	5.1	26.4	19.9	21.9	25.6
Eu151	0.3	3.7	4.0	1.8	3.0	2.2	7.4	4.5	6.1	5.8
Gd157	4.9	6.4	5.7	4.8	5.4	4.5	17.1	10.9	12.9	19.3
Tb159	0.8	0.8	0.7	0.6	0.7	0.6	2.1	1.2	1.5	2.7
Dy163	5.0	5.2	4.5	3.8	4.8	4.0	11.1	5.5	7.3	15.6
Ho165	0.9	1.1	1.0	0.8	1.0	0.9	1.8	0.9	1.2	2.7
Er167	2.3	3.0	2.7	2.0	2.8	2.4	3.7	1.9	2.3	5.6
Tm169	0.3	0.4	0.4	0.3	0.4	0.3	0.3	0.2	0.2	0.5
Yb171	1.8	2.8	2.4	2.0	2.7	2.4	1.8	1.5	1.2	2.6
Lu175	0.2	0.4	0.3	0.3	0.4	0.3	0.2	0.2	0.1	0.2

	974	974	974	974	974	974	974	974	841	841
	349_86	349_86	349_86	349_86	349_86	291_01	291_01	291_01	530_1	530_1
[ppm]	C_5	C_4	C_3	C_2	C_1	gt_3	gt_2	gt_1	A_8	A_7
B11										
Al27	1902	558	560	637	3224	105343	97136	101597	50	14
Si29	172970	176395	175825	175567	179916	227653	210912	225369	182024	178690
Ca43	243427	240068	237924	238710	241998	261938	251861	264797	244499	243927
Sc45	1.2	1.3	1.2	1.2	1.3	2.5	1.6	1.5	1.4	1.4
Ti49	159.0	174.7	268.8	195.4	235.7	1771.3	1034.8	867.1	1.7	0.6
V51	46.5	56.3	59.5	42.3	51.1	23.8	12.6	6.5	0.0	<0.01
Cr53	1.8	2.0	2.0	1.6	1.1	4.8	<2.1	2.7	1.4	0.8
Mn55	650	353	<0.1	<0.1	649	<0.4	<0.3	<0.2	835	<0.1
Co59										
Cu65	<0.1	0.1	0.5	<0.1	0.3	<0.3	0.5	0.3	0.1	0.1
Zn66	1.7	3.4	6.0	5.1	3.2	2.7	5.4	4.2	2.9	28.9
Ga71										
Ge72										
As75										
Sr88	0.4	0.5	1.2	0.5	0.2	1.4	0.2	0.0	0.0	0.0
Y89	1.1	0.1	0.2	0.1	0.8	8.8	0.9	0.2	0.1	0.1
Zr90	0.1	0.0	0.1	0.0	0.1	31.1	7.1	3.4	0.1	0.0
Nb93	0.7	0.1	0.2	0.2	4.3	6.7	4.9	3.2	0.0	0.0
Cd111										
In115										
Sn119	25.4	14.4	35.5	36.0	85.2	163.7	630.8	336.3	168.6	33.4
Sn118	28.3	16.2	40.5	41.1	95.9	185.1	707.4	381.8	190.7	38.5
Ta181										
Th232	0.2	0.0	0.0	0.0	0.8	0.0	0.0	0.0	0.0	0.0
U238	1.5	0.1	0.2	0.4	6.3	0.0	0.0	0.1	0.1	0.0
Sn115										
Dy160										
La139	2.4	1.7	2.7	4.1	3.1	<0.003	0.0	0.0	2.8	0.5
Ce140	10.5	2.9	3.5	6.2	19.9	2.3	0.0	0.0	8.7	1.4
Pr141	1.4	0.2	0.2	0.4	3.3	0.0	0.0	0.0	0.6	0.1
Nd143	3.5	0.5	0.4	0.7	9.5	0.2	0.3	0.2	1.2	0.2
Sm147	0.3	0.0	0.0	0.0	0.7	0.5	0.3	0.2	0.1	0.0
Eu151	0.2	0.0	0.0	0.0	0.8	0.1	0.0	0.1	0.2	0.0
Gd157	0.3	0.0	0.0	0.1	0.5	1.0	0.2	0.2	0.1	0.0
Tb159	0.0	0.0	0.0	0.0	0.0	0.2	0.0	0.0	0.0	0.0
Dy163	0.1	0.0	0.0	0.0	0.1	1.5	0.2	0.1	0.0	0.0
Ho165	0.0	0.0	0.0	0.0	0.0	0.3	0.0	0.0	0.0	0.0
Er167	0.1	0.0	0.0	0.0	0.0	0.8	0.1	0.0	0.0	0.0
Tm169	0.0	0.0	0.0	0.0	0.0	0.1	0.0	0.0	<0.001	0.0
Yb171	0.1	0.0	0.0	0.0	0.0	0.8	0.0	<0.03	0.0	0.0
Lu175	0.0	0.0	0.0	0.0	0.0	0.1	0.0	0.0	0.0	0.0

	841 530_1	841 530_1	841 530_1	841 530_1	841 530_1	841 530_1	890W6	890W6	890W6	890W6
[ppm]	A_6	A_5	A_4	A_3	A_2	A_1	C_5	C_4	C_3	C_2
B11										
Al27	41	37	133	11	33	103	10034	2682	4545	12445
Si29	181573	177351	179157	177161	178954	178126	180935	174110	176660	181908
Ca43	245714	243141	244571	244070	243427	244070	238281	232921	234065	239353
Sc45	1.4	1.3	1.3	1.5	1.4	1.3	1.5	1.5	1.6	2.1
Ti49	2.2	0.8	1.0	<0.1	3.8	0.6	60.5	103.8	96.5	230.7
V51	<0.01	<0.01	0.0	<0.01	0.0	<0.01	6.2	23.2	14.4	35.9
Cr53	1.0	1.2	<0.55	1.4	<0.55	0.8	1.2	2.2	0.8	11.9
Mn55	151	<0.1	1053	<0.1	<0.1	849	<0.1	<0.1	<0.1	<0.1
Co59										
Cu65	<0.1	<0.1	<0.1	<0.1	<0.1	<0.1	<0.1	0.1	<0.1	<0.1
Zn66	26.1	35.3	4.1	30.1	27.7	5.7	10.6	10.5	8.8	7.2
Ga71										
Ge72										
As75										
Sr88	0.1	0.1	0.0	0.1	0.0	0.0	0.1	0.1	0.1	0.0
Y89	0.3	0.2	1.5	0.1	1.4	0.3	8.3	0.1	1.8	12.7
Zr90	0.0	0.0	0.0	0.0	0.2	0.0	4.0	1.7	2.3	7.6
Nb93	0.0	0.0	0.0	0.0	0.0	0.0	10.1	0.1	0.3	0.3
Cd111										
In115										
Sn119	33.5	46.8	44.6	36.3	48.2	317.1	2576.8	2798.7	2419.9	2016.9
Sn118	38.1	53.3	51.2	41.2	55.4	357.2	<0.1	<0.1	<0.1	<0.1
Ta181										
Th232	0.0	0.0	0.0	0.0	0.0	0.0	1.0	0.3	0.5	0.1
U238	0.1	0.0	0.2	0.1	<0.01	0.2	1.3	2.6	2.1	0.1
Sn115										
Dy160										
La139	0.8	0.3	3.5	0.9	0.5	0.8	0.5	7.2	3.7	0.3
Ce140	2.4	0.5	10.8	3.7	1.7	5.6	6.5	13.8	7.7	3.6
Pr141	0.4	0.0	1.1	0.4	0.2	0.6	2.1	0.8	0.6	1.3
Nd143	0.7	0.2	3.0	1.3	0.9	1.4	14.7	1.3	2.5	10.9
Sm147	0.2	0.1	0.5	0.1	0.2	0.2	4.8	0.1	1.0	5.3
Eu151	0.1	0.0	0.1	0.1	0.1	0.2	0.8	0.3	0.3	0.8
Gd157	0.2	0.0	0.4	0.1	0.2	0.2	2.5	0.1	0.6	3.3
Tb159	0.0	0.0	0.0	0.0	0.0	0.0	0.3	0.0	0.1	0.4
Dy163	0.1	0.0	0.2	0.0	0.2	0.1	1.4	0.0	0.3	2.3
Ho165	0.0	0.0	0.0	0.0	0.0	0.0	0.2	0.0	0.0	0.4
Er167	0.0	0.0	0.1	0.0	0.1	0.0	0.5	0.0	0.1	0.9
Tm169	0.0	0.0	0.0	<0.002	0.0	0.0	0.1	0.0	0.0	0.1
Yb171	0.0	0.0	0.0	<0.001	0.0	0.0	0.4	0.0	0.1	0.7
Lu175	0.0	0.0	0.0	0.0	0.0	0.0	0.0	0.0	0.0	0.1

	890W6	939 1103_2	939 1103_2	939 1103_2	939 1103_2	939 1103_2	939 1103_2	939 1103_2	859 765_8	859 765_8
[ppm]	C_1	C_1	C_2	C_3	C_4	C_5	C_7	C_8	B_1	B_2
B11										
Al27	10790	4812	2282	4180	5063	4875	4225	2285	1237	1976
Si29	179242	194872	191132	194672	200843	197595	200485	200094	171744	179191
Ca43	241497	241569	240140	242141	241855	241355	241069	243070	240640	240068
Sc45	1.4	1.7	2.1	2.2	2.1	2.1	1.6	1.2	1.1	1.3
Ti49	44.0	274.1	371.4	570.5	644.3	272.3	148.9	26.5	5.3	5.6
V51	5.8	19.2	19.4	32.7	41.2	18.7	7.9	1.1	0.2	0.2
Cr53	1.7	<1.2	3.8	2.1	<2.1	<2.7	<2.5	<2.4	<1.1	2.6
Mn55	<0.09	1209	1217	1255	1234	1261	1603	983	205	1038
Co59										
Cu65	<0.1	<0.2	<0.2	1.7	<0.3	<0.3	<0.3	<0.3	0.8	<0.2
Zn66	5.5	13.2	22.8	93.6	10.3	10.8	11.9	5.1	19.6	13.4
Ga71										
Ge72										
As75										
Sr88	0.0	0.3	0.3	0.6	0.2	1.2	0.1	0.1	13.2	14.3
Y89	1.6	104.1	44.5	120.8	36.6	38.8	102.1	11.5	1.2	1.3
Zr90	0.2	1.3	2.2	3.2	3.7	1.6	0.9	0.1	0.1	0.1
Nb93	0.1	25.5	18.6	25.4	24.1	14.8	8.8	4.6	0.2	0.1
Cd111										
In115										
Sn119	2143.5	160.0	697.1	392.4	120.9	148.4	311.3	79.8	1864.1	2809.7
Sn118	<0.054	181.6	789.7	443.3	137.0	166.2	353.7	89.9	2082.7	1796.0
Ta181										
Th232	0.0	2.4	1.8	1.8	2.8	2.6	1.9	0.7	0.0	0.0
U238	0.0	4.1	7.0	5.6	3.1	4.2	4.9	1.5	2.4	3.3
Sn115										
Dy160										
La139	0.5	3.6	10.9	6.3	3.8	4.0	2.6	1.4	17.7	35.9
Ce140	2.3	53.1	85.1	62.2	41.0	57.9	53.9	22.2	21.2	33.1
Pr141	0.4	13.4	15.4	14.2	9.2	13.6	13.9	5.3	1.7	2.3
Nd143	2.3	72.7	64.8	80.2	48.6	62.8	69.6	25.0	4.6	5.0
Sm147	0.9	28.5	15.4	30.8	17.2	17.1	22.8	6.9	0.6	0.5
Eu151	0.3	1.2	1.7	1.8	0.9	0.9	1.7	0.5	2.0	2.7
Gd157	0.4	22.8	11.3	25.6	10.8	10.5	19.2	5.0	0.5	0.5
Tb159	0.1	3.2	1.5	3.8	1.3	1.3	2.7	0.5	0.0	0.0
Dy163	0.3	19.6	8.9	23.3	7.5	7.2	16.9	2.5	0.2	0.2
Ho165	0.0	3.6	1.6	4.4	1.3	1.3	3.1	0.4	0.0	0.0
Er167	0.1	8.7	3.6	11.0	3.7	3.5	7.9	0.9	0.1	0.1
Tm169	0.0	1.1	0.5	1.4	0.6	0.4	1.0	0.1	0.0	0.0
Yb171	0.1	6.4	2.9	8.3	4.3	3.5	5.9	0.6	0.0	0.0
Lu175	0.0	0.7	0.3	0.9	0.5	0.4	0.7	0.1	0.0	0.0

	859 765_8	859 765_8	859 765_8	859 765_8	859 765_8	949 165_80	949 165_80	949 165_80	949 165_80	949 165_80
[ppm]	B_3	B_4	B_5	B_6	B_7	D_1	D_2	D_3	D_4	D_5
B11						21	17	17	14	17
Al27	1106	167	687	848	481	24671	21847	27292	12274	11187
Si29	178362	176366	172973	180636	104350	192196	186670	192924	180048	193782
Ca43	241569	241569	241212	239639	237995	244285	239210	245571	239353	247858
Sc45	1.2	1.2	1.3	1.4	0.9	3.3	5.1	4.2	11.8	1.0
Ti49	1.8	1.1	1.0	5.1	21.6	485.3	1095.7	1017.0	838.5	70.6
V51	0.1	<0.02	0.0	0.2	0.5	15.6	20.1	23.1	16.9	4.9
Cr53	1.4	1.5	<0.94	2.2	1.0	5.9	19.8	17.8	48.8	3.4
Mn55	<0.2	<0.2	<0.2	1748	842	1536	1372	1384	925	1912
Co59						<0.1	<0.1	0.2	0.3	<0.1
Cu65	0.4	<0.1	0.3	<0.1	0.3	<0.6	<0.6	1.0	<0.4	<0.6
Zn66	28.2	12.0	20.2	15.1	14.1	2.1	2.6	2.0	2.5	1.6
Ga71						9.0	10.1	11.0	7.3	7.1
Ge72						4.6	5.6	5.4	4.8	4.2
As75						3.8	5.7	3.2	37.2	17.5
Sr88	15.5	0.6	26.0	0.7	9.8	0.0	0.1	0.6	1.8	0.0
Y89	1.2	0.6	1.3	1.6	1.2	16.9	16.4	19.8	8.6	3.8
Zr90	0.0	0.0	0.0	0.2	0.4	22.1	39.0	33.1	31.7	3.9
Nb93	0.1	0.1	0.1	0.2	0.2	1.6	3.3	3.0	2.6	0.3
Cd111						<0.1	<0.1	<0.1	<0.1	<0.1
In115						2.2	2.1	1.2	1.7	0.7
Sn119	2072.6	1505.4	817.0	1640.3	733.7	102.0	117.2	100.4	70.6	40.0
Sn118	2309.9	<0.083	924.4	1841.2	829.4	104.9	123.2	104.4	70.7	42.3
Ta181						0.1	0.2	0.2	0.3	0.0
Th232	0.0	0.0	0.0	0.0	0.1	5.8	4.1	4.8	2.0	1.3
U238	1.7	1.1	1.2	2.0	2.7	0.7	0.5	0.5	0.4	0.5
Sn115						1.9	1.9	1.0	1.5	0.7
Dy160						2.8	2.1	2.9	0.7	0.8
La139	20.5	32.5	19.3	38.3	8.0	0.5	0.5	0.4	1.4	1.8
Ce140	23.6	17.7	18.7	29.3	7.9	5.8	5.3	4.0	7.0	8.5
Pr141	1.8	1.1	1.5	1.8	0.8	2.1	1.7	1.6	1.3	1.6
Nd143	4.7	2.9	3.8	4.1	2.6	16.2	12.4	12.7	5.3	6.9
Sm147	0.5	0.3	0.4	0.5	0.4	3.9	3.0	3.5	0.7	1.3
Eu151	2.5	3.7	1.0	1.9	0.9	1.3	1.2	1.2	0.5	0.6
Gd157	0.5	0.3	0.4	0.5	0.3	2.9	2.2	3.0	0.6	
Tb159	0.0	0.0	0.0	0.1	0.0	0.4	0.3	0.4	0.1	0.1
Dy163	0.2	0.2	0.3	0.4	0.2	2.1	2.0	2.5	0.9	0.5
Ho165	0.0	0.0	0.0	0.1	0.0	0.4	0.4	0.5	0.2	0.1
Er167	0.1	0.1	0.1	0.1	0.1	1.0	1.1	1.3	0.6	0.2
Tm169	0.0	0.0	0.0	0.0	0.0	0.1	0.1	0.2	0.1	0.0
Yb171	0.0	0.0	0.0	0.0	0.0	1.0	1.0	1.1	0.5	0.2
Lu175	0.0	0.0	0.0	0.0	0.0	0.1	0.1	0.1	0.1	0.0

	949 165_80	949 165_80	952 575_2_III	952 575_2_III	952 575_2_III	952 575_2_III	952 575_2_III	952 575_2_III	952 575_2_III
[ppm]	D_6	D_7	A_1	A_2	A_3	A_4	A_5	A_6	A_7
B11	17	17	12	13	11	12	10	10	10
Al27	10792	25284	638	1675	4260	8566	3756	7001	1066
Si29	183646	192394	183119	183472	187948	185943	183086	182597	180389
Ca43	240068	247787	234779	238567	237638	238710	239639	238925	232349
Sc45	1.5	2.6	1.0	1.2	6.8	1.9	1.4	6.6	0.7
Ti49	129.8	326.3	13.0	281.4	390.1	661.3	235.1	420.7	9.6
V51	5.4	12.4	0.7	3.7	14.1	22.3	12.6	3.9	0.1
Cr53	3.8	<1.6	4.2	4.2	19.3	6.1	6.7	14.7	6.2
Mn55	1661	2373	3866	4196	3243	3366	2912	2533	3709
Co59	<0.1	<0.1	0.4	0.4	0.3	0.4	0.3	<0.1	0.4
Cu65	<0.5	<0.6	<0.5	<0.5	<0.5	<0.6	<0.5	<0.5	<0.5
Zn66	1.5	1.9	5.2	152.2	2.8	1.9	5.4	3.2	3.2
Ga71	6.1	12.0	23.7	16.2	35.7	43.6	35.5	21.9	25.5
Ge72	4.3	4.1	30.4	31.8	41.6	94.2	53.9	46.2	29.6
As75	24.8	35.3	48.0	30.0	27.0	8.8	15.4	17.5	6.1
Sr88	0.1	0.0	0.1	0.2	0.1	0.0	0.1	0.1	0.1
Y89	3.9	9.7	0.6	4.3	2.5	10.1	2.6	2.0	0.3
Zr90	5.0	13.7	0.9	6.1	7.8	16.2	3.7	9.6	0.4
Nb93	0.5	1.1	0.1	1.0	0.3	2.0	0.3	1.2	0.0
Cd111	<0.1	<0.1	0.1	0.9	0.2	0.3	0.3	0.1	0.2
In115	0.9	7.7	35.4	26.1	40.2	29.3	33.3	24.3	40.7
Sn119	50.8	1578.7	124.9	135.2	213.2	453.2	386.8	737.4	1066.8
Sn118	53.8	1630.3	129.4	141.4	219.5	468.0	401.6	765.2	1106.0
Ta181	0.0	0.1	0.0	0.1	0.0	0.1	0.0	0.1	<0.001
Th232	0.9	2.5	0.1	1.1	0.8	2.2	0.8	1.4	0.1
U238	0.6	0.8	0.0	0.1	0.3	0.6	0.3	0.5	0.2
Sn115	0.8	6.8	31.3	23.0	35.6	25.9	29.4	21.5	36.0
Dy160	0.5	1.3	0.1	0.4	0.2	1.0	0.3	0.2	0.0
La139	3.2	2.1	10.1	3.8	4.5	1.2	1.7	2.1	2.1
Ce140	13.7	11.8	1.3	0.9	5.4	3.6	3.8	7.0	3.4
Pr141	2.0	2.3	0.1	0.2	0.4	0.7	0.4	1.1	0.3
Nd143	7.1	9.8	0.3	1.0	1.4	4.1	1.8	3.3	0.6
Sm147	0.8	1.4	0.1	0.3	0.2	1.0	0.3	0.3	0.1
Eu151	0.7	1.3	0.0	0.0	0.1	0.2	0.1	0.2	0.1
Gd157	0.5				0.2		0.3	0.2	
Tb159	0.1	0.2	0.0	0.1	0.0	0.1	0.0	0.0	0.0
Dy163	0.4	1.2	0.1	0.4	0.2	1.0	0.3	0.2	0.0
Ho165	0.1	0.2	0.0	0.1	0.1	0.2	0.1	0.0	0.0
Er167	0.3	0.7	0.0	0.3	0.1	0.6	0.2	0.1	0.0
Tm169	0.0	0.1	0.0	0.0	0.0	0.1	0.0	0.0	0.0
Yb171	0.2	0.6	0.1	0.3	0.2	0.8	0.2	0.1	0.0
Lu175	0.0	0.1	0.0	0.0	0.0	0.1	0.0	0.0	0.0

	952 575_2_III	952 575_2_III	859 612_5	859 612_5	859 612_5	859 612_5	859 612_5	859 612_5	859 612_5	952 574_42
[ppm]	A_8	A_9	A_1	A_2	A_3	A_4	A_5	A_6	A_7	A_1
B11	9	218	10	8	7	7	8	8	8	15
Al27	5553	3021	300	346	1659	1112	1535	88	17	687
Si29	173887	182481	180334	178126	162556	188546	181231	176929	176051	165158
Ca43	237495	234636	230205	240997	237995	243427	241783	239496	244428	233564
Sc45	3.5	1.4	0.6	0.5	2.5	1.3	1.9	1.0	0.9	0.5
Ti49	77.8	194.8	25.4	18.4	28.1	972.1	19.9	<0.4	<0.5	10.9
V51	1.8	4.4	2.2	2.4	2.0	5.0	5.3	0.1	<0.06	0.4
Cr53	6.5	10.5	4.9	4.1	14.8	16.2	15.4	2.1	4.9	<1.9
Mn55	2623	4598	10685	10414	3688	10457	2116	3301	4608	6535
Co59	<0.1	0.2	<0.2	0.2	0.1	<0.2	0.2	3.4	3.1	<0.2
Cu65	<0.5	<0.5	<0.6	0.6	0.9	<0.6	<0.5	<0.5	<0.6	<0.7
Zn66	1.8	4.9	15.8	8.9	1.7	9.7	3.7	45.4	23.8	15.6
Ga71	15.9	39.9	2.4	2.1	1.6	3.4	2.2	18.7	5.6	121.8
Ge72	28.5	58.5	7.7	7.4	16.1	8.4	21.9	55.3	16.6	236.8
As75	37.7	27.1	1146.7	873.0	200.2	906.5	1527.6	210.8	545.5	282.4
Sr88	0.1	0.1	0.1	0.1	0.0	0.1	0.0	0.1	0.1	0.1
Y89	3.6	1.2	0.1	0.1	0.5	5.1	0.3	0.0	<0.01	0.8
Zr90	3.2	1.7	0.3	0.3	0.6	21.2	0.2	<0.03	0.0	0.1
Nb93	0.6	0.4	0.0	0.0	0.1	1.9	0.1	<0.01	<0.01	<0.02
Cd111	0.1	<0.1	0.3	0.2	<0.1	0.2	0.2	0.3	0.3	0.1
In115	56.6	159.8	4.8	4.7	10.6	9.5	224.1	763.0	479.9	205.1
Sn119	696.5	4498.4	78.9	68.6	523.7	123.8	516.0	11635.9	1263.6	16375.3
Sn118	723.9	4657.2	81.2	72.3	551.3	128.2	538.1	10890.4	1312.8	15410.1
Ta181	0.0	0.0	<0.001	0.0	0.0	0.5	<0.001	<0.002	<0.001	<0.002
Th232	0.8	0.3	0.0	0.0	0.9	1.9	0.3	0.0	0.0	0.0
U238	1.0	1.1	0.5	0.7	0.7	2.0	0.6	0.0	0.0	0.0
Sn115	50.1	141.3	4.2	4.2	9.3	8.4	198.1	674.7	424.4	181.3
Dy160	0.5	0.3	0.0	0.0	0.1	0.4	0.1	0.0	0.0	0.2
La139	5.5	2.1	0.4	0.4	0.3	0.5	1.2	0.3	0.3	2.4
Ce140	13.4	7.1	0.4	0.5	0.4	0.9	3.9	0.2	0.1	1.7
Pr141	1.3	0.7	0.0	0.1	0.1	0.2	0.6	0.0	0.0	0.2
Nd143	3.9	2.0	0.1	0.2	0.3	0.9	1.7	0.1	0.0	0.6
Sm147	0.7	0.3	0.0	<0.004	0.0	0.3	0.2	<0.01	<0.02	0.1
Eu151	0.3	0.2	0.0	0.0	0.1	0.1	0.2	0.4	0.1	0.1
Gd157	0.5	0.3	0.0	0.0	0.1			0.0	0.0	0.2
Tb159	0.1	0.0	0.0	0.0	0.0	0.1	0.0	<0.002	<0.002	0.0
Dy163	0.4	0.1	0.0	0.0	0.1	0.4	0.0	<0.01	<0.01	0.1
Ho165	0.1	0.0	0.0	0.0	0.0	0.1	0.0	0.0	<0.001	0.0
Er167	0.2	0.1	0.0	0.0	0.0	0.3	<0.01	<0.004	0.0	0.1
Tm169	0.0	0.0	0.0	0.0	0.0	0.1	0.0	<0.001	<0.002	0.0
Yb171	0.1	0.1	<0.01	<0.01	0.0	0.5	<0.01	<0.02	0.0	0.1
Lu175	0.0	0.0	0.0	0.0	0.0	0.1	0.0	<0.001	<0.001	0.0

	952 574_42	952 574_42	952 574_42	952 574_42	952 574_42	952 574_42	952 574_42	952 574_42	952 574_42
[ppm]	A_2	A_3	A_4	A_5	A_6	A_7	A_8	A_9	A_10
B11	13	11	14	11	20	14	9	8	8
Al27	538	1099	1181	1239	5652	3619	482	1423	10436
Si29	167319	169528	173860	173903	174607	171723	183890	169046	175574
Ca43	232921	230848	233993	235423	235137	227775	242855	233707	232993
Sc45	0.9	0.9	0.4	1.1	1.3	1.4	0.8	0.9	1.1
Ti49	7.4	46.2	23.7	20.6	83.9	83.7	12.1	13.9	255.8
V51	0.3	1.6	0.6	0.6	1.4	1.5	0.4	0.4	10.7
Cr53	4.6	4.8	3.5	4.0	2.1	5.9	4.8	7.2	6.4
Mn55	7063	4773	7940	7175	6914	7433	5161	5984	5119
Co59	0.3	0.3	0.4	0.4	0.4	<0.2	0.3	0.3	<0.3
Cu65	<0.8	<0.9	<0.9	<0.8	<0.8	<0.7	<0.9	<0.8	<0.8
Zn66	32.7	21.4	21.7	13.6	25.8	24.6	7.9	12.7	4.2
Ga71	117.9	106.4	221.8	220.1	420.7	431.8	916.5	999.2	781.2
Ge72	575.9	401.8	259.0	271.1	307.6	408.5	242.3	283.4	229.9
As75	116.4	152.3	499.8	487.9	273.8	109.3	78.3	37.0	30.3
Sr88	0.0	0.1	0.1	0.1	1.0	0.4	<0.02	0.0	<0.01
Y89	0.1	0.9	0.6	0.4	3.9	3.5	0.0	0.1	4.9
Zr90	<0.03	0.2	0.3	0.1	2.9	1.3	0.1	0.2	4.3
Nb93	0.0	0.1	0.0	0.0	0.4	0.2	<0.02	0.0	0.3
Cd111	<0.2	<0.1	<0.1	<0.1	0.1	<0.1	0.3	<0.1	0.2
In115	394.5	508.6	262.8	216.9	254.7	186.6	358.5	315.4	384.3
Sn119	28956.6	19720.2	15278.7	13550.1	26996.5	24631.7	20188.9	29105.4	13501.8
Sn118	32999.6	18630.2	14608.9	13223.5	25586.7	23495.1	19301.3	27487.8	12883.7
Ta181	0.0	<0.002	0.0	<0.004	0.0	0.0	<0.002	<0.003	0.0
Th232	0.0	0.0	0.0	0.0	0.2	0.1	0.0	0.0	0.6
U238	0.1	0.1	0.0	0.0	0.3	0.2	0.5	1.4	3.1
Sn115	348.8	449.7	232.3	191.8	225.2	165.0	317.0	278.9	339.8
Dy160	0.3	0.3	0.2	0.1	0.8	0.6	0.1	0.2	1.3
La139	12.8	2.3	4.2	2.6	6.5	6.8	6.3	3.0	3.9
Ce140	14.6	2.3	2.9	2.2	11.7	9.9	13.9	12.3	23.1
Pr141	1.1	0.3	0.3	0.2	1.5	1.3	1.2	2.0	5.8
Nd143	2.3	1.0	0.7	0.7	5.0	4.0	2.1	5.6	26.9
Sm147	0.2	0.2	0.1	0.1	0.7	0.5	<0.02	0.2	3.1
Eu151	2.0	0.1	0.3	0.1	2.2	2.0	1.0	2.7	4.3
Gd157	0.3	0.3	0.2	0.1	0.8	0.6	0.2	0.2	1.4
Tb159	0.0	0.0	0.0	0.0	0.1	0.1	0.0	0.0	0.1
Dy163	0.0	0.1	0.0	0.0	0.4	0.5	0.0	0.0	0.6
Ho165	0.0	0.0	0.0	0.0	0.1	0.1	<0.004	0.0	0.1
Er167	<0.01	0.0	0.0	0.0	0.2	0.2	0.0	0.0	0.2
Tm169	0.0	0.0	0.0	0.0	0.0	0.0	<0.002	<0.002	0.0
Yb171	<0.01	0.0	0.1	<0.02	0.1	0.1	0.0	<0.01	0.2
Lu175	0.0	0.0	0.0	0.0	0.0	0.0	<0.004	0.0	0.0

	949 179_15	949 179_15	949 179_15	949 179_15	949 179_15	949 179_15
[ppm]	D_1	D_2	D_3	D_4	D_5	D_6
B11	9	12	10	10	10	7
Al27	26224	14781	11500	18994	18340	31098
Si29	188242	184317	178252	185957	179309	187080
Ca43	243927	242069	236209	241497	236137	243427
Sc45	11.9	1.7	0.6	4.9	5.6	4.7
Ti49	9290.7	3364.7	686.4	2367.4	2901.4	3675.4
V51	171.5	48.3	13.8	81.2	76.6	146.6
Cr53	20.4	6.0	4.0	17.2	21.1	11.3
Mn55	17925	8531	9011	6483	6844	7145
Co59	2.1	0.8	0.9	0.3	0.3	0.6
Cu65	<0.6	<0.6	<0.6	<0.6	0.7	<0.6
Zn66	49.7	19.8	18.6	7.7	11.2	6.1
Ga71	13.2	6.9	5.5	8.4	8.2	13.8
Ge72	12.9	84.8	91.7	21.4	24.8	18.6
As75	15.4	303.4	377.0	230.0	266.9	19.6
Sr88	4.8	0.2	0.1	0.2	0.2	0.0
Y89	99.1	75.4	18.1	27.5	26.6	19.7
Zr90	286.6	105.4	23.8	77.6	70.5	134.7
Nb93	25.1	11.0	2.6	10.0	12.1	18.6
Cd111	<0.1	0.2	0.1	0.1	0.1	<0.1
In115	2.3	11.9	14.5	7.9	8.2	4.7
Sn119	312.2	936.1	1230.3	350.0	337.4	435.4
Sn118	330.5	966.5	1273.6	357.2	353.0	449.7
Ta181	2.0	0.8	0.2	0.7	0.9	1.2
Th232	4.6	4.2	1.4	2.0	1.5	1.1
U238	1.6	2.2	2.2	4.1	4.5	1.0
Sn115	2.0	10.5	12.8	6.9	7.3	4.1
Dy160	6.1	5.0	1.2	4.2	3.8	4.0
La139	0.6	7.4	8.2	5.7	6.3	0.8
Ce140	4.2	13.3	13.9	18.5	18.8	5.8
Pr141	1.1	1.7	1.6	3.0	2.9	1.5
Nd143	7.2	7.6	5.6	14.1	14.8	10.0
Sm147	3.2	2.7	0.9	3.9	3.5	3.8
Eu151	0.5	0.4	0.3	0.8	0.7	0.6
Gd157	5.9	4.8	1.2	4.3	3.9	4.2
Tb159	1.1	0.9	0.2	0.7	0.5	0.5
Dy163	9.1	7.0	1.8	4.0	3.6	3.2
Ho165	2.4	1.8	0.4	0.7	0.7	0.6
Er167	7.2	5.5	1.4	1.7	1.8	1.3
Tm169	1.1	0.7	0.2	0.2	0.2	0.1
Yb171	7.3	3.7	1.0	1.1	1.3	0.8
Lu175	1.1	0.5	0.1	0.1	0.2	0.1

Appendix 10: LA-ICP-MS analyses of clinopyroxene

	949 443.68	**949 443.68**	**949 443.68**	**949 443.68**	**949 443.68**	**949 443.68**	**949 443.68**
[ppm]	D_1	D_2	D_3	D_4	B_1	B_2	B_3
B11	8.0	7.7	8.3	6.1	9.6	7.5	7.6
Ca43	158020	159879	157306	159021	162166	156305	160164
Sc45	3.4	1.6	1.1	2.3	1.9	1.8	0.8
Ti49	107.7	58.2	44.0	60.9	46.3	58.2	54.5
V51	2.7	2.6	1.5	1.7	1.4	1.6	2.2
Cr53	16.0	6.3	3.3	6.4	<1.9	<1.6	2.6
Mn55	8409.0	8272.6	9397.5	8740.7	10200.4	9821.6	11903.6
Co59	24.1	17.5	16.6	17.2	16.3	18.5	18.6
Cu65	0.7	<0.6	<0.6	<0.4	1.4	<0.5	<0.5
Zn66	569.3	340.4	358.7	347.1	342.5	381.0	334.7
Ga71	9.0	10.6	4.8	5.9	7.7	6.3	10.7
Ge72	31.4	48.7	56.3	39.9	64.9	32.5	29.0
As75	<0.6	<0.6	<0.6	0.8	<0.6	<0.6	1.1
Sr88	1.7	0.7	0.4	0.5	0.4	1.0	1.7
Y89	6.2	10.2	10.3	6.7	14.2	7.6	10.7
Zr90	8.0	6.2	5.7	4.2	7.6	3.4	2.0
Nb93	0.0	0.0	<0.01	<0.01	0.0	0.0	0.3
Cd111	<0.1	0.1	<0.1	<0.1	0.2	<0.1	<0.04
In115	11.5	7.3	24.2	7.1	32.1	3.9	2.5
Sn119	12.9	9.0	5.1	3.9	7.8	2.4	7.4
Sn118	13.1	9.6	5.2	3.5	7.5	2.6	8.4
Ta181	0.01	0.01	0.00	0.00	0.00	<0.001	0.01
Th232	0.02	0.02	0.03	0.01	0.03	0.03	0.34
U238	0.02	0.01	0.03	0.01	0.03	0.04	0.26
Sn115	10.13	6.41	21.38	6.31	28.36	3.42	2.17
Dy160	0.74	1.13	1.29	0.84	1.62	0.89	1.20
La139	0.37	0.56	0.52	0.37	0.51	0.53	2.11
Ce140	2.09	3.19	3.06	1.86	3.14	2.76	7.86
Pr141	0.46	0.69	0.72	0.40	0.76	0.56	1.31
Nd143	2.67	3.73	3.69	2.38	4.16	2.71	5.55
Sm147	0.68	1.07	1.35	0.74	1.41	0.80	1.22
Eu151	0.12	0.23	0.26	0.12	0.25	0.18	0.31
Gd157	0.74	1.12	1.29	0.85		0.90	1.20
Tb159	0.13	0.21	0.21	0.12	0.26	0.16	0.21
Dy163	0.84	1.41	1.53	0.81	1.85	0.94	1.41
Ho165	0.18	0.30	0.31	0.17	0.40	0.21	0.30
Er167	0.56	0.67	0.79	0.60	1.27	0.71	0.74
Tm169	0.08	0.12	0.14	0.10	0.18	0.10	0.10
Yb171	0.73	0.59	1.11	0.56	1.32	0.73	0.63
Lu175	0.09	0.08	0.17	0.08	0.20	0.09	0.05

blank cells: not analysed; <0.0.. below minimum detection limit

	974 291.01	974 291.01	939 1103.2	939 1103.2	939 1103.2	939 1103.2	890W6 787.56	890W6 787.56
[ppm]	A_1	A_2	A_2	A_3	B_1	B_2	A_1	A_2
B11								
Ca43	186323	186323	154161	161522	161522	158449	182392	182392
Sc45	56.8	52.1	18.7	15.2	20.4	15.3	2.0	1.9
Ti49	33.6	21.9	94.6	92.9	105.7	149.9	8.5	2.3
V51	248.8	206.3	7.6	5.0	6.5	8.6	1.8	0.2
Cr53	356.7	353.7	4.1	<2.3	3.1	<1.9	1.3	1.9
Mn55	<0.2	<0.3	3380.3	3892.8	4449.5	3741.9	<0.1	<0.1
Co59								
Cu65	2.3	3.5	0.6	0.9	0.3	0.4	2.1	2.0
Zn66	342.9	341.8	799.2	833.4	1072.3	846.9	564.9	642.0
Ga71								
Ge72								
As75								
Sr88	14.1	4.0	3.7	4.3	4.3	4.5	1.9	1.9
Y89	0.1	0.1	7.7	12.6	5.4	16.3	0.1	<0.002
Zr90	1.0	1.0	4.8	4.0	5.6	7.4	0.0	<0.01
Nb93	0.0	0.0	<0.03	0.6	0.3	0.5	0.0	0.0
Cd111								
In115								
Sn119	3.7	1.5	<0.4	2.6	3.3	3.8	2.8	1.8
Sn118	1.5	1.7	2.6	2.7	3.8	4.6	3.17	2.07
Ta181								
Th232	0.03	<0.02	0.26	0.26	0.26	0.23	0.09	0.01
U238	0.00	0.22	0.16	0.11	0.24	0.13	0.04	0.01
Sn115								
Dy160								
La139	0.10	0.01	0.69	0.94	0.69	1.16	0.46	0.06
Ce140	0.42	0.11	4.17	5.10	3.77	8.67	0.33	0.11
Pr141	0.05	0.01	0.84	0.90	0.65	1.86	0.02	0.01
Nd143	0.27	0.07	4.12	4.50	3.22	10.02	0.06	0.03
Sm147	0.04	0.00	1.77	1.86	1.30	4.17	0.01	<0.003
Eu151	0.01	<0.001	0.04	0.05	0.02	0.08	0.00	<0.001
Gd157	0.05	0.02	1.64	1.80	1.20	3.65	0.01	<0.01
Tb159	0.00	<0.001	0.31	0.32	0.20	0.65	<0.002	<0.0002
Dy163	0.02	0.00	2.10	2.20	1.43	4.40	0.00	0.00
Ho165	0.00	0.00	0.46	0.52	0.28	1.01	0.01	<0.002
Er167	0.01	<0.01	1.51	1.96	1.02	3.54	<0.003	<0.003
Tm169	0.00	<0.00	0.33	0.45	0.26	0.76	0.00	<0.0004
Yb171	0.04	0.03	3.26	4.31	3.31	7.56	0.00	<0.002
Lu175	0.01	0.00	0.72	0.81	0.96	1.59	0.0	0.0

Appendix 11: LA-ICP-MS analyses of sphalerite

[ppm]	983 885_71 D_1	983 885_71 D_2	983 885_71 D_3	983 885_71 D_4	983 885_71 D_5	983 885_71 A_1	983 885_71 A_2	983 885_71 A_3	983 885_71 A_4	983 885_71 A_5	983 885_71 A_6	888 710_7 C_1	888 710_7 C_3	888 710_7 C_4	888 710_7 C_5
Zn67	688541	674850	702005	741842	712988	710187	622122	723857	703710	711446	723225	665815	696858	695291	686401
Fe57	9794	9250	9328	9872	10183	10027	8939	9483	9483	9716	9950	26973	27672	28216	26973
Co59	1	1	1	1	1	0	0	0	0	0	0	<0.05	<0.06	0	<0.05
In115	31	25	21	23	19	33	31	41	37	40	41	47	49	49	48
Se77	10	9	9	9	5	6	5	6	7	7	10	56	57	54	56
Cd111	2402	2368	2426	2536	2465	2592	2249	2630	2562	2579	2593	1781	1850	1881	1835
Mn55	748	813	867	892	867	886	790	755	809	826	850	119	125	124	114
Ga71	19.5	8.0	9.2	8.1	9.5	7.3	4.6	4.1	7.0	6.7	12.1	4.7	5.4	4.9	4.7
Ge72	2.6	2.7	2.6	2.8	2.7	2.5	2.6	2.8	2.7	2.8	3.1	2.6	2.4	2.6	2.5
Sn118	3.8	4.6	14.7	13.2	6.2	87.8	4.1	2.8	4.9	3.8	107.7	1.3	2.2	3.3	1.4
Sn119	3.5	4.6	13.7	12.3	5.8	82.8	3.5	2.7	4.5	3.6	101.2	1.2	2.0	2.9	1.3
Sn115	27.5	22.4	19.1	21.1	17.3	29.3	27.5	37.1	33.2	35.7	36.9	41.8	44.2	43.7	43.0
Ag107	3.0	2.8	3.0	3.2	2.9	4.0	5.7	4.9	8.4	4.8	4.1	2.6	2.9	2.8	2.8
Pb208	2.0	1.4	1.3	2.2	1.3	8.1	3.5	3.0	2.1	2.8	4.0	1.1	1.3	1.6	1.3
Bi209	1.6	1.9	1.6	2.0	2.5	4.6	10.6	9.4	13.9	7.2	3.5	0.0	0.0	0.0	0.0
Sb121	1.1	0.7	1.1	2.8	0.9	7.8	6.3	5.3	118.6	4.3	9.3	0.1	0.1	0.2	0.2
As75	0.5	0.3	0.3	0.3	0.3	8.8	1.3	0.8	33.1	2.0	11.9	1.1	1.3	0.8	1.0
Cu65	38	26	36	37	28	137	39	33	195	38	167	64	133	168	79
Cr52	2.4	1.7	2.6	2.8	2.9	2.5	<0.4	1.6	1.8	1.9	1.6	2.2	1.2	3.0	1.6
Ni60	<0.7	<0.7	<0.7	<0.8	<0.7	1	<0.5	<0.7	<0.6	1	<0.7	<0.7	<0.8	<0.7	<0.7
Mo95	0.0	0.0	0.1	0.1	0.1	0.1	0.1	0.0	0.0	0.1	0.1	<0.02	<0.02	0.0	<0.02
Te125	<0.04	0.1	<0.04	0.1	<0.06	0.4	1.3	0.6	0.2	0.7	0.6	0.3	0.3	0.3	0.3

<0.0.. below minimum detection limit

	888 710_7	888 710_7	888 710_7	888 710_7	888 710_7	888 710_7	937W4 1133	937W4 1133	937W4 1133	937W4 1133	937W4 1133	937W4 1133	937W4 1133	937W4 1133	937W4 1133	937W4 1133
[ppm]	C_6	C_7	C_10	D_2	D_4	D_6	A_1	A_2	A_3	A_4	A_5	A_6	B_1	B_2	B_3	B_4
Zn67	650211	692149	647075	664024	661308	681058	726483	745464	740512	716139	748617	678672	498541	524173	527386	518813
Fe57	26429	27361	26429	24641	24408	24718	65450	65761	67782	67315	66149	66926	56277	57366	57132	59697
Co59	<0.05	0	<0.04	0	<0.05	<0.05	0	0	0	0	0	0	0	0	0	1
In115	46	49	43	36	46	49	124	115	109	105	108	93	52	52	51	49
Se77	53	54	54	56	59	59	5	2	4	5	2	1	3	1	2	<0.6
Cd111	1736	1854	1717	1789	1796	1852	2008	2057	2124	2076	2188	2172	1702	1726	1763	1729
Mn55	112	116	117	187	160	146	204	230	245	248	273	270	268	274	269	271
Ga71	5.9	4.9	4.7	5.5	4.6	5.0	2.3	6.4	11.8	7.7	10.7	12.8	1.5	6.5	7.1	4.5
Ge72	2.5	2.5	2.6	2.7	2.4	2.5	3.0	3.3	2.8	2.9	3.1	3.2	2.1	2.1	2.4	2.2
Sn118	3.3	3.3	1.7	2.7	14.8	1.0	0.5	0.6	0.6	1.1	0.8	0.9	0.6	0.5	12.7	0.5
Sn119	3.1	3.3	1.5	2.5	13.7	0.9	0.7	0.5	0.5	1.0	0.7	0.7	0.7	0.5	11.3	3.1
Sn115	41.1	43.9	38.4	32.8	40.9	44.4	111.2	103.6	98.2	94.5	97.4	83.9	46.7	46.4	46.0	44.1
Ag107	2.6	3.0	2.6	2.5	2.8	2.8	8.3	5.4	4.1	4.3	5.3	8.4	17.5	4.1	35.6	7.8
Pb208	4.9	6.2	2.2	1.5	1.9	1.1	2.7	1.7	1.0	0.6	0.5	3.5	6.9	0.3	4.9	2.1
Bi209	3.6	1.8	0.1	0.2	0.1	0.1	8.9	0.4	0.2	0.5	0.1	8.7	4.3	0.1	8.9	0.9
Sb121	1.1	0.9	0.1	0.1	0.2	0.2	0.4	0.1	0.1	0.7	0.0	0.7	0.5	0.0	0.4	0.1
As75	1.4	1.2	2.0	1.0	1.5	0.7	<0.2	<0.2	<0.2	0.3	0.2	0.3	<0.1	0.2	1.0	<0.1
Cu65	83	123	93	82	104	68	344	109	93	82	105	689	3904	47	57	880
Cr52	2.3	1.9	1.2	2.1	2.7	2.4	2.8	3.8	2.6	2.5	1.9	2.2	1.5	1.4	2.0	2.9
Ni60	<0.6	<0.7	<0.6	1	<0.6	<0.6	<0.7	1	1	<0.7	<0.4	<0.7	<0.5	<0.5	<0.6	<0.5
Mo95	269.4	307.0	0.1	0.0	<0.01	<0.01	0.0	<0.02	0.1	0.0	0.1	0.2	0.5	<0.02	0.0	0.0
Te125	0.5	0.3	0.2	0.3	0.1	0.4	0.1	<0.7	0.1	<0.03	0.1	0.3	0.1	0.1	31.7	<0.03

	937W4 1133	937W4 1133	849W1 579	849W1 579	849W1 579	849W1 579	849W1 579	849W1 579	849W1 579	849W1 579	849W1 579	849W1 579	849W1 579	849W1 579	849W1 579	849W1 579
[ppm]	B_5	B_6	A_1	A_2	A_3	A_4	A_5	A_6	A_7	A_8	A_9	A_10	B_2	B_4	B_6	B_8
Zn67	572875	600575	605501	619909	596429	575213	561038	604225	596199	615848	592159	592319	581022	601939	464201	485920
Fe57	60553	62729	90401	93277	91800	92111	93666	96853	94288	97242	96231	97863	70502	72445	68248	58143
Co59	0	0	16	18	20	22	29	40	44	49	46	42	19	19	25	11
In115	49	51	115	133	137	137	136	140	139	153	154	113	118	124	55	72
Se77	1	1	3	5	3	2	<0.9	2	2	3	3	3	4	3	1	2
Cd111	1934	2053	4924	5213	5151	4991	4691	4755	4488	4514	4460	4556	4824	4418	3717	4142
Mn55	290	300	2734	3520	4478	5447	6553	7927	8024	8283	7849	7953	4195	2243	6549	2014
Ga71	8.5	2.3	0.8	1.0	1.0	1.1	1.0	1.7	1.1	1.3	1.0	0.6	1.1	1.1	0.2	0.6
Ge72	2.6	2.7	2.8	2.4	2.9	2.8	2.7	2.9	3.3	3.1	3.5	2.8	3.0	3.2	2.0	2.4
Sn118	0.6	2.0	1.5	13.7	15.6	15.2	24.0	26.8	25.2	26.0	19.7	10.3	11.8	23.4	2.2	6.7
Sn119	0.5	2.1	1.7	12.8	14.8	14.0	22.7	24.6	24.7	23.4	18.8	9.5	11.3	22.4	2.0	6.2
Sn115	43.7	45.6	103.1	119.3	123.2	122.9	122.4	125.7	125.0	137.4	138.1	101.5	105.8	111.6	49.5	64.5
Ag107	5.9	6.3	12.6	8.1	8.7	8.2	7.2	13.6	14.2	15.1	15.5	7.8	57.4	96.5	27.1	42.1
Pb208	1.1	0.8	2.3	3.8	0.2	0.3	0.6	1.8	1.3	2.9	0.3	0.7	104.5	130.1	19.5	80.2
Bi209	0.2	0.4	0.4	0.2	0.1	0.0	0.0	0.1	0.0	0.0	0.0	0.0	2.0	3.4	0.2	5.7
Sb121	0.0	0.1	<0.03	0.5	0.0	0.0	0.0	0.2	0.0	<0.02	<0.02	0.1	8.2	41.6	0.1	7.1
As75	<0.2	0.3	<0.2	0.4	<0.2	<0.2	0.6	<0.2	<0.2	<0.2	<0.2	<0.2	0.3	2.5	<0.1	1.8
Cu65	323	193	1169	1055	195	149	165	356	316	379	277	756	29068	37842	14778	24451
Cr52	0.9	1.6	2.9	2.6	1.4	2.2	3.2	2.2	2.6	3.2	1.8	1.4	2.2	1.5	1.8	1.2
Ni60	1	<0.7	<0.6	<0.7	<0.7	<0.7	<0.7	<0.7	<0.6	1	<0.68	<0.7	<0.7	<0.6	<0.5	<0.6
Mo95	0.1	<0.01	0.2	0.2	0.4	0.4	0.5	0.7	0.8	0.7	0.7	0.6	0.4	0.2	0.6	0.3
Te125	0.1	0.1	0.1	0.1	<0.1	0.0	<0.06	<0.6	<0.04	<0.1	<0.03	0.1	0.1	0.2	<0.03	<0.1

[ppm]	949 165_80 B_1	949 165_80 B_2	949 165_80 B_3	949 165_80 B_4	949 165_80 B_5	949 165_80 B_6	949 165_80 B_7	949 165_80 B_8	949 165_80 B_9	949 165_80 B_10	949 165_80 B_11	949 165_80 B_12	949 165_80 B_13	949 179_15 C_1	949 179_15 C_2
Zn67	542512	581392	539103	471579	536527	568218	609707	656081	692266	724228	630852	563195	617648	626871	632574
Fe57	79752	66538	60475	63351	69569	74700	79830	80063	74078	72290	67393	67859	83561	30471	30393
Co59	119	145	145	133	151	158	168	174	182	186	152	123	123	240	237
In115	84	111	70	80	75	70	71	83	102	83	97	91	60	8	9
Se77	6	7	5	7	4	4	6	6	6	5	5	7	2	41	43
Cd111	3419	3438	3395	3215	3679	3892	4262	4396	4487	4532	3867	3476	3903	2579	2585
Mn55	6731	6558	5893	5389	6577	6924	7654	7773	7479	7554	6967	6789	6872	5133	5038
Ga71	0.6	0.2	0.1	0.8	0.7	0.9	0.9	0.7	2.9	1.4	0.7	0.3	0.5	0.3	0.4
Ge72	2.3	2.8	2.2	2.0	2.4	2.6	2.6	3.0	3.1	2.9	2.8	2.8	2.8	2.6	2.7
Sn118	2.0	2.0	3.1	8.3	12.4	11.8	8.6		1.9	1.8	1.8	1.5	2.2	1.2	1.4
Sn119	2.0	1.8	2.9	7.9	11.7	11.0	8.0	9.3	1.5	1.8	1.9	1.4	1.8	1.3	1.2
Sn115	75.2	99.4	63.1	71.6	67.3	62.9	63.4	74.3	91.4	74.8	87.4	81.7	53.6	7.3	8.1
Ag107	3.0	3.5	4.6	7.8	6.4	8.1	7.7	4.0	4.5	5.8	3.7	4.7	7.3	2.2	2.6
Pb208	0.4	0.4	0.4	77.2	0.2	2.2	0.2	0.4	0.2	0.2	0.2	0.2	0.9	0.6	0.5
Bi209	0.1	0.1	0.6	2.8	0.0	0.7	0.1	0.2	0.0	0.0	0.0	0.1	0.5	0.2	0.3
Sb121	<0.03	<0.03	<0.02	0.2	<0.02	0.0	<0.02	0.0	<0.03	<0.3	<0.02	<0.03	<0.02	<0.02	<0.02
As75	0.2	<0.2	<0.2	0.2	<0.2	<0.2	<0.2	0.3	0.3	<0.2	<0.2	<0.2	<0.2	0.3	<0.2
Cu65	54	66	43	277	59	205	57	60	64	54	58	56	140	9	12
Cr52	1.6	0.9	2.1	1.5	2.8	2.3	1.0	1.3	2.3	2.3	1.3	1.5	<0.62	3.6	2.9
Ni60	1	1	3	3	7	4	4	3	4	3	1	1	<0.71	14	14
Mo95	0.6	0.5	0.4	0.5	0.6	0.6	0.6	0.7	0.6	0.6	0.5	0.6	0.6	0.1	0.4
Te125	<0.1	0.1	<0.1	0.1	<0.04	<0.04	<0.04	<0.04	<0.04	<0.1	<0.04	<0.1	<0.04	0.0	0.1

[ppm]	949 179_15 C_3	949 179_15 C_4	949 179_15 C_5	949 179_15 C_6	949 179_15 C_7	949 179_15 C_8	949 179_15 C_9	949 179_15 B_2	949 179_15 B_3	949 179_15 B_4	949 179_15 B_6	949 179_15 B_7	949 179_15 B_8
Zn67	644179	632375	621559	627775	633160	608124	630803	638586	668323	715574	640511	646545	651327
Fe57	31092	31481	31481	33036	34046	33813	35523	19355	20288	22697	20832	20366	21998
Co59	244	237	234	242	245	240	248	245	252	276	244	247	250
In115	12	14	14	11	9	8	8	17	17	20	17	15	13
Se77	43	43	47	47	42	44	49	47	48	52	50	47	49
Cd111	2693	2693	2641	2762	2823	2770	2881	2842	2913	3172	2814	2864	2857
Mn55	5171	5190	5235	5548	5738	5730	5993	3588	3743	4218	3856	3749	4082
Ga71	0.2	0.3	0.3	0.2	0.3	0.3	0.6	0.3	0.3	0.2	0.2	0.2	0.4
Ge72	2.3	2.6	2.4	2.1	2.4	2.4	2.6	2.7	2.7	2.7	2.8	2.8	2.9
Sn118	1.3	1.2	1.3	1.2	1.4	1.4	1.5	0.8	0.9	1.0	0.8	0.9	0.9
Sn119	1.3	1.3	1.3	1.2	1.3	1.1	1.3	0.7	0.9	1.1	0.9	0.7	0.9
Sn115	11.0	12.6	12.2	10.1	8.4	7.3	7.6	14.8	15.3	17.8	15.4	13.9	11.9
Ag107	2.5	2.5	2.5	2.7	2.4	2.4	2.4	2.6	2.7	2.8	2.6	2.6	2.5
Pb208	0.4	0.3	0.3	1.1	0.4	0.1	0.2	0.2	0.2	0.2	0.3	0.3	0.2
Bi209	0.0	0.2	0.2	4.5	0.5	0.2	0.1	0.2	0.1	0.0	0.4	0.4	0.0
Sb121	<0.02	<0.03	<0.02	0.5	<0.03	<0.02	<0.02	<0.02	<0.02	<0.02	0.0	<0.02	<0.02
As75	0.2	<0.2	<0.2	<0.2	<0.2	<0.2	<0.2	<0.2	<0.2	<0.2	<0.2	<0.2	<0.2
Cu65	12	11	10	12	12	10	11	11	12	13	13	11	12
Cr52	2.9	2.2	2.8	2.1	2.9	2.5	2.6	2.6	1.8	1.4	1.2	0.6	0.6
Ni60	14	13	14	13	14	13	15	13	14	15	12	13	13
Mo95	0.4	0.4	0.4	0.5	0.5	0.5	0.6	0.3	0.3	0.3	0.4	0.3	0.4
Te125	0.1	<0.1	0.1	0.0	<0.03	<0.1	0.1	0.1	0.0	<0.1	<0.04	0.1	<0.1

Appendix 12: LA-ICP-MS analyses of zircon

[ppm]	949-1	949-2	949-3	949-4	949-5b	949-5a	949-6	949-7a	949-7b	949-8a
P31	343	691	525	819	602	426	424	612	693	538
Ca44	<29	121	92	74	84	41	31	82	81	93
Ti49	16	10	2	9	9	8	5	13	13	10
Sr88	0.1	0.2	0.2	0.2	0.2	0.2	0.1	0.2	0.1	0.2
Y89	797	3144	1712	1632	1793	1338	1079	1642	1323	1722
Nb93	1	2	7	2	4	3	2	1	2	4
La139	<0.004	0	0	0	<0.004	0	0	0	<0.004	0
Ce140	2	5	6	3	9	6	4	2	2	9
Pr141	0	0	0	0	0	0	0	0	0	0
Nd143	1	6	1	2	1	1	1	3	2	2
Sm147	2	14	3	5	4	3	2	6	4	5
Eu151	0	1	0	0	0	0	0	0	0	0
Gd160	15	81	25	30	28	21	17	35	26	29
Tb159	5	26	10	11	10	8	6	12	9	10
Dy163	68	328	152	145	146	109	90	150	117	146
Ho165	27	123	64	57	60	45	36	57	45	60
Er167	123	532	303	259	285	215	171	254	211	284
Tm169	25	101	63	52	59	44	36	50	43	58
Yb171	236	893	576	477	557	425	335	447	399	544
Lu175	49	172	114	96	113	87	67	88	81	111
Th	41	294		138			132	85	94	112
U	115	15		314			356	184	235	247
Th/U	0.4	0.6		0.4			0.4	0.5	0.4	0.5
Hf	10115	10965	13260	9945	12835	10625	10370	10795	10540	10540
Zr/Hf	49	44	36	49	38	46	47	45	47	46
Hf/Y	13	3	8	6	7	8	10	7	8	6
∑REE	554	2280	1318	1136	1273	965	766	1104	939	1259
T [°C]	783	741	611	730	731	725	690	763	764	744
Sm/La		1067	195	1271		591	785	2743		1347
Ce/Ce*		13	48	24		65	64	21		98
Lu/Gd	26	17	37	25	33	33	32	21	25	31
Eu/Eu*	0.12	0.06	0.03	0.07	0.08	0.09	0.05	0.06	0.06	0.11

blank cells: not analysed, <0.0 below minimum detection limit

[ppm]	949-8b	949-18	949-9	949-10	949-11	949-12	949-14	949-15	949-16a	949-16b
P31	478	893	748	667	493	919	639	346	301	346
Ca44	31	78	102	127	95	68	111	72	70	47
Ti49	9	15	10	19	9	9	10	8	12	13
Sr88	0.1	0.2	0.2	0.2	0.1	0.2	0.2	<0.2	0.1	0.1
Y89	1404	1496	2429	1935	975	2007	1805	854	601	1177
Nb93	3	2	2	2	2	3	2	2	1	1
La139	0	<0.004	0	0	<0.004	<0.003	0	0	0	0
Ce140	7	2	5	3	3	3	4	3	1	2
Pr141	0	0	0	0	0	0	0	0	0	0
Nd143	1	1	4	4	1	2	3	1	1	3
Sm147	4	4	8	8	2	6	8	2	2	5
Eu151	0	0	0	1	0	0	0	0	0	0
Gd160	24	25	50	44	17	36	42	14	11	
Tb159	9	9	17	14	6	13	13	5	4	8
Dy163	118	124	224	175	82	174	172	71	51	107
Ho165	47	50	86	66	33	69	65	29	20	41
Er167	220	238	385	286	152	324	285	134	94	180
Tm169	45	49	75	56	31	65	55	27	19	35
Yb171	414	471	684	502	286	601	493	253	180	324
Lu175	83	99	134	99	58	121	97	51	37	65
Th	109		105	75		79	139	62	60	
U	277		266	192		172	249	172	112	
Th/U	0.4		0.4	0.4		0.5	0.6	0.4	0.5	
Hf	10965	13600	13345	14025	10880	10455	11135	11050	8585	9350
Zr/Hf	45	36	37	34	45	47	44	44	58	52
Hf/Y	8	9	5	7	11	5	6	13	14	8
∑REE	973	1073	1675	1258	670	1415	1238	590	420	770
T [°C]	735	778	742	800	733	735	745	719	760	766
Sm/La	1151		194	784			1715	1243	790	1062
Ce/Ce*	93		9	12			26	85	26	12
Lu/Gd	28	32	22	18	27	27	19	29	28	
Eu/Eu*	0.09	0.04	0.07	0.10	0.08	0.05	0.08	0.07	0.11	

[ppm]	949-17	952W1-1-a	952W1-1-b	952W1-2	952W1-3-a	952W1-3-b	952W1-6	952W1-4
P31	638	654	429	555	462	359	329	849
Ca44	<22	68	70	52	76	64	39	115
Ti49	8	9	13	13	7	5	13	12
Sr88	0.2	0.2	0.1	0.1	0.1	0.2	0.1	0.3
Y89	1250	1951	1038	873	1195	1207	702	2695
Nb93	3	2	2	2	3	2	1	2
La139	0	0	<0.003	0	0	0	<0.003	0
Ce140	3	3	3	2	7	4	2	3
Pr141	0	0	0	0	0	0	0	0
Nd143	1	4	1	1	1	2	1	6
Sm147	3	8	3	3	3	4	2	11
Eu151	0	0	0	0	0	0	0	1
Gd160	22		19	16	22	25		65
Tb159	8	14	7	5	8	8	4	21
Dy163	107	179	87	74	103	111	59	275
Ho165	43	68	35	29	41	43	23	104
Er167	196	298	166	135	185	193	108	453
Tm169	40	58	34	28	37	38	22	87
Yb171	371	517	326	262	337	351	212	770
Lu175	75	103	68	54	67	70	44	150
Th	105	95		128	132		96	99
U	260	274		278	289		163	279
Th/U	0.4	0.4		0.5	0.5		0.6	0.4
Hf	9775	9860	10795	10710	11730	10625	9605	11050
Zr/Hf	50	49	45	46	42	46	51	44
Hf/Y	8	5	10	12	10	9	14	4
∑REE	869	1252	749	610	812	848	478	1945
T [°C]	718	727	762	763	706	681	765	755
Sm/La	993	1412		844	938	575		1046
Ce/Ce*	41	16		26	98	27		11
Lu/Gd	27		29	28	25	23		19
Eu/Eu*	0.05		0.08	0.07	0.08	0.09		0.07

[ppm]	952W1-5	952W1-7	952W1-8	952w1-9-a	952W1-9-b	952W1-10	952W1-11-a	952W1-11-b
P31	485	772	709	606	502	561	458	384
Ca44	98	100	73	140	88	100	66	50
Ti49	9	14	16	8	9	8	14	8
Sr88	0.2	0.2	0.2	0.2	0.1	0.2	0.1	0.1
Y89	2291	2242	1826	2621	1125	2312	1426	727
Nb93	2	2	1	2	2	2	1	2
La139	0	0	0	0	<0.003	0	0	0
Ce140	8	3	2	5	3	6	2	3
Pr141	0	0	0	0	0	0	0	0
Nd143	4	4	4	5	1	5	4	1
Sm147	9	8	8	11	3	11	7	2
Eu151	1	0	0	1	0	1	0	0
Gd160	51	48	42	60	20		34	13
Tb159	17	16	13	20	7	18	11	5
Dy163	222	213	172	261	95	225	132	60
Ho165	85	82	65	99	38	83	50	24
Er167	373	365	292	435	177	358	215	113
Tm169	73	72	57	84	36	68	41	23
Yb171	648	653	517	745	333	601	375	221
Lu175	127	130	103	143	67	116	74	45
Th	245	157	229	66		136	54	68
U	448	277	581	218		288	133	195
Th/U	0.5	0.6	0.4	0.3		0.4	0.4	0.3
Hf	9520	9350	10795	10710	10370	11305	9775	12495
Zr/Hf	51	52	45	46	47	43	50	39
Hf/Y	4	4	6	4	9	5	7	17
∑REE	1617	1595	1275	1870	780	1491	945	509
T [°C]	728	771	783	719	727	720	771	721
Sm/La	985	886	575	963		981	2261	538
Ce/Ce*	34	10	8	20		21	18	61
Lu/Gd	20	22	20	19	28		18	29
Eu/Eu*	0.12	0.08	0.07	0.06	0.05		0.08	0.06

[ppm]	952W1-12-a	952W1-12-b	952W1-13	952W1-14	952W1-15	952W1-16	952W1-17
P31	530	355	380	474	577	410	725
Ca44	97	81	61	61	35	80	46
Ti49	10	2	14	8	16	11	10
Sr88	0.1	0.2	0.2	0.2	0.1	0.1	0.2
Y89	1604	1134	1396	1405	917	1284	1381
Nb93	1	3	1	3	1	1	2
La139	0	<0.003	0	0	<0.003	0	0
Ce140	3	2	3	7	1	2	4
Pr141	0	0	0	0	0	0	0
Nd143	3	0	3	1	1	2	1
Sm147	7	1	6	3	3	5	3
Eu151	0	0	1	0	0	0	0
Gd160	39	13	32	22	16	28	22
Tb159	12	6	10	8	6	9	8
Dy163	156	87	128	114	76	119	115
Ho165	58	39	48	47	31	45	46
Er167	252	193	213	224	144	204	217
Tm169	49	42	42	46	30	40	45
Yb171	438	405	380	445	284	367	423
Lu175	86	83	75	92	58	73	86
Th	54	46	73	109	62	64	82
U	141	161	135	254	176	137	231
Th/U	0.4	0.3	0.5	0.4	0.4	0.5	0.4
Hf	10030	14195	10625	10880	10200	10200	10625
Zr/Hf	48	34	46	45	47	48	46
Hf/Y	6	13	8	8	11	8	8
∑REE	1102	871	940	1010	649	895	970
T [°C]	741	628	773	725	785	748	738
Sm/La	3824		854	1320		620	1552
Ce/Ce*	33		18	103		15	65
Lu/Gd	18	52	19	34	29	21	32
Eu/Eu*	0.06	0.04	0.12	0.10	0.07	0.08	0.07

	BE1-2	BE1-15	BE1-17	BE1-20	BE1-22	BE1-3	BE1-5	BE1-19	BE1-21	BE1-7
P31	735	694	551	355	458	488	523	720	231	568
Ca44	104	56	81	59	52	31	54	87	<18	71
Ti49	13	7	12	11	10	10	13	14	12	15
Sr88	0.1	0.1	0.1	0.1	0.1	0.1	0.2	0.2	0.1	0.2
Y89	1954	998	1036	711	1230	1071	1770	2086	555	1488
Nb93	1	2	1	1	2	2	1	3	1	2
La139	0	0	<0.04	<0.002	<0.003	0	0	0	0	0
Ce140	14	11	6	7	16	15	11	13	6	11
Pr141	0	0	0	0	0	0	0	0	0	0
Nd143	4	1	1	1	1	1	3	3	0	2
Sm147	7	2	3	2	3	3	7	6	1	5
Eu151	1	0	0	0	1	0	1	1	0	1
Gd160	42	13	20	12	20	17	39		9	29
Tb159	14	5	7	4	7	6	12	13	3	10
Dy163	178	73	90	59	100	84	162	182	44	132
Ho165	69	31	35	24	40	34	61	72	18	51
Er167	306	157	156	108	189	165	269	329	86	233
Tm169	59	35	31	22	40	35	52	66	18	46
Yb171	535	352	281	202	386	347	459	603	164	422
Lu175	106	77	56	41	81	73	89	124	34	86
Th	118	120	53	42	248	175	144	67	73	149
U	160	243	87	69	278	298	159	129	90	164
Th/U	0.7	0.5	0.6	0.6	0.9	0.6	0.9	0.5	0.8	0.9
Hf	11560	12495	10455	9860	11305	11390	10625	11135	10030	10795
Zr/Hf	42	39	47	50	43	43	46	44	49	45
Hf/Y	6	13	10	14	9	11	6	5	18	7
∑REE	1335	756	686	483	884	781	1166	1413	383	1028
T [°C]	764	712	758	753	745	740	765	770	755	779
Sm/La	1434	648				458	1883	634	1458	1414
Ce/Ce*	80	243				169	73	60	282	92
Lu/Gd	20	49	23	27	33	36	19		31	24
Eu/Eu*	0.19	0.17	0.17	0.19	0.20	0.21	0.20		0.21	0.19

[ppm]	BE1-10	949-13	BE1-8	883W3-1	883W3-2a	883W3-2b	883W3-4	883W3-7a	883W3-7b
P31	451	394	437	453	418	379	423	403	320
Ca44	74	<32	<19	97	81	83	75	52	52
Ti49	8	15	13	10	13	4	11	9	6
Sr88	0.1	0.1	0.1	0.3	0.1	0.1	0.2	0.1	0.1
Y89	978	742	438	2674	1270	1037	1073	1339	956
Nb93	1	1	1	3	2	2	2	3	2
La139	0	0	0	0	0	0	<0.003	0	0
Ce140	13	8	1	20	12	18	11	13	15
Pr141	0	0	0	1	0	0	0	0	0
Nd143	1	2	1	10	3	2	2	3	1
Sm147	3	3	5	17	5	4	4	5	3
Eu151	0	1	0	4	1	1	1	1	1
Gd160	17	13	31	82	26	20	21	28	18
Tb159	6	5	9	24	8	7	7	9	6
Dy163	80	59	73	286	109	89	88	121	80
Ho165	32	22	14	105	43	35	36	48	32
Er167	149	104	31	448	201	162	171	220	151
Tm169	31	22	4	86	41	34	36	44	31
Yb171	288	219	27	764	391	313	346	407	304
Lu175	59	48	5	151	81	65	74	84	64
Th	137	53	117	204	128		100	157	
U	173	176	326	332	239		154	277	
Th/U	0.8	0.3	0.4	0.6	0.5		0.6	0.6	
Hf	9945	12835	12920	9690	9180	11560	10200	9435	10710
Zr/Hf	49	38	38	50	53	42	49	52	46
Hf/Y	10	17	30	4	7	11	10	7	11
∑REE	678	505	200	1995	923	748	796	982	705
T [°C]	718	780	762	743	766	674	752	732	692
Sm/La	814	1091	2523	349	568	623		817	845
Ce/Ce*	198	90	23	22	61	159		84	159
Lu/Gd	29	29	1	15	25	26	29	24	28
Eu/Eu*	0.18	0.35	0.01	0.30	0.32	0.22	0.30	0.29	0.27

[ppm]	883W3-5	883W3-6	883W3-8	883W3-9	883W3-10	883W3-11a	883W3-11b	883W3-12
P31	567	325	394	370	317	498	330	373
Ca44	37	30	81	48	45	82	78	39
Ti49	9	6	4	7	6	4	6	5
Sr88	0.3	0.1	0.2	0.2	0.1	0.1	0.2	0.1
Y89	1960	957	1424	1366	929	1293	1250	972
Nb93	5	2	6	3	2	1	2	3
La139	0	0	<0.003	0	0	0	0	0
Ce140	35	15	12	18	14	11	17	16
Pr141	0	0	0	0	0	0	0	0
Nd143	3	1	1	3	1	3	3	1
Sm147	6	3	4	5	3	5	5	3
Eu151	1	1	1	1	1	1	1	1
Gd160	36	17	25	28	17	28		19
Tb159	12	6	9	9	6	9	8	6
Dy163	165	78	119	121	76	113	109	84
Ho165	65	32	48	48	31	44	43	33
Er167	298	150	223	224	146	202	203	153
Tm169	62	32	45	46	31	42	42	31
Yb171	573	306	418	433	296	393	403	289
Lu175	117	64	84	88	62	82	84	59
Th		145		136	115	127		113
U		227		221	205	185		237
Th/U		0.6		0.6	0.6	0.7		0.5
Hf	9860	10115	10370	9095	9945	9690	10710	10965
Zr/Hf	49	49	47	53	50	51	46	44
Hf/Y	5	11	7	7	11	7	9	11
∑REE	1374	705	987	1025	683	933	918	696
T [°C]	728	691	660	705	698	674	695	688
Sm/La	429	935		2408	1281	1005	582	1577
Ce/Ce*	128	195		201	233	76	94	248
Lu/Gd	26	30	27	26	30	24		25
Eu/Eu*	0.21	0.24	0.21	0.32	0.27	0.29		0.21

[ppm]	883W3-13	883W3-14	883W3-15	883W2-11	883W2-a	883W2-13	883W2-1	883W2-3
P31	536	230	278	478	293	506	476	487
Ca44	<31	51	62	245	63	259	128	107
Ti49	6	2	9	5	3	2	3	5
Sr88	0.1	0.1	0.2	0.4	0.3	0.4	0.3	0.3
Y89	1285	1050	1524	4313	1329	4244	3092	4264
Nb93	3	2	1	7	6	7	14	10
La139	0	<0.003	0	0	0	0	<0.01	0
Ce140	20	8	10	18	6	10	18	18
Pr141	0	0	0	1	0	0	0	0
Nd143	2	1	5	10	1	4	3	8
Sm147	4	3	8	25	3	13	9	22
Eu151	1	0	2	4	0	2	1	3
Gd160	23	17		134	23	87	63	122
Tb159	8	6	12	39	8	30	22	37
Dy163	103	85	145	468	114	402	291	450
Ho165	43	35	54	166	46	155	113	162
Er167	205	166	239	694	210	674	491	676
Tm169	43	34	47	128	42	126	95	124
Yb171	413	327	426	1086	376	1087	832	1061
Lu175	89	67	86	205	74	205	157	198
Th		68	111	594		613	664	667
U		198	131	417		628	542	465
Th/U		0.5	0.9	1.4		1.0	1.2	1.4
Hf	10625	11390	8670	10370	11050	11815	12070	10200
Zr/Hf	46	43	57	47	44	41	40	48
Hf/Y	8	11	6	2	8	3	4	2
∑REE	953	750	1035	2978	903	2795	2095	2883
T [°C]	699	612	734	680	647	631	654	684
Sm/La	153		513	1432	297	728		1246
Ce/Ce*	76		27	34	62	31		40
Lu/Gd	31	31		12	26	19	20	13
Eu/Eu*	0.27	0.15		0.19	0.18	0.19	0.18	0.19

[ppm]	883W2-4	883W2-14	883W2-2	883W2-8	883W2-19	883W2-18	883W2-6	883W2-c	883W2-b
P31	564	353	513	562	458	487	441	677	383
Ca44	188	103	162	169	176	148	104	139	157
Ti49	4	2	2	2	2	3	3	<2	2
Sr88	0.3	0.2	0.2	0.3	0.4	0.4	0.2	0.3	0.2
Y89	4111	1751	3478	3655	4499	3638	2561	4771	2392
Nb93	7	12	6	30	11	10	6	10	9
La139	0	<0.01	0	0	0	0	0	0	0
Ce140	14	7	8	18	12	10	7	11	11
Pr141	0	0	0	0	0	0	0	0	0
Nd143	9	1	3	2	4	3	2	4	2
Sm147	22	4	11	7	15	11	7	14	7
Eu151	3	1	2	1	2	2	1	2	1
Gd160	120	27		67	112	80	51	98	47
Tb159	36	10	24	25	38	28	17	33	16
Dy163	439	147	325	345	496	363	238	444	223
Ho165	157	61	128	136	186	138	92	174	87
Er167	655	282	554	608	802	602	409	754	388
Tm169	121	56	105	116	150	112	78	142	75
Yb171	1032	524	911	1023	1292	980	682	1212	659
Lu175	192	102	172	192	234	181	128	225	124
Th	606	352	471	635	493	453	372		
U	423	380	538	748	647	512	441		
Th/U	1.4	0.9	0.9	0.8	0.8	0.9	0.8		
Hf	10625	11900	11050	11475	12580	11900	11900	11815	11815
Zr/Hf	46	41	44	42	38	40	41	41	41
Hf/Y	3	7	3	3	3	3	5	2	5
∑REE	2800	1221	2243	2539	3343	2511	1714	3114	1638
T [°C]	658	610	626	603	615	635	645		615
Sm/La	1030		510	877	3526	1026	216	1667	196
Ce/Ce*	27		26	130	85	47	22	50	33
Lu/Gd	13	30		23	17	18	20	19	21
Eu/Eu*	0.19	0.16		0.17	0.17	0.19	0.19	0.18	0.20

[ppm]	983-1	983-2	983-3	936-18	936-7	936-17	936-15	936-12	936-10	936-13
P31	1082	<595	1524	624	1255	503	683	744	614	541
Ca44	312	<1249	132	250	<113	180	180	<168	227	226
Ti49	4	<30	<2	<2	3	<3	<2	<4	7	4
Sr88	0.7	20.7	0.5	0.5	0.2	0.3	0.4	0.2	0.6	0.5
Y89	5557	9614	3606	4937	2074	2008	5311	2466	4220	4430
Nb93	78	86	29	12	15	16	14	19	37	35
La139	0	1	0	1	0	0	1	1	0	1
Ce140	28	33	10	12	7	10	15	17	21	22
Pr141	0	2	0	0	0	0	0	0	0	0
Nd143	2	16	1	4	2	1	5	3	3	4
Sm147	11	27	6	15	4	6	17	7	10	10
Eu151	1	5	1	2	0	1	2	1	2	1
Gd160	105			104	30	37		48		85
Tb159	40	59	21	35	12	13	39	16	31	31
Dy163	550	791	298	473	172	179	514	229	421	435
Ho165	219	304	124	181	70	70	197	87	163	170
Er167	973	1311	567	787	328	313	849	390	726	745
Tm169	187	236	111	148	66	61	156	73	137	143
Yb171	1630	2082	983	1264	584	528	1330	631	1211	1249
Lu175	305	374	187	237	115	102	249	120	227	234
Th	1678	2026	2159	711	902	762	1009	648	636	1013
U	1701	1824	2129	884	918	864	1096	561	681	965
Th/U	1.0	1.1	1.0	0.8	1.0	0.9	0.9	1.2	0.9	1.1
Hf	12521	13600	0	12410	12410	12325	12070	13090	12240	13260
Zr/Hf	38	35		39	39	39	40	37	40	36
Hf/Y	2	1		3	6	6	2	5	3	3
∑REE	4051	5243	2310	3263	1390	1322	3375	1624	2952	3131
T [°C]	666				640				711	671
Sm/La	1421	53	499	47	16	105	44	15	58	23
Ce/Ce*	207	6	72	8	6	29	7	7	20	9
Lu/Gd	24			19	31	23		20		22
Eu/Eu*	0.11			0.16	0.11	0.16		0.13		0.15

[ppm]	936-5	936-4	936-a	984-2	984-3	984-1	984-a	984-6	984-7	984-9
P31	983	1553	531	792	584	425	778	374	483	556
Ca44	237	111	<80	83	<90	104	108	116	171	188
Ti49	3	6	4	3	3	3	3	4	3	4
Sr88	0.4	0.2	0.3	0.2	0.3	0.3	0.2	0.2	0.3	0.5
Y89	3173	3883	2621	1720	5232	2600	1991	2151	2825	5139
Nb93	11	27	23	7	12	19	9	12	18	10
La139	0	<0.01	0	<0.004	0	<0.003	<0.004	0	0	0
Ce140	7	12	13	6	21	13	8	14	15	17
Pr141	0	0	0	0	0	0	0	0	0	0
Nd143	2	2	2	1	10	1	1	2	2	8
Sm147	8	7	6	4	25	6	4	7	6	22
Eu151	1	1	1	1	4	1	1	1	1	4
Gd160	58	60	46	28	149	51			51	139
Tb159	21	24	17	11	44	18	12	16	19	45
Dy163	287	333	237	150	535	256	172	211	264	576
Ho165	112	136	93	61	192	101	70	83	104	213
Er167	500	624	413	286	800	453	320	367	466	903
Tm169	95	120	80	57	148	87	64	71	90	169
Yb171	825	1055	695	524	1254	772	572	634	788	1440
Lu175	159	205	133	103	236	146	111	121	150	269
Th	383	607			842	627		390	449	445
U	524	582			522	634		340	500	452
Th/U	0.7	1.0			1.6	1.0		1.1	0.9	1.0
Hf	12580	12665	12920	12665	10795	12325	11390	11900	11815	11900
Zr/Hf	39	38	38	38	45	40	43	41	41	41
Hf/Y	4	3	5	7	2	5	6	6	4	2
∑REE	2074	2577	1736	1232	3418	1906	1336	1527	1957	3804
T [°C]	638	694	663	642	655	651	647	675	655	667
Sm/La	222		59		1160			2732	200	382
Ce/Ce*	24		20		41			172	58	20
Lu/Gd	22	27	23	29	13	23			24	16
Eu/Eu*	0.17	0.16	0.16	0.17	0.18	0.17			0.19	0.20

[ppm]	984-10	984-12	984-13	984-14	984-15	984-16	984-17	995-8	995-1	995-11
P31	691	442	600	482	499	462	368	350	374	729
Ca44	205	161	173	<63	140	197	62	102	<158	86
Ti49	3	3	4	5	2	4	3	4	<4	3
Sr88	0.4	0.4	0.4	0.2	0.2	0.4	0.2	0.2	0.3	0.3
Y89	5011	4213	3637	2713	2616	4084	1784	2095	1397	2122
Nb93	14	8	30	16	16	8	11	11	7	6
La139	0	0	0	<0.01	0	0	<0.003	<0.01	0	0
Ce140	15	10	19	18	17	12	9	12	10	7
Pr141	0	0	0	0	0	0	0	0	0	0
Nd143	5	4	2	2	2	6	1	2	2	2
Sm147	17	13	8	7	7	17	4	5	3	6
Eu151	3	2	1	1	1	2	1	1	1	1
Gd160	118	87	70	54	49			38	26	38
Tb159	39	31	26	19	18	34	12	13	9	14
Dy163	518	407	351	253	244	443	159	186	120	192
Ho165	197	158	136	98	93	167	63	74	49	76
Er167	839	683	605	430	408	722	286	333	217	344
Tm169	158	130	117	81	78	135	55	64	45	68
Yb171	1348	1110	1021	706	673	1156	492	571	394	620
Lu175	248	206	192	132	125	217	94	109	76	120
Th	893	346	654	641	319	630	483	320	309	357
U	834	446	787	579	402	498	357	360	312	379
Th/U	1.1	0.8	0.8	1.1	0.8	1.3	1.4	0.9	1.0	0.9
Hf	11815	12410	11985	11305	11390	10795	11050	11390	10540	10965
Zr/Hf	41	39	40	43	43	46	44	43	46	44
Hf/Y	2	3	3	4	4	3	6	5	8	5
∑REE	3504	2842	2548	1802	1714	2910	1177	1408	953	1487
T [°C]	642	653	672	685	611	669	645	658		647
Sm/La	1824	2497	254		732	1880			11	693
Ce/Ce*	59	57	66		99	45			7	51
Lu/Gd	17	19	22	20	21			23	24	26
Eu/Eu*	0.18	0.20	0.17	0.20	0.19			0.19	0.28	0.19

[ppm]	995_10	995_h	995-5	995-g	995-f	995-e	995-d	995-c	995-b
P31	369	288	279	337	369	267	958	416	400
Ca44	113	130	83	70	122	98	94	124	104
Ti49	5	3	2	4	4	3	4	6	4
Sr88	0.3	0.3	0.3	0.2	0.3	0.2	0.6	0.8	0.3
Y89	2237	3089	2732	2009	1925	2905	3705	4156	2558
Nb93	12	4	3	11	8	3	9	11	15
La139	0	0	0	0	0	0	0	0	0
Ce140	14	8	8	12	9	8	9	12	17
Pr141	0	0	0	0	0	0	0	0	0
Nd143	2	4	4	2	3	4	7	6	2
Sm147	6	11	10	5	6	11	15	15	7
Eu151	1	2	2	1	1	2	4	3	1
Gd160	44	73	62	39	40	67	92	96	52
Tb159	16	24	20	14	14	21	31	32	19
Dy163	219	319	262	189	196	276	397	415	253
Ho165	87	122	100	75	77	105	142	157	99
Er167	383	532	435	332	340	457	593	679	435
Tm169	74	100	82	64	66	86	109	128	83
Yb171	656	869	717	567	597	743	930	1108	724
Lu175	125	164	136	108	113	142	172	204	136
Th	402		228						
U	441		302						
Th/U	0.9		0.8						
Hf	10965	10115	11050	10540	10200	10795	11135	10795	10540
Zr/Hf	44	48	44	46	48	45	44	45	46
Hf/Y	5	3	4	5	5	4	3	3	4
∑REE	1626	2230	1838	1408	1462	1923	2499	2856	1829
T [°C]	684	652	628	672	661	643	664	692	675
Sm/La	3329	3690	693	1340	48	3727	110	160	2464
Ce/Ce*	209	64	30	122	9	59	7	12	197
Lu/Gd	23	18	18	22	23	17	15	17	21
Eu/Eu*	0.19	0.19	0.20	0.18	0.21	0.18	0.29	0.20	0.19

[ppm]	995-15	995-21	995-16	995-17
P31	318	444	442	336
Ca44	124	<119	199	130
Ti49	3	4	5	3
Sr88	0.2	0.2	0.5	0.2
Y89	1966	3664	2598	2038
Nb93	11	5	14	11
La139	0	<0.01	0	0
Ce140	11	9	15	12
Pr141	0	0	0	0
Nd143	2	4	2	2
Sm147	5	12	7	5
Eu151	1	2	1	1
Gd160	36	75	47	38
Tb159	13	26	17	14
Dy163	183	341	238	190
Ho165	72	131	92	76
Er167	323	571	407	342
Tm169	63	108	78	67
Yb171	555	926	690	588
Lu175	107	176	130	113
Th	253	228	629	257
U	321	268	584	312
Th/U	0.8	0.8	1.1	0.8
Hf	11135	10880	11305	11220
Zr/Hf	44	45	43	44
Hf/Y	6	3	4	6
∑REE	1371	2382	1724	1448
T [°C]	648	671	690	645
Sm/La	2137		751	1100
Ce/Ce*	168		100	118
Lu/Gd	24	19	22	24
Eu/Eu*	0.18	0.19	0.17	0.20

Appendix 13: U-Pb dataset of zircons

	949-1	949-2	949-3	949-4	949-5	949-6	949-7	949-8	949-9	949-10	949-11	949-12	949-13	949-14	949-15	949-16	949-17	949-19	949-20
Th [ppm]	41	294	128	132	94	85	112	109	132	105	75	52	87	79	188	139	265	215	62
U [ppm]	115	468	314	356	235	184	247	277	296	266	192	141	211	172	371	249	461	408	172
Th/U ratio	0.355	0.627	0.407	0.372	0.401	0.461	0.453	0.394	0.447	0.394	0.390	0.367	0.412	0.457	0.505	0.560	0.575	0.527	0.361
Isotope ratio																			
Pb207/Pb206	0.0548	0.0518	0.0539	0.0528	0.0534	0.0540	0.0533	0.0528	0.0530	0.0546	0.0525	0.0532	0.0522	0.0519	0.0529	0.0526	0.0525	0.0525	0.0527
± 2 Se	0.0019	0.0017	0.0018	0.0018	0.0018	0.0019	0.0018	0.0018	0.0018	0.0018	0.0018	0.0019	0.0018	0.0018	0.0018	0.0018	0.0018	0.0017	0.0018
Pb206/U238	0.0480	0.0496	0.0487	0.0492	0.0495	0.0493	0.0498	0.0504	0.0488	0.0502	0.0490	0.0493	0.0495	0.0507	0.0496	0.0502	0.0496	0.0485	0.0497
± 2 Se	0.0006	0.0006	0.0006	0.0006	0.0006	0.0006	0.0006	0.0006	0.0006	0.0006	0.0006	0.0007	0.0006	0.0007	0.0006	0.0006	0.0006	0.0006	0.0006
Pb207/U235	0.363	0.353	0.364	0.360	0.372	0.365	0.365	0.370	0.356	0.388	0.353	0.360	0.362	0.367	0.364	0.367	0.363	0.354	0.366
± 2 Se	0.008	0.006	0.006	0.006	0.007	0.007	0.007	0.006	0.006	0.007	0.007	0.009	0.007	0.007	0.006	0.007	0.007	0.006	0.008
Pb208/Th232	0.0156	0.0159	0.0162	0.0157	0.0160	0.0158	0.0160	0.0166	0.0157	0.0167	0.0160	0.0158	0.0159	0.0164	0.0167	0.0164	0.0156	0.0153	0.0160
± 2 Se	0.0006	0.0006	0.0006	0.0006	0.0006	0.0006	0.0006	0.0006	0.0006	0.0006	0.0006	0.0006	0.0006	0.0006	0.0006	0.0006	0.0006	0.0005	0.0006
Isotope age																			
Pb207/Pb206	403	279	366	322	344	371	339	322	330	395	307	339	296	282	324	311	307	307	318
± 2 Se	42	35	33	34	37	38	35	34	35	34	38	46	38	38	33	37	36	33	41
Pb206/U238	302	312	307	310	312	310	313	317	307	316	308	310	311	319	312	316	312	305	313
± 2 Se	4	4	4	4	4	4	4	4	4	4	4	4	4	4	4	4	4	4	4
Pb207/U235	314	307	315	312	321	316	316	319	309	333	307	312	314	317	315	318	315	308	317
± 2 Se	7	5	5	5	6	6	6	6	6	6	6	7	6	6	5	6	6	5	7
Pb208/Th232	314	319	325	314	321	318	320	332	316	335	321	317	318	330	334	328	313	307	321
± 2 Se	11	11	12	11	12	11	11	12	11	12	12	12	11	12	12	12	11	11	12

	949-21	949-22	949-23	949-24	949-25	952W1-1	952W1-2	952W1-3	952W1-4	952W1-5	952W1-6	952W1-7	952W1-8	952W1-9	952W1-10	952W1-11	952W1-12	952W1-13
Th [ppm]	43	105	60	42	128	95	128	132	96	245	99	157	229	66	136	73	54	68
U [ppm]	91	260	112	224	308	274	278	289	163	448	279	277	581	218	288	174	133	195
Th/U ratio	0.473	0.405	0.536	0.188	0.417	0.347	0.460	0.457	0.590	0.547	0.356	0.569	0.394	0.303	0.474	0.420	0.404	0.346
Isotope ratio																		
Pb207/Pb206	0.0524	0.0522	0.0517	0.0524	0.0543	0.0518	0.0522	0.0540	0.0525	0.0523	0.0521	0.0542	0.0528	0.0523	0.0540	0.0540	0.0532	0.0527
± 2 Se	0.0020	0.0018	0.0019	0.0018	0.0018	0.0017	0.0017	0.0018	0.0018	0.0017	0.0017	0.0018	0.0017	0.0019	0.0018	0.0018	0.0019	0.0018
Pb206/U238	0.0468	0.0497	0.0466	0.0476	0.0465	0.0477	0.0492	0.0471	0.0472	0.0470	0.0477	0.0483	0.0510	0.0476	0.0486	0.0489	0.0489	0.0486
± 2 Se	0.0006	0.0006	0.0006	0.0006	0.0006	0.0006	0.0006	0.0006	0.0006	0.0006	0.0006	0.0006	0.0007	0.0007	0.0006	0.0006	0.0006	0.0006
Pb207/U235	0.342	0.363	0.339	0.350	0.355	0.347	0.359	0.354	0.347	0.342	0.345	0.364	0.372	0.344	0.367	0.370	0.367	0.364
± 2 Se	0.009	0.007	0.008	0.007	0.006	0.006	0.006	0.006	0.007	0.005	0.006	0.006	0.005	0.009	0.006	0.007	0.008	0.007
Pb208/Th232	0.0146	0.0167	0.0148	0.0154	0.0157	0.0149	0.0153	0.0147	0.0144	0.0147	0.0150	0.0153	0.0160	0.0157	0.0150	0.0152	0.0154	0.0155
± 2 Se	0.0005	0.0006	0.0005	0.0006	0.0006	0.0005	0.0005	0.0005	0.0005	0.0005	0.0005	0.0005	0.0006	0.0006	0.0005	0.0005	0.0006	0.0006
Isotope age																		
Pb207/Pb206	305	293	273	305	385	276	294	370	305	298	291	379	318	297	369	370	337	314
± 2 Se	52	38	49	39	35	34	34	32	38	30	33	33	29	50	32	37	40	36
Pb206/U238	295	312	294	300	293	300	310	297	298	296	300	304	321	300	306	308	308	306
± 2 Se	4	4	4	4	4	4	4	4	4	4	4	4	4	4	4	4	4	4
Pb207/U235	299	315	296	305	309	302	311	308	302	299	301	315	321	300	317	320	318	315
± 2 Se	8	6	7	6	6	5	5	5	6	4	5	5	5	8	5	6	7	6
Pb208/Th232	293	334	297	310	315	299	307	295	289	295	300	307	321	315	301	304	308	312
± 2 Se	11	12	11	12	11	11	11	10	10	10	11	11	11	12	11	11	11	11

	952W1-14	952W1-15	952W1-16	952W1-17	952W1-18	952W1-19	952W1-20	952W1-22	952W1-21	952W1-23	952W1-24	952W1-25	BE1-1	BE1-2	BE1-4	BE-11	BE-12	BE-13
Th [ppm]	54	46	73	109	101	62	64	82	123	178	111	150	222	118	285	228	302	132
U [ppm]	141	161	135	254	177	176	137	231	253	320	243	372	521	160	392	301	379	201
Th/U ratio	0.380	0.285	0.536	0.430	0.572	0.353	0.466	0.353	0.484	0.556	0.456	0.404	0.426	0.738	0.726	0.756	0.797	0.655
Isotope ratio																		
Pb207/Pb206	0.0529	0.0523	0.0520	0.0522	0.0537	0.0531	0.0520	0.0528	0.0530	0.0531	0.0524	0.0530	0.0525	0.0533	0.0529	0.0532	0.0532	0.0535
± 2 Se	0.0018	0.0018	0.0018	0.0017	0.0019	0.0019	0.0018	0.0018	0.0018	0.0018	0.0018	0.0017	0.0007	0.0009	0.0007	0.0008	0.0007	0.0009
Pb206/U238	0.0484	0.0495	0.0493	0.0510	0.0491	0.0511	0.0493	0.0498	0.0477	0.0492	0.0498	0.0492	0.0478	0.0503	0.0488	0.0498	0.0485	0.0479
± 2 Se	0.0006	0.0006	0.0006	0.0007	0.0006	0.0007	0.0006	0.0006	0.0006	0.0006	0.0006	0.0006	0.0004	0.0005	0.0004	0.0005	0.0004	0.0004
Pb207/U235	0.357	0.359	0.353	0.368	0.369	0.374	0.355	0.366	0.348	0.358	0.363	0.359	0.345	0.372	0.356	0.366	0.358	0.358
± 2 Se	0.007	0.007	0.007	0.006	0.007	0.008	0.007	0.006	0.006	0.006	0.006	0.006	0.005	0.007	0.005	0.006	0.005	0.006
Pb208/Th232	0.0157	0.0161	0.0157	0.0167	0.0158	0.0168	0.0156	0.0158	0.0153	0.0155	0.0159	0.0156	0.0151	0.0166	0.0153	0.0155	0.0156	0.0150
± 2 Se	0.0006	0.0006	0.0006	0.0006	0.0006	0.0006	0.0006	0.0006	0.0005	0.0005	0.0006	0.0005	0.0002	0.0002	0.0002	0.0002	0.0002	0.0002
Isotope age																		
Pb207/Pb206	326	298	284	292	358	331	286	318	329	331	303	331	309.2	339.5	324.4	335.1	335.5	348.8
± 2 Se	39	38	41	34	39	40	41	34	33	32	34	31	28.9	38.1	30.4	32.8	30.4	36.5
Pb206/U238	305	311	310	321	309	321	310	314	300	309	313	310	300.9	316.3	307.1	313.4	305.4	301.5
± 2 Se	4	4	4	4	4	4	4	4	4	4	4	4	2.7	2.8	2.7	2.8	2.6	2.6
Pb207/U235	310	312	307	318	319	323	309	317	303	311	315	312	300.9	321.4	309.0	317.0	310.7	310.9
± 2 Se	6	6	6	5	6	7	6	6	5	5	5	5	3.4	5.1	3.7	4.2	3.7	4.6
Pb208/Th232	314	323	316	336	316	336	313	317	306	310	319	313	303.7	333.4	307.7	311.2	311.9	300.7
± 2 Se	11	12	11	12	11	12	11	11	11	11	11	11	3.1	3.6	3.0	3.2	3.0	3.2

	BE-14	BE-15	BE-16	BE-17	BE-18	BE-22	BE-23	BE-24	BE-25	BE1-3	BE1-5	BE1-6	BE1-7	BE1-9	BE1-10	BE-19	BE-20	BE-21
Th [ppm]	283	120	50	53	181	248	123	153	357	175	144	115	149	175	137	67	42	73
U [ppm]	549	243	79	87	214	278	159	190	401	298	159	214	164	368	173	129	69	90
Th/U ratio	0.516	0.496	0.626	0.606	0.846	0.890	0.773	0.803	0.890	0.585	0.902	0.537	0.909	0.476	0.794	0.521	0.612	0.811
Isotope ratio																		
Pb207/Pb206	0.0526	0.0529	0.0518	0.0534	0.0523	0.0533	0.0524	0.0526	0.0530	0.0529	0.0522	0.0558	0.0539	0.0526	0.0527	0.0548	0.0557	0.0501
± 2 Se	0.0007	0.0008	0.0012	0.0011	0.0010	0.0008	0.0009	0.0009	0.0008	0.0008	0.0010	0.0009	0.0011	0.0007	0.0010	0.0011	0.0013	0.0012
Pb206/U238	0.0493	0.0495	0.0493	0.0482	0.0491	0.0491	0.0488	0.0487	0.0492	0.0467	0.0464	0.0472	0.0453	0.0467	0.0438	0.0462	0.0481	0.0466
± 2 Se	0.0005	0.0005	0.0005	0.0005	0.0005	0.0004	0.0005	0.0005	0.0004	0.0004	0.0005	0.0004	0.0004	0.0004	0.0004	0.0004	0.0005	0.0005
Pb207/U235	0.360	0.368	0.351	0.342	0.359	0.360	0.361	0.364	0.364	0.343	0.340	0.369	0.343	0.340	0.319	0.356	0.390	0.327
± 2 Se	0.005	0.006	0.009	0.008	0.008	0.006	0.007	0.007	0.005	0.005	0.007	0.007	0.007	0.005	0.007	0.008	0.010	0.008
Pb208/Th232	0.0155	0.0153	0.0152	0.0150	0.0152	0.0153	0.0177	0.0151	0.0152	0.0151	0.0144	0.0158	0.0143	0.0145	0.0133	0.0151	0.0151	0.0143
± 2 Se	0.0002	0.0002	0.0002	0.0002	0.0002	0.0002	0.0002	0.0002	0.0002	0.0002	0.0002	0.0002	0.0002	0.0002	0.0002	0.0002	0.0002	0.0002
Isotope age																		
Pb207/Pb206	309.5	325.3	277.2	345.7	297.6	339.9	302.2	312.4	330.6	324.4	294.4	443.9	368.3	313.1	316.1	405.1	441.9	198.6
± 2 Se	29.6	33.2	49.8	47.2	43.2	32.8	39.4	38.5	32.2	32.2	41.6	36.8	44.2	31.5	43.8	45.7	51.0	52.7
Pb206/U238	310.2	311.4	310.0	303.4	308.8	308.9	307.3	306.5	309.8	294.1	292.6	297.4	285.3	294.3	276.1	291.0	302.9	293.8
± 2 Se	2.8	2.8	3.0	2.9	3.0	2.7	2.8	2.8	2.7	2.6	2.8	2.6	2.6	2.6	2.7	2.7	3.0	2.9
Pb207/U235	312.1	317.8	305.4	299.0	311.2	311.9	312.8	314.9	315.1	299.6	297.0	318.8	299.5	297.2	281.4	309.1	334.2	287.5
± 2 Se	3.6	4.2	6.5	6.0	5.7	4.1	5.1	5.0	4.0	3.9	5.2	4.9	5.6	3.7	5.2	6.1	7.5	6.4
Pb208/Th232	311.4	306.9	304.7	301.5	304.7	305.8	355.3	303.1	305.7	303.7	289.0	317.4	287.6	291.3	267.9	302.6	303.2	287.9
± 2 Se	3.2	3.3	4.0	3.9	3.6	3.0	3.8	3.3	3.0	3.1	3.2	3.6	3.3	3.1	3.2	4.0	4.3	3.6

	BE1-8	949-18	883W3-1	883W3-2	883W3-3	883W3-4	883W3-5	883W3-6	883W3-7	883W3-8	883W3-9	883W3-10	883W3-11	883W3-12	883W3-13	883W3-14	883W3-15	883W3-16
Th [ppm]	117	53	128	79	204	381	209	100	121	145	171	230	136	115	111	127	113	374
U [ppm]	326	176	239	111	332	642	490	154	200	227	225	427	221	205	131	185	237	720
Th/U ratio	0.358	0.303	0.537	0.715	0.614	0.594	0.426	0.650	0.606	0.639	0.762	0.540	0.615	0.560	0.853	0.686	0.477	0.520
Isotope ratio																		
Pb207/Pb206	0.0982	0.0996	0.0530	0.0518	0.0543	0.0530	0.0535	0.0528	0.0527	0.0522	0.0546	0.0527	0.0528	0.0517	0.0522	0.0530	0.0539	0.0541
± 2 Se	0.0011	0.0032	0.0018	0.0019	0.0018	0.0018	0.0017	0.0018	0.0018	0.0018	0.0018	0.0017	0.0018	0.0018	0.0018	0.0018	0.0019	0.0018
Pb206/U238	0.2678	0.2670	0.0482	0.0479	0.0476	0.0497	0.0480	0.0470	0.0479	0.0475	0.0494	0.0486	0.0482	0.0481	0.0486	0.0492	0.0493	0.0498
± 2 Se	0.0022	0.0034	0.0006	0.0006	0.0006	0.0006	0.0006	0.0006	0.0006	0.0006	0.0006	0.0006	0.0006	0.0006	0.0006	0.0006	0.0007	0.0006
Pb207/U235	3.639	3.695	0.356	0.342	0.359	0.364	0.347	0.346	0.351	0.348	0.371	0.354	0.354	0.342	0.355	0.365	0.375	0.371
± 2 Se	0.044	0.060	0.006	0.008	0.006	0.006	0.005	0.007	0.006	0.006	0.007	0.005	0.006	0.006	0.007	0.007	0.008	0.006
Pb208/Th232	0.0789	0.0793	0.0149	0.0152	0.0152	0.0157	0.0151	0.0147	0.0149	0.0151	0.0161	0.0161	0.0153	0.0152	0.0157	0.0158	0.0155	0.0164
± 2 Se	0.0007	0.0028	0.0005	0.0005	0.0005	0.0006	0.0005	0.0005	0.0005	0.0005	0.0006	0.0006	0.0005	0.0005	0.0006	0.0006	0.0006	0.0006
Isotope age																		
Pb207/Pb206	1590.1	1616	329	277	382	330	348	319	317	293	395	317	320	272	294	330	368	373
± 2 Se	20.4	23	34	45	35	32	29	38	36	37	35	30	35	37	42	37	41	30
Pb206/U238	1529.4	1526	304	301	300	313	302	296	301	299	311	306	303	303	306	309	310	313
± 2 Se	11.4	19	4	4	4	4	4	4	4	4	4	4	4	4	4	4	4	4
Pb207/U235	1558.2	1570	309	299	311	315	303	302	305	303	320	308	308	299	308	316	323	321
± 2 Se	9.6	26	5	7	6	5	4	6	6	6	6	5	5	6	6	6	7	5
Pb208/Th232	1535.6	1542	299	305	304	315	302	295	299	302	324	322	307	306	314	316	310	329
± 2 Se	13.9	55	11	11	11	11	11	10	11	11	11	11	11	11	11	11	11	12

	883W3-17	883W3-18	883W3-19	883W3-20	883W2-1	883W2-2	883W2-3	883W2-4	883W2-5	883W2-6	883W2-7	883W2-8	883W2-9	883W2-10	883W2-11	883W2-12	883W2-14	883W2-15
Th [ppm]	68	83	238	221	613	471	606	667	287	372	661	635	530	674	594	499	352	890
U [ppm]	198	173	292	376	628	538	423	465	357	441	746	748	517	836	417	491	380	905
Th/U ratio	0.342	0.482	0.814	0.588	0.975	0.875	1.432	1.436	0.803	0.842	0.886	0.849	1.025	0.806	1.422	1.015	0.927	0.984
Isotope ratio																		
Pb207/Pb206	0.0533	0.0517	0.0519	0.0524	0.0543	0.0533	0.0538	0.0536	0.0538	0.0538	0.0607	0.0534	0.0620	0.0540	0.0532	0.0570	0.0650	0.0606
± 2 Se	0.0018	0.0018	0.0017	0.0017	0.0016	0.0016	0.0016	0.0016	0.0017	0.0017	0.0018	0.0016	0.0019	0.0016	0.0016	0.0018	0.0020	0.0019
Pb206/U238	0.0501	0.0487	0.0470	0.0499	0.0518	0.0513	0.0518	0.0525	0.0513	0.0509	0.0520	0.0522	0.0515	0.0520	0.0506	0.0517	0.0519	0.0512
± 2 Se	0.0007	0.0006	0.0006	0.0006	0.0007	0.0007	0.0007	0.0007	0.0007	0.0007	0.0007	0.0007	0.0007	0.0007	0.0007	0.0007	0.0007	0.0007
Pb207/U235	0.373	0.352	0.339	0.361	0.393	0.380	0.389	0.392	0.381	0.379	0.434	0.383	0.440	0.384	0.371	0.405	0.470	0.424
± 2 Se	0.007	0.007	0.006	0.006	0.007	0.007	0.007	0.007	0.007	0.008	0.008	0.007	0.008	0.007	0.007	0.009	0.009	0.009
Pb208/Th232	0.0173	0.0159	0.0151	0.0163	0.0164	0.0159	0.0166	0.0169	0.0164	0.0163	0.0181	0.0172	0.0177	0.0168	0.0165	0.0172	0.0182	0.0171
± 2 Se	0.0006	0.0006	0.0005	0.0006	0.0006	0.0006	0.0006	0.0006	0.0006	0.0006	0.0007	0.0006	0.0007	0.0006	0.0006	0.0006	0.0007	0.0006
Isotope age																		
Pb207/Pb206	341	271	279	302	382.6	342.3	362.4	355.5	360.9	362.4	629.3	344.8	675.2	372.6	336.7	490.8	773.4	625.9
± 2 Se	37	37	33	31	27.6	31.4	30.0	30.1	31.5	33.2	28.3	27.8	27.8	27.5	31.7	36.2	29.1	34.2
Pb206/U238	315	307	296	314	325.6	322.5	325.3	329.9	322.6	319.7	326.7	328.1	323.7	326.6	318.2	324.8	325.9	321.6
± 2 Se	4	4	4	4	4.5	4.6	4.5	4.5	4.4	4.4	4.6	4.5	4.4	4.5	4.5	4.4	4.4	4.5
Pb207/U235	322	306	296	313	336.5	327.3	333.5	336.1	327.6	326.3	365.7	329.4	370.4	330.3	320.7	344.9	391.1	359.2
± 2 Se	6	6	5	5	6.0	6.4	6.3	6.3	6.3	6.6	6.9	5.9	6.8	5.8	6.3	7.5	7.6	7.7
Pb208/Th232	347	318	303	327	328.6	319.7	331.7	338.6	328.1	327.3	362.6	344.7	353.8	337.1	330.9	345.2	365.0	341.8
± 2 Se	12	11	11	11	12.2	12.0	12.3	12.6	12.3	12.3	13.6	12.8	13.2	12.6	12.4	13.0	13.6	13.0

	883W2-16	883W2-17	883W2-18	883W2-19	883W2-20	936-1	936-2	936-3	936-4	936-5	936-6	936-7	936-8	936-9	936-10	936-11	936-12	936-13
Th [ppm]	407	1060	453	493	326	432	732	1047	607	383	530	903	1012	1143	636	978	648	1013
U [ppm]	443	1163	512	647	389	497	735	836	582	524	634	918	1039	1144	681	1358	561	965
Th/U ratio	0.917	0.912	0.886	0.763	0.837	0.870	0.996	1.252	1.044	0.732	0.836	0.983	0.974	1.000	0.935	0.720	1.155	1.050
Isotope ratio																		
Pb207/Pb206	0.0536	0.0631	0.0545	0.054	0.055	0.0645	0.0548	0.0534	0.0580	0.0563	0.0555	0.0533	0.0553	0.0551	0.0561	0.0584	0.0549	0.0543
± 2 Se	0.0016	0.0019	0.0017	7E-04	0.001	0.0020	0.0007	0.0007	0.0011	0.0008	0.0007	0.0006	0.0007	0.0007	0.0007	0.0007	0.0007	0.0007
Pb206/U238	0.0525	0.0519	0.0509	0.051	0.053	0.0521	0.0506	0.0514	0.0506	0.0513	0.0485	0.0499	0.0509	0.0526	0.0517	0.0518	0.0528	0.0511
± 2 Se	0.0007	0.0007	0.0007	5E-04	5E-04	0.0007	0.0007	0.0007	0.0008	0.0007	0.0007	0.0007	0.0007	0.0007	0.0007	0.0007	0.0007	0.0007
Pb207/U235	0.390	0.445	0.385	0.378	0.396	0.467	0.382	0.379	0.406	0.379	0.371	0.365	0.388	0.392	0.402	0.405	0.400	0.381
± 2 Se	0.008	0.009	0.008	0.005	0.011	0.009	0.007	0.007	0.010	0.007	0.007	0.006	0.007	0.007	0.007	0.007	0.007	0.007
Pb208/Th232	0.0169	0.0179	0.0166	0.017	0.017	0.0179	0.0161	0.0163	0.0172	0.0171	0.0157	0.0157	0.0175	0.0170	0.0172	0.0250	0.0174	0.0168
± 2 Se	0.0006	0.0007	0.0006	2E-04	3E-04	0.0007	0.0006	0.0006	0.0007	0.0006	0.0006	0.0006	0.0007	0.0006	0.0006	0.0009	0.0006	0.0006
Isotope age																		
Pb207/Pb206	354.9	712.3	389.8	358.6	394.5	758	404	344	528	463	430	342	423	418	456	544	407	383
± 2 Se	31.4	30.1	34.7	28.56	53.39	27	27	28	41	29	28	27	27	27	28	26	28	30
Pb206/U238	329.7	326.0	320.3	323	335.2	328	318	323	318	323	305	314	320	331	325	326	332	322
± 2 Se	4.5	4.7	4.5	2.82	3.26	4	4	4	5	4	4	4	4	5	4	4	5	5
Pb207/U235	334.4	373.5	330.4	325.7	339	389	329	326	346	326	320	316	333	336	343	345	342	328
± 2 Se	6.4	7.5	7.0	3.58	7.94	7	6	6	9	6	6	5	6	6	6	6	6	6
Pb208/Th232	338.8	359.1	332.7	331.3	341	358	322	327	344	343	315	315	351	340	345	499	349	337
± 2 Se	12.6	13.6	12.5	3.28	5.32	13	12	12	13	13	12	12	13	13	13	19	13	13

	936-14	936-15	936-16	936-17	936-18	936-19	936-20	984-1	984-2	984-3	984-4	984-5	984-6	984-7	984-8	984-9	984-10	984-11	984-12
Th [ppm]	767	1009	1202	762	711	537	776	627	229	842	695	430	390	449	474	445	893	836	346
U [ppm]	823	1096	1082	864	884	635	836	634	303	522	723	497	340	500	421	452	834	482	446
Th/U ratio	0.932	0.921	1.111	0.881	0.804	0.846	0.928	0.988	0.757	1.613	0.962	0.865	1.146	0.898	1.126	0.985	1.071	1.735	0.774
Isotope ratio																			
Pb207/Pb206	0.0551	0.0561	0.0536	0.0567	0.0540	0.0552	0.0556	0.0545	0.0538	0.0562	0.0533	0.0550	0.0528	0.0527	0.0535	0.0583	0.0589	0.0708	0.0611
± 2 Se	0.0007	0.0007	0.0006	0.0007	0.0007	0.0007	0.0007	0.0012	0.0013	0.0013	0.0012	0.0013	0.0012	0.0013	0.0012	0.0014	0.0014	0.0017	0.0014
Pb206/U238	0.0492	0.0512	0.0515	0.0526	0.0509	0.0511	0.0519	0.0511	0.0520	0.0519	0.0515	0.0512	0.0517	0.0518	0.0510	0.0516	0.0520	0.0542	0.0535
± 2 Se	0.0007	0.0007	0.0007	0.0007	0.0007	0.0007	0.0007	0.0005	0.0005	0.0005	0.0005	0.0005	0.0005	0.0005	0.0005	0.0005	0.0005	0.0005	0.0006
Pb207/U235	0.378	0.393	0.378	0.410	0.377	0.389	0.396	0.386	0.387	0.402	0.378	0.390	0.382	0.381	0.375	0.411	0.423	0.536	0.454
± 2 Se	0.007	0.007	0.006	0.007	0.007	0.007	0.007	0.005	0.007	0.006	0.005	0.005	0.006	0.006	0.005	0.006	0.007	0.008	0.007
Pb208/Th232	0.0156	0.0218	0.0162	0.0173	0.0164	0.0165	0.0169	0.0157	0.0166	0.0167	0.0163	0.0162	0.0161	0.0165	0.0163	0.0176	0.0169	0.0182	0.0181
± 2 Se	0.0006	0.0008	0.0006	0.0006	0.0006	0.0006	0.0006	0.0005	0.0006	0.0006	0.0006	0.0006	0.0006	0.0006	0.0006	0.0006	0.0006	0.0006	0.0006
Isotope age																			
Pb207/Pb206	415	456	354	479	370	421	435	392.4	363.4	461.2	340.9	410.9	319.8	316.4	351.0	539.5	562.7	950.8	641.9
± 2 Se	29	26	26	26	27	28	26	27.4	35.4	28.7	28.1	28.5	31.3	33.3	30.4	32.2	31.5	28.2	29.4
Pb206/U238	309	322	324	330	320	322	326	321.3	326.7	325.9	323.9	321.6	325.1	325.3	320.9	324.1	326.5	340.2	336.0
± 2 Se	4	4	4	5	4	4	4	3.3	3.5	3.4	3.2	3.3	3.3	3.3	3.3	3.2	3.2	3.4	3.5
Pb207/U235	326	337	326	349	325	334	339	331.4	331.9	343.3	325.6	334.3	328.4	327.9	323.5	349.5	358.2	436.0	380.0
± 2 Se	6	6	6	6	6	6	6	4.3	5.8	4.8	4.2	4.6	4.9	5.3	4.7	5.5	5.6	6.6	5.7
Pb208/Th232	313	436	325	347	329	331	338	314.9	333.3	334.0	327.5	325.3	323.6	330.5	326.0	351.6	338.6	365.1	363.1
± 2 Se	12	16	12	13	12	12	13	10.9	11.7	11.6	11.3	11.2	11.2	11.5	11.3	12.2	11.8	12.7	12.7

	984-13	984-14	984-15	984-16	984-17	984-18	984-19	984-20	995-2	995-3	995-5	995-6	995-7	995-8	995-9	995-10	995-11	995-12	995-13
Th [ppm]	654	641	319	630	483	663	1130	551	266	201	228	235	309	320	493	402	357	447	291
U [ppm]	787	579	402	498	357	464	689	411	290	210	302	285	312	360	441	441	379	486	282
Th/U ratio	0.831	1.106	0.792	1.266	1.353	1.431	1.640	1.342	0.916	0.959	0.756	0.825	0.989	0.890	1.118	0.911	0.940	0.921	1.032
Isotope ratio																			
Pb207/Pb206	0.0539	0.0740	0.0529	0.1137	0.0536	0.0664	0.0553	0.0547	0.0536	0.0520	0.0533	0.0543	0.0549	0.0536	0.0543	0.0641	0.0537	0.0529	0.0543
± 2 Se	0.0012	0.0018	0.0013	0.0025	0.0012	0.0016	0.0012	0.0013	0.0013	0.0014	0.0013	0.0013	0.0014	0.0013	0.0015	0.0016	0.0013	0.0013	0.0014
Pb206/U238	0.0529	0.0535	0.0521	0.0522	0.0520	0.0518	0.0520	0.0509	0.0486	0.0486	0.0498	0.0489	0.0500	0.0498	0.0503	0.0506	0.0502	0.0497	0.0512
± 2 Se	0.0006	0.0006	0.0005	0.0005	0.0005	0.0006	0.0005	0.0005	0.0005	0.0005	0.0005	0.0005	0.0005	0.0005	0.0006	0.0006	0.0005	0.0005	0.0006
Pb207/U235	0.392	0.542	0.386	0.820	0.386	0.482	0.401	0.395	0.366	0.348	0.374	0.37	0.386	0.375	0.376	0.449	0.375	0.364	0.391
± 2 Se	0.006	0.009	0.007	0.010	0.006	0.008	0.005	0.006	0.007	0.008	0.006	0.006	0.007	0.006	0.009	0.008	0.006	0.007	0.008
Pb208/Th232	0.0168	0.0190	0.0168	0.0225	0.0168	0.0185	0.0170	0.0165	0.015	0.015	0.016	0.015	0.016	0.016	0.016	0.017	0.016	0.016	0.017
± 2 Se	0.0006	0.0007	0.0006	0.0008	0.0006	0.0006	0.0006	0.0006	0.0005	0.0005	0.0006	0.0005	0.0006	0.0006	0.0006	0.0006	0.0006	0.0006	0.0006
Isotope age																			
Pb207/Pb206	366.2	1040.7	322.7	1859.6	355.1	819.1	425.2	398.4	355	286	341	383	407	356	383	743	359	326	383
± 2 Se	29.6	28.8	35.1	21.0	30.4	32.0	27.4	32.8	37	45	34	35	36	35	46	33	34	37	41
Pb206/U238	332.5	335.7	327.3	327.7	326.5	325.3	326.5	320.3	306	306	314	308	315	314	316	318	316	313	322
± 2 Se	3.6	3.7	3.4	3.4	3.3	3.5	3.3	3.3	3	3	3	3	3	3	4	3	3	3	3
Pb207/U235	336.1	440.0	331.5	607.8	331.1	399.5	342.2	337.8	317	303	322	320	331	323	324	377	323	316	335
± 2 Se	4.8	7.2	5.7	7.7	4.8	6.9	4.5	5.5	6	7	5	6	6	6	8	7	5	6	7
Pb208/Th232	335.9	381.0	336.5	450.6	336.5	371.2	340.2	330.2	310	300	319	307	318	323	315	345	321	317	336
± 2 Se	11.7	13.3	11.8	15.6	11.6	13.0	11.8	11.4	11	11	11	11	11	11	11	12	11	11	12

	995-14	995-15	995-16	995-17	995-18	995-19	995-20	995-21	983-1	983-2	983-3	983-4	983-5	885_71_c1	885-71_c2	885-71-c3	885-71-c4	885-71-c5
Th [ppm]	437	253	629	257	1476	1106	517	228	1678	2026	2312	3550	2159	1521	1022	902	1422	1345
U [ppm]	454	321	584	312	778	754	475	268	1701	1824	1880	2755	2129	1328	1019	985	1216	1162
Th/U ratio	0.962	0.789	1.077	0.823	1.897	1.467	1.087	0.849	0.986	1.111	1.230	1.288	1.014	1.145	1.002	0.915	1.170	1.158
Isotope ratio																		
Pb207/Pb206	0.0531	0.0534	0.0532	0.0550	0.0566	0.0529	0.0538	0.0549	0.0536	0.0541	0.1252	0.1026	0.0854	0.0543	0.0557	0.0557	0.0551	0.0557
± 2 Se	0.0014	0.0013	0.0013	0.0015	0.0013	0.0013	0.0013	0.0014	0.0017	0.0017	0.0040	0.0034	0.0028	0.0009	0.0009	0.0010	0.0009	0.0009
Pb206/U238	0.0500	0.0504	0.0496	0.0496	0.0492	0.0490	0.0476	0.0489	0.0527	0.0522	0.0519	0.0546	0.0511	0.0515	0.0540	0.0508	0.0517	0.0505
± 2 Se	0.0005	0.0005	0.0005	0.0006	0.0005	0.0005	0.0005	0.0005	0.0007	0.0007	0.0007	0.0008	0.0007	0.0005	0.0005	0.0005	0.0005	0.0005
Pb207/U235	0.366	0.376	0.361	0.381	0.385	0.355	0.356	0.374	0.378	0.377	0.863	0.754	0.583	0.3718	0.4092	0.3838	0.3801	0.3745
± 2 Se	0.007	0.006	0.006	0.008	0.006	0.006	0.006	0.007	0.005	0.005	0.012	0.013	0.009	0.0068	0.0071	0.0081	0.0074	0.0070
Pb208/Th232	0.016	0.016	0.016	0.016	0.016	0.015	0.016	0.016	0.0165	0.0167	0.0224	0.0211	0.0191	0.0154	0.0175	0.0158	0.0165	0.0160
± 2 Se	0.0006	0.0006	0.0005	0.0006	0.0005	0.0005	0.0005	0.0006	0.0006	0.0006	0.0008	0.0008	0.0007	0.0004	0.0004	0.0005	0.0005	0.0004
Isotope age																		
Pb207/Pb206	333	347	337	410	476	324	363	409	356	375	2032	1672	1323	384.4	438.8	437.9	416.3	439
± 2 Se	40	35	33	43	31	34	36	38	27	25	20	27	24	35.33	33.14	39.25	36.66	35.27
Pb206/U238	315	317	312	312	310	308	300	308	331	328	326	343	321	323.5	339.3	319.6	324.7	317.5
± 2 Se	3	3	3	3	3	3	3	3	4	4	4	5	4	2.93	3.09	2.98	2.88	2.75
Pb207/U235	317	324	313	328	330	309	309	323	325	325	632	571	466	321	348.3	329.8	327.1	323
± 2 Se	6	6	5	7	5	5	5	6	5	4	9	10	7	5.03	5.1	5.93	5.42	5.17
Pb208/Th232	319	320	315	323	311	294	312	324	331	335	449	421	382	309.7	351.3	317.6	329.9	321.4
± 2 Se	11	11	11	11	11	10	11	11	12	12	16	15	13	7.92	8.19	9.29	9.21	8.6

	885-71-c6	885-71-c7	885-71-c8	880-28-E1	880-28-E2	880-28-D	880-28-B	880-28-C
Th [ppm]	1409	1464	2110	1672	2553	3661	3437	1132
U [ppm]	1151	1187	2097	1487	1932	2610	2383	1103
Th/U ratio	1.224	1.232	1.006	1.124	1.322	1.403	1.442	1.026
Isotope ratio								
Pb207/Pb206	0.0535	0.0593	0.0526	0.0569	0.0545	0.0518	0.0535	0.0565
± 2 Se	0.0009	0.0008	0.0007	0.0011	0.0010	0.0010	0.0009	0.0009
Pb206/U238	0.0539	0.0535	0.0523	0.0507	0.0513	0.0514	0.0512	0.0518
± 2 Se	0.0005	0.0005	0.0005	0.0005	0.0005	0.0006	0.0005	0.0005
Pb207/U235	0.3917	0.4277	0.3703	0.3876	0.3748	0.3518	0.3653	0.3896
± 2 Se	0.0072	0.0062	0.0053	0.0089	0.0086	0.0082	0.0068	0.0070
Pb208/Th232	0.0147	0.0149	0.0154	0.0169	0.0156	0.0146	0.0172	0.0173
± 2 Se	0.0004	0.0003	0.0003	0.0006	0.0006	0.0005	0.0005	0.0005
Isotope age								
Pb207/Pb206	347.8	576.7	312.4	485.6	389.9	275.1	350.8	471.6
± 2 Se	35.9	28.23	29.28	41.86	42.02	43.48	35.88	34.27
Pb206/U238	338.4	335.7	328.5	318.5	322.4	323	321.8	325.3
± 2 Se	3	3.09	3.01	2.92	2.95	3.45	2.85	2.93
Pb207/U235	335.6	361.6	319.9	332.6	323.2	306.1	316.2	334.1
± 2 Se	5.28	4.39	3.92	6.49	6.34	6.13	5.07	5.09
Pb208/Th232	295.4	299.6	309.1	338.9	312	293.4	345.6	346.2
± 2 Se	7.92	5.74	6.11	11.88	11.11	10.28	10.16	9.48

Appendix 14: Re-Os dataset of molybdenite

	950**	**950**	**955**	**982**	**983**	**890W6**
wt sample [g]	0.2547	0.0998	0.0512	0.1501	0.2025	0.1941
Wt. Re spike [g]	0.0863	0.1073	0.2181	0.0459	0.0191	0.0207
Wt Os spike [g]	0.0152	0.0205	0.0588	0.0103	0.0104	0.0106
(^{185}Re/^{187}Re)FC	1.8585	4.0706	3.2522	5.9956	4.5644	8.3854
% SE	0.0010%	0.0090%	0.0096%	0.0017%	0.0405%	0.0040%
(^{187}Os/^{192}Os)FC	2.3008	0.7028	0.6793	0.4067	0.2633	0.1495
% SE	1.9286%	0.0050%	0.0018%	0.0115%	0.0370%	0.0189%
umol ^{187}Re	0.00793	0.00335	0.00914	0.00087	0.00052	0.00025
2SE	2.53E-07	7.83E-07	2.32E-06	3.85E-08	5.40E-07	2.74E-08
[Re] ppm	9.26	10.00	53.12	1.72	0.76	0.385
2SE	0.03	0.23	1.35	0.01	0.08	0.004
(^{192}Os/^{187}Os)FC	0.43463	1.42289	1.47218	2.45899	3.79738	6.68997
^{187}Os ppb	30.64	30.92	166.47	5.69	2.61	1.35
2SE	117.99	0.33	0.65	0.15	0.23	0.07
^{187}Os/^{187}Re	5.263E-03	4.919E-03	4.987E-03	5.260E-03	5.467E-03	5.590E-03
2SE	2.029E-04	1.666E-06	1.458E-06	1.580E-06	1.050E-05	3.501E-06
Age [Ma]	**315.1**	**294.5**	**298.6**	**314.9**	**327.2**	**334.6**
total uncertainty [Ma]	**13.1**	**1.0**	**1.0**	**1.0**	**1.6**	**1.2**

** considered unreliable due to possible incomplete spike-sample equilibration

FC = fractionation corrected

Appendix 15: Lu–Hf dataset of zircons

Sample	$^{176}Hf/^{177}Hf_m$	2s	$^{176}Lu/^{177}Hf_m$	2s	$^{176}Yb/^{177}Hf_m$	2s	$^{176}Hf/^{177}Hf_i$	2s	εHf(t)	2s
***Redcap dacite (949), crystallisation age 310* ± 2 Ma**										
949_ar	0.282384	0.000010	0.000935	0.000005	0.0258	0.0002	0.282379	0.000010	-7.5	0.6
949_ac	0.282403	0.000012	0.000934	0.000065	0.0245	0.0017	0.282398	0.000012	-6.8	0.7
949_c	0.282358	0.000012	0.001271	0.000013	0.0351	0.0003	0.282351	0.000012	-8.5	0.7
949_b	0.282337	0.000012	0.001394	0.000116	0.0403	0.0035	0.282328	0.000012	-9.3	0.7
949_24r	0.282372	0.000012	0.000578	0.000030	0.0151	0.0008	0.282369	0.000012	-7.8	0.7
949_24c	0.282417	0.000013	0.000600	0.000011	0.0163	0.0003	0.282413	0.000013	-6.3	0.7
949_23	0.282367	0.000018	0.000657	0.000009	0.0172	0.0002	0.282363	0.000018	-8.0	0.8
949_22r	0.282346	0.000013	0.000756	0.000007	0.0201	0.0002	0.282342	0.000013	-8.8	0.7
949_22	0.282333	0.000016	0.001347	0.000046	0.0364	0.0013	0.282325	0.000016	-9.4	0.8
949_20r	0.282377	0.000021	0.000720	0.000006	0.0193	0.0002	0.282373	0.000021	-7.7	0.9
949_20c	0.282249	0.000020	0.001152	0.000067	0.0309	0.0020	0.282242	0.000020	-12.3	0.9
949_19r	0.282383	0.000015	0.001024	0.000002	0.0288	0.0001	0.282378	0.000015	-7.5	0.8
949_19c	0.282373	0.000013	0.000583	0.000015	0.0162	0.0005	0.282370	0.000013	-7.8	0.7
949_16	0.282357	0.000015	0.001354	0.000057	0.0410	0.0017	0.282349	0.000015	-8.5	0.7
949_14	0.282371	0.000021	0.001349	0.000035	0.0424	0.0010	0.282363	0.000021	-8.0	0.9
949_13	0.282363	0.000016	0.000905	0.000036	0.0272	0.0013	0.282358	0.000016	-8.2	0.8
949_11	0.282346	0.000021	0.000756	0.000029	0.0232	0.0009	0.282341	0.000021	-8.8	0.9
949_4	0.282343	0.000015	0.001289	0.000051	0.0415	0.0015	0.282335	0.000015	-9.0	0.8
949_3	0.282375	0.000016	0.001184	0.000035	0.0375	0.0013	0.282368	0.000016	-7.9	0.8
949_2	0.282368	0.000020	0.001860	0.000068	0.0605	0.0020	0.282358	0.000020	-8.2	0.9
949_1	0.282363	0.000015	0.000643	0.000017	0.0200	0.0006	0.282359	0.000015	-8.2	0.7

Sample	$^{176}Hf/^{177}Hf_m$	2s	$^{176}Lu/^{177}Hf_m$	2s	$^{176}Yb/^{177}Hf_m$	2s	$^{176}Hf/^{177}Hf_i$	2s	εHf(t)	2s
Redcap dacite (952W1), crystallisation age 306 **± 2 Ma**										
952W1_a	0.282357	0.000013	0.001638	0.000058	0.0451	0.0017	0.282348	0.000013	-8.6	0.7
952W1_22c	0.282375	0.000015	0.000869	0.000012	0.0259	0.0004	0.282370	0.000015	-7.9	0.7
952W1_22r	0.282380	0.000016	0.000897	0.000015	0.0263	0.0005	0.282375	0.000016	-7.7	0.8
952W1_20	0.282346	0.000014	0.000908	0.000057	0.0274	0.0018	0.282341	0.000014	-8.9	0.7
952W1_19	0.282353	0.000017	0.001165	0.000014	0.0346	0.0004	0.282346	0.000017	-8.4	0.8
952W1_17	0.282385	0.000012	0.001129	0.000012	0.0331	0.0003	0.282378	0.000012	-7.2	0.7
952W1_16	0.282351	0.000015	0.000817	0.000031	0.0241	0.0010	0.282346	0.000015	-8.7	0.7
952W1_15	0.282332	0.000012	0.000568	0.000015	0.0159	0.0005	0.282329	0.000012	-9.3	0.7
952W1_14	0.282338	0.000014	0.001028	0.000020	0.0300	0.0005	0.282332	0.000014	-9.2	0.7
952W1_11	0.282351	0.000022	0.001111	0.000087	0.0314	0.0026	0.282344	0.000022	-8.8	0.9
952W1_9	0.282390	0.000023	0.001114	0.000059	0.0288	0.0019	0.282383	0.000023	-7.4	1.0
952W1_7	0.282348	0.000026	0.001751	0.000063	0.0468	0.0019	0.282338	0.000026	-9.0	1.0
952W1_2	0.282263	0.000013	0.000886	0.000004	0.0227	0.0001	0.282258	0.000013	-11.8	0.7
952W1_1	0.282342	0.000013	0.000882	0.000016	0.0227	0.0003	0.282337	0.000013	-9.0	0.7
Belgravia granodiorite (BE-1,P-I), crystallisation age 309 **± 2 Ma**										
BE_25	0.282465	0.000023	0.001987	0.000138	0.0543	0.0039	0.282453	0.000023	-4.9	1.0
BE_22	0.282421	0.000013	0.001275	0.000042	0.0353	0.0012	0.282414	0.000013	-6.3	0.7
BE_15r	0.282445	0.000011	0.000622	0.000010	0.0157	0.0004	0.282441	0.000011	-5.3	0.7
BE_15	0.282452	0.000015	0.001191	0.000061	0.0355	0.0020	0.282445	0.000015	-5.1	0.7
BE_12	0.282427	0.000022	0.001226	0.000051	0.0336	0.0011	0.282420	0.000022	-6.0	0.9
BE_1	0.282458	0.000013	0.001104	0.000033	0.0336	0.0011	0.282452	0.000013	-4.9	0.7

Sample	$^{176}Hf/^{177}Hf_m$	2s	$^{176}Lu/^{177}Hf_m$	2s	$^{176}Yb/^{177}Hf_m$	2s	$^{176}Hf/^{177}Hf_i$	2s	εHf(t)	2s
Belgravia granodiorite (BE-1,P-II), crystallisation age 297 ± 2 Ma										
BE_5	0.282332	0.000014	0.001170	0.000050	0.0336	0.0015	0.282325	0.000014	-9.7	0.7
BE_3	0.282412	0.000013	0.000957	0.000026	0.0272	0.0006	0.282407	0.000013	-6.8	0.7
BE_23	0.282344	0.000013	0.000960	0.000054	0.0272	0.0015	0.282338	0.000013	-8.9	0.7
BE_17	0.282326	0.000015	0.001064	0.000007	0.0318	0.0001	0.282320	0.000015	-9.8	0.8
BE_13	0.282352	0.000015	0.000809	0.000006	0.0230	0.0002	0.282348	0.000015	-8.9	0.7
***Inherited grains (BE 1523* ± 13 Ma, 949 1516 ± 20 Ma)**										
BE_8r	0.281696	0.000023	0.000047	0.000008	0.0016	0.0002	0.281694	0.000023	-4.3	1.0
BE_8	0.281703	0.000015	0.000027	0.000004	0.0009	0.0001	0.281702	0.000015	-4.0	0.8
949_18r	0.281725	0.000039	0.000661	0.000144	0.0189	0.0044	0.281706	0.000039	-4.1	1.5
949_18	0.281707	0.000024	0.000360	0.000013	0.0087	0.0003	0.281697	0.000024	-4.4	1.0
Mungana rhyolitic porphyry (883W2), crystallisation age 324 ± 2 Ma										
883_W2_a	0.282373	0.000031	0.003912	0.000695	0.1391	0.0271	0.282350	0.000031	-8.2	1.2
883_W2_18	0.282352	0.000027	0.002019	0.000049	0.0627	0.0017	0.282340	0.000027	-8.5	1.1
883_W2_16	0.282359	0.000019	0.001285	0.000016	0.0395	0.0005	0.282352	0.000019	-8.1	0.8
883_W2_14	0.282359	0.000017	0.002476	0.000152	0.0783	0.0055	0.282344	0.000017	-8.4	0.8
883_W2_12	0.282362	0.000014	0.002195	0.000076	0.0714	0.0037	0.282349	0.000014	-8.2	0.7
883_W2_11	0.282348	0.000023	0.001864	0.000089	0.0556	0.0028	0.282337	0.000023	-8.6	1.0
883_W2_9	0.282370	0.000018	0.002330	0.000115	0.0755	0.0053	0.282356	0.000018	-8.0	0.8
883_W2_8	0.282362	0.000018	0.003124	0.000119	0.0964	0.0037	0.282343	0.000018	-8.4	0.8
883_W2_7	0.282340	0.000020	0.001970	0.000094	0.0598	0.0028	0.282328	0.000020	-8.9	0.9
883_W2_6	0.282345	0.000021	0.001444	0.000017	0.0437	0.0006	0.282336	0.000021	-8.7	0.9
883_W2_5	0.282347	0.000022	0.001951	0.000070	0.0606	0.0022	0.282335	0.000022	-8.7	0.9
883_W2_4	0.282346	0.000016	0.002239	0.000016	0.0697	0.0006	0.282332	0.000016	-8.8	0.8
883_W2_2	0.282352	0.000020	0.001251	0.000002	0.0381	0.0001	0.282344	0.000020	-8.4	0.9
883_W2_1	0.282386	0.000015	0.002898	0.000270	0.0905	0.0091	0.282368	0.000015	-7.5	0.7

Sample	$^{176}Hf/^{177}Hf_m$	2s	$^{176}Lu/^{177}Hf_m$	2s	$^{176}Yb/^{177}Hf_m$	2s	$^{176}Hf/^{177}Hf_i$	2s	εHf(t)	2s
Mungana granite (883W3), crystallisation age 305 ± 2 Ma										
883W3_b	0.282264	0.000012	0.000629	0.000022	0.0185	0.0007	0.282260	0.000012	-11.8	0.7
883W3_a2	0.282338	0.000017	0.001405	0.000075	0.0382	0.0022	0.282330	0.000017	-9.3	0.8
883W3_17	0.282264	0.000015	0.001116	0.000030	0.0302	0.0008	0.282258	0.000015	-11.9	0.7
883W3_16	0.282343	0.000016	0.002171	0.000112	0.0632	0.0033	0.282330	0.000016	-9.3	0.8
883W3_14	0.282288	0.000014	0.001408	0.000046	0.0391	0.0015	0.282280	0.000014	-11.1	0.7
883W3_13	0.282291	0.000013	0.001168	0.000013	0.0322	0.0004	0.282285	0.000013	-10.9	0.7
883W3_12	0.282255	0.000016	0.000886	0.000040	0.0251	0.0013	0.282250	0.000016	-12.2	0.8
883W3_11	0.282264	0.000022	0.001364	0.000087	0.0391	0.0031	0.282256	0.000022	-11.9	1.0
883W3_10	0.282258	0.000020	0.000998	0.000007	0.0281	0.0002	0.282253	0.000020	-12.0	0.9
883W3_9	0.282284	0.000017	0.001296	0.000145	0.0370	0.0044	0.282276	0.000017	-11.2	0.8
883W3_8	0.282277	0.000015	0.001111	0.000017	0.0302	0.0006	0.282271	0.000015	-11.4	0.7
883W3_7	0.282286	0.000016	0.000822	0.000006	0.0220	0.0001	0.282282	0.000016	-11.0	0.8
883W3_5	0.282267	0.000015	0.001379	0.000034	0.0394	0.0010	0.282259	0.000015	-11.8	0.7
883W3_4	0.282321	0.000023	0.002252	0.000062	0.0624	0.0018	0.282308	0.000023	-10.1	1.0
883W3_3	0.282261	0.000023	0.001317	0.000026	0.0346	0.0007	0.282253	0.000023	-12.0	1.0
Red Dome mineralised quartz vein (983), crystallisation age 322 ± 2 Ma										
983_5	0.282321	0.000022	0.003002	0.000191	0.0904	0.0061	0.282302	0.000022	-9.9	1.0
983_4	0.282340	0.000026	0.004151	0.000107	0.1354	0.0040	0.282314	0.000026	-9.5	1.1
983_3	0.282347	0.000034	0.003692	0.000134	0.1152	0.0050	0.282325	0.000034	-9.1	1.3
983_2	0.282320	0.000024	0.003031	0.000057	0.0893	0.0017	0.282302	0.000024	-9.9	1.0
983_1	0.282314	0.000019	0.003334	0.000055	0.0983	0.0020	0.282294	0.000019	-10.2	0.9

Sample	$^{176}Hf/^{177}Hf_m$	2s	$^{176}Lu/^{177}Hf_m$	2s	$^{176}Yb/^{177}Hf_m$	2s	$^{176}Hf/^{177}Hf_i$	2s	εHf(t)	2s
Red Dome quartz-feldspar porphyry (936), crystallisation age 322 ± 2 Ma										
936_a	0.282346	0.000028	0.003629	0.000052	0.1138	0.0019	0.282324	0.000028	-9.1	1.1
936_19	0.282349	0.000025	0.001896	0.000035	0.0580	0.0012	0.282337	0.000025	-8.7	1.0
936_18	0.282374	0.000022	0.002661	0.000038	0.0844	0.0012	0.282358	0.000022	-7.9	0.9
936_17	0.282351	0.000019	0.002214	0.000029	0.0688	0.0008	0.282337	0.000019	-8.7	0.9
936_12	0.282296	0.000023	0.001905	0.000027	0.0585	0.0009	0.282285	0.000023	-10.5	1.0
936_11	0.282342	0.000023	0.002679	0.000083	0.0824	0.0026	0.282326	0.000023	-9.1	1.0
936_10	0.282345	0.000020	0.001909	0.000108	0.0577	0.0035	0.282333	0.000020	-8.8	0.9
936_7	0.282358	0.000023	0.001934	0.000085	0.0607	0.0027	0.282346	0.000023	-8.3	1.0
936_5	0.282354	0.000020	0.001568	0.000095	0.0451	0.0028	0.282345	0.000020	-8.4	0.9
936_3	0.282309	0.000020	0.002452	0.000063	0.0737	0.0020	0.282294	0.000020	-10.2	0.9
936_2	0.282307	0.000022	0.002304	0.000170	0.0696	0.0053	0.282293	0.000022	-10.2	0.9
Red Dome quartz-feldspar porphyry (984), crystallisation age 324 ± 2 Ma										
984_b	0.282357	0.000017	0.002643	0.000057	0.0845	0.0020	0.282341	0.000017	-8.5	0.8
984_a	0.282357	0.000013	0.001990	0.000062	0.0603	0.0019	0.282344	0.000013	-8.4	0.7
984_20	0.282364	0.000022	0.003928	0.000304	0.1464	0.0152	0.282340	0.000022	-8.5	0.9
984_18	0.282356	0.000013	0.001879	0.000008	0.0606	0.0003	0.282345	0.000013	-8.4	0.7
984_17	0.282344	0.000016	0.001739	0.000027	0.0548	0.0008	0.282333	0.000016	-8.8	0.8
984_15	0.282375	0.000020	0.001540	0.000040	0.0480	0.0013	0.282366	0.000020	-7.6	0.9
984_14	0.282364	0.000019	0.002520	0.000113	0.0798	0.0037	0.282349	0.000019	-8.2	0.9
984_13	0.282336	0.000021	0.002380	0.000042	0.0748	0.0015	0.282321	0.000021	-9.2	0.9
983_12	0.282358	0.000018	0.001793	0.000065	0.0555	0.0020	0.282347	0.000018	-8.3	0.8
984_9	0.282343	0.000016	0.001822	0.000038	0.0572	0.0013	0.282332	0.000016	-8.8	0.8
984_6	0.282333	0.000014	0.001089	0.000024	0.0329	0.0008	0.282327	0.000014	-9.0	0.7
984_3	0.282357	0.000015	0.003046	0.000250	0.0990	0.0097	0.282338	0.000015	-8.6	0.8

Sample	$^{176}Hf/^{177}Hf_m$	2s	$^{176}Lu/^{177}Hf_m$	2s	$^{176}Yb/^{177}Hf_m$	2s	$^{176}Hf/^{177}Hf_i$	2s	εHf(t)	2s
Red Dome dacitic porphyry (995), crystallisation age 311 ± 2 Ma										
995_c	0.282380	0.000022	0.001606	0.000100	0.0461	0.0028	0.282371	0.000022	-7.7	0.9
995_21	0.282388	0.000022	0.001503	0.000063	0.0432	0.0019	0.282379	0.000022	-7.4	0.9
995_17	0.282368	0.000027	0.003160	0.000094	0.0955	0.0034	0.282350	0.000027	-8.5	1.1
995_16	0.282389	0.000026	0.001983	0.000033	0.0568	0.0012	0.282377	0.000026	-7.5	1.1
995_15	0.282378	0.000013	0.001391	0.000010	0.0397	0.0003	0.282370	0.000013	-7.7	0.7
995_14	0.282380	0.000017	0.002359	0.000200	0.0700	0.0064	0.282367	0.000017	-7.9	0.8
995_11	0.282386	0.000012	0.001554	0.000019	0.0478	0.0007	0.282377	0.000012	-7.5	0.7
995_8	0.282390	0.000023	0.003160	0.000180	0.0993	0.0059	0.282371	0.000023	-7.7	1.0
995_5	0.282393	0.000016	0.002067	0.000142	0.0646	0.0046	0.282381	0.000016	-7.4	0.8
995_3	0.282389	0.000016	0.001065	0.000041	0.0306	0.0013	0.282382	0.000016	-7.3	0.8
995_1	0.282397	0.000015	0.001740	0.000027	0.0552	0.0009	0.282387	0.000015	-7.2	0.7